이학박사 학위논문

A Multiscale View of Active Galactic Nuclei Jets: from the Formation and Acceleration to High Energy Outbursts

활동성은하핵 제트의 여러 규모에서의 모습: 제트의 형성과 가속부터 고에너지 분출 현상까지

2019년 8월

서울대학교 대학원

물리·천문학부 천문학전공

박 종 호

A Multiscale View of Active Galactic Nuclei Jets: from the Formation and Acceleration to High Energy Outbursts

by

Jongho Park
(jhpark@astro.snu.ac.kr)

A dissertation submitted in partial fulfillment of the requirements for
the degree of

Doctor of Philosophy

in
Astronomy

in
Astronomy Program
Department of Physics and Astronomy
Seoul National University

Committee:

Professor	Bon-Chul Koo
Professor	Sascha Trippe
Professor	Jong-Hak Woo
Professor	Sang-Sung Lee
Professor	Taehyun Jung

ABSTRACT

Active Galactic Nuclei (AGNs) often produce highly collimated relativistic jets, one of the most energetic phenomena in the Universe. In this thesis, we probe the mechanism of launching, propagation, and energy dissipation of AGN jets by using various methodologies. We study the jet of a nearby radio galaxy M87 with very long baseline interferometry observations and find that the jet is collimated by the pressure of non-relativistic winds launched from hot accretion flows and accelerated to relativistic speeds by strong magnetic fields in the jet. We investigate the frequency dependence of Faraday rotation of many AGN jets and reveal that recollimation shocks in the jets may play an important role in dissipation of the jet kinetic energy. We examine the association of strong γ-ray flares occurred in 2015 in the jet of PKS 1510–089 and its peculiar kinematic behavior and find that the flares may originate from compression of the jet knots by a standing shock in the core. We study the long-term radio variability of many radio-loud AGNs by employing temporal Fourier transform of the light curves and reveal that the radio variability can be controlled by the accretion processes. We constrain the properties of the radio-emitting source known as Sagittarius A*, which is potentially powered by jets, by a very long baseline interferometry observation during the passage of the gas cloud G2 through the vicinity of the supermassive black hole.

Keywords: galaxies: active – galaxies: jets – relativistic processes – radiation mechanisms: non-thermal – polarization – accretion, accretion disks – techniques: interferometric

Student Number: 2013-20392

Contents

List of Figures

List of Tables

Chapter 1

Introduction

1.1 Jets in Active Galactic Nuclei

Collimated outflows, called jets, are a ubiquitous phenomenon associated with the accretion of material onto a compact object. Jets have been observed in various astronomical objects such as active galactic nuclei (AGNs), young stellar objects (YSOs), Gamma-ray bursts (GRBs), and black hole X-ray binaries (BHXRBs). Figure 1.1 shows representative images of the jets in the various systems. Among these, jets in AGNs have been of interest for many decades because they are closely related with many astronomical phenomena and fundamental physics, e.g., the spin of central supermassive black holes (Doeleman et al. 2012), the accretion of gas and the growth of the black holes (Yuan & Narayan 2014), particle acceleration in the jets producing high energy (up to TeV) photons (Hartman et al. 1992) and even neutrinos (Aartsen et al. 2018), and heating of the interstellar/intergalactic medium which may control star formation and the evolution of galaxies (Fabian 2012). AGN jets are usually highly collimated, moving at relativistic speeds, and emit non-thermal synchrotron radiation.

1.1.1 Phenomenology

There are many observational features that make AGN jets interesting and important to study as follows.

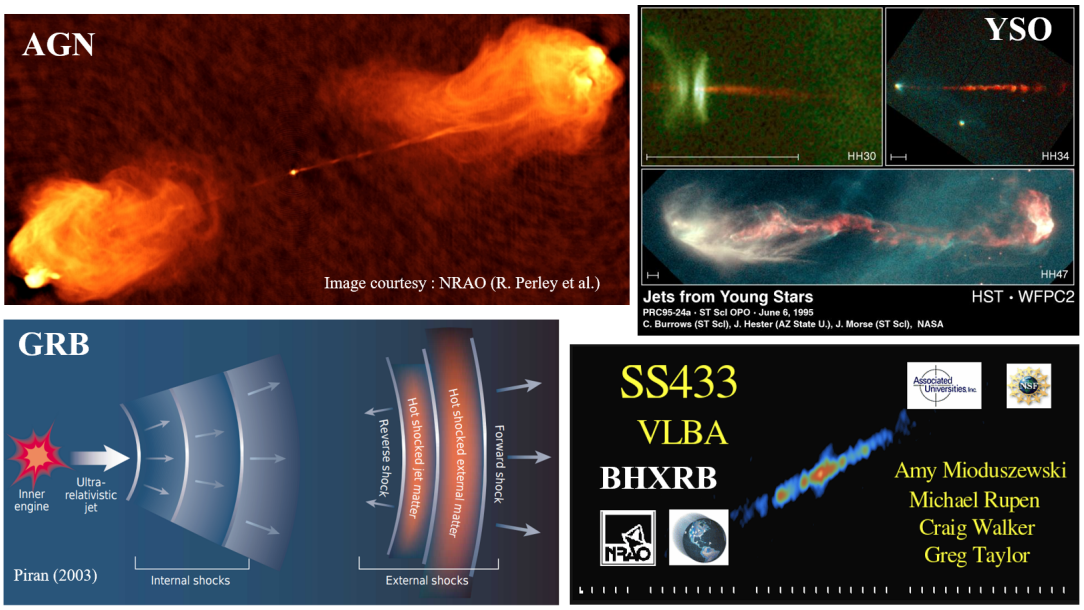

Figure 1.1. Images of jets in various astronomical systems. *Top left :* two-sided jets observed in a nearby radio galaxy Cygnus A, which extend on a spatial scale several tens of times larger than that of host galaxies (Perley et al. 1984). *Top right :* jets observed in several YSOs (image courtesy : Burrows et al.). *Bottom left :* a schematic diagram to explain the phenomena known as a GRB (Piran 2003). Jets are believed to eject from the central star in its late stage, which are the source of high energy photons. *Bottom right :* two-sided jets observed in a BHXRB SS 433 (image courtesy : NRAO).

(Apparently) Superluminal motions. One of the most representative characteristics of AGN jets is superluminal motions. Superluminal motions of the jets at high apparent speeds, up to $\sim 78c$ in an extreme case, where c is the speed of light, are frequently observed in many AGN jets (e.g., Jorstad et al. 2017). Figure 1.2 shows a series of jet images of the famous quasar 3C 279 taken between 1991 and 1998. When we assume that the leftmost bright feature in different epochs is stationary over time, the rightmost bright feature appears to have moved 25 light years on the plane of the sky over seven years, indicating that this feature moves at a speed of ≈ 3.6 times the speed of light.

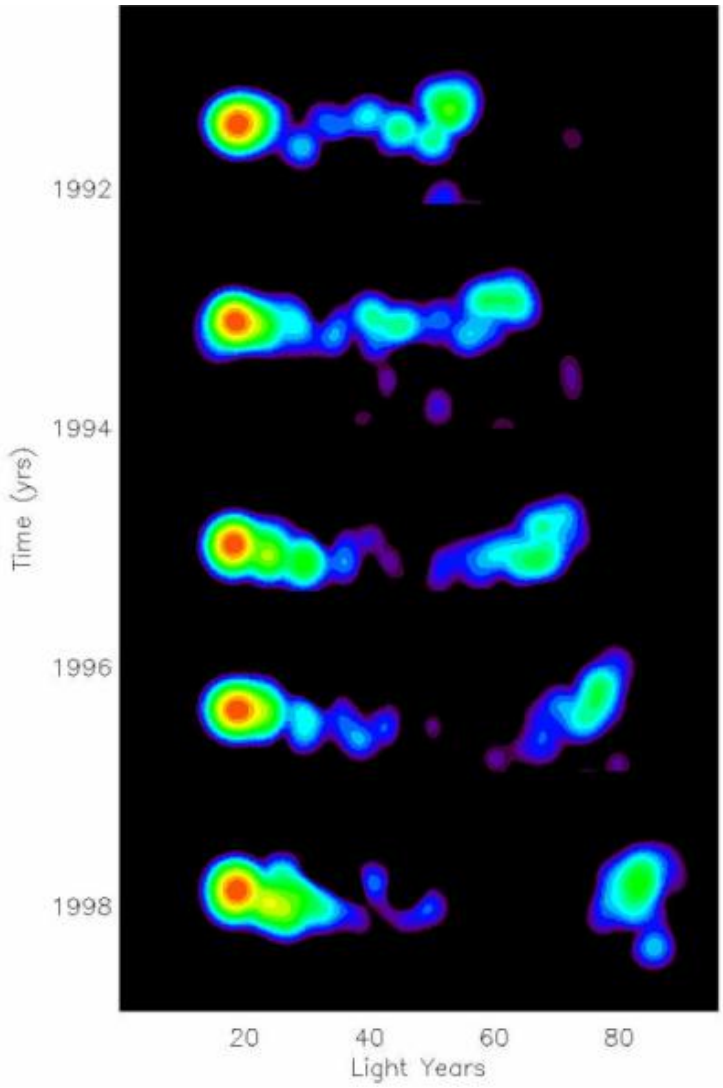

Figure 1.2. Apparently superluminal motions of the radio jet of the bright quasar 3C 279 (image courtesy : NRAO). The bright component at the left is taken to be the fixed reference position, also referred to as the "radio core", and the bright spot at the right appears to have moved 25 light years on the sky plane between 1991 and 1998, giving a speed of ≈ 3.6 times the speed of light.

This phenomenon occurs because of light travel time effect, as illustrated in Figure 1.3. Consider a clump moving from point B1 to point B2 over time t with an angle

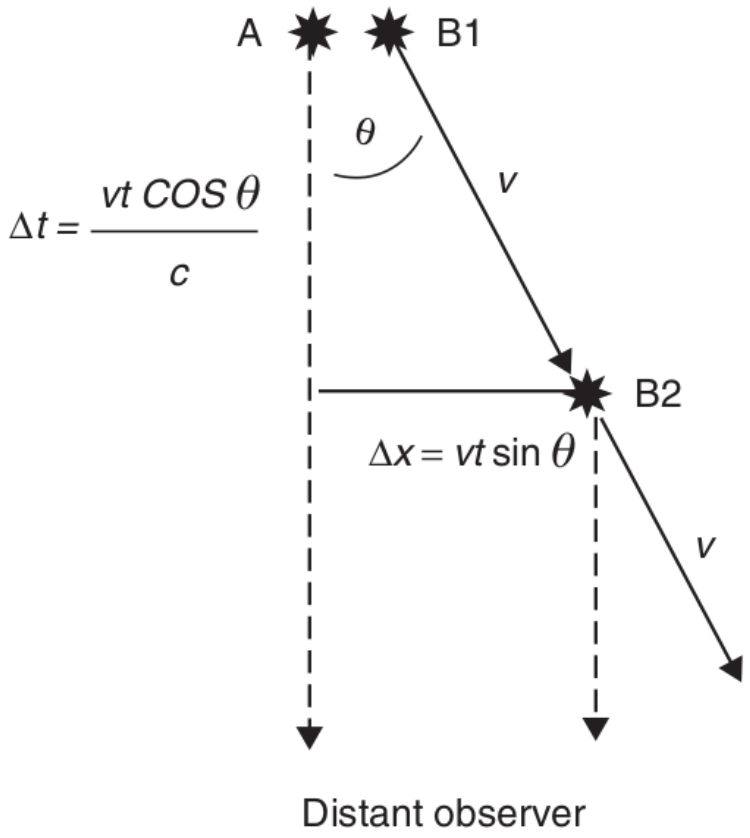

Figure 1.3. Simple geometry to explain superluminal motions. Clump B is moving from point B1 to point B2 at velocity v over time t.

θ to the line of sight of a distant observer. The distance that the clump moves on the projected sky plane is $vt\sin\theta$. The time interval between B1 and B2 in the point view of the observer is $t - vt\cos\theta/c$. Thus, the speed of this clump in the point of view of the observer in units of the speed of light is

$$\beta_{\rm obs} = \frac{vt\sin\theta/c}{t - vt\cos\theta/c} = \frac{\beta\sin\theta}{1-\beta\cos\theta}. \tag{1.1}$$

One can see that when the speed of this clump is non-relativistic, $\beta_{\rm obs} \approx \beta\sin\theta$ is recovered, as one may easily guess in the daily life. However, as the speed approaches the speed of light, the time interval between the two positions shrinks rapidly (in the observer's frame) and the clump appears to move at a superluminal speed.

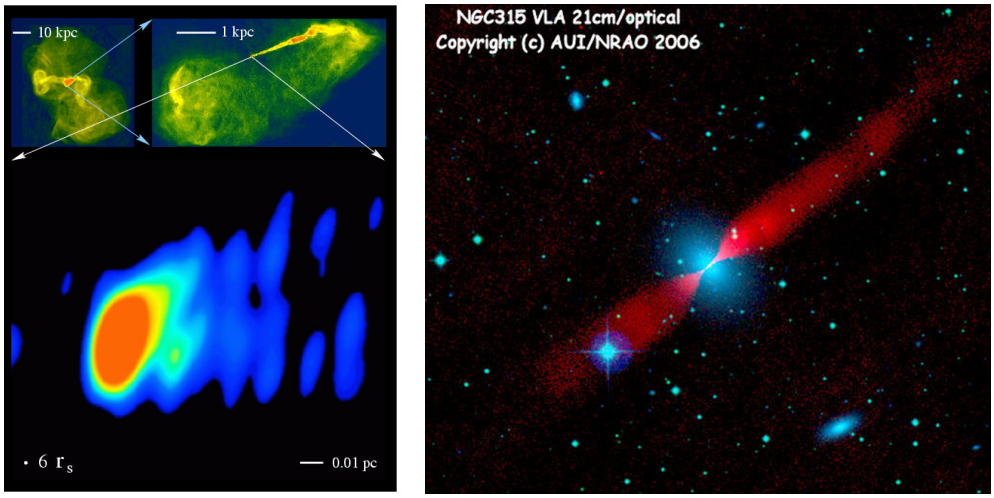

Figure 1.4. Images of the jet in M87 (left) and NGC 315 (right). The M87 jet appears to be one-sided on various spatial scales, while the jets in NGC 315 are two-sided. This difference can be understood by the fact that the former has a relatively small jet viewing angle ($\theta \approx 17°$), whereas the latter has a large angle ($\theta \approx 38°$), so that the approaching (receding) jet is significantly Doppler boosted (de-boosted). Image courtesy : NRAO.

Because of the relativistic speeds of AGN jets, jet emission is affected by relativistic abberation, time dilation, and Doppler shift. These effects are often referred to as relativistic Doppler beaming effect. This effect substantially boosts the observed flux density of the jet approaching the observer with a relatively small jet viewing angle, the angle between the jet axis and our line of sight, to a high power of the "Doppler factor". The Doppler factor is given by $D = 1/\Gamma(1-\beta\cos\theta)$, where Γ is the bulk Lorentz factor, β is the intrinsic jet speed, and θ is the jet viewing angle. The jet emission receding from the observer is highly de-boosted analogously. An example of this effect is shown in Figure 1.4. The radio galaxy M87 shows a jet on only one side on various spatial scales, while another radio galaxy NGC 315 shows jets on both sides with respect to the central host galaxy. M87 is believed to have a relatively small jet viewing angle ($\theta \approx 17°$, Mertens et al. 2016), while NGC 315 has a large jet viewing angle ($\theta \approx 38°$,

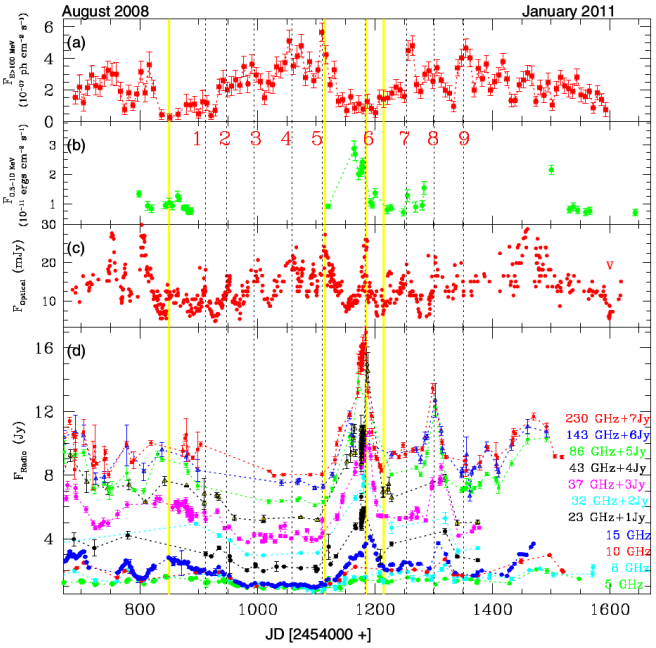

Figure 1.5. Light curves of a blazar S5 0716+714 at γ-ray (top), X-ray (second from the top), optical (third from the top), and radio wavelengths (bottom), taken from Rani et al. (2013).

Canvin et al. 2005). Accordingly, the brightness difference between the approaching and receding jets in M87 is significant due to the Doppler boosting effect, whereas that in NGC 315 is insignificant.

Rapid variability across the whole electromagnetic spectrum. The time interval between any two events in the jet shrinks in the observer's frame by the relativistic beaming effect (by the Doppler factor). This results in rapid variability in the light curves of AGNs which have jets closely aligned with our line of sight, called *blazars*. Figure 1.5 shows an example light curve of a blazar S5 0716+714, showing rapid variability in the γ-ray, X-ray, optical, and multi-frequency radio light curves (Rani et al. 2013).

Another characteristic of blazars is that they are bright across the entire electromagnetic spectrum from radio to γ-ray. Photons at energies above TeV are frequently

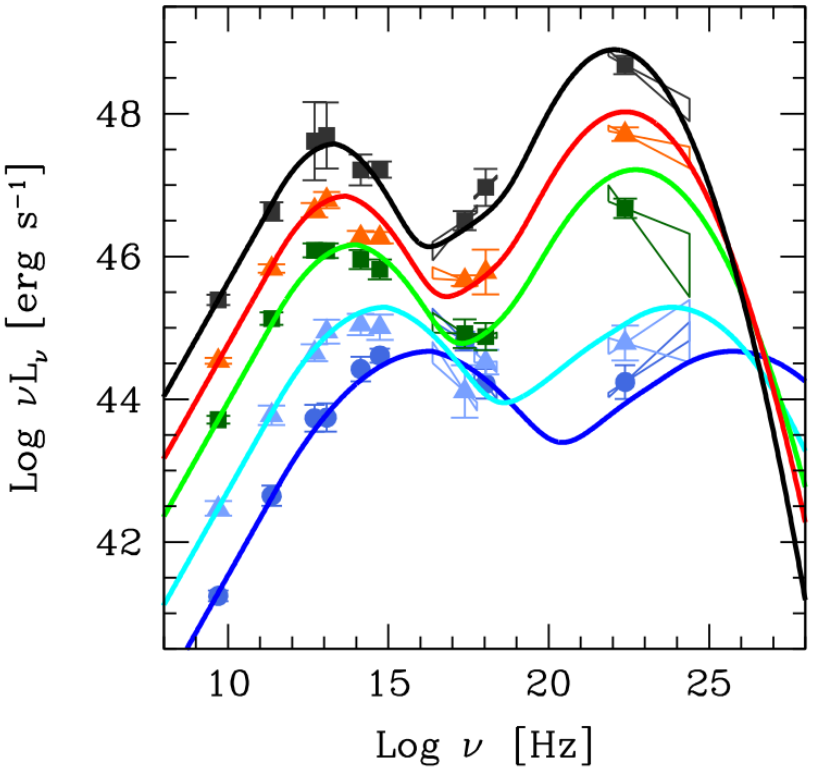

Figure 1.6. Spectral energy distributions of blazars, which was introduced in the framework of "blazar sequence" (Fossati et al. 1998; Ghisellini et al. 1998). The data points are obtained from average SEDs of 126 blazars and the solid lines are corresponding model SEDs. Different colors represent different radio luminosity bins.

observed in blazars (e.g., Aleksić et al. 2011a,b), indicating that they are efficient particle accelerators. Figure 1.6 shows average spectral energy distributions (SEDs) of many blazars, grouped into different radio luminosity bins (Fossati et al. 1998). Their SEDs are characterized as two humps; one at lower (higher) energy is believed to originate from synchrotron (inverse-Compton) emission of their jets. The SEDs of blazars having higher luminosity tend to show (i) synchrotron and IC bumps peaking at lower observing frequencies, and (ii) a larger IC bump in comparison to the synchrotron one, forming the so-called "blazar sequence". This behavior has been interpreted due to the efficient cooling of the relativistic electrons in the jets in the higher luminosity blazars.

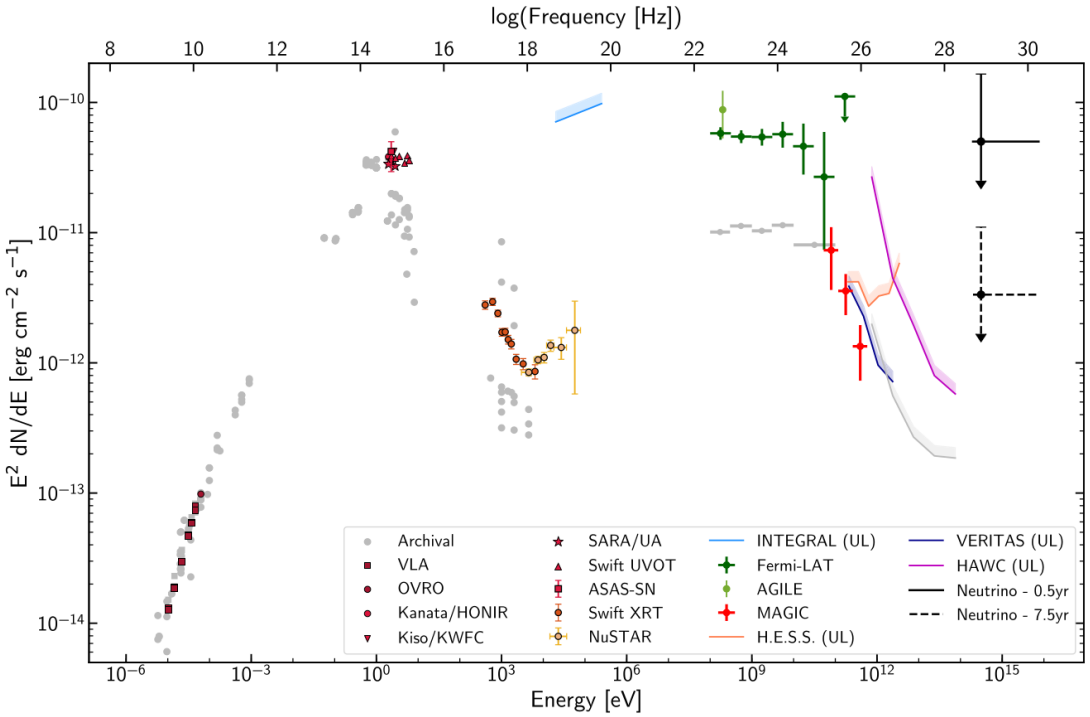

Figure 1.7. SED of the blazar TXS 0506+056 in which neutrino was detected by Icecube (Aartsen et al. 2018).

Those blazars are thought to have a large amount of soft photons originating in the broad line region, which results in the efficient cooling.

Figure 1.7 shows an extreme case which demonstrates that blazars are sources of high energy photons and particles. The SED of the blazar TXS 0506+056 shows two humps, similar to the typical blazar SEDs shown in Figure 1.6, but the high energy hump has a tail extending to TeV energies. A high-energy neutrino with an energy of ≈ 290 TeV was detected in this blazar (Aartsen et al. 2018), indicating that extremely high energy particles can be generated in blazars. The mechanism of generating such high energy particles and photons is still under debate. However, there is a general consensus that kinetic energy of relativistic jets is converted into particle or photon energies via dissipation processes such as shocks or magnetic reconnection (e.g., Giannios et al. 2009; Sironi & Spitkovsky 2014).

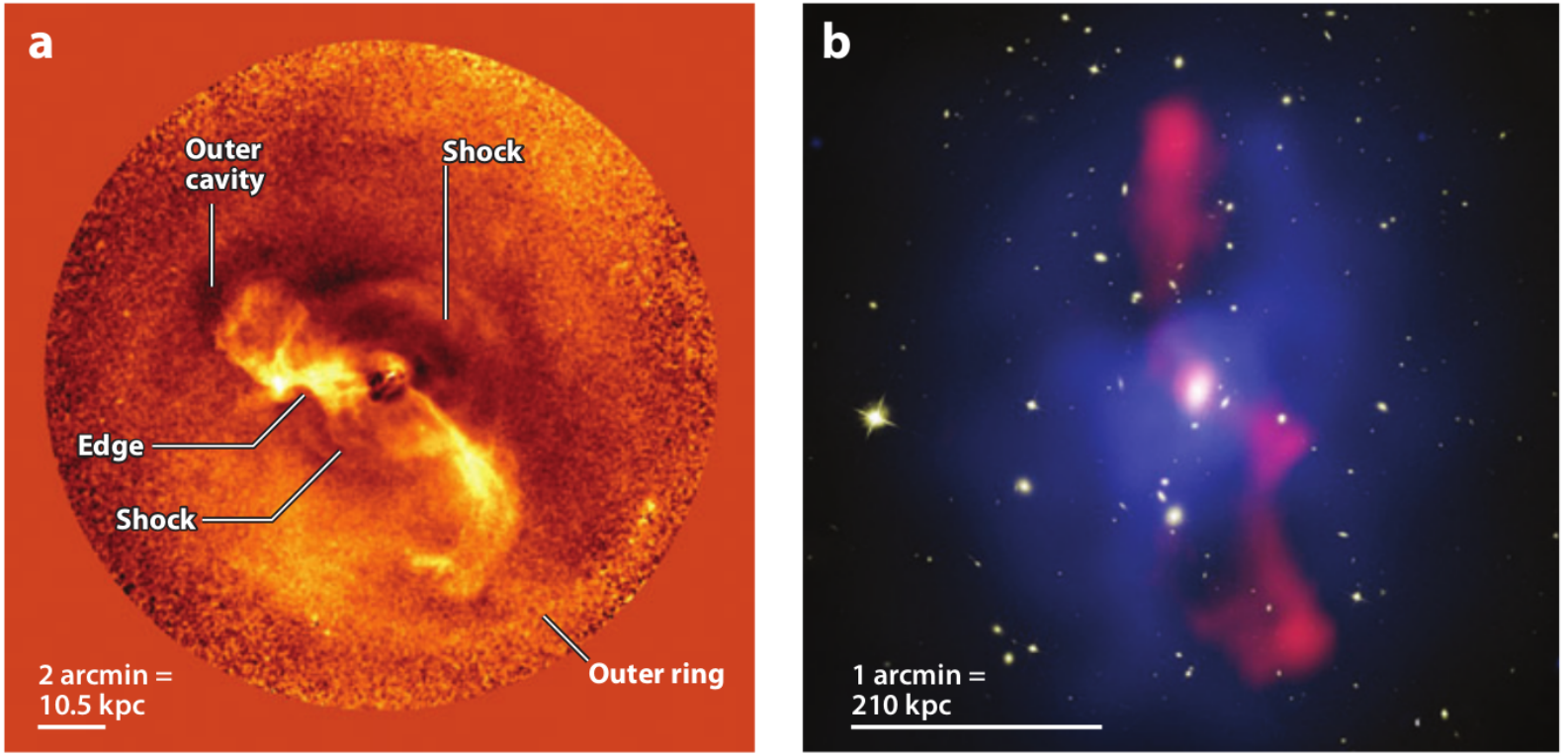

Figure 1.8. *Left :* various features such as shocks or arms that may originate from the interaction of the jets in M87 with the ambient medium. *Right :* jets shown in red color fill in the cavities of X-ray emitting hot gas (blue color) in MS0735.6. The jets are thought to push away the hot gas, implying that they may control heating, cooling, and star formation in this cluster. Images are taken from Fabian (2012).

Interaction of jets with interstellar/intergalactic medium. AGN jets moving at relativistic speeds interact with interstellar or intergalactic medium. Also, they are believed to suffer from various instabilities such as magnetic kink instability which prevent them from maintaining their well collimated structure at large distances (e.g., Bromberg & Tchekhovskoy 2016). A huge amount of kinetic energy initially retained in the jets is delivered to the ambient medium, which may control the evolution of galaxies and clusters. For example, X-ray observations of hot gas in massive galaxies at the centers of groups and clusters suggest that its radiative cooling time is quite short. The rapid cooling of the gas would result in forming new stars at a rate larger than hundreds or thousands of solar mass in a year (Fabian 2012). However, the observed star formation rates in those galaxies are much smaller than what was predicted. This phenomena are known as a "cooling flow problem".

Although there may be various elements that prohibit the gas from cooling, jets are obvious candidates because massive galaxies at the centers of groups and clusters usually have jets. Figure 1.8 illustrates how jets affect the structure of surrounding hot gases. The left panel shows various features such as shocks and arms which may be generated by the jet in M87. The right panel shows that the cavities of X-ray emitting hot gases in the cluster MS0735.6 are filled with the radio jets. This image demonstrates that AGN jets may play an important role in suppressing cooling of nearby gas and star formation in galaxies.

1.1.2 How are AGN jets produced?

One of the fundamental questions in AGN jet astrophysics is how they are produced. Understanding the mechanism of launching and propagation of AGN jets has improved significantly in the last couple of decades. Figure 1.9 compares the basic picture of AGN jets proposed in 1985 (Marscher & Gear 1985) and in 2008 (Marscher et al. 2008). About 30 years ago, it was assumed that relativistic electrons and strong magnetic fields, produced by an unknown central energy generator, are injected into a conically expanding jet through a "pipeline". Now it is evident that the energy generator is

an accreting supermassive black hole (Kormendy & Ho 2013). Also, there is growing evidence that the pipeline is an acceleration of the jet to relativistic speeds by magnetic fields, which can occur under the condition that the jet is systematically collimated by the pressure of an external medium confining the jet, known as the "collimation–acceleration paradigm" (Vlahakis 2015). Thus, two important physical processes which can produce highly collimated relativistic jets as observed in many radio loud AGNs are (i) jet launching and (ii) acceleration and collimation of jet.

Although the details of jet launching mechanisms bring in quite complicated mathematical descriptions, a simplified explanation is shown in Figure 1.10. Two most important ingredients for jet launching are (i) vertical magnetic fields and (ii) coiling of the fields due to rotation of their roots. Consider a magnetic field line attached on one end to a "ceiling" and on the other end to a conducting sphere rotating at an angular frequency Ω (**a**). As the sphere keeps rotating, the field line is progressively twisted like a spring (**b**). This magnetic spring pushes against the ceiling due to the pressure of the toroidal field. When the spring is more strongly twisted, the magnetic pressure becomes so strong that the spring pushes the ceiling away (**c**). Any plasma attached to the field is accelerated and forms a jet. In the end, the rotation of the sphere continuously coils the poloidal field into new toroidal loops at a rate that balances the rate at which the loops move downstream together with plasma within the loops (**d**).

If the rotating sphere in the above illustration is a spinning black hole, the frame-dragging effect inside the ergosphere of the black hole can produce the "magnetic coils". This mechanism is known as the Blandford-Znajek (BZ) process (Blandford & Znajek 1977). In this case, rotational energy of the spinning black hole can be extracted to power the jets. On the other hand, the differential rotation of an accretion disk can also produce the coils. In this case, the jet is launched by a magneto-centrifugal process, known as the Blandford-Payne (BP) mechanism (Blandford & Payne 1982). It is still under debate which mechanism is responsible for AGN jets. However, there is a growing consensus that the BZ mechanism is more probable. The jets launched by the accretion disk suffer from high mass-loading and it is very difficult to accelerate the massive

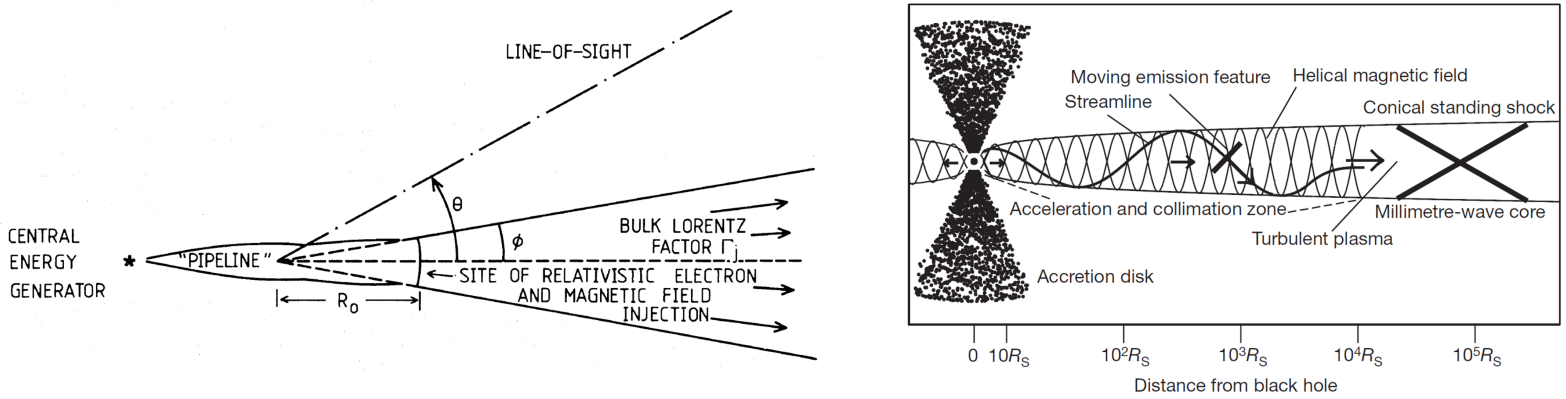

Understanding of AGN jets in 1985
(Marscher & Gear 1985)

Understanding of AGN jets in 2008
(Marscher et al. 2008)

Figure 1.9. Schematic diagrams of the models for AGN jet proposed in 1985 (left, Marscher & Gear 1985) and in 2008 (right, Marscher et al. 2008).

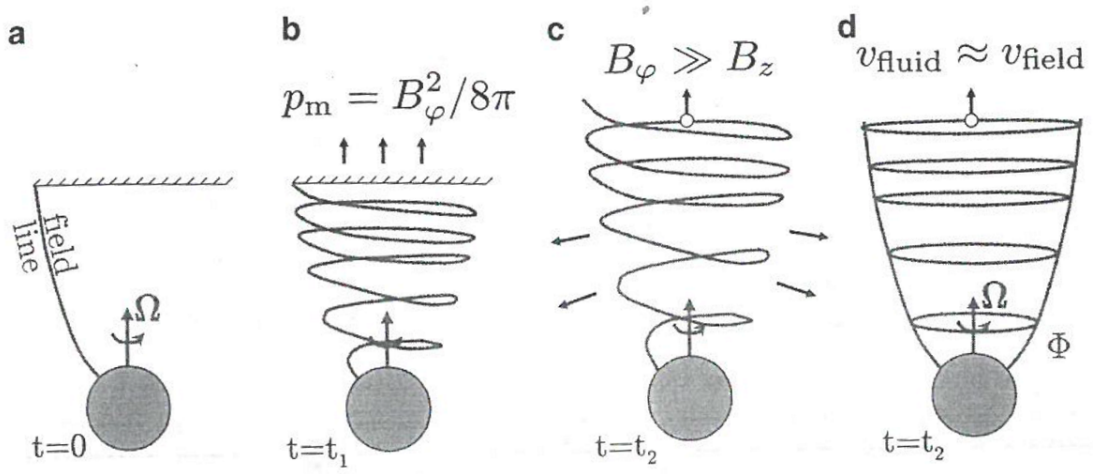

Figure 1.10. Illustration of jet launching mechanism that involves poloidal magnetic fields and a rotation of the central object to which the field lines are attached. This figure is taken from Tchekhovskoy (2015).

plasmas to relativistic speeds, while strong magnetic fields and low mass-loading in the vicinity of a black hole makes it easier to launch the jets. One of the observational evidences for the BZ mechanism favored is shown in Figure 1.11. The power of jets in many blazars inferred from the SED modeling is larger than their accretion power ($\dot{M}_{\rm BH}c^2$, where $\dot{M}_{\rm BH}$ is the mass accretion rate). This indicates that the output power is larger than the input power, which means that there must be an additional source of energy that powers the jets. Rotational energy of spinning black holes is a natural candidate for the additional energy.

However, how AGN jets can be highly collimated with opening angles of a few degrees and accelerated to relativistic speeds requires a totally different process. To obtain solutions for such outflows, one has to solve a full set of equations involving Ohm's law, Maxwell equations, conservation of mass, momentum, and energy of the flow simultaneously. The combined magnetohydrodynamic (MHD) equations are very complicated and highly nonlinear, preventing us from obtaining exact solutions. Previous studies have relied on assuming self-similarity (e.g., Vlahakis et al. 2000) or numerical simula-

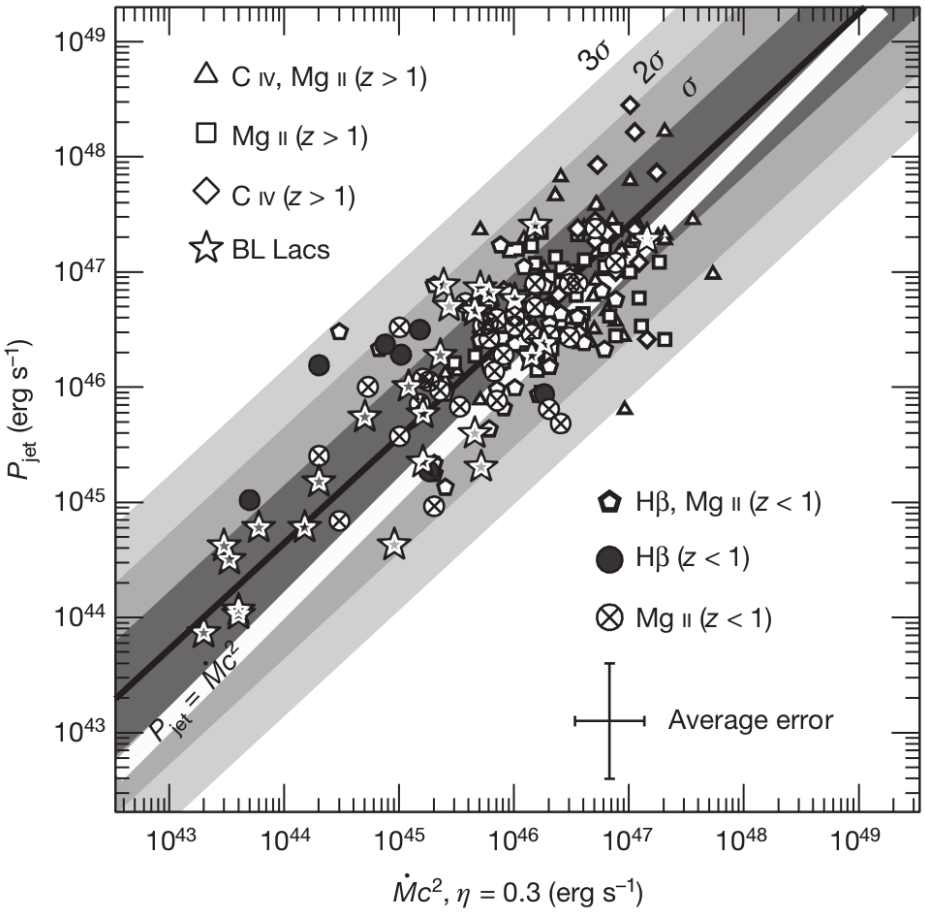

Figure 1.11. Jet power as a function of accretion power ($\dot{M}_{\rm BH}c^2$) of many blazars (Ghisellini et al. 2014). The white diagonal line shows a one-to-one line between the two quantities. For many sources, the jet power is similar to or exceeds the accretion power, indicating that there must be an additional source of energy that powers the jets.

tions (e.g., McKinney 2006; Komissarov et al. 2007, 2009; Tchekhovskoy et al. 2008). Indeed, those studies showed that jets can be accelerated to relativistic speeds by converting strong electromagnetic energy near the central object into kinetic energy of the flow.

The left panel of Figure 1.12 shows the evolution of various quantities of the flow

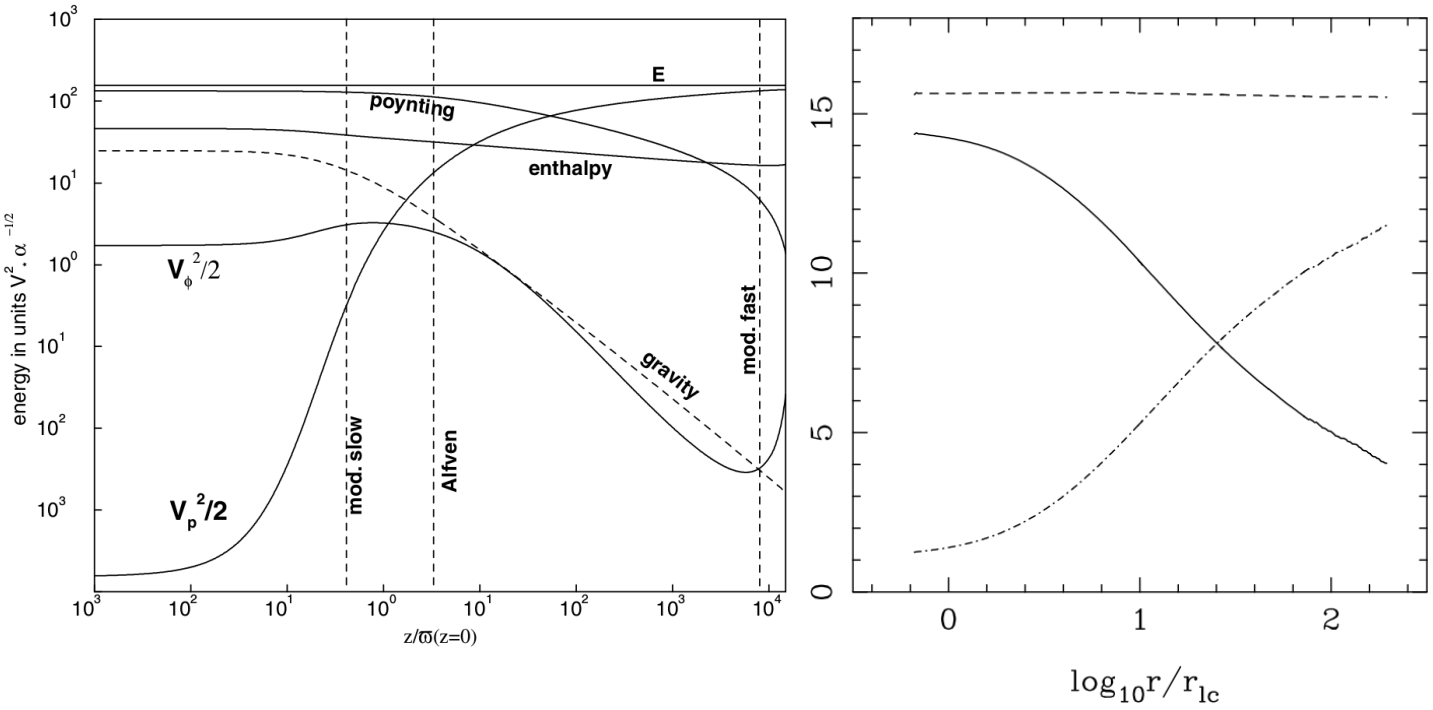

Figure 1.12. *Left :* Various quantities derived by solving MHD equations assuming a radial self-similarity (Vlahakis et al. 2000). Poynting flux gradually decreases with distance, while kinetic energy flux of the poloidal velocity component ($V_p{}^2/2$) keeps increasing, indicating that the electromagnetic energy initially dominant near the jet base is converted into the kinetic energy. *Right :* similar to the left figure but showing the results of numerical simulations by Komissarov et al. (2007). The total energy flux, Poynting flux, and kinetic flux per unit rest-mass energy flux are shown by the dashed, solid, and dot-dahsed lines, respectively.

obtained by solving the MHD equations and assuming a radial self-similarity (Vlahakis et al. 2000). Remarkably, Poynting energy flux (per unit of mass flux density) gradually decreases with increasing distance, while kinetic energy flux of the flow keeps increasing. On the other hand, the right panel shows the results of numerical simulations which do not suffer from the limitation of self-similarity assumptions (Komissarov et al. 2007). Similar to the case of the analytic solutions, Poynting flux conversion takes place with a high efficiency, i.e., the kinetic energy flux reaching more than 60 percent of the total energy flux. These results manifest that magnetic driving of relativistic outflows in AGNs is a highly probable process.

Figure 1.13 illustrates how the Poynting flux conversion takes place and the jet is collimated and accelerated. The poloidal (B_p) and toroidal (B_ϕ) magnetic field, electric field (E), and the poloidal current (J_p) driven by the magnetic field are shown. The Lorentz force ($J_p \times B_\phi$) consists of components along and perpendicular to the poloidal field line. The former accelerates the jet, while the latter collimates the jet. Thus, the magnetic field twisted by a central rotating object (a black hole or an accretion disk) shown in Figure 1.10 are basically able to accelerate and collimate the jet. However, an ideal MHD condition requires $E + \frac{V}{c}B = 0$, where V is the flow velocity. Thus, the electric force is almost negligible compared to the Lorentz force when the flow is non-relativistic. However, the two forces become comparable to each other and nearly cancel out each other as the flow speed reaches the speed of light, indicating that other processes are needed for continued collimation and acceleration of the jet.

One can guess that the Lorentz force component along the poloidal field line is dependent on the angle between the field line and the current. In other words, if the poloidal current is parallel to the field line, the jet would not be accelerated. Then, what determines the distribution of the field lines and current lines? Again, one cannot just choose these lines but must solve the full MHD equations. Theoretical studies found the condition for efficient jet acceleration, described by the following equation:

$$\frac{\Gamma}{\mu} \approx 1 - \frac{B_p}{\Phi/(\pi R^2)}, \tag{1.2}$$

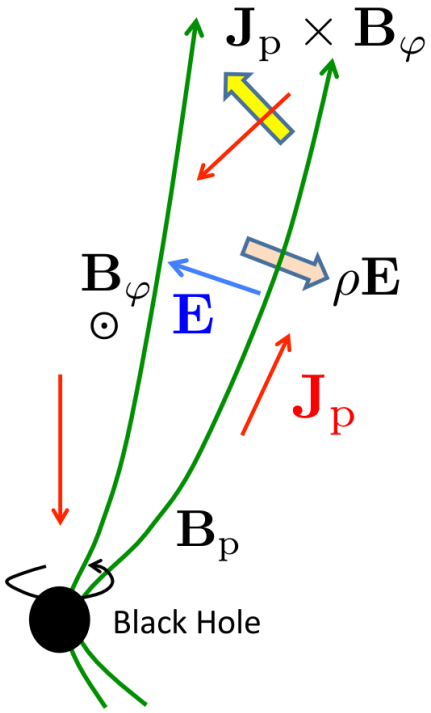

Figure 1.13. Schematic diagram of magnetic jet acceleration and collimation process taken from the presentation file of Dr. Toma in the *Challenges of AGN jets* meeting held in 2017 (`http://www.miz.nao.ac.jp/vera/en/system/files/collegium_and_conference/208/attached_560.pdf`). Poloidal magnetic fields (B_p) are attached to the central rotating black hole (the black filled circle). Poloidal currents (J_p) driven by the magnetic fields are shown with the red arrows. The Lorentz force ($J_p \times B_\phi$) and the electric force (ρE) are shown with the yellow and pink arrows, respectively.

where μ is the ratio of the total energy flux to the rest-mass flux and is a conserved quantity along a field line, Φ is the magnetic flux interior to the field line, and R is the distance from the jet axis to the field line (Tchekhovskoy et al. 2009). Since μ is a constant, Γ increases with distance when B_p becomes smaller than the mean enclosed field $\Phi/(\pi R^2)$. This situation is realized when the inner (poloidal) field lines closer to the axis are more collimated than the outer field lines, often called *differential* bunching/collimation of field lines. This is because the magnetic field strength is determined

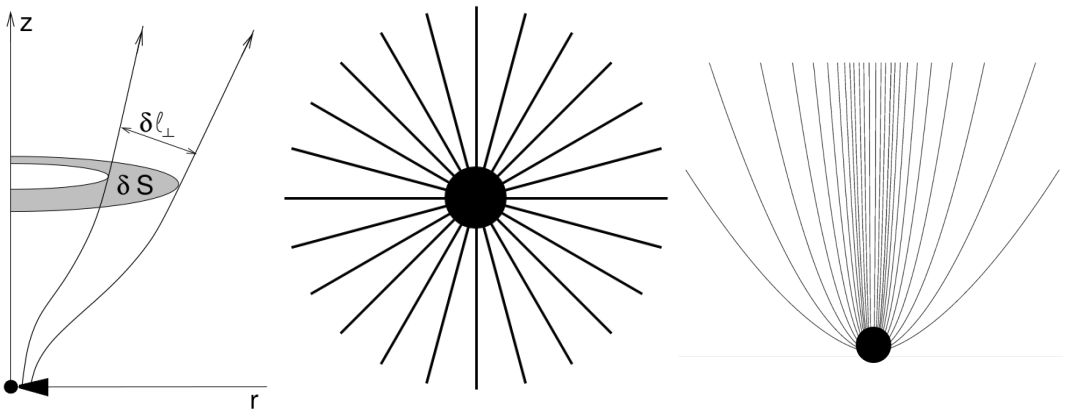

Figure 1.14. *Left :* schematic diagram showing the concept of differential collimation of field lines. The distance between streamlines $\delta l_\perp$ must increase faster than the cylindrical distance r of the inner field line for efficient jet acceleration. *Middle :* monopole-like magnetic field lines cannot accelerate jets. *Right :* inner (poloidal) field lines being more collimated than outer lines are ideal for efficient jet acceleration.

by how many field lines pass through unit surface area. The left panel of Figure 1.14 shows the concept of the differential collimation. When the distance between streamlines $\delta l_\perp$ increases faster than the cylindrical distance r, the inner field line is more collimated than the outer one. The monopole-like field line distribution shown in the central panel cannot accelerate the jet because $B_p/(\Phi/\pi R^2)$ would be a constant at any distance. The field lines such as those in the right panel are ideal for efficient jet acceleration.

Therefore, collimation and acceleration of jets are intimately related to each other. This is the reason why the magnetic acceleration mechanism is often called the "collimation–acceleration mechanism". However, as we discussed above, jets cannot be collimated enough by the magnetic hoop stress of toroidal fields because it would be counterbalanced by the electric force when the jets are relativistic. This indicates that the jets must be confined by an external medium to be collimated and accelerated continuously at larger distances as observed in nearby radio galaxies such as M87 (Asada & Nakamura 2012; Mertens et al. 2016) and Cygnus A (Boccardi et al. 2016). What can

serve as the external medium? Both observations and numerical simulations suggest that winds, non-relativistic gas outflows launched from the accretion disk, are the most probable candidate.

1.1.3 Accretion flows and winds

AGNs, including their jets, are powered by strong gravitational potential energy of accreting gas. Therefore, understanding the accretion process is essential to study AGN jets. Two types of accretion flows distinct from each other have been successful in explaining the observational features of AGNs. One is a cold and optically thick flows, accreted onto the central black hole by forming a geometrically thin disk. This type of accretion is believed to operate when the disk luminosity is larger than $\approx 1\%$ of the Eddington luminosity, i.e., in rapidly accreting AGNs. Most of the gravitational potential energy of the accreting gas is released as radiation and the disk remains to be cold at temperature of $10^4 - 10^7\ K$. Thus, the gas pressure is negligible compared to the gravity of the disk and the disk scale height (H) is quite small, forming a razor thin disk. The kinematic viscosity coefficient ν is parameterized as $\nu \equiv \alpha c_s H$, where α is a mathematical prescription to introduce turbulence needed for the disk materials accreted onto the black hole within a reasonable timescale (Shakura & Sunyaev 1973), c_s is the sound speed. Accordingly, this accretion model is often called an α-disk model. Later studies found that magneto-rotational instability (MRI) can naturally drive the turbulence (Balbus & Hawley 1991) and the α prescription is reasonable with its value of $0.05 - 0.2$ (Hawley & Balbus 2002; Penna et al. 2013b).

Since the accreting gas is concentrated in a thin disk, it is optically thick and emits blackbody radiation (Netzer 2013). The disk temperature decreases with radius to the power of $-3/4$ and the resulting emission can be described by superposition of blackbody spectra having various temperatures. Its spectrum is characterized by a bump peaking at ultraviolet wavelengths, called the "big blue bump", which has been observed in many quasars and Seyfert galaxies. The left panel of Figure 1.15 shows a typical SED of AGNs accreting at relatively high rates (taken from Harrison 2014),

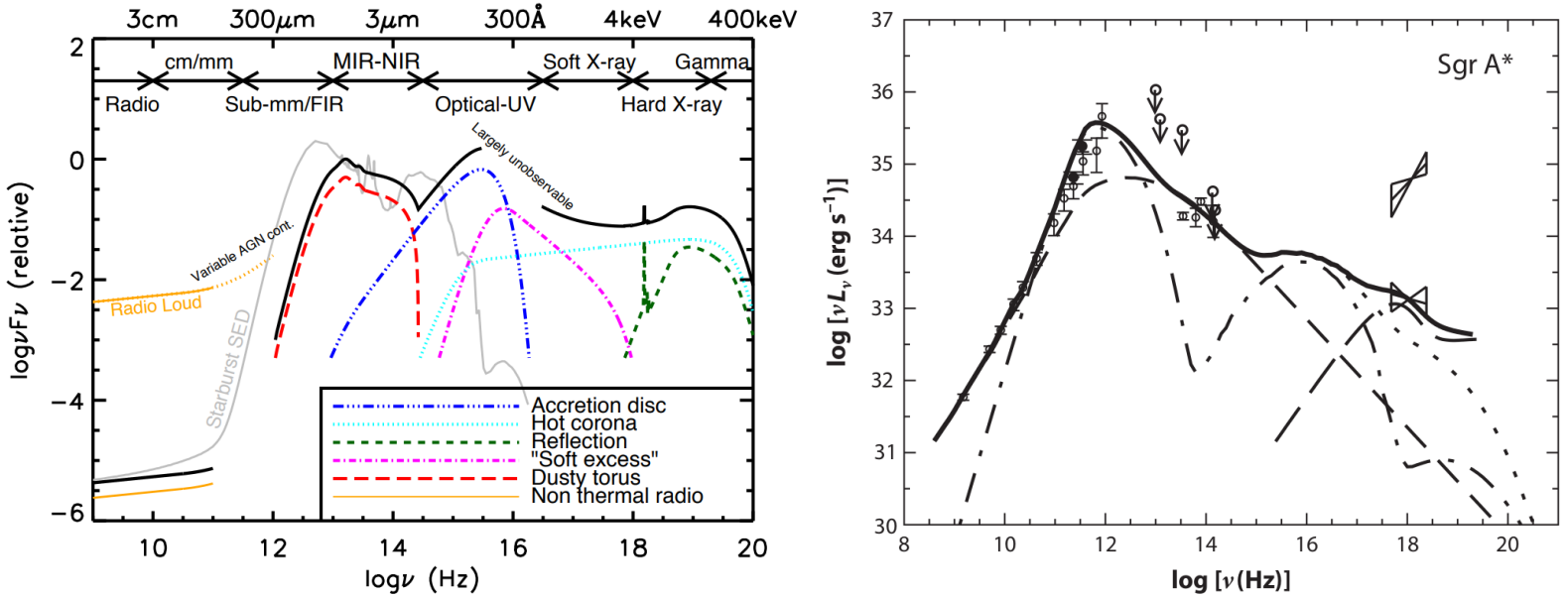

Figure 1.15. *Left :* a schematic representation of the SED of an AGN for which the disk luminosity is larger than $\approx 1\%$ of the Eddington luminosity, taken from Harrison (2014). One of the notable features is the bump peaking at UV wavelengths, often called the "big blue bump". This bump has been successfully modeled by the blackbody radiation originating in a cold, geometrically thin, and optically thick accretion disk (Shakura & Sunyaev 1973). *Right :* the SED of the radio source Sagittarius A* at the center of our Galaxy (Yuan et al. 2003), taken from Yuan & Narayan (2014). The model spectrum (thick solid line) consists of three different emission components: synchrotron emission and its Compton counterpart from thermal electrons (dot-dashed line), synchrotron emission from nonthermal electrons (short-dashed line), and bremsstrahlung emission from electrons near the Bondi radius (long-dashed line).

where the big blue bump clearly exists. This example plot demonstrates that AGNs having high luminosity (larger than $\approx 1\%$ of the Eddington luminosity) are powered by the cold accretion flows.

However, most ($\approx 98\%$) of the supermassive black holes in the local Universe do not have such high luminosities (relative to the Eddington luminosities). One of the best examples is the radio source associated with the supermassive black hole at the center of our Galaxy, Sagittarius A* (Sgr A*). Its bolometric luminosity is about 10^{36} erg s^{-1}. Considering its mass of $M_{\rm BH} = 4.1 \times 10^6 M_\odot$ (Meyer et al. 2012), the luminosity is only $\sim 2 \times 10^{-9} L_{\rm Edd}$. This kind of black holes do show some activities but have low luminosities (in units of the Eddington luminosities), and called low-luminosity AGNs (LLAGNs, Ho 2008). The SED of Sgr A*, shown in the right panel of Figure 1.15, is very different from that of quasars and Seyfert galaxies; there is no big-blue bump! This indicates that different types of accretion flows are operating in LLAGNs.

There has been significant progress in understanding the accretion process in the low accretion rate limit during the last few decades. One of the most important characteristics that need to be taken into account in those accretion models is to reproduce the observed low luminosities. Many solutions satisfying this condition were found and a representative model is known as an advection-dominated accretion flows (ADAFs, Ichimaru 1977; Narayan & Yi 1994) model. In this accretion flows, most of the gravitational potential energy of gas is advected into the black hole instead of being radiated. The gas temperature is very high and almost virial (with a temperature profile of $T \sim (10^{12}/r)K$), making this type of accretion flows belong to *hot accretion flows* (Yuan & Narayan 2014). Accordingly, the gas pressure is high and the accretion flow is geometrically quite thick. The gas density is much smaller than the case of a thin disk, while the radial velocity is much faster, leading to the advection timescale shorter than the cooling timescale. Another important characteristic of ADAFs is that the ions and electrons are expected to have different temperatures. This is because (i) electrons cool much more efficiently than do ions, (ii) compressional heating is more efficient for ions than electrons when the electrons become relativistic (i.e., temperature larger than

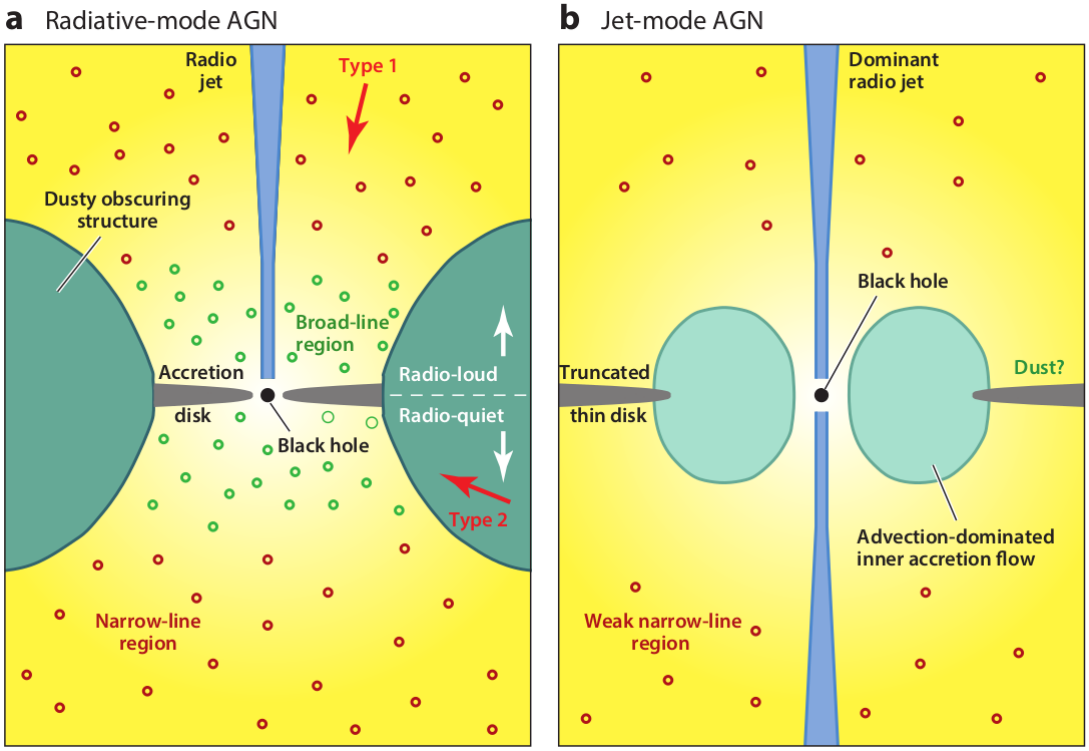

Figure 1.16. Schematic diagrams of AGNs powered by a cold, thin accretion disk (left) and by a geometrically thick hot accretion flow (right), taken from Heckman & Best (2014). The former is often called radiative-mode AGNs because it delivers most of its energy to the ISM by strong radiation, while the latter called jet-mode AGNs because its radiation is relatively weak but it usually has strong jets.

$\approx 6\times10^9 K$), and (iii) ions and electrons rarely change energy with each other due to the low density and weak Coulomb collisions. The right panel of Figure 1.15 shows that the SED of Sgr A* is successfully explained by the ADAF model. Synchrotron, Compton, and Bremsstrahlung emission are dominant, which is clearly distinct from the case of cold accretion flows. Schematic diagrams of AGNs having cold and hot accretion flows are presented in Figure 1.16.

There are two important characteristics of the ADAF solutions; (i) the solutions are unstable to convection and (ii) the Bernoulli parameter, the sum of the kinetic energy,

potential energy, and enthalpy, is positive, indicating that the accretion flows should have strong outflows or jets. Based on these characteristics, alternative accretion models have been proposed, so-called convection-dominated accretion flows (CDAFs, Narayan et al. 2000; Quataert & Gruzinov 2000) and advection-dominated inflow-outflow solutions (ADIOS, Blandford & Begelman 1999, 2004; Begelman 2012). In the former model, the gas constantly moves in and out in turbulent convective eddies and not much gas at outer radii can be actually accreted onto the black hole. The situation is similar for the latter model but the gas escapes from the accretion flows, bringing in a genuine mass loss in a wind.

The difference between these models can be described by two quantities: the radial mass accretion rate profile and density profile.

$$\dot{M}_{\rm in}(r) \propto r^s, \tag{1.3}$$

$$\rho \propto r^{-p}, \tag{1.4}$$

where $\dot{M}_{\rm in}(r)$ denotes the mass inflow rate at a given radius r. There is a relation between s and p such that $p = 1.5 - s$ (to satisfy the mass conservation law in one-dimensional fluid equations). The ADAF model predicts $s = 0$ and $p = 1.5$ (Narayan & Yi 1994). The ADIOS model predicts $0 < s < 1$ and $0.5 < p < 1.5$ (Blandford & Begelman 1999). The CDAF model predicts $s = 1$ and $p = 0.5$ (Quataert & Gruzinov 2000). While the ADAF model suggests that the accretion flows consist of pure inflows, the ADIOS and CDAF models show that most of gas captured by the black hole's gravity cannot actually reach the vicinity of the black hole due to strong outflows and convection.

A number of numerical simulations have been performed to understand the dynamics and properties of hot accretion flows. Remarkably, most of those simulations found that the mass inflow rate is not constant over radius but its profile has $s = 0.4 - 0.8$ (e.g., Yuan et al. 2012b). An example plot is presented in Figure 1.17, showing the results of hydrodynamic simulations performed by Stone et al. (1999). Both the mass inflow and outflow rates decrease with decreasing radius and only a small fraction of

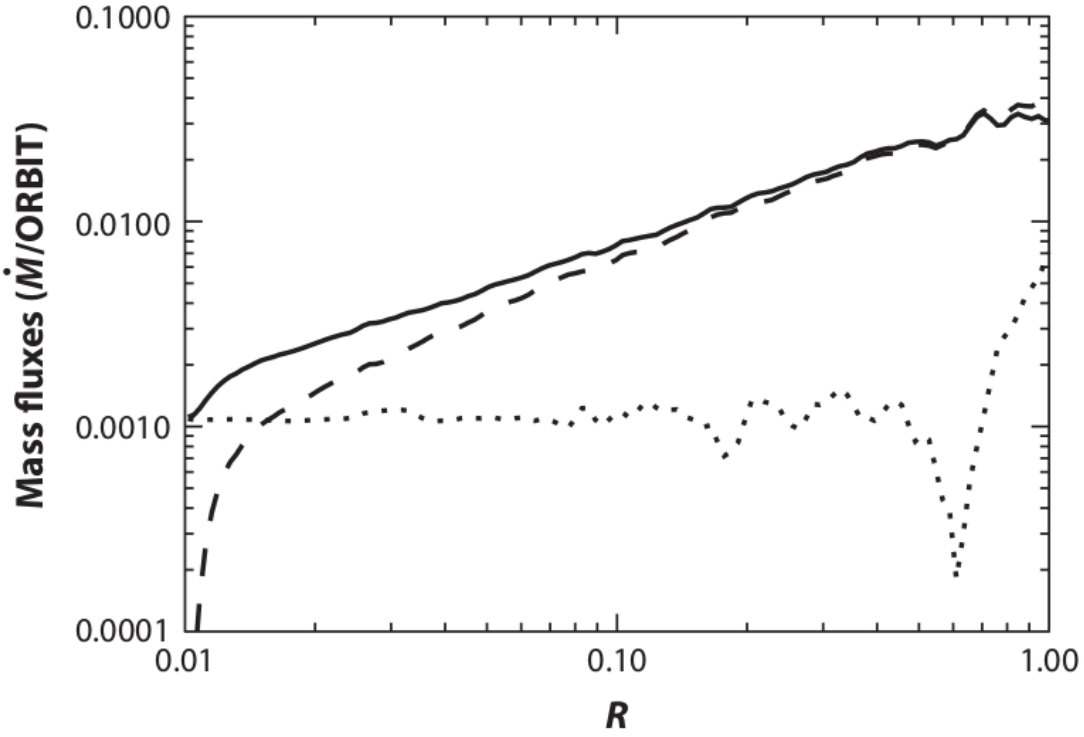

Figure 1.17. Radial mass accretion rate profile of hydrodynamic numerical simulations of hot accretion flows (Stone et al. 1999). The mass inflow and outflow rate are shown with the black solid and dashed lines, respectively. The net rate, i.e., the difference between the mass inflow and outflow rate, is shown with the dotted line.

gas captured by the black hole's gravity is actually accreted onto the black hole. Therefore, the results of those simulations appear to be consistent with the ADIOS model, indicating that hot accretion flows are subject to lose a significant amount of mass in the form of outflows. Then, why convection is not dominant in hot accretion flows even though the ADAF solutions are unstable to convection? Numerical simulations showed that magnetic fields, ignored in the original ADAF solutions but surely exist in hot accretion flows, can suppress convection (Narayan et al. 2012; Yuan et al. 2012a).

Figure 1.18 shows three-dimensional visualization of different components of the black hole inflow–outflow system, based on the results of general relativistic magentohydrodynamic (GRMHD) simulations (Sadowski et al. 2013). Equatorial regions are

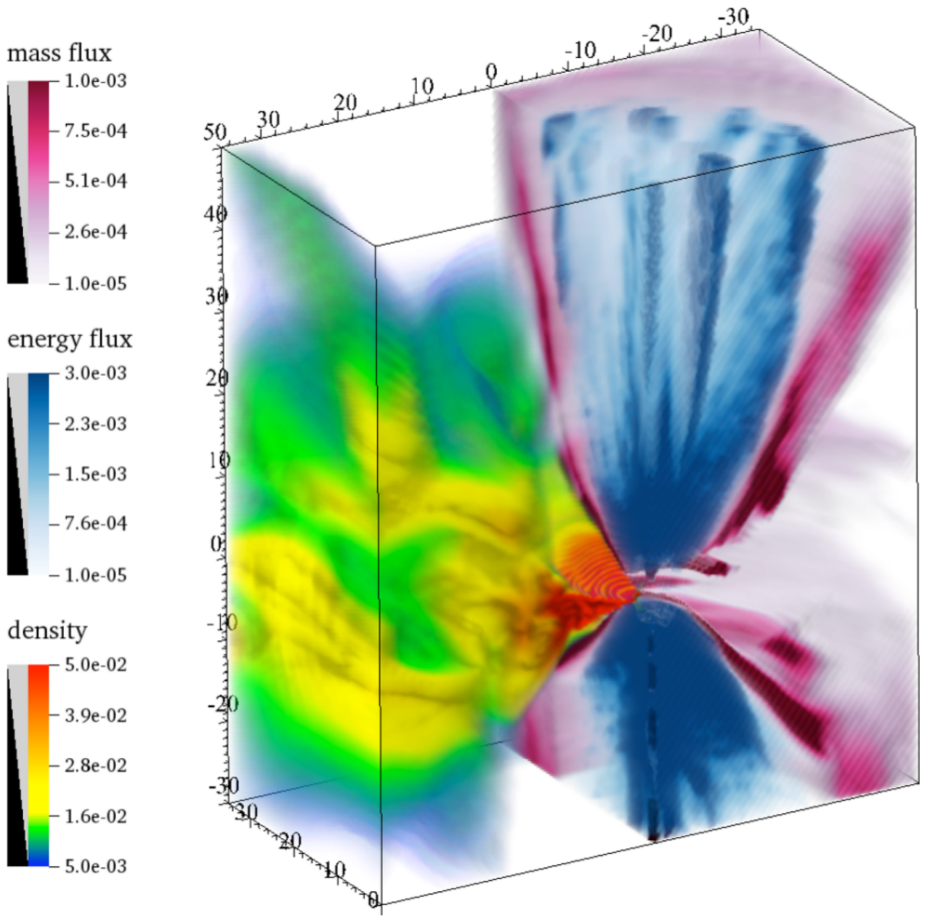

Figure 1.18. Three-dimensional visualization of a black hole inflow–outflow system based on the results of GRMHD simulations (Sadowski et al. 2013). There are three different components with different characteristics: highly magnetized, collimated relativistic jets (blue), weakly magnetized hot accretion flows with high density (green and yellow), and un-collimated non-relativistic winds launched from hot accretion flows (magenta).

filled in by hot accretion flows having high density. Bi-polar outflows in the polar regions carrying a large amount of energy flux, equivalent to jets, are launched by the central rotating black hole. The jets are highly collimated and moving at relativistic speeds. One can see that there is an additional component between the jets and the

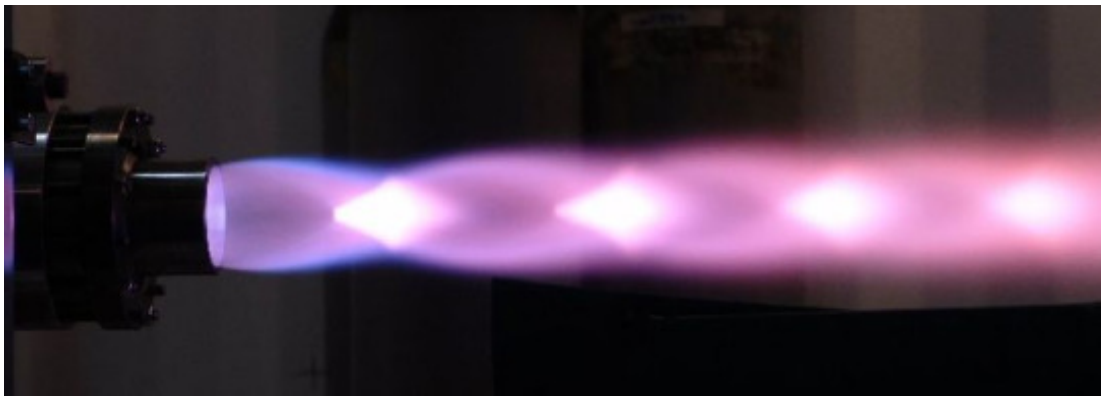

Figure 1.19. Shock diamonds in a flow exiting a nozzle in an aircraft taken from `https://www.zmescience.com/other/science-abc/diamond-rings-aircraft-0423423/`.

accretion flows, having high mass flux. This is called winds, which are un-collimated non-relativistic gas outflows launched from hot accretion flows. Winds are surrounding jets and can serve as an external confining medium, which is very important for continued acceleration and collimation of jets at large distances (see Section 1.1.2).

The cold and hot accretion flows, which are distinct in many aspects as described above, may represent different evolutionary stages of a black hole accretion process. Black hole X-ray binaries (BHXRBs) show two distinct states, known as *high soft state* and *low hard state*. In the former state, BHXRBs' emission is dominated by a high-luminosity thermal X-ray component, which usually peaks at relatively low energies and thus its X-ray spectrum is soft. In the latter state, their spectra are characterized by low luminosity and hard X-ray emission and low-power radio jets can be often found. The soft and hard states have been successfully modeled by the cold accretion and hot accretion models, respectively (e.g., Narayan & McClintock 2008). BHXRBs are observed to traverse from one state to another, suggesting that the two accretion modes represent different evolutionary stages of black hole accretion.

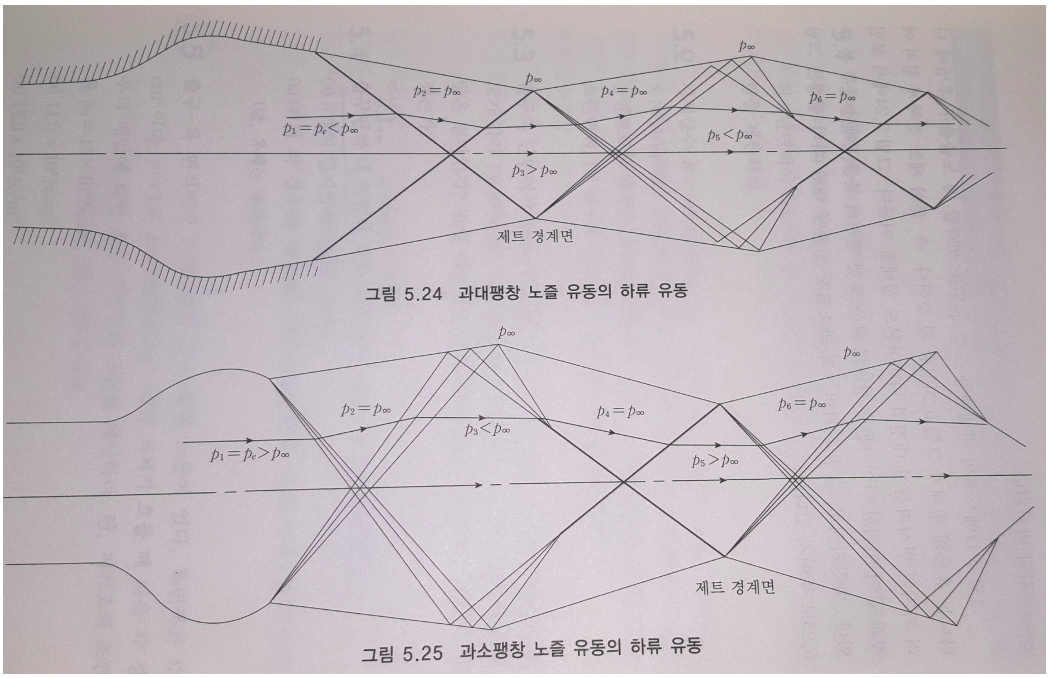

Figure 1.20. Schematic diagrams of over-expanded (upper) and under-expanded (lower) flows exiting a nozzle, taken from 노오현 (2004). Several oblique shocks and expansion/compression fans are formed to obtain the pressure balance between the flow and the ambient medium. The shocks and fans are reflected at the boundary.

1.1.4 Recollimation shocks and energy dissipation

In Section 1.1.2, how AGN jets can be highly collimated and accelerated to relativistic speeds is briefly explained. As seen in Figure 1.12, the jets initially carry a large amount of energy in the form of Poynting flux, which is gradually converted into the jet kinetic flux at larger distances. The Poynting flux conversion is thought to be almost completed when they start to freely expand into an interstellar medium (ISM) not governed by the black hole's gravity (i.e., outside the Bondi radius). At this point, the jet moves relativistically, meaning that the jet is a supersonic flow. If there is pressure mismatch between the jet and the ISM, the jet tries to expand or contract to obtain the pressure balance. However, a supersonic flow can change its direction only through shocks or an expansion fan because any information from the downtream gas flows such as changing

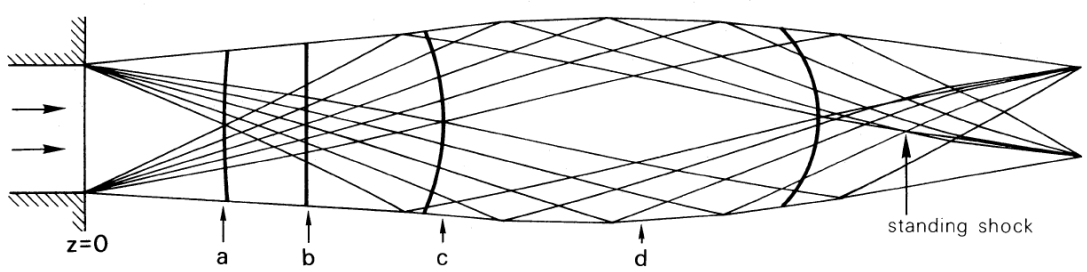

Figure 1.21. Formation of a standing shock in the case of a jet experiencing a drop in external pressure, calculated by solving HD equations with the method of characteristics (Daly & Marscher 1988). The expansion and compression characteristic lines cross each other in the downstream region, forming a conical, recollimation shock.

the flow direction cannot be delivered to the upstream flows in advance. This behavior can result in a series of standing shocks, often called "recollimation shocks", and expansion and contraction of the jet.

Although the details of the formation mechanism of recollimation shocks in AGN jets require quite complicated mathematical calculations, we can find an analogous situation in our daily life: when a flow exits a nozzle in an aircraft or a rocket at supersonic speeds. An example is shown in Figure 1.19 where a series of standing shocks forms "shock diamonds". If the supersonic exhaust from the aircraft's nozzle has a smaller or larger pressure compared to the ambient pressure at the exit, the flow must contract or expand to obtain the pressure balance. This requires chaning the flow direction, which can only be done by oblique shocks or expansion/compression fans. These shocks or fans must be reflected at the boundary or at the axis to satisfy the pressure balance (i) at the boundary and (ii) at the axis, as illustrated in Figure 1.20.

Similar explanations have been applied to AGN jets. Figure 1.21 shows the formation of a standing, recollimation shock in a jet which exits a nozzle and experience a drop in external pressure, calculated by solving HD equations with the method of characteristics (Daly & Marscher 1988). The jet expansion and compression are described by the expanding and reflected characteristic lines, similar to the expansion and com-

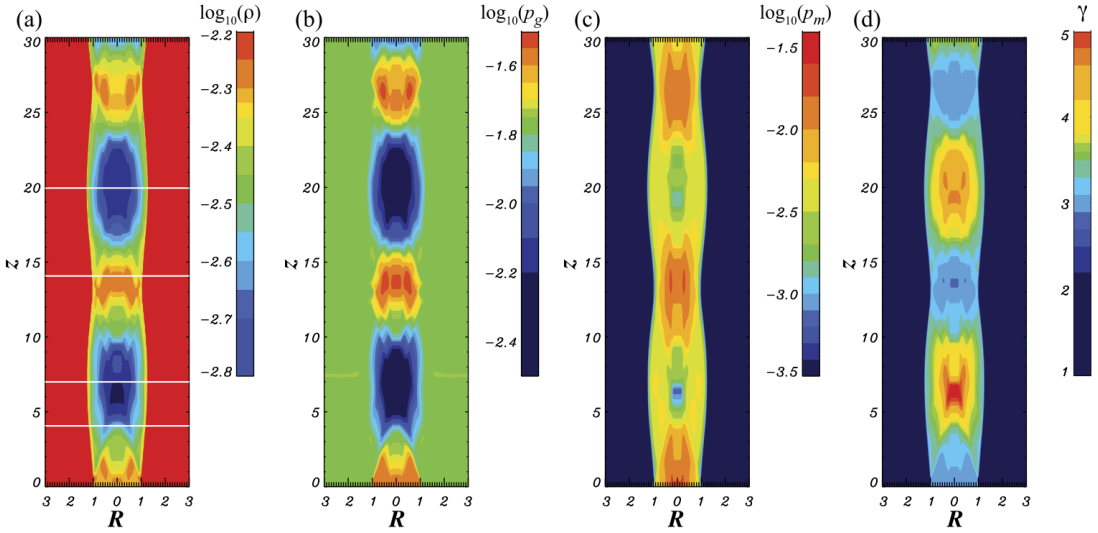

Figure 9. Case MHD−c. Same as in Figure 3, but for the helical magnetic-field case with $B_0 = 0.2$.

Figure 1.22. Formation of recollimation shocks in the case of over-pressured relativistic jets, shown in the results of special relativistic MHD simulations (Mizuno et al. 2015). The distributions of rest-mass density (a), gas pressure (b), magnetic pressure (c), and Lorentz factor (d) are shown with colors.

pression fans in Figure 1.20. A characteristic line shares the same quantity consisting of the flow speed and the sound speed. In the downstream compression region, several characteristic lines merge into a conical shape, indicating that a standing shock in a conical shape forms in this region.

Recollimation shocks can form even in the case of the jet permeated by an ordered magnetic field, which appears to be realistic at least for several AGN jets (e.g., Asada et al. 2002; Zamaninasab 2013; Gómez et al. 2016; Gabuzda et al. 2018). Figure 1.22 shows the results of numerical simulations (Mizuno et al. 2015) assuming that a jet is permeated by a helical, ordered magnetic field and injected into an ambient medium having smaller pressure than the jet (also called an over-pressured jet). Similar to the case of HD, recollimation shocks repeatedly appear which increase the gas density and pressure and decrease the bulk Lorentz factor. Recollimation shocks can convert the kinetic energy into other forms of energy such as heat and radiation.

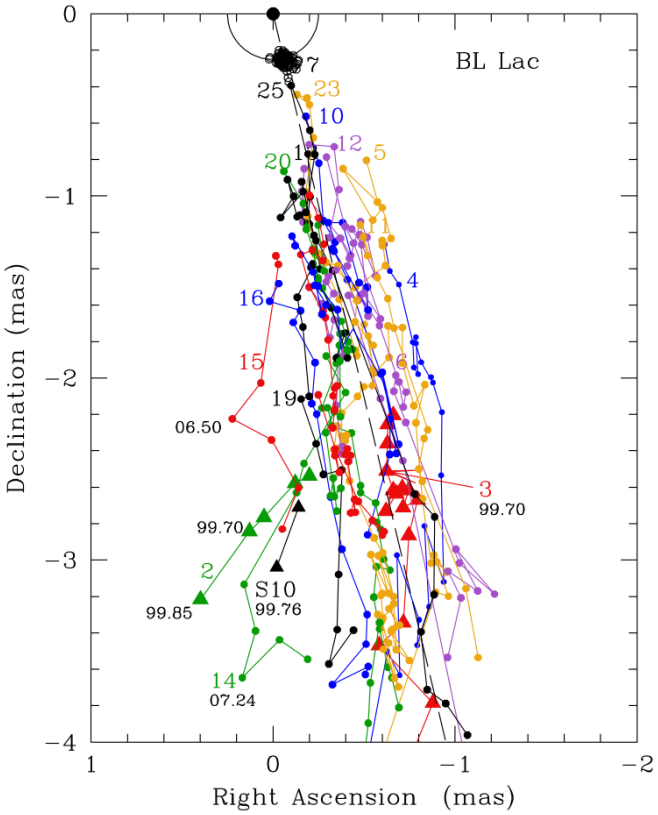

Figure 1.23. Trajectories of many jet blobs (also called "components") of the blazar BL Lacertae resolved by the very long baseline array (VLBA) (Cohen et al. 2014). While most of the components show outward motions in the southern direction, one component at the origin, called the "core", and another at ≈ 0.35 mas from the core remain at the same positions over time.

Then, a question that naturally arises is whether we can observe those recollimation shocks in the maps of AGN jets. Since recollimation shocks are expected to form after exiting a nozzle, presumably outside the Bondi radius (i.e., when the jet is moving through a free ISM), observations with high angular resolution are required. Indeed, very long baseline interferometry (VLBI) monitoring observations of many AGN jets have shown that there are stationary features in those jets, usually located close to the jet base ($\lesssim 1$ mas), in addition to many relativistically moving jet "blobs" (Lister et al.

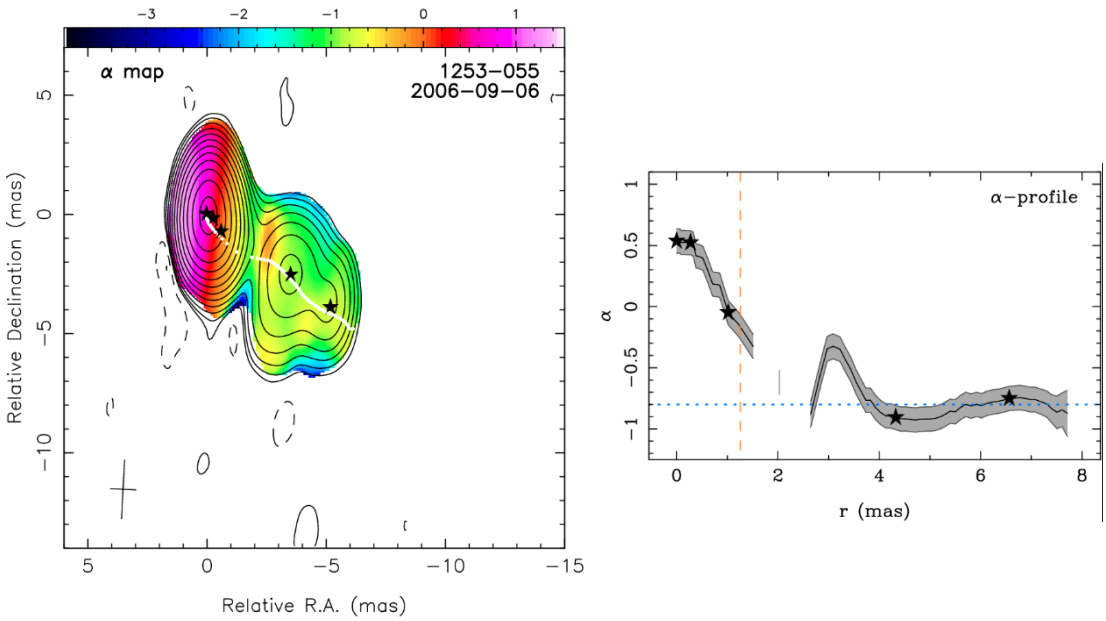

Figure 1.24. *Left :* a spectral index map of 3C 279 obtained at frequencies of 8.1 – 15.2 GHz with the VLBA (Hovatta et al. 2012). Colors show the distribution of α in $S_\nu \propto \nu^\alpha$, where S_ν is the flux density and ν is the observing frequency. *Right :* a spectral index curve along the jet ridge line shown in the left map.

2016; Jorstad et al. 2017). Figure 1.23 shows an example of BL Lacertae, the prototype of BL Lac objects, where many jet blobs, also called "components", move outwards in the southern direction. However, two components, one at the origin of the map and the other at ≈ 0.35 mas from the origin are stationary over time. Can these stationary components be identified with recollimation shocks?

The answer seems to be yes. Nearly every blazars shows a compact and bright emission feature upstream of their jets in the VLBI maps. This "core" region usually shows an optically thick spectrum at radio frequencies and new superluminal jet blobs appear to be ejected from the core, as seen in Figure 1.3 for the quasar 3C 279. Figure 1.24 shows a spectral index map of 3C 279 obtained at frequencies of 8.1 – 15.2 GHz with the VLBA (Hovatta et al. 2012). The core and downstream jet emission are characterized by an optically thick and thin spectrum, respectively. Initially, the core was

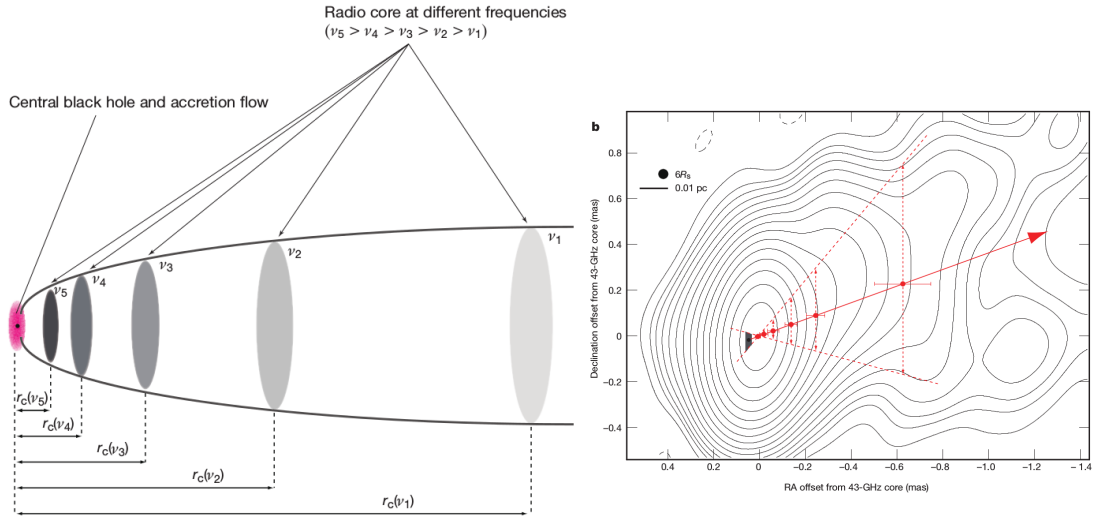

Figure 1.25. *Left :* a schematic diagram showing the core-shift effect, a shift of the core position closer to the jet base at higher observing frequencies due to the frequency dependence of synchrotron self-absorption. The darker shaded ellipses which represent the core positions at higher frequencies become closer to the jet base. This image is taken from Hada et al. (2011). *Right :* the observed core-shift in a nearby radio galaxy M87 by astrometric observations at multiple frequencies with the VLBA (Hada et al. 2011). The core positions at different frequencies are shown with the red circles and the inferred location of the jet base is shown with the black shaded area.

thought to be a transition location where jet synchrotron emission becomes optically thick. The jet expands as it moves from the central engine, meaning that its electron density and magnetic field strength, and thus the absorption coefficient of synchrotron emission are higher at smaller distances. This indicates that the jet emission upstream of a certain distance, where the optical depth becomes about unity ($\tau \approx 1$), would not be detectable due to strong absorption. The core marks this transition location because it is apparently stationary and optically thick. According to this scenario, the core positions at higher observing frequencies must be closer to the jet base because of the frequency dependence of synchrotron self-absorption, known as the "core-shift" effect

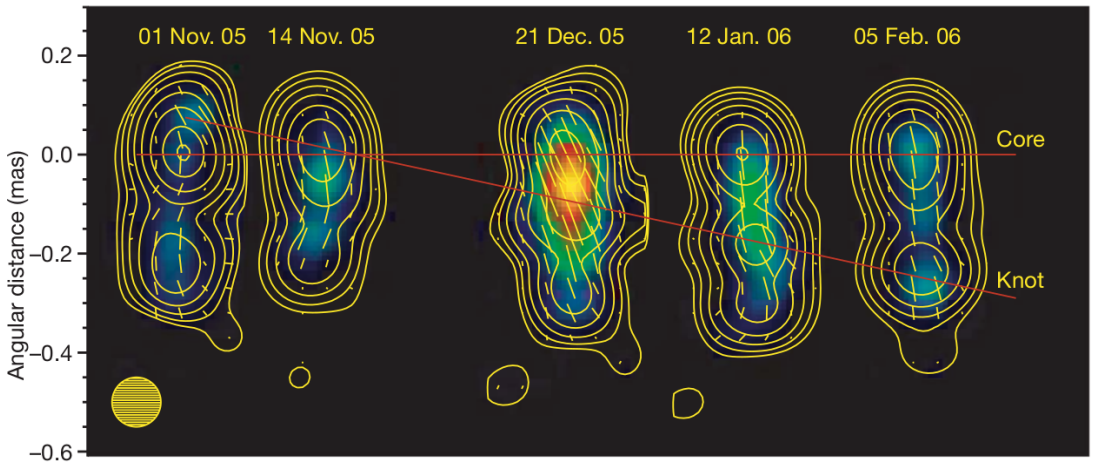

Figure 1.26. A series of maps of BL Lacertae observed at 43 GHz with the VLBA (Marscher et al. 2008). A jet knot, initially located upstream of the core, gradually moves downward in the later epochs. When the knot passes through the core, strong flares in both total intensity emission (contours) and linear polarization emission (colors) occur. Multi-wavelength flares as well as a systematic rotation of optical linear polarization angle occur near in time to the passage, indicating that the interaction of the knot and the core may be responsible for the onset of the flares.

(see Figure 1.25). Indeed, this core-shift effect has been observed in many radio-loud AGNs (e.g., O'Sullivan & Gabuzda 2009a; Pushkarev et al. 2012) and an example for M87 is shown in the right panel (Hada et al. 2011).

However, there is a growing consensus that the core cannot only be a simple $\tau = 1$ surface but be a physical structure such as a recollimation shock. Multi-wavelength monitoring observations and VLBI jet kinematic analysis of many blazars have found that strong flares at multiple wavelengths from radio to γ-ray occur when new superluminal knots pass through the cores. For example, $\approx 83\%$ of the γ-ray flares in the VLBA monitoring program of about 40 blazars occurred near in time to the passage of new superluminal knots through the cores (Jorstad & Marscher 2016). The coincidence of the brightening of the jet emission from BL Lacertae with the passage of a

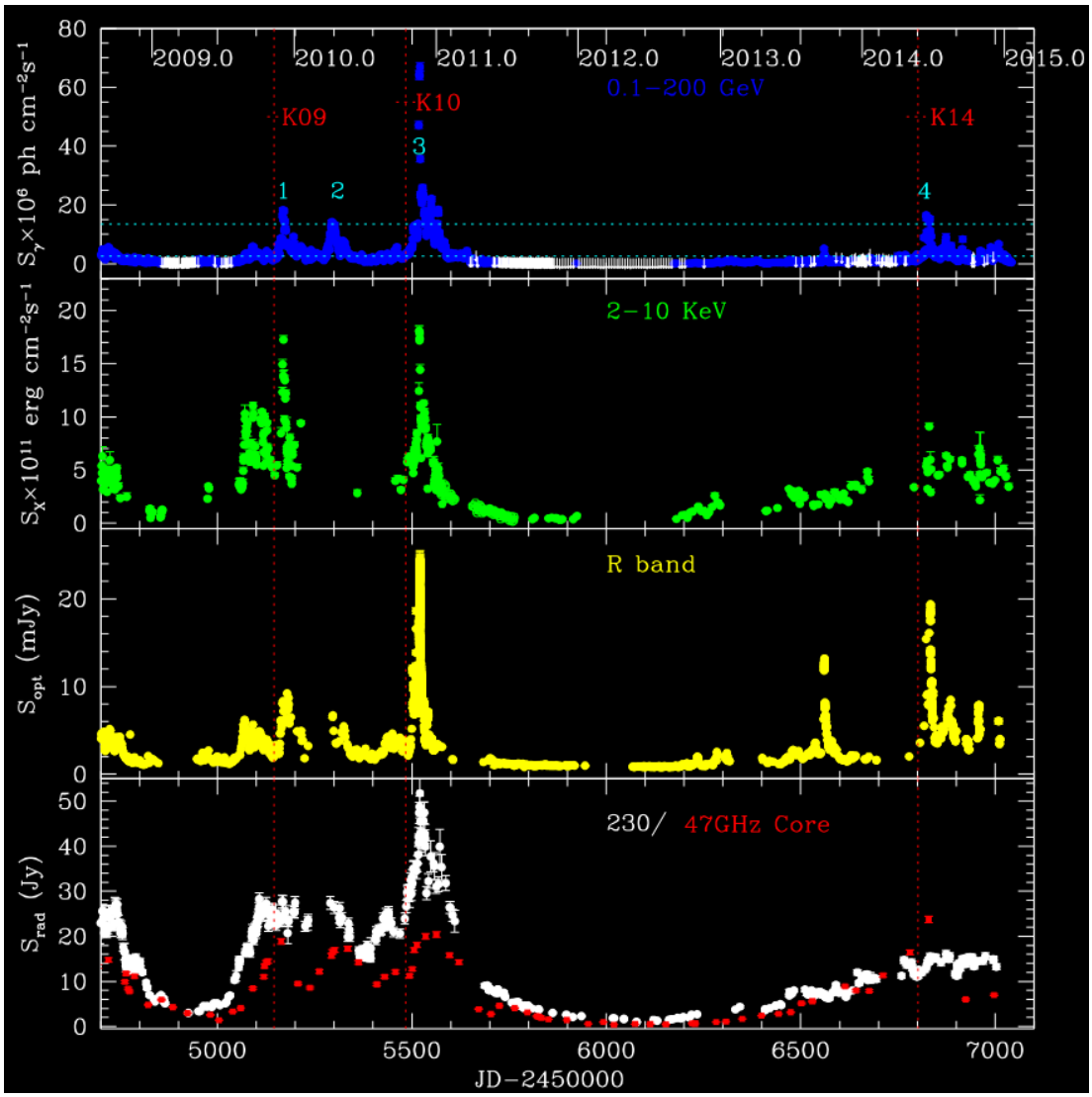

Figure 1.27. Light curves of the quasar 3C 454.3 at γ-ray (top), X-ray (second from the top), optical (third from the top), and radio (bottom) wavelengths (Jorstad & Marscher 2016). The red vertical dotted lines show the time when new superluminal knots pass through the core, inferred from the kinematic analysis of the VLBA monitoring data at 43 GHz.

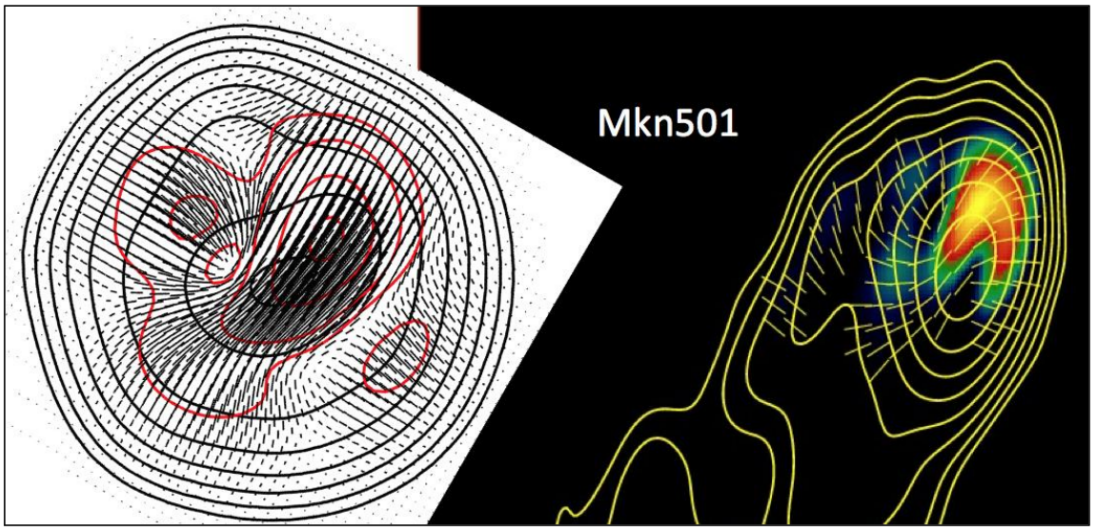

Figure 1.28. *Left :* total intensity emission (black contours), linear polarization emission (red contours), and linear polarization angle (black sticks) distributions of a blazar core reconstructed by a recollimation shock model (Marscher 2016). *Right :* observed total intensity (yellow contours), linear polarization emission (colors), and linear polarization angle (yellow sticks) distributions of the blazar Mrk 501 at 43 GHz with the VLBA (Marscher 2016).

knot through the core is shown in Figure 1.26 as an example (Marscher et al. 2008). Also, the passage of superluminal knots through the core in the quasar 3C 454.3 associated with strong multi-waveleng flares is presented in Figure 1.27. Furthermore, the observed total intensity and linear polarization emission in the core of the blazar Mrk 501 is successfully reproduced by a recollimation shock model (Figure 1.28, Marscher 2016).

These phenomena can be explained by interaction of moving shocks and a recollimation shock. Figure 1.29 shows the results of special relativistic HD numerical simulations showing the interaction (Fromm et al. 2016). As we already saw above, recollimation shocks form due to the pressure mismatch between the jet and the surrounding medium (high pressure regions in the top panel). In addition, pressure perturbations injected

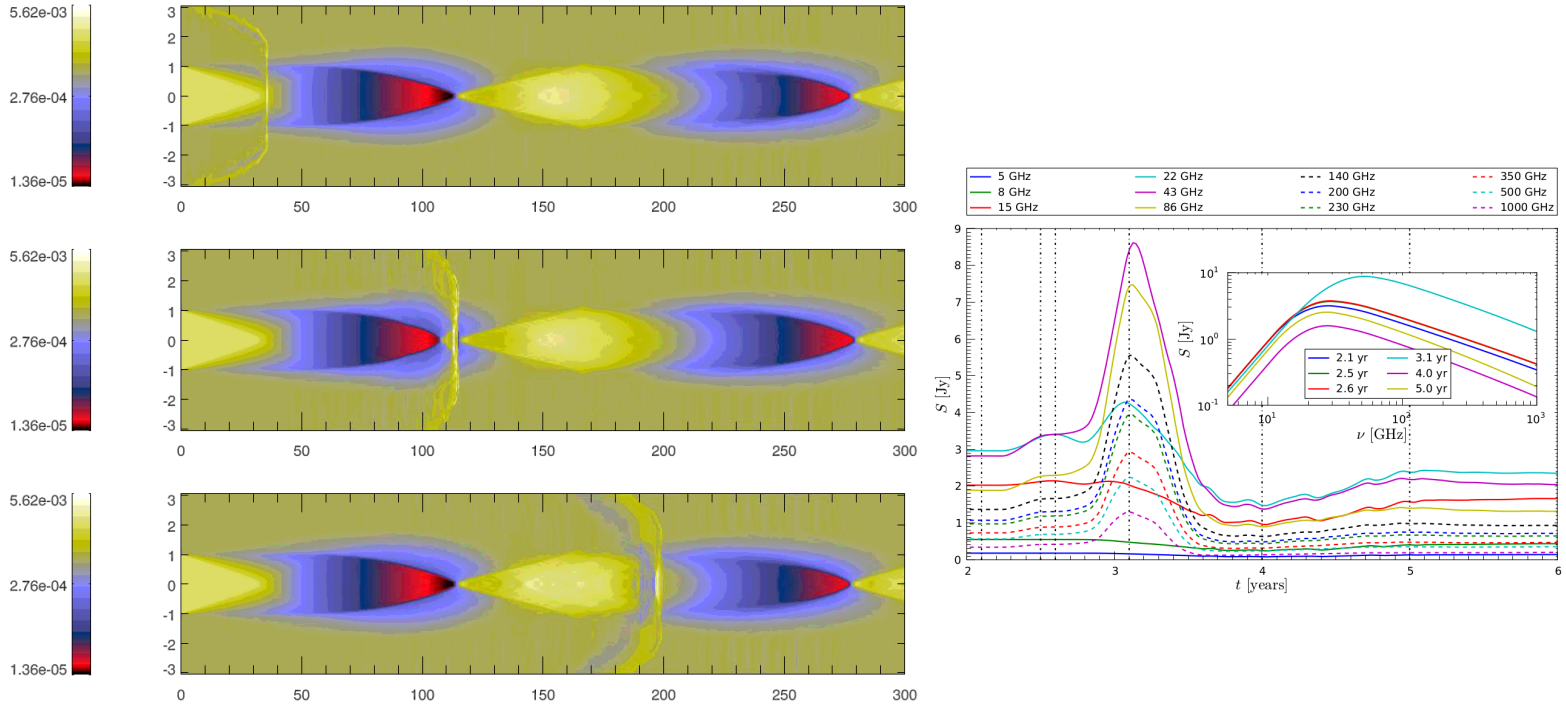

Figure 1.29. *Top :* snapshots (lower panels at later time) for pressure distribution obtained by the special relativistic HD simulations of AGN jets (Fromm et al. 2016). The high pressure regions represent recollimation shocks. A traveling shock generated by pressure perturbation injected at the jet nozzle propagates downstream the jet. *Bottom :* Light curves at different radio frequencies reconstructed from the simulations, where strong flares are observed at $t \approx 3.1$ year when the traveling shock passes through the recollimation shock at distance ≈ 110 in the left figure.

at the jet nozzle are developed into traveling shocks. When the moving shock passes through the standing recollimation shock, strong flares at multiple radio frequencies occur due to the energy dissipation during the interaction (at $t \approx 3.1$ years in the bottom panel). If the blazar cores are recollimation shocks and the superluminal blobs are traveling shocks, the interaction between those shocks can result in multi-wavelength flares, which has been indeed observed in many sources. The recollimation shocks also suffer from synchrotron self-absorption and the core-shift effect is naturally expected in this case as well.

1.1.5 M87: the best target for AGN jet astrophysics

So far, we have briefly discussed the mechanisms of jet launching, acceleration and collimation, and formation of recollimation shocks which may play an important role in energy dissipation. However, it is generally quite difficult to test the theoretical predictions with observations because most of those processes are expected to occur in small regions or at short distances from the jet base. For example, jet acceleration and collimation zone is thought to be at $\lesssim 10^6$ Schwarzschild radii from the jet base (Marscher et al. 2008). This distance corresponds to an angular projected distance of ≈ 0.5 milliarcseconds for an AGN at a redshift of 0.1 and having a black hole with mass of 10^8 $M_\odot$ and a jet viewing angle of 5°. Resolving this region is challenging even for VLBI.

Therefore, nearby radio galaxies have been of special interest for AGN jet astrophysicist. M87 has one of the best studied AGN jets, thanks to its proximity (located at 16.8 Mpc, EHT Collaboration et al. 2019f) and an extremely massive black hole (with the mass of $\approx 6.5 \times 10^9$ $M_\odot$, EHT Collaboration et al. 2019f). The Event Horizon Telescope (EHT) collaboration has revealed the shadow of the black hole in M87, which ensures that the power source of this active galaxy (and its jet) is the black hole (EHT Collaboration et al. 2019a). The jet appears on only one side with respect to the central core at most distances, presumably due to strong Doppler boosting and deboosting of the approaching and receding jet, respectively. However, there is indication

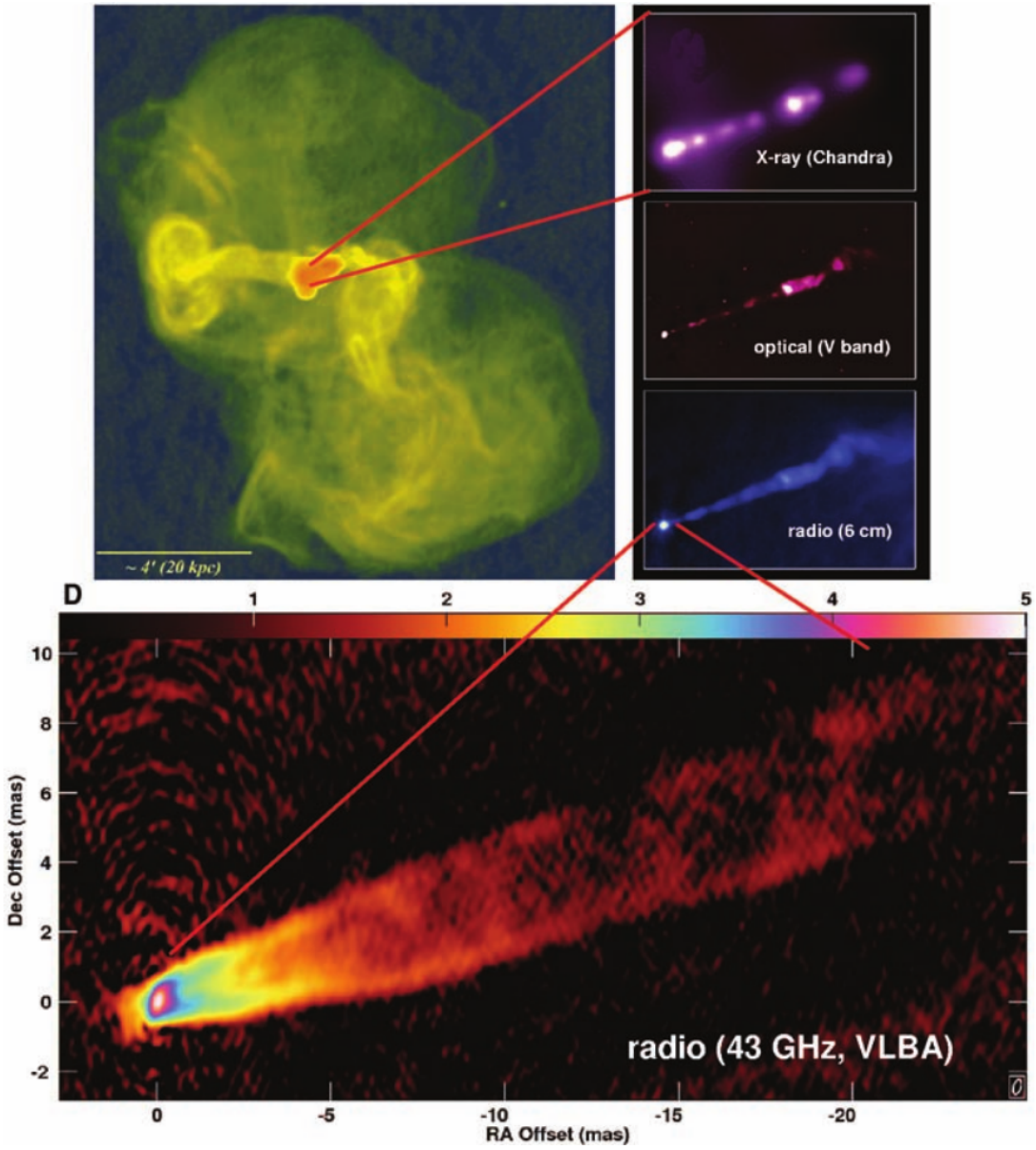

Figure 1.30. Images of the M87 jet on different scales. The large-scale radio jet and lobe (top left), the kpc-scale jet at X-ray, optical, and radio wavelengths (top right), and the mas-scale radio jet (bottom) are shown. Tenuous counterjet emission is detected at distances $\lesssim 2$ mas. This image is taken from Acciari et al. (2009).

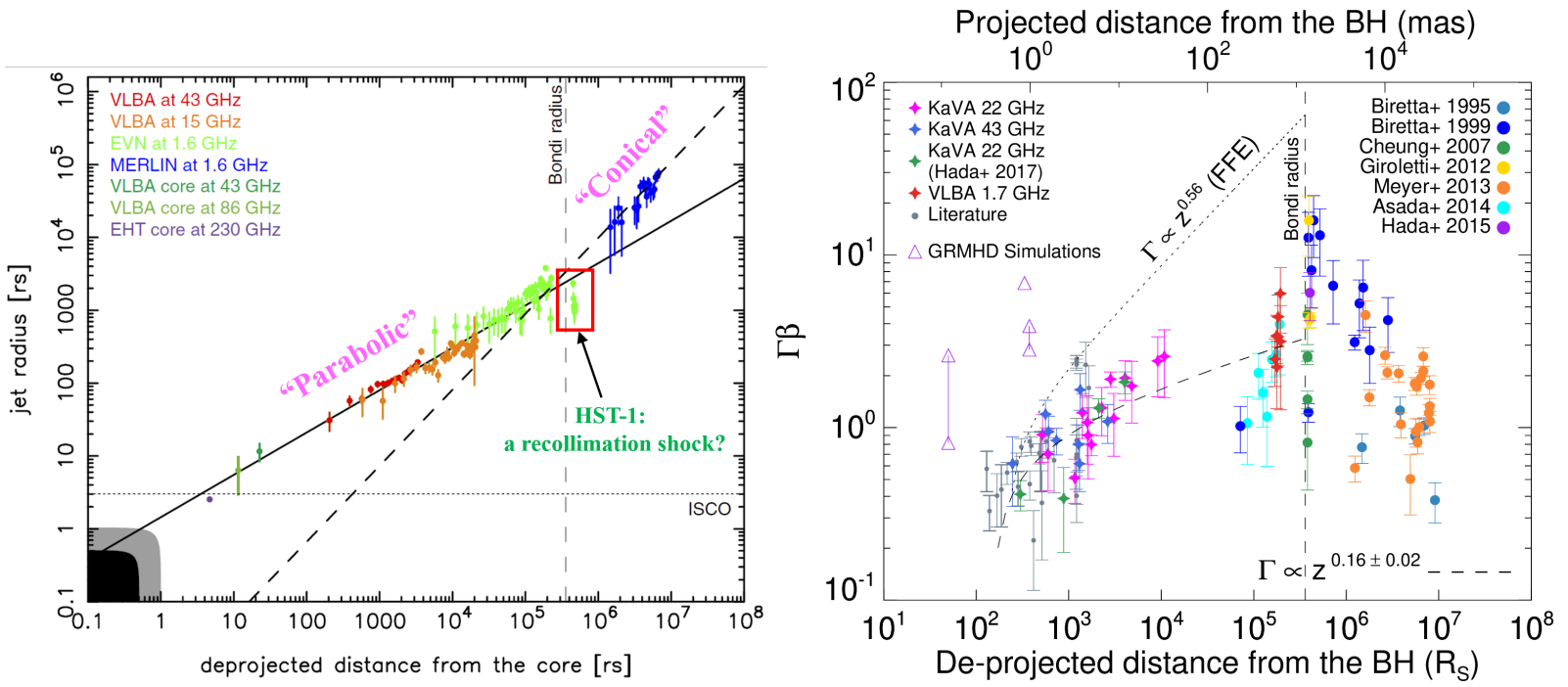

Figure 1.31. *Left :* jet radius of M87 as a function of de-projected distance from the core in units of Schwarzschild radii (R_S), taken from Nakamura & Asada (2013). The jet shape transitions from parabolic to conical near the Bondi radius, indicating that the jet is being collimated inside the Bondi radius. Near the Bondi radius, the jet radius suddenly drops. This is where HST-1, which has been modeled as a recollimation shock, is located (see Figure 1.32). *Right :* $\Gamma\beta$ of the M87 jet as a function of de-projected distance. The jet is gradually accelerated to relativistic speeds inside the Bondi radius. See Chapter 3 for more details about this figure.

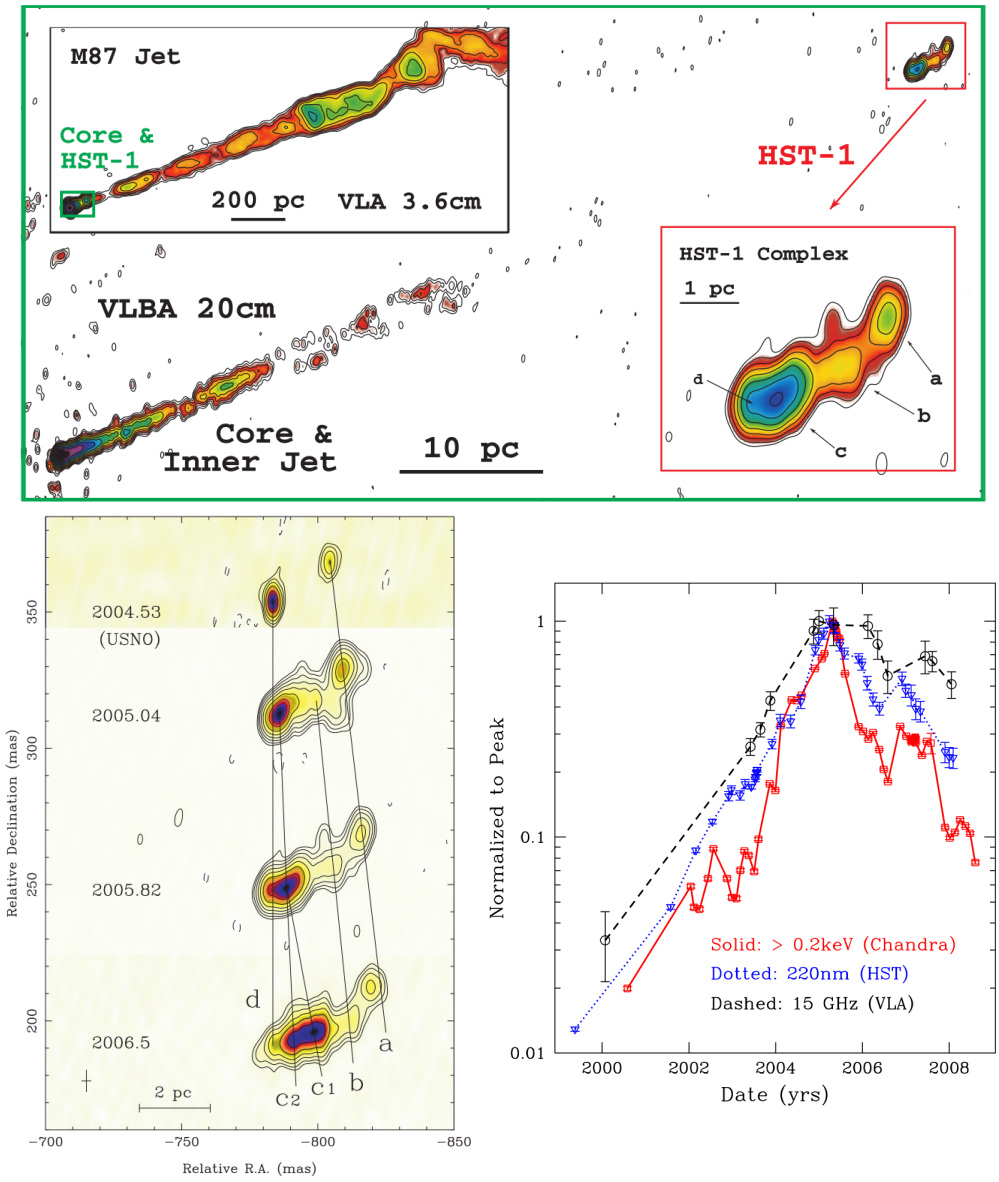

Figure 1.32. *Top :* total intensity emission of the ACZ of M87 and HST-1 (Cheung et al. 2007). The image in the upper left box shows the large-scale jet. *Bottom left :* maps showing the evolution of HST-1. Superluminal knots emerge from a quasi-stationary feature upstream of the complex. *Bottom right :* normalized light curves of HST-1 at multiple frequencies.

of a counterjet at small distances from the core, e.g., $\lesssim 2$ mas (Ly et al. 2007; Kovalev et al. 2007), where the jet is probably sub-relativistic. The jet extends up to less than 10 kpc from the core, beyond which it is disrupted and forms large-scale diffuse gas backflows (Owen et al. 1990). On kpc scales, the jet consists of many bright knots and fainter inter-knot regions emitting synchrotron radiation up to X-ray energies (see Figure 1.30).

Then, one may ask questions; "Does the M87 jet show gradual acceleration and collimation at distances $\lesssim 10^6 R_S$?"; "Does it have a recollimation shock?" The answer seems to be yes. Figure 1.31 shows the jet radius and $\Gamma\beta$ as a function of de-projected distance. The jet shape transitions from parabolic to conical near the Bondi radius, indicating that the jet is being collimated inside the Bondi radius (a parabolic jet shape means that jet opening angle decreases with distance). Furthermore, jet velocity increases from sub-relativistic to relativistic speeds inside the Bondi radius. Therefore, the jet is gradually accelerated and collimated simultaneously at $\lesssim 4 \times 10^5 R_S$ as the MHD theories predicted (Section 1.1.2). Right beyond the acceleration and collimation zone (ACZ), the jet radius suddenly drops by a factor of a few. This is where the HST-1 complex is located. Figure 1.32 shows the structure of the ACZ and HST-1. Several knots moving at relativistic speeds (with apparent speeds $\approx 4c$) emerge from a quasi-stationary upstream feature of HST-1. Besides, a strong multifrequency flare occurred in 2005 in radio to X-ray energies, implying that this region is a site for efficient particle acceleration. Combining the above observational results, many studies have suggested that HST-1 consists of a recollimation shock and several traveling fast MHD shock waves (e.g., Stawarz et al. 2006; Bromberg & Levinson 2009; Nakamura et al. 2010; Nakamura & Meier 2014).

1.2 The gas cloud G2 passing through the vicinity of Sagittarius A*

The radio-emitting source known as Sagittarius A* (Sgr A*) is associated with the supermassive black hole with a mass of $M_{\rm BH} \approx 4.3 \times 10^6 M_\odot$ (see, e.g., Genzel et al. 2010). Its emission mechanism is a matter of ongoing debate. Some studies show that its spectrum can be explained well by radiatively inefficient accretion flows (e.g., Yuan et al. 2003). However, other studies have pointed out that the larger scale jet-like features indicate that the emission need to originate from jets (e.g., Yusef-Zadeh et al. 2012; Li, Morris & Baganoff 2013).

In 2011, a gas cloud labeled G2 with the estimated mass of three times the Earth's mass was observed to move toward Sgr A*, on a nearly radial orbit (Gillessen et al. 2012, see the left panel of Figure 1.33). It was expected that interactions with the accretion flows toward Sgr A* might cause G2 to lose angular momentum, and as a result, parts of it may be accreted onto the black hole (Schartmann et al. 2012). Accordingly, an increased radio luminosity as well as an increase in source size might be expected. In addition, radio-bright outflows such as jets or winds launched from hot accretion flows (Yuan et al. 2003; Mościbrodzka et al. 2012), which have been proposed by previous studies but not been clearly detected, might become observable on spatial scales of $\lesssim 1$ mas.

However, there was no notable activity found in Sgr A* during the pericenter passage of G2. Sgr A* was quiescent from radio to X-rays in 2013 and 2014 (Akiyama et al. 2013; Brunthaler & Falcke 2013; Chandler & Sjouwerman 2014; Degenaar et al. 2014). Besides, our observations of Sgr A* with the global millimeter VLBI array (GMVA, Kim et al. 2018a) during the pericenter passage found that the closure phases for all the triangles of stations are consistent with zero within errors (Park et al. 2015, see Chapter 8). This indicates that brightness distribution of the source is centrally symmetric and there was no indication of asymmetric structures such as one-sided jets observed in many other AGNs. It seems that G2 was not disrupted and smoothly

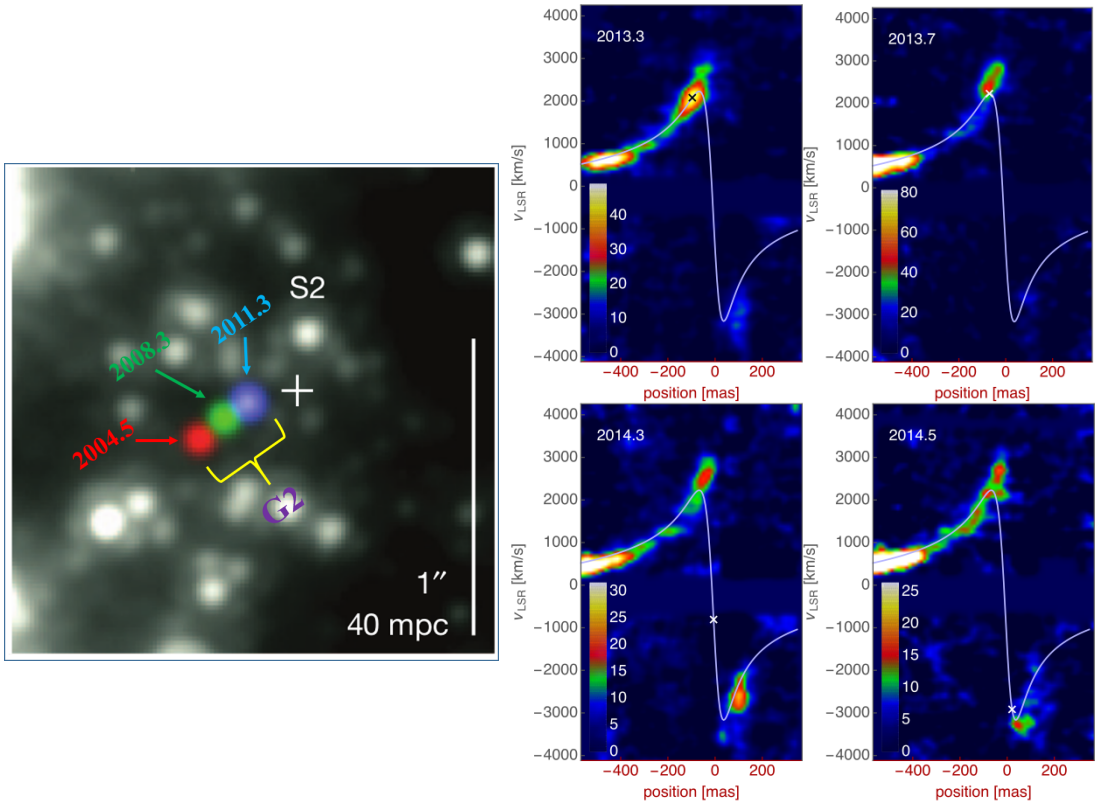

Figure 1.33. *Left :* position of the gas cloud G2 in three different time (red for 2004.5, green for 2008.3, and blue for 2011.3) with the location of Sgr A* marked as the white cross (Gillessen et al. 2012). *Right :* position-velocity diagrams of G2, which had passed through its pericenter near 2014 (Pfuhl et al. 2015).

passed through its pericenter (see the right panel of Figure 1.33). This may imply that G2 might be a star enshrouded by gas and/or dust (Witzel et al. 2014) or it is a gas cloud but it takes more years, comparable to viscous timescale (Schartmann et al. 2012), for a part of its gas to be accreted onto the black hole and to induce any enhanced AGN-like activity in Sgr A* (Kawashima et al. 2017).

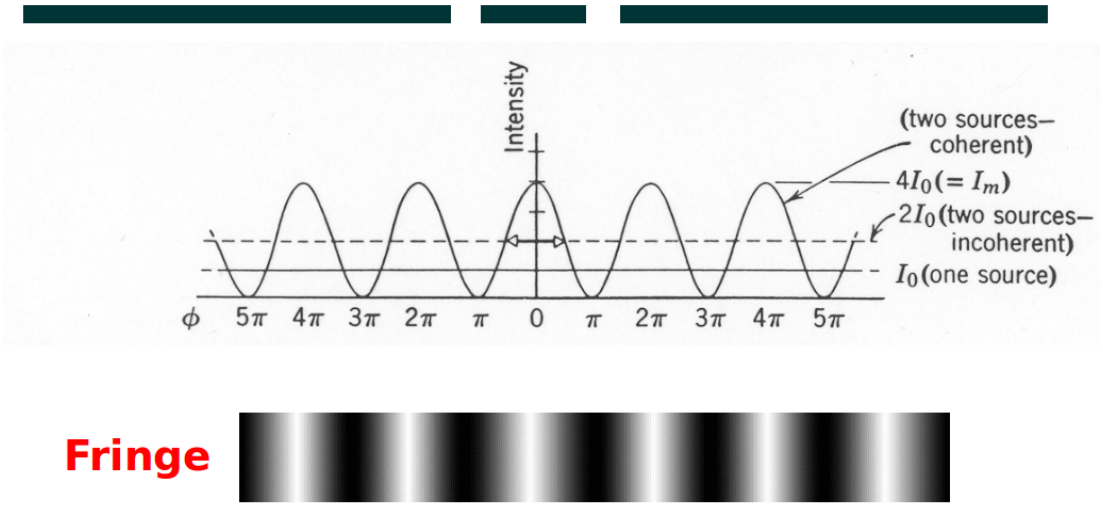

Figure 1.34. A schematic figure showing the well-known Young's double-slit experiment (taken from Prof. Yong-Sun Park's lecture note). The "fringe" pattern is produced by constructive and destructive interference between the two waves originating in the two slits.

1.3 Very Long Baseline Interferometry

In this thesis, we extensively use the VLBI technique to study AGN jets. This technique provides us with a ultra-high angular resolution, on the order of mas for most existing VLBI observatories at centimeter wavelengths, and even down to μas for global VLBI arrays at millimeter wavelengths like the EHT and GMVA. It uses a simple and fundumental physics: photons interfere with each other.

Figure 1.34 shows the well-known Young's double-slit experiment. The "fringe" pattern is produced by constructive and destructive interference between the two waves originating in the two slits (in the case of monochromatic planar wave). Similar to this experiment, when we observe the same light source with two telescopes, one can obtain an interference or fringe pattern by multiplying the signals detected at the telescopes. The only difference is that the Young's experiment records "intensity" of the interference pattern, which is positive only, while the radio telescope interference

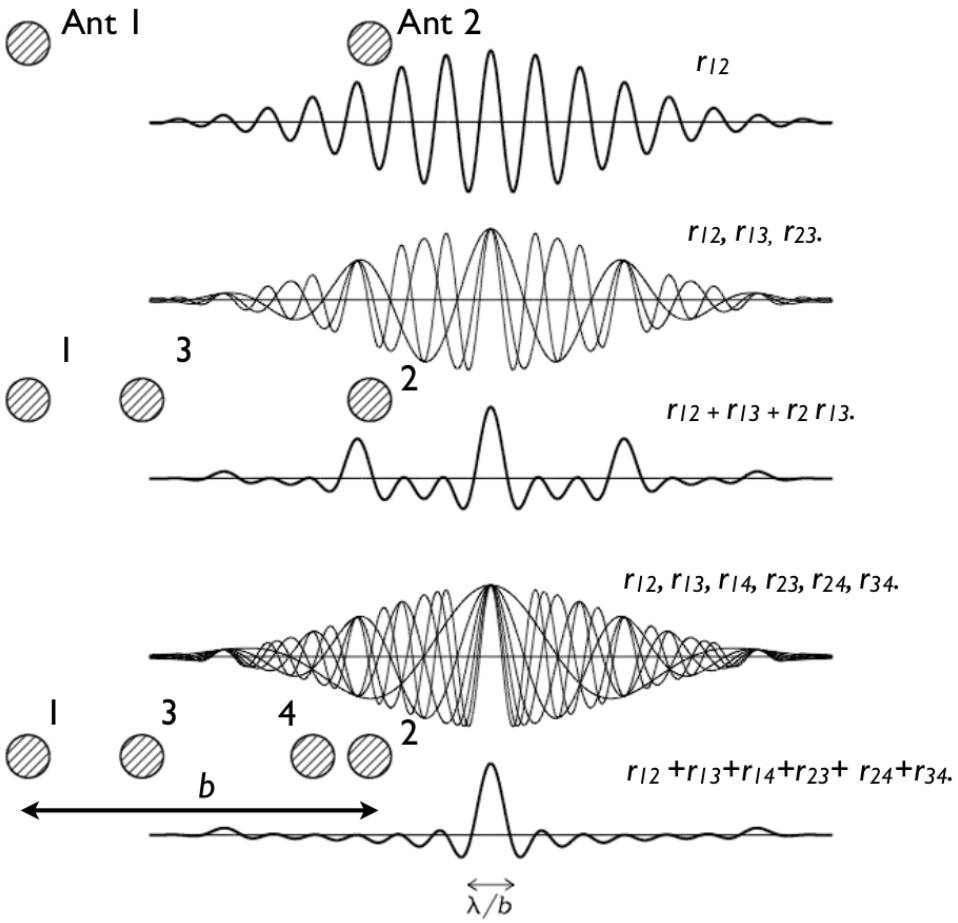

Figure 1.35. A schematic figure showing how interferometric fringe or beam patterns are produced (Condon & Ransom 2016). The top panel shows a fringe pattern made by two antennas ("Ant 1" and "Ant 2") having a finite bandwidth. The second and third panels from the top show three fringe patterns made by three different combinations of three antennas (r_{12}, r_{13}, r_{23}), and their superposition. Since the baseline lengths between different antenna pairs are different from each other, the fringe pattern after the superposition has "side lobes" with reduced amplitudes. The fourth and fifth panels show the case of four antennas. Now the fringe pattern has a strong "main lobe" and significantly suppressed side lobes. The width of the main lobe can be approximated by λ/b, where b is the maximum distance between different antennas.

pattern can have both positive and negative values because the full sinusoidal wave signals are recorded by the telescopes. The width of the central fringe hump is on the order of λ/b, where λ is the wavelength and b is the distance between the two slits.

Now, let us consider that the telescopes have a finite bandwidth. The resulting fringe pattern would be described by superposition of various fringe patterns having different fringe widths because waves having different λ are superposed. The fringe patterns for different λ waves other than the central hump are not the same anymore and their amplitudes become smaller compared to the case of monochromatic wave. This is shown in the top panel of Figure 1.35. Now suppose that we have three antennas having different distances between different pairs. The fringe pattern produced by these antennas can be described by superposition of the three fringe patterns produced by the three different antenna pairs (the second panel from the top). Since the baseline lengths between different antenna pairs are different from each other, the fringe pattern after the superposition has "side lobes" with reduced amplitudes compared to the two antennas case (the third panel from the top). Nevertheless, the amplitude of the strongest side lobe is still larger than half of the "main lobe". In the case of four antennas, the fringe pattern has a strong "main lobe" and significantly suppressed side lobes. The width of the main lobe can be approximated by λ/b, where b is the maximum distance between antennas (the fourth and fifth panels from the top).

Figure 1.35 illustrates how we can achieve very high angular resolution with VLBI. One can either increase the maximum baseline b or decrease the wavelength λ to obtain finer resolution. However, this example assumes one-dimensional distribution of different antennas (and thus of fringe patterns), while beam patterns must be two-dimensional to map the source's brightness distribution projected on the sky plane. Also, the fringe widths are determined by the "projected" baseline lengths, not by the physical distance between antennas. Both the "length" and "direction" of this projected baseline is varying over time due to the rotation of the Earth. Now one can easily imagine the following situation; as we obtain fringe patterns between different antennas having various projected baseline "vectors" (so both lengths and direction are

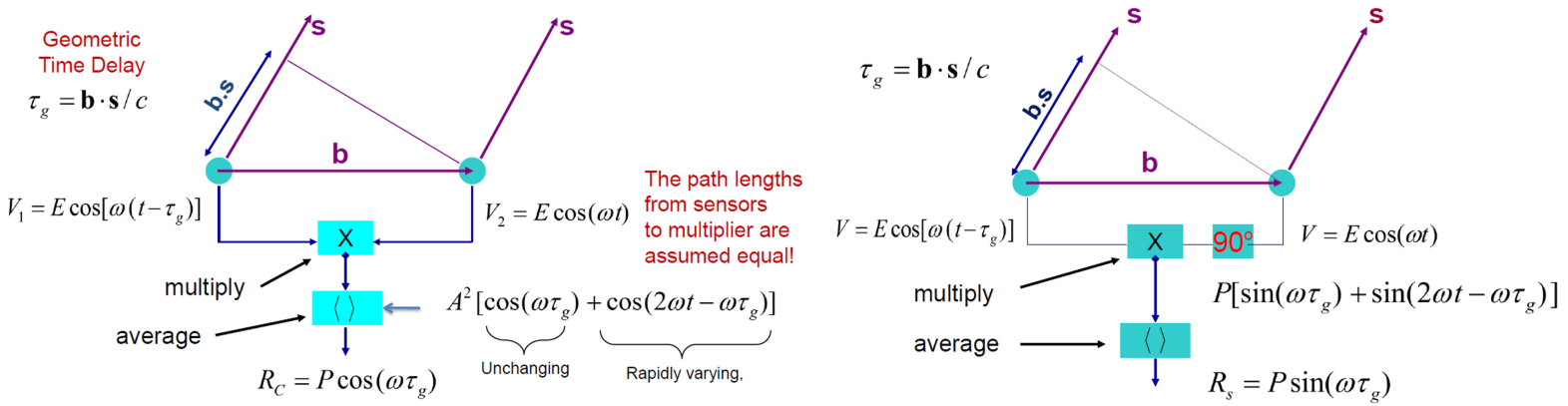

Figure 1.36. *Left :* a schematic diagram showing the output after (i) multiplying the signals obtained from two antennas and (ii) taking the time average. The baseline vector ($\mathbf{b}$) and the vector toward the source ($\mathbf{s}$) makes the geometric time delay ($\mathbf{b}\cdot\mathbf{s}/c$) for one of the antennas. *Right :* same as the left figure but after inserting a 90° phase shift in one of the signal paths. A complex function called visibility ($V_\nu(\mathbf{b})$) constructed by combining the two output signals is related with the source's brightness distribution ($I_\nu(\mathbf{s})$).

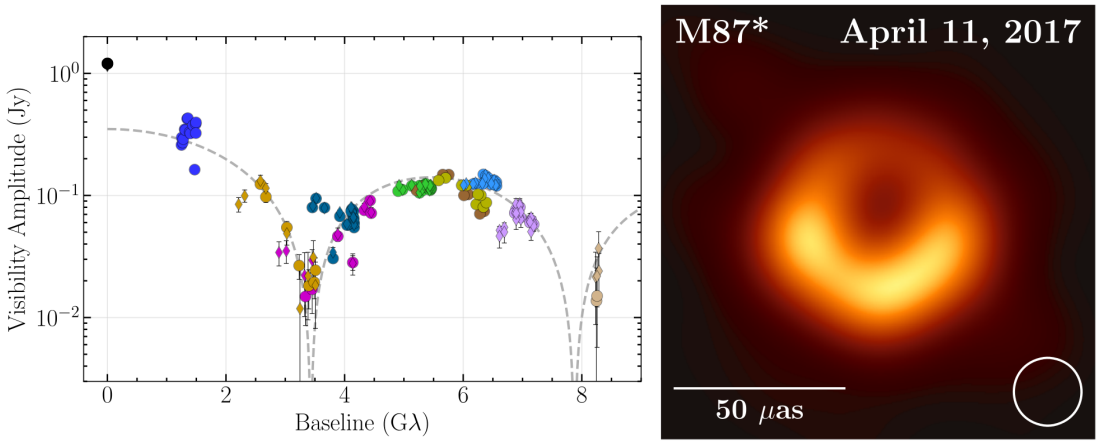

Figure 1.37. *Left :* calibrated visibility amplitudes of M87 as a function of projected baseline length observed by the EHT on 2017 April 11. The Fourier transform of an azimuthally symmetric thin ring model with a diameter of 46 μas is shown with a dashed line. *Right :* EHT image of M87 reproduced by the visibility data presented in the left figure.

involved), we can obtain a better beam pattern.

This concept can be mathematically expressed by the van Cittert- Zernike theorem. The left panel of Figure 1.36 shows the output of correlation of the signals received by two antennas. The geometrical time delay between the signals is $\tau_g = \mathbf{b} \cdot \mathbf{s}/c$, where $\mathbf{b}$ denotes the baseline vector and $\mathbf{s}$ is a vector toward the source. By multiplying the two signals and taking the time average, one can obtain $R_C \equiv P\cos(\omega\tau_g)$, where $P \equiv |E|^2$ represents the source's intensity. One can also obtain $R_S \equiv P\sin(\omega\tau_g)$ by inserting a 90° phase shift in one of the signal paths. Now we can define a complex function $V_\nu(\mathbf{b}) \equiv R_C - iR_S = \int\int I_\nu(\mathbf{s}) e^{-2\pi i \mathbf{b}\cdot\mathbf{s}/c} d\Omega$. Note that R_C and R_S include signals from the whole brightness distribution of a target source and thus integration over solid angle is taken. This relation indicates that the source's brightness distribution can be obtained by performing inverse Fourier transform of $V_\nu(\mathbf{b})$, which we call "visibility".

Therefore, to obtain the image of our target, what we need is to obtain the visibility. $\mathbf{b}$ is a vector on a plane which is parallel to the sky plane and can be decomposed into

two components that are orthogonal to each other, namely u and v. If we obtain the correlated signals for various baseline vectors (thus having wide ranges of u and v), then we fill in the visibilities in the uv-plane. Of course, one cannot obtain visibilities for an infinite range of u and v, which would distort the source's brightness distribution after inverse Fourier transform. This effect can be expressed as:

$$I^D(l,m) = \int\int S(u,v)V(u,v)e^{+i(lu+vm)}dudv, \tag{1.5}$$

where l and m are the components of $\mathbf{s}$ on the sky plane that are orthogonal to each other. $S(u,v)$ is called a "sampling function", which satisfies $S(u,v) = 1$ for sampled (u,v) and $S(u,v) = 0$ otherwise. Thus, the source's brightness distribution obtained from the "sampled" visibilities ($I^D(l,m)$) is not coincident with the real brightness distribution ($I(l,m)$) due to the imperfect sampling. According to the convolution theorem, $I(l,m)*s(l,m) = I^D(l,m)$, where $s(l,m)$ is the Fourier transform of the sampling pattern ($S(u,v)$) and corresponds to the "beam pattern" (Figure 1.35). Therefore, one needs to "deconvolve" the observed "dirty image" ($I^D(l,m)$) with the sampling pattern to obtain the real image. Figure 1.37 shows an example of observed visilibity data and an image obtained by Fourier transform of the data and by some deconvolution procedures (EHT Collaboration et al. 2019a).

1.4 Power spectrum of light curve

Similar to the distortion of source's brightness distribution by the limited sampling patterns, temporal power spectra (often called periodograms) of AGN light curves are also subject to be distorted by the limited sampling patterns. Variability in light curves is one of the main characteristics of AGNs. A lot of studies have focused on finding any periodic signal in the light curves, which would be related to rotation of "hot spots" around the black holes, precession of AGN jets, motion of binary black holes, and so on. However, one cannot obtain continuous and infinite light curves and there must be distortion in the power spectra obtained by Fourier transform of the light curves. Figure 1.38 shows an example. The power spectra (solid black lines in the

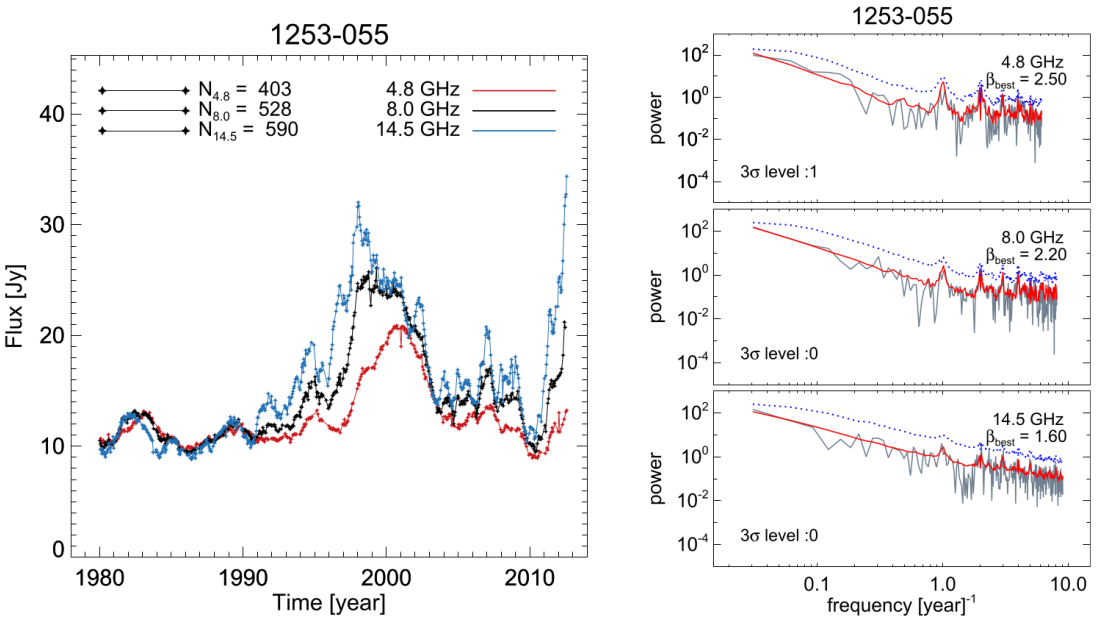

Figure 1.38. Light curves of the quasar 3C 279 (left) observed by the University of Michigan Radio Astronomy Observatory at three radio frequencies. If we obtain power spectra of these light curves by performing Fourier transform (black solid lines in the right figure), then we can find that there are local peaks at several frequency bins. These are not generated by periodic signals intrinsic to the source but by the sampling pattern of light curves. The red curves are model power spectra obtained by assuming no significant periodic signal and taking into account the limited sampling of the light curves. See Chapter 7.1 for more details.

right figure) of the light curves of 3C 279 (shown in the left figure) show several local peaks. These peaks are reproduced by the model power spectra assuming no significant periodic signal and distorted by the sampling patterns of the observed light curves. This means that the peaks in the power spectra are not produced by periodic signals intrinsic to the source but by the limited sampling of the light curves. Therefore, one must carefully take into account possible effects of sampling pattern when investigating temporal power spectra of AGN light curves.

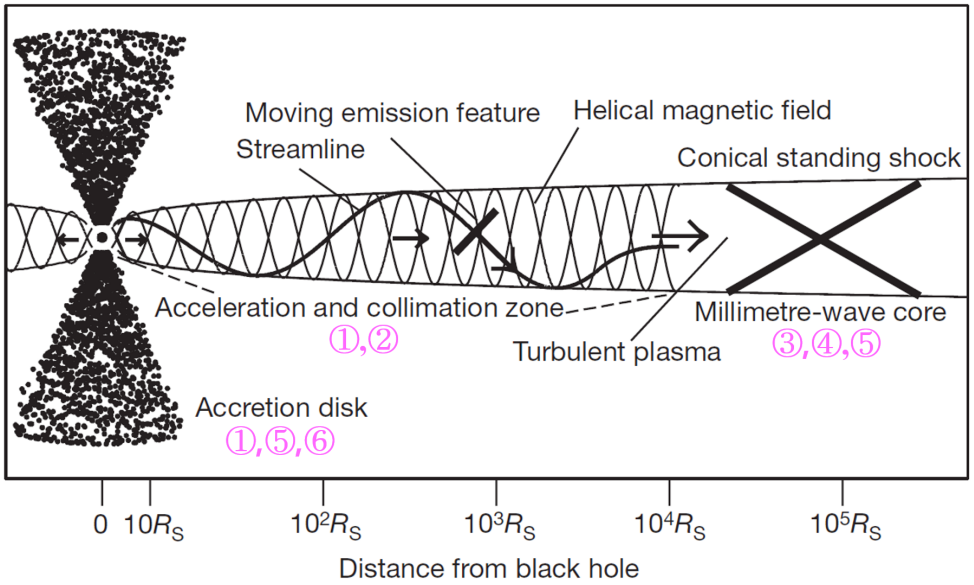

Methodologies

Flares &Variability
④,⑤,⑥

Jet Kinematics
②,④

Linear Polarization & Faraday Rotation
①,③,④

High Energy emission
④

① **Faraday Rotation in the Jet of M87 inside the Bondi radius (Chapter 2).**
② **Intensive Monitoring of the M87 Jet with KaVA (Chapter 3).**
③ **Revealing the Nature of Blazar Cores through Multifrequency Polarimetry with KVN (Chapter 4).**
④ **Ejection of Double Knots from the Core of PKS 1510-089 during the 2015 γ-ray flares (Chapter 5).**
⑤ **The long-term centimeter variability of AGN (Chapter 6, 7).**
⑥ **No Asymmetric Outflows from Sagittarius A* during the Pericenter Passage of G2 (Chapter 8).**

Figure 1.39. A schematic diagram of the AGN jet model (Marscher et al. 2008), which is already presented in Figure 1.9. Jets are launched in the vicinity of the central black hole by the accreteion of matter, propagate through the acceleration and collimation zone, and end up with a conical standing shock. The circled numbers indicate different physical regions that different chapters in this thesis probe (listed in the lower part) with different methodologies listed on the right side.

1.5 Thesis outline

The thesis is structured as follows. In Chapter 2, we study Faraday rotation in the jet of M87 with multifrequency VLBI observations. Investigating Faraday rotation allows us to study the properties of hot accretion flows in M87 and their role in jet collimation and acceleration. Referring to Section 1.1.2, 1.1.3, and 1.1.5 will be helpful for understanding the background of this study. In Chapter 3, we investigate kinematics of the M87 jet to understand the jet acceleration mechanism (see also Section 1.1.2 and 1.1.5). In Chapter 4, we try to reveal the nature of the blazar's radio cores through multifrequency Faraday rotation observations with the KVN (see also Section 1.1.4). In Chapter 5, we study the mechanism of high energy emission in the bright quasar PKS 1510-089 at γ-ray energy bands by exploiting the long-term, multi-wavelength light curves and performing the jet kinematic and linear polarimetric analysis (see also Section 1.1.4). In Chapter 6 and 7, we investigate the long-term radio variability of many AGNs and its relation to the accretion process (see also Section 1.1.3 and 1.4). In Chapter 8, we constrain the possible effects of the passage of the gas cloud G2 through the vicinity of Sgr A* (see also Section 1.2).

To sum up, this thesis covers various "components" of AGNs and the related physics. Figure 1.39 shows the basic picture of AGN jets based on the current understanding (Marscher et al. 2008). Jets are launched in the vicinity of the central black hole by the accreteion of matter, propagate through the acceleration and collimation zone, and end up with a conical standing shock. This figure outlines how different studies presented in various chapters are related with different physical regions. Each region shows different characteristics and spans various spatial scales, which requires different methodologies and tools for studying. However, the physical processes which govern different regions are closely related to each other and one needs to have a "multi-scale view" of AGN jets for a better understanding.

We note that the results presented in this thesis were published in or submitted to some journals (Park & Trippe 2014, 2017; Park et al. 2015, 2018, 2019a,b,c).

Chapter 2

Faraday Rotation in the Jet of M87 inside the Bondi Radius: Indication of Winds from Hot Accretion Flows Confining the Relativistic Jet[†]

Abstract

We study Faraday rotation in the jet of M87 inside the Bondi radius using eight Very Long Baseline Array data sets, one at 8 GHz, four at 5 GHz, and three at 2 GHz. We obtain Faraday rotation measures (RMs) measured across the bandwidth of each data set. We find that the magnitude of RM systematically decreases with increasing distance from the black hole from 5,000 to 200,000 Schwarzschild radii. The data, showing predominantly negative RM sign without significant difference of the RMs on the northern and southern jet edges, suggest that the spatial extent of the Faraday

[†]The contents of this chapter was originally published in the Astrophysical Journal (Park et al. 2019a)

screen is much larger than the jet. We apply models of hot accretion flows, thought to be prevalent in active galactic nuclei having relatively low luminosity such as M87, and find that the decrease of RM is described well by a gas density profile $\rho \propto r^{-1}$. This behavior matches the theoretically expected signature of substantial winds, nonrelativistic uncollimated gas outflows from hot accretion flows, which is consistent with the results of various numerical simulations. The pressure profile inferred from the density profile is flat enough to collimate the jet, which can result in gradual acceleration of the jet in a magneto-hydrodynamical process. This picture is in good agreement with the observed gradual collimation and acceleration of the M87 jet inside the Bondi radius. The dominance of negative RMs suggests that jet and wind axis are misaligned such that the jet emission exposes only one side of the toroidal magnetic fields permeating the winds.

2.1 Introduction

Active galactic nuclei (AGNs) are powered by accretion of gas onto supermassive black holes at the centres of galaxies. It is now widely believed that there are two distinct modes of black hole accretion: cold and hot. A cold accretion flow forms an optically thick but geometrically thin disk, radiating thermal blackbody emission with the gas temperature in the range of $10^4 - 10^7$ K (Shakura & Sunyaev 1973, see e.g., Netzer 2013 for a review). On the other hand, hot accretion flows are thought to be optically thin but geometrically thick with a large portion of the gravitational binding energy of the accreted gas advected into the black hole (e.g., Ichimaru 1977; Narayan & Yi 1994, see e.g., Yuan & Narayan 2014 for a review). The most critical factor in determining the accretion mode is the mass accretion rate ($\dot{M}$) relative to the Eddington rate ($\dot{M}_{\rm Edd}$) or, equivalently, the disk luminosity ($L_{\rm disk}$) relative to the Eddington luminosity ($L_{\rm Edd}$). Observationally, $L_{\rm disk}/L_{\rm Edd} \approx 1\%$ is usually assumed to be a dividing line between the two accretion modes (e.g., Ghisellini et al. 2011; Heckman & Best 2014).

Most ($\approx 98\%$) nearby AGNs spend their lives in a low accretion state, making them low-luminosity AGNs (LLAGNs, Ho 2008; Netzer 2013) which are thought to

be powered by hot accretion flows. One of the representative models of hot accretion flows is the advection-dominated accretion flows (ADAFs, Ichimaru 1977; Narayan & Yi 1994; Narayan & Yi 1995a,b), which is characterized by self-similar solutions with a density profile of $\rho \propto r^{-1.5}$ and a constant mass accretion rate as a function of spherical radius (r). Two important properties found in ADAFs are that (i) the flows are convectively unstable and (ii) the Bernoulli parameter of the flow is positive, indicating that strong outflows are a natural outcome of hot accretion flows (e.g., Narayan & Yi 1994; Narayan & Yi 1995a). These properties led to two variants of ADAF, convection-dominated accretion flow (CDAF, e.g., Narayan et al. 2000; Quataert & Gruzinov 2000; Igumenshchev & Narayan 2002) and adiabatic inflow-outflow solution (ADIOS, e.g., Blandford & Begelman 1999, 2004; Begelman 2012), respectively.

A number of numerical simulations have been performed to better understand the dynamics of hot accretion flows (e.g., Stone et al. 1999; Igumenshchev & Abramowicz 2000; Machida et al. 2001; Igumenshchev et al. 2003; Pen et al. 2003, see Yuan et al. 2012b for a review). One of the most important findings consistently seen in those simulations is that the mass accretion rate decreases with decreasing radius, namely $\dot{M}_{\rm in}(r) \propto r^s$ with $s > 0$, or, equivalently, the density profile flatter than the one of ADAF self-similar solutions, i.e., $\rho \propto r^{-q}$ with $q < 1.5$. The CDAF model explains the inward decrease of $\dot{M}_{\rm in}$ with large fluxes of both inflowing and outflowing gas in turbulent convective eddies and predicts $s = 1$ and $q = 0.5$ (e.g., Narayan et al. 2000; Quataert & Gruzinov 2000; Igumenshchev & Narayan 2002). In the ADIOS model, the inward decrease of $\dot{M}_{\rm in}$ is due to a genuine mass loss via gas outflows; the model predicts $0 < s < 1$ and $0.5 < q = 1.5 - s < 1.5$ (Blandford & Begelman 1999, 2004). Values of $s = 0.4 - 0.8$ and $q = 0.5 - 1$ were preferentially found in simulations (see Yuan et al. 2012b and references therein), which is in general consistent with the ADIOS model. Indeed, both three-dimensional (3D) general relativistic magneto-hydrodynamic (GRMHD) simulations of hot accretion flows (Narayan et al. 2012) and 2D simulations of hot accretion flows including magnetic fields (Yuan et al. 2012a) showed that hot accretion flows are convectively stable, supporting that hot accretion flows can lose

substantial mass via gas outflows (but see Bu et al. 2016a,b for gas outflows on large spatial scales when the gravitational potential of the nuclear star cluster is included).

Nevertheless, knowledge of the properties of outflows from hot accretion flows has been limited due to the difficulty in tracing the actual outflows by discriminating them from turbulent motions. Yuan et al. (2015) used a "virtual particle trajectory" approach and overcame the difficulty in their 3D GRMHD simulations. They found that the outflows from hot accretion flows are dominant in the polar region, while inflows are filling in the equatorial regions, and the geometry of the outflows can be described as conical. Similar results were obtained in another GRMHD simulation in which the collimated and relativistic jet launched from a spinning black hole is surrounded by non-relativistic gas outflows (Sadowski et al. 2013). We clarify the terminology of gas outflows with different physical properties: hereafter, *jet* refers to a highly magnetized, collimated and relativistic gas outflow possibly launched from a spinning black hole (Blandford & Znajek 1977) or from the innermost region of an accretion disk (Blandford & Payne 1982), whereas *wind* refers to a moderately magnetized, un-collimated and non-relativistic gas outflow launched from the accretion flow.

Winds have been frequently observed in luminous AGNs for which cold accretion is thought to be operating (e.g., Crenshaw et al. 2003; Tombesi et al. 2010). However, it is challenging to confirm the presence of winds from hot accretion flows, i.e., in LLAGNs, because the winds are believed to be very hot and generally fully ionized (Yuan et al. 2018). Even though UV and X-ray absorption lines with high outflow velocities have been found in some LLAGNs (e.g., Tombesi et al. 2014), due to limited angular resolution it is unclear whether those outflows originate from the accretion flows or from outside regions (e.g., Crenshaw & Kraemer 2012). Accordingly, there have been attempts to directly determine the radial density profiles of hot accretion flows in a few nearby LLAGNs with X-ray observations. For example, Wong et al. (2011, 2014) presented a density profile of NGC 3115 broadely consistent with $\rho \propto r^{-1}$ inside the Bondi radius, within which the gravitational potential energy of the central black hole is larger than the thermal energy of the gas, using Chandra X-ray observations. Russell

et al. (2015) showed a similar density profile of $\rho \propto r^{-1}$ for M87 inside the Bondi radius and Russell et al. (2018) found a possible difference between the density profiles in the polar region, i.e., along the jet axis, with $\rho \propto r^{-0.93}$, and in the equatorial region, with $\rho \propto r^{-1.5}$, from Chandra observations. Although these results are consistent with the ADIOS model and possibly indicate the presence of winds in those LLAGNs, they were obtained near the Bondi radius; measurements of density profiles well inside the Bondi radius are needed for a firm conclusion. We note that there are some studies which favor the presence of winds in the supermassive black hole in our Galactic Center, Sagittarius A* (Sgr A*), using spectral energy distribution modelling (Yuan et al. 2003), modelling of the X-ray emission lines (Wang et al. 2013), numerical simulations reproducing the *Fermi* Bubbles possibly inflated by those winds (Mou et al. 2014), and modelling of the motion of the gas cloud G2 slowed down by a drag force (Gillessen et al. 2018).

Winds have important astrophysical implications. The actual rate of mass accreted onto the black hole could be substantially smaller than the accretion rate measured through X-ray observations at the Bondi radius (Bondi accretion rate, $\dot{M}_{\rm Bondi}$) due to the mass loss via winds. Therefore, a major factor in the faintness of LLAGNs might be the reduced mass accretion rate (Bower et al. 2003), not a very low radiative efficiency as usually assumed (Xie & Yuan 2012). Also, rotational energy of spinning black holes must be extracted efficiently to explain the observed high kinetic jet powers with small mass accretion rate (Nemmen & Tchekhovskoy 2015). Furthermore, winds have a large cross section and may regulate star formation in the host galaxies via momentum transfer (Yoon et al. 2018; Yuan et al. 2018).

Another important role played by winds is their effect on the collimation of AGN jets. It has been a long-standing problem how jets in AGNs can be highly collimated and accelerated to nearly the speed of light. It is widely accepted that the acceleration and collimation zone in AGN jets are co-spatial and located within about 10^5 Schwarzschild radii ($r_{\rm s}$, Marscher et al. 2008). MHD models predict that magnetic fields can accelerate AGN jets to relativistic speeds if the jets are systematically collimated (e.g., Vlahakis 2015). It is difficult for the jets to be confined by themselves (e.g., Eichler 1993; Begel-

man & Li 1994; Komissarov et al. 2007) and an external confining medium is necessary to produce the observed highly collimated jets. Previous theoretical studies suggest that winds are the primary candidates for this medium (Tsinganos & Bogovalov 2002; McKinney & Gammie 2004; Bogovalov & Tsinganos 2005; De Villiers et al. 2005; Gracia et al. 2005; Globus & Levinson 2016; Nakamura et al. 2018).

M87 serves as a unique laboratory for studying AGN jets and their formation, collimation, and acceleration thanks to its proximity with a distance of 16.7 Mpc (Mei et al. 2007) and its extremely massive black hole with a mass of $M_{\rm BH} = (3.5-6.6)\times10^9 M_\odot$ (Gebhardt & Thomas 2009; Gebhardt et al. 2011; Walsh et al. 2013). Accordingly, this source has been studied extensively especially on scales corresponding to the jet acceleration and collimation zone. One of the most notable results is the discovery of an edge-brightened jet structure with a systematic collimation of the jet on scales $\gtrsim 100\ r_{\rm s}$ (Junor et al. 1999). The large-scale collimation profile shows a transition from a semi-parabolic jet with $z \propto R^{1.7}$, where z and R denote the jet distance and the jet radius, respectively, to a conical jet at a transition location near the Bondi radius (Asada & Nakamura 2012). The precise constraint on the location of the black hole by core-shift analysis (Hada et al. 2011) together with the source size measured with the Event Horizon Telescope (EHT) at 1.3 mm (Doeleman et al. 2012) allowed to constrain the innermost collimation profile. The profile is consistent with a parabolic geometry (Nakamura & Asada 2013) but shows indication of a slight deviation from the larger scale profile (Hada et al. 2013, see also Hada et al. 2016; Mertens et al. 2016; Kim et al. 2018a; Walker et al. 2018).

There has been growing evidence for gradual acceleration of the jet inside the Bondi radius as well, though the scale on which bulk jet acceleration occurs is a matter of debate. Observations of HST-1, a peculiar feature that consists of a quasi-stationary component from which superluminal components are emerging and is the location of the multiwavelength flare observed around 2005 (Cheung et al. 2007), show superluminal motions with velocities larger than $6c$ (with c being the speed of light) at optical wavelengths (Biretta et al. 1999), and with velocities of $\approx 4c$ at radio wavelengths

(Cheung et al. 2007; Giroletti et al. 2012). Asada et al. (2014) found a systematic acceleration of the jet at a distance of $\approx 10^5\ r_{\rm s}$, supported by the slow velocities obtained on smaller scales with the Very Long Baseline Array (VLBA) at 15 GHz (Kovalev et al. 2007). However, as already noted in Kovalev et al. (2007), the observed one-sideness of the jet at a distance of only ≈ 3 milliarcseconds from the radio core is difficult to explain with sub-luminal motions at the same distance. Other studies suggest that the jet acceleration occurs on a much smaller scale (Mertens et al. 2016; Hada et al. 2017; Walker et al. 2018) and constraining the acceleration profile at various jet distances is still on-going (Park et al. 2018, in prep.).

The observation of jet collimation and acceleration on the same spatial scales is consistent with the scenario that the jet is collimated by an external medium with a relatively shallow pressure profile, which results in gradual acceleration of the jets in an MHD process (Komissarov et al. 2009; Lyubarsky 2009). However, it has not been possible to either probe the external medium with observations or to verify the general picture of jet collimation and acceleration. In this study, we investigate Faraday rotation, the rotation of the plane of linear polarization by intervening magnetic fields, in the jet of M87. When linearly polarized emission passes through a magnetized medium, Faraday rotation occurs. The amount of rotation of the electric vector position angle (EVPA), $\Delta\chi$, is related to the Faraday rotation measure (RM) via $\Delta\chi = {\rm RM}\lambda^2$, where λ is the wavelength. RM is proportional to the integral of the product of free electron density (n_e) and line of sight component of the magnetic field (B) along the path from emitter to observer (l), meaning ${\rm RM} \propto \int n_e(l)B(l)dl$ (e.g., Gardner & Whiteoak 1966). Thus, observations of the Faraday rotation of polarized jets can probe the magnetized medium between the jet and the observer, i.e., the external medium. Unfortunately, the jets in nearby LLAGNs are usually very weakly polarized (see e.g., Bower et al. 2017 for more discussion) and the Faraday rotation observations have been limited to specific emitting regions in some sources such as Sgr A* (e.g., Bower et al. 2003, 2018; Marrone et al. 2006, 2007; Liu et al. 2016), 3C 84 (e.g., Taylor et al. 2006; Plambeck et al. 2014; Nagai et al. 2017; Kim et al. 2018b), and M87 (e.g., Zavala & Taylor 2002;

Kuo et al. 2014). In this work, we obtain RM values at various locations in the M87 jet by exploiting multifrequency VLBA data from multiple epochs and present the radial RM profile of the jet between 5,000 and 200,000 $r_{\rm s}$. Then, we test the conjecture that winds are launched from hot accretion flows and serve as the external confining medium of the jet using the RM data.

2.2 Archival data and data reduction

We searched the VLBA archive for data suitable for a study of linear polarization and Faraday rotation in the M87 jet. We selected those data in which (i) different sub-bands are sufficiently separated in wavelength, (ii) both parallel and cross-hand visibilities are available, and (iii) M87 is observed as a primary target in full-track observing mode. Using these criteria, we are left with one data set at 8 GHz, four data sets at 5 GHz, and many data sets at 2 GHz. We note that there are multifrequency VLBA data obtained quasi-simultaneously in 7 different sub-bands from 8.1 and 15.2 GHz in the literature (Zavala & Taylor 2002) which we could not find in the VLBA archive. Therefore, these data are not included in our analysis but we show that our results are consistent with the results of their work in Section 2.3.4. We found that the distribution of RM in the jet in different data sets at 2 GHz are more or less the same and chose three data sets among them for which all 10 VLBA antennas are available and the weather was good. We show the list of the eight VLBA archive data sets we analyzed and the basic information for each observation in Table 2.1. In total, we analyzed eight different polarization data sets of M87 taken by the VLBA (one at 8 GHz, four at 5 GHz, and three at 2 GHz).

A standard data post-correlation process was performed with the National Radio Astronomy Observatory's (NRAO) Astronomical Image Processing System (AIPS, Greisen 2003). We corrected ionospheric dispersive delays using the ionospheric model provided by the Jet Propulsion Laboratory, antenna parallactic angles, and instrumental delays using scans on bright calibrators. Amplitude calibration was performed by using the antenna gain curves and system temperatures with an opacity correction.

Table 2.1. Summary of VLBA archive data

Project code (1)	Obs. date (2)	Frequency [GHz] (3)	D Term cal. (4)	EVPA cal. (5)
BJ020A	1995 Nov 22	8.11, 8.20, 8.42, 8.59	OQ 208	OJ 287 (UMRAO)
BJ020B	1995 Dec 09	4.71, 4.76, 4.89, 4.99	OQ 208	3C 273 (UMRAO)
BC210B	2013 Mar 09	4.85, 4.88, 4.92, 4.95 4.98, 5.01, 5.04, 5.08	M87	N/A
BC210C	2014 Jan 29	4.85, 4.88, 4.92, 4.95 4.98, 5.01, 5.04, 5.08	M87	N/A
BC210D	2014 Jul 14	4.85, 4.88, 4.92, 4.95 4.98, 5.01, 5.04, 5.08	M87	N/A
BH135F	2006 Jun 30	1.65, 1.66, 1.67, 1.68	M87	3C 286
BC167C	2007 May 28	1.65, 1.66, 1.67, 1.68	M87	3C 286
BC167E	2007 Aug 20	1.65, 1.66, 1.67, 1.68	M87	3C 286

Note. — (1) Project code of VLBA observations. (2) Observation date. (3) Observing frequency for all sub-bands. (4) Source used for calibration of instrumental polarization. (5) Source used for EVPA calibration. '(UMRAO)' means that we corrected the EVPA by comparing the VLBI integrated EVPAs with the EVPAs obtained from contemporaneous single dish observations by the University of Michigan Radio Astronomy Observatory. N/A implies that EVPA calibration was not available. 3C 286 has a stable integrated EVPA of 33° at the frequencies of our interest (Perley & Butler 2013).

We performed global fringe fitting with a solution interval between 10 and 30 seconds assuming a point source model. Bandpass calibration was performed by using scans on bright calibrators. The cross-hand R-L phase and delay offsets were calibrated by using scans on bright calibrators. We used the Caltech Difmap package (Shepherd 1997) for imaging and phase and amplitude self-calibration. We determined the feed polarization leakage (D-terms) for each antenna and for each sub-band by using the task LPCAL (Leppänen et al. 1995) in AIPS with a total intensity model of the D-term calibrators. We used OQ 208 or M87 for the D-term correction (Table 2.1) because of their very low degree of linear polarization (usually $\lesssim 1\%$).

The EVPA calibration was performed by comparing the integrated EVPAs of the VLBI maps of the calibrators with the EVPAs obtained in contemporaneous single dish polarization observations of the University of Michigan Radio Astronomy Observatory (UMRAO), or by using 3C 286 for which a stable integrated EVPA of $\approx 33^\circ$ is known at the frequencies of our interest (Perley & Butler 2013), if available. However, we note that EVPA calibration is not critical for our purpose because the expected amount of EVPA correction for different sub-bands is almost the same. For example, we present the RM map and EVPA as a function of λ^2 at the map center of one of the calibrators in BC210B session, 0716+714, in Figure 2.1. Even though we could not perform EVPA correction for this epoch (see Table 2.1), the difference in EVPAs in different sub-bands is much smaller than the error bars and the obtained RM value is consistent with the previous measurements with the VLBA (Hovatta et al. 2012). We check the RM of the calibrators in all the data we analyzed to ensure that the detected RM for M87 is not due to potential errors in EVPA calibration but is intrinsic to the source itself.

We obtained RM values at various positions in the M87 jet from measuring EVPAs in different sub-bands (intermediate frequencies) in each dataset (see Table 2.1). We considered four error sources in EVPA: random error, systematic error induced by imperfect CLEAN procedures, by imperfect D-term calibration, and by imperfect EVPA calibration. We present the details of error estimation in Appendix A.1. For obtaining RM maps, we first convolved the maps in different sub-bands with the synthesized

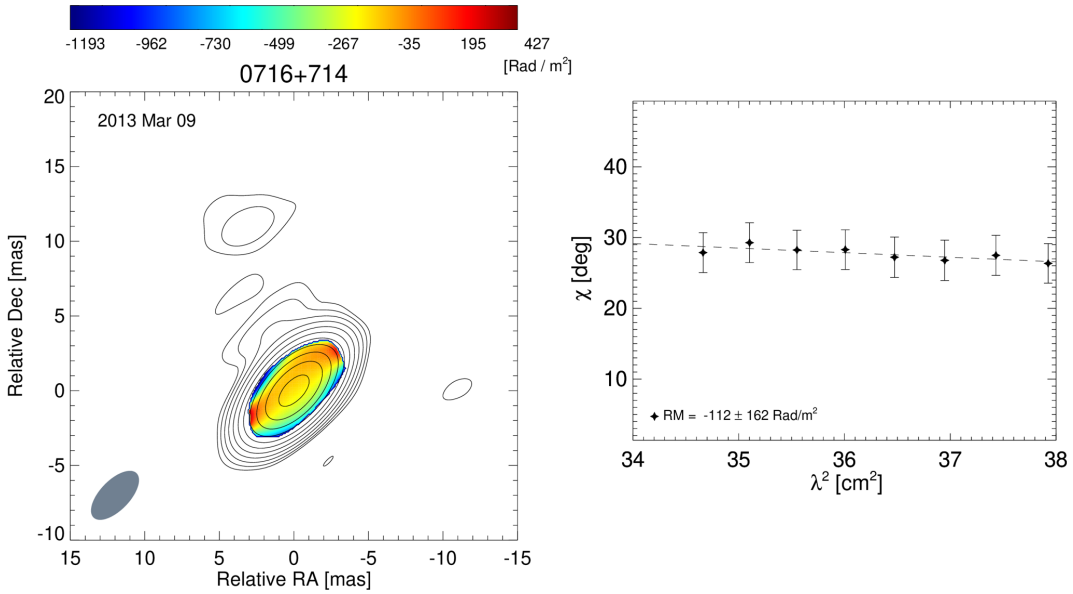

Figure 2.1. *Left:* Color map of the distribution of RM overlaid on contours of the total intensity of the calibrator 0716+714 in the BC210B session observed at 5 GHz. The colorscale of RM in units of rad/m^2 is shown at the top. The beam size is illustrated by the gray shaded ellipse. Contours start at 0.79 mJy per beam and increase by factors of 2. *Right:* EVPA as function of λ^2 at the center of the map shown in the left panel. The dashed line is the best-fit λ^2-law with RM $= -112 \pm 162$ rad/m^2.

beam of the sub-band at the lowest frequency. Then, we fitted a linear function to the EVPAs from different sub-bands versus λ^2 for each pixel where the linear polarization intensity exceeds 1.5σ in all sub-bands, with σ being the full uncertainty including D-term errors and CLEAN errors (Hovatta et al. 2012). We discuss the significance levels of the observed RMs in Appendix A.2. We fitted the EVPA data several times including potential $n\pi$ rotations and used the fit that provided us with the lowest χ^2 value.

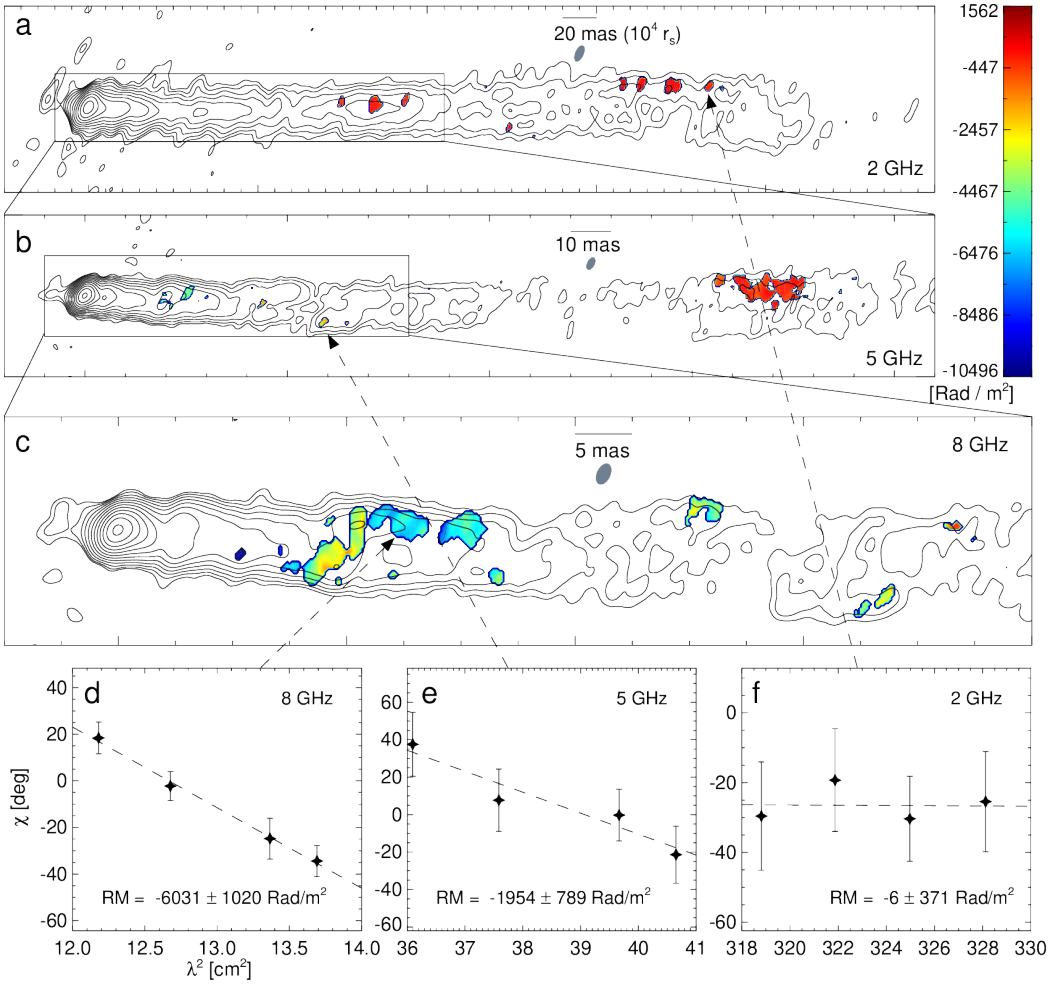

Figure 2.2. Colormap of the RM distribution, overlaid on contours of the total intensity of the M87 jet in three VLBA data sets (out of eight) at 2 (**a**), 5 (**b**), and 8 GHz (**c**). Contours start at 0.79, 0.54, and 0.53 mJy per beam for the 2 GHz, 5 GHz, and 8 GHz maps, respectively, and increase by factors of 2. The RM colorscale in units of rad/m^2 is shown at the top-right corner. Beam sizes are illustrated by the gray shaded ellipses. All maps are rotated clockwise by 23° relative to astronomical R.A.–Dec coordinates for better visualization. EVPA as function of λ^2, along with the best-fit λ^2 laws at the locations indicated by the black dashed arrows, is shown in **d**–**f**. We note that all RMs measured at different locations show good λ^2 fits (see Figure 2.3). We omitted the jet and RMs at $\approx$ 900 mas from the core at 2 GHz for better visualization (see Figure 2.3).

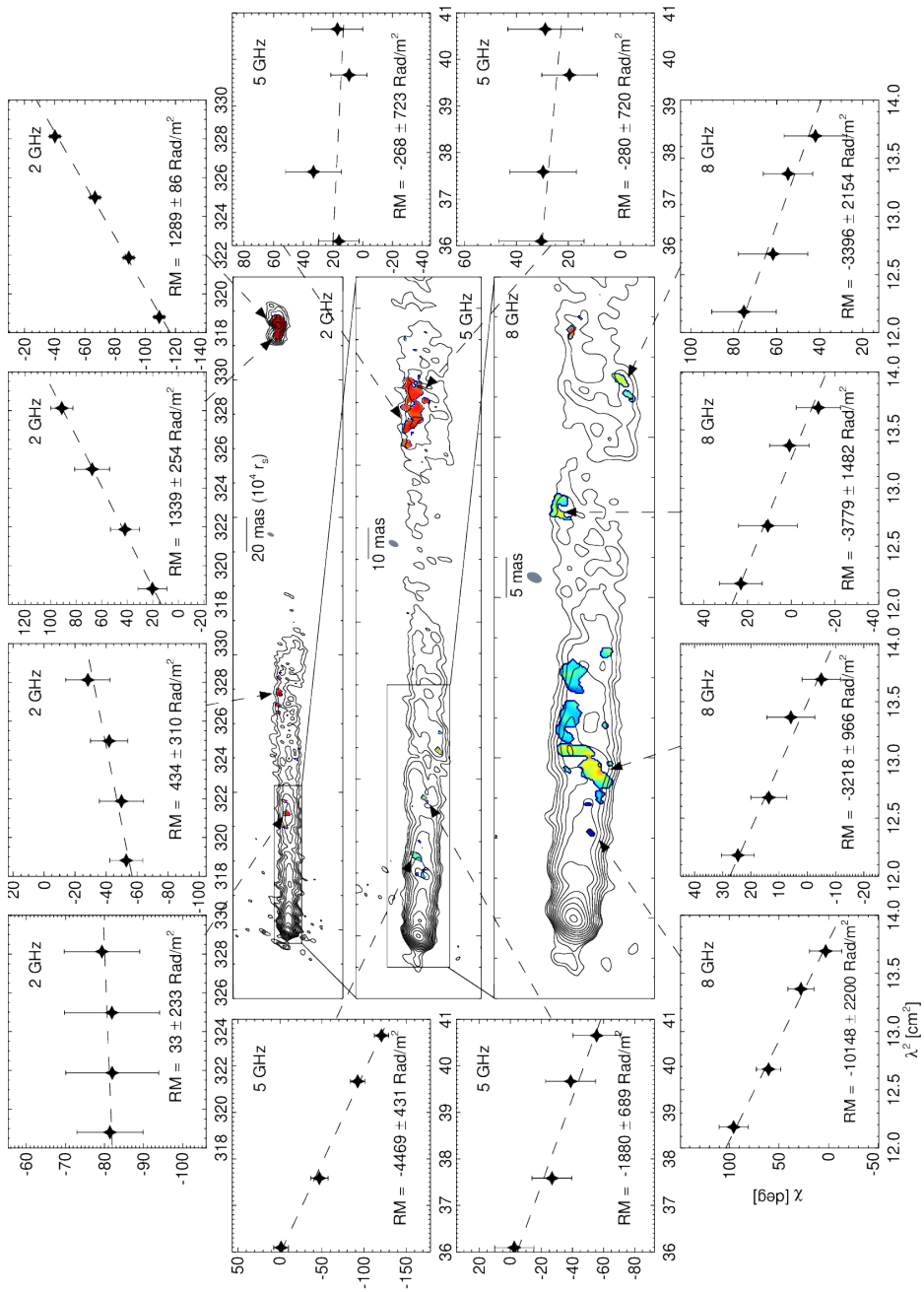

Figure 2.3. Same as Figure 2.2 but including HST-1 at $\approx$ 900 mas from the core at 2 GHz and showing EVPA–λ^2 diagrams for various jet locations where significant Faraday rotation is detected.

2.3 Analysis and Results

2.3.1 RM maps

In Figure 2.2, we present example RM maps overlaid on the total intensity distribution of the jet for one observation at each frequency. The EVPA as function of λ^2 at three different locations of the jet is shown with good λ^2 fits. We obtained good λ^2 fits for the other RMs measured at different locations as well (some of them are shown in Figure 2.3) and also in the other five data sets not presented in Figure 2.2. We omitted the jet and RMs at $\approx$ 900 mas from the core at 2 GHz for better visualization; those data are presented in Figure 2.3. At lower frequencies, Faraday rotation is observable in more outward regions of the jet due to longer cooling times of the jet plasma. At higher frequencies, Faraday rotation is observable closer to the compact upstream emission thanks to better angular resolution and less depolarization. We note that the RM distributions are patchy at all frequencies because significant linear polarization is detected only in some parts of the jet, possibly due to substantial de-polarization in the other parts. We also note that it is unlikely that those patchy RMs are artifacts because we found that the RMs in different epochs at the same observing frequency are detected in similar locations of the jet (see Appendix A.3).

2.3.2 Radial RM profile

To obtain a radial RM profile along the jet, we calculated spatially binned RM by taking the weighted mean of all values in each separated region of the map with similar RM values. A priori, taking a weighted mean over a part of a map assumes that all individual pixels are independent from each other, which is not the case here. Pixels values are correlated across the extension of a resolution element (here, the synthesized beam). Thus, we first calculated a mean value, then its formal error (which assumes all pixels to be uncorrelated), and then multiplied this formal error by $\sqrt{n\Sigma_{\rm FWHM}/\Sigma_{\rm RM}}$, where n is the number of the pixels used for taking the mean, $\Sigma_{\rm RM}$ the size of the map region with RM values, and $\Sigma_{\rm FWHM}$ the area within the full width at half maximum of

the synthesized beam. We present the mean distance from the black hole, the binned RM values, and corresponding RM errors in Table 2.2. This data is used for our further analysis.

In Figure 2.4, we present the absolute values of RM as function of de-projected distance from the black hole in units of $r_{\rm s}$. We assumed a black hole mass of $M_{\rm BH} = 6 \times 10^9 M_{\odot}$ (Gebhardt et al. 2011), a viewing angle of 17 deg[1] (Mertens et al. 2016), and a distance between black hole and radio core as estimated by core-shift analysis of the M87 jet (Hada et al. 2011) to convert the observed projected jet distance from the radio cores into the de-projected distance from the black hole. Remarkably, the RM decreases systematically along the jet over nearly two orders of magnitude in distance (from 5,000 to 200,000 $r_{\rm s}$) inside the Bondi radius ($3.6 \times 10^5 r_{\rm s}$; Russell et al. 2015). Our results substantially improved the radial RM profile of the M87 jet that was previously limited to a specific jet location at ≈ 20 mas from the core obtained in the pioneering RM study of the M87 jet (Zavala & Taylor 2002). The sign of the rotation measure is preferentially negative inside the Bondi radius except in the outer jet region (at distance of $\approx 2 \times 10^5$ $r_{\rm s}$) where RM errors are comparable to the RM values, which makes the RM sign ambiguous. However, at the location of HST-1 (at $\approx 4 \times 10^5$ $r_{\rm s}$), the observed RMs suddenly increase by a factor of ≈ 10 compared with those at $\approx 2 \times 10^5$ $r_{\rm s}$ and their signs are always positive, which is opposite to the signature observed in the inner jet region (Figure 2.4). This result is in good agreement with the previous measurements by the Very Large Array (VLA) observations (Chen et al. 2011). Since we focus on the behavior of RMs inside the Bondi radius in this paper, we briefly discuss the results of RMs at HST-1 in Section 2.4.6 and more detailed results will be presented in a forthcoming paper (Park et al. 2018, in prep.).

[1]We note that the viewing angle of the M87 jet is a matter of on-going discussion. Some studies suggest relatively large angles of $\theta \gtrsim 30^\circ$ (e.g., Owen et al. 1989; Ly et al. 2007; Hada et al. 2016), while other studies reported rather small viewing angles of $\theta \lesssim 19^\circ$ (e.g., Biretta et al. 1999; Wang & Zhou 2009; Perlman et al. 2011; Mertens et al. 2016; Walker et al. 2018). In this study, we adopt a viewing angle 17° based on the results of Mertens et al. (2016) and consideration of the upper limit of $\theta \lesssim 19^\circ$ derived from the velocity measurement at HST-1 (Biretta et al. 1999), as in Walker et al. (2018).

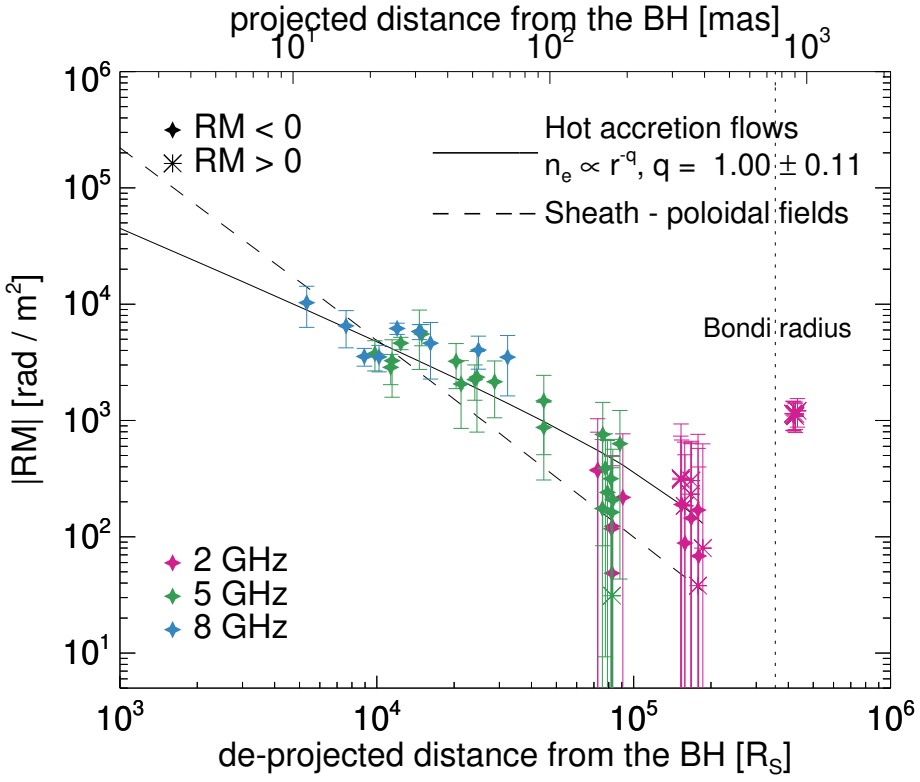

Figure 2.4. Absolute values of RM as function of de-projected distance from the black hole (bottom abscisa) and projected angular distance (top abscissa). The red, green, and blue data points are obtained at 2, 5, and 8 GHz, respectively. Diamonds and asterisks denote negative and positive RMs, respectively. The vertical dotted line indicates the Bondi radius (Russell et al. 2015). The solid (dashed) line is the best-fit function of the hot accretion flows (the sheath) model to the data points (see Section 2.3.5). The hot accretion flows model describes the observed data better than the sheath model (see Section 2.4.1). The electron density n_e scales like $n_e \propto r^{-q}$ with $q = 1.00 \pm 0.11$ in the best-fit function of the hot accretion flows model. All RM values displayed here were obtained after subtracting 130 rad/m^2 from our measurement results; the RM errors were obtained after adding 300 rad/m^2 in quadrature to our measurement uncertainties (see Section 2.3.3).

2.3.3 Contribution of RM sources outside the Bondi radius

We investigate the source of RMs inside the Bondi radius in this paper. However, there are three candidates other than gas within the Bondi radius which can contribute to the observed RM values: the Galactic interstellar medium (ISM), the intergalactic medium (IGM) in the Virgo cluster, and the diffuse gas not bound by the black hole's gravity in M87. The Galactic ISM would contribute less than ≈ 20 rad/m^2 because of the large galactic latitude of $b = 74.5^\circ$ for M87 (Taylor et al. 2009). The IGM in the Virgo cluster is expected to contribute less than ≈ 30 rad/m^2, based on the RM observations of other galaxies in the cluster (Weżgowiec et al. 2012). However, the contribution of the diffuse gas in M87 outside the Bondi radius would not be negligible. Previous VLA observations of M87 showed that RMs of the larger scale jet outside the Bondi radius are typically ≈ 130 rad/m^2 but values as low as ≈ -250 rad/m^2 and as high as ≈ 650 rad/m^2 are also seen in some parts of the jet (Owen et al. 1990; Algaba et al. 2016). Therefore, we subtracted 130 rad/m^2 from our observed RM values and added 300 rad/m^2 to the RM errors quadratically, which is used in Figure 2.4 and for our further analysis.

2.3.4 Variability

Our data are obtained in different periods from 1996 to 2014, so RM variability might affect the results. We also included the results of a previous study of RM of the M87 jet (Zavala & Taylor 2002) for investigating potential RM variability. One can divide our data into four time groups, obtained in 1995–1996, 2000.48, 2006–2008, and 2013–2015. We show the absolute values of RM from different groups with different colors as a function of distance from the black hole in the left panel of Figure 2.5. The data obtained in different periods do not show significant deviation from each other. We also present the RM values as a function of time obtained in four different jet distance ranges, 15–40, 40–70, 100–200, and 200–400 mas, with different colors (the right panel of Figure 2.5). The mean values from different groups in the same jet distance range are consistent with each other within 1σ in almost all cases, suggesting that there is no

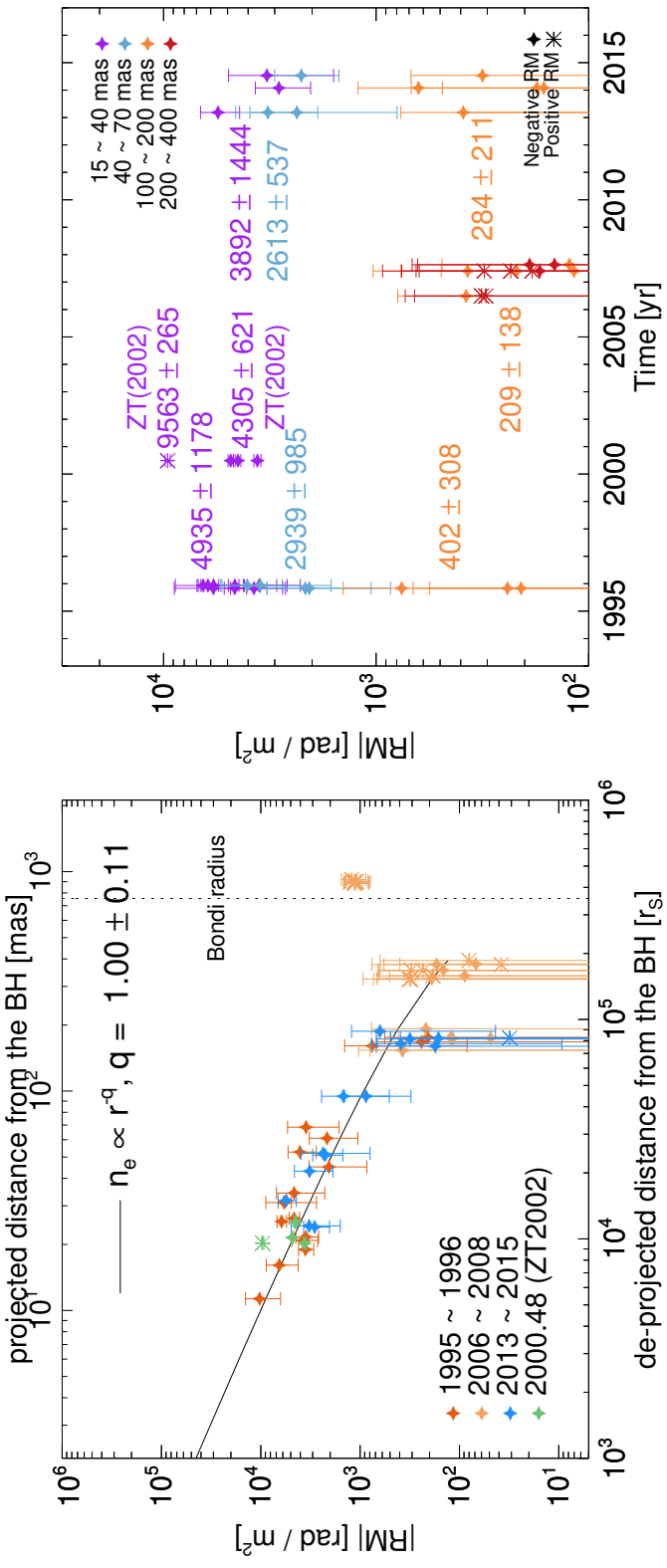

Figure 2.5. *Left:* Same as Figure 2.4 but with data points obtained in different epochs shown in different colors. *Right:* Absolute value of RM as a function of time. Values obtained at different angular distance ranges from the black hole are shown in different colors. The mean and standard deviation of RM values for each group (obtained in each time period for each jet distance) are noted next to the data points. The diamonds and asterisks denote negative and positive RMs, respectively. The data points obtained in the middle of 2000 are from a previous RM study of the M87 jet (Zavala & Taylor 2002).

significant temporal variability in RM. However, one exception is the case of positive RMs detected at ≈ 25 mas from the radio core in 2000.48 presented in the literature (Zavala & Taylor 2002). This value is larger than others obtained at similar jet distance by a factor of ≈ 2 and its sign is opposite. It is reasonable to consider that the positive RMs might be locally transient and not related to a global behavior of RM of the M87 jet because (i) the region of positive RMs is much smaller than that of negative RMs at a similar jet distance by a factor of ≈ 20 (Zavala & Taylor 2002) and (ii) positive RMs are not detected in other epochs and at other jet distances except in the outer jet region where RM errors are comparable to the RM values, which makes the RM sign ambiguous.

2.3.5 The Faraday screen

Internal Faraday rotation and depolarization

If the Faraday rotating electrons are intermixed with the synchrotron emitting jet plasma, internal Faraday rotation can occur. Burn (1966) showed that the complex polarization ($\mathcal{P}$) of a synchrotron-emitting uniform slab with a purely regular magnetic field (see Sokoloff et al. 1998 for the case of a non-uniform or an asymmetric slab) is given by

$$\mathcal{P} \equiv Q + iU = p_0 I \frac{\sin \phi\lambda^2}{\phi\lambda^2} \mathrm{e}^{2i(\chi_0 + \frac{1}{2}\phi\lambda^2)}, \tag{2.1}$$

where Q, U, and I are intensity in Stokes Q, U, and I maps, respectively, p_0 is the intrinsic fractional polarization, χ_0 the intrinsic EVPA, and ϕ the Faraday depth. However, internal Faraday rotation in sources with more realistic geometries and magnetic field structures usually results in deviation from a λ^2 law after total rotations $\gtrsim 45^\circ$ (Burn 1966; Sokoloff et al. 1998; Homan 2012).

We tested whether the observed degree of polarization and Faraday rotation can be explained with Equation 2.1 or not. We compared the degree of linear polarization expected in this model, $p_{\mathrm{L,internal}} = p_0 |\mathrm{sinc}(2\mathrm{RM}\lambda^2)|$, with the observed one, $p_{\mathrm{L,obs}}$. We assumed $p_0 \approx 0.75$ because this is the maximum allowed degree of linear polarization for optically thin synchrotron radiation (Pacholczyk 1970). In Figure 2.6, we present

Table 2.2. Binned rotation measure values

Session (1)	Proj. dist. [mas] (2)	RM [rad/m^2] (3)	$\sigma_{\rm RM}$ [rad/m^2] (4)
BJ020A	10.87	-10163.47	3965.69
	15.55	-6381.18	2278.09
	18.35	-3421.25	541.23
	20.97	-3391.10	849.69
	24.69	-6054.02	615.75
	30.23	-5688.09	804.28
	33.37	-4489.37	2327.39
	51.38	-3908.49	1239.84
	66.79	-3374.41	1852.78
BJ020B	20.07	-3628.40	1049.11
	25.39	-4495.79	472.80
	30.05	-5698.63	3064.56
	43.83	-1932.51	1169.71
	59.31	-2022.79	1056.72
	156.90	-627.96	603.85
	163.58	-110.87	312.19
	171.72	-77.88	194.93
BC210B	30.73	-5414.65	1117.57
	41.89	-3101.13	1317.59
	50.59	-2229.21	1535.19
	92.36	-742.15	478.03
	160.65	-259.05	232.85
	170.49	161.17	201.12
BC210C	23.18	-2736.92	779.55
	92.35	-1345.83	919.99
	156.32	-45.10	414.45
	170.03	-32.60	136.35
	183.02	-501.42	505.80

Note. — (1) Project code of VLBA observations. (2) Mean projected distance from the black hole of the region where the RMs are measured, in units of milliarcseconds. (3) Binned RM values in units of rad/m^2. (4) 1σ errors of the binned RMs. All RM values are those before subtracting 130 rad/m^2 and the RM errors are before adding 300 rad/m^2 in quadrature to the uncertainties (see Section 2.3.3).

Table 2.2. Binned rotation measure values

Session (1)	Proj. dist. [mas] (2)	RM [rad/m^2] (3)	$\sigma_{\rm RM}$ [rad/m^2] (4)
BC210D	23.47	-3135.18	1653.81
	49.63	-2119.48	693.08
	168.70	-185.79	221.31
BH135F	149.44	-247.30	288.74
	170.00	81.37	198.19
	315.35	449.35	285.42
	347.12	434.49	196.92
	370.33	61.64	137.53
	873.80	1242.69	36.47
	899.69	1340.05	143.18
BC167C	149.35	-240.64	592.94
	169.17	12.77	233.97
	187.30	-88.17	460.41
	316.27	439.96	547.68
	326.85	314.65	358.40
	345.39	362.52	262.42
	368.23	-39.88	508.98
	865.47	1270.15	102.53
	883.03	1269.38	44.13
BC167E	170.44	6.70	217.93
	317.98	-59.62	388.00
	327.55	41.67	292.40
	346.71	-14.73	394.56
	368.51	167.98	446.63
	384.56	209.87	460.24
	866.06	1276.49	117.15
	883.04	1221.10	48.23

Note. — Continued.

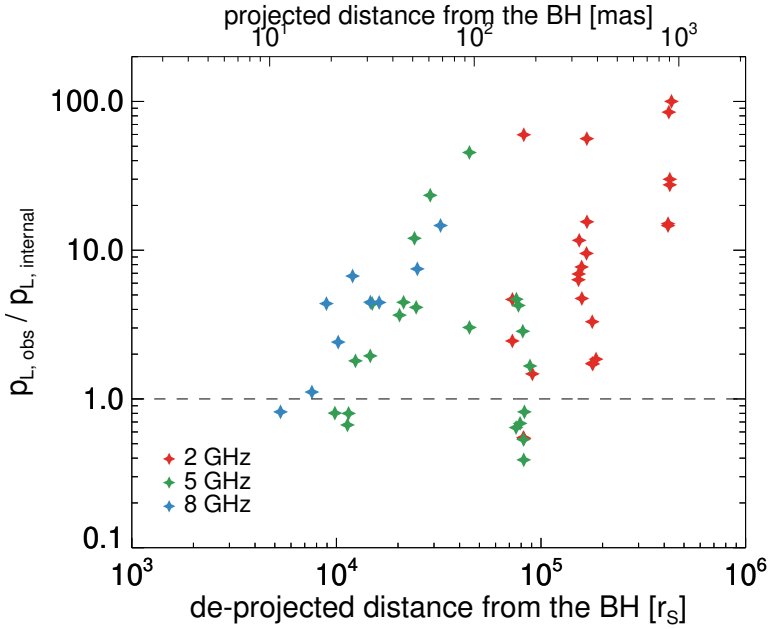

Figure 2.6. Ratio of the observed degree of linear polarization to the expected one in the internal Faraday rotation model (Equation 2.1, Burn 1966) as a function of distance from the black hole. The horizontal dashed line shows unity ratio.

$p_{\rm L,obs}/p_{\rm L,internal}$ as a function of de-projected distance from the black hole. Most of the data points are much larger than unity, indicating that internal Faraday rotation in a uniform slab permeated by a regular magnetic field is not responsible for the observed jet RM. In addition, we frequently measure EVPA rotations larger than 45° with good λ^2 fits at various locations in the jet at all frequencies as shown in Figure 2.3. The fact that we could not find any statistically significant difference in RMs obtained at different frequencies at a given distance also supports an external origin (Figure 2.4). Thus, the systematic decrease of RM shown in Figure 2.4 must originate from the magnetized plasma outside the jet (external Faraday rotation).

However, internal Faraday rotation might still be responsible for depolarization. As already noted in Section 2.3.1, at many locations of the jet linearly polarized emission is not detected in our data, making the RM distributions patchy. In general, depolarization originates from either internal Faraday rotation or spatial variations in the RMs of

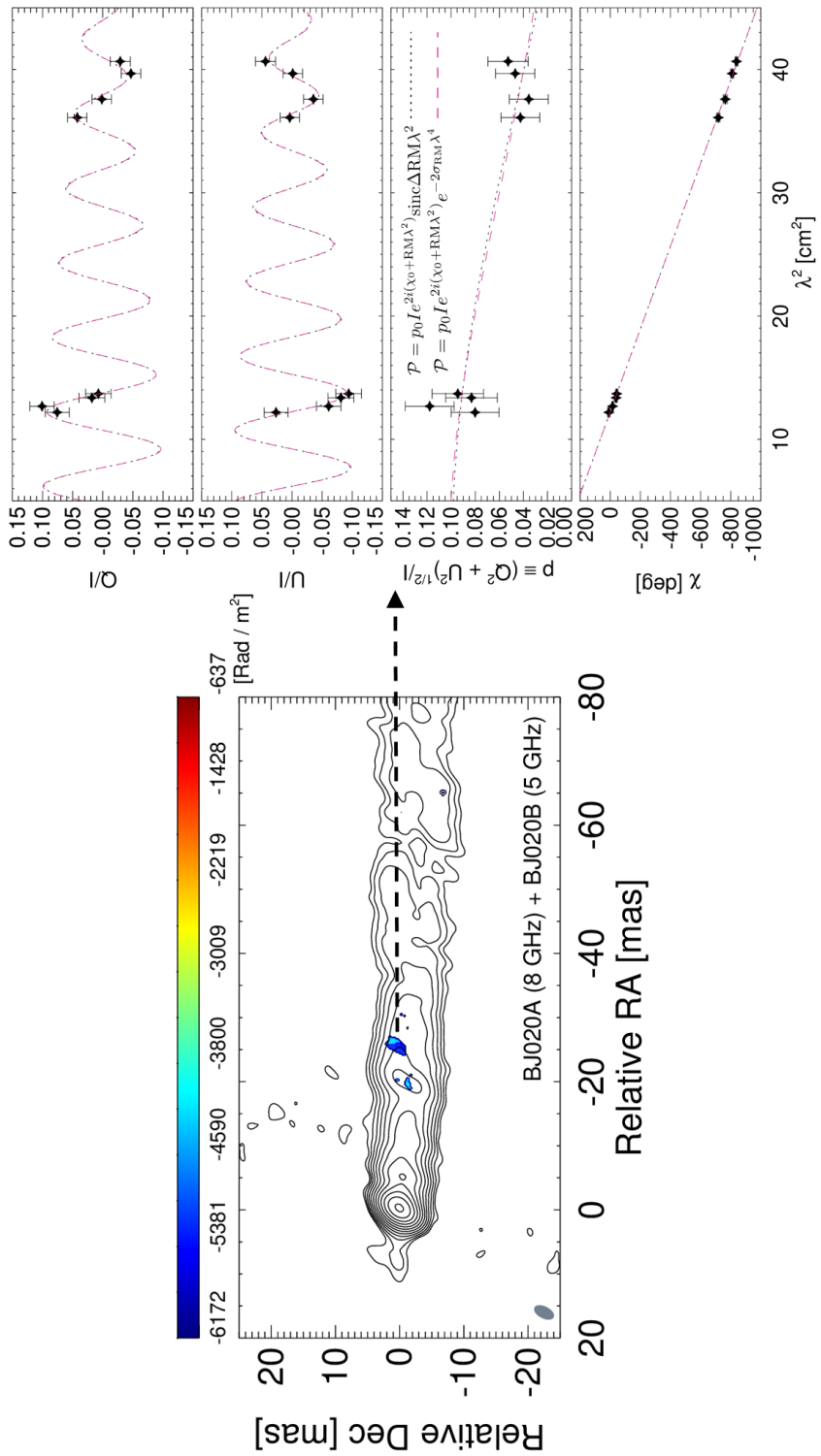

Figure 2.7. *Left:* an RM map obtained by combining BJ020A and BJ020B data sets. Contours start at 0.54 mJy per beam and increase by factors of 2. *Right:* Q/I, U/I, p, and χ as functions of λ^2 from top to bottom. The black dotted line and the red dashed line are the best-fit of model 1 ($\sigma_{\mathrm{RM}} = 0$ in Equation 2.2) and model 2 ($\Delta\mathrm{RM} = 0$) to the data points, respectively. (see Section 2.3.5 for more details).

the external Faraday screen on scales smaller than the resolution of the observations (e.g., Burn 1966; Tribble 1991; Sokoloff et al. 1998; Homan 2012). The depolarization mechanism of AGN jet emission has been extensively investigated recently, thanks to observations with large bandwidths (e.g., O'Sullivan et al. 2012, 2017; Hovatta et al. 2018; Pasetto et al. 2018), or VLBI observations at many different observing frequencies (e.g., Kravchenko et al. 2017). Investigating the depolarization mechanism of the M87 jet is difficult for us because we have a limited number of observing frequencies with relatively short λ^2 spacings available. However, we found that the data collected in the BJ020A and BJ020B sessions could be combined because their observing dates and frequencies are relatively close to each other (Table 2.1).

We obtained the RM map as described in Section 2.2 after considering a core-shift effect between 5 and 8 GHz by employing two-dimensional cross correlation of the optically thin emission regions in the image plane (Croke & Gabuzda 2008) and present the map in the left panel of Figure 2.7. We note that the results are not significantly affected by the core-shift. Significant RMs were detected in small parts of the jet because linear polarization at 5 GHz has not been detected in most parts of the jet in the inner jet region (at distances less than ≈ 60 mas), where the jet emission could be detected at 8 GHz. Nevertheless, an RM patch was detected at ≈ 25 mas from the core over a region with a size comparable to the beam size. In the right panel of Figure 2.7, we present Q/I, U/I, $p \equiv \sqrt{Q^2+U^2}/I$, and χ as a function of λ^2 in this region.

In order to investigate the depolarization mechanism, we tried to model the Stokes I, Q, and U intensity simultaneously at different wavelengths, known as the qu-fitting technique (e.g., Farnsworth et al. 2011; O'Sullivan et al. 2012). We used a model for the complex polarization which includes the effect of depolarization due to random magnetic fields ($\sigma_{\rm RM}$) and ordered magnetic fields (ΔRM), given by

$$\mathcal{P} = p_0 I e^{2i(\chi_0 + {\rm RM}\lambda^2)} e^{-2\sigma_{\rm RM}^2\lambda^4} {\rm sinc}\Delta{\rm RM}\lambda^2, \tag{2.2}$$

(Sokoloff et al. 1998). We followed a recent study which detected a very high rotation measure of $(3.6\pm0.3)\times10^5$ rad/m^2 in the quasar 3C 273 with Atacama Large Millimeter Array (ALMA) observations at 1 mm (Hovatta et al. 2018) and fitted Equation 2.2 with

$\sigma_{\rm RM} = 0$ (model 1, the black dotted lines in the right panel of Figure 2.7) and with $\Delta{\rm RM} = 0$ (model 2, the red dashed lines) to the data points. The best-fit parameters are ($p_0 = 0.10 \pm 0.01$, $\Delta{\rm RM} = 532 \pm 62$ rad/m^2, $\chi_0 = 184 \pm 6^\circ$, ${\rm RM} = -5195 \pm 43$ rad/m^2) and ($p_0 = 0.10 \pm 0.01$, $\sigma_{\rm RM} = 171 \pm 25$ rad/m^2, $\chi_0 = 184 \pm 6^\circ$, ${\rm RM} = -5194 \pm 43$ rad/m^2) for model 1 and 2, respectively. Both models can explain the data well with the reduced chi-square $\chi^2_r \equiv \chi^2/{\rm d.o.f}$, where d.o.f is the degree of freedom, of 0.66 and 0.64 for model 1 and 2, respectively. This is due to the sparse sampling of the data in the λ^2 space, which prevented us from solving the degenaracy. Nonetheless, the observed depolarization at $\approx$ 25 mas from the core is likely due to a gradient in RM by $\approx$ 532 rad/m^2 either in the jet or in the external Faraday screen across the beam or due to random magnetic fields with $\sigma_{\rm RM} \approx 171$ rad/m^2 in the external screen (Sokoloff et al. 1998; O'Sullivan et al. 2017; Hovatta et al. 2018; Pasetto et al. 2018). We also obtained good λ^2 fits for the EVPA rotation larger than 4π, supporting an external origin of the observed RM. The observed RM of $\approx -5194 \pm 43$ rad/m^2 for model 2 is consistent with that obtained in the same location by using only BJ020A (8 GHz) data, -5535 ± 1226 rad/m^2, within 1σ and BJ020B (5 GHz) data, -4469 ± 431 rad/m^2, within less than 2σ. The deviation larger than 1σ in the latter case might be due to a non-negligible time gap of $\approx$ 18 days between the two data sets.

A jet sheath

If the Faraday screen is placed in the immediate vicinity of the jet, e.g., like a sheath surrounding the jet as claimed for other distant AGNs (e.g., Zavala & Taylor 2004; Jorstad et al. 2007; O'Sullivan & Gabuzda 2009a; Hovatta et al. 2012; Park et al. 2018), then one expects significant RM gradients across the jet with a possible change of the sign of the RM; this is seen in numerical simulations (Broderick & McKinney 2010). This signature has indeed been frequently observed in the jets of many blazars (e.g., Asada et al. 2002, 2008; Gabuzda et al. 2004, 2015, 2018; Hovatta et al. 2012). The transverse RM gradients are related to toroidal magnetic fields in the jet and/or in the sheath, which can be naturally produced in the inner part of the accretion disk and/or

in the black hole's ergosphere. These magnetic fields play a crucial role in launching and powering of relativistic jets (Meier 2012). MHD theories predict that poloidal magnetic fields which are dominant near the jet base become rapidly weak at larger distance and toroidal fields become dominant relatively far from the black hole (e.g., Vlahakis & Königl 2004; Komissarov et al. 2009).

However, for M87 the observed sign of RM is negative almost everywhere inside the Bondi radius (Figure 2.4). Furthermore, we found that there is no significant difference between the RMs on the northern and southern jet edges at a given distance and the RMs appear to vary only as function of radial distance (see Appendix A.4). Recently, linear polarization structure of the core of the M87 jet at 43 GHz has been revealed, showing the inferred magnetic field vectors wrapped around the core[2] (Walker et al. 2018). This suggests that toroidal fields might be dominant already on scales of $\approx 100\, r_{\rm s}$, which makes it difficult to explain the observed single (negative) RM sign and no significant difference in RMs between the north and south edges with the Faraday screen consisting of a jet sheath.

We checked whether the observed RMs can be explained by the sheath model or not if poloidal magnetic fields are somehow dominant in the sheath at distance $\gtrsim$ 5,000 $r_{\rm s}$, as indicated by a recent study of time variable RM in the radio core of a nearby BL Lac object Mrk 421 (Lico et al. 2017). We assumed (i) the same parabolic geometry of the sheath as that observed for the jet, i.e., $z \propto R^{1.73}$ (Asada & Nakamura 2012; Nakamura & Asada 2013) with the radius of the outer boundary of the sheath being twice the radius of the jet (see the left panel of Figure 2.8), (ii) a constant velocity of the sheath at different distances, (iii) no reversal in the magnetic field direction along the line of sight, and (iv) the sheath consisting of non-relativistic cold plasma. These assumptions led us to the scaling relations of $n_e(z) \propto R^{-2} \propto z^{-1.16}$ and $B_p(z) \propto R^{-2} \propto z^{-1.16}$ with R being the radius of the sheath and B_p the poloidal magnetic field strength. We integrated RM $\propto \int n_e(l) B(l) dl$ numerically along each line of sight for each RM

[2]We note that we could not obtain intrinsic (RM-corrected) EVPAs with our data sets because the data are sampled in limited wavelength ranges relatively far from $\lambda = 0$. This leads to very large uncertainties in the intrinsic EVPAs usually larger than 90° .

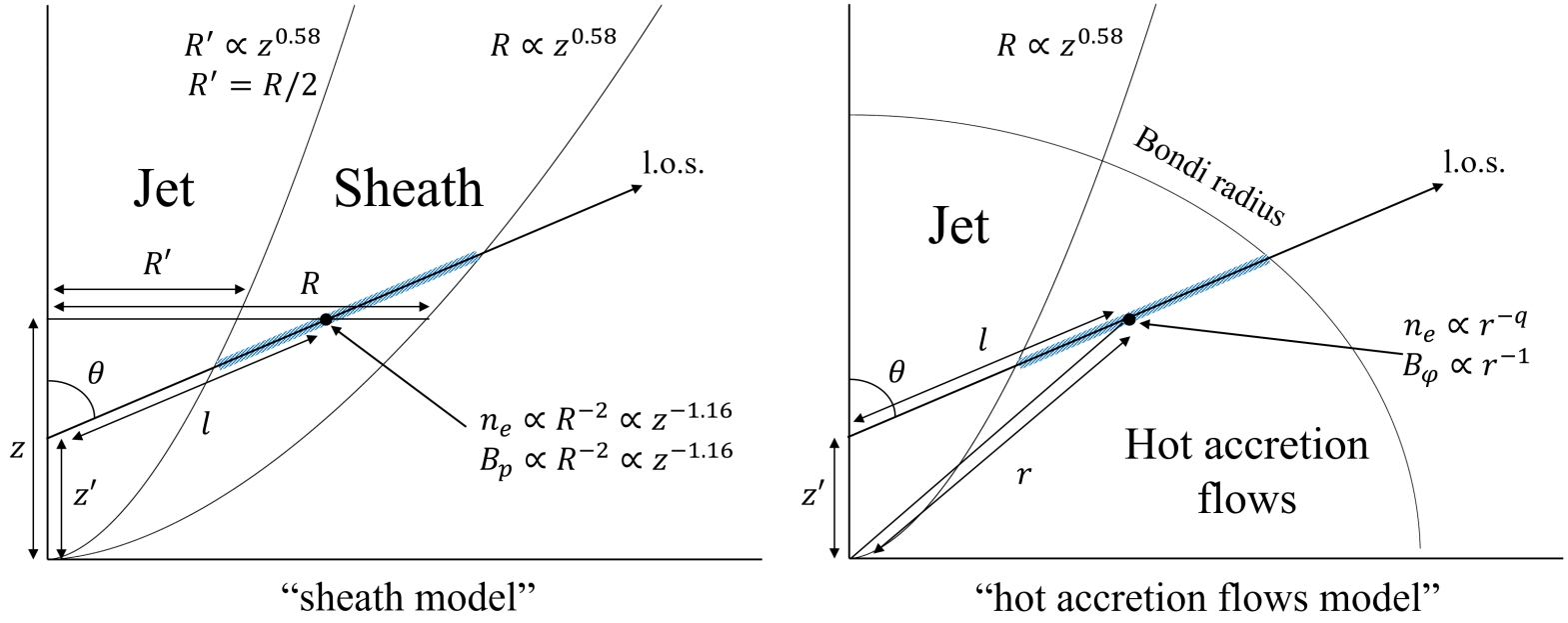

Figure 2.8. *Left:* Schematic diagram showing the sheath model. l denotes the path from the emitter to the observer at the jet distance z'. θ is the jet viewing angle and R is the radius of the sheath. We performed numerical integration of RM $\propto \int n_e(l)B(l)dl$ in the sheath region along each line of sight for each z' (the blue shaded line), with the scaling relations of $n_e(z) \propto R^{-2} \propto z^{-1.16}$ and $B_p(z) \propto R^{-2} \propto z^{-1.16}$ provided (see Section 2.3.5 for details). *Right:* Same as the left panel but showing the case of the hot accretion flows model. r denotes the spherical radius and $n_e(r) \propto r^{-q}$ and $B(r) \propto r^{-1}$ are used for numerical integration of RM $= 8.1 \times 10^5 \int n_e(l)B(l)dl$ for each jet distance (see Section 2.3.5 for details). We note that the jet radius and θ are much smaller than those shown in these diagrams in reality.

data point between the jet boundary and the sheath boundary (see the left panel of Figure 2.8) and fitted this function to the data points at different distances with a coefficient left as a free parameter. The best-fit model is indicated by the dashed line in Figure 2.4.

Hot accretion flows

We use the scaling relations $n_e(r) = n_{e,\mathrm{out}}(r/r_{\mathrm{out}})^{-q}$ with $0.5 \leq q \leq 1.5$ and $B(r) = B_{\mathrm{out}}(r/r_{\mathrm{out}})^{-1}$, where r is the radial distance from the black hole and $n_{e,\mathrm{out}}$ and B_{out} are the electron number density and the magnetic field strength at r_{out}, respectively. The former is based on self-similar solutions of hot accretion flows (Blandford & Begelman 1999; Yuan & Narayan 2014). The latter is based on the assumption that toroidal magnetic fields are dominant in the accretion flows (e.g., Hirose et al. 2004). We note that we are restricted to 1D scaling relations due to the limitations of the 2D accretion flow models including non-negligible magnetic fields currently available, especially at small polar angles which is of our interest because of the small jet viewing angle (e.g., Mosallanezhad et al. 2016; Bu & Mosallanezhad 2018). In other words, we assume here that the quantities of the flows would be spherically symmetric for regions with a polar angle smaller than the jet viewing angle of 17°.

We employed $\mathrm{RM} = 8.1 \times 10^5 \int n_e(l)B(l)dl$ (RM in units of rad/m^2, n_e in units of cm^{-3}, B in units of Gauss, and l in units of parsec; Gardner & Whiteoak 1966) for 'cold' non-relativistic plasma, which applies to the relatively large spatial scales probed in this study (Yuan & Narayan 2014). We also performed numerical integration along each line of sight between the jet boundary and the Bondi radius (see the right panel of Figure 2.8, see also Section 2.3.3 for discussion of the potential contribution by gas outside the Bondi radius). The result of fitting this function to the observed RM values measured inside the Bondi radius is indicated by the solid line in Figure 2.4 with the best-fit parameter of $q = 1.00 \pm 0.11$, which indicates $\rho \propto r^{-1}$ with ρ being the mass density. We could also obtain $n_{e,\mathrm{out}}B_{\mathrm{out}}$ from the fitting and when using $n_{e,\mathrm{out}} \approx 0.3$ cm^{-3} at the Bondi radius measured by the X-ray observations (Russell et

al. 2015), we obtain $B_{\rm out} = (2.8 \pm 0.8) \times 10^{-6}$ G.

2.4 Discussion

2.4.1 Jet sheath vs hot accretion flows

In Section 2.3.5, we considered three different sources of Faraday rotation, (i) the jet itself, (ii) a sheath surrounding the jet, and (iii) hot accretion flows. Given that the observed EVPA rotations are larger than 45° at various locations in the jet with good λ^2 scalings and the observed degree of linear polarization is usually much higher than that expected in the internal Faraday rotation model, we excluded the scenario (i) in Section 2.3.5. Although the hot accretion flows model (the solid line in Figure 2.4) apparently fits the data better than the sheath model (the dashed line in Figure 2.4), a statistical analysis is necessary to properly determine the better model. In Table 2.3, we present the values of reduced chi-square (χ^2_r) and Bayesian information Criterion (BIC) obtained in the best-fit for each model. The BIC is defined as BIC $\equiv -2\ln\mathcal{L}_{\rm max} + k\ln N$, where $\mathcal{L}_{\rm max}$ is the maximum likelihood and $-2\ln\mathcal{L}_{\rm max}$ is equivalent to the χ^2 value for the best-fit model in case for Gaussian errors (when neglecting a constant term), k the number of free parameters in the model, and N the number of data points used in the fit. The BIC allows one to compare the goodness of fit of different models having different numbers of free parameters (Schwarz 1978). The difference between the BIC values (ΔBIC) for two models quantifies how strongly one model is preferred over the other one, where a model with a lower BIC value is more favored by the data. Conventionally, $0 < \Delta{\rm BIC} < 2$ represents weak evidence, $2 < \Delta{\rm BIC} < 6$ positive evidence, $6 < \Delta{\rm BIC} < 10$ strong evidence, and $10 < \Delta{\rm BIC}$ very strong evidence (e.g., Jeffreys 1961; Kass & Raftery 1995; Mukherjee et al. 1998; Liddle 2004). The value of BIC for the hot accretion flows model is smaller than that for the jet sheath model by ≈ 24 (Table 2.3), indicating that the former is strongly favored by the data.

We note that the above conclusion is based on the results obtained by using several assumptions on the jet sheath. For example, we assumed that the sheath geometry

Table 2.3. Comparison of the models

Model	n_e profile	B profile	χ^2_r	BIC
(1)	(2)	(3)	(4)	(5)
Jet sheath	$n_e(z) \propto z^{-1.16}$ (fixed)	$B(z) \propto z^{-1.16}$ (fixed)	1.73	86.8
Hot accretion flows	$n_e(r) \propto r^{-1.00\pm0.11}$ (fit)	$B(r) \propto r^{-1}$ (fixed)	1.16	62.4

Note. — (1) Model applied to the RM data. (2) Density profile. The definition of z and r is explained in Figure 2.8. (fixed) means that the fixed profile is used in the model, whereas (fit) means that the index in the power-law is left as a free parameter in the fitting. (3) Magnetic field strength profile. (4) Reduced chi-square for the best-fit. (5) Bayesian Information Criteria for the best-fit. The number of data points used in the fitting is 49.

is the same as the jet, which may not be true. When we relax this assumption and leave the power-law index in the width profile of the sheath as a free parameter, i.e., $z_{\rm sheath} \propto R^{\eta}_{\rm sheath}$, and fit the sheath model to the data points, then we obtain the best-fit with $\eta = 2.49 \pm 0.17$. This indicates that the sheath is more strongly collimated than the jet, which is unlikely because the inner part (closer to the axis) of streamlines is thought to be more collimated than the outer part for collimated outflows (e.g., Komissarov et al. 2007, 2009; Tchekhovskoy et al. 2008; Nakamura et al. 2018). Or, if we assume that toroidal fields are dominant in the sheath and fix the sheath geometry, we obtain a relatively good fit with a BIC value comparable to that of the hot accretion flows model. However, as noted in Section 2.3.5, it is difficult to explain the absence of a systematic difference between the RMs on the south and north edges in this case.

An alternative scenario is that the Faraday screen consists of dense clouds with ordered magnetic fields that are entrained by the jet (suggested by Zavala & Taylor 2002). The volume filling factor of these clouds, if they exist, is expected to be very small and this might explain why the RMs are detected in only small parts of the jet. Although we could not exclude this possibility, the observed depolarization at longer

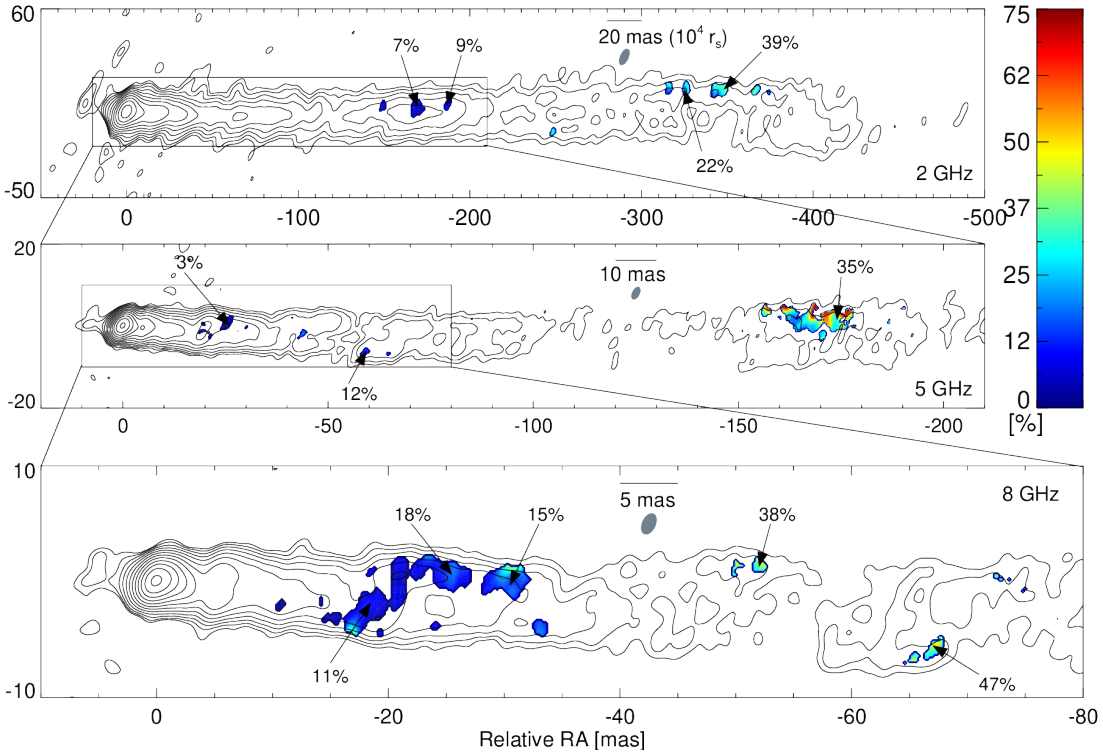

Figure 2.9. Same as Figure 2.2 but colors show degree of linear polarization for the first sub-band data at each frequency. Contours start at 0.79, 0.54, and 0.53 mJy per beam for the 2 GHz, 5 GHz, and 8 GHz maps, respectively, and increase by factors of 2. The values of fractional polarization at various locations of the jet are noted.

wavelengths does not seem to support this scenario. We present the distribution of the degree of linear polarization overlaid on the contours of total intensity emission for one observation at each frequency in Figure 2.9. At higher observing frequencies, the distribution of significant linear polarization becomes more continuous and the degree of linear polarization becomes higher at a given distance, notably at ≈ 20 and ≈ 170 mas from the core. This suggests that the Faraday screen consists of a continuous and extended medium such as winds but significant depolarization in large parts of the jet makes the observed patchy RM distributions especially at lower frequencies. We will investigate the depolarization mechanism at various locations of the jet with dedicated

multi-frequency polarimetric observations in the near future, which will allow us to identify the Faraday screen more rigorously.

Taken as a whole, we conclude that attributing the Faraday screen to hot accretion flows is most consistent with the data presented in this paper and we discuss the results obtained by applying the hot accretion flows model hereafter.

2.4.2 Winds and the Faraday screen

The density profile we derived is significantly flatter than the profile $\rho \propto r^{-1.5}$ from the ADAF with pure gas inflows (Narayan & Yi 1994; Narayan & Yi 1995a), at a level of $> 3\sigma$. Instead, our observations are in good agreement with the ADIOS model (Blandford & Begelman 1999; Yuan & Narayan 2014), suggesting that substantial winds from hot accretion flows exist in M87. Our results are consistent with the results of various numerical simulations of hot accretion flows, i.e., $\rho \propto r^{-q}$ with $q = 0.5 - 1$ (see Yuan et al. 2012b and references therein). Since our study probes regions relatively far from the central engine, i.e., $\gtrsim$ 5,000 $r_{\rm s}$, the results of Pang et al. (2011) would be the most suitable to compare with our observations among various simulations. They performed a numerical survey with various parameters of the accretion flows in their 3D MHD simulations, in which the outer boundary is extended up to ten times the Bondi radius, and found the most favored value of $q \approx 1$. This result is in good agreement with our finding. We note that previous observations of Faraday rotation at 1 mm with the Submillimeter Array already ruled out the pure inflow scenario (Kuo et al. 2014), which is consistent with our results. However, we could further constrain the accretion model of M87 from the radial RM profile measured at distances over nearly two orders of magnitude.

GRMHD simulations also found the production of winds, which are non-relativistic, moderately magnetized gas outflows surrounding the highly magnetized and collimated jets[3] (e.g., Sadowski et al. 2013; Nakamura et al. 2018). Since the viewing angle of the

[3]The geometry of winds is approximated as conical (Sadowski et al. 2013; Yuan et al. 2015) and the use of $B_\phi \propto r^{-1}$ in our modelling (Section 2.3.5) would be valid because $B_\phi \propto R^{-1} \propto r^{-1}$.

M87 jet is relatively small ($\theta \approx 17^\circ$ Mertens et al. 2016), it is reasonable to regard the winds as a dominant source of the observed RMs and thus as an external medium confining the jet. Nevertheless, we note that the contribution of weakly magnetized inflows to the observed RMs is probably non-negligible. From the derived pressure profile and the assumed magnetic field configuration for winds, one expects $\beta \equiv p_{\rm gas}/p_{\rm mag} \approx 68$ at $r_{\rm out}$ assuming $\beta \approx 1$ close to the black hole (De Villiers et al. 2005) because $p_{\rm gas} \propto r^{-5/3}$ and $p_{\rm mag} \propto r^{-2}$ with $p_{\rm mag}$ being the magnetic pressure (see Section 2.4.3). However, we obtained $\beta \approx 1400$ at $r_{\rm out}$ using $B_{\rm out} \approx 2.8\ \mu G$ from the fitting (Section 2.3.5) and the pressure at $r_{\rm out}$ measured by X-ray observations (Russell et al. 2015). This β is larger than that for winds by an order of magnitude and we expect some contribution of weakly magnetized inflows to the observed RMs (Yuan & Narayan 2014). Thus, the Faraday screen of the M87 jet might consist of a complex mixture of inflows and winds.

2.4.3 Jet collimation by winds

The pressure profile of an external medium surrounding the jet can be estimated from the density profile. Assuming an adiabatic equation of state for non-relativistic monatomic gas, the pressure scales like $p_{\rm gas} \propto \rho^\gamma \propto r^{-5/3}$, where $\gamma = 5/3$ is the specific heat ratio. According to MHD models, AGN jets are gradually accelerated by transferring the electromagnetic energy of the flow to its kinetic energy (e.g., Komissarov et al. 2009; Lyubarsky 2009; Toma & Takahara 2013). Jet collimation is critical for the conversion; therefore the acceleration and collimation zones in AGN jets are expected to be co-spatial (Marscher et al. 2008). It has been shown that the flow acceleration is very inefficient without an external confinement (e.g., Eichler 1993; Begelman & Li 1994). If the pressure profile of the external medium follows a power-law, i.e., $p_{\rm ext} \propto r^{-\alpha}$, the power-law index must satisfy $\alpha \leq 2$ to permit for a parabolic jet shape (Begelman & Li 1994; Lyubarsky 2009; Komissarov et al. 2009; Vlahakis 2015). Our results, $\alpha = 1.67$ for the external medium, and the observed parabolic geometry up to the Bondi radius (Junor et al. 1999; Asada & Nakamura 2012; Nakamura & Asada 2013; Hada et al.

2013), are consistent with the MHD collimation-acceleration scenario[4] (Komissarov et al. 2009; Lyubarsky 2009; Vlahakis 2015). Indeed, systematic acceleration of the M87 jet inside the Bondi radius has been discovered (Asada et al. 2014; Mertens et al. 2016; Hada et al. 2017; Walker et al. 2018). Remarkably, recent GRMHD simulations presented that non-relativistic winds launched from hot accretion flows play a dynamical role in jet collimation and the jet is accelerated to relativistic speeds (Nakamura et al. 2018). We note that our conclusion is also supported by the fact that the observed collimation profile of the M87 jet was successfully modelled by a two-zone MHD model, where an inner relativistic jet is surrounded by highly magnetized (Gracia et al. 2005, 2009) or weakly magnetized (Globus & Levinson 2016) non-relativistic outer disk winds. We also note that the confinement of the jet by hot accretion flows and/or winds on smaller scales has been suggested by Hada et al. (2016), where a complicated innermost collimation profile with a local constricted jet structure was observed.

2.4.4 Mis-alignment

The dominance of a single RM sign for M87 implies that the background light source, i.e., the jet, exposes only one side of the toroidal magnetic loops in the Faraday screen. This situation can be realized when there is a mis-alignment between the jet axis and the symmetry axis of the toroidal field loops (Figure 2.10). This is another indication for winds or inflows as the dominant source of Faraday rotation because the jet sheath is tightly attached to the jet and cannot be tilted relative to the jet axis. Since the jet is

[4]We note, however, that $\alpha = 1.67$ leads to an asymptotic jet shape with $z \propto R^{2.4}$ in the MHD models (Lyubarsky 2009), which deviates from the observed one, $z \propto R^{1.73}$ (Nakamura & Asada 2013). Also, the fact that the jet appears stable over a large distance range can be explained by the loss of causual connectivity across the jet, if $\alpha > 2$ (Porth & Komissarov 2015). However, the jet becomes conical in this case. We note that if the same temperature profile as in the ADAF self-similar solutions, $T \propto r^{-1}$, can be applied to the ADIOS model (Yuan et al. 2012b), then we obtain $\alpha = 2$ which allows $1 < a < 2$ in $z \propto R^a$ (Komissarov et al. 2009). However, this requires a remarkable coincidence, considering the non-negligible error in the obtained density profile $\rho \propto r^{-1.00\pm0.11}$. Therefore, we adopt $\alpha = 1.67$ obtained from the assumption of a simple equation of state, which generally allows a parabolic jet geometry (see Section 5 in Porth & Komissarov 2015 for more discussion).

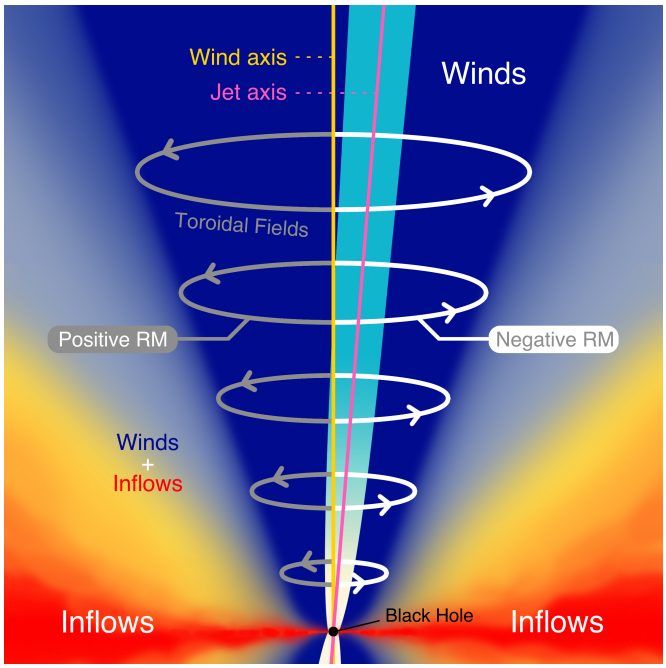

Figure 2.10. Schematic diagram of the black hole inflow–outflow system in M87. Different colors represent regions dominated by dense, hot, and turbulent inflows (red and yellow), collimated and highly magnetized jets (cyan), non-relativistic and moderately magnetized winds (dark blue), and a complex mixture of inflows and winds (light blue). The winds are permeated by toroidal magnetic fields indicated by gray and white loops. The jet axis (purple vertical line) is tilted with respect to the wind axis (yellow vertical line) and the jet exposes only one side of the toroidal fields, resulting in a single (negative) RM sign from the point of view of a distant observer.

highly collimated and narrow (Junor et al. 1999; Asada & Nakamura 2012; Doeleman et al. 2012), only a slight misalignment by $\approx 5^\circ$ can result in observations of a fixed RM sign over a large distance range. Such small misalignments seem to be quite common in hot accretion flows even when the magneto-spin alignment effect, an alignment of the accretion disk and jets with the black hole spin by strong magnetic fields near the black hole, operates (McKinney et al. 2013).

We note that it is unlikely that poloidal magnetic fields are responsible for the

observed RMs of M87 because in that case one expects $\rho \propto r^0$ from $B \propto r^{-2}$, which is impossible to explain with the accretion models currently available (Yuan & Narayan 2014). However, there is indication of non-negligible poloidal fields as well as toroidal fields – resulting in helical magnetic fields – in the jet environment of other distant AGNs, which results in transverse RM gradients with no sign changes (e.g., Asada et al. 2002; Zamaninasab 2013; Gómez et al. 2016; Gabuzda et al. 2018, see also Section 2.3.5). The existence of non-negligible poloidal fields was indicated even for the M87 jet at HST-1 from the observed moving knots with both fast and slow velocities which could be explained by quad relativistic MHD shocks in a helical magnetic field permeating the jet (Nakamura et al. 2010; Nakamura & Meier 2014). In Section 2.3.5 and Section 2.4.1, we explained that poloidal magnetic fields might be very weak at distances $\gtrsim$ 5,000 $r_{\rm s}$ probed in this study and we concluded that hot accretion flows and winds are more probable to be the Faraday screen than the jet sheath. However, if the jet experiences recollimation, which may lead to formation of standing shocks (e.g., Daly & Marscher 1988; Gómez et al. 1995; Agudo et al. 2001; Mizuno et al. 2015; Martí et al. 2016; Fuentes et al. 2018), then the strength of poloidal fields could be substantially enhanced. Indeed, the width of HST-1 is significantly smaller than expected from the parabolic (conical) width profile inside (outside) the Bondi radius (Asada & Nakamura 2012), which has been explained with a hydrodynamic recollimation shock (e.g., Stawarz et al. 2006; Bromberg & Levinson 2009; Asada & Nakamura 2012). Also, the core of blazars is often identified with a recollimation shock (e.g., Daly & Marscher 1988; Marscher 2008; Cawthorne et al. 2013). This may explain the presence of non-negligible poloidal fields in the sheath of blazar jets and in HST-1, but not in the M87 jet inside the Bondi radius.

2.4.5 Mass accretion rate

The presence of winds indicates that the actual rate of mass accreted onto the black hole could be substantially smaller than the Bondi accretion rate. If the density profile in the equatorial plane is similar to the one we observe, i.e., if a radial self-similarity

holds, one expects $\dot{M}(r) = \dot{M}_{\rm ADAF}(r/r_{\rm out})^{1.5-q}$ (e.g., Blandford & Begelman 2004; Yuan et al. 2012b; Yuan & Narayan 2014), where $\dot{M}_{\rm ADAF}$ is the mass accretion rate in the classical ADAF model. Using $\dot{M}_{\rm Bondi} = 0.1 M_\odot {\rm yr}^{-1}$ (Russell et al. 2015) and $\dot{M}_{\rm ADAF} = 0.3\dot{M}_{\rm Bondi}$ with a viscosity parameter $\alpha = 0.1$ (Narayan & Fabian 2011), assuming a constant mass accretion rate inside 10 $r_{\rm s}$ (Yuan et al. 2012b), the rate of mass passing through the event horizon of M87 would be $\dot{M}_{\rm BH} \approx 0.3\dot{M}_{\rm Bondi}(10r_{\rm s}/3.6\times 10^5 r_{\rm s})^{0.5} = 1.6\times10^{-4} M_\odot {\rm yr}^{-1}$.

This is consistent with the upper limit on the accretion rate of $9.2\times10^{-4} M_\odot {\rm yr}^{-1}$ obtained from previous polarimetric observations of M87 at 1 mm (Kuo et al. 2014). We obtained a radiative efficiency $\epsilon \equiv L_{\rm disk}/\dot{M}_{\rm BH}c^2 \approx 3.8\%$ for a disk luminosity of $L_{\rm disk} = 3.4\times10^{41}$ erg s^{-1} (Prieto et al. 2016) and $\dot{M}_{\rm BH}/\dot{M}_{\rm Edd} \approx 1.2\times10^{-6}$, where $\dot{M}_{\rm Edd} \equiv 10L_{\rm Edd}/c^2$ with $L_{\rm Edd}$ being the Eddington luminosity (Yuan & Narayan 2014). This is consistent with recent theoretical studies which found that the radiative efficiency of hot accretion flows might not be as small as previously thought even at very low accretion rates (Xie & Yuan 2012; Yuan & Narayan 2014). The obtained radiative efficiency is consistent with the case of $\delta = 0.5$ in Xie & Yuan (2012), where δ is the fraction of the viscously dissipated energy in the accretion flows used to directly heat electrons. Remarkably, this is similar to the value found for Sgr A* in the SED modelling (Yuan et al. 2003). Our results indicate that a very low accretion rate due to the mass loss via winds is probably the main reason for the faintness of the active nucleus of M87 and a similar conclusion was drawn for Sgr A* from the measured RMs (Bower et al. 2003).

The accretion rate we derive suggests a jet production efficiency of $\eta \equiv P_{\rm jet}/\dot{M}_{\rm BH}c^2 \gtrsim 110\%$ with a jet power $P_{\rm jet} \gtrsim 10^{43}$ erg s^{-1} for M87 (e.g., Bicknell & Begelman 1996; Owen et al. 2000; Allen et al. 2006; Rafferty et al. 2006; Stawarz et al. 2006; Bromberg & Levinson 2009, see Broderick et al. 2015 for more discussion). This is higher than the efficiency of gravitational binding energy of accretion flows released as radiation in a maximally rotating black hole by a factor of three (Thorne 1974) and indicates that almost all of input rest mass power is released as jet power. This is possible only when (i) the accretion disk of M87 is in magnetically arrested disk (MAD) state in which the

magnetic pressure of the poloidal magnetic fields is balanced by the ram pressure of the accreting gas (Narayan et al. 2003; Tchekhovskoy et al. 2011; McKinney et al. 2012) and (ii) there is extraction of rotational energy of a spinning black hole that powers the jet, the Blandford-Znajek (BZ) process (Blandford & Znajek 1977). GRMHD simulations find that the efficiency of winds launched from hot accretion flows or of jets launched not in a MAD state is $\lesssim 10\%$ (Sadowski et al. 2013) but can go up to $\approx 300\%$ with the BZ process in a MAD state (Tchekhovskoy et al. 2011, 2012; McKinney et al. 2012; Sadowski et al. 2013). This is also in agreement with recent observational evidence that most radio-loud active galaxies, including M87, are in a MAD state (Zamaninasab et al. 2014). The jet power larger than or comparable to the accretion power $\dot{M}_{\rm BH}c^2$ has also been found for many blazars (Ghisellini et al. 2014).

We note that the estimation of mass accretion rate and the related quantities above is based on an assumption that the gas contents of the accretion flows are dominated by hot gas. However, a recent study showed that significant amounts of cold and chaotic gas can form near or inside the Bondi radius via non-linear growth of thermal instabilities, resulting in the accretion rate being boosted up to two orders of magnitude compared to the case of hot gas only (Gaspari et al. 2013). However, as already noted in Nemmen & Tchekhovskoy (2015), the amount of cold gas is unlikely to be much larger than the amount of hot gas in the accretion flows because of (i) no correlation between the jet power and the total mass of cold molecular gas in many radio galaxies (McNamara et al. 2011) and (ii) not very tight but significant correlation between the jet power and the Bondi accretion power of nearby radio galaxies (e.g., Allen et al. 2006; Balmaverde et al. 2008; Russell et al. 2013; Nemmen & Tchekhovskoy 2015). In addition, even if the true accretion rate is an order of magnitude larger than the one we estimated due to the cold gas, the jet production efficiency would be still very large, possibly close to $\approx 100\%$. The jet power of $\approx 10^{43}$ erg s^{-1} we used above is estimated from observations of X-ray cavities, which represents the mechanical power of the jet averaged over the cavity buoyance time of about $\gtrsim 1$ Myr (Broderick et al. 2015). Also, this power should be in general regarded as a lower limit on the total mechanical power of the jet due

to possibly missing cavities and the significant contribution of weak shocks and sound waves to the jet power, which was not considered in the cavity analysis (Russell et al. 2013). Other estimates of the jet power which reflect more recent ($\lesssim$ a few $\times 10^3$ yr) jet activities of M87 provide $\approx 10^{44}$ erg s^{-1} (e.g., Bicknell & Begelman 1996; Owen et al. 2000; Stawarz et al. 2006; Bromberg & Levinson 2009; Broderick et al. 2015). This may compensate for the increased mass accretion rate due to cold gas and a high jet production efficiency would still be maintained.

The magnetic flux near the event horizon in a MAD state is saturated at $\Phi_{\rm MAD} \sim 50\left(\dot{M}_{\rm BH} r_{\rm g}^2 c\right)^{1/2}$ G cm^2, where $r_{\rm g} \equiv GM_{\rm BH}/c^2$ is the black hole gravitational radius, G the gravitational constant (Tchekhovskoy et al. 2011). One can estimate the magnetic field strength at the horizon via $B_{\rm MAD} \approx \Phi_{\rm MAD}/2\pi r_{\rm g}^2 = 10^{10}(M/M_\odot)^{-1/2}(\dot{M}_{\rm BH}/\dot{M}_{\rm Edd})^{1/2}$ G (Yuan & Narayan 2014). We obtain $B_{\rm MAD} \approx 142$ G, which is roughly consistent with the magnetic field strength limit provided by Kino et al. (2015b), $50 \lesssim B_{\rm tot} \lesssim 124$ G, in the presence of an optically thick region with synchrotron self-absorption near the jet base. This indicates that the jet base might be highly magnetized and the jet can be accelerated by the Poynting flux conversion (McKinney 2006; Komissarov et al. 2007, 2009; Lyubarsky 2009).

2.4.6 RM at HST-1

The sudden increase of RM at HST-1 by a factor of ≈ 10 compared to those values at $\approx 2 \times 10^5\ r_{\rm s}$ with positive RM sign may require explanations that are different from the case of RMs inside the Bondi radius. This is because HST-1 is located outside the Bondi radius and thus the contribution of inflows and outflows to the observed RMs is probably small. A simple explanation would be a compact gas cloud located in the line of sight toward HST-1 with very high electron density and/or magnetic field strengths, which might be the case for a nearby radio galaxy 3C 84 (Nagai et al. 2017). However, this requires a remarkable coincidence because most of the jet region on relatively large spatial scales observed with the VLA show much smaller RMs well represented by ≈ 130 rad/m^2 (Algaba et al. 2016). We could not observe any significant jump in RM

at a specific distance from the black hole in the inner jet region and it is unlikely that a compact cloud with high Faraday depth is located only in the line of sight toward HST-1.

Another possible explanation is a recollimation shock which has been proposed to explain the compactness of HST-1 and its temporal variability (e.g., Stawarz et al. 2006; Bromberg & Levinson 2009, see Section 2.4.4 for more details). Emission from the shock is expected to concentrate near the jet axis where the pressure of the shocked gas is very high, surrounded by a relatively low-pressure region (Bodo & Tavecchio 2018). In this scenario, the emitting region would be quite compact and the dominant source of Faraday rotation would be the surrounding shocked jet region. This is consistent with (i) our finding that external Faraday rotation is dominant also in HST-1 and (ii) the large RM values in HST-1 which could be explained by the enhancement of thermal electron density and strong magnetic fields in the shock, on the order of mG (Harris et al. 2003, 2009; Giroletti et al. 2012). We will investigate the origin of the enhanced RM at HST-1 more deeply with more data sets in a forthcoming paper (Park et al. 2018, in prep.).

2.4.7 EHT observations

Our results indicate the presence of winds on relatively large spatial scales of $\gtrsim$ 5,000 $r_{\rm s}$. The observed continuous jet collimation profile from the vicinity of the jet base to the distance of $\lesssim$ 200,000 $r_{\rm s}$ (Junor et al. 1999; Doeleman et al. 2012; Asada & Nakamura 2012; Hada et al. 2013) implies that a similar mechanism of jet collimation by the winds may be at work on smaller scales as well. On-going and future full-polarimetric observations with the EHT (e.g., Doeleman et al. 2008, 2012; Lu et al. 2013; Akiyama et al. 2015; Johnson et al. 2015, 2018; Fish et al. 2016; Lu et al. 2018) in conjunction with the phased-up ALMA at 230 and 345 GHz will provide an unprecedented view of polarization and RM structures in the jet on scales down to a few $r_{\rm s}$ together with an image of the black hole shadow (e.g., Broderick & Loeb 2009; Dexter et al. 2012; Lu et al. 2018; Chael et al. 2016; Mościbrodzka et al. 2016, 2017; Akiyama et al. 2017; Pu et

al. 2017), enabling a definitive test for the origin of winds and the jet.

2.5 Conclusions

We studied Faraday rotation in the jet of M87 with eight VLBA data sets. We found that the magnitude of RM systematically decreases with increasing distance from the black hole from 5,000 to 200,000 $r_{\rm s}$. Our work leads us to the following principal conclusions:

1. We found that the degree of linear polarization in the jet is usually much higher than that expected in the case of internal Faraday rotation in a uniform slab with regular magnetic fields. In addition, we found that EVPA rotations are larger than 45° at various locations in the jet and always follow λ^2 scalings, which is difficult to reproduce with internal Faraday rotation in a synchrotron emitting region with a realistic geometry and magnetic field structure. We conclude that the systematic decrease of RM must originate from the magnetized plasma outside the jet, supporting an external Faraday rotation scenario.

2. We found that the observed sign of RM is predominantly negative inside the Bondi radius, without indication of significant difference in RMs detected on the north and south edges. The observed radial RM profile is difficult to explain with a sheath surrounding the jet permeated by poloidal magnetic fields being the Faraday screen. This implies that the Faraday screen consists of hot accretion flows, not of the jet sheath.

3. We applied hot accretion flows model to the RM data points and obtained a best-fit function consistent with $\rho \propto r^{-1}$. This result is in good agreement with the ADIOS model in which substantial winds, non-relativistic un-collimated gas outflows, are launched from hot accretion flows. The winds are likely surrounding the highly collimated relativistic jet and probably a dominant source of the observed RMs (Figure 2.10). However, we see indication for non-negligible contribution of inflows to the observed RMs as well.

4. The density profile we obtained leads to the pressure profile of the winds, an external medium surrounding the jet, which is $p_{\rm gas} \propto r^{-5/3}$. This profile is consistent with a scenario in which the jet is substantially collimated by the winds, resulting in gradual acceleration of the jet in an MHD process. This is in agreement with the observed gradual collimation and acceleration of the jet inside the Bondi radius.

5. The negative RM sign preferentially found inside the Bondi radius indicates that the jet exposes only one side of the toroidal magnetic loops in the Faraday screen (Figure 2.10). We conclude that the jet axis and the wind axis are mis-aligned with respect to each other. Since the jet is narrow, a slight mis-alignment by only $\approx 5^\circ$ can lead to a fixed RM sign at distances $\gtrsim$ 5,000 $r_{\rm s}$. According to recent GRMHD simulations (McKinney et al. 2013), such a (small) mis-alignment seems to be common in hot accretion flows, depending on the history of gas accretion, even when the magneto-spin alignment effect operates.

6. The mass accretion rate can be substantially lower than the Bondi accretion rate due to the winds; we obtained $\dot{M}_{\rm BH} = 1.6 \times 10^{-4} M_\odot {\rm yr}^{-1}$, assuming a radial self-similarity of the density profile. This leads to a radiative efficiency of 3.8% at $\dot{M}_{\rm BH}/\dot{M}_{\rm Edd} = 1.2 \times 10^{-6}$, which indicates that the radiative efficiency is not as small as usually assumed and the faintness of the nucleus of M87 is mainly due to the reduced mass accretion rate. Also, we obtained a jet production efficiency of $\gtrsim$ 110%, implying that extraction of rotational energy of a spinning black hole might be at work in a MAD state.

7. The rotation measure at HST-1, located outside the Bondi radius, is larger by an order of magnitude and shows the opposite sign compared to the RM profile inside the Bondi radius. We conclude that this might be related with a recollimation shock that possibly forms in HST-1.

We conclude with several caveats that need to be addressed in future studies. We used simple one-dimensional self-similar solutions for the density and magnetic field

strength in the hot accretion flows model, while it is unclear whether this is valid or not. Studies of two dimensional solutions of hot accretion flows showed a breakdown of spherical symmetry (e.g., Mosallanezhad et al. 2016; Bu & Mosallanezhad 2018), though the behavior of physical parameters measured close to the jet axis is poorly constrained yet. We assumed ≈ 130 rad/m^2 for the contribution of the diffuse gas in M87 outside the Bondi radius based on the results of RM studies of the large scale jet but this could be uncertain. We assumed that the same radial density profile holds for the polar region and for the equatorial region to estimate the mass accretion rate. This may not be true as seen in a recent study by Russell et al. (2018), though their results are obtained relatively close to the Bondi radius. We conclude that a sheath surrounding the jet is unlikely to be the Faraday screen based on the fact that the RMs detected on the southern and northern sides of the jet at a given distance are similar to each other. However, we could not test whether there are significant transverse RM gradients in the jet due to limited sensitivity and/or substantial depolarization. We plan to perform polarimetric observations with high sensitivity and having both short and long λ^2 spacings to constrain the origin of Faraday rotation more robustly and to investigate the depolarization mechanism in the near future.

Chapter 3

Intensive Monitoring of the M87 Jet with KaVA: Jet Kinematics based on Observations in 2016 at 22 and 43 GHz[†]

Abstract

We study the kinematics of the M87 jet using the first year data of the KVN and VERA Array (KaVA) large program, which has densely monitored the jet at 22 and 43 GHz since 2016. We find that the apparent jet speeds increase from $\approx 0.3c$ at ≈ 0.5 mas from the core to $\approx 2.5c$ at ≈ 22 mas, indicating that the jet is accelerated from subluminal to superluminal speeds on these scales. We complement the acceleration profile with an additional analysis of archival Very Long Baseline Array monitoring data observed in $2005 - 2009$ at 1.7 GHz, confirming that the jet is moving at relativistic speeds of $1.9 - 5.1c$ at distances $340 - 410$ mas. We combine the two kinematic results and find that the jet is gradually accelerated over a broad distance range that coincides with

[†]The contents of this chapter was submitted to the Astrophysical Journal and is under review (Park et al. 2019c)

the jet collimation zone, implying that conversion of Poynting flux to kinetic energy takes place in the jet region we probe. However, the observed trend of jet acceleration is relatively slow compared to the models of a highly magnetized jet and the results of numerical simulations, which suggests that Poynting flux conversion through the differential collimation of poloidal magnetic fields may not be very efficient. We discuss the possibility that the jet emission consists of multiple streamlines following different acceleration profiles, causing a non-negligible dispersion in the observed speeds at a given distance.

3.1 Introduction

Active galactic nuclei (AGNs) often produce highly collimated relativistic jets (e.g., Blandford et al. 2018). Superluminal motions of the jets at high apparent speeds up to tens of times the speed of light (c) are frequently observed in many radio-loud AGNs, indicating that they are traveling at nearly the speed of light (e.g., Lister et al. 2016; Jorstad et al. 2017). It is widely believed that the jets, after they are launched in the vicinity of the central supermassive black holes by the accretion of matter (Meier 2012), are collimated and accelerated simultaneously at distances $\lesssim 10^4 - 10^6\ R_{\rm S}$ from the black hole, where $R_{\rm S}$ is the Schwarzschild radius (e.g., Meier et al. 2001; Marscher et al. 2008). Very long baseline interferometry (VLBI) observations, providing a high angular resolution to resolve the jet acceleration and collimation zone, has been extensively used as a powerful tool for studies of jet acceleration and collimation mechanisms (e.g., Homan et al. 2015).

M87 is a primary target for studies of AGN jets. The black hole shadow revealed by recent Event Horizon Telescope (EHT) observations (EHT Collaboration et al. 2019a,b,c,d,e,f) demonstrates that the power source of this active galaxy is a black hole with a large mass of $M_{\rm BH} = 6.5 \times 10^9 M_\odot$ (EHT Collaboration et al. 2019f, see also Gebhardt et al. 2011). It is located at a distance of 16.8 Mpc (EHT Collaboration et al. 2019c; based on distance measurements of Blakeslee et al. 2009; Bird et al. 2010; Cantiello et al. 2018), giving a scale of 1 mas $\approx 130\ R_{\rm S}$. Previous VLBI observations

revealed that the jet is edge-brightened with an apparent jet opening angle becoming larger at smaller distances from the core on mas scales (up to $\gtrsim 100^\circ$ at ≈ 0.1 mas from the core, e.g., Reid et al. 1989; Junor et al. 1999; Hada et al. 2016; Kim et al. 2018a; Walker et al. 2018), indicating that the jet is being substantially collimated. The collimation continues at larger distances up to about 400 mas following a semi-parabolic profile of $R \propto z^{0.56}$, where R and z denote the jet radius and distance, respectively (Asada & Nakamura 2012; Hada et al. 2013; Nakamura & Asada 2013). Recent general relativistic magnetohydrodynamic (GRMHD) simulations (Nakamura et al. 2018) and a study of Faraday rotation in the jet (Park et al. 2019a) suggested that an external medium surrounding the jet, possibly non-relativistic winds launched from the accretion flows, may play a dynamical role in the jet collimation process.

While the jet collimation profile is constrained precisely in a broad range of jet distances, the jet acceleration profile is under debate. A bright knot known as HST-1, located at an angular distance ~ 900 mas from the core, shows superluminal motions of several components at apparent speeds up to $\approx 6.1c$ at optical wavelengths (Biretta et al. 1999) and up to $\approx 5.1c$ at radio wavelengths (Cheung et al. 2007; Giroletti et al. 2012; Hada et al. 2015). The jet apparent speeds become smaller at larger distances (Biretta et al. 1995, 1999; Meyer et al. 2013), implying that the jet acceleration mostly occurs inside the location of HST-1, which is almost coincident with the Bondi radius (Russell et al. 2015). Kovalev et al. (2007) reported subluminal motions of several components within the distance of ≈ 25 mas from the monitoring of the jet over ≈ 12 years at 15 GHz with the Very Long Baseline Array (VLBA). Similar results of very slow or no apparent motions were obtained at lower observing frequencies (Reid et al. 1989; Dodson et al. 2006). Asada et al. (2014) found that the jet motions remain subluminal until ≈ 200 mas and the jet is substantially accelerated to relativistic speeds between ~ 200 and ~ 400 mas by using the data observed in three epochs in 2007–2009 at 1.6 GHz with the European VLBI Network. However, recent studies using densely-sampled data with the VLBA at 43 GHz (Mertens et al. 2016; Walker et al. 2018) and with the KaVA (KVN and VERA Array, Niinuma et al. 2014) at 22 GHz (Hada et al. 2017) have

detected superluminal motions at distances $\lesssim 20$ mas, which is in contradiction with the earlier studies. Besides, these studies showed that the jet is substantially accelerated already at projected distances $\gtrsim 0.5$ mas.

To resolve the reason for the discrepancy between different studies and to constrain the jet acceleration profile more accurately, we started a dedicated monitoring program of M87 in the framework of a KaVA Large Program in 2016 (Kino et al. 2015a; Hada et al. 2017). In this program, M87 is observed biweekly over four to seven months every year at both 22 and 43 GHz quasi-simultaneously. The good sensitivity (with a typical dynamic range of $\approx 2000 - 4000$ for M87 at 22 GHz, Hada et al. 2017), the reasonably good angular resolution (≈ 1.2 mas and ≈ 0.6 mas at 22 and 43 GHz, respectively), and the good *uv*-coverage of the KaVA especially for short baselines (Figure 3.1) make it possible to investigate the jet velocity field at various distances from the core up to ≈ 25 mas (at 22 GHz). Besides, our quasi-simultaneous observations at 22 and 43 GHz enable to probe an evolution of the spectral properties of synchrotron-emitting plasma in the jet, which will be presented in a forthcoming paper (H. Ro et al. 2019, in preparation). The KaVA has recently expanded to the East Asian VLBI Network (EAVN) which includes 21 telescopes in total and covers a wide range of observing frequencies from 2.3 to 43 GHz (Wajima et al. 2016; An et al. 2018), and our large program also makes use of the EAVN since 2017. In this paper, we report the results of the jet kinematics of M87 by using the KaVA-only observations performed in 2016. More results using the EAVN data will be presented elsewhere (Y. Cui et al. 2019, in preparation).

The paper is organized as follows. We describe the observations, the KaVA large program, and data reduction in Section 3.2. We summarize the methods used for the M87 jet kinematics in previous studies in Section 3.3. We present the results of jet kinematics obtained with KaVA observations in Section 4. In Section 5, we supplement our jet proper motion measurements with archival VLBA data observed in 2005–2009 at 1.7 GHz, which can trace the jet motion beyond 100 mas. We discuss possible implications of our results in Section 3.6 and conclude in Section 3.7.

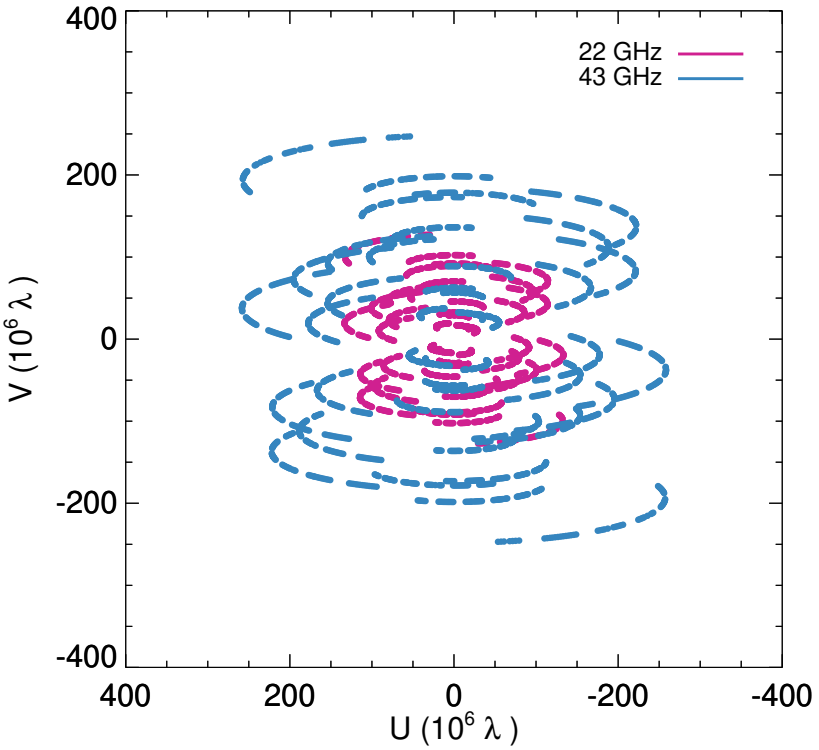

Figure 3.1. Typical *uv*-coverage of KaVA observations of M87 taken from the first epoch data at 22 (red) and 43 GHz (blue) in units of 10^6 times the wavelength.

In this work, we adopt a jet viewing angle of 17° which was constrained by using three independent methods (Mertens et al. 2016), considering the upper limit of $\theta \lesssim 19°$ derived from the maximum observed the apparent speed of $6.1c$ at HST-1 (Biretta et al. 1999), as in Walker et al. (2018).

3.2 Observations and Data Reduction

We observed M87 with the KaVA in nine epochs in 2016. Observations in each epoch were performed in two sessions, one at 22 GHz and the other at 43 GHz, separated from each other by one or two days. The monitoring interval between adjacent epochs is typically two weeks. The on-source time for M87 is about four and a half hours out

of the total observing time of seven hours for each epoch at each frequency, allowing us to achieve a good *uv*-coverage (Figure 3.1). The typical beam size is about 1.2 and 0.6 mas at 22 and 43 GHz, respectively. Under the natural weighting of the visibility data, the beam shape is close to a circular shape, as seen in previous KaVA observations (e.g., Niinuma et al. 2014; Oh et al. 2015; Hada et al. 2017). All seven KaVA stations successfully participated in the observations in most epochs, except for one that performed on 2016 Jun 01 at 22 GHz which lost two VERA (Mizusawa and Ishigaki) stations, and on 2016 Jun 02 at 43 GHz which lost the Mizusawa station; the 22 GHz observation data of this epoch is not included in the current paper. The weather condition was very good in general, providing us with a set of high-quality images with a typical dynamic range of 3000–4000 and 2000–3000 at 22 and 43 GHz, respectively. However, the data observed on 2016 May 05 at 43 GHz suffer from a severe weather condition in various stations, and we excluded this data from our analysis. Thus, we use the data observed in eight epochs in total at each frequency. We summarize the basic information of our observations in Table 3.1.

Our data were recorded in left-hand circular polarization with two-bit quantization in 8 IFs (baseband channels) at a recording rate of 1 Gbps, yielding a total bandwidth of 256 MHz, and correlated by the Daejeon correlator at the Korea-Japan Correlation Center (KJCC, Lee et al. 2014, 2015a). We performed a standard data post-correlation process with the NRAO's Astronomical Image Processing System (AIPS, Greisen 2003). A priori amplitude calibration was performed by using the antenna gain curves and system temperatures. We obtained models of the amplitudes of the antenna bandpass shapes by using the auto-correlation data of scans on bright calibrators, with which we normalized the bandpass shapes of all data. We scaled up the amplitudes by a factor of 1.3 to account for the known (constant) amplitude loss of the Daejeon hardware correlator (Lee et al. 2015b; Hada et al. 2017). We corrected antenna parallactic angles for the three KVN antennas only because the field rotators in the receiving rooms of VERA antennas fix the parallactic angle during observations. We also corrected instrumental delays in the visibility phases by using scans on bright calibrators. We

Table 3.1. Summary of KaVA observations in 2016

Exp. Code (1)	Obs. Date (2)	Stations (3)	Beam size (4)	$I_{\rm peak}$ (5)	$I_{\rm rms}$ (6)	$I_{\rm peak}/I_{\rm rms}$ (7)
			22 GHz			
k16mk02a	2016 Feb 25 (56d)	KaVA	$1.34 \times 1.20, -6.1$	1.41	0.42	3300
k16mk02c	2016 Mar 09 (69d)	KaVA	$1.42 \times 1.20, -0.2$	1.42	0.50	2805
k16mk02e	2016 Mar 21 (81d)	KaVA	$1.50 \times 1.25, -12.0$	1.45	0.51	2860
k16mk02g	2016 Apr 08 (99d)	KaVA	$1.35 \times 1.16, -10.3$	1.29	0.30	4336
k16mk02i	2016 Apr 21 (112d)	KaVA	$1.32 \times 1.23, -10.9$	1.28	0.36	3630
k16mk02k	2016 May 03 (124d)	KaVA	$1.35 \times 1.10, -13.4$	1.17	0.32	3748
k16mk02m	2016 May 23 (144d)	KaVA	$1.27 \times 1.10, -12.6$	1.15	0.32	3646
k16mk02q	2016 Jun 13 (165d)	KaVA	$1.25 \times 1.13, -3.1$	1.21	0.68	1776
			43 GHz			
k16mk02b	2016 Feb 26 (57d)	KaVA	$0.76 \times 0.63, 16.2$	1.10	0.42	2624
k16mk02d	2016 Mar 10 (70d)	KaVA	$0.79 \times 0.68, -0.24$	1.08	0.44	2405
k16mk02f	2016 Mar 20 (80d)	KaVA	$0.72 \times 0.64, -30.3$	1.04	0.33	3255
k16mk02h	2016 Apr 09 (100d)	KaVA	$0.71 \times 0.62, -7.5$	0.95	0.35	2665
k16mk02j	2016 Apr 22 (113d)	KaVA	$0.70 \times 0.61, -26.0$	0.90	0.38	2390
k16mk02n	2016 May 24 (145d)	KaVA	$0.64 \times 0.57, 2.1$	0.86	0.48	1794
k16mk02p	2016 Jun 02 (154d)	KaVA, -MIZ	$0.83 \times 0.65, 43.1$	0.82	0.42	1978
k16mk02r	2016 Jun 15 (167d)	KaVA	$0.71 \times 0.52, -34.0$	0.78	0.62	1240

Note. — (1) Experiment code of KaVA observations. (2) Observation date. Those in the parentheses denote the number of days elapsed since 2016 Jan 1. (3) Stations participating in observations. KaVA means that all seven stations successfully participated in observations. In the observation performed on 2016 Jun 02 at 43 GHz, the VERA Mizusawa station (MIZ) could not participate due to technical problems. (4) Full width at half maximum of the synthesized beam of M87 data with a natural weighting scheme in units of (mas $\times$ mas, deg). (5) Peak intensity of M87 with a natural weighting scheme in units of Jy per beam. (6) Off-source rms noise of M87 maps with a natural weighting scheme in units of mJy per beam. (7) Dynamic range of M87 images calculated from $I_{\rm peak}$ and $I_{\rm rms}$.

performed a global fringe fitting with a solution interval between 10 and 30s for each IF, depending on the weather conditions. The data were averaged over an each IF bandwidth, and we performed imaging with an iterative procedure of CLEAN and phase/amplitude self-calibration in the Caltech Difmap package (Shepherd 1997). We present naturally weighted CLEAN images at 22 and 43 GHz in Figures 3.2 and 3.3, respectively.

3.3 Summary of Previous Studies of the M87 Jet Kinematics

One of the most important issues in the jet kinematics is how to identify each part of the jet in different epochs. Different studies of the M87 jet kinematics used various methods, which may contribute to the discrepancy between their results. Thus, we summarize different methods implemented in different studies below.

(i) `Modelfit` with Gaussian components. This method fits several components of circular or elliptical Gaussian brightness distributions to the visibility data, describing the observed jet structure with several distinct regions having Gaussian brightness distributions. This is the standard method for the jet kinematics of radio-loud AGNs (e.g., Lister et al. 2016; Jorstad et al. 2017) since their jet structures usually consist of several knots. One of the biggest advantages of this method is that it is easy to identify different components in different epochs, especially when the total number of components in different epochs is the same. However, the M87 jet shows a complex jet structure with a prominent limb-brightening (e.g., Junor et al. 1999; Kovalev et al. 2007; Hada et al. 2016; Kim et al. 2018a; Walker et al. 2018), making it controversial whether the assumption of a simple Gaussian brightness distribution for each jet region can be applied to M87 or not. Kovalev et al. (2007) applied this method to their long-term monitoring data of the M87 jet obtained with the VLBA at 15 GHz and found apparent speeds $\lesssim 0.05c$. Asada et al. (2014) obtained the jet acceleration profile between ≈ 200 and ≈ 400 mas, by making use of this method as well. Hada et al. (2017) also used this

method for their KaVA monitoring data obtained in 2014 and derived relatively fast motions at apparent speeds up to $\approx 2c$ with an indication of jet acceleration at $\lesssim 10$ mas. We note that they also 'grouped' two components at distances of 3–6 mas and treated them as a single component to obtain the velocity because of the complicated component identification for this region. Britzen et al. (2017) obtained circular Gaussian components for the north and south jet edges separately for some epochs by using the MOJAVE program (Lister & Homan 2005, part of this data were presented in Kovalev et al. 2007), and obtained hints of jet acceleration at distances $\lesssim 10$ mas.

(ii) Visual inspection. The complex jet structure and the complicated component identification led several studies to pick characteristic patterns in the jet brightness distributions by visual inspection and to obtain the velocities. Ly et al. (2007) measured the apparent speeds of $0.25 - 0.4c$ at distances $\approx 2 - 4$ mas from the three locally brightened positions forming a triangular shape in two epochs of 2001.78 and 2002.42 of their VLBA observations at 43 GHz. Hada et al. (2016) identified four and five locally brightened components along the north and south jet limbs, respectively, and one component in the counterjet, using their VLBA observations at 43 and 86 GHz. They fitted an elliptical Gaussian function to each component in the image plane to determine the component position and found the apparent speeds of $0.15-0.48c$. Walker et al. (2018) visually determined the locations of local maxima in the total intensity maps and identified components in different epochs by blinking rapidly back and forth between the maps in different epochs. They found an indication of jet acceleration at $\lesssim 5$ mas for both north and south jet limbs with a range of apparent speeds of $\approx 0 - 5c$. Although this method is straightforward, the component identification would suffer from a lack of objectivity, especially when the total numbers of components in different epochs are not the same.

(iii) Subtracting the average image from the individual epoch images. Acciari et al. (2009) subtracted the average image of 11 epochs data observed in 2007 with the VLBA at 43 GHz from the individual epoch images in 2008, and they traced the bright regions in the subtracted images, obtaining an apparent speed of $1.1c$ at 0.77 mas. This

method assumes that the brightness enhancement near the core (at $\lesssim 0.5$ mas) is due to a new moving component ejected from the core. We note that they could use this method thanks to a significant increase in flux density of the inner jet observed in 2008 which was coincident with a flare seen at TeV energies and this method might not be applicable in general cases. We also note that Walker et al. (2018) could not detect such a high apparent speed at the given distance, even if they used more data sets including those used in Acciari et al. (2009).

(iv) The Wavelet-based Image Segmentation and Evaluation (WISE). This method allows one to decompose and segment images and to identify significant structural patterns (SSPs) in different epochs through the multiscale cross-correlation (MCC) method, providing an automated or unsupervised way to obtain the jet velocity field (Mertens & Lobanov 2015). Mertens et al. (2016) applied this method to the VLBA monitoring data of M87 observed in 11 epochs in 2007 at 43 GHz and revealed rich information about the velocity field at $\lesssim 6$ mas with a clear indication of jet acceleration on these scales. They also applied the stacked cross-correlation (SCC) algorithm (Mertens & Lobanov 2016) and found that there are at least two layers in the jet at 1–4 mas, one moving at a superluminal speed of $\gtrsim 2c$ and the other at a subluminal speed of $\lesssim 0.5c$. However, this method has not yet been applied for jet kinematics of many sources observed with different VLBI instruments. It needs to be tested whether or not this method works well for various data sets having different *uv*-coverage, angular resolution, imaging sensitivity, and sampling intervals.

(v) The brightness ratio of the jet and counterjet. Previous VLBI observations showed that there is tenuous but significant jet emission on the opposite side to the extended jet in the western direction with respect to the core (e.g., Ly et al. 2007; Kovalev et al. 2007; Hada et al. 2016; Mertens et al. 2016; Walker et al. 2018; Kim et al. 2018a). The location of the jet base, probably coincident with the location of the black hole, was constrained to be quite close to the positions of the core at cm wavelengths, i.e., $\lesssim 0.04$ mas from the 43 GHz core (Hada et al. 2011), indicating that the weak jet emission on the eastern side of the core is a counterjet. When assuming that

the jet and the counterjet are intrinsically symmetric, and that there is no substantial free-free absorption towards the counterjet by the accretion flows (which seems to be the case for M87, see Ly et al. 2007, see also, e.g., Jones et al. 1996; Jones & Wehrle 1997; Walker et al. 2000; Fujita & Nagai 2017 for other nearby radio galaxies), then the brightness ratio between the jet and counterjet at the same distance from the jet base can be explained by the result of Doppler boosting. Specifically, the brightness ratio is related to the intrinsic jet speed in units of the speed of light (β) as follows[1]:

$$\frac{I_{\rm jet}}{I_{\rm cjet}} = \left(\frac{1+\beta\cos\theta}{1-\beta\cos\theta}\right)^{2-\alpha}, \tag{3.1}$$

where $I_{\rm jet}$ and $I_{\rm cjet}$ denote the jet and counterjet intensity, respectively, α is the spectral index of the synchrotron radiation ($I_\nu \propto \nu^\alpha$), and θ is the jet viewing angle. The intrinsic jet speed can be converted into the apparent speed ($\beta_{\rm app}$) via

$$\beta_{\rm app} = \frac{\beta\sin\theta}{1-\beta\cos\theta}. \tag{3.2}$$

This method does not suffer from the complicated characterization and identification of jet 'components' in different epochs. However, imaging the counterjet emission in VLBI observations is usually subject to relatively large calibration and deconvolution errors, which may introduce relatively large errors in the measured brightness ratio (e.g., Ly et al. 2004). Combining the measurements of the brightness ratio in different studies, using the adopted jet viewing angle of 17° and the spectral index of $\alpha = -0.7 \pm 0.2$ for the inner jet region at 43 GHz (Hada et al. 2016), one can obtain the apparent speeds of $\sim 0.1-0.4c$ at $\sim 0.2-1.0$ mas (Ly et al. 2007; Hada et al. 2016; Mertens et al. 2016; Walker et al. 2018; Kim et al. 2018a).

[1]We consider the case of a continuous jet for the beaming factor (Ghisellini et al. 1993).

3.4 Jet Kinematics on Scales of $\lesssim 20$ mas Based on KaVA Observations

Among the five methods of the jet kinematics listed above, we applied three methods, (i), (ii), and (iv) to our data, and the application of each method is described in detail in Section 3.4.1, 3.4.2, and 3.4.3, respectively. We could not find significant brightening of the core and the inner jet emission during the period of our observations so that we could not apply the method (iii). Instead, the core intensity decreases with time (Table 3.1), which will be examined in a forthcoming paper by combining with other data sets observed in different periods (Y. Cui et al. 2019, in preparation). Although we found an indication of the counterjet emission in our data, similarly to our previous observations in 2013–2014 at 22 GHz (Hada et al. 2017), the limited angular resolution of the KaVA makes it difficult to apply the method (v). We describe how we obtain the kinematic results with each method below.

3.4.1 Modelfit with Circular Gaussian Components

We fitted several circular Gaussian components to the visibility data with the task `modelfit` in Difmap. We restricted the total number of components to be about five and four[2] for the 22 and 43 GHz data, respectively, which allows us to identify the components in different epochs. We found that those circular Gaussian components could reproduce the overall jet structure well with the peak intensity in the residual images less than 10 mJy per beam at both observing frequencies, similarly to the case of our previous study of the M87 jet kinematics with the KaVA data observed in 2013–2014 (Hada et al. 2017). We present the fitted Gaussian components on top of the CLEAN maps at 22 and 43 GHz in the left panels of Figures 3.2 and 3.3, respectively. At 22 GHz, the distributions of different identified components, labeled as KG1, KG2,

[2]When we increase the number of Gaussian components, we encountered that some of the components have very small sizes, becoming point source models during the `modelfit` iterations. This is not consistent with the basic assumption of this method, using a set of circular Gaussian components with finite sizes.

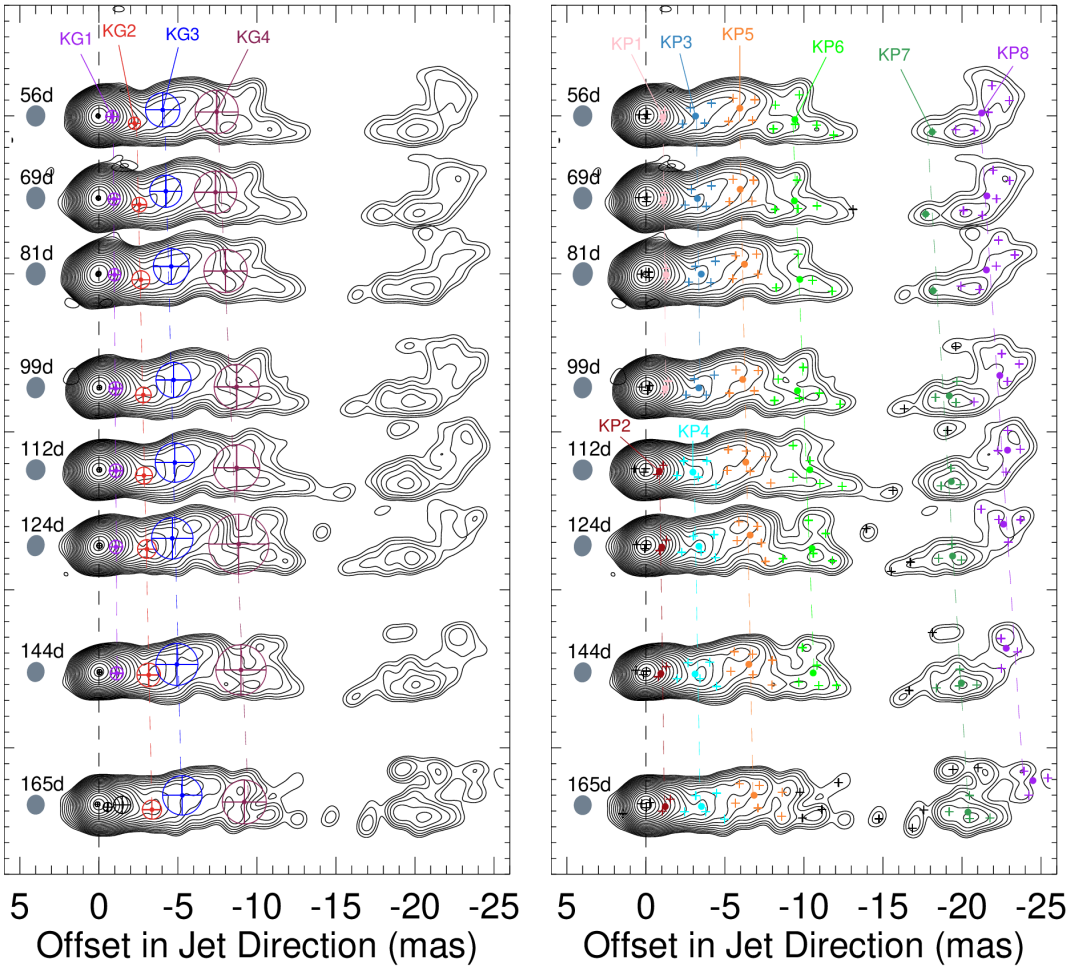

Figure 3.2. Contours show CLEAN images of the M87 jet obtained with the KaVA observations in 2016 at 22 GHz. The model components obtained in the `modelfit` analysis with circular Gaussian components (Section 3.4.1) and with point source components (Section 3.4.2) are drawn on top of the contours in the left and right panels, respectively. The components with the same color in different epochs are identified to represent the same parts of the jet. The point source models in the right panel are grouped and treated as a single component and their mean positions weighted by flux density are shown with the small filled circles. The dashed lines show the best-fit linear motions of the components. All maps are rotated clockwise by 18° with respect to the map center in each epoch.

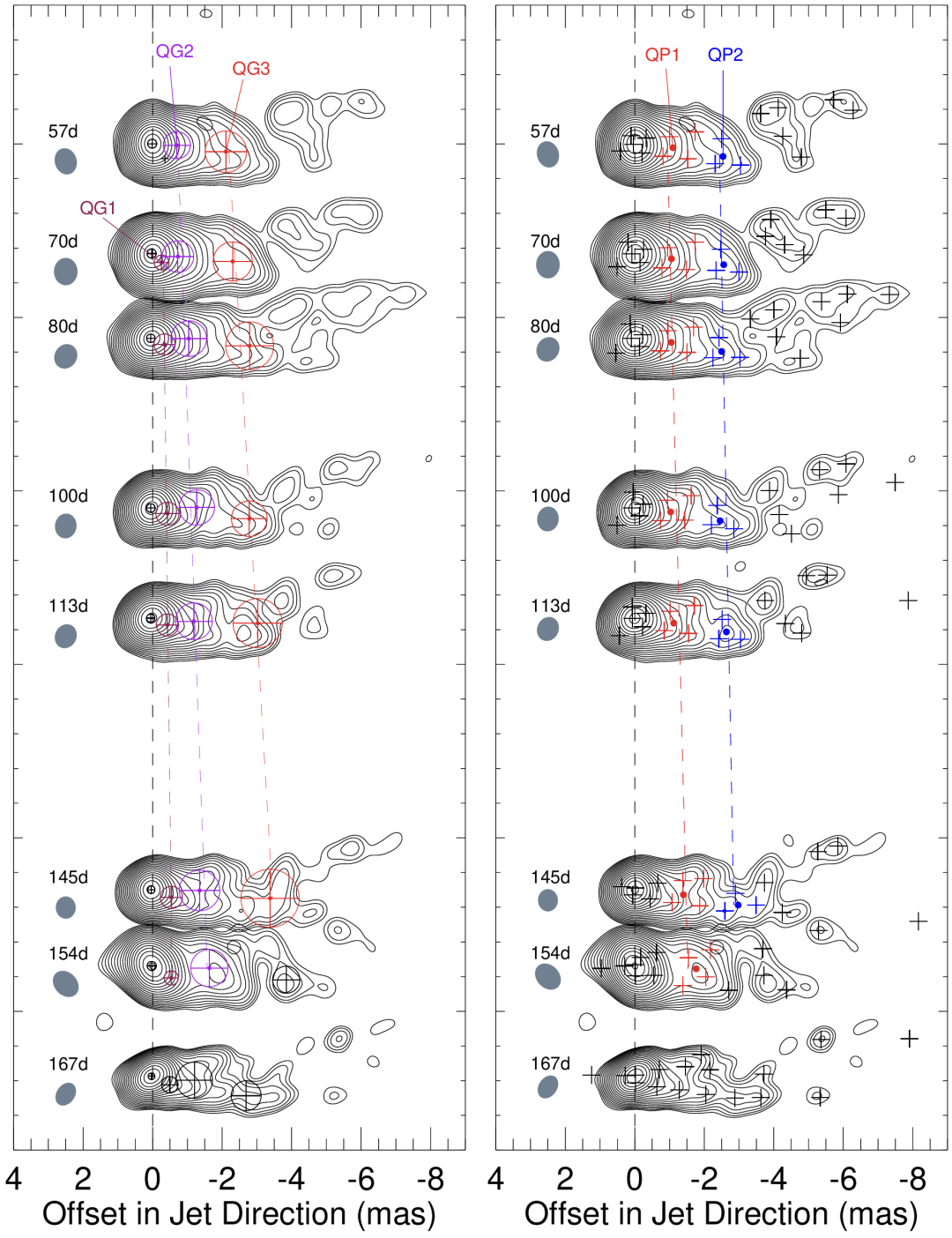

Figure 3.3. Same as Figure 3.2 but at 43 GHz. Contours start at 2.2 mJy per beam and increase by factors of $\sqrt{2}$.

KG3, and KG4, in different epochs are quite similar. We note that we were forced to put two components at ≈ 1 mas for the last epoch unlike other epochs, which prevented us from identifying KG1 for that epoch. We also note that we did not attempt to model the evolution of highly complex jet structures at ≈ 20 mas with simple one or two Gaussian components; we did it with another method in Section 3.4.2. We fitted a linear function to the separation from the core with time for each identified component, obtaining jet velocities at different distances. At 43 GHz, we identify three components, labeled as QG1, QG2, and QG 3, showing similar distributions in different epochs, except in the last epoch when the locations of the fitted components abruptly move inward compared to the earlier epochs. Thus, we did not include the components in this epoch for the kinematics because they may not trace the same parts of the jet as the earlier epochs. Besides, the component at ≈ 0.5 mas in the first epoch has a size much smaller than the later epochs, and we did not include this component.

We present the flux, size, and separation from the core as functions of time for the identified components in Figure 3.4. The properties of each identified component vary smoothly in general, suggesting that the components in different epochs may trace the same part of the jet indeed. Remarkably, separation from the core for the components KG1 and QG2, and KG2 and QG3 are consistent with each other, gradually increasing with time. This result indicates that each outflowing jet region is successfully traced at both observing frequencies.

Estimating the errors of component position is not straightforward. We assumed that the error is one-fifth of the synthesized beam size at a zero distance from the core and linearly increases with distance to become comparable to the synthesized beam size at the distances of the observed maximum jet extension, ≈ 25 and ≈ 7 mas at 22 and 43 GHz, respectively. This approach is based on the fact that the position errors of faint components at larger jet distances would be larger than those of bright components close to the core (Fomalont 1999) and that a similar approach was adopted in previous studies of jet collimation (e.g., Mertens et al. 2016).

3.4.2 Modelfit with Point Sources and Grouping

Since the jet shows a limb-brightening, fitting models with several circular Gaussian components to the data (Section 3.4.1) cannot reproduce the observed jet emission accurately, which may introduce additional errors in the jet kinematics. Thus, we increase the number of model components this time until the residual images become dominated by noise, similarly to the usual `modelfit` analysis that has been applied to the jet kinematics of many radio-loud AGNs (e.g., Lister et al. 2016; Jorstad et al. 2017). During the `modelfit` procedure, we found that the sizes of many Gaussian components become virtually zero. The distribution of those models with zero size is changed from epoch to epoch, which makes component identification almost impossible. Thus, we used point source component with zero sizes instead of using circular Gaussian components to be consistent in different epochs. The distribution of fitted components on top of naturally-weighted CLEAN images at 22 and 43 GHz is shown in the right panels of Figures 3.2 and 3.3, respectively.

We also introduced grouping of different point source components for the jet kinematics and component identification. This is because each point source model may not represent a distinct jet emitting region, which must have a finite size, though fitting with many point source models would reproduce the observed jet structures quite well mathematically. Besides, we are interested in obtaining the jet bulk speeds and grouping different components would be a good strategy when the jet structure is complex (see, e.g., Lisakov et al. 2017 for the case of 3C 273). We obtained the positions of grouped components by averaging the positions of individual components weighted by their flux densities.

We adopt different grouping schemes for different jet regions, and we explain in details for the 22 GHz data first. There are six and seven components at $\lesssim 5$ mas in the first four and the last four epochs, respectively. We found that the distribution of these components is very similar in the first and the last four epochs, separately. Thus, we group two components at ≈ 1 mas and identify them as a single component in the two periods separately (KP1, KP2). The four and five components at ≈ 3 mas are

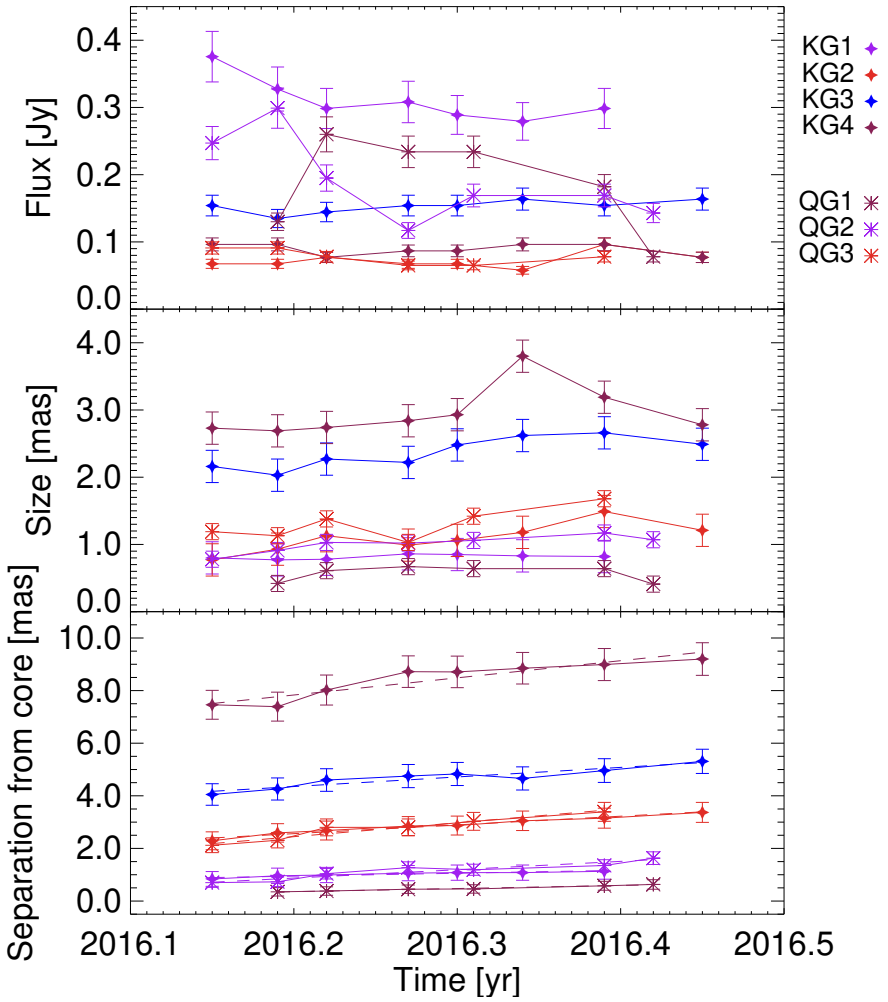

Figure 3.4. Flux density (top), size (middle), and separation from core (bottom) as functions of time for different identified components in the `modelfit` analysis with circular Gaussian components (Section 3.4.1) at 22 (diamonds) and 43 GHz (asterisks). The names of identified components are noted in the top right. The dashed lines in the bottom panel show the best-fit lines.

grouped and identified in the two periods separately as well (KP3, KP4). This grouping scheme is based on our assumption that each grouped component represents the same jet region, provided that individual components used for the grouping have the same total number of components and a similar spatial distribution in different epochs. At a

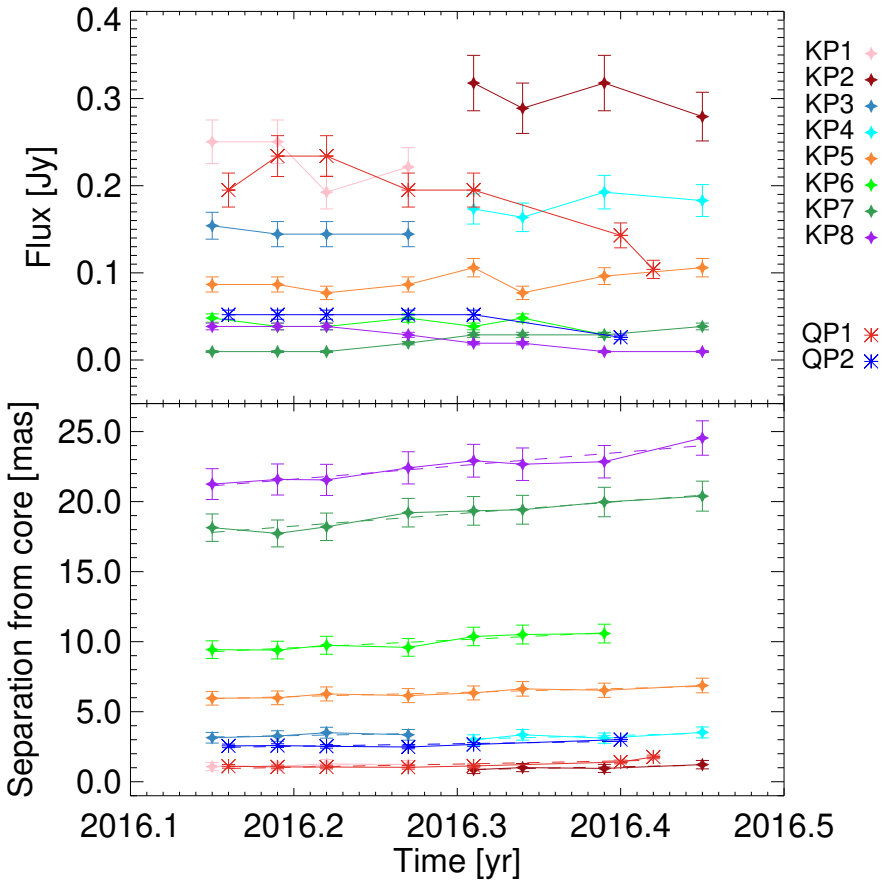

Figure 3.5. Flux density (top) and separation from core (bottom) as functions of time for different identified components in the `modelfit` analysis with point source components (Section 3.4.2) at 22 (diamonds) and 43 GHz (asterisks). The names of identified components are noted in the top right. The dashed lines in the bottom panel show the best-fit lines.

distance of $\approx 8 - 13$ mas, a triangle-like jet shape is detected in all epochs except the last epoch, which led us to group and to identify the components in this region (KP6). Then, the remaining components at $\approx 5 - 8$ mas are grouped and identified (KP5).

At a distance $\approx$ 20 mas, the jet re-brightens and significant emission is detected in all epochs. The shape of this emitting region is arc-like, which is reminiscent of the

filamentary jet structures detected on pc scales (e.g., Reid et al. 1989; Walker et al. 2018) and on kpc scales (e.g., Owen et al. 1989; Perlman et al. 2001; Lobanov et al. 2003). The bright knot in the southern limb at $\approx$ 20 mas apparently moves inward from the first to the fifth epochs and then moves outward in the last four epochs again. We consider that this apparent inward motion is likely caused by the fact that a new jet component enters this area from the upstream side, shifting the effective brightness centroid of this structure inward. We group and identify the components based on this assumption (KP7 and KP8). This region is where a subluminal motion of a knot ($\lesssim 0.3c$) was reported in previous low-frequency observations (Reid et al. 1989), and our result suggests that the underlying flow speed would actually be quite fast. Since the jet becomes brighter at this location, when there are materials flowing out from this region and flowing into this region, it may appear as a stationary or slowly moving feature when observed with a limited angular resolution and with relatively long intervals between epochs.

At 43 GHz, we could detect four point source components at 1–2 mas and three components at 2–3 mas in many epochs. We group and identify these components and obtain the jet speeds. We present the flux density and separation from the core as functions of time for different grouped components in Figure 3.5. Similarly to the case of our `modelfit` analysis with circular Gaussian components (Section 3.4.1), the properties of the grouped components vary smoothly, indicating that they may trace the same parts of the jet in different epochs. We estimate the errors of the positions of grouped components as follows. For those who have the same numbers and similar distributions of individual components in different epochs, i.e., KP1, KP2, KP3, KP4, QP1, and QP2, we assumed the errors which provide us with $\chi^2/d.o.f. = 1$ for the fitting of linear functions to the separation from the core, where $d.o.f.$ denotes the degree of freedom. This is because there would not be much errors introduced by the grouping or component identification in this case. For other grouped components, we estimated the position errors in the same manner as in Section 3.4.1.

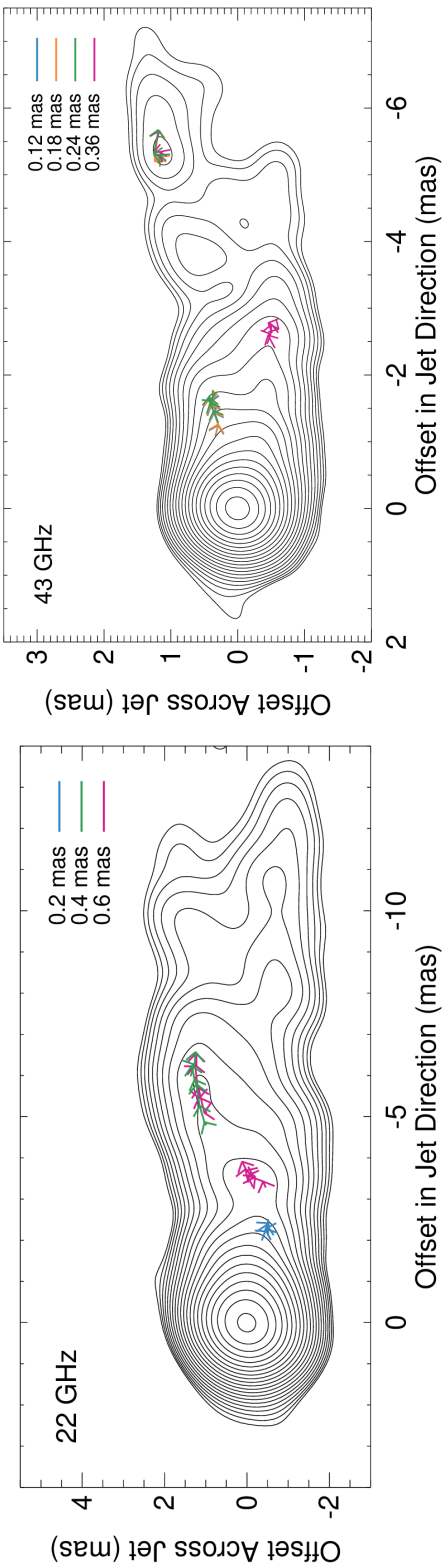

Figure 3.6. Stacked map of the CLEAN images at 22 (left) and 43 GHz (right) rotated clockwise by 18° with respect to the map center. Contours start at 0.8 mJy per beam and increase by factors of $\sqrt{2}$. The displacements of several SSPs between adjacent epochs detected in the WISE analysis are shown with the arrows. Different colors denote different spatial scales applied to the SWD and IWD (Section 3.4.3).

3.4.3 Wise

We applied a WISE analysis (Mertens & Lobanov 2015) to our KaVA images of the M87 jet. We decomposed each map with the segmented wavelet decomposition (SWD) method to detect a set of SSPs with a 3σ detection threshold. We implemented the intermediate wavelet decomposition (IWD[3]) as well for a robust detectability of displacements of SSPs (Mertens et al. 2016). We applied the SWD on two spatial scales of 0.2 (0.12) and 0.4 (0.24) mas and amended them with the IWD on scales of 0.3 (0.18) and 0.6 (0.36) mas at 22 (43) GHz. We identify SSPs in adjacent epochs by using the MCC method with a tolerance factor of 1.5 and a correlation threshold of 0.65. We obtained velocity vectors for SSPs detected in at least four adjacent epochs by fitting linear functions to their separation from the core with time.

We found that the observed displacement vectors of SSPs consist of two groups: one showing radial, outward motions consistently in many different epochs and the other showing quasi-stationary or inward motions with relatively large dispersion in the positions of SSPs. We assumed that the latter group does not represent intrinsic jet motions but might be affected by the limited angular resolution of our KaVA observations. We discuss the validity of this assumption in detail in Appendix B.1. We present the displacement vectors in the former group in Figure 3.6. We note that the displacement vectors obtained on different SWD/IWD scales in the same parts of the jet are significantly different from each other at several locations, demonstrating the dependence of the WISE results on SWD/IWD scales for our KaVA data (see Appendix B.1). In those cases, we used the results obtained from the finest scale for our further analysis to be less affected by potential resolution effects. We show the mean radial distances from the core and the observed radial speeds of the jet components obtained by the three methods in Table 3.2.

[3]IWD allows one to cover intermediate scales between SWD scales and to improve cross identification of the individual features (see Appendix A in Mertens et al. 2016)

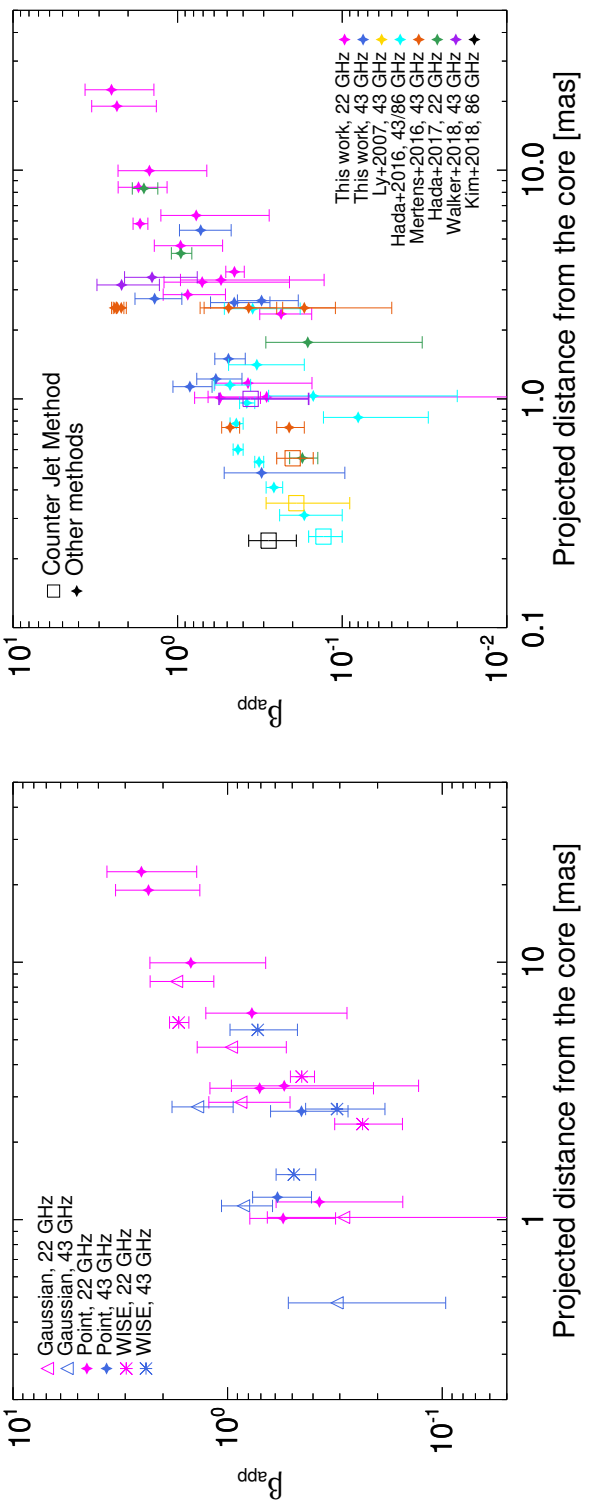

Figure 3.7. Left: apparent speed as a function of projected distance from the core from the KaVA observations at 22 (magenta) and 43 (blue) GHz. The different symbols are from different methods applied to the jet kinematics (Section 3.4). Right: same as the left panel but adding the apparent speeds obtained in other studies to the diagram (Ly et al. 2007; Hada et al. 2016; Mertens et al. 2016; Hada et al. 2017; Walker et al. 2018; Kim et al. 2018a). The data points obtained by the jet to counterjet brightness ratio analysis are shown in the open squares, while those obtained by other methods are shown in the filled diamonds.

3.4.4 Jet Apparent Speeds and Comparison with Other Studies

We present the apparent jet speeds obtained from the three different kinematics analysis at two frequencies in the left panel of Figure 3.7. The apparent speeds, in general, increase from $\approx 0.3c$ at a distance ≈ 0.5 mas to $\approx 2.5c$ at ≈ 20 mas. However, there is non-negligible dispersion in the speeds at a given distance, especially at 2–4 mas. The dispersion might be produced by the velocity stratification intrinsic to the jet or by potential systematic errors in different methods we applied. As already explained in Section 3.3, the first method, `modelfit` with circular Gaussian components, has an advantage of a straightforward component identification in different epochs. However, the results can be affected by non-negligible residual emission in the maps which could not be properly modeled by a few Gaussian components only. The second method, `modelfit` with point sources and grouping of different components for cross-identification in different epochs, is not affected by the residual jet emission. However, it relies on visual inspection for grouping and identification and could be quite subjective. The WISE analysis is based on statistical methods and does not lose an objectivity. However, we encountered the displacement vectors of SSPs showing two distinct groups and adopted only one of the groups, which needs to be investigated more carefully with other KaVA/EAVN data (see Appendix B.1).

In the right panel of Figure 3.7, we compare our results with other previous VLBI observations. We include the results obtained from the data observed with relatively small sampling intervals (e.g., $\lesssim 3$ weeks) in many epochs, i.e., more than five epochs, to avoid possible effects of a large sampling interval on the results, or from the analysis of jet to counterjet brightness ratio. We converted the observed brightness ratio in different studies into the apparent speeds with the adopted viewing angle of 17° and the spectral index of $\alpha = -0.7$ for the inner jet (at 0.2–1.2 mas) obtained at 22–86 GHz (Hada et al. 2016). As for the results of Mertens et al. (2016), we included the values derived by their stacked cross-correlation analysis which are representatives of a large number of jet speeds derived by the WISE analysis. Also, we present an average of the component speeds measured at core distances greater than 1.8 mas reported by

Walker et al. (2018).

Although there is general scatter as noted above, all different studies using various methods and instruments show a consistent trend of jet acceleration. The dispersion in the observed speeds at a given distance is also present in other studies as well. It is notable that the observed speeds derived by the jet to counterjet brightness ratio, not much affected by the complicated component identification in different epochs or by the limited cadence of observations, and those derived by other methods are consistent with each other. This result suggests that the jet is moving at subluminal speeds at distances $\lesssim 1$ mas from the core. We note that our results are consistent with those of Mertens et al. (2016) and Walker et al. (2018) at distances $\lesssim 1$ mas, while the speeds we obtained are smaller than the fast motions of Mertens et al. (2016) and are marginally consistent with Walker et al. (2018) at distances $\gtrsim 2$ mas.

3.5 Jet Kinematics on Scales of $\approx 340 - 410$ mas Based on VLBA Archive Data

While there is rich information about the jet velocity measurements available at relatively small distances of $\lesssim 20$ mas thanks to many recent studies with VLBI observations at relatively high frequencies of $\gtrsim 15$ GHz, the velocity measurements at outer jet distances is still limited. Asada et al. (2014) showed pioneering results which connect the velocity fields between mas scales and arcsecond scales, indicating substantial jet acceleration from subluminal to superluminal speeds occurring at $\approx 180 - 450$ mas. However, recent studies including our present study have found that the jet shows superluminal motions already at $\lesssim 20$ mas (see Figure 3.7). Therefore, the scale where bulk jet acceleration occurs in M87 is still under debate.

One of the possible explanations for the rapid jet acceleration observed at $\gtrsim 180$ mas (Asada et al. 2014) is that fast jet motions could not be traced by their observations due to the limited angular resolution (with the FWHM of the synthesized beam of 19.9×14.6 mas) and the large time interval between adjacent epochs (about one year).

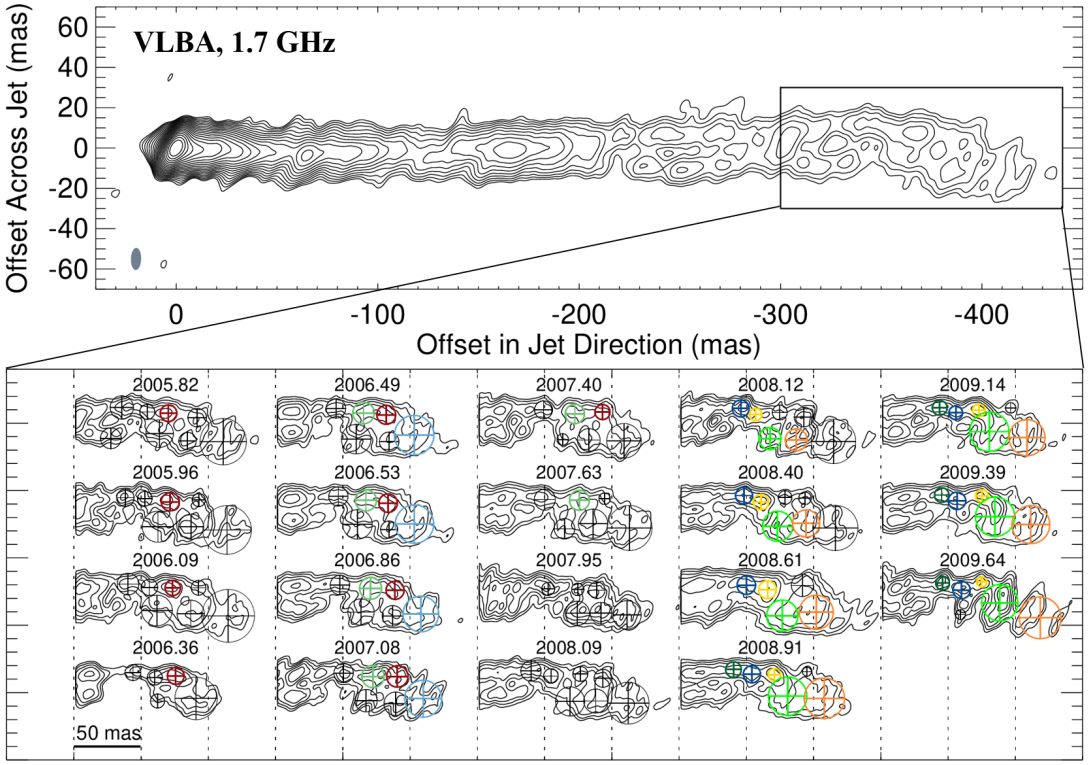

Figure 3.8. Top: a CLEAN image of the M87 jet observed with the VLBA on 2005 Oct 27 at 1.7 GHz. The gray shaded ellipse in the lower left part denotes a typical size of the full width at half maximum of the synthesized beam. Contours start at 1 mJy per beam. The map is rotated clockwise by 23°. Bottom: CLEAN maps showing the region in the rectangular box in the top panel for 19 VLBA archival data we analyzed (Section 3.5). The observation date in units of year is noted for each map. The circular Gaussian components fitted to the visibility data are shown with the crosses surrounded by circles. The components with the same color in different epochs are identified as the same component.

To investigate this possibility and to probe the jet velocity field over a wide distance range, we performed a complementary jet kinematic analysis by using the archival VLBA monitoring data observed in 19 epochs between 2005 and 2009 at 1.7 GHz. These data were presented in previous studies of HST-1 (Cheung et al. 2007; Giroletti

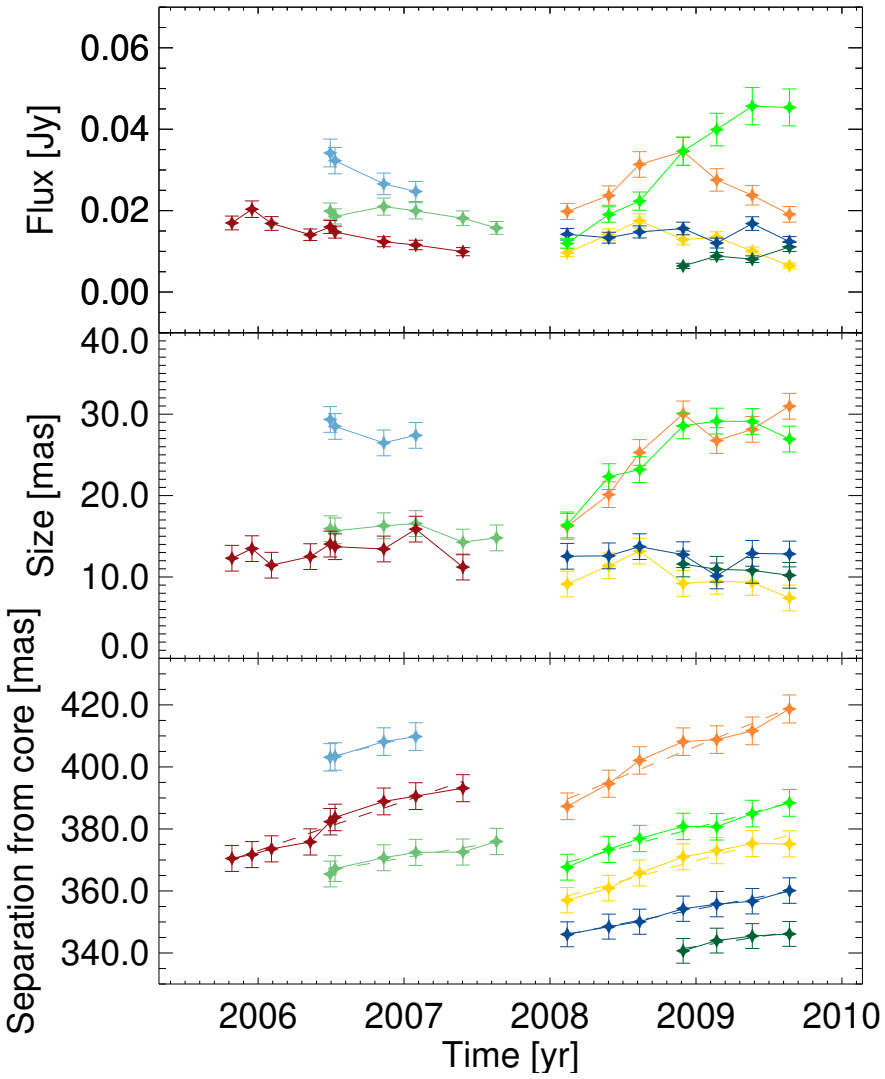

Figure 3.9. Same as Figure 3.4 but for the VLBA archival data observed at 1.7 GHz (Figure 3.8). The same color scheme for the identified components as in Figure 3.8 is used.

et al. 2012). We revisited these data in our recent study of Faraday rotation in the M87 jet (Park et al. 2019a), where the details of the data reduction process are shown. In this paper, we present our kinematic analysis using these data at distances $\lesssim 450$ mas.

We show a naturally-weighted CLEAN image of the first epoch data in the upper

panel of Figure 3.8. A typical size of the full width at half maximum of the synthesized beam is 11×5 mas with a position angle of $-2°$, improved by a factor of two compared to the observations of Asada et al. (2014), and a typical rms noise level is ≈ 0.2 mJy per beam. Although the whole jet structure between the core and the extended jet down to ≈ 450 mas was successfully imaged, we found that there are locally brightened jet regions at ≈ 20, 65, and 165 mas in all epochs. The positions of these regions are almost the same in different epochs, making them appear stationary, as already seen in the previous observations (Reid et al. 1989; Asada et al. 2014). Besides, the jet structure between ≈ 200 and ≈ 320 mas is quite smooth, and it was almost impossible to trace each part of the jet in different epochs. Fortunately, at $\gtrsim 320$ mas, the jet shows a distinct shape like a 'head' consisting of several knotty structures, allowing us to trace the motions in this region. We present the evolution of this structure in the bottom panel of Figure 3.8.

We performed the `modelfit` analysis with circular Gaussian components. Thanks to the high resolution of the VLBA and the large width of the jet in the region of our interest, the jet emission is modeled well with several circular Gaussian components along the north and south limbs separately. We identify components in different epochs only when (i) the distribution of neighboring components is similar and (ii) the properties of components, i.e., flux density, size, and separation from the core, vary smoothly over more than four successive epochs. This tight criterion allows us to avoid potential misidentification of the components. The components identified to be the same part of the jet are shown with the same color in different epochs (Figure 3.8). We present the properties of these components as functions of time in Figure 3.9, showing that all the quantities vary smoothly over time. Similarly to the case of our KaVA analysis presented in Section 3.4.1, we assumed position errors linearly increasing from one-fifth of the synthesized beam size at a zero distance to one beam size at ≈ 450 mas. We present the results of jet kinematics using the VLBA data in Table 3.2.

The apparent jet speeds obtained in our study are consistent with those reported by Asada et al. (2014) at corresponding distances. Thus, we confirm the presence of

superluminal motions at apparent speeds $\approx 2-5c$ at $\approx 340-410$ mas, by using the data more densely sampled, observed in many more epochs with a higher angular resolution compared to the previous study (Asada et al. 2014). However, our VLBA results were focused (limited) to the distance range of 340-410 mas. One may expect an increase in the jet apparent speed by $\approx 1c$ within this range according to the jet acceleration trend of Asada et al. (2014), which is almost comparable to the errors of our VLBA results (Table 3.2). Therefore, we could not test whether there is a rapid jet acceleration from subluminal to superluminal speeds at distances between 180 and 450 mas with the data presented in this paper only. In this aspect, probing the velocity field at distances $\lesssim 300$ mas with future observations will be critical. As mentioned above, we found the re-brightening of the jet at several locations (at ≈ 20, 65, and 165 mas, see Figure 3.8) and the smooth jet brightness distribution for this region, which makes it difficult to obtain reliable kinematic results. We note that we found an indication of underlying fast jet flows for one of the re-brightened, apparently stationary region at ≈ 20 mas with our KaVA observations at 22 GHz (Section 3.4.2) which have a higher angular resolution and cadence compared to the previous observations (e.g., Reid et al. 1989). This result indicates that we are probably missing fast jet motions at $\lesssim 300$ mas as well and this possibility needs to be tested by dedicated VLBI monitoring observations with a high cadence and a high angular resolution in the future.

Table 3.2. Results of jet kinematics

Methods (1)	$\langle R \rangle$ (mas) (2)	μ_r (mas yr^{-1}) (3)	$\beta_{\rm app}$ (4)
	KaVA 22 GHz		
Circular Gaussian	1.02 ± 0.10	1.09 ± 1.38	0.29 ± 0.37
	2.86 ± 0.34	3.28 ± 1.35	0.87 ± 0.36
	4.68 ± 0.39	3.63 ± 1.61	0.96 ± 0.43
	8.42 ± 0.70	6.54 ± 2.15	1.73 ± 0.57
Point Sources	1.01 ± 0.16	2.08 ± 0.90	0.55 ± 0.24
	1.17 ± 0.09	1.41 ± 0.84	0.37 ± 0.22
	3.31 ± 0.15	2.06 ± 1.57	0.54 ± 0.42
	3.24 ± 0.24	2.68 ± 1.89	0.71 ± 0.50
	6.34 ± 0.32	2.92 ± 1.87	0.77 ± 0.49
	9.95 ± 0.52	5.61 ± 3.10	1.48 ± 0.82
	19.05 ± 0.94	8.84 ± 3.75	2.34 ± 0.99
	22.47 ± 1.06	9.54 ± 4.27	2.52 ± 1.13
WISE	2.35 ± 0.08	0.89 ± 0.31	0.24 ± 0.08
	3.59 ± 0.18	1.71 ± 0.22	0.45 ± 0.06
	5.83 ± 0.68	6.40 ± 0.66	1.69 ± 0.17
	5.84 ± 0.56	4.96 ± 0.89	1.31 ± 0.24
	KaVA 43 GHz		
Circular Gaussian	0.47 ± 0.11	1.17 ± 0.80	0.31 ± 0.21
	1.13 ± 0.34	3.19 ± 0.85	0.84 ± 0.23
	2.74 ± 0.46	5.22 ± 1.65	1.38 ± 0.44
Point Sources	1.22 ± 0.27	2.22 ± 0.68	0.59 ± 0.18
	2.64 ± 0.19	1.71 ± 0.67	0.45 ± 0.18
WISE	1.50 ± 0.21	1.86 ± 0.39	0.49 ± 0.10
	1.58 ± 0.15	1.37 ± 0.39	0.36 ± 0.10
	2.69 ± 0.13	1.17 ± 0.47	0.31 ± 0.12
	5.46 ± 0.23	2.74 ± 0.95	0.72 ± 0.25
	5.50 ± 0.21	2.67 ± 0.45	0.71 ± 0.12

Table 3.2 (cont'd)

Methods (1)	$\langle R \rangle$ (mas) (2)	μ_r (mas yr^{-1}) (3)	$\beta_{\rm app}$ (4)
	5.53 ± 0.17	2.23 ± 0.47	0.59 ± 0.12
	VLBA 1.7 GHz		
Circular Gaussian	344.07 ± 2.43	7.30 ± 7.36	1.93 ± 1.94
	353.07 ± 5.02	9.13 ± 3.04	2.41 ± 0.80
	368.32 ± 7.23	12.88 ± 3.11	3.40 ± 0.82
	370.73 ± 3.83	7.96 ± 4.05	2.10 ± 1.07
	378.98 ± 7.00	12.65 ± 3.17	3.34 ± 0.84
	381.14 ± 8.58	15.91 ± 2.86	4.20 ± 0.76
	404.47 ± 10.68	19.22 ± 3.30	5.08 ± 0.87
	406.11 ± 3.37	11.92 ± 9.13	3.15 ± 2.41

Note. — (1) Methods of the jet kinematics used. (2) Mean radial distance from the core and 1σ scatter of the distances. (3) Angular radial speed and 1σ uncertainty. (4) Radial speed in units of the speed of light and 1σ uncertainty.

3.6 Discussion

In Figure 3.10, we present the four-velocities $\Gamma\beta$, where Γ is the bulk Lorentz factor and β the intrinsic jet speed in units of the speed of light, converted from the apparent jet speeds obtained from our KaVA and VLBA results with the adopted jet viewing angle of 17°, as a function of de-projected distance from the black hole (after correcting for the core positions with respect to the jet base by using the core-shift measurements by Hada et al. 2011) in units of $R_{\rm S}$. We include four data points from our recent study of KaVA monitoring data observed in 2013–2014 at 22 GHz (Hada et al. 2017). We also include the results obtained in the literature to compare with our results and to show an overall trend of jet acceleration and deceleration at distances from sub-pc to kpc scales. We discuss several implications of our results below.

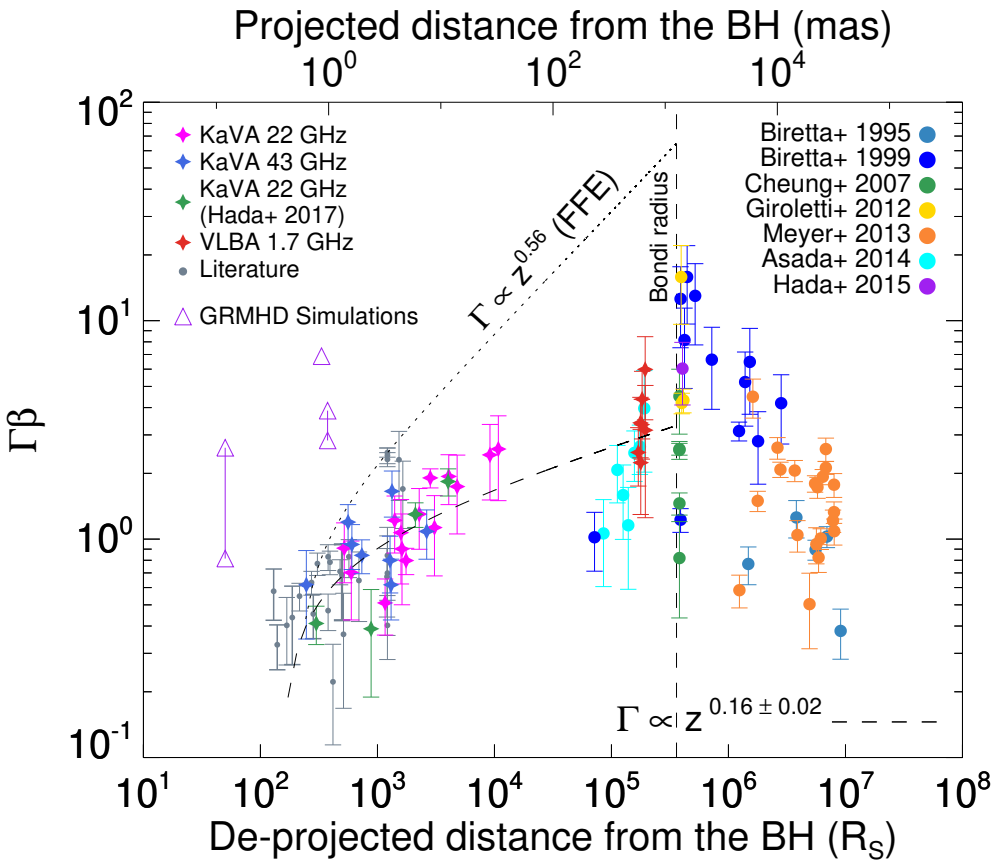

Figure 3.10. Four-velocity $\Gamma\beta$, obtained from the measured apparent speeds with the adopted jet viewing angle of 17°, as a function of de-projected distance from the black hole in units of $R_{\rm S}$. The data points obtained in this study and our previous study using the KaVA observations at 22 GHz (Hada et al. 2017) are shown with the diamonds, while those obtained in the literature presented in the right panel of Figure 3.7 are shown with the grey filled circles. We include the data points in the literature for the jet speeds on large scales as well (Biretta et al. 1995, 1999; Cheung et al. 2007; Giroletti et al. 2012; Meyer et al. 2013; Asada et al. 2014; Hada et al. 2015). The distances between the radio cores and the black hole are corrected by using the core-shift measurement (Hada et al. 2011). We also include the results obtained by GRMHD simulations shown with the purple open upward triangles (McKinney 2006; Penna et al. 2013; Nakamura et al. 2018). The best-fit function, assuming a power-law function for the bulk Lorentz factor and converting it into the four-velocity, to the data points obtained in this study and our previous study (the magenta, blue, red, green diamonds) is $\Gamma \propto z^{0.16\pm0.02}$ and shown with the black dashed line. The linear jet acceleration profile of $\Gamma \propto z^{0.56}$, expected in the FFE model (see texts), is shown as a reference with the black dotted line.

3.6.1 Slow Jet Acceleration

One of the notable features we found is that the jet is moving at subluminal speeds at distances $\lesssim 1$ mas, corresponding to de-projected distances $\lesssim 500\ R_{\rm S}$. This is consistent with the results of other studies, especially with the speeds obtained by the jet to counterjet brightness ratio (see Section 3.4.4 and the right panel of Figure 3.7). This result indicates that it is less likely that VLBI observations are missing very fast jet motions due to the limited angular resolution or cadence on this scale. The jet becomes relativistic at a distance $\approx 10^3 R_{\rm S}$, though it is difficult to determine an exact location because of the dispersion in the observed speeds. This distance is relatively far from the central engine compared to the results of various GRMHD simulations which obtain $\Gamma \gtrsim$ a few already at distances less than a few hundred $R_{\rm S}$ (e.g., McKinney 2006; Penna et al. 2013; Nakamura et al. 2018, see also Figure 3.10).

Besides, the observed jet acceleration profile seems to be relatively flat compared to the prediction of magnetic jet acceleration models. We fit a function, assuming a power-law function for the bulk Lorentz factor and converting it into the four-velocity, to the data points obtained in our study and our previous study (Hada et al. 2017), and obtain the best fit of $\Gamma \propto z^{0.16\pm0.02}$. We note, however, that this profile assumes that all the data points follow the same power-law, which may not be necessarily the case (see Section 3.6.2). Theoretical studies of highly magnetized jets in the highly relativistic limit ($\sigma \gg 1$, where σ is the Poynting flux per unit matter energy flux, so-called the magnetization parameter) or in the far zone ($r \gg r_{\rm lc}$, where $r_{\rm lc} = c/\Omega$ is the light cylinder radius with Ω being the angular velocity of a given streamline) show that an evolution of the Lorentz factor would be described as $\Gamma \propto R \propto z^a$ near the jet base (so-called a linear acceleration regime because of the linear proportionality between Γ and R), where the latter proportionality comes from the jet collimation profile, with a transition to a slower acceleration profile at a certain distance (e.g., Tchekhovskoy et al. 2008; Komissarov et al. 2009; Lyubarsky 2009). Previous VLBI observations found $a \approx 0.56$ for M87 in the regions we are probing in this study (Asada & Nakamura 2012; Hada et al. 2013; Nakamura & Asada 2013), which is translated into the linear

acceleration profile of $\Gamma \propto z^{0.56}$. Thus, the observed trend of jet acceleration appears to be much flatter than what the model predicts.

Taken as a whole, our results suggest that the M87 jet is gradually accelerated over a large jet distance range that coincides with the jet collimation zone, which is one of the essential characteristics of the magnetic jet acceleration mechanism (e.g., Vlahakis & Königl 2004; Lyubarsky 2009). However, the observed acceleration does not seem to be as efficient as in the models or the results of GRMHD simulations of a highly magnetized jet. There are two essential ingredients necessary for efficient jet acceleration in the models: the degree of jet magnetization near the jet base (often given by σ) and the "differential collimation" of poloidal magnetic fields. The former tells us about the amount of electromagnetic energy available for being converted into the jet kinetic energy and thus determines the upper limit of jet bulk Lorentz factor. The latter is realized when the inner streamlines closer to the jet axis are more collimated than the outer ones, also known as the "magnetic nozzle" effect (e.g., Li et al. 1992; Vlahakis & Königl 2003), and it determines the efficiency of conversion from electromagnetic to kinetic energy.

Therefore, the observed slow jet acceleration may be explained if the M87 jet is not highly magnetized at its base. Mertens et al. (2016) have found a transition from an efficient linear acceleration ($\Gamma \propto z^{0.56}$) to a slower acceleration ($\Gamma \propto z^{0.16}$) occurring at $\approx 10^3\ R_{\rm S}$. The latter profile at outer jet distances is in good agreement with the acceleration profile we found, while the former at inner distances is much steeper, which might be related with the fact that they used the fastest jet motions at a given distance bin for deriving the profiles (see Section 3.6.2 for related discussions). They applied the asymptotic solution of relativistic, axisymmetric MHD equations in the far zone derived by Lyubarsky (2009) for the case of the pressure of an external confining medium ($P_{\rm ext}$) rapidly decreasing with distance from the central engine, i.e., $\kappa > 2$ in $P_{\rm ext} \propto z^{-\kappa}$. This solution predicts a transition of jet acceleration and collimation profiles from the linear acceleration ($\Gamma \propto R \propto z^{\kappa/4}$) with a parabolic jet shape to a slower acceleration ($\Gamma \propto z^{(\kappa-2)/2}$) with a conical jet shape. While Mertens et al. (2016)

obtained a good fit with the inferred value of $\kappa \approx 2.4$ using this model, a transition to the conical jet shape was not found in the region they probed[4] (Asada & Nakamura 2012). They explained this contradiction with early saturation of the Poynting flux, resulting in a quenched acceleration. If this is the case, the assumptions of a Poynting flux dominated jet, i.e., $\sigma \gg 1$, used in the models may not hold. The jet may have relatively small initial magnetization parameter if it is launched in the inner part of the accretion disk[5] (e.g., Mertens et al. 2016; Kim et al. 2018a).

In contrast, previous studies constrained the degree of magnetization near the jet base of M87, based on VLBI observations (Kino et al. 2014, 2015b; Kim et al. 2018a). They suggested that the jet base is highly magnetized, which is in line with indirect observational evidence that M87 is in a magnetically arrested disk (MAD, Narayan et al. 2003; Tchekhovskoy et al. 2011) state (e.g., Zamaninasab et al. 2014; Park et al. 2019a). If this is the case, the distance at which the jet transitions from the linear acceleration regime to a slower acceleration regime would be given by steady axisymmetric force-free electrodynamic (FFE) solutions (Tchekhovskoy et al. 2008):

$$z_{\rm tr} = z_{\rm fp} \left[\frac{1}{\Omega_{\rm fp} z_{\rm fp}} \frac{C}{2\sin^2(\theta_{\rm fp}/2)\sqrt{(2-\nu)\nu}} \right]^{1/(1-\nu)}, \tag{3.3}$$

where $z_{\rm fp}$, $\Omega_{\rm fp}$, and $\theta_{\rm fp}$ are the distance from the central engine, the rotational frequency, and the colatitude angle at the footpoint of the local field line, respectively, C is a numerical factor that depends on the field line rotational profile, ν is the radial power-law index in the poloidal flux function of the initial magnetic field configuration which describes the asymptotic shape of the field line as $z \propto R^{2/(2-\nu)}$. Recent GRMHD simulations found that the jet collimation profile of M87 is in good agreement with the outermost parabolic streamline of the FFE solution anchored to the black hole

[4]We note that our recent study of Faraday rotation in the jet at distances $\lesssim 2 \times 10^5$ $R_{\rm S}$ suggests $\kappa \lesssim 2$ (Park et al. 2019a), which allows a parabolic jet shape without a transition to a conical shape (Komissarov et al. 2009), as observed in this region.

[5]We note, however, that GRMHD simulations consistently found that gas outflows launched from the disk cannot reach relativistic speeds due to high mass-loading (e.g., Sadowski et al. 2013; Yuan et al. 2015; Nakamura et al. 2018; Qian et al. 2018).

event horizon on the equatorial plane (Nakamura et al. 2018). Based on this result, one may use $\theta_{\rm fp} = \pi/2$, $\nu = 0.89$, and $C = \sqrt{3}$. $\Omega_{\rm fp}$ and $z_{\rm fp}$ depend on the black hole spin which was estimated to be $a \gtrsim 0.2$ for M87 (Doeleman et al. 2012, see also EHT Collaboration et al. 2019e; Nokhrina et al. 2019). Thus, the expected transition distance is $z_{\rm tr} \gtrsim 2.5 \times 10^7\ R_{\rm S}$, indicating that the linear acceleration profile of $\Gamma \propto z^{0.56}$ would be maintained in the observed jet acceleration zone according to the FFE model.

Therefore, the observed trend of jet acceleration is difficult to explain with the FFE model. It may indicate that, if the jet is initially highly magnetized as previous studies suggested, there may be a lack of the differential collimation of poloidal fields in the M87 jet. Indeed, recent GRMHD simulations showed that the differential collimation proceeds in a complicated manner, depending on the distance from the central engine and the black hole spin, indicating that the efficient jet acceleration through the Poynting flux conversion predicted in the FFE models may not be always achieved (Nakamura et al. 2018). In this case, the jet would still remain Poynting flux dominated even beyond the acceleration and collimation zone (outside the location of HST-1) because not all of the Poynting flux would be converted into the kinetic energy[6]. We note that several studies have pointed out that the M87 jet may be highly magnetized on kpc scales from the observed morphology and linear polarization structure (e.g., Owen et al. 1989), the high energy γ-ray observations (Stawarz et al. 2005), and the conical jet expansion observed in the region where a surrounding interstellar medium is nearly uniformly distributed (Asada & Nakamura 2012).

In our analysis and discussion above, we assumed that the jet viewing angle is constant over the distance range of our interest. However, one can see that local changes of the direction of the jet ridge on the sky plane are present in the VLBA images (Figure 3.8). Also, the jet opening angle decreases with increasing distance (e.g., Junor et al. 1999; Asada & Nakamura 2012), which can change the effective jet viewing angles at different distances. These effects may contribute to the observed jet acceleration profile

[6]unless much of the jet electromagnetic energy is dissipated into other forms of energy instead of being transferred into the jet kinetic energy (e.g., Ostrowski 1998; Stawarz & Ostrowski 2002; Giannios et al. 2009; Sironi & Spitkovsky 2014)

and the scatter of data points (Section 3.6.2). However, the viewing angle constraints on mas scales (e.g., Mertens et al. 2016) and arcsecond scales (Biretta et al. 1999) are consistent with each other. Furthermore, the VLBA images in Figure 3.8 suggest that the jet morphology is globally straight on the sky plane at $\lesssim 420$ mas, indicating that the variation of the jet viewing angle with jet distance would not be significant. Therefore, we expect that the observed jet acceleration profile would not be much affected by the assumption of constant jet viewing angle, though quantitative examination is needed in future studies.

3.6.2 Multiple Streamlines and Velocity Stratification

The above discussion is based on the best-fit function of a simple power-law for the bulk Lorentz factor, which may hold only for a single streamline in the FFE models. However, it is possible that the observed jet emission consists of multiple streamlines. In this case, a more complicated jet velocity field is expected. Different streamlines may have different magnetization parameters (e.g., Tomimatsu & Takahashi 2003) and different collimation profiles (e.g., Komissarov et al. 2007), which can result in a lateral stratification in jet velocity. The distribution of electric current flows within the jet, which is likely associated with the rotation velocity profile of the footpoint of jet (e.g., Komissarov et al. 2007; Tchekhovskoy et al. 2008; Komissarov et al. 2009), determines which streamlines are more efficiently accelerated than other streamlines. If the dispersion in the observed speeds at a given distance (Figure 3.10) originates from different streamlines having different speeds at the same distance, then it is difficult to discuss the efficiency of Poynting flux conversion by comparing with the bulk Lorentz factor profiles prediced by the FFE models. In this case, the dispersion observed at $\approx 10^5$ $R_{\rm S}$ by our present study and Asada et al. (2014) may also be contributed by multiple stream lines, instead of representing a rapid jet acceleration there. We note that the different speeds observed at HST-1 between optical (Biretta et al. 1999) and radio wavelengths (Cheung et al. 2007; Giroletti et al. 2012; Hada et al. 2015, see also Figure 3.10) may originate from jet emission at different frequencies dominated by dif-

ferent jet layers (e.g., Mertens et al. 2016; Kim et al. 2018a; Walker et al. 2018). This scenario may also be supported by observations of different jet widths and linear polarization structure between radio and optical on kpc scales (e.g., Sparks et al. 1996; Perlman et al. 1999)

Alternatively, the fastest motions at a given distance may represent the jet bulk motions, while slower motions are associated with instability pattern or outer winds moving at sub-relativistic speeds launched by the accretion disk, as suggested by Mertens et al. (2016). They selected the fastest 10% of the speeds measured within individual distance bins, and found a transition from an efficient linear acceleration ($\Gamma \propto z^{0.56}$) to a slower acceleration ($\Gamma \propto z^{0.16}$) occurring at $\approx 10^3\ R_{\rm S}$. In this case, the presence of a transition may imply that the jet is not initially highly magnetized and early saturation of the Poynting flux conversion results in the quenched acceleration, as discussed in Section 3.6.1.

3.6.3 Current Limitations and Future Prospects

We remark on the limitations of our present study and address the need for future studies. As we explained in Section 3.4.4, we applied various methods for the jet kinematics because each method has its own advantage and disadvantage. Therefore, the dispersion in the observed speeds at a given distance bin (the left panel of Figure 3.7) may just simply arise due to potential systematic errors in different methods. However, the dispersion may not be solely due to the errors because many previous studies which use a single kinematic method have shown non-negligible dispersion at a given distance bin (see, e.g., the right panel of Figure 3.7 and references therein). Also, we showed that jet kinematics for regions at distances $\lesssim 300$ mas (corresponding to de-projected distances $\lesssim 1.4 \times 10^5\ R_{\rm S}$) using data observed with a low angular resolution is complicated due to the smooth jet brightness distribution and the re-brightening of the jet at several locations (Section 3.5). We also note that bulk jet speeds of $\Gamma \gtrsim 6 - 11$ are required if the fast motions detected in HST-1 represent relativistic MHD shocks propagating in the jet (Nakamura et al. 2010; Nakamura & Meier 2014). Thus, the bulk jet speeds

comparable or slightly smaller than this limit need to be present in the inner region, which appears to be missing in the present and previous observations possibly due to the limited capability of those observations. The above limitations require dedicated monitoring observations with a high angular resolution, sensitivity, and an observing cadence in the future. On-going and future monitoring observations with the EAVN will be important in this aspect (Y. Cui et al. 2019, in preparation).

We list several issues that can be addressed by future observations specifically. Firstly, probing the jet velocity field in the distance range of $10^4 - 10^5$ $R_{\rm S}$ will allow us to figure out whether the dispersion in the observed speeds is produced by multiple streamlines or by instability patterns or outer slow winds. If the lower envelope of the velocity field shows a systematic acceleration with distance over a wide range, which would be difficult to be reproduced by instability patterns (e.g., Hardee 2000; Lobanov et al. 2003; Hardee & Eilek 2011) or winds launched from hot accretion flows (e.g., Yuan et al. 2015), the dispersion may originate from multiple streamlines following different acceleration profiles. Secondly, resolving the re-brightened jet regions is necessary to determine whether the jet is stationary or there is underlying fast flows in those regions. Multifrequency observations and linear polarization observations will be beneficial to determine the origin of the re-brightening. Thirdly, high-sensitivity observations will provide an opportunity to detect very fast motions, e.g., $\beta_{\rm app} \gtrsim 4c$ at $\lesssim 10^5$ $R_{\rm S}$, if there are such motions in the jet as the FFE models predict. The Doppler beaming factor peaks at $\Gamma\beta \approx 3.3$ for a jet viewing angle of 17°, indicating that the jet motions faster than this speed would be preferentially less detected when the jet indeed consists of multiple streamlines and is observed with a limited sensitivity. Finally, no jet emission has been detected, to our knowledge, between the distance $\approx$ 450 mas and HST-1 in previous VLBI observations. If the emission in this region can be detected with high-sensitivity observations at low frequencies, one can infer the jet bulk speed of this region, which will be beneficial for constraining the jet acceleration profile more accurately.

3.7 Conclusions

We studied the kinematics of the M87 jet with the KaVA monitoring observations performed in eight epochs in 2016 quasi-simultaneously at 22 and 43 GHz. We also performed a complementary kinematic analysis of the VLBA archive data observed in 19 epochs between 2005 and 2009 at 1.7 GHz. Our work leads us to the following principal conclusions:

1. We found that the apparent jet speeds increase from $\approx 0.3c$ at ≈ 0.5 mas from the core to $\approx 2.5c$ at ≈ 22 mas, which indicates that the jet is accelerated from subluminal to superluminal speeds on this scale, as recent studies have suggested (Mertens et al. 2016; Hada et al. 2017; Walker et al. 2018).

2. We confirmed that the jet moves at relativistic apparent speeds $\approx 2 - 5c$ at distances $\approx 340 - 410$ mas, which is consistent with the previous observations of the jet in three epochs at 1.6 GHz (Asada et al. 2014). Combined with the kinematic results for inner jet regions, the M87 jet seems to accelerate over a broad distance range from 10^2 to a few $\times 10^5$ $R_{\rm S}$, while it is being gradually collimated simultaneously, as the magnetic jet acceleration models predict.

3. Both jet kinematic analysis using VLBI monitoring observations and an analysis of the brightness ratio of the jet and counterjet suggest that the jet is moving at subluminal speeds at de-projected distances $\lesssim 500$ $R_{\rm S}$. This result indicates that the jet is in a non-relativistic regime up to distances considerably larger than what previous GRMHD simulations predicted.

4. We found that the best-fit function of $\Gamma \propto z^{0.16\pm0.02}$ can describe the observed radio data well in general. This profile is much flatter than that predicted by the models of highly magnetized jets. This result indicates that the jet is not highly magnetized near its base and early saturation of Poynting flux leads to the flat acceleration profile, or the jet is highly magnetized but Poynting flux conversion through the differential collimation of poloidal magnetic fields in the jet may not

be very efficient.

5. However, the above interpretation is based on the assumption that the observed velocity field is contributed solely by a single streamline. We found that there is non-negligible dispersion in the observed speeds at a given distance, as already suggested by previous studies (e.g., Mertens et al. 2016). If this dispersion is caused by multiple streamlines following different acceleration profiles in the jet, which is naturally expected in analytical models and from the results of numerical simulations, then one cannot compare the observed velocity field with a simple power-law function which may hold only for a single streamline. Alternatively, only the fastest motions at a given distance may represent the jet bulk motion, while the slower motions are produced by instability patterns or outer slow winds. Future VLBI monitoring observations which can probe the distance range of $10^4 - 10^5$ $R_{\rm S}$ will play an important role in investigating the origin of the observed dispersion.

We finally remark on that the results presented in this paper are derived from the radial kinematic analysis using the first year data observed with the KaVA in our large program. Different types of analysis such as the spectral evolution between 22 and 43 GHz and jet motions in the transverse direction to the jet axis using these data will be presented elsewhere (H. Ro, et al. 2019, in preparation). Furthermore, our program started using the EAVN extensively since 2017 with shorter intervals down to ~ 5 days for specific periods, which allows us to obtain high-quality images of the jet extended down to ~ 30 and ~ 10 mas at 22 and 43 GHz, respectively. The results using these data will be presented in forthcoming papers (Y. Cui, et al. 2019, in preparation). Thanks to the advent of millimeter VLBI arrays such as the EHT (e.g., EHT Collaboration et al. 2019a) and the global millimeter VLBI array (GMVA; e.g., Kim et al. 2018a), resolving the horizon-scale structure of accreting and outflowing matters has been realized. We stress that continued monitoring observations with centimeter VLBI arrays such as the EAVN in accordance with the mm-VLBI observations will contribute to complete the picture of jet launching, acceleration, and collimation.

Chapter 4

Revealing the Nature of Blazar Radio Cores through Multi-Frequency Polarization Observations with the Korean VLBI Network[†]

Abstract

We study the linear polarization of the radio cores of eight blazars simultaneously at 22, 43, and 86 GHz with observations obtained by the Korean VLBI Network (KVN) in three epochs between late 2016 and early 2017 in the frame of the Plasma-physics of Active Galactic Nuclei (PAGaN) project. We investigate the Faraday rotation measure (RM) of the cores; the RM is expected to increase with observing frequency if core positions depend on frequency due to synchrotron self-absorption. We find a systematic increase of RMs at higher observing frequencies in our targets. The RM–ν relations

[†]The contents of this chapter was originally published in the Astrophysical Journal (Park et al. 2018)

follow power-laws with indices distributed around 2, indicating conically expanding outflows serving as Faraday rotating media. Comparing our KVN data with contemporaneous optical polarization data from the Steward Observatory for a few sources, we find indication that the increase of RM with frequency saturates at frequencies of a few hundreds GHz. This suggests that blazar cores are physical structures rather than simple $\tau = 1$ surfaces. A single region, e.g. a recollimation shock, might dominate the jet emission downstream of the jet launching region. We detect a sign change in the observed RMs of CTA 102 on a time scale of $\approx$1 month, which might be related to new superluminal components emerging from its core undergoing acceleration/deceleration and/or bending. We see indication for quasars having higher core RMs than BL Lac objects, which could be due to denser inflows/outflows in quasars.

4.1 Introduction

Blazars, characterized by violent flux variability across the entire electromagnetic spectrum, are a sub-class of active galactic nuclei (AGNs) which show highly collimated, one-sided relativistic jets (see Urry & Padovani 1995 for a review). Large-scale magnetic fields which are strongly twisted in the inner part of the accretion disc or the black hole's ergosphere play a crucial role in launching and powering of relativistic jets (Blandford & Znajek 1977; Blandford & Payne 1982). Jets appear to be gradually accelerated and collimated magneto-hydrodynamically (Vlahakis & Königl 2004; Komissarov et al. 2007, 2009; Asada & Nakamura 2012; Toma & Takahara 2013; Hada et al. 2013; Asada et al. 2014; Mertens et al. 2016; Hada et al. 2017; Walker et al. 2018) and they are directly linked to accretion process onto supermassive black holes (Marscher et al. 2002a; Chatterjee et al. 2009, 2011; Ghisellini et al. 2014; Park & Trippe 2017). Their parsec-scale radio morphology is characterized by (a) the 'VLBI core', a (radio) bright, optically thick, compact feature, and (b) an extended, optically thin, jet (e.g., Fromm et al. 2013).

The nature of the core is a matter of ongoing debate. The standard Blandford & Königl jet model describes the core as the upstream region where the conical jet

becomes optically thin, i.e., at unity optical depth (e.g., Blandford & Königl 1979). In this scenario, the observed core position shifts closer to the physical location of the jet base at higher observing frequencies – the well-known 'core shift effect' (Lobanov 1998). Core shift has been observed in blazars (e.g., O'Sullivan & Gabuzda 2009b; Sokolovsky et al. 2011; Algaba et al. 2012; Pushkarev et al. 2012; Fromm et al. 2013; Hovatta et al. 2014) as well as in nearby radio galaxies (e.g., Hada et al. 2011; Martí-Vidal et al. 2011), supporting the idea that the radio core marks the transition between the optically thick and thin jet regimes.

However, the plain 'optical depth interpretation' of the radio core ignores the physical structure of AGN jets. Especially, a standing conical shock, located at the end of the jet acceleration and collimation zone (e.g., Marscher et al. 2008), is expected (see also Potter & Cotter 2013a,b for a discussion of the transition region from a parabolic to a conical jet shape that is dominating jet synchrotron emission of blazars). Such a (quasi-)stationary feature – a 'recollimation shock' – may appear when there is a mismatch between the gas pressures in the jet and the confining medium (e.g., Daly & Marscher 1988; Gómez et al. 1995, 1997; Agudo et al. 2001; Mizuno et al. 2015; Martí et al. 2016). Observations of the nearby radio galaxy M87 indeed reveal a stationary feature (known as HST-1) at the end of the jet collimation region (Asada & Nakamura 2012), showing blazar-like activity such as rapid variability and high energy emission (Cheung et al. 2007). In addition, recent studies have discovered that most γ-ray flares in blazars occur when new (apparently) superluminal jet components pass through the core (Jorstad & Marscher 2016, see also Ramakrishnan et al. 2014; Casadio et al. 2015; Rani et al. 2015 for the case of individual sources and Jorstad et al. 2001; León-Tavares et al. 2011 for investigation of statistical significance between the two phenomena). This indicates that the core supplies the jet plasma electrons with large amounts of energy, with the possible formation of a shock as the source of high energy emission.

At first glance, these two models and corresponding observational support seem to be in contradiction. This conflict is resolved if the core consists of (a) a standing shock which is optically thin only at (sub)-mm wavelengths, plus (b) extended jet flows

downstream of the shock. In this case, there is no core shift expected at millimeter wavelengths where the core becomes transparent. Interestingly, a recent study which used a bona-fide astrometric technique showed that the core shift between 22 and 43 GHz for BL Lacertae is significantly smaller than the expected one from lower frequency data, indicating that the core at these frequencies might be identified with a recollimation shock (Dodson et al. 2017). However, a number of previous studies did not find such a trend at the same frequencies (e.g., O'Sullivan & Gabuzda 2009b; Algaba et al. 2012; Fromm et al. 2013). This might be because the core position accuracy of previous VLBI observations is comparable to the expected amount of core shift at those frequencies.

An alternative route is provided by multi-frequency polarimetric observations of the core that provide RMs, defined as $\mathrm{EVPA_{obs}} = \mathrm{EVPA_{int}} + \mathrm{RM}\lambda^2$, where $\mathrm{EVPA_{obs}}$ and $\mathrm{EVPA_{int}}$ are observed and intrinsic electric vector position angles (EVPAs) of linearly polarized emission and λ is observing wavelength. If the core is the $\tau = 1$ surface of a continuous conical jet and the jet is in a state of energy equipartition, then the core RM obeys the relation $|\mathrm{RM_{core},\nu}| \propto \nu^a$, where a is the power-law index of the electron density distribution given by $N_e \propto d^{-a}$, with d being the distance from the jet base (Jorstad et al. 2007). In this scenario, we observe polarized emission from regions closer to the jet base at higher frequencies due to the core shift effect, where one may expect higher particle densities and stronger magnetic fields. Looking at this argument the other way around, we would expect *no increase* in RM as a function of frequency at millimeter wavelengths *if* the core is indeed a standing recollimation shock. This provides the opportunity to uncover the nature of blazar VLBI cores, and thus the intrinsic structure of blazar jets, through multi-frequency polarimetric observations at millimeter wavelengths.

At centimeter wavelengths, many studies showed that the power law index a is usually distributed around $a = 2$ (e.g., O'Sullivan & Gabuzda 2009a; Algaba 2013; Kravchenko et al. 2017), corresponding to a spherical or conical outflow (Jorstad et al. 2007). A conical outflow is more likely than a spherical one because Pushkarev et

al. (2017) showed that conical jet geometries are common in blazars. $a \approx 2$ found in many blazars is in agreement with the fact that many blazars show core shift at these wavelengths. However, to the best of our knowledge, there are only a few studies of the core RM of blazars at (sub-)mm frequencies. Jorstad et al. (2007) analyzed 7, 3, and 1 mm polarization data and obtained an average $\langle a \rangle = 1.8 \pm 0.5$ by comparing with other studies done at cm wavelengths. This result indicates that the dependence of RM on observing frequency might continue up to mm wavelengths. Some of their sources are not fitted well by λ^2 laws even at the highest frequencies, indicating that a frequency dependence of RM exists even at around 1 mm. Another study using the IRAM 30-m telescope at 3 and 1 mm found RMs (a few times 10^4 rad/m^2) that are much larger than those at cm wavelengths (a few hundred rad/m^2, Hovatta et al. 2012), albeit within large errors (Agudo et al. 2014, see also Agudo et al. 2018a,b; Thum et al. 2018).

A recent observation with the Atacama Large Millimeter Array (ALMA) at 1 mm has revealed a very high rotation measure of $(3.6 \pm 0.3) \times 10^5$ rad/m^2 in 3C 273 with the core RM scaling with frequency like $|\mathrm{RM}| \propto \nu^{1.9 \pm 0.2}$ from cm to mm wavelengths. Martí-Vidal et al. (2015) observed even larger RMs ($\approx 10^8$ rad/m^2 in the rest frame) in the gravitationally lensed quasar PKS 1830–211 through ALMA observations at up to 300 GHz (about 1 THz in the rest frame). These results may suggest that (i) blazar core RMs rapidly increase as a function of frequency, as predicted by Jorstad et al. (2007); (ii) polarized (sub-)mm radiation might originate near the jet base, not from a recollimation shock (which presumably is located quite far from the jet base). However, it is uncertain whether this is a common behaviour of blazars or if these quasars are special. Therefore, a systematic study of blazar core RMs with multi-frequency polarimetric observations at (sub)mm wavelengths is necessary.

The Korean VLBI Network (KVN) has the unique capability of observing simultaneously at four frequencies, 22, 43, 86, and 129 GHz, or at two of these frequencies in dual polarization mode (Lee et al. 2011, 2014). Thanks to the simultaneous observation at multiple frequencies, one can overcome rapid phase variations at high frequencies

caused by tropospheric delay that reduce the coherence time by applying the fringe solutions obtained at lower frequencies to higher ones, i.e., frequency phase transfer (FPT) (Rioja et al. 2011, 2014; Algaba et al. 2015; Zhao et al. 2018). This technique increases the fringe detection rate to values larger than 80% even at 129 GHz for sources brighter than ≈ 0.5 Jy, making the KVN a powerful instrument for multi-frequency mm polarimetry of AGNs.

In early 2017, we launched a KVN large program, the Plasma-physics of Active Galactic Nuclei (PAGaN) project (see Kim et al. 2015; Oh et al. 2015 for related studies), for monitoring about 14 AGNs at the four KVN frequencies in dual polarization mode almost every month. One of the main scientific goals of the project is a systematic study of RMs of blazars at mm wavelengths and their evolution in time. In this paper, we present the results from three observation epochs located between late 2016 and early 2017, which were performed as test observations for the initiation of the large program. We describe observations and data calibration in Section 4.2. Results are shown and discussed in Section 4.3 and 7.4, respectively. In Section 4.5, we summarize our findings.

4.2 Observations and Data Reduction

We observed a total of 11 sources in the 22, 43, and 86 GHz bands with the KVN on 2016 December 9–10 and in the four bands including the 129 GHz band on 2017 January 16–17 and 2017 March 22–24 with observation time of $\approx$ 48 hours for each epoch. Since KVN can observe at two frequencies simultaneously in dual polarization mode, we allocated the first half of the observing time to 22/86 GHz observations and the other half to 43/129 GHz. Although we obtained the data at 129 GHz in the two epochs observations, we had a difficulty in polarization calibration of the data and thus we did not include them in this paper. More sophisticated investigation of the 129 GHz data will be presented in a forthcoming paper (Kam et al. in preparation). All sources were observed in 6–15 scans of 5–20 minutes in length, depending on source declination and brightness. We performed cross-scan observations at least twice per hour to cor-

KVN Observation Log

Project code	Obs. date	Frequency	D Term cal.	σ_D[%]	EVPA cal.	$\Delta\chi$ [°]	$\sigma_{\Delta\chi}$ [°]
(1)	(2)	(3)	(4)	(5)	(6)	(7)	(8)
p16st01i	2016 Dec 09	21.650 GHz	OJ 287	1.22	3C 279, OJ 287	-28.79	1.04
		86.600 GHz	3C 84	2.25	3C 279, OJ 287	112.76	0.90
p16st01j	2016 Dec 10	43.300 GHz	OJ 287	0.70	3C 279, OJ 287	-19.52	2.37
		86.600 GHz	OJ 287	1.86	3C 279, OJ 287	125.86	2.65
p17st01a	2017 Jan 16	21.650 GHz	3C 84	0.57	3C 279, OJ 287	11.53	0.94
		86.600 GHz	OJ 287	1.25	3C 279, OJ 287	5.55	1.80
p17st01b	2017 Jan 17	43.100 GHz	3C 84	1.07	3C 279, OJ 287	54.29	0.33
		129.300 GHz	–	–	–	–	–
p17st01e	2017 Mar 22	21.650 GHz	3C 84	1.04	3C 279, OJ 287	-28.72	0.87
		86.600 GHz	OJ 287	1.59	3C 279, OJ 287, 3C 454.3	32.42	1.04
p17st01f	2017 Mar 24	43.100 GHz	OJ 287	0.90	3C 279, OJ 287, BL LAC	9.07	1.37
		129.300 GHz	–	–	–	–	–

Table 4.1. (1) KVN observations project code (2) observation date (3) *starting* observing frequency (4) sources used for instrumental polarization calibration (5) Errors of D-terms estimated by comparing the D-terms obtained from different instrumental polarization calibrators (6) sources used for EVPA calibration by comparing with contemporaneous KVN single dish observations (7) amount of EVPA rotation applied (8) Errors of EVPA calibration estimated from $\Delta\chi$ values of different sources in (6). We note that we did not include the 129 GHz observations in our analysis due to the complicated polarization calibration at this frequency.

rect antenna pointing offsets that might lead to inaccurate correlated amplitudes. The received signals were 2-bit quantized and divided into 4 sub-bands (IFs) of 16 MHz bandwidth for each polarization and each frequency. Mark 5B recorders were used at recording rates of 1024 Mbps. The data were correlated with the DiFX software correlator in the Korea-Japan Correlator Center (Lee et al. 2015a). Table 4.1 summarizes our observations.

A standard data post-correlation process was performed with the NRAO Astronomical Image Processing System (AIPS). Potential effects of digital sampling on the amplitudes of cross-correlation spectra were estimated by the AIPS task ACCOR. Amplitude calibration was done by using the antennas gain curves and opacity corrected system temperatures provided by the observatory. The fringe amplitudes were re-normalized by taking into account potential amplitude distortion due to quantization, and the quantization and re-quantization losses (Lee et al. 2015b).

The instrumental delay residuals were removed by using the data in a short time range of bright calibrators, either 3C 279 or 3C 454.3. To apply the FPT technique, a global fringe fitting was performed with a solution interval of 10 seconds for the lower frequency first (22 or 43 GHz), which led us to very high fringe detection rates $\gtrsim 95\%$ in most cases. Then, we transferred the obtained fringe solutions to the simultaneously observed higher frequency (86 GHz). This process corrects rapidly varying tropospheric errors in the visibility phases at high frequencies (though not the ionospheric errors that vary more slowly). Then, the residual phases have much longer coherence times, typically larger than a few minutes. Thus, we performed a global fringe fitting with a much longer solution interval of ≈ 3 minutes for the high frequency data, which resulted in quite high fringe detection rates – usually larger than 95% at 86 GHz for our sources. Bandpass calibration was performed by using scans on bright sources such as 3C 279.

The cross-hand R-L phase and delay offsets were calibrated by using the data for bright sources, such as OJ 287, 3C 84, 3C 279 and 3C 454.3, located within short time ranges, with the task RLDLY. We used the Caltech Difmap package for imaging and phase self-calibration (Shepherd 1997). Typical beam sizes are 5.6×3.2, 2.8×1.6, and

1.4×0.8 mas at 22, 43, and 86 GHz, respectively. We determined the feed polarization leakage (D-terms) for each antenna by using the task LPCAL (Leppänen et al. 1995) with a total intensity model of the D-Term calibrators. 3C 84 usually serves as a good D-Term calibrator thanks to its high flux density and very low degree of linear polarization ($\lesssim$0.5%) at lower frequencies but less so at high frequency (86 GHz) where its linear polarization becomes non-negligible (Kam et al., in preparation). Thus, we also used a compact, bright, and polarized source OJ 287 at 86 GHz. We chose the D-Term calibrator for each epoch and for each frequency by comparing the behaviour of observed visibility ratios on the complex plane with the D-Term models of different calibrators (see Appendix C.1). The EVPA calibration was performed by comparing the integrated EVPAs of the VLBI maps of the EVPA calibrators after the instrumental polarization calibration with contemporaneous KVN single dish polarization observations. We performed KVN single dish observations within two days of each VLBI observations as described in Kang et al. (2015). For the 2016 data, we have two 86 GHz data separated by 1 day. We note that the maps for all sources after the calibration are almost identical to each other and we used the average of Stokes I, Q, and U maps of the two data for our further analysis.

Estimating errors for degree of linear polarization (m) and EVPA is important but not straightforward. Errors for each polarization quantity can be derived from the following relations:

$$\sigma_p = \frac{\sigma_Q + \sigma_U}{2} \tag{4.1}$$

$$\sigma_{\mathrm{EVPA}} = \frac{\sigma_p}{2p} \tag{4.2}$$

$$\sigma_m = \frac{\sigma_p}{I} \tag{4.3}$$

where σ_Q and σ_U denote rms noise in the Stokes Q and U images, respectively, $p = \sqrt{Q^2 + U^2}$, and $m = p/I$ (Hovatta et al. 2012). In most cases, random errors are quite small and systematic errors are much more dominant in the above quantities. Imperfect D-term calibration is usually the most dominant source of errors in m. For EVPAs, both the D-term uncertainty and EVPA correction error are important. Following Roberts

et al. (1994), errors of m and EVPA caused by residual D-terms can be expressed as:

$$\sigma_{m,\mathrm{D}} = \sigma_D (N_a N_{\mathrm{IF}} N_s)^{-1/2} \tag{4.4}$$

$$\sigma_{\mathrm{EVPA,D}} \approx \frac{\sigma_{m,\mathrm{D}}}{2m} \tag{4.5}$$

where σ_D is the D-term error, N_a and N_{IF} are the number of antennas and IFs, respectively, and N_s is the number of scans having independent parallactic angles which depend on the source declination. We estimated the D-term errors by comparing the D-terms obtained from different D-Term calibrators (see (5) in Table 4.1 and Appendix C.1) and estimated $\sigma_{m,\mathrm{D}}$ and $\sigma_{\mathrm{EVPA,D}}$ using Equation 4.4 and 4.5. Thanks to the number of IFs being four and the large parallactic angle coverage of our sources, we could achieve errors in m (typically $0.1 - 0.3\%$) much smaller than the D-Term errors (typically $1 - 2\%$). We also assessed the EVPA correction error, $\sigma_{\Delta\chi}$, by comparing the amount of EVPA rotation calculated from different EVPA calibrators (see (6) and (8) in Table 4.1). Then, we added σ_m and $\sigma_{m,\mathrm{D}}$ quadratically for m and σ_{EVPA}, $\sigma_{\mathrm{EVPA,D}}$, and $\sigma_{\Delta\chi}$ quadratically for EVPA.

In the Appendix, we show the results of D-term calibration and the temporal evolution of the D-terms. The overall D-terms are usually less than $\approx 10\%$, except for Ulsan station at 86 GHz which showed D-terms as large as $\approx 20\%$. The D-terms obtained from different calibrators are quite consistent with each other, showing standard deviations of $\lesssim 2\%$ (see (5) in Table 4.1). The D-terms are more or less stable over ≈ 3 months, showing standard deviations of $\lesssim 2\%$. We also compare our KVN 22/43 and 86 GHz data of 3C 273 observed in 2016 December with contemporaneous Very Long Baseline Array (VLBA) 15/43 GHz data, respectively. Both fractional polarization and EVPAs at a few different locations in the jet are in good agreement within errors between the data of the different instruments, considering non-negligible time gaps between the observations and the expected RM of a few hundred rad/m^2 in the jet (e.g., Hovatta et al. 2012).

4.3 results

4.3.1 RM at radio wavelengths

In Figure 4.1, we present polarization maps for multiple frequencies convolved with the KVN 22 GHz beam size (left panels), EVPAs at the core as a function of λ^2 (central panels), and RMs as a function of geometric mean observing frequency (right panels). We obtained one RM value from each adjacent data pair in the EVPA–λ^2 plots because we could not obtain good λ^2 fits across the three bands in most cases. We have to rotate the 22 and 43 GHz EVPAs by more than 720° and 180° to explain this behavior with $n\pi$ ambiguity, which translates into RM $\gtrsim 10^5$ rad/m^2. This RM value is too large especially at 22 GHz because almost all of the detected core RM of blazars are less than 1000 rad/m^2 at $\lesssim$ 15 GHz (Hovatta et al. 2012). Alternatively, different optical depths of the cores at different frequencies might be responsible for the non-λ^2 fits. Especially, EVPA rotations by 90° are expected in case of a transition of the core from optically thick to optically thin (Pacholczyk 1970). We provide the spectral index, α in $S_\nu \propto \nu^\alpha$, between adjacent frequencies in columns (3) and (4) in Table 4.1 and in the center panels of Figure 4.1 (blue asterisks). We found that values of α measured at different frequency pairs differ from each other by more than 1σ in only four cases, 3C 279 in 2017 January, OJ 287 in 2017 January, 3C 345 in 2017 January, and BL Lac in 2017 March. When we rotate the EVPAs at the lowest frequency by 90° for these cases, we are left with even worse λ^2 fits (higher χ^2 values) compared to the case of no rotation. In addition, the degree of polarization is not much different, less than a factor of ≈ 2, at different frequencies (Section 4.3.3), while it should decrease by a factor of ≈ 7 if there were a 90° flip (Pacholczyk 1970). Therefore, the progressively steeper EVPA rotations at higher frequencies are more likely to be due to the core shift effect, as shown in the numerical simulations of special relativistic magnetohydrodynamic jets (Porth et al. 2011).

We identified the origin (0,0) of the maps with the location of the cores. This might not be always the case exactly; however, the beam size is quite large and thus the effect

of an offset of the core position from the origin would be insignificant. We summarize our sources' basic information and their observed polarization quantities in Table 4.2. We note that we did not consider the effect of the integrated (Galactic) RM because it is a few hundreds rad/m^2 at most (e.g., Taylor et al. 2009); this is much smaller than the typical RM error we obtain, and at the KVN frequencies the EVPA rotation due to the integrated RM is negligible.

Since the beam sizes are quite different at different frequencies, we need to quantify the errors in polarization quantities introduced by the convolution of all maps with the 22 GHz beam. We compared m and EVPA at the core found with and without using convolution for each source at each frequency and added the differences quadratically to the errors of m and EVPA found from convolved maps, respectively. Using contemporaneous BU VLBA maps, We identified and excluded sources which have complex polarization structure near the core that cannot be resolved with the KVN; this leaves us with eight sources. We briefly describe the results for individual sources below.

3C 279

This source is characterized by longitudinal (i.e., parallel to the jet direction) EVPAs that show a smooth distribution from the core to the inner jet[1] (e.g., Jorstad et al. 2005). Similarly, our KVN maps show basically longitudinal EVPAs but rotated by up to $\approx 20^\circ$ as function of frequency. RMs between adjacent frequency pairs range from $\approx 10^3$ to $\approx 10^4$ rad/m^2. We fitted a power law function to the RMs as a function of geometrical mean observing frequency and obtained the power law index a in the relation $|\mathrm{RM}| \propto \nu^a$. Since we calculate each RM value from only two data points, the RM errors are relatively large, which results in relatively large errors in a. However, a values in all three epochs show a good agreement with $a = 2$–3, which is quite consistent

[1]The term 'inner jet' denotes any polarized component in the jet that can be resolved from the core by instruments with higher angular resolution than the KVN but cannot be (well) resolved by the KVN itself, like the extended linear polarization structure of 3C 279 at ≈ 1 mas from the core seen in the BU map of 14 January 2017 (see `https://www.bu.edu/blazars/VLBA_GLAST/3c279/3C279jan17\_map.jpg`)

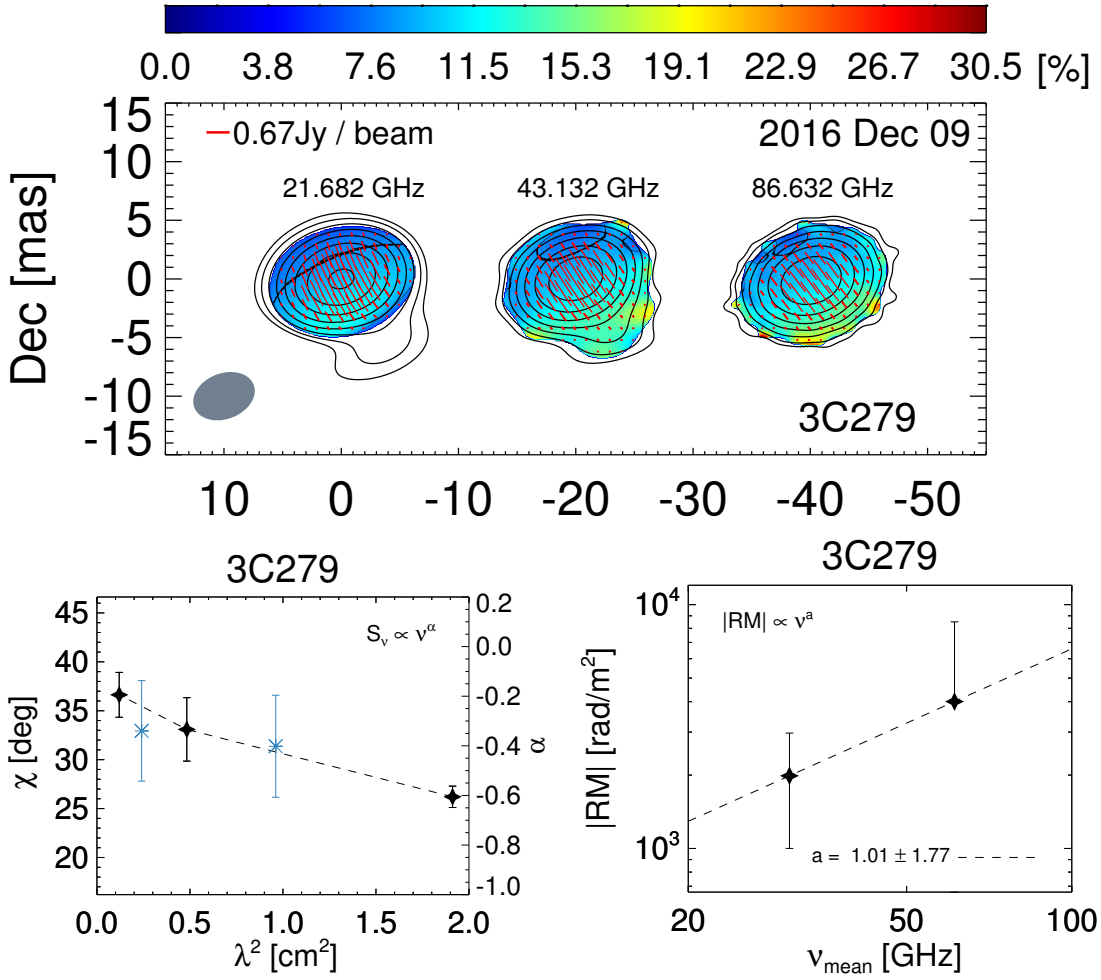

Figure 4.1. *Top*: Contours show naturally weighted CLEAN maps. Colors show the degree of linear polarization in units of %. Red ticks show distribution of EVPAs. The maps at different observing frequencies are shifted by 20 mas along the x-axis. The gray shaded ellipses show the beam size of the KVN at 22 GHz. All maps from different frequencies are convolved with this beam. For OJ 287, we include contemporaneous MOJAVE data at 15 GHz in our analysis (see Section 4.3.1). *Bottom left*: EVPA (black diamonds, values on the left axis) and spectral index (blue asterisks, values on the right axis) at the core as function of λ^2 (geometrical mean λ^2 for spectral index). *Bottom right*: RM as function of geometric mean observing frequency. Each data point is obtained from two adjacent data points for EVPAs in the corresponding central panel. All RM values are rest frame values.

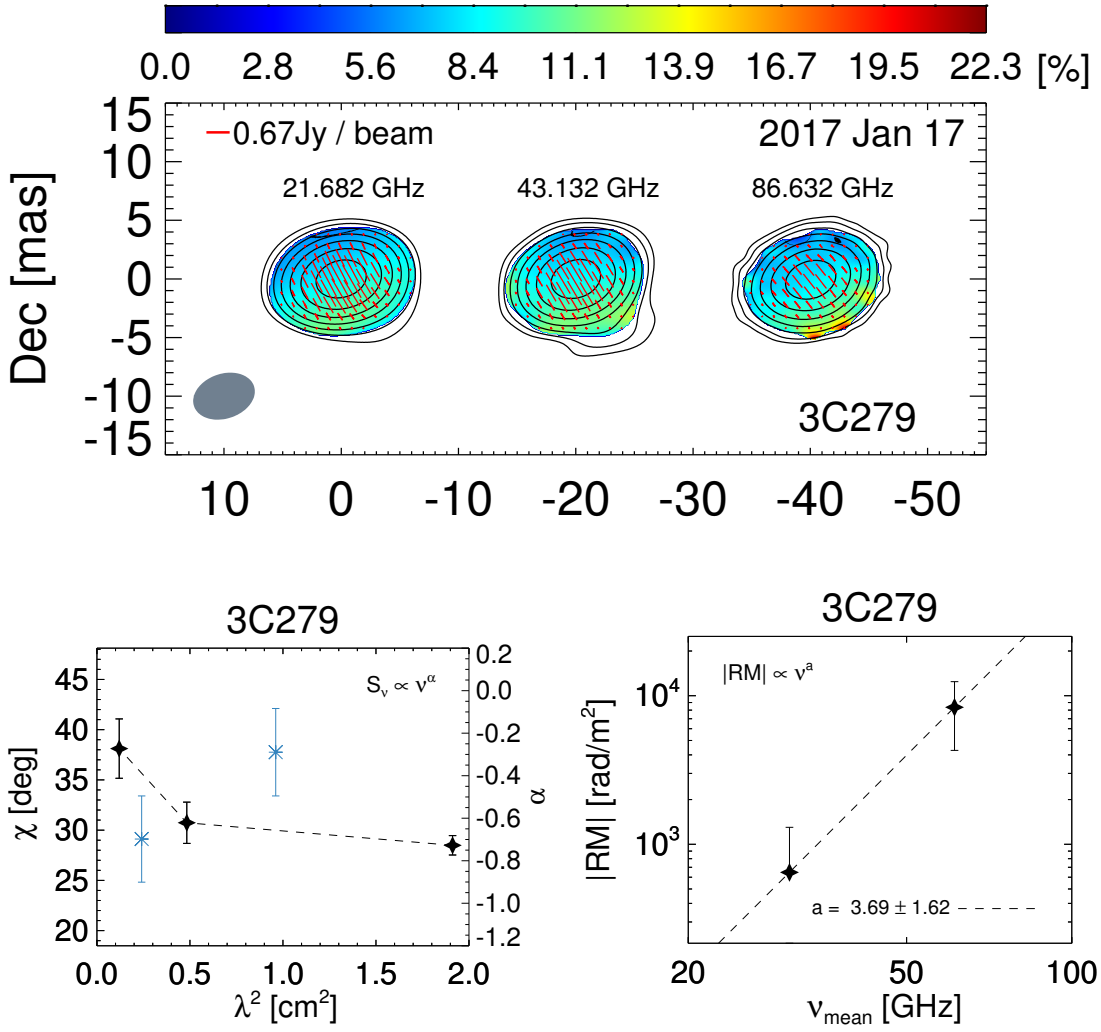

Figure 4.1. *Continued.*

with the results of previous KVN single-dish polarization monitoring of 3C 279 (Kang et al. 2015). We note that the core EVPAs of this source might be contaminated by polarization from the inner jet. However, EVPA rotation of the inner jet region is expected to be very small at $\gtrsim$ 22 GHz because of a relatively small RM in that region ($\lesssim$ 250 rad/m^2; Hovatta et al. 2012). Therefore, we conclude that the observed EVPA rotation over frequency of this source is dominated by the core polarization.

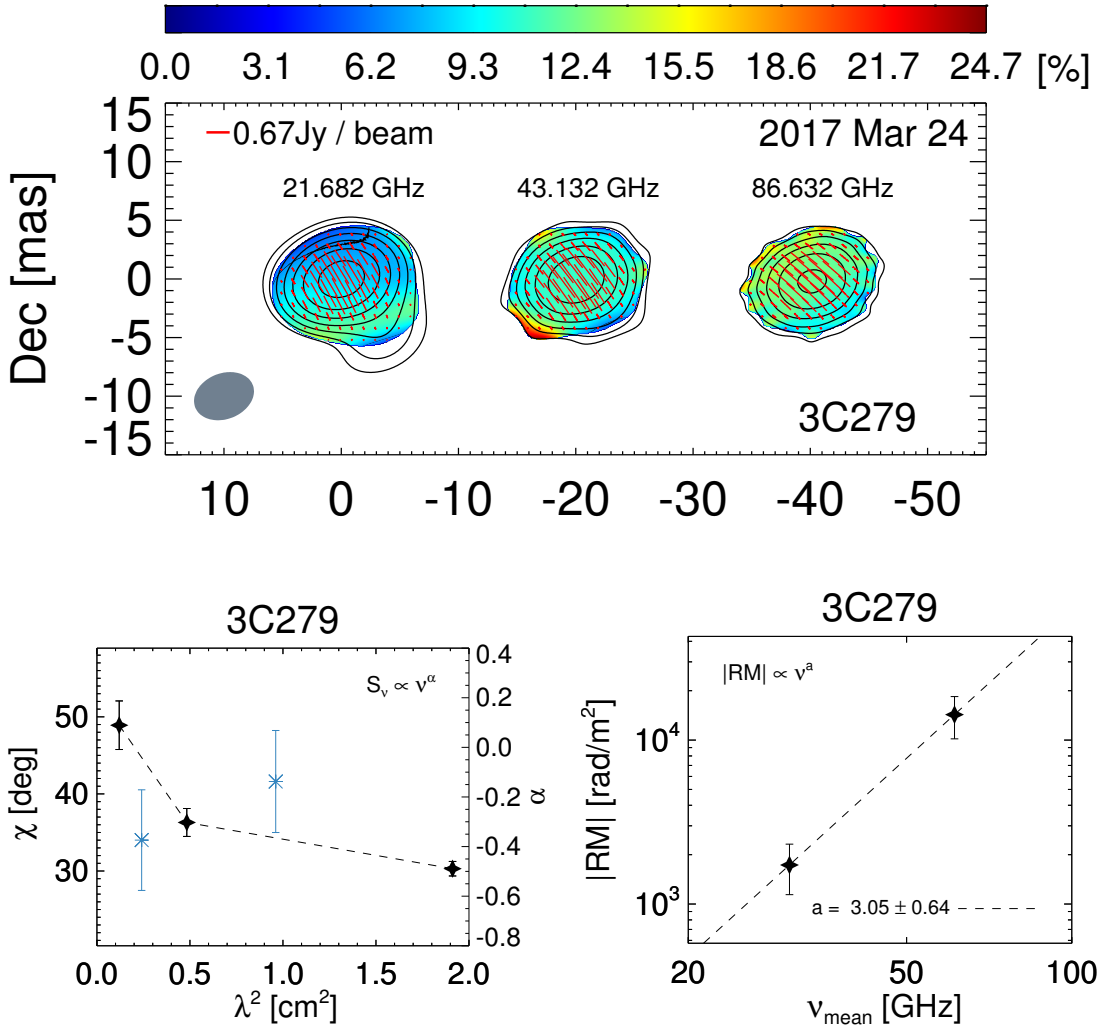

Figure 4.1. *Continued.*

OJ 287

For this source, we could find contemporaneous VLBA data at 15 GHz from the MOJAVE program[2], observed on 2017 January 28 and March 11, with our KVN data being obtained on 2017 January 17–18 and March 22–24, respectively. We included those data in our analysis after convolving the 15 GHz maps with the KVN 22 GHz beam (because the KVN beam is larger than the VLBA one even though it is at a higher frequency.)

[2] `http://www.physics.purdue.edu/astro/MOJAVE/index.html`

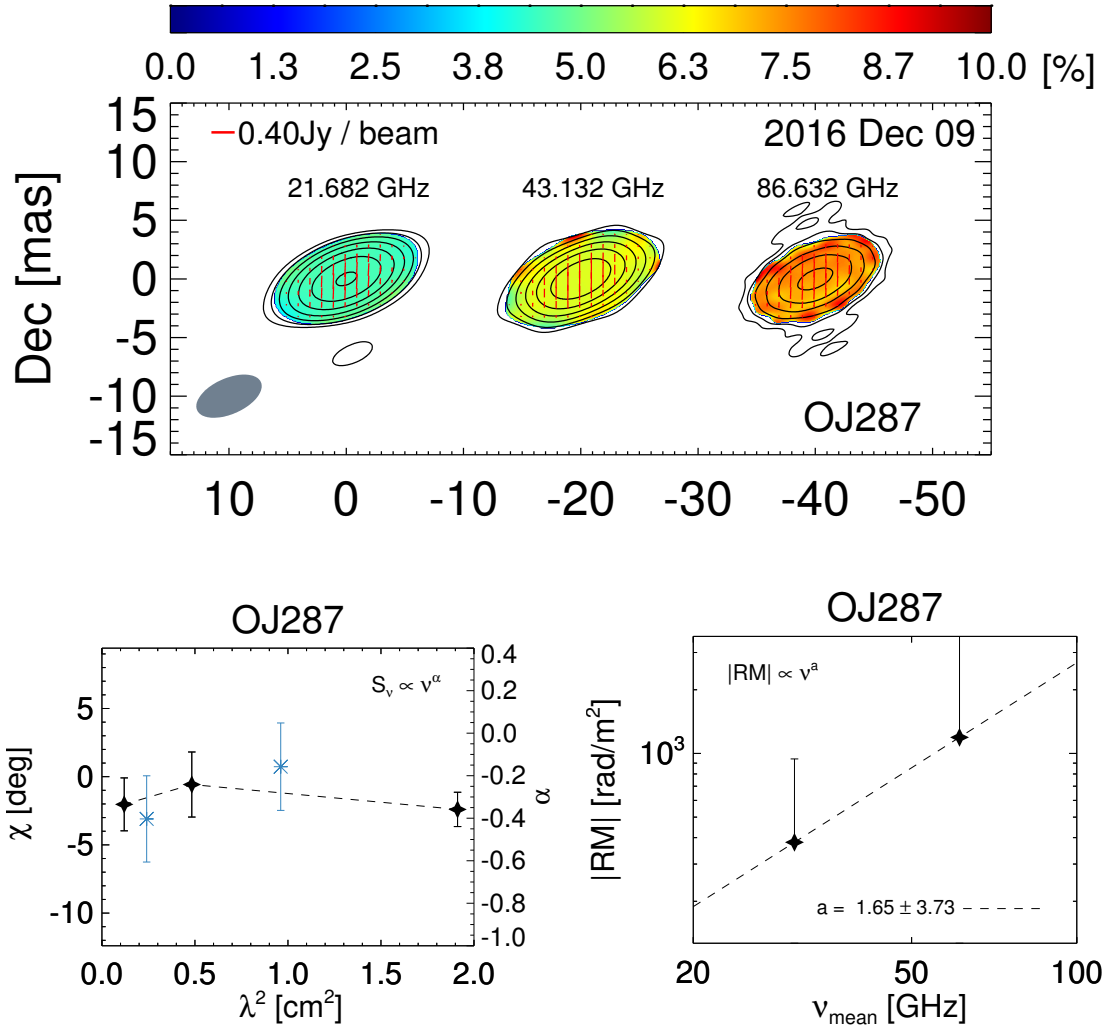

Figure 4.1. *Continued.*

This source has shown slow and gradual EVPA variation in time and thus a potential variability during the time gap between the MOJAVE and our KVN observations ($\lesssim 2$ weeks) would not be significant (see the AGN monitoring database of the 26-meter University of Michigan Radio Astronomy Observatory[3]). In addition, OJ 287 has been known for relatively small RMs at cm wavelengths (e.g., Hovatta et al. 2012). Our KVN maps are consistent with zero RM (within errors) in 2016 December. However, in the 2017 January data, EVPA rotations from 15 to 86 GHz in the same direction being

[3]`https://dept.astro.lsa.umich.edu/obs/radiotel/gif/0851\_202.gif`

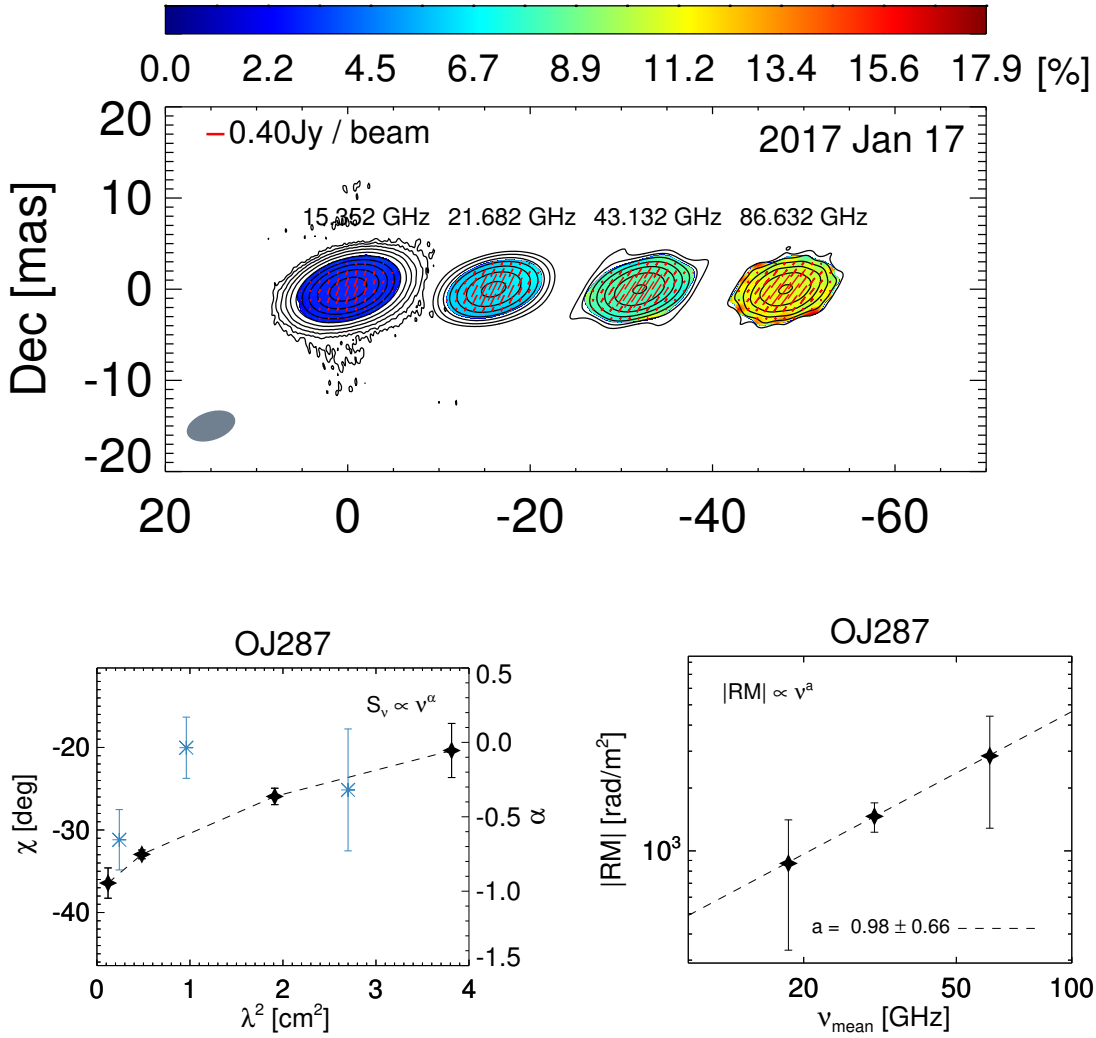

Figure 4.1. *Continued.*

steeper at higher frequency pairs are observed, which results in $a = 0.98 \pm 0.66$. In the 2017 March data, the EVPA rotations between 15 and 43 GHz were almost zero within errors but a relatively large rotation with $|\mathrm{RM}| \approx 5 \times 10^3 \mathrm{rad/m^2}$ was detected at 43/86 GHz.

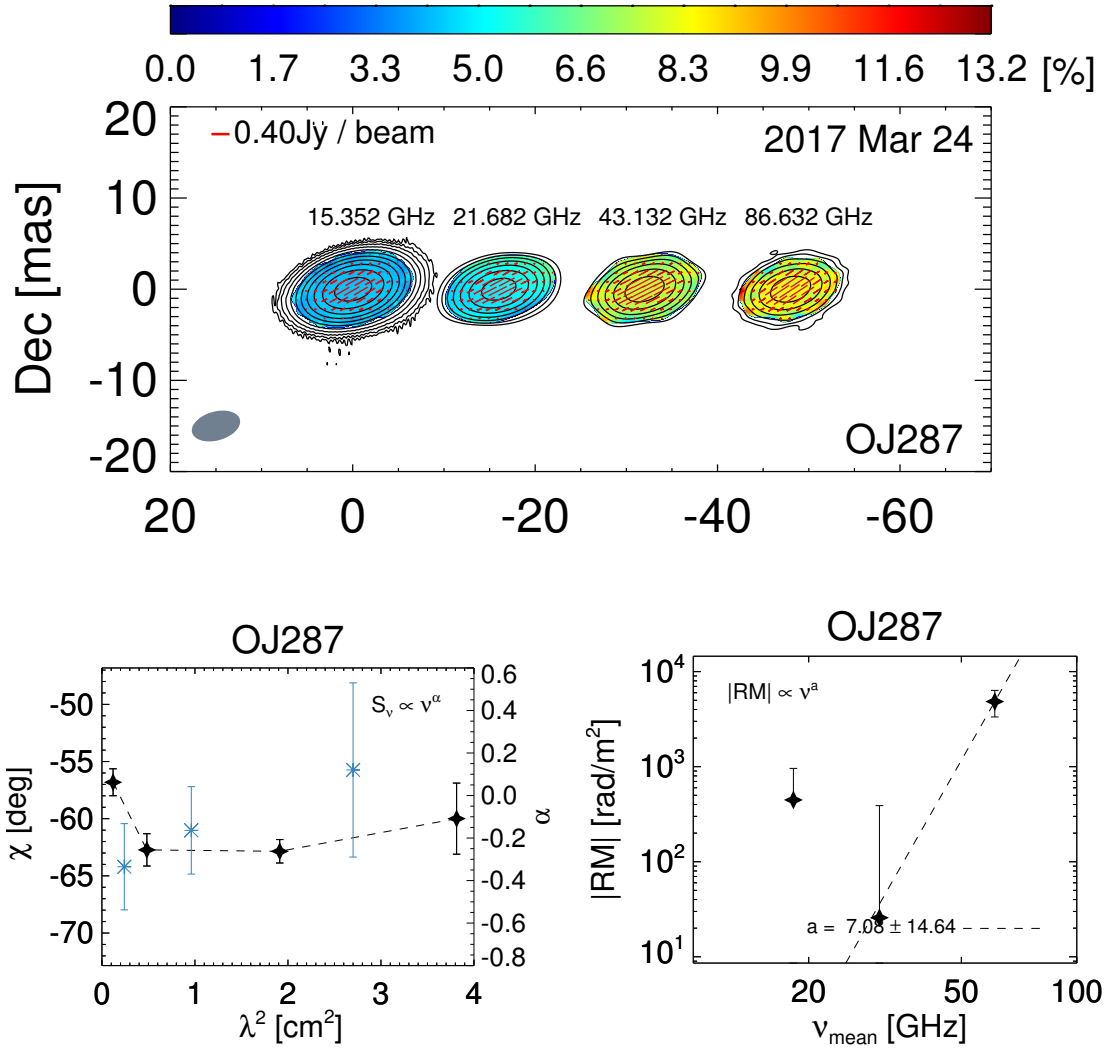

Figure 4.1. *Continued.*

CTA 102

This source shows a high degree of polarization, up to ≈ 40%, in its jet at 22 GHz but becomes compact at higher frequencies. The EVPAs rotate rapidly as function of frequency, with different slopes in the EVPA–λ^2 diagram between 22/43 GHz and 43/86 GHz. RMs at 43/86 GHz are a few times 10^4 rad/m^2 in the source rest frame in both epochs. However, a value in the 2016 December data is much larger than that in the 2017 January data. The signs of RMs are different in our two epochs, while

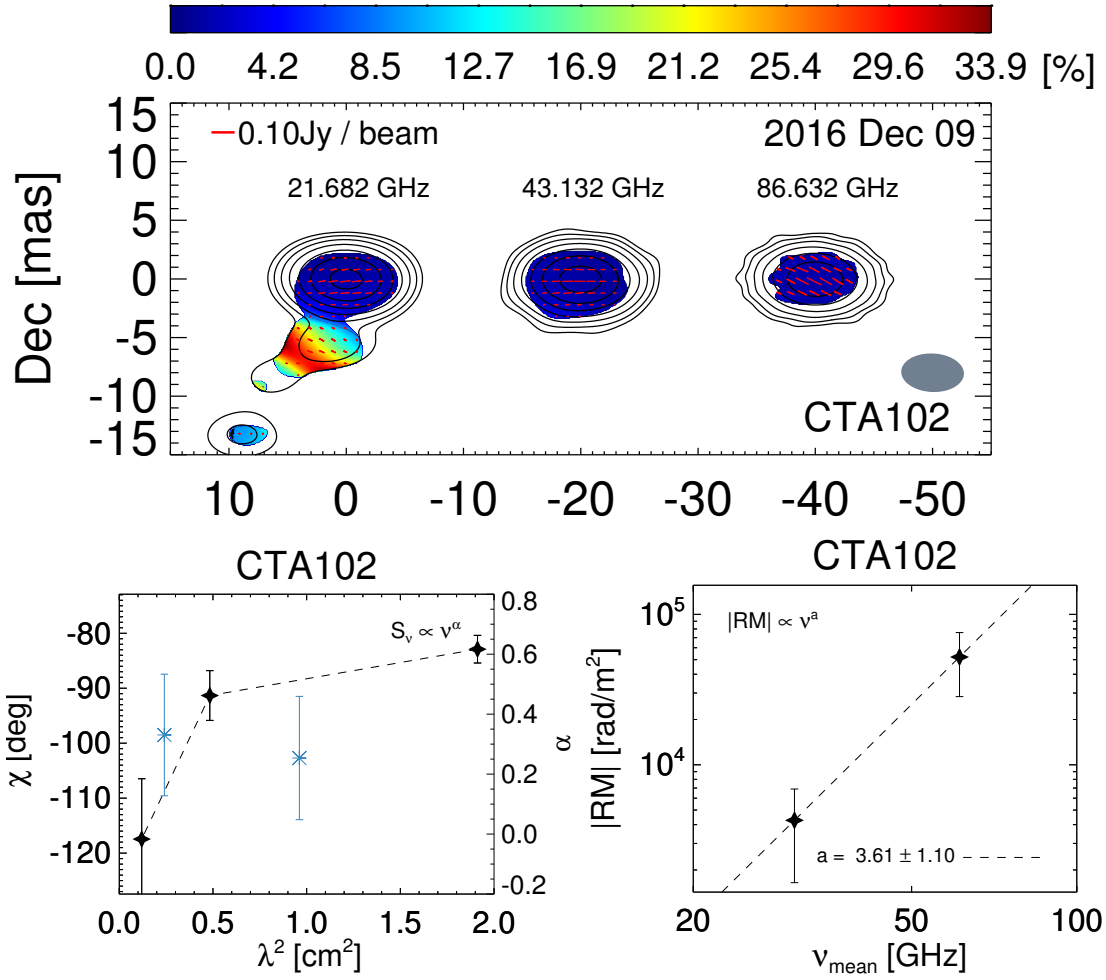

Figure 4.1. *Continued.*

their absolute values are of the same order of magnitude. This behavior suggests that the line-of-sight component of the jet magnetic field changed its direction within ≈ 1 month, while magnetic field strength and electron density (or at least their product) did not vary substantially. This sign change might be related to a strong flare that occurred during our KVN observations (Raiteri et al. 2017). We discuss possible reasons for the sign flip in CTA 102 in Section 4.4.4.

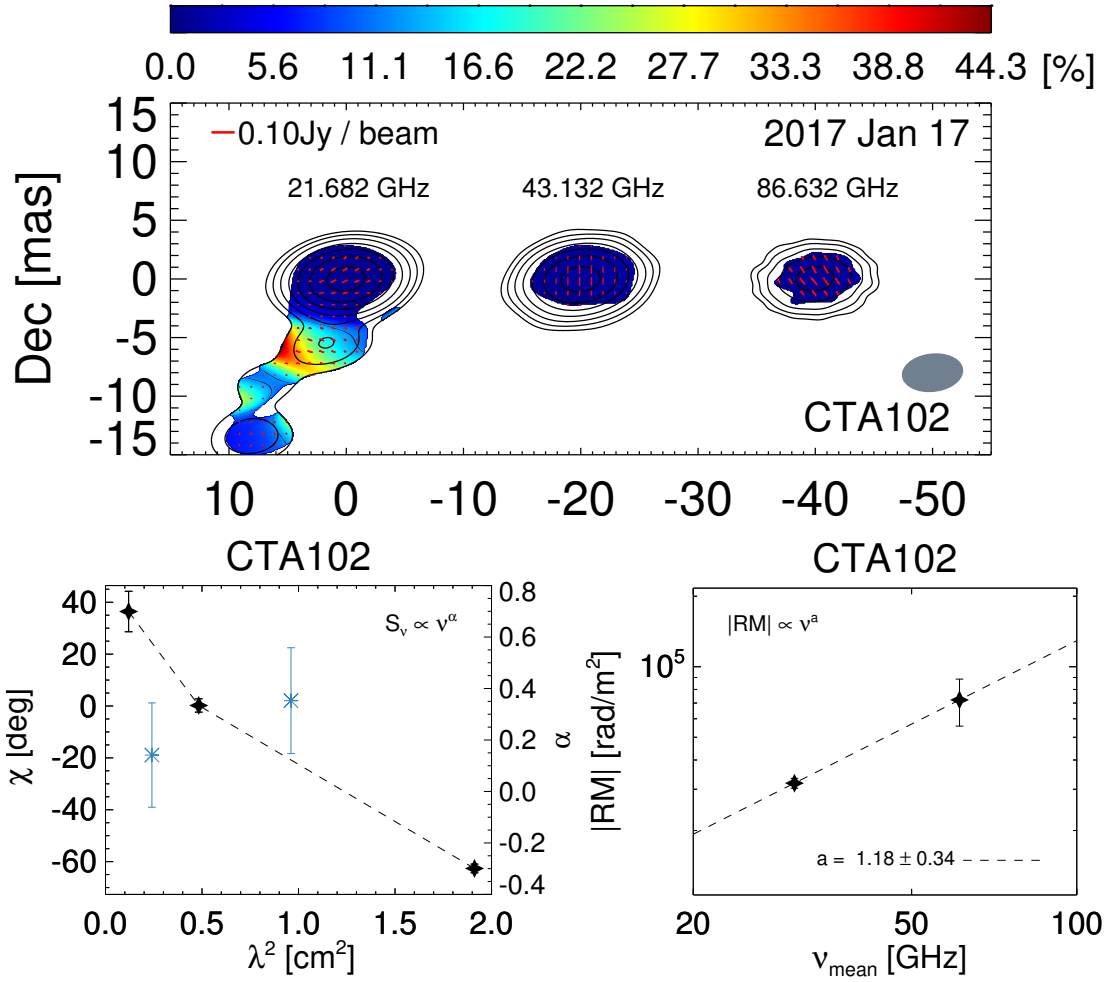

Figure 4.1. *Continued.*

3C 345

This source shows almost the same RMs at 22/43 and 43/86 GHz, $|\mathrm{RM}| \approx 10^4$ rad/m^2 in the 2016 December data, with a being consistent with zero within errors. However, the RM at 43/86 GHz is much larger than that at 22/43 GHz about one month later, resulting in $a = 1.86 \pm 0.3$. These results indicate that there is substantial time variability in this source. Similarly to the case of CTA 102, this source shows a flare during our KVN observations and the flux density in early 2017 is almost three times higher

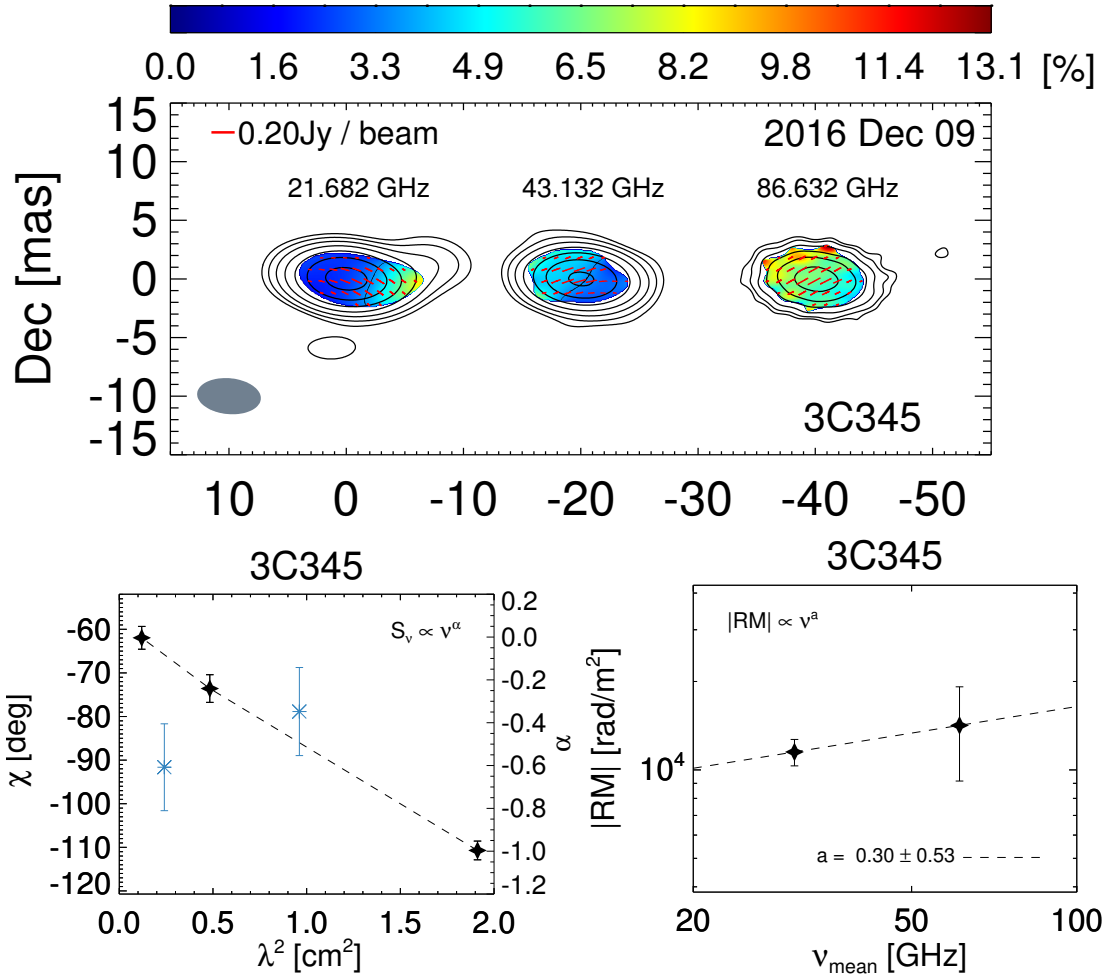

Figure 4.1. *Continued.*

than that in mid 2016 at 1 mm.[4]

1749+096

This source displays a rather compact jet geometry at all frequencies and in both epochs (2016 December and 2017 March). Interestingly, the degree of linear polarization is

[4] `http://sma1.sma.hawaii.edu/callist/callist.html?plot=1642\%2B398` This might be related to a substantial change in a within $\approx$ 1 month for this source, though the sign of RM does not change during the period.

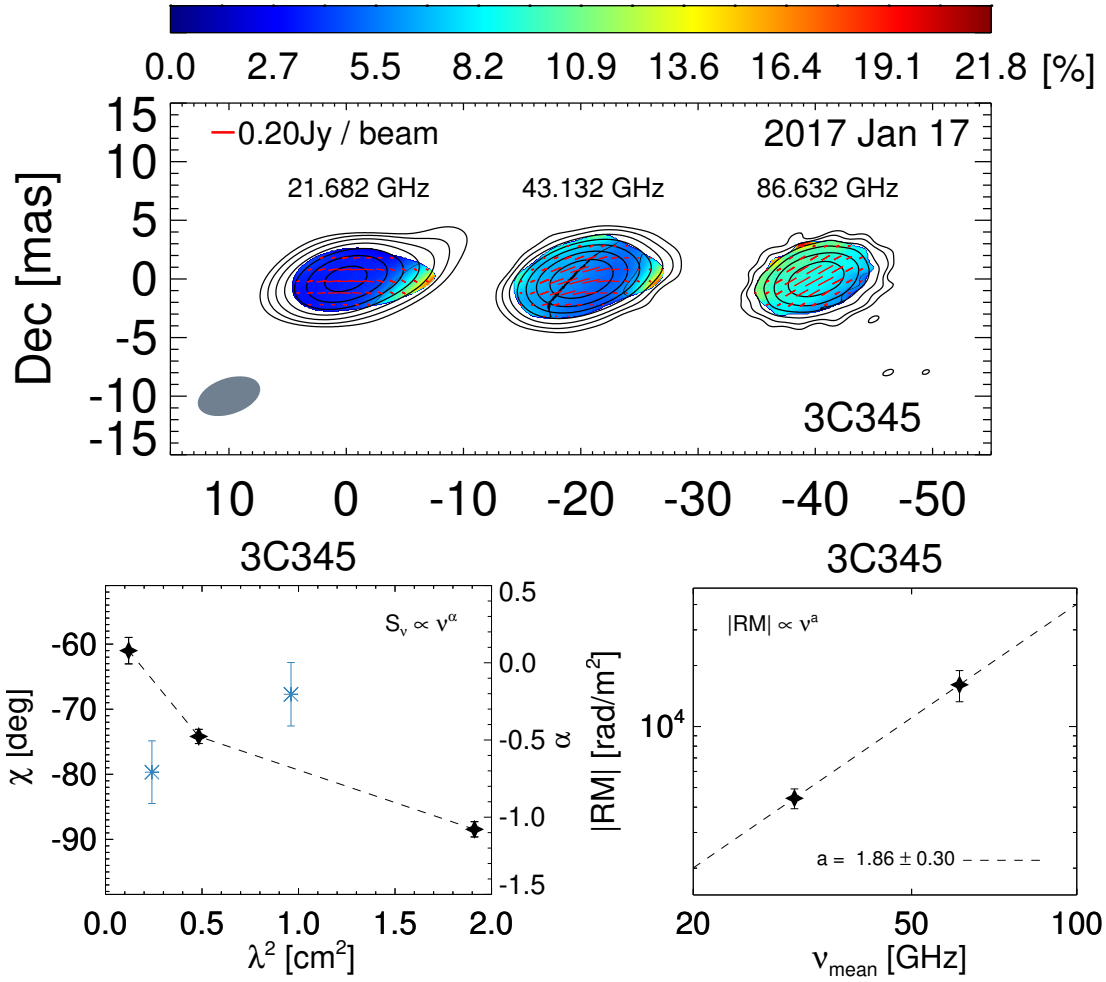

Figure 4.1. *Continued.*

larger at lower frequencies, which is not usually seen in other sources (Section 4.3.3). This might suggest that we are looking at a mixture of different polarization components with different EVPAs and/or RMs or that internal Faraday rotation occurs in this source (Section 4.4.3). The values of RM range from $\approx 10^3$ to $\approx 10^4$ rad/m^2 in both epochs data. The values of a are consistent within errors. Therefore, the sign, absolute value, and frequency dependence of RM appear to be stable over ≈ 3 months.

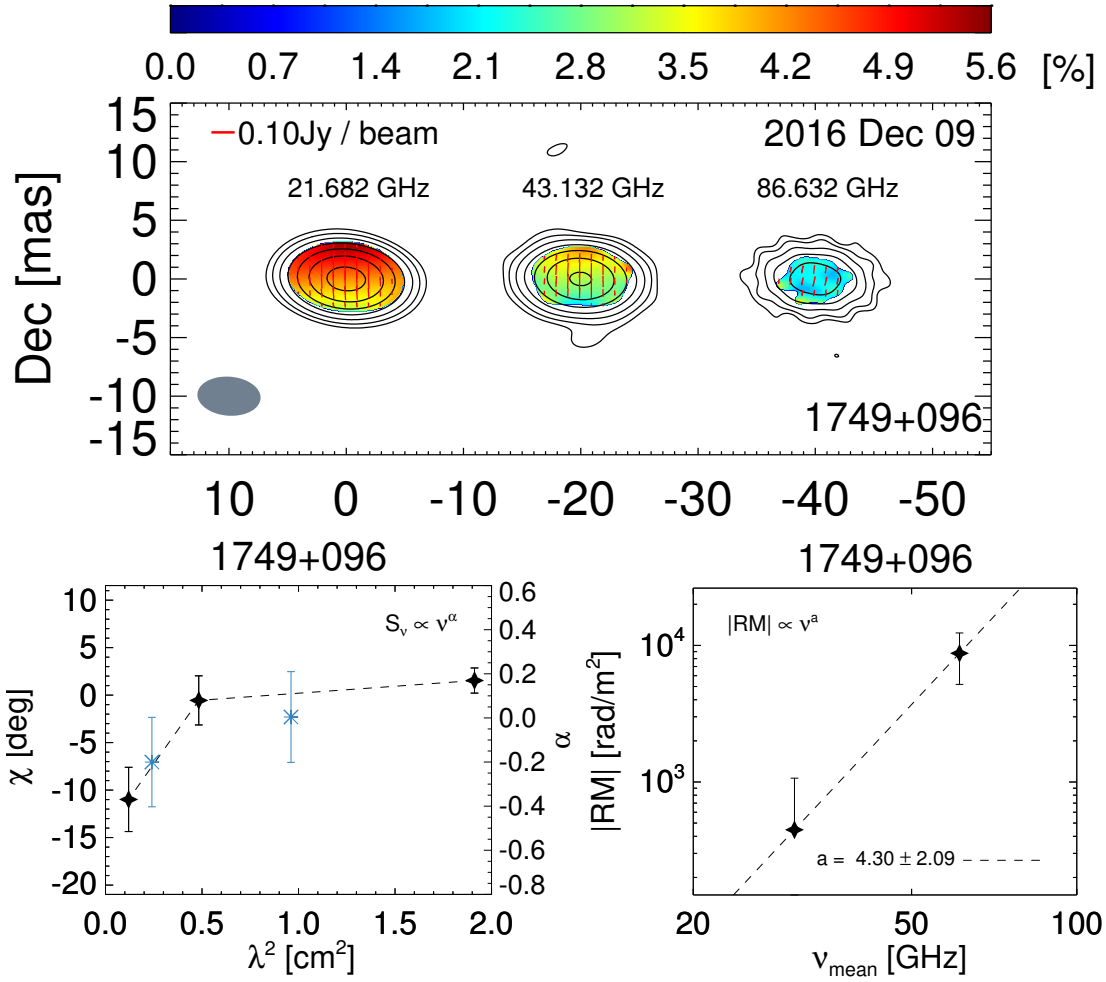

Figure 4.1. *Continued.*

0235+164

This source shows a rather compact jet geometry. A systematic rotation of EVPAs in the same sense as function of frequency can be seen from 22 to 86 GHz. RMs range from $\approx 10^3$ to $\approx 2 \times 10^4$ rad/m^2, with a substantially larger RM at a higher frequency pair, resulting in $a = 3.47 \pm 1.18$.

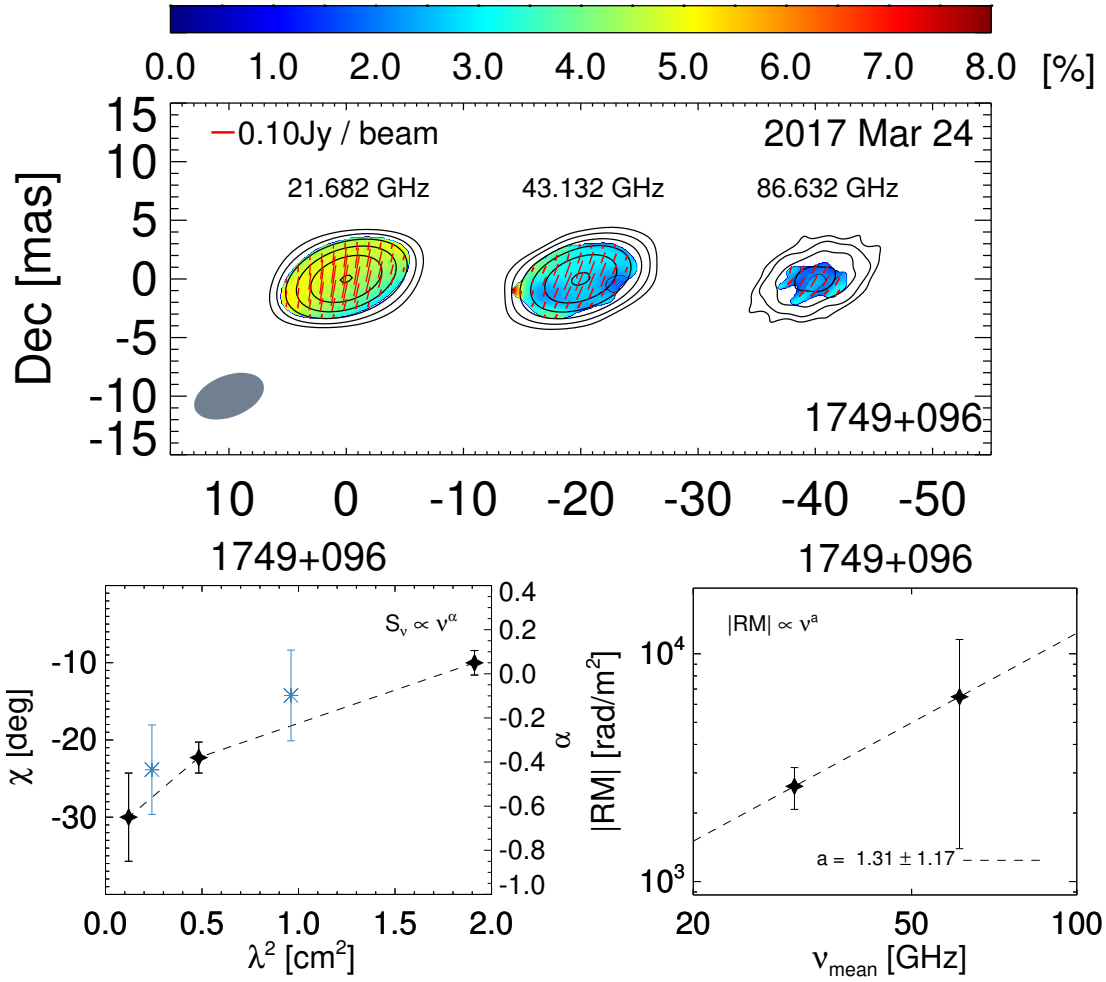

Figure 4.1. *Continued.*

BL LAC

The EVPA–λ^2 diagram shows a steeper slope between 43 and 86 GHz than between 22 and 43 GHz, providing $a = 2.65 \pm 0.61$. RM values range from $\approx 10^3$ to $\approx 6 \times 10^3$ rad/m^2. This is consistent with previous measurements of the core RM between 15 and 43 GHz (O'Sullivan & Gabuzda 2009a; Gómez et al. 2016). However, the high resolution *RadioAstron* space VLBI image shows a complex RM structure in the core region including a sign change, indicating the presence of helical magnetic fields there (Gómez et al. 2016). Therefore, we may be looking at a blend of those structures in our KVN

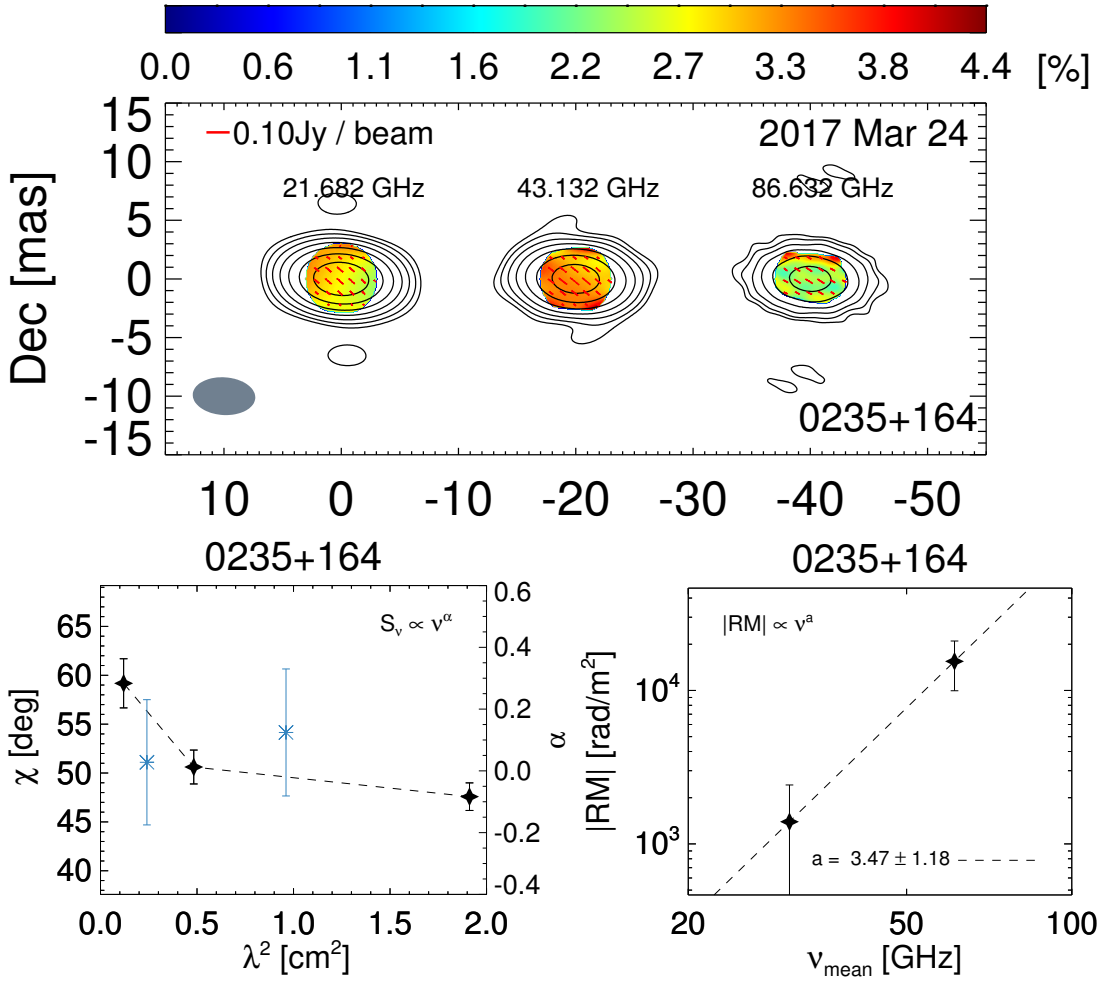

Figure 4.1. *Continued.*

images (see Section 4.4.7).

1633+38

This source is relatively faint and shows a low degree of linear polarization ($\approx 2\%$) which leads to relatively large EVPA errors. Thus, the RM at 43/86 GHz is comparable to its error and the obtained $a = 1.91 \pm 1.96$ has also a large error. When fitting a single linear function to the EVPAs at the three frequencies available, we obtained RM = 974 ± 509 rad/m^2. This is surprisingly low because a very high RM, $\approx 2.2 \times 10^4$ rad/m^2,

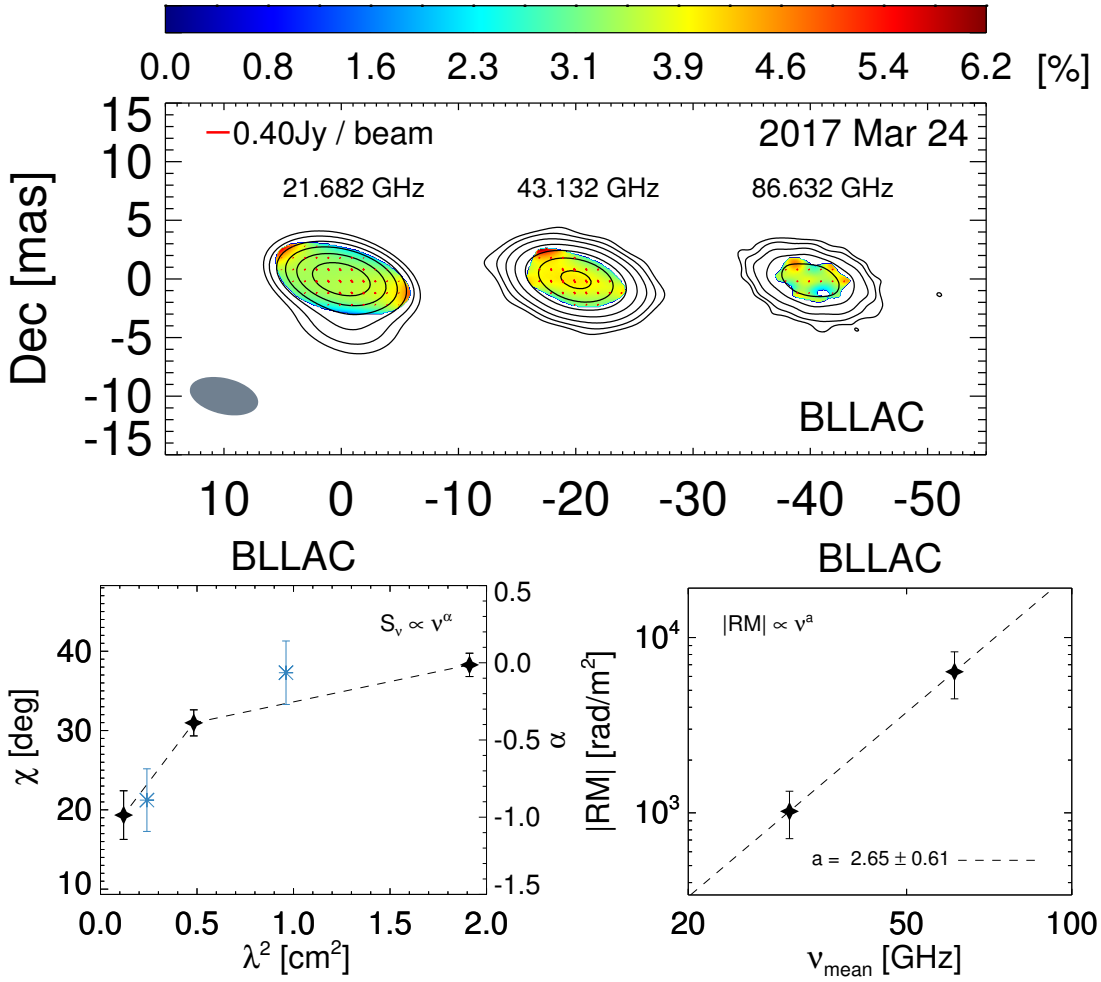

Figure 4.1. *Continued.*

was reported previously for the core of this source using six different frequencies from 12 GHz to optical wavelength (Algaba et al. 2012). We found that EVPAs at the core of this source in the MOJAVE program are 44° and 32° in 2016 November and 2017 April, respectively. If there is no substantial EVPA variability in between these two epochs, then a simple λ^2 fit can explain the data from 15 to 86 GHz, suggesting that there is no $n\pi$ ambiguity in our data and that the core RM of this source is indeed quite small. The observations in Algaba et al. (2012) were performed in 2008 November which indicates that there is substantial temporal variability of the EVPA rotation in 1633+38. Four

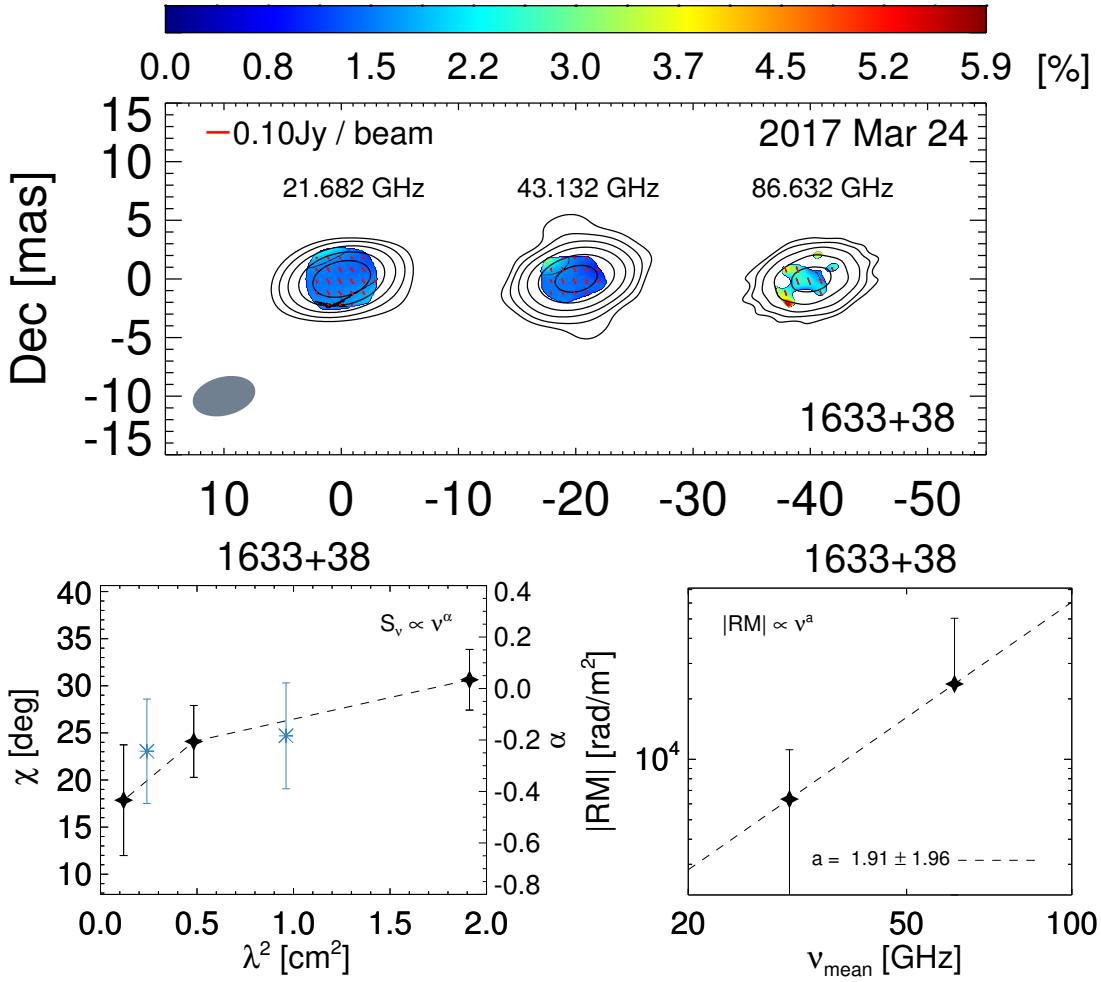

Figure 4.1. *Continued.*

years before their observations, core EVPAs could not be fitted with a single λ^2 law and the obtained RM value was much smaller, RM $= -570 \pm 430$ rad/m^2 (Algaba et al. 2011). This also suggests substantial temporal RM variability in 1633+38.

4.3.2 Optical EVPAs from the Steward observatory

For a few sources, we obtained quasi-contemporaneous (taken within $\lesssim$1 week) optical polarization data from the Steward Observatory blazar monitoring program[5] (see

[5] `http://james.as.arizona.edu/~psmith/Fermi`

Our targets and the polarization properties of their cores

Source	Type	z	l	Epoch	$\alpha_{22/43}$	$\alpha_{43/86}$	22 GHz		43 GHz		86 GHz		β	$\mathrm{RM}_{22/43}$[rad/m^2]	$\mathrm{RM}_{43/86}$	a
							m[%]	χ [°]	m	χ	m	χ				
	(1)	(2)	(3)		(4)	(5)							(6)	(7)	(8)	(9)
3C279	FSRQ	0.54	20	12/09-10/16	-0.4 ± 0.2	-0.3 ± 0.2	9.9±0.1	26±1	10.3±0.5	33±3	10.5±2.2	37±2	-0.05	(-2.0±1.0)×10^3	(-4.0±4.5)×10^3	1.0±1.8
				01/16-17/17	-0.3 ± 0.2	-0.7 ± 0.2	8.8±0.1	28±1	8.8±0.4	31±2	8.2±0.9	38±3	0.03	(-6.5±6.5)×10^2	(-8.4±4.1)×10^3	3.7±1.6
				03/22-24/17	-0.1 ± 0.2	-0.4 ± 0.2	8.6±0.1	30±1	11.2±0.2	36±2	12.4±0.4	49±3	-0.31	(-1.7±0.6)×10^3	(-1.4±0.4)×10^4	3.1±0.6
OJ287	BLO	0.31	14	12/09-10/16	-0.2 ± 0.2	-0.4 ± 0.2	4.6±0.1	-2±1	6.1±0.1	-1±2	7.4±0.5	-2±2	-0.38	(-3.8±5.6)×10^2	(1.2±2.5)×10^3	1.7±3.7
				01/16-17/17	0.0 ± 0.2	-0.7 ± 0.2	6.6±0.1	-26±1	8.3±0.1	-33±1	10.9±0.1	-36±2	-0.73	(1.5±0.2)×10^3	(2.8±1.6)×10^3	1.0±0.7
				03/22-24/17	-0.2 ± 0.2	-0.3 ± 0.2	5.0±0.1	-63±1	7.6±0.1	-63±1	8.3±0.2	-57±1	-0.43	(-0.3±3.6)×10^2	(-4.8±1.5)×10^3	7.1±14.6
CTA102	FSRQ	1.04	26	12/09-10/16	0.3 ± 0.2	0.3 ± 0.2	1.6±0.1	-83±3	1.5±0.2	-91±5	1.8±0.4	-117±11	0.02	(4.3±2.6)×10^3	(5.2±2.4)×10^4	3.6±1.1
				01/16-17/17	0.4 ± 0.2	0.1 ± 0.2	1.1±0.1	-63±2	1.4±0.2	0±3	1.4±0.1	36±8	-0.13	(-3.2±0.2)×10^4	(-7.2±1.6)×10^4	1.2±0.3
3C345	FSRQ	0.59	21	12/09-10/16	-0.3 ± 0.2	-0.6 ± 0.2	2.6±0.2	-111±2	3.9±0.2	-74±3	6.6±0.8	-62±3	-0.65	(-1.2±0.1)×10^4	(-1.4±0.5)×10^4	0.3±0.5
				01/16-17/17	-0.2 ± 0.2	-0.7 ± 0.2	3.7±0.1	-88±1	5.8±0.2	-74±1	9.0±0.7	-61±2	-0.65	(-4.4±0.5)×10^3	(-1.6±0.3)×10^4	1.9±0.3
1749+096	BLO	0.32	15	12/09-10/16	0.0 ± 0.2	-0.2 ± 0.2	4.2±0.1	2±1	3.2±0.1	-1±3	2.2±0.5	-11±3	0.42	(4.5±6.2)×10^2	(8.8±3.6)×10^3	4.3±2.1
				03/22-24/17	-0.1 ± 0.2	-0.4 ± 0.2	4.6±0.2	-10±2	2.9±0.1	-22±2	2.5±0.8	-30±6	0.63	(2.6±0.5)×10^3	(6.5±5.1)×10^3	1.3±1.2
0235+164	FSRQ	0.94	25	03/22-24/17	0.1 ± 0.2	0.0 ± 0.2	2.8±0.1	48±1	3.3±0.1	51±2	2.4±0.3	59±3	-0.09	(-1.4±1.0)×10^3	(-1.5±0.6)×10^4	3.5±1.2
BLLAC	BLO	0.07	4	03/22-24/17	0.0 ± 0.2	-0.9 ± 0.2	3.5±0.1	38±1	4.1±0.3	31±2	3.8±0.4	19±3	-0.11	(1.0±0.3)×10^3	(6.4±1.9)×10^3	2.7±0.6
1633+38	FSRQ	1.81	27	03/22-24/17	-0.2 ± 0.2	-0.2 ± 0.2	1.5±0.2	31±3	1.4±0.2	24±4	2.2±0.7	18±6	-0.09	(6.3±4.8)×10^3	(2.4±2.7)×10^4	1.9±2.0

Table 4.2. (1) Source types: FSRQ: flat spectrum radio quasars; BLO: BL Lac objects; taken from the MOJAVE web site. (2) Redshifts are taken from the NASA/IPAC Extragalactic Database (NED). (3) Linear size probed for each source in units of parsec corresponding to the typical size of the minor axis of the KVN beam at 22 GHz, using the scaling factors provided by the MOJAVE web site. (4) Total intensity spectral index, defined as $S_\nu \propto \nu^\alpha$ between 22 and 43 GHz. (5) Total intensity spectral index between 43 and 86 GHz. (6) Polarization spectral index, defined as $m \propto \lambda^\beta$. (7) RM between 22 and 43 GHz in source rest frame. (8) RM between 43 and 86 GHz in source rest frame. (9) Power-law index in $|\mathrm{RM}| \propto \nu^a$ (see Figure 4.1).

Optical Data from the Steward Observatory

Source	Obs. date	$\chi_{\rm opt}$ [°]	$\nu_{\rm trans}$ [GHz]
CTA 102	11/30/16–12/02/16	-216.5 ± 31.4	244^{+701}_{-93}
	01/10/17–01/13/17	111.7 ± 12.6	591^{+1467}_{-276}
3C 279	01/10/17–01/14/17	85.2 ± 2.7	209^{+697}_{-71}
BL LAC	03/29/17–03/30/17	-8.9 ± 26.1	138^{+298}_{-65}

Table 4.3. $\chi_{\rm opt}$ is the EVPA at optical wavelengths taken from the blazar monitoring program of the Steward Observatory. We used the mean value of the EVPAs observed in the noted period as $\chi_{\rm opt}$ (see text for explanation of $n\pi$ ambiguity and error estimation). $\nu_{\rm trans}$ shows the frequency on the source's rest frame at which the power-law increase of RM at radio frequencies is expected to stop (see the right panel of Figure 4.2).

Smith et al. 2009 for details) for some epochs. We summarize the optical data we used in Table 4.3. (We excluded some additional datasets due to their large errors.) The optical polarimetry errors are usually quite small, $\lesssim 1°$, unless sources are very weakly polarized. However, optical polarization of blazars often show rapid variability on short time scales (e.g., Jorstad et al. 2013) presumably due to a smaller size of the emission region at higher frequencies (Marscher 1996). In order to take into account the uncertainty arising from the time gap between optical and radio observations we estimated errors from source variability as follows.

The Steward Observatory blazar monitoring program usually observes each source multiple times for a specified period spanning a few days in a broad optical band from 500 to 700 nm. We selected all data in the periods that are close to our KVN observations and used the mean and standard deviation of the data points as representatives of optical EVPA and typical error, respectively. We assumed that their optical EVPAs show random-walk type variations with time. (In addition to statistical variability, many blazars occasionally show smooth, systematic optical EVPA rotations that might be associated with high energy flares; e.g., Blinov et al. 2015). We multiplied the ob-

served standard deviation by the square root of the ratio of the time gap between optical and radio observations to the duration of the period in which a set of optical data was obtained. Under this assumption, the longer the time separation, the larger the formal uncertainty of an optical EVPA at the time of the corresponding radio observation.

Due to lack of frequency coverage between 86 GHz and optical wavelengths, we suffered from potential $n\pi$ rotation of the optical EVPAs. Therefore, we assumed that the optical EVPAs of our sources rotate in the same direction as the ones at mm wavelengths and that the EVPA rotation between 86 GHz and the optical band does not exceed π. We present the optical EVPA values of three sources in Table 4.3 and plot them with the core EVPAs from our KVN observations in the left panel of Figure 4.2. We also show the RMs obtained from each adjacent frequency pair in the RM–frequency diagram (the right panels of Figure 4.2). Our assumption on $n\pi$ rotation appears reasonable because the optical EVPAs follow the trend of EVPA rotation established at radio frequencies, although we cannot rule out the possibility of coincidence because of the low number of sample. The RMs obtained from the EVPA difference between 86 GHz and the optical frequencies are about an order of magnitude higher than the values obtained from the frequency pair 43/86 GHz. We note that the observed RMs between 86 GHz and optical light exceed the minimum possible measurable RM by an order of magnitude except for BL Lac for which the observed RM is about two times the minimum measurable RM.

The power-law increase of RM as a function of frequency does not continue to optical wavelengths but saturates at a certain frequency (right panel of Figure 4.2). We used the term *transition frequency*, $\nu_{\rm trans}$, for this frequency. We calculated asymmetric errors on $\nu_{\rm trans}$ via Monte-Carlo simulations by adding Gaussian random numbers to the best-fit parameters of the radio RM–ν power-law relation with standard deviations identical to their 1σ errors. The obtained $\nu_{\rm trans}$ are distributed from 138 to 591 GHz in the source rest frame for different sources and in different epochs (Table 4.3). We note that $\nu_{\rm trans}$ for BL Lac is consistent with the observed frequency of 86 GHz within 1σ because of the relatively large minimum measurable RM.

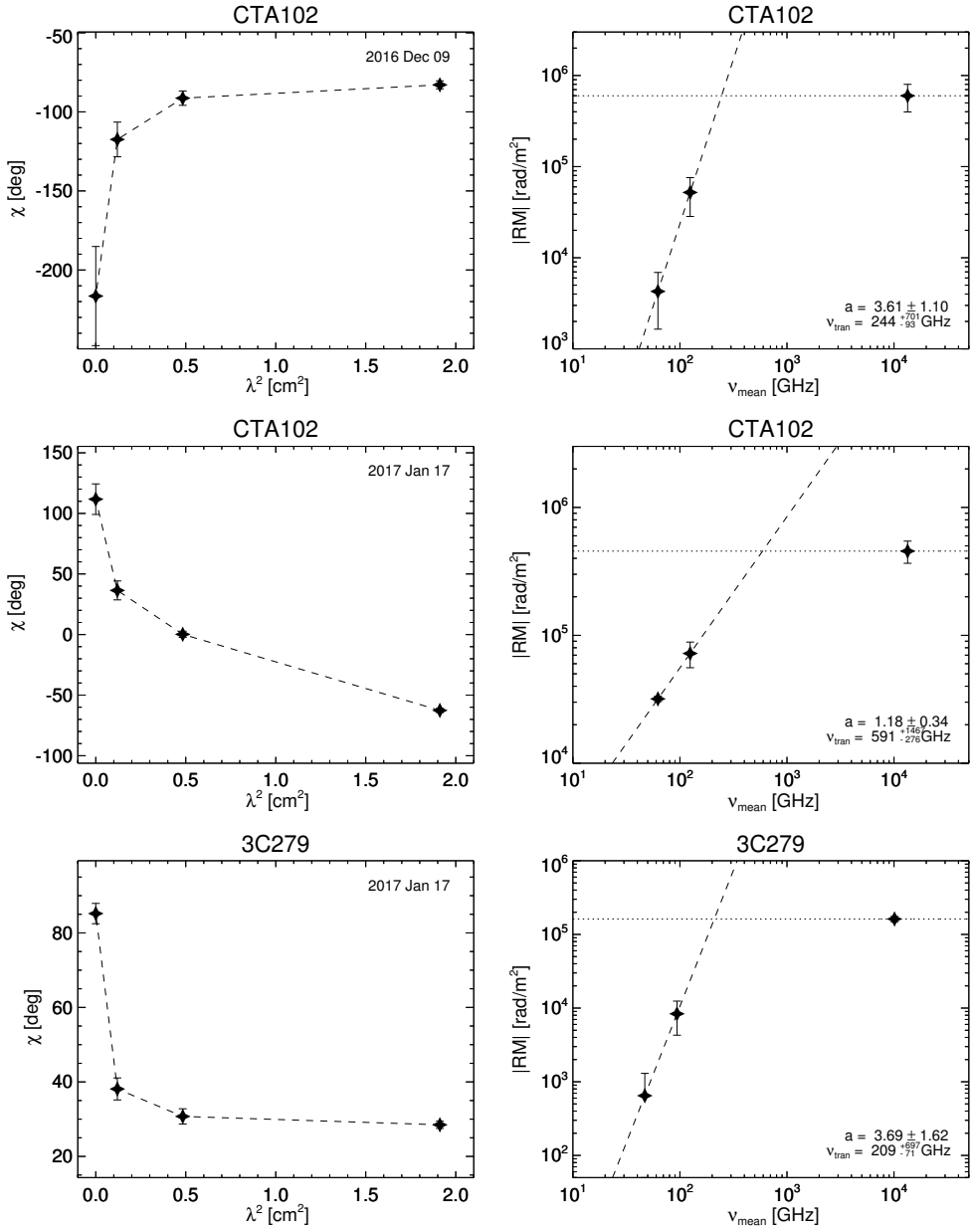

Figure 4.2. Same as the central and right panels of Figure 4.1 but combined with contemporaneous optical data (see Table 4.3). We obtained the frequency $\nu_{\rm trans}$ where the power-law increase of the RM measured at radio frequencies intersects with the RM obtained with the optical data points (horizontal dotted lines). The values of the power-law index a and $\nu_{\rm trans}$ are given at the bottom right of the right panels. All RM and frequency values are in the source rest frame.

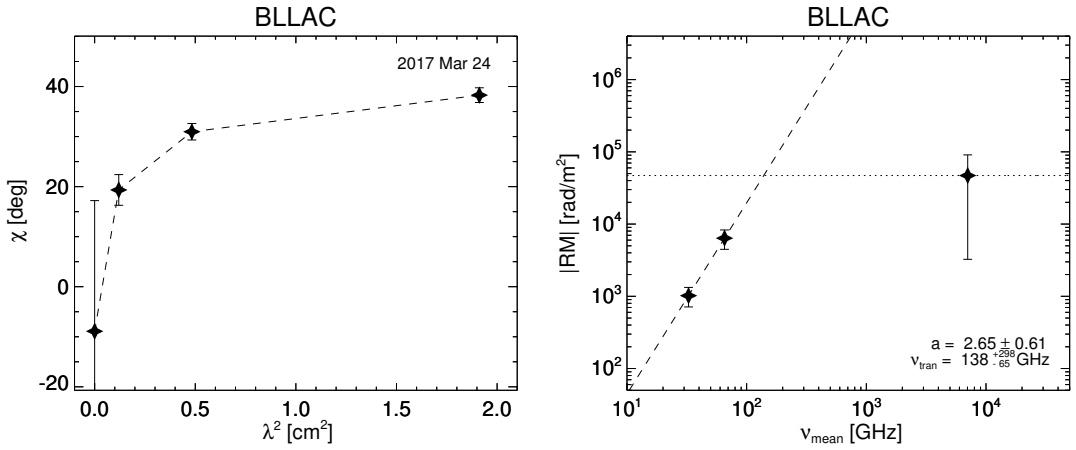

Figure 4.2. *Continued.*

4.3.3 fractional polarization

We present the degree of linear polarization m as function of λ in Figure 4.3. Various de-polarization models are available to explain the evolution of m with wavelength (see O'Sullivan et al. 2012; Farnes et al. 2014 for summaries). In principle, $m-\lambda$ scalings can be used to determine whether the emitting region and the Faraday screen are co-spatial or not, whether magnetic fields in the screen are regular or turbulent, whether there are multiple components with different polarization properties on scales smaller than the spatial resolution, and so on (Burn 1966; Conway et al. 1974; Tribble 1991; Sokoloff et al. 1998). However, we did not try to apply those models to our data because (i) our data provide sparse frequency sampling over a limited frequency range, (ii) the models are mostly appropriate for optically thin emitters while we are dealing with (partially) optically thick cores, and (iii) different observing frequencies might probe different physical regions, as suggested by the complicated $\chi - \lambda^2$ scalings of the EVPAs. Instead, we obtain a polarization spectral index β by fitting $m \propto \lambda^\beta$ to our data (Table 4.1, see Farnes et al. 2014), which could be used for future theoretical studies (e.g., Porth et al. 2011) and for comparison with observations at lower frequencies (e.g., Farnes et al. 2014). We refer the readers to detailed studies of degree of linear polarization at different wavelengths of AGNs using broadband radio spectro-polarimetric observations

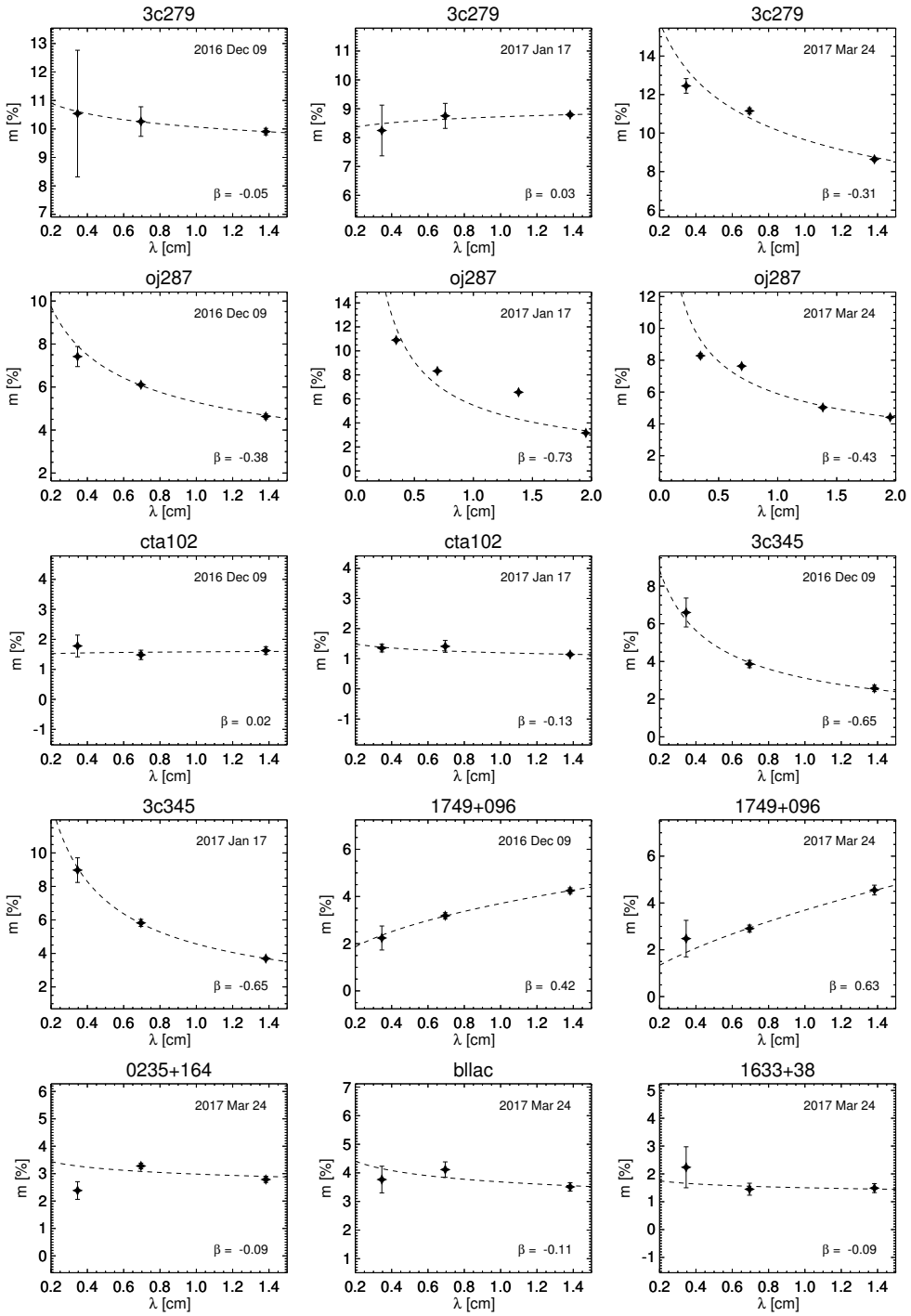

Figure 4.3. Degree of core linear polarization as function of λ. The dashed lines are the best-fit power-law functions, $m \propto \lambda^{\beta}$, to the data points. The polarization spectral indices, β, are noted in each panel.

(e.g., O'Sullivan et al. 2012, 2017; Hovatta et al. 2018; Pasetto et al. 2018) and investigating spatially resolved optically thin emitting regions with multi-frequency VLBI observations (e.g., Hovatta et al. 2012; Kravchenko et al. 2017). The median, mean, and standard deviation of β are -0.11, -0.17, and 0.38, respectively. All sources show $\beta \lesssim 0$ except for 1749+096 which showed $\beta \approx 0.5$ in both epochs (2016 December and 2017 March).

4.4 discussion

In this section, we interpret the results of the core polarization properties of eight blazars, five flat spectrum radio quasars (FSRQs) and three BL Lac objects (BLOs).

4.4.1 RM distributions at different frequencies

We present the distributions of the absolute RM values for different frequency pairs in the left panel of Figure 4.4. We excluded RM values whose absolute values are smaller than their 1σ errors. The histograms show that the median RM increases with frequency. We note that the minimum possible measurable RMs are 440 and 2038 rad/m^2 at 22/43 and 43/86 GHz, respectively, assuming a typical EVPA error of 2°, 3°, and 3° at 22, 43, and 86 GHz, respectively. As is evident in Figure 4.4, the RM values we found are much larger than these minimum possible measurable RMs. Notably, the trend of increasing RMs with increasing observing frequencies cannot be produced artificially.

We collected the median core RMs at cm wavelengths for our sources from Hovatta et al. (2012) and show all median RM values as function of frequency in the right panel of Figure 4.4. As expected, RMs increase with increasing frequency (355, 2620, and 14200 rad/m^2 for 8.1–15.4, 22–43, and 43–86 GHz, respectively). Un-weighted fitting of a power-law function returns a best-fit power-law index $a = 2.42$. Although the sample size is small and the standard deviations of the RM distributions are large, the obtained power-law index is quite close to $a = 2$, indicating that Faraday rotating media of blazars core can be represented as conical outflows statistically (Jorstad et al. 2007).

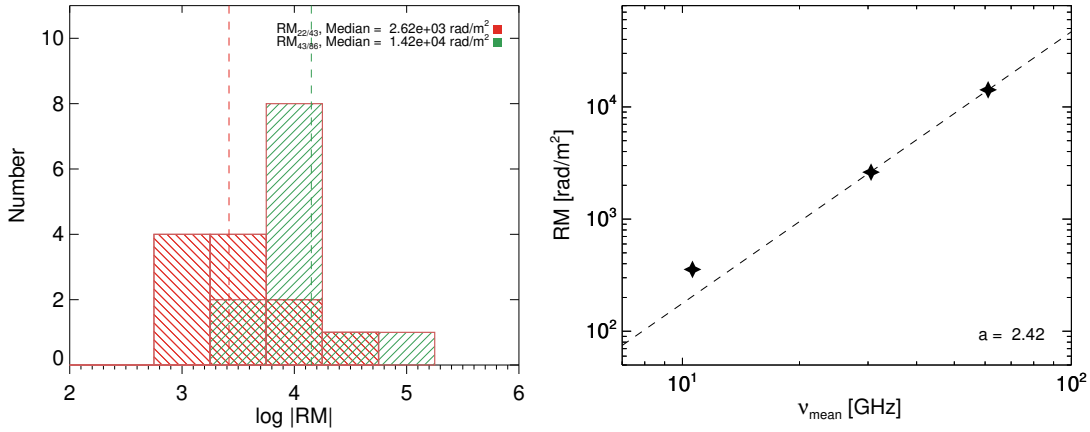

Figure 4.4. *Left:* Histograms of the logarithms of absolute RM values between 22 and 43 GHz (red) and 43 and 86 GHz (green). Values smaller than their 1σ errors are not included. The median values for each frequency pair are noted at the top right and are marked with vertical dashed lines. All RM values are rest frame values. *Right:* Median RM values as function of geometric mean observing frequency, combined with that obtained at 8.1–15.4 GHz for the same sources used for the left histogram by Hovatta et al. (2012). The dashed line is an un-weighted power-law fit with a best-fit power-law index $a = 2.42$.

Instead of comparing RM distributions of all sources at different frequencies, we collected the power-law indices a obtained for each source in Figure 4.5. We have 13 measurements in total, with some sources having more than one measurement. The mean and standard deviation of all a values are $a = 2.25 \pm 1.28$, which is consistent with $a = 2$ and the fitting results for the median values of RM distributions at different frequencies. Our results are also consistent with previous studies of blazars at both cm and mm wavelengths (e.g., Jorstad et al. 2007; O'Sullivan & Gabuzda 2009a; Algaba 2013; Kravchenko et al. 2017; Hovatta et al. 2018). However, many a values are located far from the mean value, which potentially indicates a bimodal distribution. Assuming a power-law electron density distribution as function of jet distance (d), $N_e \propto d^{-a}$, toroidal magnetic fields dominant in the Faraday screen, $B \propto d^{-1}$, a conical geometry

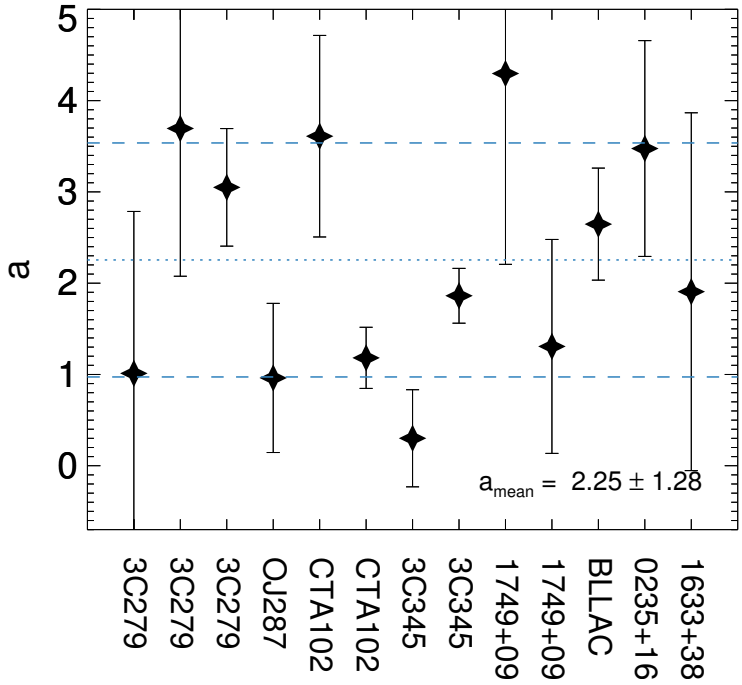

Figure 4.5. a values obtained from fitting $|\mathrm{RM}| \propto \nu^a$ to the data of each source (right panels of Figure 4.1). Multiple values for the same source correspond to different epochs. The blue dotted and dashed lines mark the mean and standard deviation of the full set of measurements, respectively; the values are noted on the bottom right.

of the Faraday screen, $dl \propto d$ and $a = 2$, and energy equipartition, $d_{\mathrm{core}} \propto \nu^{-1}$, one obtains $\mathrm{RM}_{\mathrm{core}} \propto \int N_e B dl \propto \nu^2$ (Jorstad et al. 2007). If some of these assumptions are not satisfied, one might expect deviations from a $a = 2$ scaling. For example, there is growing evidence for a parabolic geometry of the blazar cores (e.g., Algaba et al. 2017; Pushkarev et al. 2017). In some cases, a need for helical magnetic fields instead of dominant toroidal fields in blazars has been pointed out (e.g., Zamaninasab 2013). Likewise, the assumption of energy equipartition between radiating particles and magnetic fields may not hold for some sources (e.g., Homan et al. 2006). However, it is difficult to determine accurate a values for each source with the current data only due to source variability and relatively large errors in a. For example, the values of a are likely

related with source's flaring activity as seen in the case of CTA 102 and 3C 345 (see Section 4.3.1 and 4.3.1). We expect that our monthly monitoring program will allow us to investigate the reason for potential difference in a values for different sources and in different epochs, together with the detailed information of the compact core region provided by the ultra high resolution arrays such as the Global Millimeter-Very Long Baseline Interferometry Array (GMVA, see e.g., Kim et al. 2016) or the Radioastron space VLBI (e.g., Gómez et al. 2016).

4.4.2 Change of core opacities from optically thick to thin

In Section 4.3.2, we show that the power-law increase of RM as a function of frequency might not continue to optical wavelengths but flatten out at a certain frequency, $\nu_{\rm trans}$. We suggest that the cores of blazars become fully transparent at $\nu > \nu_{\rm trans}$, meaning no core-shift and thus no more frequency dependence of RM at those frequencies. Accordingly, the radio core may be a standing recollimation shock at $\nu > \nu_{\rm trans}$. For CTA 102, $\nu_{\rm trans}$ increased substantially from $\approx$ 240 GHz to $\approx$ 590 GHz within one month, albeit within large errors (Table 4.3). This might be related to a strong flare that occurred at the time of our observations (see Section 4.3.1) which ejected a large amount of relativistic electrons into the core, causing it to become optically thick. We obtained $\nu_{\rm trans} \approx$ 210 and 140 GHz for 3C 279 and BL Lac, respectively. This result seems to be in line with recent astrometric observations of BL Lac which found a systematic deviation of the amount of core-shift from the one expected for a Blandford–Königl type jet at 22/43 GHz (Dodson et al. 2017). Likewise, the scaling of synchrotron cooling time with frequency in BL Lac matches a standing shock better than an optically thick jet (Kim et al. 2017). In summary, one may expect no frequency dependence of RM and no core-shift above $\approx$ 140 GHz for BL Lac and above $\approx$ 210 GHz for 3C 279 and CTA 102. However, we stress that the conclusions presented in this section are valid only when the assumptions of (a) no $n\pi$ ambiguity and (b) EVPA rotations in the same sense from mm to optical hold. We will study core opacity evolution and RM saturation further with dedicated upcoming multi-frequency observations at mm and

sub-mm, combining data from KVN and ALMA (Park et al., in preparation).

4.4.3 The Faraday screen

Identifying the source of Faraday rotation is very difficult. As the amount of Faraday rotation is inversely proportional to the square of the mass of charged particles, thermal electrons and/or low-energy end of radiating non-thermal electrons would be the dominant source of the observed RM. If those Faraday rotating electrons are mixed in with the emitting plasma in jets, internal Faraday rotation occurs. However, if the rotating medium is located outside the jet, e.g., in a sheath surrounding the jet or the broad/narrow line regions (BLRs/NLRs), then the observed Faraday rotation is external to the jet. Theoretical models assuming an optically thin jet with spherical or slab geometries showed that it is very difficult for internal Faraday rotation to cause EVPA rotations larger than 45° without severe depolarization (Burn 1966). Multiple studies showed that many blazars indeed have EVPA rotations larger than 45° without significant depolarization, indicating that the source of Faraday rotation is external to the jets usually (e.g., Zavala & Taylor 2003, 2004; Jorstad et al. 2007; O'Sullivan & Gabuzda 2009a; Hovatta et al. 2012). A sheath surrounding the jet is considered to be the most viable candidate for an external Faraday rotating medium; in addition, BLRs/NLRs are unlikely sources of RM given the time variability of RMs in jets and volume filling factor arguments (Zavala & Taylor 2002, 2004; Hovatta et al. 2012). Nevertheless, there is indication for potential internal Faraday rotation in some sources (Hovatta et al. 2012).

We cannot identify the Faraday screen from our data because of their limitations (Section 4.3.3). Nevertheless, we note that the observed RM–frequency relations having $a \approx 2$ (Section 4.4.1) and the polarization spectral indices being predominantly negative ($\beta \lesssim 0$) for our sources support the conclusion of previous studies that an external jet sheath acts as Faraday screen (Zavala & Taylor 2002, 2004; Hovatta et al. 2012). However, for 1749+096 we observed the degree of fractional polarization at high frequencies to be smaller than the one at lower frequencies, with $\beta \approx 0.5$ in both

epochs (2016 December 9 and 2017 March 24) – which is almost impossible to explain with any standard external depolarization model (Hovatta et al. 2012). Such 'inverse depolarization' can be due to blending of different polarized inner jet components at different frequencies (Conway et al. 1974) or internal Faraday rotation in helical or loosely tangled random magnetic field configurations (Homan 2012).

4.4.4 RM sign change

We observed a RM sign change for CTA 102 within ≈1 month, while the absolute values of RM did not change much (Figure 4.1). Previous studies found temporal sign reversals in RMs for other sources (e.g., Mahmud et al. 2009; Lico et al. 2017), sign reversals between core and jet (e.g., Mahmud et al. 2013), and sign reversals in the cores at different frequencies intervals (e.g., O'Sullivan & Gabuzda 2009a). Scenarios proposed to explain such RM sign changes include: (i) a reversal of the magnetic pole of the black hole facing the Earth; (ii) torsional oscillations of the jet; (iii) a 'nested-helix' magnetic field structure; and (iv) helical magnetic fields in jets seen at different orientations due to relativistic abberation, depending on whether $\theta\Gamma$ is larger or smaller than 1, where θ is the viewing angle and Γ is the bulk Lorentz factor of jets (see Mahmud et al. 2009, 2013 for (i)-(iii) and O'Sullivan & Gabuzda 2009a for (iv) for details). Although all scenarios are possible theoretically, we focus on the fact that CTA 102 underwent a relatively strong flare in the period of our KVN observations (Section 4.3.1).

Evidence for the presence of helical magnetic fields in AGN jets has been provided by many studies, starting with the detection of a transverse RM gradient in the jet of 3C 273 (Asada et al. 2002) which was later confirmed by other studies (Zavala & Taylor 2005; Hovatta et al. 2012). Similar behaviour has been found in many BL Lac objects (e.g., Gabuzda et al. 2004, 2015), radio galaxies (e.g., Kharb et al. 2009), and quasars (e.g., Asada et al. 2008; Algaba 2013; Gabuzda et al. 2015). Furthermore, general relativistic magnetohydrodynamic simulations of AGN jets showed that the combination of the rotation of the jet base and the outflow leads to the generation of a helical field and associated Faraday rotation gradients (Broderick & McKinney

2010). If helical magnetic fields pervade in the jet sheaths and if they are the main contributor of the observed RMs as speculated in Section 4.4.3), the sign of RMs would be determined by whether $\theta\Gamma$ is larger or smaller than 1, as explained in O'Sullivan & Gabuzda (2009a).

As noted in Section 4.3.1, a strong flare at multiple wavelengths occurred during our KVN observations (Raiteri et al. 2017). Flares in blazars are usually associated with new VLBI components emerging from the cores (e.g., Savolainen et al. 2002). The flare in CTA 102 would then likewise be connected to newly ejected VLBI components. Jorstad et al. (2005) found $\theta = 2.6°$ and $\Gamma = 17.2$ for CTA 102, which yields $\theta\Gamma = 0.78$. If there is bending and/or acceleration or deceleration of the ejected component, changes of $\theta\Gamma$ across the value $\theta\Gamma = 1$ can occur and the sign of RM reverses. Assuming scenario (i) or (ii) as mechanism behind the sign reversal requires coincidence with the recent strong flaring activity of this source. Furthermore, scenario (iii) can be related to flaring since a new jet component might lead to temporal increase of the relative contribution of the inner field to the outer field in the magnetic tower model. However, in this case it is difficult to explain the observation of similar RM magnitudes in the two epochs (a few times 10^4 rad/m^2 for CTA 102); the relative contributions by the inner and outer magnetic fields to the observed RMs must be almost exactly opposite in different epochs, which, again, would be a coincidence (but see Lico et al. 2017 for the case of Mrk 421 which supports this scenario). Therefore, we conclude that scenario (iv) provides the most natural way to explain the observed sign change in RMs of CTA 102 as it does not require substantial changes in the physical properties of the jets. Our interpretation is also consistent with modelling the multi-wavelength flare in this source in late 2016 with a twisted inhomogeneous jet (Raiteri et al. 2017). We note that bending and acceleration/deceleration of blazar jets are quite common indeed (e.g., Lister et al. 2013).

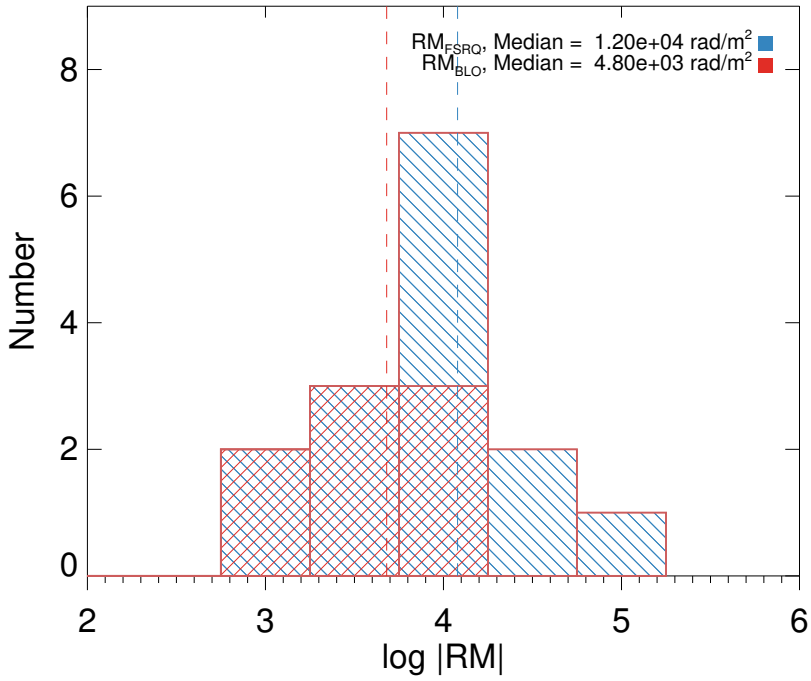

Figure 4.6. Histograms of the logarithmic absolute values of RMs of FSRQs (blue) and BLOs (red). Median values are indicated by vertical dashed lines and noted at the top right. We omitted RM values consistent with zero (within 1σ). All the RM values are rest-frame values.

4.4.5 Optical subclasses

Phenomenologically, blazars can be divided into two classes based on their optical properties: FSRQs and BLOs. Previous studies showed that FSRQs tend to have higher RMs than BLOs (Zavala & Taylor 2004; Hovatta et al. 2012). We collected all available core RM values from all frequency pairs and present the distributions of the (logarithmic) RMs of FSRQs and BLOs in Figure 4.6. The median RM values are 1.2×10^4 rad/m^2 and 4.8×10^3 rad/m^2 for FSRQs and BLOs, respectively – the value for FSRQs is higher than that for BLOs by a factor close to three. However, a Kolmogorov-Smirnov test (Press et al. 1992) finds a probability of 7% that the FSRQ and BLO values are drawn from the same parent population. Therefore, it is possible that their RM properties are

intrinsically the same.

In Section 4.4.3, we claimed that the observed Faraday rotation mostly originates from jet sheaths. Relatively slow, possibly non-relativistic winds launched by an accretion disk that surround and confine the highly relativistic jet spine are one of the candidates for a jet sheath (e.g., De Villiers et al. 2005). A fundamental difference between FSRQs and BLOs is their accretion luminosities relative to their Eddington luminosities, above and below $\approx 1\%$, respectively (e.g., Ghisellini et al. 2011, see also Potter & Cotter 2015 for further discussion). This suggests that sources in high accretion states tend to have larger RMs. A simple explanation would be that high accretion rates lead to relatively larger amounts of matter in jet sheaths. There is indeed evidence for a relation between the rate of matter injection into the jet and the accretion rate (e.g., Ghisellini et al. 2014; Park & Trippe 2017), supporting this idea. However, the strength and degree of ordering of core magnetic fields as function of blazar subclass are poorly understood yet; the difference in RM may not be solely due to the difference in particle density.

4.4.6 Intrinsic polarization orientation

Intrinsic EVPAs (projected onto the sky plane) of AGN jets can be obtained by correcting for Faraday rotation. It has been consistently shown that BLOs have intrinsic EVPAs well aligned with their jets, while a wide range of angles between EVPAs and jet orientations, sometimes seen as double-peaked distribution of relative angles, is observed for FSRQs (e.g., Lister & Homan 2005; Jorstad et al. 2007). The good alignment and the mis-alignment were associated with a transverse or oblique shock and a conical shock, respectively (Jorstad et al. 2007). These results, however, used RMs obtained from a single λ^2 law description of EVPA variation between 7 and 1 mm. The RM values were of the order 10^4 rad/m^2.

However, our results show that there is a possibility that the core RMs of blazars can increase up to $\approx 10^6$ rad/m^2 at ≈ 250 GHz (Figure 4.2). The possible difference in core RM between FSRQs and BLOs, discussed in Section 4.4.5, suggests that it is

easier for FSRQs to have high core RMs up to $\approx 10^6$ rad/m^2 than for BLOs – unless the transition frequency for BLOs is much larger than for FSRQs, which seems not to be the case (Figure 4.2). Even at 1 mm, the high RM of $\approx 10^6$ rad/m^2 leads to an EVPA rotation of ≈ 57 deg. Therefore, one needs to take the frequency dependence of RM into account – especially for FSRQs – when comparing the intrinsic EVPAs at mm wavelengths with the direction of the inner jet. However, FSRQs are unlikely to have intrinsic EVPAs aligned with their jets (see also Yuan et al. 2001; Gabuzda et al. 2006; Hovatta et al. 2016) even after correcting for Faraday rotation; even their optical EVPAs, which do not suffer from strong Faraday rotation, show bimodal distributions in the angles between jets and EVPAs (Jorstad et al. 2007, see also Lister & Smith 2000).

We observe RMs to increase with increasing frequency, meaning that intrinsic core EVPAs are different for different observing frequencies. Such a frequency dependence implies that polarized emission observed at higher frequencies comes from regions closer to the jet base. This indicates that intrinsic EVPAs can vary with distance from the jet base. A similar behaviour has been observed for a few sources in other studies. O'Sullivan & Gabuzda (2009a) found that the jet of BL Lac shows EVPAs well aligned to the jet direction in inter-knot regions and even when the jet bends. Gómez et al. (2016) showed that their high resolution polarization image of the same source shows smooth but non-negligible variations of EVPA upstream and downstream from the core. Both results were interpreted as the presence of helical magnetic fields in the jet. Similarly, different intrinsic EVPAs at different frequencies might imply the presence of helical magnetic fields in the core regions. However, a firm conclusion requires confirming the frequency dependence of RM at a wide range of observing frequencies with both short and long λ^2 spacings (see Section 4.4.7).

4.4.7 Multiple recollimation shocks in the cores

Theoretical studies have shown that a series of recollimation shocks can form in relativistic jets: in analytic works (e.g., Daly & Marscher 1988), in hydrodynamic numer-

ical simulations (e.g., Gómez et al. 1995, 1997; Agudo et al. 2001), and in magneto-hydrodynamic simulations (e.g., Mizuno et al. 2015; Martí et al. 2016). Observationally, the presence of stationary features in AGN jets in addition to their VLBI cores has been verified in many studies (e.g., Jorstad et al. 2005). Especially, high resolution images of 3C 454.3 (Jorstad et al. 2010) and BL Lac (Gómez et al. 2016) revealed that their cores may consist of multiple stationary components. For BL Lac, emission upstream the radio core, leading to multi-wavelength flares when it passes through the core, was observed (Marscher et al. 2008; Gómez et al. 2016); this supports the idea that the core can be identified with one of a series of recollimation shocks (e.g., Marscher 2009).

We found that the EVPA–λ^2 relations of our sources are usually non-linear, instead showing breaks in their slopes. We obtained the RMs for pairs of adjacent frequencies and discovered that the core RMs systematically increase with observing frequency. Based on VLBA observations at 8 different frequencies from 4.6 to 43 GHz, O'Sullivan & Gabuzda (2009a) showed that breaks in RM appear frequently, with the best-fit lines in the EVPA–λ^2 diagram connecting smoothly over a wide range of frequencies (though not for BL Lac in their sample). In contrast, Kravchenko et al. (2017) presented large discontinuities between the different EVPA–λ^2 fits at much lower frequencies (between 2 and 5 GHz). Therefore, one might expect that potential discontinuities in EVPA rotations might not be substantial at mm wavelengths and the assumption underlying our analysis – no RM discontinuities – might be justified.

Furthermore, these studies showed that core EVPA rotations could be fitted well by a λ^2 law in some frequency ranges, then breaks, and then shows another good λ^2 fit in other frequency ranges (e.g., O'Sullivan & Gabuzda 2009a; Kravchenko et al. 2017). Other studies obtained good λ^2 fits for the core EVPA rotations in most cases when they used relatively small frequency intervals, e.g., 8–15 GHz (e.g., Zavala & Taylor 2004; Hovatta et al. 2012). This indicates that polarized emission from a single emission region is dominant over relatively small frequency intervals, without showing a systematic increase of RMs as a function of frequency. However, over a wide range of frequencies, the RM–frequency relations appear to show multiple breaks; this implies

that $|\mathrm{RM}| \propto \nu^{\mathrm{a}}$ predicted by Jorstad et al. (2007) assuming a continuous core-shift effect might not hold for narrow frequency intervals. One possible explanation is that blazar cores actually consist of multiple recollimation shocks and we observe polarized emission from one of the shocks in a given narrow frequency interval. As one goes to higher frequencies, polarized emission from inner shocks close to the jet base becomes more dominant due to lower opacity, leading to another good λ^2 fit with higher RMs.

4.5 Conclusions

We studied polarization properties of 8 blazars – 5 FSRQs and 3 BLOs with multi-frequency simultaneous observations with the KVN at 22, 43, and 86 GHz. We investigated the nature of blazar radio cores by means of measuring Faraday rotation measures at different observing frequencies. Our work leads us to the following principal conclusions:

1. We found that RMs increase with frequency, with median values of 2.62×10^3 rad/m^2 and 1.42×10^4 rad/m^2 for the frequency pairs 22/43 GHz and 43/86 GHz, respectively. These values are also higher than those obtained by Hovatta et al. (2012) at 8.1–15.4 GHz for the same sources. The median values are described well by a power-law function with $|\mathrm{RM}| \propto \nu^{\mathrm{a}}$ with $a = 2.42$. When a values are obtained separately for each source, they are distributed around $a = 2$ with mean and standard deviation of $a = 2.25 \pm 1.28$. This agrees with the expectation from core-shift (Jorstad et al. 2007) for many blazars at the KVN frequencies. This finding implies that the geometry of Faraday rotating media in blazar cores can be approximated as conical.

2. We compared our KVN data with contemporaneous (within $\approx$ 1 week) optical polarization data from the Steward Observatory for a few sources. When we assume that the direction of EVPA rotation at radio frequencies is the same at optical wavelengths and that there is no $n\pi$ ambiguity, the optical data show a trend of EVPA rotation similar to that of the radio data. The RM values

obtained with the optical data indicate that the power-law increase of RM with frequency continues up to a certain frequency, $\nu_{\rm trans}$, and then saturates, with $|{\rm RM}| \approx 10^{5-6}$ rad/m^2 at ≈ 250 GHz, depending on source and flaring activity. We suggest that this saturation is due to the absence of core shift above $\nu_{\rm trans}$; instead, radio cores are standing recollimation shocks. This is in agreement with other studies which concluded that the radio cores of blazars cannot purely be explained as the unity optical depth surface of a continuous conical jet but are physical structures at least in some cases.

3. We detected a sign change in the observed RMs of CTA 102 over ≈ 1 month, while the magnitudes of RM were roughly preserved. Since this source showed strong flaring at the time of our observations, we suggest that new relativistic jet components emerging from the core undergo acceleration/deceleration and/or jet bending, thus leading to a change in the direction of the line-of-sight component of helical magnetic fields in the jet because of relativistic abberation.

4. We found indication that the absolute values of the core RMs of FSRQs are larger than those of BLOs at 22–86 GHz, which is consistent with results found at cm wavelengths. This difference might arise from FSRQs having higher accretion rates than BLOs, resulting in larger amounts of material in the central engine.

5. For those sources which show non-linear EVPAs–λ^2 relations, the RM-corrected (intrinsic) EVPAs might be different at different frequencies and thus at different locations of the jets. A recent ultra-high resolution image of BL Lac observed with space VLBI shows that its intrinsic EVPAs in the core region vary with different locations indeed.

6. We suggest that the systematic increase of RM as function of observing frequency appears only when covering sufficiently large ranges in frequency, with different λ^2 laws at different frequency ranges connecting smoothly. Combining this with the fact that linear EVPA–λ^2 relations are commonly observed over narrow frequency ranges suggests that blazars cores might consist of multiple recollimation shocks

such that polarized emission from one of the shocks is dominant in a given narrow frequency range.

Chapter 5

Ejection of Double knots from the radio core of PKS 1510–089 during the strong γ-ray flares in 2015[†]

Abstract

PKS 1510–089 is a bright and active γ-ray source that showed strong and complex γ-ray flares in mid-2015 during which the Major Atmospheric Gamma Imaging Cherenkov telescopes detected variable very high energy (VHE; photon energies >100 GeV) emission. We present long-term multi-frequency radio, optical, and γ-ray light curves of PKS 1510–089 from 2013 to 2018, and results of an analysis of the jet kinematics and linear polarization using 43 GHz Very Long Baseline Array data observed between late 2015 and mid-2017. We find that a strong radio flare trails the γ-ray flares in 2015, showing an optically thick spectrum at the beginning and becoming optically thin over time. Two laterally separated knots of emission are observed to emerge from the radio

[†]The contents of this chapter was originally published in the Astrophysical Journal (Park et al. 2019b)

core nearly simultaneously during the γ-ray flares. We detect an edge-brightened linear polarization near the core in the active jet state in 2016, similar to the quiescent jet state in 2008–2013. These observations indicate that the γ-ray flares may originate from compression of the knots by a standing shock in the core and the jet might consist of multiple complex layers showing time-dependent behavior, rather than of a simple structure of a fast jet spine and a slow jet sheath.

5.1 Introduction

The Large Area Telescope (LAT) on board the *Fermi* satellite (Atwood et al. 2009) has revealed that blazars, active galactic nuclei (AGNs) having highly collimated and relativistic jets closely aligned with our line of sight (Urry & Padovani 1995; Blandford et al. 2018), make up the largest fraction of observed γ-ray sources (e.g., Acero et al. 2015; Ackermann et al. 2015). It is commonly assumed that inverse Compton (IC) scattering of soft photons off relativistic electrons in the jets is responsible for the γ-ray emission[1]. However, both the location of the γ-ray emission sites in AGN jets and the origin of the seed photons, which are upscattered in energy by the IC process, are still a matter of debate. The seed photons could be synchrotron photons from the same electrons that up-scatter the photons (synchrotron self-Compton, SSC; e.g., Maraschi et al. 1992) or photons from sources outside the jets (external Compton, EC) such as the accretion disk (e.g., Dermer et al. 1992), the broad line region (BLR, e.g., Sikora et al. 1994), and the dusty torus (DT, e.g., Błażejowski et al. 2000), or photons from the cosmic microwave background (e.g., Tavecchio et al. 2000).

Blazars can be divided into two classes based on their optical properties: flat spectrum radio quasars (FSRQs) and BL Lac objects (BL Lacs). This classification was initially phenomenological and based on the equivalent widths of emission lines being larger (FSRQs) or smaller (BL Lacs) than 5 Å (Urry & Padovani 1995). Eventually,

[1]In addition to this leptonic model, there are also hadronic models for γ-ray emission in blazars (e.g., Mannheim 1993, see also Boettcher et al. 2012 and Böttcher et al. 2013 for review of the leptonic and hadronic models).

it turned out that the different classes originated from different accretion regimes of AGNs, with FSRQs and BL Lacs having high and low accretion rates, respectively (Ghisellini et al. 2011; Heckman & Best 2014; Yuan & Narayan 2014). Their spectral energy distributions (SEDs) are distinct from each other. Compared to BL Lacs, FSRQ SEDs tend to show (i) higher luminosity, (ii) synchrotron and IC bumps peaking at lower observing frequencies, and (iii) a larger IC bump in comparison to the synchrotron one (Fossati et al. 1998; Ghisellini et al. 1998, 2017). This behavior in FSRQs has been interpreted due to the efficient cooling of the relativistic electrons from the jets. The reason why the electrons cool so efficiently in FSRQs is thought to be because of the large amount of soft photons originating in the BLR. Since the BLR is thought to be within 10^3–10^4 $r_{\rm s}$ of the central engine (where $r_{\rm s}$ is the Schwarzschild radius), this is referred to as the "near-dissipation zone" scenario (e.g., Ghisellini et al. 1998; Hartman et al. 2001; Ghisellini et al. 2010).

However, many observations disfavor this scenario. For example, a significant fraction of γ-ray flares in blazars occur when superluminal knots in the jets pass through the radio core. The core is a (quasi-)stationary compact emission feature located at the upstream end of the jet (e.g., Jorstad et al. 2001; Jorstad & Marscher 2016) resolved by very long baseline interferometry (VLBI). The core is often identified with a recollimation shock which may form when there is a pressure mismatch between the jet and the confining medium (e.g., Sanders 1983; Wilson & Falle 1985; Daly & Marscher 1988; Gómez et al. 1995; Komissarov & Falle 1997; Agudo et al. 2001; Cawthorne et al. 2013; Mizuno et al. 2015; Fromm et al. 2016; Fuentes et al. 2018; Park et al. 2018) and is usually expected to be located quite far from the jet base, i.e., at distances $\gtrsim 1$ pc in the source frame (e.g., O'Sullivan & Gabuzda 2009b; Pushkarev et al. 2012). This distance is larger than 10^4 $r_{\rm s}$ for most blazars and supports the "far-dissipation zone" scenario for the γ-ray flares. Likewise, the detection of very high energy (VHE, where VHE is defined as photon energies >100 GeV and high energy, HE, as >100 MeV) emission in several FSRQs (e.g., Aleksić et al. 2011a,b, 2014) is challenging to explain with the near-dissipation zone scenario because it is difficult for the VHE photons to

escape the intense radiation field of the BLR (e.g., Liu & Bai 2006; Tavecchio & Mazin 2009; Barnacka et al. 2014). On the other hand, it has been pointed out that the external seed photon field at the VLBI core would be too weak to produce the observed γ-ray emission (e.g., Marscher et al. 2010; Aleksić et al. 2014).

PKS 1510–089 is one of the brightest and most active blazars observed by *Fermi*-LAT (e.g., Abdo et al. 2010) and has been detected at VHE bands (H.E.S.S. Collaboration 2013; Aleksić et al. 2014; Ahnen et al. 2017; MAGIC Collaboration et al. 2018; Zacharias et al. 2019). Marscher et al. (2010) detected a systematic rotation of the optical electric vector position angle (EVPA), followed by strong optical and γ-ray flaring that was also coincident with an ejection of a new superluminal knot from the core in 2009. They concluded that the γ-ray flares occurred in the superluminal knot as it passed through the core (Marscher et al. 2008). The origin of the seed photons was discussed in the context of a spine-sheath jet structure, where a relatively slow jet sheath surrounds a fast jet spine (see, e.g., Fig. 1 of Ghisellini et al. 2005, see also Sol et al. 1989; Laing 1996). In contrast, based on (a) the absence of a correlation between X-ray and γ-ray fluxes in 2008 and 2009 and (b) a comparison of observed γ-ray-to-optical flux ratios to simulated ones, Abdo et al. (2010) concluded that the γ-ray emission is dominated by the EC process with the seed photons originating in the BLR. Dotson et al. (2015) suggested that some of the γ-ray flares in 2009 occurred at the distance of the DT, while others occurred in the vicinity of the radio core, by investigating the energy dependence of the flare decay time to infer the source of the seed photons.

Orienti et al. (2013) found a γ-ray flare from PKS 1510-089 in late 2011 after the onset of a strong radio flare and located the γ-ray emitting site to be about 10 pc downstream of the jet base. On the other hand, Saito et al. (2015) suggested that the γ-ray flares in 2011 occurred at the distance of 0.3–3 pc from the central engine with the seed photons provided by the BLR and DT, based on the model of internal shocks formed by colliding blobs of the jet plasma. Aleksić et al. (2014) showed the HE and VHE γ-ray spectra in 2012 smoothly connected with each other. The γ-ray light curves were correlated with the millimeter-wave light curves, and a superluminal knot emerged

from the core near in time with the γ-ray flares. They showed that the observed SEDs could be explained well by two scenarios, (i) EC in the jet about 1 pc downstream of the central engine with seed photons from the DT and (ii) EC in the core at ≈ 6.5 pc downstream of the central engine with the seed photons being provided by the sheath. A recent study, using the Very Long Baseline Array (VLBA) at 43 GHz when the jet was in a quiescent state, revealed that the degree of linear polarization near the core increases toward the edges of the jet with the EVPAs predominantly perpendicular to the jet direction (MacDonald et al. 2015; see also MacDonald et al. 2017 for the case of other blazars). This result indicates that there may be a relatively slow sheath of jet plasma surrounding the fast jet spine, as predicted in previous studies of γ-ray flares in this source (e.g., Marscher et al. 2010; Aleksić et al. 2014). The sheath could be an important source of seed photons in the far-dissipation zone scenario, and also can provide seed photons for "orphan" γ-ray flares that show little or no corresponding variability detected at longer wavelengths (MacDonald et al. 2015).

In 2015, PKS 1510–089 showed variable VHE emission on time scales of a few days during its long, elevated HE γ-ray state (Ahnen et al. 2017). This event was accompanied by a systematic optical EVPA rotation and the ejection of a knot from the core which was observed with the VLBA at 43 GHz, similar to the flares in 2009 (Marscher et al. 2010) and 2012 (Aleksić et al. 2014). However, the knot (named K15) moved away from the core at a position angle (PA) radically different (by $\sim 90^\circ$) from the historic jet direction (Jorstad et al. 2017). K15 was detected for five successive epochs from 2015 December to 2016 April and is unlikely to be an imaging artifact. Ahnen et al. (2017) could not determine if the ejection of this component is indeed related to the VHE or γ-ray emission in 2015 because of uncertainties in the kinematic analysis.

The primary goal of this paper is to investigate the unusual kinematics and linear polarization structure of the jet in 2016 and 2017 and to probe a potential connection of the jet activity to the HE and VHE flares in 2015. Therefore, we extend the observational timeline of the kinematic analysis by Ahnen et al. (2017) by one year

and four months. We refer the reader to other studies for detailed modeling of SEDs of our source with good spectral coverage in various periods (e.g., Abdo et al. 2010; D'Ammando et al. 2011; H.E.S.S. Collaboration 2013; Aleksić et al. 2014; Saito et al. 2015; Ahnen et al. 2017; MAGIC Collaboration et al. 2018).

This paper is organized as follows. We first present multi-wavelength light curves of PKS 1510–089 between 2013 and 2018 in Section 5.2. In Section 5.3, we focus on the peculiar behavior of the jet after the strong and complex multi-wavelength flare in 2015, by performing kinematic and linear polarization analysis. We discuss our results and draw our conclusions in Sections 7.4 and 5.5, respectively. In this paper, we adopt the following cosmological parameters: $H_0 = 70$ km s^{-1} Mpc^{-1}, $\Omega_{\rm m} = 0.3$, and $\Omega_\Lambda = 0.7$, giving a projected scale of 5.0 pc mas^{-1} for PKS 1510-089 at a redshift of 0.36 (Thompson et al. 1990).

5.2 Multi-wavelength Light Curves

In this section, we present the long-term light curves of PKS 1510-089 at radio, optical, and γ-ray wavelengths, which is shown in Figure 5.1. We did not include X-ray light curves in our analysis because of relatively large time gaps in the *Swift*-XRT light curve during the period of our interest; we refer the reader to MAGIC Collaboration et al. (2018) for the long-term activity of our source at X-ray.

5.2.1 iMOGABA

The iMOGABA program observes about 30 γ-ray bright blazars with the Korean VLBI Network (KVN; Lee et al. 2011, 2014) at 22, 43, 86, and 129 GHz simultaneously (see Lee et al. 2016 for details of the program). PKS 1510–089 has been observed almost every month since 2012 December. A standard data post-correlation process with the NRAO Astronomical Image Processing System (AIPS, Greisen 2003) was performed by using the automatic pipeline for KVN data (Hodgson et al. 2016). We achieved high fringe detection rates and reliable imaging at up to 86 GHz by using the frequency phase transfer (FPT) technique (Middelberg et al. 2005; Rioja et al. 2011, 2014; Algaba

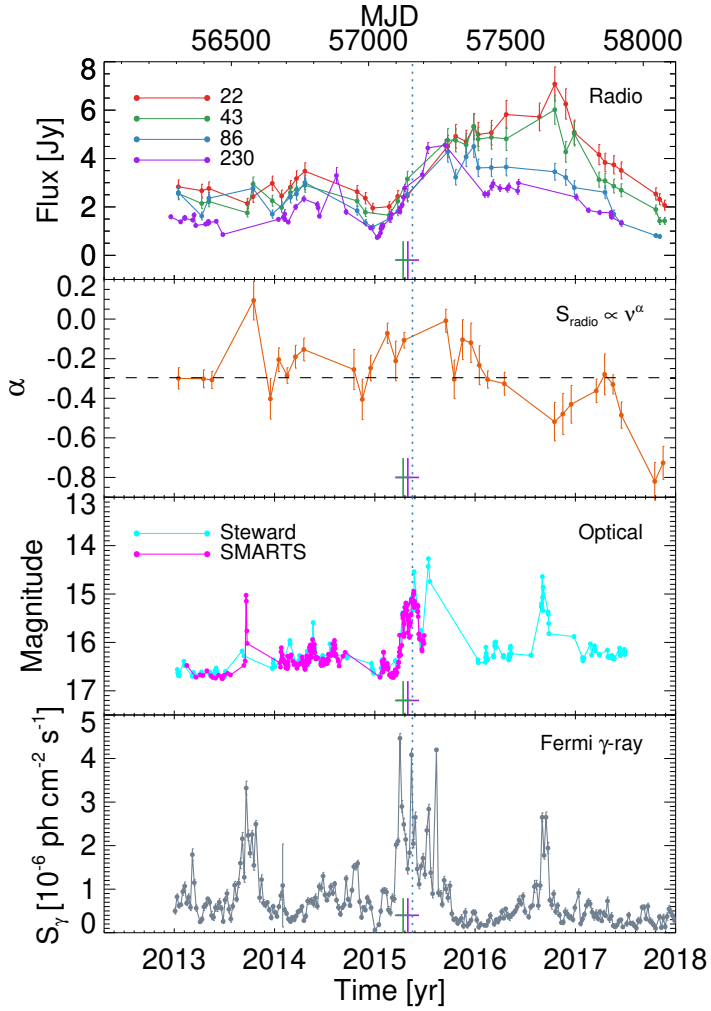

Figure 5.1. *Top panel:* Light curves of PKS 1510–089 from 2013 to 2018 at radio frequencies (22, 43, 86 GHz from the iMOGABA program, 230 GHz from the SMA). *Second panel from top:* Spectral index obtained by fitting a simple power-law function to the radio spectra available for each time bin (see Section 5.2.3). *Third panel from top:* Light curves at optical wavelengths (cyan: Steward observatory; magenta: SMARTS program). *Bottom panel:* γ-ray light curve from *Fermi*-LAT data. The crosses at the bottom show the epochs of zero separation of the knots K15 and J15 (vertical lines) with their 1σ errors (horizontal lines, see Section 5.3 and Figure 5.4 for details). The blue vertical dotted line marks the time of VHE emission in mid-2015 (Ahnen et al. 2017).

et al. 2015; Zhao et al. 2018) which overcomes the rapid tropospheric phase variations characteristic for high frequencies. Nevertheless, the data at 129 GHz usually suffer from severe observing conditions such as relatively large sky opacity and low aperture efficiencies, which makes the detection rate lower than at other frequencies. Moreover, the 129 GHz results have larger uncertainties originating from inaccurate pointing and large gain errors (e.g., Kim et al. 2017). Thus, we excluded the 129 GHz data from our analysis. We used the Caltech *Difmap* package for imaging and phase self-calibration (Shepherd 1997). We performed a `modelfit` analysis in *Difmap* using circular Gaussian components. We note that we found a single component at the radio core in most epochs at all frequencies due to the compact source geometry and the relatively large beam size of the KVN. We generated radio light curves by using the flux density of the core component when a single component was detected and the total flux density when multiple components were detected (see the top panel of Figure 5.1).

5.2.2 SMA

The 230 GHz (1.3 mm) flux density data were obtained at the Submillimeter Array (SMA) near the summit of Mauna Kea (Hawaii). PKS 1510–089 is included in an ongoing monitoring program at the SMA to determine the fluxes of compact extragalactic radio sources that can be used as calibrators at mm wavelengths (Gurwell et al. 2007). Observations of available potential calibrators are from time to time observed for 3 to 5 minutes, and the measured source signal strength calibrated against known standards, typically solar system objects (Titan, Uranus, Neptune, or Callisto). Data from this program are updated regularly and are available at the SMA website[2] database (Gurwell et al. 2007). The light curve is shown in the top panel of Figure 5.1.

5.2.3 Radio Spectral Index

We obtained the radio spectral index as a function of time (the second panel from the top in Figure 5.1) by binning the light curves at 22, 43, 86, and 230 GHz into monthly

[2] `http://sma1.sma.hawaii.edu/callist/callist.html`

time intervals. We then fitted the radio spectra with a simple power-law function, i.e., $S_\nu \propto \nu^\alpha$, for bins where flux data are available in at least three different frequency bands. One has to take into account synchrotron self-absorption to obtain more reliable fits to the radio spectra as done in other studies (e.g., Fromm et al. 2011; Rani et al. 2013; Algaba et al. 2018). However, we used simple power-law fitting in this work because of the limited spectral coverage in many time bins and because we could not find any significant deviation of the data from power-law fits within errors. The simple power-law fitting would be enough to show the long-term evolution of the radio spectral index, which fits our purpose.

5.2.4 Optical Photometric Data

We collected publicly available optical photometric data from the Steward Observatory blazar monitoring program[3] measured in the 500-to-700 nm band (see Smith et al. 2009 for details) for the same period for which we obtained the *Fermi* γ-ray data. We also obtained optical V band data from 2013 to mid-2015 from the Small and Moderate Aperture Research Telescope System (SMARTS[4]) monitoring program of *Fermi* blazars (see Bonning et al. 2012 for details). The optical light curves from the two datasets are shown in the second panel from the bottom in Figure 5.1.

5.2.5 Fermi-LAT

We followed MAGIC Collaboration et al. (2018) for extracting the LAT γ-ray light curves. We used the *Fermi*-LAT data observed in survey mode.[5] We analyzed photons in the "source event" class using the standard ScienceTools (software version v11r5p3) and instrument response functions P8R2_SOURCE_V6 and the *gll_iem_v06.fits* and *iso_P8R2_SOURCE_V6_v06.txt* models for the Galactic and isotropic diffuse emission (Acero et al. 2016), respectively. We analyzed a region of interest (ROI) of 20° radius centered at the position of PKS 1510–089. A zenith angle cut of $< 90°$ was applied to

[3] `http://james.as.arizona.edu/~psmith/Fermi`

[4] `http://www.astro.yale.edu/smarts/glast`

[5] `https://fermi.gsfc.nasa.gov/cgi-bin/ssc/LAT/LATDataQuery.cgi`

reduce contamination from the Earth's limb. We first performed an unbinned likelihood analysis using gtlike (Acero et al. 2015) for the events recorded from 2013 February 1 to June 30 (MJD 56324–56474) in the energy range between 100 MeV and 300 GeV. The model parameters for the sources within 10° of the center of the ROI were left free, while the parameters for the sources from 10° to 20° were fixed to their 3FGL catalog values for this first unbinned likelihood analysis. MAGIC Collaboration et al. (2018) found no new strong sources within 20° of PKS 1510–089 in other time ranges; we conclude that the best-fit parameters obtained from the unbinned likelihood analysis for the five-month period we studied are representative for other periods of interest. For further analysis, we removed sources with a test statistic (TS; Mattox et al. 1996) less than 9, corresponding to $\approx 3\sigma$ detections. We then generated a light curve binned to one-week time intervals of PKS 1510–089 at $E > 100$ MeV by fixing the model parameters for all the sources using the output model in the first unbinned likelihood analysis, except for our target and the variable sources reported in the 3FGL catalog (Acero et al. 2015). We fitted a power law spectrum with both the flux normalization and the spectral index being free parameters for these sources. We note that the normalization of the Galactic and isotropic diffuse emission models were also left free. The γ-ray light curve is shown in the bottom panel of Figure 5.1.

5.3 Jet kinematics and linear polarization analysis

We used the calibrated VLBA data observed over 21 epochs from 2015 December to 2017 September taken from the VLBA-BU-BLAZAR program[6] except for 2016 October 6 because two antennas were unable to observe at that time. The details of the observations and the data reduction are described in Jorstad et al. (2005, 2017). We performed a `modelfit` analysis of the visibility data in *Difmap* for each epoch using multiple circular Gaussian components. We present the `modelfit` components overlaid on the CLEAN images in Figure 5.2. We first identified the radio core as the compact and bright component located at the upstream end of the jet. We assumed that the

[6] `https://www.bu.edu/blazars/VLBAproject.html`

core is stationary and identified its location with the origin of each map; we then identified other components (shown in the same color in different epochs in Figure 5.2). A triple-component structure is consistently found in the first 11 epochs. The two jet components labeled K15 (following Ahnen et al. 2017) and J15, are moving away from the core. K15 fades out and is no longer detected after 2016.91, while J15 is continuously moving with an average PA (measured north through east with respect to the core) of $-37°$. Since 2017.21, J15 appears to have split into two components, labeled J15a and J15b.

Interestingly, both K15 and J15 are seen in the five epochs of the VLBA 43 GHz data from 2015.93 to 2016.31 presented in Ahnen et al. (2017) – however, they identified J15 as the core probably because the distance between the core and J15 is quite small, ≈ 0.1 mas, in these epochs. Casadio et al. (2017) presented a map obtained using the global millimeter VLBI array (GMVA) at 86 GHz in 2016 May and found a compact triple component structure within the central ~ 0.5 mas. Their results motivated us to fit models with three Gaussian components near the core to the data and we found that they provide us with better fits in terms of reduced χ^2 in all five epochs. Specifically, the reduced χ^2 is 0.5, 5.6, 0.7, 4.1, and 2.8 in the `modelfit` results we present here[7] and is 2.0, 26.6, 2.7, 9.7, and 20.9 when using two Gaussian components, respectively, in chronological order. To demonstrate how the three components improve the goodness of fit, we selected an epoch within a month of the GMVA observation and present the visibility amplitudes of the data as a function of uv-radius (black data points in Figure 5.3). We can see that the model with three Gaussian components (red) describe the observed data better than the model with two components (blue) at various uv-radius. In addition, K15 and J15 are also consistently seen in later epochs, making it highly unlikely that they are artifacts. While the PA of J15 ($\approx -37°$ on average) seems to be generally consistent with the global jet direction on the same spatial scale (PA of $\approx -34°$, Jorstad et al. 2017), the PA of K15 ($\approx +28°$ on average) is significantly

[7] We excluded the components outside the region around the core, e.g., at distances larger than 0.3 mas from the map center, to ensure a proper comparison.

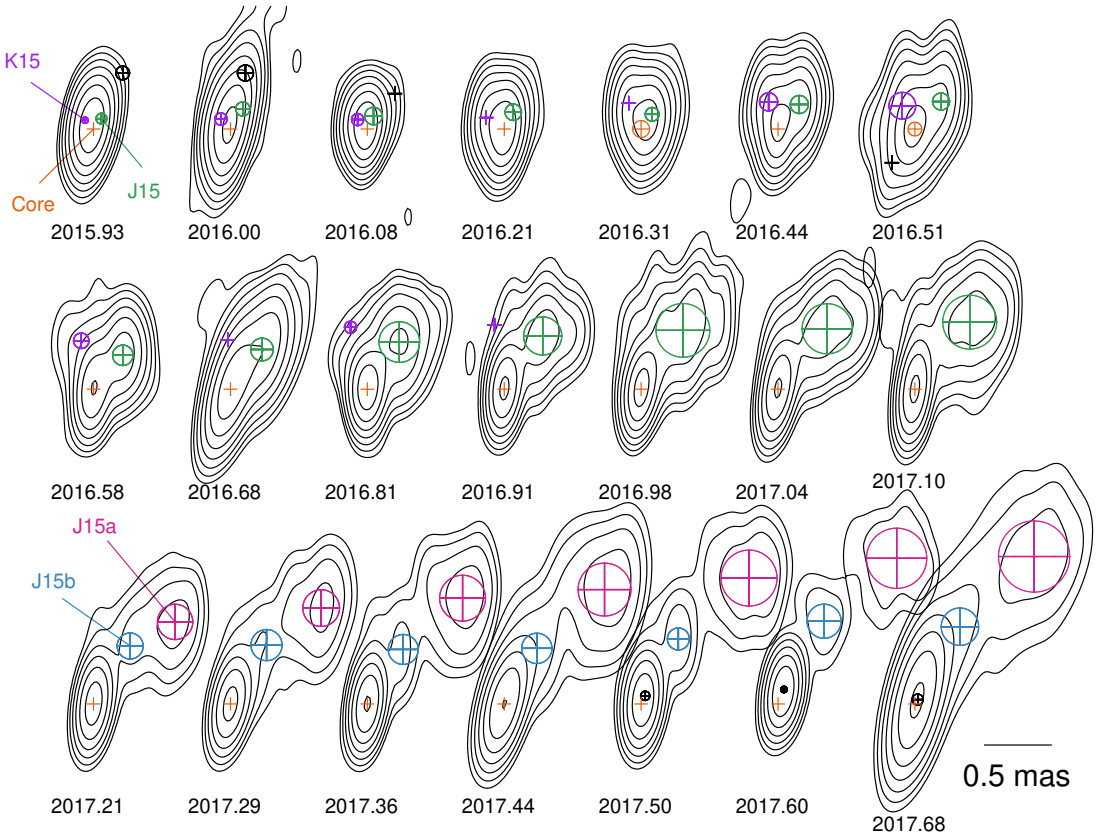

Figure 5.2. A series of CLEAN maps of PKS 1510–089 obtained by the VLBA 43 GHz data. Contours start from 25 mJy/beam and increase by factors of two. Circular Gaussian `modelfit` components are shown as crosses surrounded by circles overlaid on the contours. Crosses without surrounding circles show components with sizes smaller than 0.04 mas, corresponding to $\approx 1/5$ of the synthesized beam size. Components of the same color in different epochs are identified as being the same object. Black components are not used for component identification. The epoch of observation of each map in decimal years is noted below the contours. The dark solid line in the bottom right corner illustrates the angular scale in the images.

different.

We present the flux density and the separation from the core as functions of time for different components in Figure 5.4. The light curves for each component show moderate

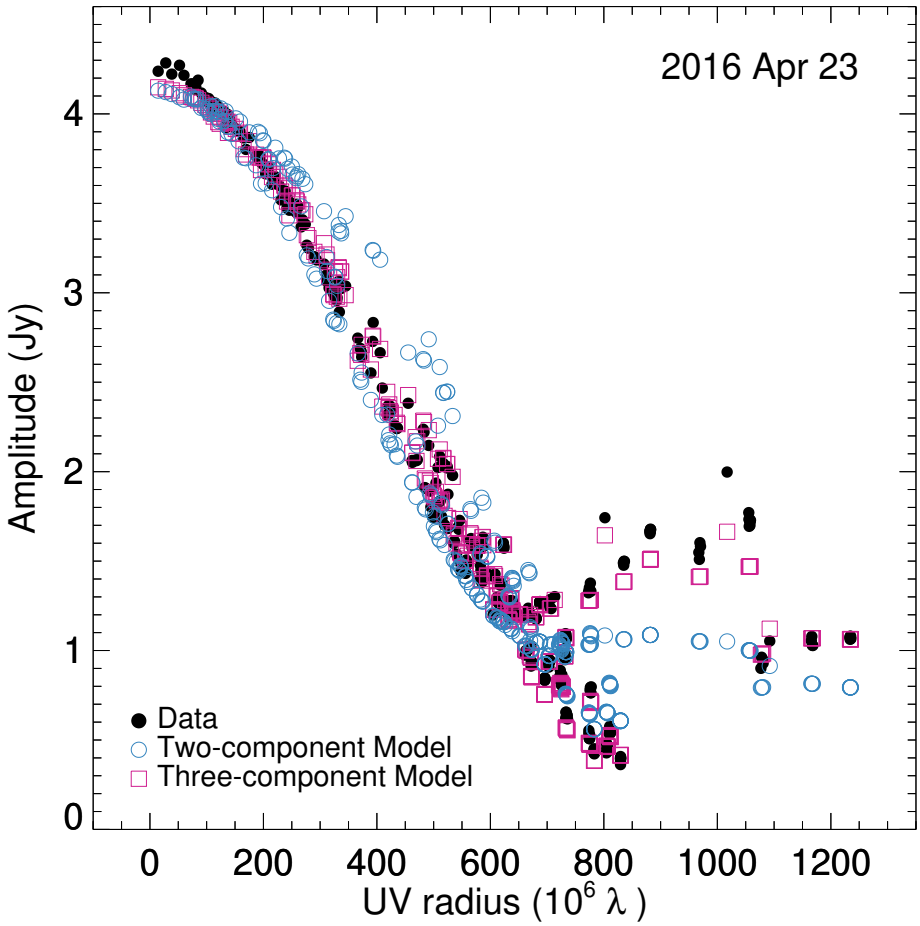

Figure 5.3. Visibility amplitude as a function of *uv*-distance. The VLBA 43 GHz data observed on 2016 Apr 23 are shown with the black data points, while the models fitted with two and three circular Gaussian components are shown with the blue and red data points, respectively. The model with three Gaussian components fits the data better than that with two Gaussian components (see Section 5.3 for details).

variability but are continuous across multiple epochs in general, suggesting that the identification of components with specific jet regions is reliable. As for the separation from the core, we fitted both linear functions (i.e., motions with constant velocities) and parabolic functions (i.e., accelerated motions) to K15 and J15 and found that the latter provides us with better fits in terms of reduced χ^2 (see Figure 5.4). The

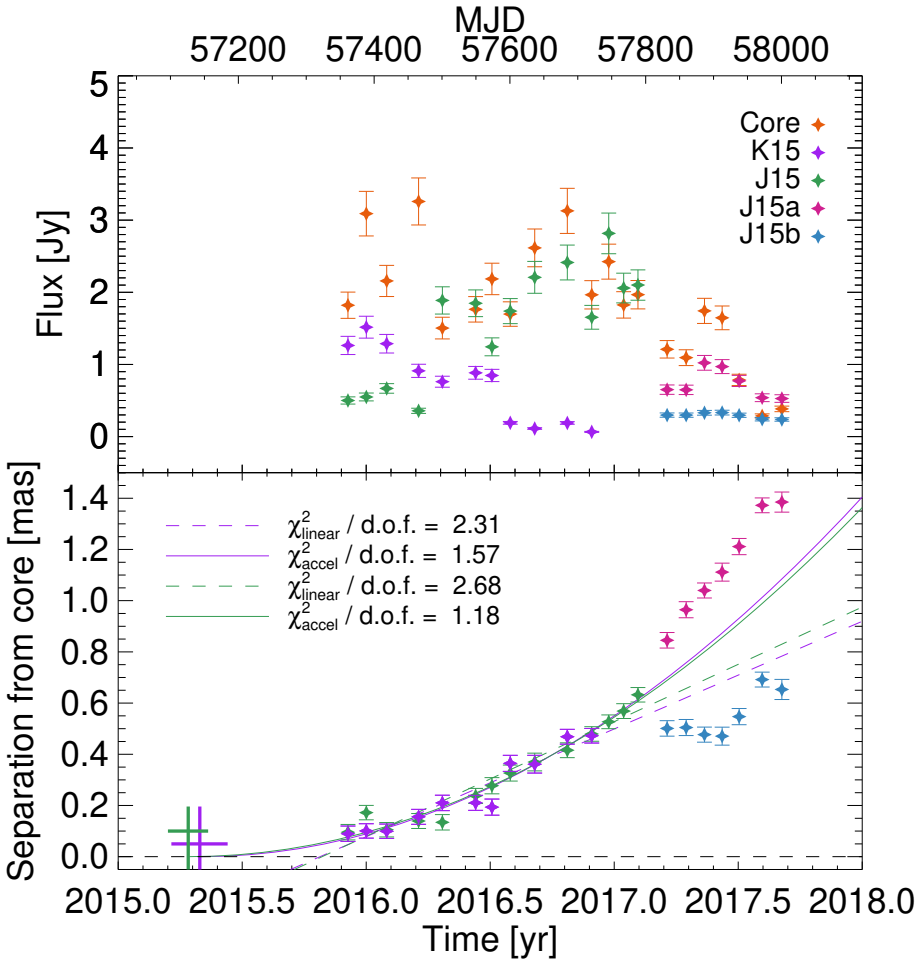

Figure 5.4. Flux density (top) and separation from core (bottom) as functions of time for all identified components (with the same color coding as in Figure 5.2). The solid curves and the dashed lines in the bottom panel (purple for K15 and green for J15) are the best-fit curves assuming acceleration and constant velocity, respectively. The reduced χ^2 ($\chi^2/d.o.f.$, where $d.o.f.$ denotes the degree of freedom) values are noted for each best-fit function. The crosses in the bottom left corner show the zero-separation epochs (vertical lines) with their 1σ errors (horizontal lines).

separation from the core for J15a, which might be the same knot as J15 but cannot be tested straightforwardly, is in a better agreement with the acceleration motion of J15 than with the linear motion. The zero-separation epochs, i.e., the time when the

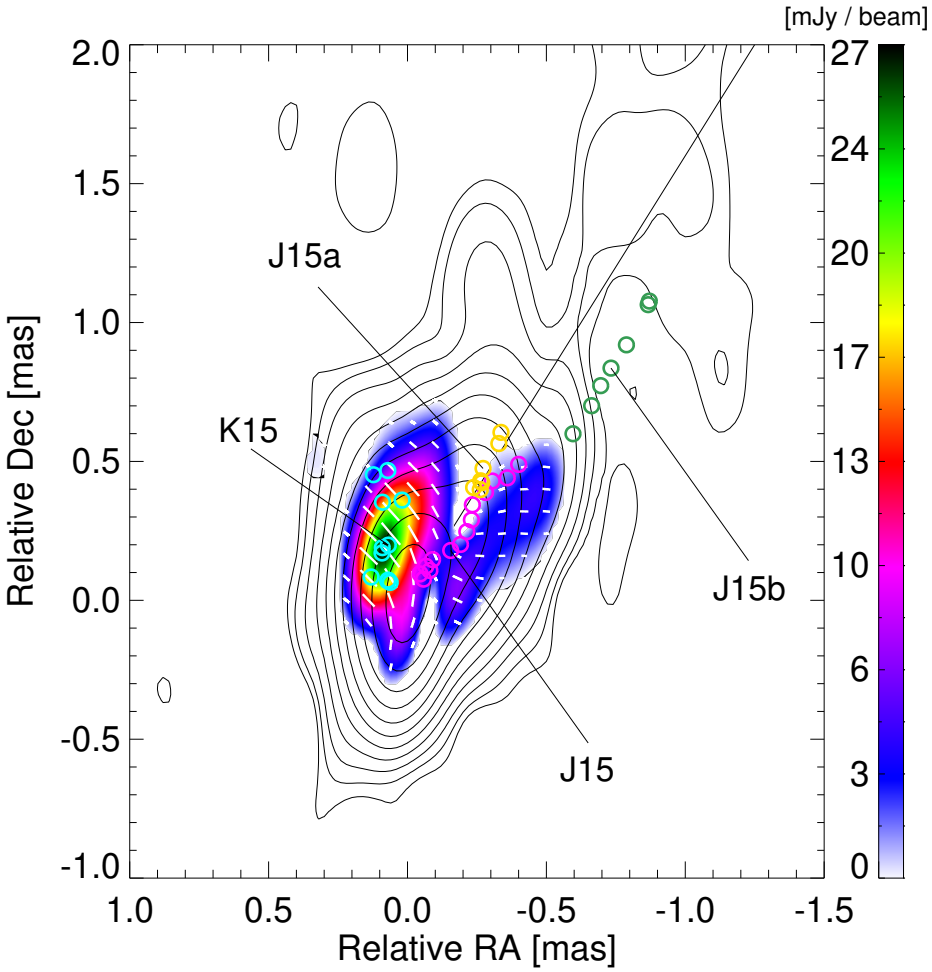

Figure 5.5. Stacked linear polarization map of the data observed in 11 epochs between 2015.93 and 2016.91 (see Section 5.3 for details). Color shows linear polarization intensity; contours show total intensity. A color scale is shown in the vertical bar on the right side. White ticks show EVPAs. We present the positions of identified components in different epochs with open circles in the map (cyan for K15, magenta for J15, yellow for J15a, and green for J15b). The black solid line indicates the global jet direction on mas scales, with a PA of $-34°$ (Jorstad et al. 2017).

components are expected to emerge from the core, are 2015.33 ± 0.11 and 2015.28 ± 0.08 for K15 and J15 (corresponding to MJD 57144 ± 42, 57127 ± 30), respectively. These estimates are slightly earlier than the ones by Ahnen et al. (2017), MJD 57230 ± 52, by

1–2σ, presumably because of different component identification and a smaller number of data points in their work.

We further checked if the two distinct emission regions can also be detected in linear polarization maps. Following MacDonald et al. (2015), we generated a stacked polarization image by (i) convolving maps for all Stokes parameters from different epochs with the same beam (average full width at half maximum with major axis, minor axis, and PA of 0.41 mas, 0.15 mas, $-6.62°$, respectively), (ii) aligning the maps such that the radio core is at the origin, and (iii) averaging the maps for each Stokes parameter. We used the epochs between 2015.93 and 2016.91, for which we could find both K15 and J15 in the total intensity maps. The results are presented in Figure 5.5. We note that we did not take into account Faraday rotation for our further analysis because the Faraday rotation measure was observed to be 165 rad/m^2 (corresponding to EVPA rotation by $\lesssim 1°$ with respect to the intrinsic EVPA at 43 GHz) at the 15 GHz core (Hovatta et al. 2012) and K15 and J15 are most likely located downstream of the 15 GHz core. We found that significant polarized emission is detected in the regions corresponding to K15 and J15. The eastern polarization component shows relatively strong and compact polarized emission with EVPAs almost perpendicular to the jet axis, while the western component shows polarized emission extended along the direction close to the global jet direction with EVPAs oblique to the jet axis.

5.4 Discussion

5.4.1 Comparison of the γ-ray flares in 2015 with previous flares

In 2015, PKS 1510–089 was in an active γ-ray state which lasted for more than six months (Figure 5.1, see also Ahnen et al. 2017; Prince et al. 2017; MAGIC Collaboration et al. 2018). Optical flares also occurred at about the same time as the γ-ray flares, while a strong radio flare lasting $\gtrsim 2$ years started in 2015. The 37-GHz radio light curve presented in a recent study indicates that the radio flare consists of two separate flares, one starting near MJD 57000 and the other near MJD 57600 (MAGIC Collaboration

et al. 2018). The latter seems to be related to the γ-ray and optical flares in mid-2016. Variable VHE emission was detected by the MAGIC telescopes on MJD 57160 and 57165. The VHE radiation seems to originate from the same region that emitted the HE γ-ray and optical flares (Ahnen et al. 2017). This is consistent with the time when K15 and J15 emerged from the core, which suggests that these components may be responsible for the multi-wavelength flares, including the VHE emission, in mid-2015.

The flares in 2015 are remarkably similar to the ones in 2009 (Marscher et al. 2010) in the sense that (i) the γ-ray flares are nearly simultaneous with the optical flares, (ii) a systematic rotation of EVPAs at optical wavelengths is detected (Ahnen et al. 2017), (iii) new jet components emerge from the core during the flares, and (iv) VHE emission is detected (H.E.S.S. Collaboration 2013). Therefore, a similar interpretation based on the far-dissipation zone scenario, compression of the knots by a standing conical shock in the core leading to strong γ-ray flares (Marscher et al. 2008, 2010; Marscher 2014), can be applied to the 2015 flares. Indeed, the radio light curves show optically thick spectra when the emerging knots are close to the core (with α in the range from -0.3 to 0 as seen in Figure 5.1), while they become optically thin after the knots are well separated from the core in later epochs (α from -0.8 to -0.3). This behavior is in good agreement with the prediction of the shock-in-jet model (e.g., Marscher & Gear 1985; Valtaoja et al. 1992; Fromm et al. 2011; Hughes et al. 2011), supporting the above interpretation. However, there is a remarkable difference in the behavior of the jet: we found two laterally separated moving knots emerging nearly simultaneously from the core, whereas a single knot was detected in 2009 (Marscher et al. 2010).

5.4.2 Double-knot Jet Structure

Blazars usually display a ridge-brightened, knotty jet structure[8] (e.g., Jorstad et al. 2005, 2017; Lister et al. 2013, 2016) and the double knot structure seen in PKS 1510–089 is uncommon. We found that the linear polarization structure near the core is

[8]We note, however, that some blazars show rapid changes in apparent jet position angles in projection on the sky plane, which might be related to radio flares and γ-ray flares in those sources (e.g., Agudo et al. 2012; Hodgson et al. 2017).

characterized as two distinct polarized regions (see Figure 5.5). Interestingly, this behavior was observed in the active state, when the two knots (K15 and J15) emerge from the core and propagate outwards during the period of 2015.93 – 2016.91, while a rather similar linear polarization structure was observed in the quiescent jet state in 2008 – 2013 also (MacDonald et al. 2015). We present the positions of identified `modelfit` components (see Section 5.3 and Figure 5.2) on top of the stacked polarization map. The compact polarized emission on the east side of the core is overlapped with the positions of K15, while the extended polarized emission on the west side of the core is distributed along with the trajectory of J15. Thus, the eastern and western polarized emission seems to be associated with the moving knots K15 and J15, respectively.

One of the possible origins of the double knot structure and the corresponding linear polarization structure is a large-scale helical magnetic field permeating in the jet (e.g., Lyutikov et al. 2005; Clausen-Brown et al. 2011; Murphy et al. 2013; Zamaninasab 2013). Evidence for helical magnetic fields in the jets of at least some blazars was provided by VLBI observations of Faraday rotation in the jets (e.g., Asada et al. 2002; Algaba 2013; Zamaninasab 2013; Gómez et al. 2016; Gabuzda et al. 2018). The helical field, depending on the jet viewing angle and the field pitch angle, can produce asymmetric profiles of both total intensity emission and linear polarization emission transverse to the jet. However, the transverse total intensity profile for blazars is expected to be more or less symmetric (see the case of $\theta_{\rm ob}\Gamma = 1/1.2$ or $1/2$ in Figure 2 in Clausen-Brown et al. 2011). PKS 1510–089 is a highly beamed blazar for which $\theta_{\rm ob}\Gamma = 0.47 - 1.23$ is expected ($\theta_{\rm ob} = 1.2 - 3.4^{\circ}$ and $\Gamma = 20.6 - 36.6$; Jorstad et al. 2005, 2017; Hovatta et al. 2009; Savolainen et al. 2010), and the observed complicated evolution of the total intensity profile, characterized by gradually decreasing and increasing flux densities of K15 and J15 over time, respectively (Figure 5.4), would be difficult to explain with the helical field scenario.

Another possible explanation is a spine-sheath structure in the jet, with a relatively slow sheath of jet plasma surrounding the fast jet spine. Such a structure is suggested by the *limb brightening* of the jets observed in several sources (e.g., Giroletti et al. 2004;

Nagai et al. 2014; Hada 2017; Giovannini et al. 2018) and was also introduced in theoretical modeling to explain the discrepancy between high Doppler factors[9] necessary to explain the TeV-detected BL Lacs and FR I (Fanaroff & Riley 1974) radio galaxies and the rather slow jet motions observed in those sources (see e.g., Ghisellini et al. 2005, see also Tavecchio & Ghisellini 2008, 2014). One of the observational signatures of a spine-sheath structure is an orientation of EVPAs perpendicular to the jet axis in the sheath (e.g., Attridge et al. 1999; Pushkarev et al. 2005). The sheath is thought to be generated by shear between the relativistic jet plasma and the ambient medium. At the boundary, the plasma jet and the embedded helical or tangled magnetic field are stretched along the direction of propagation of the jet due to the velocity gradients between the two layers (Wardle et al. 1994). This leads to an increase in the fractional polarization towards the jet edges, with the magnetic field being predominantly parallel to the jet direction, and thus EVPAs being perpendicular to the jet direction for an optically thin jet (Pacholczyk 1970). Remarkably, MacDonald et al. (2015) suggested that the edge-brightened linear polarization structure near the core observed in the quiescent jet state in 2008 – 2013 is consistent with the presence of a jet sheath, which can be an important source of seed photons for the orphan γ-ray flare observed in this source in 2009.

At a first glance, the observed features of K15, i.e., (i) a significant offset of PA from the global jet direction, and (ii) significant polarized emission with EVPAs perpendicular to the jet direction, are reminiscent of the sheath[10] on the east side of the core detected in the quiescent jet state (MacDonald et al. 2015). On the other hand, those of J15, i.e., (i) a trajectory in agreement with the global jet direction, and (ii) the extended polarized emission region along its trajectory with EVPAs oblique to the jet axis, are

[9] $\delta = 1/\Gamma(1 - \beta\cos\theta_{\rm ob})$ with Γ, β, and $\theta_{\rm ob}$ being the jet bulk Lorentz factor, intrinsic velocity, and the viewing angle, respectively

[10] In this scenario, a possible reason for the sheath appearing on only one side of the jet (K15) is that the interaction of the jet with the ambient medium is strongest on this side. The trajectory of J15 (Figure 5.5) follows the jet axis in the first five epochs but then shows a slightly curved trajectory towards the opposite side to K15, supporting this conjecture (see Attridge et al. 1999 for a similar case observed in 1055+018).

in agreement with a jet spine which is possibly a propagating shock (e.g., Hughes 2005; Jorstad et al. 2007). However, our kinematic results suggest that both knots are moving at similar apparent speeds (Figure 5.4), which is not consistent with the scenario that K15 and J15 are a slow jet sheath and a fast jet spine, respectively. This indicates that a simple spine-sheath scenario may not be able to explain the observed kinematics of these knots.

5.4.3 Acceleration motions and Spine-sheath Scenario

The apparent motions of K15 and J15 gradually accelerate from $\approx 5c$ to $\approx 13c$, with c being the speed of light (corresponding to Γ from ≈ 11 to ≈ 19 for $\theta_{\rm ob} = 1.2^\circ$ and from ≈ 7 to ≈ 13 for $\theta_{\rm ob} = 3.4^\circ$ for the fixed viewing angles), and possibly up to $\approx 28c$ for J15 if it can be identified with J15a in later epochs. The observed acceleration of apparent speeds of these knots could be due to a change of the viewing angles, or the bulk Lorentz factors, or both. On the one hand, the acceleration is observed within the physical, de-projected distance (from the core) of ≈ 75 pc, corresponding to $\lesssim 3{\times}10^6\ r_{\rm s}$, when using a jet viewing angle of 2.3°, an average of 1.2° (Jorstad et al. 2017) and 3.4° (Hovatta et al. 2009; Savolainen et al. 2010), and a black hole mass of $M_{\rm BH} \approx 2.5 \times 10^8\ M_\odot$ (Park & Trippe 2017). This is beyond the scale of a so-called an acceleration and collimation zone, where AGN jets are expected to be substantially collimated and accelerated to relativistic speeds through a magnetohydrodynamic process (e.g., Meier et al. 2001; Vlahakis & Königl 2004; Komissarov et al. 2007, 2009; Tchekhovskoy et al. 2008; Lyubarsky 2009). This process is believed to occur within the distances of $\lesssim 10^4 - 10^6\ r_{\rm s}$ from the jet base (e.g., Marscher et al. 2008), and has been observed for the nearby radio galaxies M87 and Cygnus A (Asada & Nakamura 2012; Asada et al. 2014; Boccardi et al. 2016; Mertens et al. 2016; Hada 2017; Walker et al. 2018). On the other hand, bulk jet acceleration of blazars within deprojected distances of ≈ 100 pc from the core was found to be common (e.g., Homan et al. 2015) and the exact scale of the acceleration and collimation zone of blazars is under debate (e.g., Hada et al. 2018). Thus, we could not exclude the possibility that the observed acceleration of K15

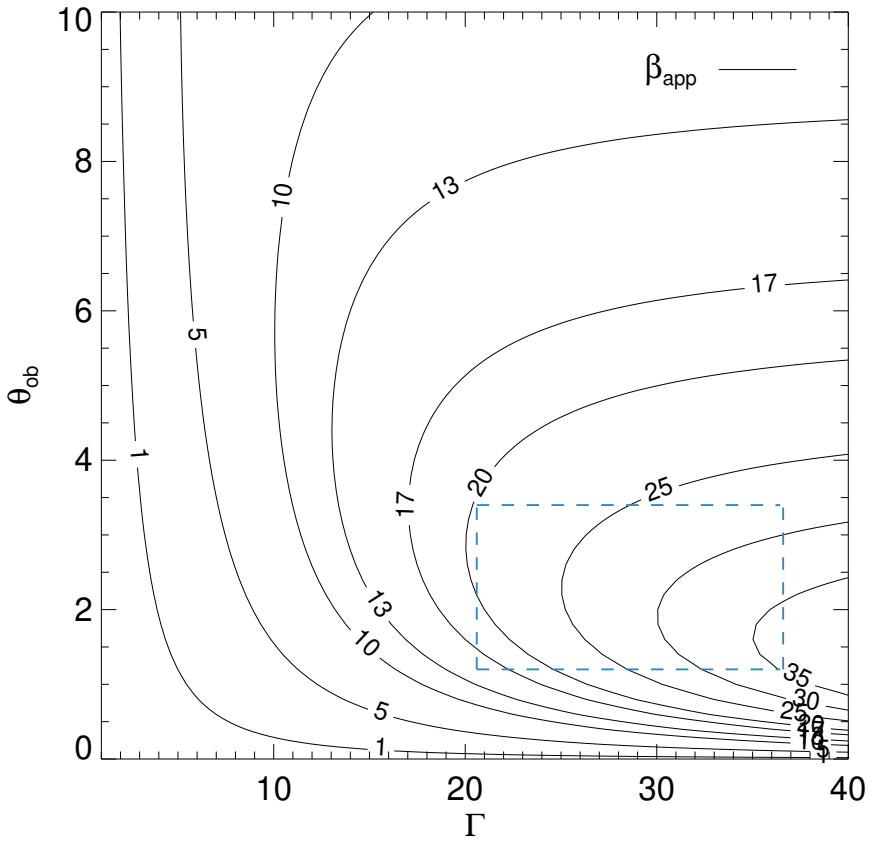

Figure 5.6. Contours show apparent speed in units of the speed of light on a $\Gamma - \theta_{\rm ob}$ plane with the value for each contour noted. The blue rectangle shows the expected range of Γ and $\theta_{\rm ob}$ based on previous studies (Jorstad et al. 2005, 2017; Hovatta et al. 2009; Savolainen et al. 2010).

and J15 is due to a change in the Lorentz factors.

Given that the PA and linear polarization properties of K15 and J15 could be consistent with a spine-sheath structure but their apparent motions are not necessarily consistent with this scenario (Section 5.4.2), we considered the possibility that J15 is *intrinsically* much faster than K15, i.e., $\Gamma_{\rm J15} \gg \Gamma_{\rm K15}$, but that both components show similar *apparent* motions due to different viewing angles. In Figure 5.6, we present a contour plot of apparent speed on a Γ–$\theta_{\rm ob}$ plane. Assuming that the acceleration of the apparent speeds of K15 and J15 is purely due to a gradual increase in the viewing angle,

$\Gamma_{\rm K15} \gtrsim 13$ is necessary. Even if we assume that the intrinsic speed of J15 is very fast with $\Gamma_{\rm J15} = 30$ based on previous studies (Jorstad et al. 2005, 2017; Hovatta et al. 2009; Savolainen et al. 2010; Lister et al. 2016), the ratio of $\Gamma_{\rm J15}$ to $\Gamma_{\rm K15}$ would be only a few, while the spine-sheath model usually assumes the ratio of $\Gamma_{\rm spine}$ to $\Gamma_{\rm sheath}$ to be ≈ 10 to explain the observed SEDs (e.g., Ghisellini et al. 2005; Aleksić et al. 2014; MacDonald et al. 2015). We note that the results of jet kinematics could also change if the absolute position of the core is changing during the radio flare (e.g., Lisakov et al. 2017; Hodgson et al. 2017), though we could not find any obvious systematic shifts in the positions of the downstream jet components. If a similar double knot structure is detected in the future, phase-referencing observations would help constrain the velocities of those knots more accurately (e.g., Niinuma et al. 2015).

We note that similar laterally extended jet emission, so-called off-axis jet emission, was observed in other γ-ray bright blazars such as 3C 279 (Lu et al. 2013) and Mrk 501 (Koyama et al. 2016). Koyama et al. (2016) proposed two possible explanations for the off-axis jet emission. It could be either (i) an internal shock formed on an axis different from the global jet axis, or (ii) a part of a dim and slow outer layer that is Doppler boosted at the time of observation. The latter scenario is in agreement with the spine-sheath scenario. We note that, in any case, the off-axis emission (corresponding to K15 in our case) must be significantly Doppler-boosted at the time of observations with a similar Doppler factor to that of the main jet, otherwise, we would not observe the off-axis emission unless its synchrotron emissivity was much higher than the main jet emission, which we consider unlikely. The jet has previously only shown knots along the global jet direction (e.g., Lister et al. 2016; Jorstad et al. 2017), yet has shown evidence for a layered structure from linear polarization observations (MacDonald et al. 2015). Taken as a whole, we conjecture a scenario that the jet emission from the off-axis layer, persistently existing in this source, would be visible only when it is significantly Doppler-boosted, which was realized after the strong optical and γ-ray flares in 2015 and during the strong radio flare in 2016 (Figure 5.1).

5.4.4 Origin of the 2015 γ-ray flare

Our jet kinematic results imply that the strong HE and VHE flares in 2015 could be related to the ejection of K15 and J15 from the core (Figures 5.1 and 5.4). As already noted in Section 5.4.1, the ejection of new knots coincident with γ-ray flares was observed many times during previous HE and VHE flares in this source, which led previous studies to conclude that the core might be a dominant emission site of those flares (e.g., Marscher et al. 2010; Orienti et al. 2013; Aleksić et al. 2014). The location of the core at 43 GHz, as derived from a core-shift analysis (Pushkarev et al. 2012), is 5.3 – 15.0 pc downstream of the jet apex, depending on the assumed jet viewing angle. This is too distant for the DT to provide the relativistic electrons in the core with enough seed photons (Marscher et al. 2010; Aleksić et al. 2014). Accordingly, additional seed photons from a slower sheath surrounding the jet spine, which may not be detected in usual cases due to small Doppler boosting, have been considered. This could explain (i) the highly variable γ-ray-to-optical flux ratio for different flares during the active γ-ray state in 2009 (Marscher et al. 2010), (ii) the SEDs, including the VHE emission, observed in 2012 (Aleksić et al. 2014), and (iii) the orphan γ-ray flare in 2009 (MacDonald et al. 2015).

However, our results show that the situation might be more complicated for the 2015 flares. In the spine-sheath model (Ghisellini et al. 2005), the EC intensity from the spine is amplified by a factor of $\delta_{\rm spine}^{3-\alpha}(\delta_{\rm spine}/\delta_{\rm sheath})^{1-\alpha}$, where $\delta_{\rm spine}$ and $\delta_{\rm sheath}$ are the Doppler factors of spine and sheath, respectively. The amplification factor for the synchrotron or SSC intensity from the spine is $\delta_{\rm spine}^{3-\alpha}$. The amplified sheath intensity is found analogously, i.e., by replacing $\delta_{\rm spine}$ by $\delta_{\rm sheath}$ and vice versa (see Ghisellini et al. 2005 and Tavecchio & Ghisellini 2008 for details). In Figure 5.7, we present the logarithmic amplification factors for synchrotron/SSC and EC emission in the spine and the sheath as functions of jet viewing angle with the assumed $\Gamma_{\rm spine} = 30$ and $\Gamma_{\rm sheath} = 13$ according to our consideration of K15 and J15 being a relatively slow jet sheath and a fast jet spine, respectively, in Section 5.4.3. We used the average spectral index of $\alpha = -0.3$ obtained in Section 5.2.3. The ratio of the amplification factors of EC

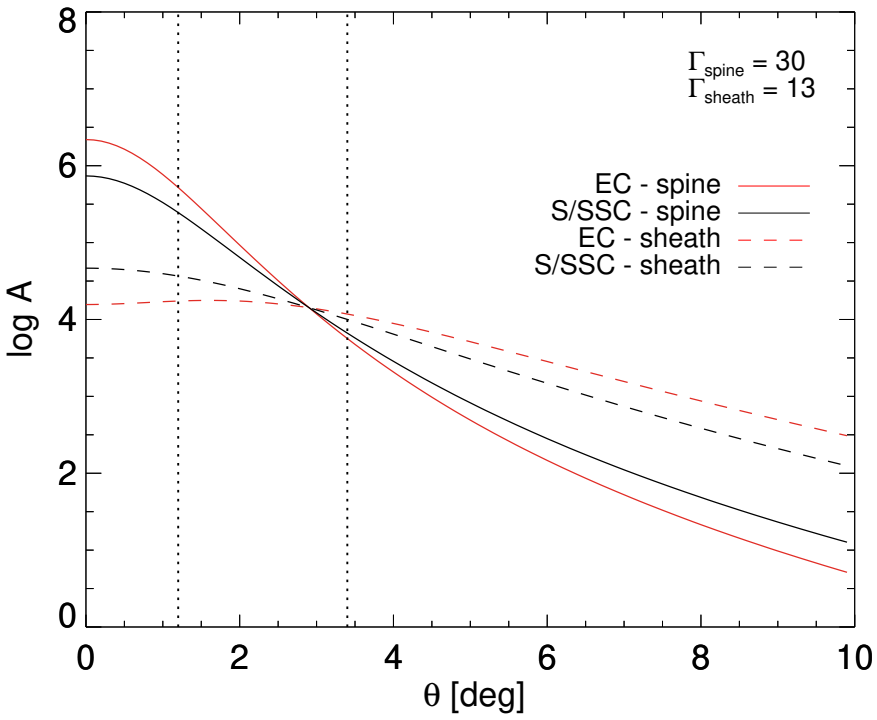

Figure 5.7. Logarithmic amplification factors for different emission components as functions of jet viewing angle in the spine-sheath model with $\Gamma_{\rm spine} = 30$ and $\Gamma_{\rm sheath} = 13$ (Ghisellini et al. 2005). The solid (dashed) lines are for the spine (sheath) emission and the red (black) lines are for EC (S/SSC) emission. (S/SSC refers to "synchrotron and SSC".) The vertical dotted lines denote the jet viewing angles estimated in the literature (Hovatta et al. 2009; Savolainen et al. 2010; Jorstad et al. 2017).

and synchrotron radiation of the spine is less than ≈ 2 for the expected viewing angle range for PKS 1510–089, while the observed peak luminosity of the IC component in 2015 is more than an order of magnitude larger than that of the synchrotron component (Ahnen et al. 2017).

Therefore, the ejection of double knots from the core near the time of the HE and VHE flares in 2015 supports the "far-dissipation zone" scenario with the core being a dominant emission site of γ-ray flares, while the observed motions of the knots make it difficult to reconcile with a spine-sheath jet structure needed for this scenario. One possible explanation is that the sheath itself may consist of multiple layers showing

time-dependent behavior. What we observed as off-axis jet emission could be a layer with relatively fast speed.

An alternative scenario as suggested by Ahnen et al. (2017) places the γ-ray emission region at ≈ 0.2 pc from the central engine. In this scenario, most of the seed photons for the external Compton processes would be provided by the DT. This one-zone model could successfully describe the observed SEDs including the VHE emission in 2015. However, the core-shift analysis of Pushkarev et al. (2012) placed the location of the 43 GHz core to be at ~ 10 pc from the jet base. If the assumptions in their core-shift study are correct, this would suggest that the kinematic association with the γ-ray flaring is coincidental. A possibility to reconcile these results could be that the assumptions underlying the core-shift analysis such as the equipartition between jet particles and magnetic field energy densities and a smooth radially expanding jet may not hold. Additionaly, the core-shift can be time-dependent (Niinuma et al. 2015), potentially explaining the discrepancy.

5.5 Conclusions

In 2015, PKS 1510–089 showed an active γ-ray state observed by *Fermi*-LAT with variable VHE emission detected by the MAGIC telescopes. We performed a jet kinematic analysis using VLBA 43 GHz data observed in 21 epochs between late 2015 and mid-2017. We found that two laterally separated knots in the jet nearly simultaneously emerge from the radio core during the period of γ-ray flaring and VHE emission in 2015. From the KVN and SMA monitoring data, we found that the onset of a strong multi-band radio flare begins near in time with the γ-ray flares, showing an optically thick spectrum at the beginning and gradually becoming optically thin as the knots become well separated from the core. Likewise, multiple complex optical flares and a systematic EVPA rotation occur along with the γ-ray flares (Ahnen et al. 2017). These observations suggest that the compression of moving knots by a standing conical shock in the core might be responsible for the HE and VHE flares. If the kinematic behavior is associated with the flaring, core-shift analysis indicates that the γ-ray emission region

is $\sim$ 10 pc downstream of the jet base, which would supports the "far-dissipation zone" scenario. We found that many of the observed properties of the double knots are consistent with a spine-sheath jet structure, which has been invoked to resolve the problem of the lack of seed photons for external Compton processes in the far-dissipation zone scenario. However, the observed speeds of the knots are difficult to explain with the fast jet spine and slow jet sheath model, indicating that the jet may consist of multiple, complex layers with different speeds which themselves could be time-dependent.

Chapter 6

Radio Variability and Random Walk Noise Properties of Four Blazars[†]

Abstract

We present the results of a time series analysis of the long-term radio lightcurves of four blazars: 3C 279, 3C 345, 3C 446, and BL Lacertae. We exploit the data base of the University of Michigan Radio Astronomy Observatory (UMRAO) monitoring program which provides densely sampled lightcurves spanning 32 years in time in three frequency bands located at 4.8, 8, and 14.5 GHz. Our sources show mostly flat or inverted (spectral indices $-0.5 \lesssim \alpha \lesssim 0$) spectra, in agreement with optically thick emission. All lightcurves show strong variability on all time scales. Analyzing the time lags between the lightcurves from different frequency bands, we find that we can distinguish high-peaking flares and low-peaking flares in accord with the classification of Valtaoja et al. The periodograms (temporal power spectra) of the observed lightcurves are consistent with random-walk powerlaw noise without any indication of (quasi-)periodic variabil-

[†]The contents of this chapter was originally published in the Astrophysical Journal (Park & Trippe 2014)

ity. The fact that all four sources studied are in agreement with being random-walk noise emitters at radio wavelengths suggests that such behavior is a general property of blazars.

6.1 Introduction

The strong and complex temporal flux variability of Active Galactic Nuclei (AGN; see, e.g., Beckmann & Shrader 2012 and references therein for a recent review) provides valuable information on the internal conditions of accretion zones and plasma outflows. Various characteristic variability patterns have been associated with a wide range of physical phenomena, from shocks in continuous (e.g.,) or discontinuous (e.g., Spada et al. 2001) jets to orbiting plasma "hotspots" (e.g., Abramowicz et al. 1991) or plasma density waves (e.g., Kato 2000) in accretion disks. Accordingly, multiple studies have aimed at quantifying the properties of AGN variability on all time scales and throughout the electromagnetic spectrum. At radio wavelengths, variability time scales probed by observations range from tens of minutes (Schödel et al. 2007, studying the mm/radio lightcurve of M 81*; see also Kim & Trippe 2013 for a discussion of the detectability of intra-day variability) to tens of years (Hovatta et al. 2007, in a statistical analysis of the long-term flux variability of 80 AGN). Of particular interest is the possible presence of quasi-periodic oscillations (QPO) which has been reported by several studies of blazar lightcurves (e.g. Rani et al. 2009, 2010; Gupta et al. 2012).

Fourier transform, period folding, power spectrum, and periodogram methods (cf. Priestley 1981 for an exhaustive review of time series analysis) have been used extensively for quantifying the statistical properties of AGN variability and for the search for possible QPOs (e.g. Benlloch et al. 2001 for X-ray, Webb et al. 1988 for optical, Fan 1999 for near infrared, and Aller et al. 2003 for radio observations). As already noted by Press (1978), power spectra of AGN lightcurves globally follow power laws $A_f \propto f^{-\beta}$ with $\beta > 0$, corresponding to *red noise*;[1] here A_f denotes the power spectral

[1] In the context of time series analysis, the term "noise" refers to stochastic emission from a source of radiation, *not* to measurement errors or instrumental noise.

amplitude as function of sampling frequency f. Lightcurves composed of pure Gaussian *white noise* have flat power spectra ($\beta = 0$). Other important special cases are *random walk noise* ($\beta = 2$) – which is the integral of white noise – and *flicker noise* ($\beta = 1$, "$1/f$ noise") as intermediate case between white noise and random walk noise (see also Park & Trippe 2012 for a detailed technical discussion). Lawrence et al. (1987) found that power spectrum of a Seyfert galaxy NGC 4051 can be described by flicker noise. Red noise power spectra were also observed by Lawrence & Papadakis (1993) who used 12 high-quality "long look" X-ray lightcurves of AGN.

A multitude of studies illustrates the difficulties of determining the statistical significance of supposed QPO signals in the power spectra of AGN lightcurves. The analysis of Benlloch et al. (2001) concluded that a previously reported quasi-periodic signal in X-ray lightcurves of the Seyfert galaxy Mrk 766 was actually statistically insignificant. Uttley et al. (2002) pointed out the importance of sampling effects leading to *red-noise leaks* and *aliasing*. Vaughan (2005) gives an analytical approach to derive significance levels for peaks in red-noise power spectra. Do et al. (2009) demonstrated the power of Monte-Carlo techniques for deriving significance levels by comparing the red-noise power spectra of actual and simulated flux data.

The temporal flux variability of AGN can be exploited for elucidating the physical conditions within active galaxies especially at radio frequencies where monitoring observations of hundreds of targets have been conducted over several decades by various observatories. Remarkably, many studies aimed at analyzing long-term AGN radio variability do not take into account the intrinsic red-noise properties of the lightcurves. The incorrect assumption of constant (as function of f) significance levels in power spectra (following from the assumption of white-noise dominated lightcurves) has lead to reports of "characteristic" time scales which are actually not special at all (cf., e.g., Ciaramella et al. 2004; Hovatta et al. 2007; Nieppola et al. 2009).

Blazars, characterized by violent flux variability across the entire electromagnetic spectrum, are a subset of AGN which include BL Lacertae (BL Lac) objects and Flat Spectrum Radio Quasars (FSRQs). In accordance with the standard viewing angle

unification scheme of AGN (Urry & Padovani 1995), it is commonly assumed that their observed emission is generated by synchrotron radiation – dominating from radio to optical frequencies – and inverse Compton emission – dominating at frequencies higher than optical – from relativistic plasma jets (almost) aligned with the line of sight. In order to perform a thorough study of the statistical properties of blazar emission, we analyze the lightcurves of four radio-bright blazars with strong flux variability – 3C 279, 3C 345, 3C 446, and BL Lac – provided by the University of Michigan Radio Astronomy Observatory (UMRAO) monitoring program of AGN. The data set comprises data spanning ≈32 years in time and covering three frequency bands located at 4.8 GHz, 8.0 GHz, and 14.5 GHz.

6.2 Target Selection and Flux Data

For our study we exploited the AGN monitoring data base of the 26-meter University of Michigan Radio Astronomy Observatory (UMRAO); the instrument, observations, and calibration procedures are described in detail by Aller et al. (1985). Our analysis required the use of densely sampled high-quality lightcurves spanning several decades in time and obtained at several observing frequencies. Accordingly, we selected targets with (i) data available for all three UMRAO bands (4.8, 8, and 14.5 GHz); (ii) continuously spanning at least 30 years in time; (iii) dense – faster than monthly at each frequency – sampling over the entire monitoring time; (iv) a minimum flux (at all frequencies) of 2 Jy; and (v) strong flux variability by factors >2. Our very strict selection criteria left us with a sample of four blazars: 3C 279, 3C 345, 3C 446, and BL Lac. Table 6.1 provides an overview over the key properties of our targets (partially taken from the NASA/IPAC Extragalactic Database (NED)[2]) and data. The median statistical error of a flux measurement was 0.09 Jy. The lightcurves cover a time line from 1980 to 2012, slightly more than 32 years.

[2] `http://ned.ipac.caltech.edu/`

Table 6.1. Properties of our four target blazars

Object	RA	DEC	Type	Redshift	T [yr]	$N_{4.8}$	$N_{8.0}$	$N_{14.5}$
3C 279	12:56:11	−05:47:22	FSRQ	0.536	32.52	1086	1337	1473
3C 345	16:42:59	+39:48:37	FSRQ	0.593	32.54	1323	1315	1415
3C 446	22:25:47	−04:57:01	BL Lac	1.404	32.12	680	902	1088
BL Lac	22:02:43	+42:16:40	BL Lac	0.069	32.54	1256	1315	1755

Note. — J2000 coordinates, source types, and redshifts are taken from the NED. We also give the total monitoring time T (in years) and the numbers N of flux data points for 4.8, 8.0, and 14.5 GHz, respectively.

6.3 Analysis

6.3.1 Lightcurves

We selected our data for the purpose of time series analysis which can be misled by irregular sampling. In order to minimize such sampling effects, we binned our lightcurves in time such that the bin size is the time interval

$$\Delta t = 2T/N \tag{6.1}$$

where T is the total observing time and N is the number of data points; for our sources, Δt is on the order of three weeks typically. (For the special case of regular sampling, Δt corresponds to the inverse of the Nyquist frequency.) The final lightcurves are shown in Fig. 6.1; evidently, all four sources show strong variability on various time scales.

6.3.2 Spectral indices

The fast – but not simultaneous – sampling of our targets at three frequencies made it possible to study their spectral evolution. A combination of (i) non-simultaneous sampling and (ii) rapid intrinsic flux variability made it necessary to group our data

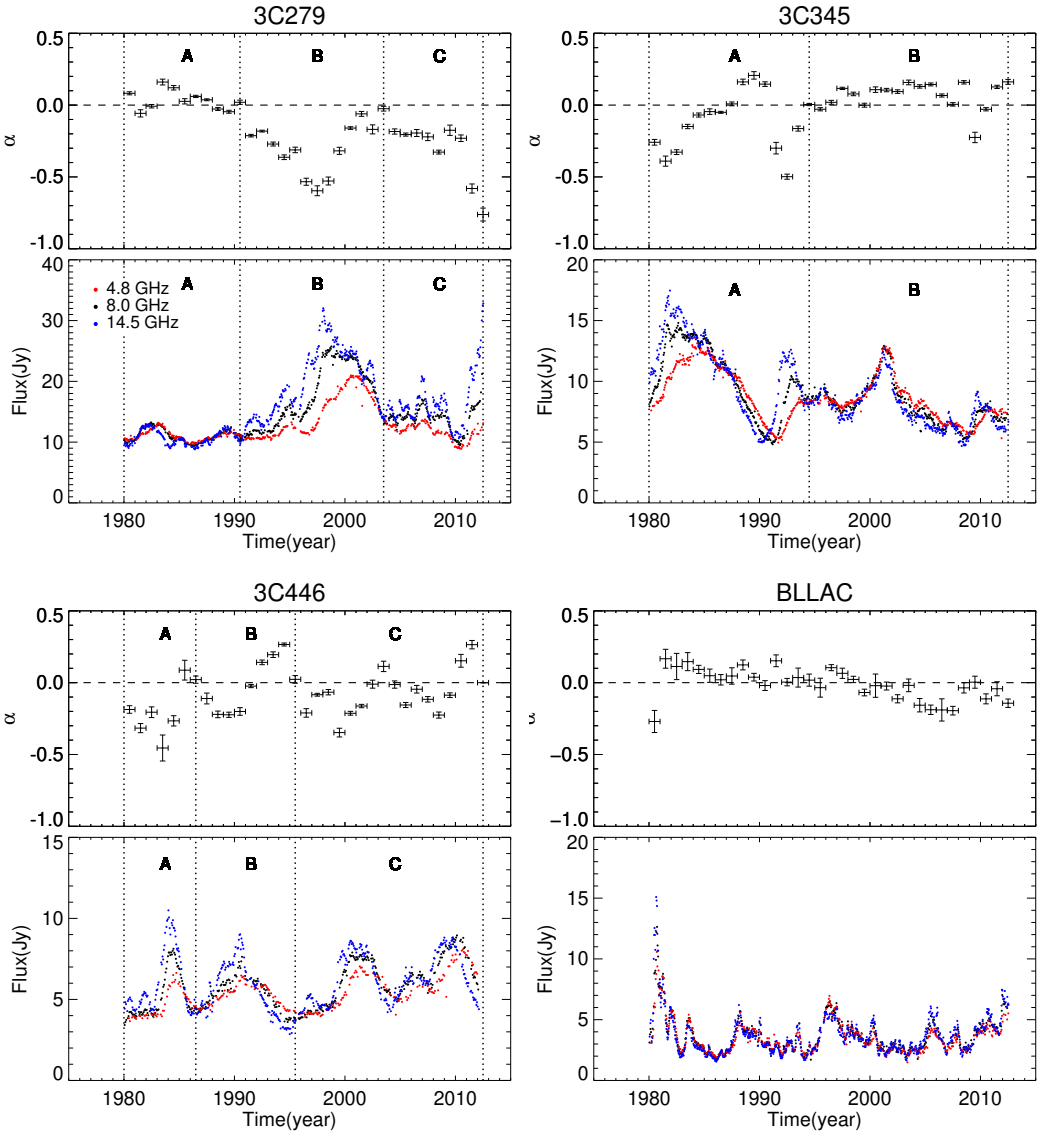

Figure 6.1. Flux densities and spectral indices α as function of time for our four blazars, spanning the years 1980 to 2012. For the spectral index diagrams, error bars along the time axes denote the size of the time windows used for the calculation of α (1 year), error bars along the α axes denote the statistical 1σ errors; horizontal dashed lines show the $\alpha = 0$ lines. In the cases of 3C 279, 3C 345, and 3C 446, we divided the lightcurves into activity phases (A, B, C) with boundaries (vertical dotted lines) given by the times when $\alpha = 0$ (cf. § 6.3.2). Red, black, and blue data points indicate fluxes at frequencies 4.8, 8, and 14.5 GHz, respectively.

into time windows; we eventually chose a time window of one year. Within each time window, we jointly described all data (covering all frequency bands) with a standard powerlaw model

$$S_\nu \propto \nu^{-\alpha} \tag{6.2}$$

where ν is the observing frequency, S_ν is the flux density, and α is the spectral index. We present the spectral index as function of time in Fig. 6.1.

6.3.3 Time offsets among spectral bands

The long overall time line and good sampling of our data made it possible to probe the data for time lags among the fluxes observed at different frequencies. We applied the discrete correlation function proposed by Edelson & Krolik (1988) to each pair of spectral bands for each source. In a first step, we computed the *unbinned discrete correlation function* (UDCF) for two discrete datasets $\{a_i\}$ and $\{b_j\}$ with $i, j = 1, 2, 3, ...,$

$$\mathrm{UDCF}_{ij}(\Delta t_{ij}) = \frac{(a_i - \bar{a})(b_j - \bar{b})}{\left[(\sigma_a^2 - \delta_a^2)(\sigma_b^2 - \delta_b^2)\right]^{1/2}} \quad . \tag{6.3}$$

Here $\bar{a}$ and $\bar{b}$ are the averages of $\{a_i\}$ and $\{b_j\}$, respectively; Δt_{ij} denotes the difference of the observing times of the data pair (a_i, b_j); $\sigma_{a,b}^2$ are the variances; and $\delta_{a,b}$ denote the mean measurement errors of a_i, b_j.

The actual *discrete correlation function* (DCF) for a given time offset τ results from averaging over all N' $\mathrm{UDCF_{ij}}(\Delta t_{ij})$ for which Δt_{ij} falls into a selected τ bin $\Delta\tau$ (i.e., $\tau - \Delta\tau/2 \leq \Delta t_{ij} < \tau + \Delta\tau/2$):

$$\mathrm{DCF}(\tau) = \frac{1}{N'} \sum_{\tau-\Delta\tau/2}^{\tau+\Delta\tau/2} \mathrm{UDCF}_{ij}(\Delta t_{ij}) \tag{6.4}$$

with (-1) $+1$ corresponding to perfect (anti-)correlation and 0 indicating the absence of any correlation. The position of the maximum of the DCF corresponds to the time offset between the lightcurves. The statistical uncertainty of $\mathrm{DCF}(\tau)$ is given by the standard error of mean

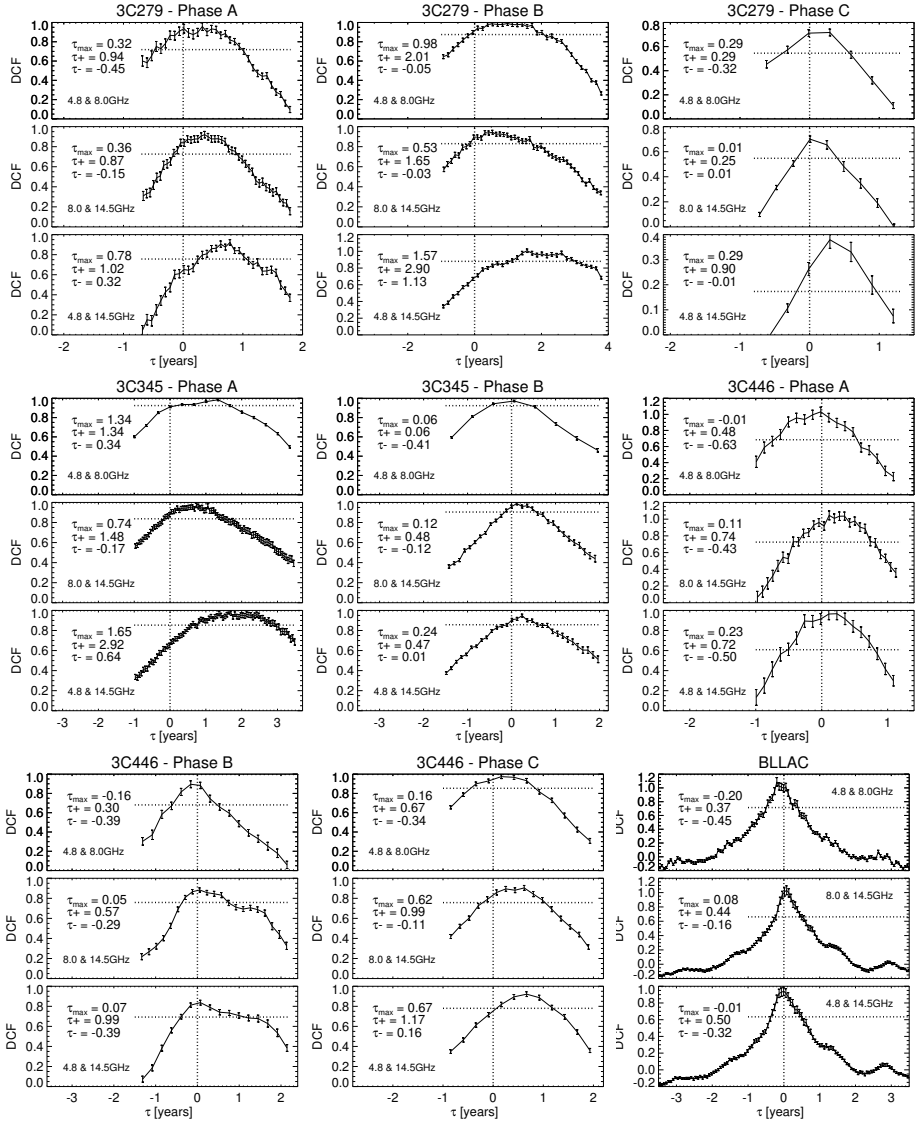

Figure 6.2. Discrete correlation function (DCF) as function of time lags τ for each pair of 4.8, 8, and 14.5-GHz lightcurves of each source. The black solid lines show the DCF, the horizontal dotted lines indicate $\max(\mathrm{DCF}) - 3\sigma_{\max(\mathrm{DCF})}$. The $\tau = 0$ lines are marked by vertical dotted lines. A positive (negative) time lag means that the higher frequency precedes (follows) the lower frequency. The values $\tau_{\max}$, τ_+, and τ_- denote the time lags corresponding to the maximum of the DCF and the upper and lower boundaries of the 3σ uncertainty intervals, respectively. $\sigma_{\mathrm{DCF}}(\tau)$ are given as the error bars for each point.

$$\sigma_{\mathrm{DCF}}(\tau) = \frac{1}{N' - 1} \left[\sum_{\tau - \Delta\tau/2}^{\tau + \Delta\tau/2} \left(\mathrm{UDCF_{ij}} - \mathrm{DCF}(\tau) \right)^2 \right]^{1/2} . \tag{6.5}$$

An important effect to be considered is the interplay between (i) variations of the spectral index α and (ii) a time delay between the lightcurves belonging to different frequency bands: an offset between spectral bands causes variations of the observed values for α even if the intrinsic (i.e., corrected for the offset) spectral index is constant. Inspection of Fig. 6.1 suggests that this might indeed be the case at several occasions in 3C 279, 3C 345, and 3C 446. Turning this argument around, this implies that we can divide our data into activity phases defined by the times when $\alpha = 0$ (i.e. the reference spectral index for flat-spectrum AGN). Accordingly, we divided our lightcurves into two or three phases (A, B, C – except for the case of BL Lac), and computed the DCF for each phase separately. We chose τ ranges sufficient for covering the largest time offsets expected between lightcurves, eventually adopting $\tau \pm 3.5$ years (except for the lightcurve pair 4.8/14.5 GHz of 3C 279 where it was necessary to extend the range to $\tau \pm 5$ years). In order to preserve a good time resolution, we usually used a τ bin size $\Delta\tau = \max[T_1/N_1, T_2/N_2]$ for two lightcurves "1" and "2". In case of the 4.8/8 GHz lightcurve pair of 3C 345 it was necessary to increase $\Delta\tau$ by factors up to six in order to suppress sampling artifacts.

We present the resulting DCF in Fig. 6.2. In our convention, a positive (negative) time lag implies that the flux at the higher frequency precedes (follows) the flux at the lower frequency. We consider the null hypothesis "the lightcurves are simultaneous" as rejected if $\mathrm{DCF}(\tau = 0)$ is located below the line defined by $\max(\mathrm{DCF}) - 3\sigma_{\max(\mathrm{DCF})}$ (with $\sigma_{\max(\mathrm{DCF})}$ denoting the statistical 1σ error of the maximum value of the DCF). We give the error of each DCF bin to check if there is any risk in using the maximum DCF value as representative for physical time lags between frequency because the DCF values are correlated between bins. If the scatter of DCF values is much smaller than the error, it would be hard to determine the correct time lags. Fortunately, this is not the case for our good quality data and we can obtain the plausible time lags by DCF.

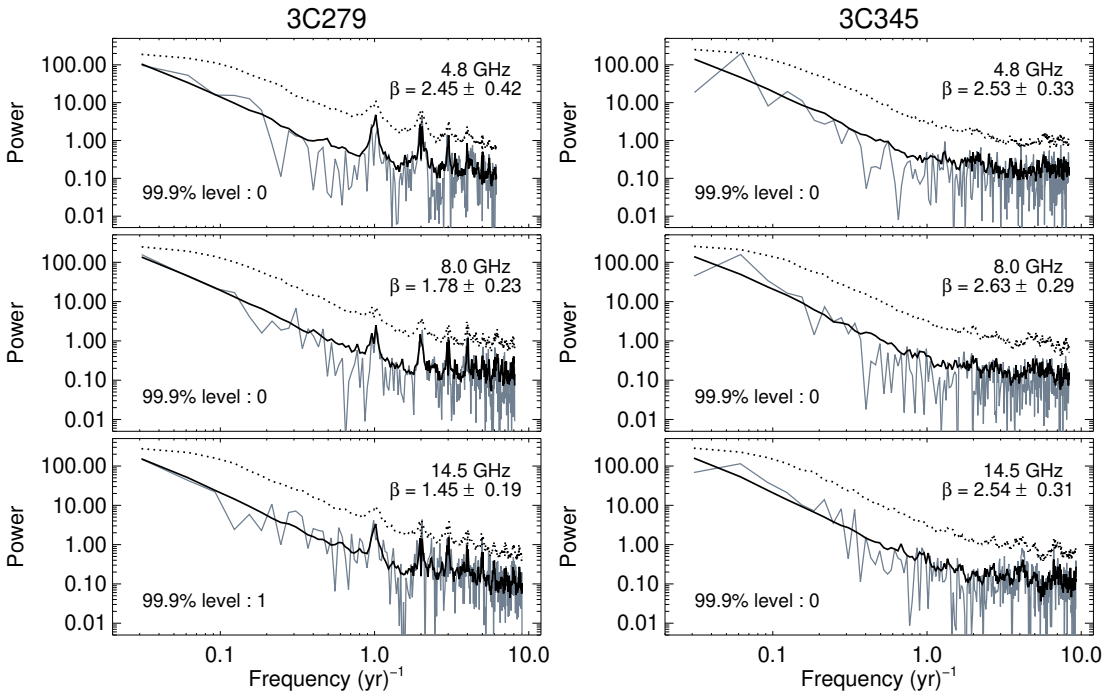

Figure 6.3. Periodograms – i.e. spectral power as function of sampling frequency (in units of yr^{-1}) – for all 12 blazar lightcurves. Solid gray lines show the observed periodograms, solid black lines indicate the expected distributions resulting from averaging over 10 000 simulated red-noise periodograms, and dotted black lines correspond to the 99.9% significance levels obtained from simulations of red-noise periodograms (cf. § 6.3.5). In each diagram the value for β found from fitting Eq. 6.8 to the data ("β = ...") and the number of data points exceeding the 99.9% significance threshold ("99.9% level: ...") are noted. The simulations used $\beta = 2$ for 3C 279, 3C 345, and 3C 446, and $\beta = 1.75$ for BL Lac. The excess values detected in the 14.5-GHz periodograms of 3C 279 (one value out of 295 frequencies probed) and BL Lac (one value out of 380) are consistent with statistical fluctuations: when taking into account the number of trials, the false alarm probabilities for these events are 26% and 32%, respectively.

6.3.4 Periodograms

For a quantitative analysis of flux variability we employed the normalized *Scargle periodogram*

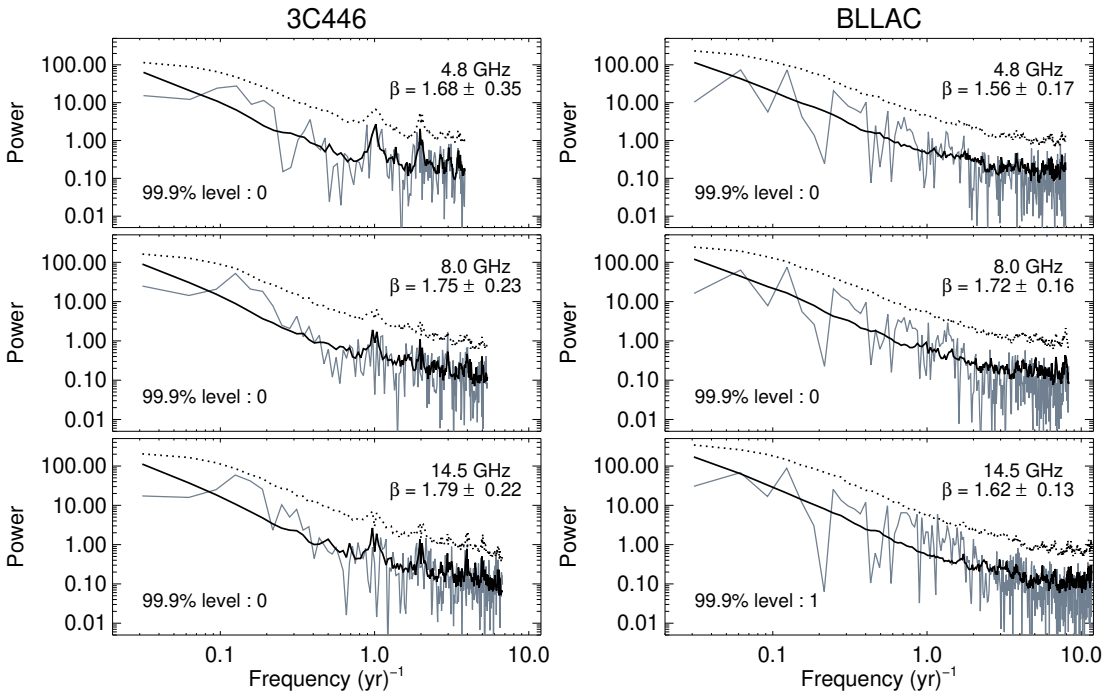

Figure 6.3. Continued.

$$A_f = \frac{1}{2\sigma^2}\left[\frac{\left(\sum_i S_i \cos\omega(t_i-\tau')\right)^2}{\sum_i \cos^2\omega(t_i-\tau')} + \frac{\left(\sum_i S_i \sin\omega(t_i-\tau')\right)^2}{\sum_i \sin^2\omega(t_i-\tau')}\right] \tag{6.6}$$

where τ' is a time offset satisfying

$$\tan(2\omega\tau') = \frac{\sum_j \sin 2\omega t_j}{\sum_j \cos 2\omega t_j} \tag{6.7}$$

(Scargle 1982). Here $\omega = 2\pi f$ is the angular frequency, A_f is the amplitude of the periodogram evaluated at sampling frequency f, S_i is the i-th flux value, t_i denotes the time when S_i was obtained, and σ^2 is the variance of the data. The base frequency is $f_{\min} = 1/T$, the sampling frequencies are $f = f_{\min}, 2f_{\min}, 3f_{\min}, \ldots, f_{\max} = N/(2T)$. Here T is the total observing time and N is the number of flux data points. The Scargle periodogram is preferable over standard Fourier transform methods because it can be applied to data with arbitrary sampling and has a well-understood statistical

behavior (Priestley 1981; Scargle 1982). We present the periodograms of our lightcurves in Fig. 6.3.

The power spectra of AGN lightcurves are known (cf. § 1) to follow red-noise powerlaws. However, when dealing with lightcurves that are sampled irregularly and show gaps, a complication arises in form of *aliasing*: the power at frequencies above the Nyquist frequency is transferred to lower frequencies because variations on time scales shorter than the sampling period cannot be distinguished from variations on longer time scales. Aliasing introduces an approximately constant offset which adds to the power spectrum (Uttley et al. 2002). As (i) the amplitudes of power spectra tend to span several orders of magnitude and (ii) are affected by multiplicative noise (Scargle 1982; Vaughan 2005), periodograms have to be treated in logarithmic space. Accordingly, we assumed the functional form

$$\log\left[A_f\right] = \log\left[af^{-\beta} + \delta\right] \tag{6.8}$$

for our analysis; here a is a scaling factor, β is the power-law index of the periodogram, and δ is the aliasing power. In order to estimate the powerlaw index β, we fit the model given by Eq. 6.8 to each empirical periodogram; the resulting values are included in Fig. 6.3.

6.3.5 Simulated lightcurves and significance levels

The detection of deviations from a red-noise powerlaw periodogram, especially of (quasi-)periodic signals at specific sampling frequencies, requires the establishment of reliable significance levels – a problem that has been notoriously difficult (cf., e.g., Vaughan 2005). Arguably the most straightforward ansatz is provided by Monte-Carlo simulations that compare simulated periodograms and lightcurves to actual data (e.g., Benlloch et al. 2001; Do et al. 2009), and this is the approach we adopted.

We simulated red-noise lightcurves using the method suggested by Timmer & König (1995). For each sampling frequency f, we drew two random numbers from Gaussian distributions with zero mean and unit variance for the real part and the imaginary

part, respectively. We multiplied both numbers with $f^{-\beta/2}$ to generate power-law noise with slope $-\beta$. The result was an array of complex numbers which corresponded to the complex Fourier transform of the artificial lightcurve. We constructed each complex array such that the values of the Fourier transform $F(f)$ obey $F(-f_i) = F^*(f_i)$, with * denoting complex conjugation, to obtain a real valued time series. We computed artificial lightcurves $S(t)$ by taking the inverse Fourier transform of the complex arrays.

Each artificial lightcurve consisted of 4096 data points initially. We then identified the time between two adjacent data points with the time scale defined in Eq. 6.1 and omitted values from the artificial lightcurve at the locations of gaps in the observed lightcurves, thus mapping the sampling pattern of the UMRAO observations into the simulated lightcurve. Eventually, we computed a periodogram from each re-mapped artificial lightcurve. As the observed indices are $\beta \gtrsim 1.5$ for all blazar lightcurves (cf. § 4), we used values of 1.5, 1.75, and 2 for β in the simulations. In order to decide which value for β to adopt for a given observed periodogram, we (i) computed 10 000 simulated periodograms for each of the three choices of β, and (ii) compared the average of the simulated periodograms to the observed periodogram via a weighted least-squares test.

From the set of 10 000 artificial periodograms for a given blazar lightcurve we determined, separately for each sampling frequency f, a 99.9% significance level (corresponding to 3.29σ in Gaussian terms) for the periodogram derived from the UMRAO data. Our simulation procedure is based on the null hypothesis "the observed periodogram originates from a red-noise lightcurve". Accordingly, the spectral power of a deviation from a red-noise periodogram, especially a candidate periodic signal, needs to exceed the aforementioned significance levels in order to be potentially significant. The results of our analysis are illustrated in Fig. 6.3.

6.4 Results

6.4.1 3C 279

Using our criteria outlined in § 6.3.3 we divided the lightcurves of 3C 279 into three activity phases (see also Fig. 6.1). Phase A, ranging from 1980 to 1990, is characterized by relatively weak variability with fluxes ranging approximately from 10 Jy to 14 Jy. Flux densities in all three frequency bands are very similar for most of the time, leading to spectral indices $\alpha \approx 0$ except of the very beginning of phase A. The DCF analysis (§ 6.3.3 and Fig. 6.2) finds that the 14.5-GHz lightcurve precedes the 4.8-GHz lightcurve by $\tau = 0.78^{+0.24}_{-0.46}$ years (3σ uncertainty interval); time lags between the other lightcurve pairs are consistent with zero. Phase B, ranging from 1990 to 2003, is characterized by a strong increase in emission from ≈10 Jy to ≈30 Jy (at 14.5 GHz). This outburst occurs the earlier the higher the frequency; for the frequency pair 4.8/14.5 GHz, the time lag between the lightcurves is $\tau = 1.57^{+1.33}_{-0.44}$ years. The observed spectral index becomes inverted, with α as low as about -0.7. Phase C, starting in 2003, is characterized by multiple flux density fluctuations in the range 10–20 Jy for most of the time, with a strong increase – up to 35 Jy at 14.5 GHz – since 2010. The spectral index remains mildly inverted ($\alpha \approx 0.2$) for most of the time but reaches $\alpha \approx -0.8$ in 2012, coinciding with the observed flux maximum at the end of the monitoring. The time lags are consistent with zero for all frequency pairs.

The periodograms (§ 6.3.4, Fig. 6.3) of all three lightcurves decrease toward increasing sampling frequencies – as is characteristic for red noise – and show a flattening at the highest sampling frequencies – as expected in case of notable aliasing. By fitting the model given by Eq. 6.8 to the spectra we find approximate powerlaw indices β of 2.5, 1.8, and 1.5 for the 4.8-GHz, 8-GHz, and 14.5-GHz periodograms, respectively, with statistical errors between 0.2 and 0.4 (1σ confidence intervals). Comparison of observed periodograms to the ones found from Monte-Carlo simulations (averages of 10 000 realizations of red-noise periodograms; cf. § 6.3.5) leads to the conclusion that all three observed power spectra are consistent with being generated by random-walk noise

($\beta = 2$) lightcurves. None of the observed periodograms shows statistically significant excess power with respect to a red-noise power spectrum.

6.4.2 3C 345

We divided the lightcurves into two activity phases. Phase A, ranging from 1980 to 1994, is characterized by strong variability, with fluxes (at 14.5 GHz) moving between 5 and 17 Jy. This variability is also expressed in the spectral index α which fluctuates between -0.4 and 0.2. The DCF analysis finds a time lag of $\tau = 1.65^{+1.27}_{-1.01}$ years (3σ confidence intervals) between the 4.8 GHz and 14.5 GHz lightcurves, with smaller, marginally significant, lags between the other frequency pairs. Phase B, beginning in 1994, is characterized by strong flux variability between 5 and 13 Jy and a mostly flat ($\alpha \approx 0.2$) spectrum. Time lags between the lightcurves are (marginally) consistent with zero.

The periodograms of all three lightcurves are consistent with pure red-noise spectra. The best-fitting parametric model solutions (Eq. 6.8) show quite extreme powerlaw slopes $\beta \approx 2.5$ with statistical (1σ confidence) uncertainties of about 0.3. When comparing the data to the results of Monte-Carlo simulations, we find that all three observed periodograms are consistent with random-walk noise spectra.

6.4.3 3C 446

During the entire observing time this source shows strong variability in both flux density – with values ranging from 3 Jy to 10 Jy (at 14.5 GHz) – and spectral index – with values fluctuating between -0.5 and 0.3. According to our criteria (§ 6.3.3) we divided the lightcurves into three phases, ranging from 1980 to 1986 (phase A), 1986 to 1995 (phase B), and from 1995 onward (phase C). Whereas in phases A and B the lightcurves of all three frequencies are consistent with being simultaneous, we find a time lag of $\tau = 0.67^{+0.5}_{-0.51}$ years (3σ confidence interval) for the pair 4.8/14.5 GHz.

The periodograms of all three lightcurves are consistent with being pure red-noise spectra. Our parametric model fit (Eq. 6.8) finds powerlaw slopes $\beta \approx 1.7$ for all three

periodograms, with statistical (1σ) errors between 0.2 and 0.4. From our Monte-Carlo simulations we find that the observed periodograms are consistent with random-walk noise lightcurves ($\beta = 2$).

6.4.4 BL Lac

The lightcurve of BL Lac is characterized by rapid variability throughout the entire monitoring time of 32 years. Flux densities vary between 2 Jy and 7 Jy with the notable exception of a flare that reaches about 15 Jy (at 14.5 GHz) in 1980. The spectral index varies only slowly (except at the time of the 1980 flare) – on time scales of years to decades – between $\alpha \approx 0.2$ and $\alpha \approx -0.2$. Accordingly, we did not attempt to identify separate activity phases – qualitatively, the behavior of BL Lac is actually rather uniform. The lightcurves at the three observing frequencies follow each other closely not only in amplitude but also in time: all time lags identified by the cross-correlation analysis are consistent with zero.

The periodograms of all three lightcurves are in agreement with being pure red-noise power spectra. The parametric model (Eq. 6.8) finds identical (within the 1σ errors of 0.1–0.2) $\beta \approx 1.6$ for all periodograms. Comparison to the simulation results shows the best agreement with a theoretical, intrinsic powerlaw slope of $\beta = 1.75$.

6.5 Discussion

6.5.1 Spectral indices

For all sources the spectral index remains at values that are close to zero or even negative ($\alpha \lesssim 0.3$). The low values of α imply that the emission originates from optically thick synchrotron sources, leading to approximately flat ($\alpha \approx 0$) or even inverted ($-0.5 \lesssim \alpha \lesssim 0$) spectra (Ginzburg & Syrovatskii 1965; Pacholczyk 1970; Kembhavi & Narlikar 1999; Krolik 1999). This is in agreement with blazars being AGN with jets pointing (almost) toward the observer, resulting in a high column density of matter (potentially belonging to multiple individual plasma clouds) along the line of sight – we do not find

any indication for a deviation from this (expected) behavior even over a time line of three decades.

Taking a closer look at individual flux maxima (outbursts or flares of radiation), we can distinguish two types of behavior: (i) events with (a) fluxes at higher frequencies preceding the ones at lower frequencies and (b) fluxes at higher frequencies being significantly higher than the fluxes at lower frequencies (implying $\alpha < 0$); and (ii) events with all lightcurves being simultaneous and of approximately equal amplitude (implying $\alpha \approx 0$). A noteworthy example is provided by 3C 345, where both types of events occur within about 20 years (cf. phase A vs. phase B in Fig. 6.1). An interpretation is readily provided by the "generalized shock model" of Valtaoja et al. (1992) which is based on the assumption that outbursts of radio emission in AGN are caused by shocks propagating through jets and which distinguishes two scenarios: (i) in *high-peaking flares* ("high" with respect to the observing frequency), the maximum luminosity is reached at frequencies well above the observing frequency. This implies that the flare is decaying at the time of observation, resulting in an observational signature equivalent to the shock-in-jet model by Marscher & Gear (1985). This model describes shocks in AGN jets as adiabatically expanding plasmas that become optically thin at higher frequencies first, thus causing a systematic time delay between the spectral bands with the higher frequency leading with higher amplitude of flux. In case of (ii) *low-peaking flares*, the maximum luminosity is reached at frequencies well below the observing frequency. Lightcurves at different frequencies are almost simultaneous and have almost identical amplitudes. Applying this framework to our sources, high-peaking flares are present in phase B and C of 3C 279, phase A of 3C 345, and the entire lightcurves of 3C 446. The other flux outbursts can be described as low-peaking flares.

6.5.2 Spectral time delays

We examined the presence or absence of time lags between lightcurves at different frequencies for each phase of each source via discrete correlation functions. The first feature we note is the large range of time delays – on the order of months – permitted by

the 3σ confidence limits. The different temporal evolutions of the outbursts in different spectral bands, in combination with long variability time scales on the order of years, lead to broad, asymmetric DCF curves.

As discussed already partially in the context of the spectral index analysis, we find (i) significant positive time lags, as well as (ii) phases of no or weak positive time lags between different spectral bands. Phase B of 3C 279 ($\tau \approx 0.5-1.6$ years) and phase A of 3C 345 ($\tau \approx 0.7-1.7$ years) correspond to case (i); the amplitudes reach their maxima first at 14.5 GHz, with the 8 and 4.8 GHz lightcurves trailing – as expected for high-peaking flares (Valtaoja et al. 1992). The long evolution time scales of the outbursts, on the order of years, suggest physical sizes of the expanding emission regions on the order of light-years. The remaining activity phases correspond to case (ii), with time delays close to or in agreement with zero. Here we find both low- and high-peaking flares: phase C of 3C 279 and all phases of 3C 446 show very fast spectral index variability ranging from $\alpha \approx -0.8$ to $\alpha \approx 0.3$, in agreement with the behavior of high-peaking flares; BL Lac however shows simultaneous lightcurves with approximately identical amplitudes throughout the entire monitoring time of three decades – in agreement with the behavior expected for low-peaking flares.

6.5.3 Power spectra

The periodograms of all four blazars are in good agreement with lightcurves generated by powerlaw noise with index $\beta = 2$ – i.e., random walk noise – and being affected by aliasing caused by irregular sampling. Furthermore, our statistical tests (§ 6.3.5) show that all periodograms are consistent with being pure red-noise power spectra without significant (quasi-)periodic signals (cf. Fig. 6.3). The powerlaw-noise nature of their lightcurves implies that none of our target blazars shows any "characteristic" activity time scale.

As already outlined in § 1, the red-noise nature of AGN lightcurves is observationally well established (albeit this discussion is complicated by the potential presence of multiple states of emission; cf. e.g. Dodds-Eden et al. 2011; Trippe et al. 2011; Park

& Trippe 2012). Empirically, the slopes of the power spectral density of different AGN tend to scatter over a wide range of values, roughly from $\beta \approx 0.5$ (e.g., Trippe et al. 2011) to $\beta \approx 2$ (e.g., Do et al. 2009), with "typical" values $\beta \approx 1$ (e.g., Press 1978). Indeed, the presumed flicker-noise nature of AGN lightcurves triggered a search for an underlying physical mechanism which has lasted for more than three decades (e.g., Press 1978; Lyubarskii 1997; Kelly et al. 2011), without any clear picture emerging as yet.

Given the incoherent picture of the statistical properties of temporal AGN variability, the clarity of our results comes as a surprise: we find the lightcurves of all four blazars to be consistent with being random-walk signals ($\beta \approx 2$). Within the obvious limits of low-number statistics, this suggests that random-walk noise radio lightcurves are characteristic for blazars. We note the importance of a careful treatment of data (§§ 6.3.1, 6.3.4) as well as a careful modeling of red noise lightcurves (§ 6.3.5): only the combination of good data quality, periodogram analysis, awareness of sampling effects, and Monte Carlo simulations of powerlaw noise lightcurves unveils the intrinsic random-walk noise behavior. Evidently, this raises the question if random-walk noise lightcurves could be a general feature of blazars that is frequently masked by limited data quality, irregular sampling, inappropriate modeling of power spectra, et cetera.

6.6 Conclusions

We studied high-quality radio lightcurves of four luminous blazars – 3C 279, 3C 345, 3C 446, and BL Lac – spanning 32 years in time and covering the frequencies 4.8, 8, and 14.5 GHz. We analyzed the temporal evolution of fluxes and spectral indices. Our work leads us to the following principal conclusions:

1. Our sources show mostly flat or inverted ($-0.5 \lesssim \alpha \lesssim 0$) spectral indices, in agreement with optically thick synchrotron emission. The lightcurves of different frequencies are either simultaneous (within errors) or shifted relative to each other such that the high-frequency emission leads the low-frequency emission by

up to ≈1.5 years. We are able to distinguish high-peaking and low-peaking flares according to the classification of Valtaoja et al. (1992).

2. All lightcurves show variability on all time scales. Their periodograms (power spectra) are in agreement with being pure red-noise powerlaw spectra without any indication for (quasi-)periodic signals. When taking into account the sampling patterns via dedicated Monte Carlo simulations, we find that all lightcurves are consistent with being random walk noise signals with powerlaw slopes $\beta \approx 2$. Given that we find this behavior in all four sources under study, this suggests that random walk noise lightcurves are a general feature of blazars.

Our results imply that careful time series analysis of high-quality blazars lightcurves provides information on the source structure even if a target is not resolved spatially. Obviously, it will be necessary to systematically study much larger blazar samples in order to decide if the trends we have uncovered are indeed general.

Chapter 7

The long-term centimeter variability of active galactic nuclei: A new relation between variability timescale and accretion rate[†]

Abstract

We study the long-term radio variability of 43 radio bright AGNs by exploiting the data base of the University of Michigan Radio Astronomy Observatory (UMRAO) monitoring program. The UMRAO database provides high quality lightcurves spanning $25-32$ years in time at three observing frequencies, 4.8, 8, and 14.5 GHz. We model the periodograms (temporal power spectra) of the observed lightcurves as simple power-law noise (red noise, spectral power $P(f) \propto f^{-\beta}$) using Monte Carlo simulations,

[†]The contents of this chapter was originally published in the Astrophysical Journal (Park & Trippe 2017)

taking into account windowing effects (red-noise leak, aliasing). The power spectra of 39 (out of 43) sources are in good agreement with the models, yielding a range in power spectral index (β) from $\approx$1 to $\approx$3. We find a strong anti-correlation between β and the fractal dimension of the lightcurves, which provides an independent check of the quality of our modelling of power spectra. We fit a Gaussian function to each flare in a given lightcurve to obtain the flare duration. We discover a correlation between β and the median duration of the flares. We use the derivative of a lightcurve to obtain a characteristic variability timescale which does not depend on the assumed functional form of the flares, incomplete fitting, and so on. We find that, once the effects of relativistic Doppler boosting are corrected for, the variability timescales of our sources are proportional to the accretion rate to the power of 0.25 ± 0.03 over five orders of magnitude in accretion rate, regardless of source type. We further find that modelling the periodograms of four of our sources requires the assumption of broken powerlaw spectra. From simulating lightcurves as superpositions of exponential flares we conclude that strong overlap of flares leads to featureless simple power-law periodograms of AGNs at radio wavelengths in most cases.

7.1 Introduction

Active Galactic Nuclei (AGNs) are characterized by strong temporal flux variability, which can provide valuable information on the complex physical processes of accretion and plasma outflows of AGNs (see, e.g., Ulrich et al. 1997 for a review). A number of studies have found that various types of AGNs, from Seyfert galaxies (e.g., Lawrence et al. 1987) to quasars (e.g., Kelly et al. 2009) and radio bright AGNs (e.g., Hovatta et al. 2007), show ubiquitous aperiodic variability across various wavebands. The temporal power spectra or periodograms (see Priestley 1981 for an exhaustive review of time series analysis) – i.e., the square moduli of the Fourier transforms – of lightcurves have been employed to quantify the statistical properties of AGN variability (e.g., Abramowicz et al. 1991; Fan 1999; Benlloch et al. 2001; Aller et al. 2003; Do et al. 2009; Rani et al. 2009, 2010; Trippe et al. 2011; Gupta et al. 2012). In many cases, their power spectra

globally follow power laws $P(f) \propto f^{-\beta}$ with $\beta > 0$, corresponding to *red noise*[1] (Press 1978). We note that, in time series theory, the term "noise" generically refers to random intrinsic variations in brightness (i.e., not to measurement errors or instrumental noise).

Even though the fact that AGN lightcurves show red noise power spectra was discovered almost 40 years ago (Press 1978) and many studies have confirmed since then that this is a generic property of AGNs, it is still unclear why different AGNs show different characteristic variability patterns. Especially interesting have been sources that show a break in their power spectra, resulting in different slopes (β) below and above a certain frequency (the *break frequency*) (e.g., Uttley et al. 2002; M$^{\rm c}$Hardy et al. 2004). Such behaviour is often seen in optical and/or X-ray variability of Seyfert galaxies, quasars, and even galactic black holes (GBHs; Uttley et al. 2002; M$^{\rm c}$Hardy et al. 2004; Kelly et al. 2009, 2011). The break frequencies for both GBHs and AGNs show an anti-correlation with the black hole mass (M$^{\rm c}$Hardy et al. 2004; Uttley & M$^{\rm c}$Hardy 2005; Kelly et al. 2009, 2011) and are also related to the accretion rate (M$^{\rm c}$Hardy et al. 2006). The presence of break frequencies in the power spectra indicates that there is a characteristic timescale that governs the variability. Candidate timescales are the light crossing timescale, the orbital timescale, the disk thermal timescale, and the disk viscous timescale (see e.g., Kelly et al. 2009, 2011 for more details). These timescales are functions of the size of emitting regions such as accretion disks and hot coronae. Thus, it makes sense that they scale with the black hole mass because each length scale is proportional to the Schwarzschild radius, though the actual underlying relations must involve geometry and other physical properties of the emitting system.

Compared to the optical/X-ray variability of AGNs, the understanding of radio variability of AGNs is poor. The variability mechanism of *radio bright*[2] AGNs is quite different from that of radio faint, optical and/or X-ray bright AGNs. They emit strong

[1]Technically, red noise is reserved for the case $\beta = 2$ but we use the term in more general sense in this paper.

[2]We use the term *radio bright AGNs* because not all of our sources might be radio loud, i.e., have a radio-to-optical flux density ratio higher than a certain threshold value. All sources we discuss show strong activity at radio bands, including multiple flares during the time of observation.

non-thermal emission that is usually thought to originate from relativistic jets (Blandford & Königl 1979). Characteristic variability patterns are seen, especially flares or outbursts in the lightcurves (e.g., Valtaoja et al. 1999), which have been associated with shocks in jets (e.g., Marscher & Gear 1985; Hughes et al. 1985, see also Fromm et al. 2011). Blazars, a subset of AGNs that comprises most of the radio bright AGNs show violent flux variability across the entire electromagnetic spectrum. This special property of blazars is arguably related to relativistic jets (almost) aligned with the line of sight (e.g., Jorstad et al. 2005), implying that relativistic Doppler boosting plays an important role. Accordingly, a number of physical parameters and various mechanisms are involved in generating the complicated variability of radio bright AGNs at radio wavelengths.

Additional difficulties arise from limited sampling of lightcurves of AGNs and statistical analyses that do not consider the red-noise properties intrinsic to AGN lightcurves. As already noted by Park & Trippe (2014), Monte Carlo simulations of red-noise lightcurves are essential to reveal the intrinsic statistical properties of AGN lightcurves that are usually masked by irregular, finite sampling. Despite the importance (a) of the effects of limited sampling or windowing (e.g., Uttley et al. 2002, see also Isobe et al. 2015), which are often described as *red-noise leak* and *aliasing*, (b) of using goodness-of-fit tests correctly (Papadakis & Lawrence 1993), and (c) of deriving the statistical significance of supposed quasi-periodic oscillation (QPO) signals in red noise power spectra (Benlloch et al. 2001; Vaughan 2005, 2010), multiple studies of AGN radio variability focused on apparent characteristic variability timescales while using the incorrect assumption of constant (as function of f) significance levels in power spectra, which is only valid when β is close to 0 (Ciaramella et al. 2004; Hovatta et al. 2007; Nieppola et al. 2009, but, see Max-Moerbeck et al. 2014a,b; Ramakrishnan et al. 2015 for recent progress). In line with this, the characteristic timescales derived from using structure functions (SFs; Simonetti et al. 1985; Hughes et al. 1992) have been interpreted as physical variability timescales of AGNs (Ciaramella et al. 2004; Hovatta et al. 2007; Nieppola et al. 2009). However, as argued by Emmanoulopoulos et al. (2010),

this approach is probably misleading; in their study, peaks or breaks appeared in the SFs for all their simulated lightcurves even though there was no intrinsic characteristic timescale. Although the peaks or the breaks tend to appear at timescales close to the length of the lightcurves and thus the observed characteristic timescales from the SF analysis, typically smaller than 1/10 of the length of the time series, might be real, relating the timescales with physical timescales of AGNs could be risky. Thus, alternative ways to extract variability timescales from lightcurves or power spectra must be explored.

The Ornstein-Uhlenbeck (OU) process, also referred to as continuous time first-order autoregressive process, or a mixture of several OU processes have been suggested to model the observed lightcurves and power spectra of quasars at optical (Kelly et al. 2009), of Seyferts and a GBH at X-rays (Kelly et al. 2011), and of blazars at γ-rays (Sobolewska et al. 2014). The OU process describes a time series as a superposition of exponentially decaying outbursts occuring at random times and with random amplitudes. A mixture of OU processes is a linear superposition of OU processes, which has been introduced for a better description of AGN lightcurves. These models were motivated by the "perturbation" class of astrophysical models (e.g., Lyubarskii 1997) which suggests that the propagation of random accretion rate perturbations through the accretion flow is responsible for the observed variability of AGNs and GBHs. One advantage of these models is that they fit models to lightcurves instead of power spectra, which significantly reduces windowing effects. Another advantage is that they use maximum-likelihood or Bayesian techniques to utilize all the information contained in the data. The tight correlation between timescales and black hole masses seen in Kelly et al. (2009, 2011) suggests that those models accurately extract the relevant timescales from lightcurves.

However, the emission mechanisms of radio bright and radio faint AGNs are different; the former is dominated by synchrotron radiation from relativistic jets, while the latter is dominated by radiation from geometrically thin accretion disks and/or hot coronae. If the same model is applied to systems with different radiation mechanisms

are involved, one needs to explain why and how they can share the same statistical properties (this is partially discussed in Sobolewska et al. 2014). We will see that almost all (39 out 43) of our sources do not show indications for a break frequency in their power spectra, which might indicate that they have very long characteristic timescales – if at all. Thus, we make use of Monte Carlo simulations of red noise lightcurves instead of the OU process in this study, following up on our success in unveiling the intrinsic statistical properties of four radio bright AGNs (Park & Trippe 2014).

The format of the paper is as follows. In Section 7.2, we describe our data and sample. In Section 7.3, we explain how we obtain the statistical properties of our sources and relate them with other physical parameters such as the accretion rate in Section 7.4. In Section 7.5, we summarize our results and conclude. Throughout the paper, we adopt a cosmology with $H_0 = 70$ km s^{-1} Mpc^{-1}, $\Omega_{\rm M} = 0.3$, and $\Omega_\Lambda = 0.7$. All luminosities used in our paper are corrected to our adopted cosmological parameters.

7.2 Sample and Data

We exploited the AGN monitoring database of the 26-meter University of Michigan Radio Astronomy Observatory (UMRAO; see Aller et al. 1985 for technical details) for our study. For a statistical analysis we selected all lightcurves for which the number of data points exceeds 150 after binning and flagging (cf. Section 7.3). The number of data points before binning and flagging was 448 on average. This criterion ensured that at least one data point is available every ≈2 months on average. For many sources, only one or two of the three UMRAO bands (4.8, 8, and 14.5 GHz) satisfied this criterion. Our selection left us with a sample of 43 sources (20 sources were available at 4.8 GHz, 38 at 8 GHz, 36 at 14.5 GHz). The minimum source flux was around 0.6 Jy for 1101+384 (Mrk 421), the maximum flux around 35 Jy for 1226+023 (3C 273). Our source list comprised 27 flat spectrum radio quasars (FSRQs), 13 BL Lac objects (BLOs), and 3 radio galaxies (GALs). The lightcurves of eight sources, 0235+164, 0316+413, 0420−014, 1253−055, 1641+399, 1730−130, 2200+420, 2223−052, span ≈32 years in time from 1980 to around 2012; those of the other sources span ≈25 years from

Properties of the sample

Object	Type	z	T [yr]	$\beta_{4.8}$	$\beta_{8.0}$	$\beta_{14.5}$	$\tau_{\rm med}^{4.8}$	$\tau_{\rm med}^{8.0}$	$\tau_{\rm med}^{14.5}$	$\sigma_{\rm der}^{4.8}$	$\sigma_{\rm der}^{8.0}$	$\sigma_{\rm der}^{14.5}$	δ_z
	(1)		(2)		(3)			(4)			(5)		(6)
0133+476	FSRQ	0.859	25.45	$1.8^{+0.21}_{-0.21}$	$2.0^{+0.21}_{-0.21}$	$2.2^{+0.05}_{-0.21}$	0.87	0.71	0.98	3.49	3.29	2.76	11.1
0235+164	FSRQ	0.940	32.28	$1.5^{+0.05}_{-0.11}$	$1.4^{+0.11}_{-0.05}$	$1.4^{+0.05}_{-0.05}$	0.60	0.55	0.43	3.40	3.72	4.40	12.4
0316+413	GAL	0.018	32.44	$3.3^{+0.60}_{-0.50}$	$2.6^{+0.40}_{-0.05}$	$2.6^{+0.11}_{-0.05}$	6.54	5.45	3.82	0.33	0.71	1.14	0.3
0333+321	FSRQ	1.258	25.41	...	$2.1^{+0.21}_{-0.05}$	...	...	0.97	...	...	2.98	...	9.8
0336−019	FSRQ	0.852	22.29	...	$1.4^{+0.11}_{-0.11}$	...	...	0.60	...	...	4.70	...	9.4
0355+508	FSRQ	1.520	25.56	...	$2.3^{+0.30}_{-0.21}$	$2.0^{+0.30}_{-0.05}$	...	1.81	2.17	...	1.27	1.11	5.2
0415+379	GAL	0.049	25.42	...	$1.6^{+0.21}_{-0.11}$	...	...	0.87	...	...	2.15	...	2.7
0420−014	FSRQ	0.916	32.40	$1.7^{+0.21}_{-0.11}$	$1.6^{+0.11}_{-0.05}$	$1.7^{+0.11}_{-0.05}$	1.31	0.92	0.93	2.28	2.73	2.58	10.4
0422+004	BLO	0.310	25.59	...	$1.4^{+0.11}_{-0.11}$	...	...	0.63	...	...	3.64	...	...
0430+052	GAL	0.033	25.33	$1.8^{+0.11}_{-0.05}$	$1.7^{+0.21}_{-0.11}$	$1.7^{+0.11}_{-0.11}$	0.75	0.59	0.55	2.89	4.34	4.42	4.2
0528+134	FSRQ	2.060	24.18	...	$2.2^{+0.30}_{-0.30}$	...	...	0.99	...	...	1.80	...	12.2
0607−157	FSRQ	0.323	25.28	$1.6^{+0.11}_{-0.11}$	$1.8^{+0.11}_{-0.11}$	$1.9^{+0.11}_{-0.11}$	0.89	0.88	0.93	2.62	2.64	3.03	...

Table 7.1. Redshifts are taken from the NED. (1) Source types: FSRQ: flat spectrum radio quasars; BLO: BL Lac objects; GAL: radio galaxies; taken from the MOJAVE web site. (2) Total monitoring time T (in years), averaged over data from different frequencies (see Section 7.2 for details). (3) Power spectral indices of the best-fit simple power law models (Section 7.3.1). (4) Median duration of flares, obtained from fitting peaks in lightcurves with Gaussian functions (Section 7.3.3). (5) Widths of the distributions of the derivatives of lightcurves (Section 7.3.4). (6) Doppler factors from the literature, after correction of cosmological redshifts (Section 7.4.4). [b]Doppler factor from Lico et al. (2012), see also Tavecchio et al. (1998). [c]Doppler factor from Tavecchio et al. (1998), see also Katarzyński et al. (2001).

Properties of the sample

Object	Type	z	T [yr]	$\beta_{4.8}$	$\beta_{8.0}$	$\beta_{14.5}$	$\tau_{\rm med}^{4.8}$	$\tau_{\rm med}^{8.0}$	$\tau_{\rm med}^{14.5}$	$\sigma_{\rm der}^{4.8}$	$\sigma_{\rm der}^{8.0}$	$\sigma_{\rm der}^{14.5}$	δ_z
	(1)		(2)		(3)			(4)			(5)		(6)
0716+714	BLO	0.300	24.29	...	...	$1.4^{+0.05}_{-0.11}$	...	...	0.38	...	...	5.54	8.4
0735+178	BLO	0.424	25.47	...	$2.2^{+0.21}_{-0.30}$	$2.5^{+0.30}_{-0.40}$	...	1.20	1.23	...	1.61	1.70	2.7
0851+202	BLO	0.306	25.47	$1.6^{+0.05}_{-0.05}$	$1.5^{+0.11}_{-0.05}$	$1.6^{+0.11}_{-0.11}$	0.52	0.40	0.41	3.77	4.40	4.69	11.6
0923+392	FSRQ	0.695	25.50	$2.4^{+0.21}_{-0.11}$	$2.6^{+0.05}_{-0.40}$	$2.3^{+0.21}_{-0.05}$	2.03	1.71	2.16	1.24	1.68	1.47	2.5
1055+018	FSRQ	0.890	24.13	...	$1.7^{+0.11}_{-0.11}$	$1.7^{+0.21}_{-0.11}$	...	1.04	0.91	...	3.66	3.69	6.5
1101+384	BLO	0.030	25.71	...	$0.9^{+0.21}_{-0.11}$	$1.1^{+0.21}_{-0.11}$	...	0.57	0.44	...	10.04	8.42	3^b
1156+295	FSRQ	0.725	24.53	$1.4^{+0.11}_{-0.11}$	$1.5^{+0.11}_{-0.05}$	$1.6^{+0.11}_{-0.11}$	0.66	0.60	0.61	3.42	5.07	3.72	16.5
1226+023	FSRQ	0.158	25.55	$1.9^{+0.21}_{-0.11}$	$1.7^{+0.11}_{-0.11}$	$2.0^{+0.11}_{-0.11}$	0.88	0.99	0.86	2.56	2.21	2.17	11.6
1253−055	FSRQ	0.536	32.47	$2.5^{+0.40}_{-0.21}$	$2.2^{+0.11}_{-0.21}$	$1.6^{+0.11}_{-0.05}$	1.01	1.04	0.95	1.45	1.57	1.85	15.1
1308+326	FSRQ	0.998	25.42	$2.3^{+0.21}_{-0.21}$	$1.8^{+0.11}_{-0.11}$	$1.9^{+0.21}_{-0.21}$	1.31	0.89	0.81	1.55	2.80	2.54	7.7
1335−127	FSRQ	0.539	25.48	$1.6^{+0.11}_{-0.21}$	$1.8^{+0.05}_{-0.21}$	$1.6^{+0.11}_{-0.11}$	0.72	0.74	0.61	2.81	3.46	3.06	...
1413+135	BLO	0.247	24.78	...	$1.0^{+0.05}_{-0.05}$	$1.3^{+0.05}_{-0.11}$	...	0.67	0.53	...	6.29	3.96	9.8
1418+546	BLO	0.153	25.68	...	$1.7^{+0.11}_{-0.21}$	$1.6^{+0.11}_{-0.11}$	...	0.72	0.63	...	3.29	2.91	4.4
1510−089	FSRQ	0.360	25.47	$1.5^{+0.11}_{-0.11}$	$1.3^{+0.05}_{-0.11}$	$1.4^{+0.11}_{-0.05}$	0.43	0.31	0.34	4.58	6.18	6.57	20.2
1633+382	FSRQ	1.813	22.92	...	$1.8^{+0.30}_{-0.11}$	$2.1^{+0.60}_{-0.21}$	...	0.96	0.71	...	2.51	1.78	7.6
1641+399	FSRQ	0.593	32.43	$2.3^{+0.30}_{-0.11}$	$2.5^{+0.11}_{-0.21}$	$2.1^{+0.21}_{-0.21}$	1.72	1.55	1.63	1.72	1.89	2.16	9.4
1652+398	BLO	0.034	25.74	...	$1.5^{+0.21}_{-0.21}$	...	...	0.42	...	...	5.83	...	10^c

Table 7.1. Continued

Properties of the sample

Object	Type	z	T [yr]	$\beta_{4.8}$	$\beta_{8.0}$	$\beta_{14.5}$	$\tau_{\rm med}^{4.8}$	$\tau_{\rm med}^{8.0}$	$\tau_{\rm med}^{14.5}$	$\sigma_{\rm der}^{4.8}$	$\sigma_{\rm der}^{8.0}$	$\sigma_{\rm der}^{14.5}$	δ_z
	(1)		(2)		(3)			(4)			(5)		(6)
1730−130	FSRQ	0.902	32.34	...	$1.7^{+0.11}_{-0.05}$	$1.6^{+0.05}_{-0.21}$	...	0.98	1.04	...	1.93	1.64	5.6
1749+096	BLO	0.322	25.45	$1.3^{+0.11}_{-0.05}$	$1.6^{+0.05}_{-0.11}$	$1.4^{+0.05}_{-0.11}$	0.49	0.47	0.37	5.20	5.11	5.13	9.1
1803+784	BLO	0.680	24.54	...	...	$1.4^{+0.21}_{-0.11}$	...	...	0.63	...	...	3.68	11.4
1807+698	BLO	0.051	25.72	...	$1.6^{+0.40}_{-0.21}$	...	...	0.95	...	...	5.33	...	1.0
1921−293	FSRQ	0.353	25.57	...	$1.5^{+0.11}_{-0.11}$	$1.7^{+0.21}_{-0.11}$	...	0.90	0.73	...	2.41	2.53	...
1928+738	FSRQ	0.302	21.98	$1.7^{+0.30}_{-0.21}$	...	$1.3^{+0.21}_{-0.05}$	1.00	...	0.88	2.74	...	5.24	1.5
2005+403	FSRQ	1.736	25.30	...	...	$1.7^{+0.30}_{-0.11}$	...	...	1.23	...	...	2.95	4.9
2007+777	BLO	0.342	22.94	...	...	$1.7^{+0.21}_{-0.11}$	...	...	0.59	...	...	2.63	5.9
2134+004	FSRQ	1.945	25.72	...	$2.0^{+0.40}_{-0.21}$	$2.0^{+0.21}_{-0.30}$	...	0.84	1.20	...	3.83	3.06	5.5
2145+067	FSRQ	0.990	25.39	...	$2.2^{+0.40}_{-0.11}$	$2.0^{+0.40}_{-0.21}$	...	2.37	1.22	...	1.27	2.35	7.8
2200+420	BLO	0.069	32.44	$1.6^{+0.11}_{-0.11}$	$1.6^{+0.11}_{-0.05}$	$1.6^{+0.05}_{-0.05}$	0.47	0.42	0.43	3.96	4.29	4.48	6.6
2223−052	FSRQ	1.404	31.99	$1.9^{+0.11}_{-0.21}$	$1.7^{+0.11}_{-0.05}$	$1.9^{+0.11}_{-0.21}$	1.42	1.60	0.90	1.96	1.92	2.36	6.7
2230+114	FSRQ	1.037	25.50	...	$1.6^{+0.21}_{-0.05}$	$2.0^{+0.21}_{-0.21}$	...	0.89	0.77	...	4.44	3.40	8.4
2251+158	FSRQ	0.859	25.51	$1.8^{+0.05}_{-0.05}$	$2.0^{+0.11}_{-0.21}$	$1.7^{+0.11}_{-0.11}$	1.01	0.79	0.55	2.16	2.40	2.82	14.6

Table 7.1. Continued

1980 to around 2005. Table 7.1 shows an overview over the basic properties of our sources (partially taken from the NASA/IPAC Extragalactic Database, NED[3]).

7.3 Analysis

7.3.1 Lightcurves and Power Spectra

We binned our lightcurves in time to reduce any bias from irregular sampling and flagged obvious outliers by visual inspection. We used the bin size of $\Delta t = 2T/N$, where T is the total observing time and N is the number of data points. Binning of lightcurves can change the form of resulting power spectra because binning would remove power at frequencies higher than the frequency on which binning is performed ($f_{\rm bin}$). However, this effect would not affect our result since the highest sampling frequency in power spectra, $N_{\rm bin}/2T$, where $N_{\rm bin}$ is the number of data points after binning, is always smaller than $f_{\rm bin}$ ($N_{\rm bin} < N$ in our case). In other words, we did not reduce power at high sampling frequencies but we reduced the maximum sampling frequency instead. The fraction of flagged data is less than 1% in most cases, and flagging does not alter the results significantly. We employed the normalized Scargle periodogram for obtaining power spectra from irregularly sampled lightcurves (Scargle 1982). We used the fast algorithm devised by Press & Rybicki (1989) for computing periodograms. We performed Monte Carlo simulations of red-noise lightcurves using the algorithm of Timmer & König (1995) as we did already in Park & Trippe (2014). We summarize the main steps of the simulation process below.

Simulated power spectra. Artificial lightcurves can be computed by simulating complex spectra using the algorithm of Timmer & König (1995) and Fourier transforming these spectra. We began with artificial lightcurves that covered a tenfold longer timeline than the observed ones and cut out segments of appropriate length; this procedure reproduces the effects of red-noise leak (Uttley et al. 2002). The observed lightcurves still suffer from irregular sampling, i.e., many gaps, even after binning because the size

[3] `http://ned.ipac.caltech.edu/`

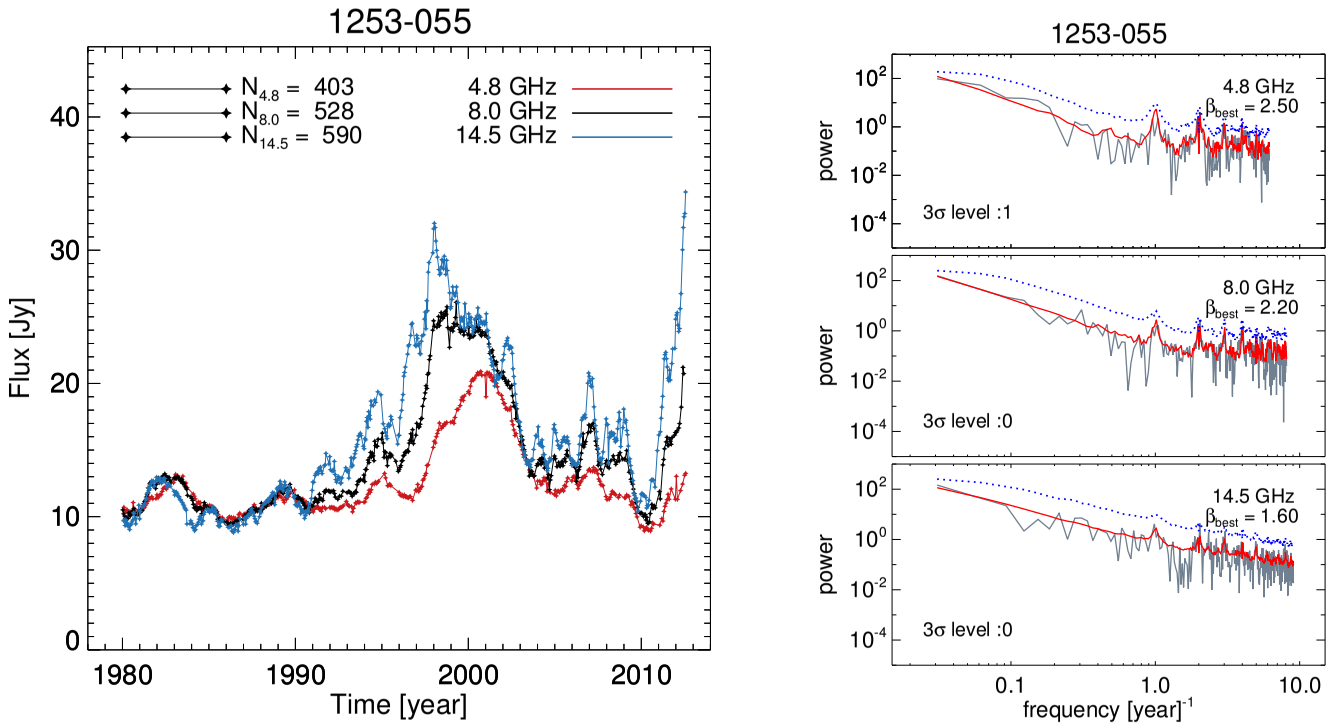

Figure 7.1. Illustration of our flux data and time series analysis. *Left*: Lightcurves of 1253−055 (after binning and flagging). Red, black, and blue lines and points are 4.8, 8, and 14.5 GHz data, respectively. The number of data points for each frequency, N, is noted. *Right*: Power spectra of the lightcurves in the left panel (black solid lines), the mean power spectra of 5 000 realizations of our simulation with the best-fit β values (red solid lines), and the 3σ significance levels for possible excess power (blue dotted lines). The best-fit β values ("$\beta_{\rm best}$ = ...") and the number of data points that exceed the significance levels ("3σ level : ...") are noted for each frequency.

of the gaps is usually much larger than the bin size. Therefore, we mapped the sampling pattern of the observed lightcurves into the simulated ones to take the effects of aliasing into account. The importance of this process was already noted in e.g., Park & Trippe (2014) and Isobe et al. (2015). We added Gaussian noise to each lightcurve; for each data point, we used the observational measurement error, multiplied by the ratio of the standard deviations of the simulated and the observed lightcurves. We note that our simulation process does not use interpolation of data.

Model fitting. For any given lightcurve, we simulated 5 000 power spectra for a range of β from 1 to 3 (from 1 to 4 for 0316+413) in steps of 0.1. At this stage, using a weighted least-squares 'goodness-of-fit' test is not possible because red-noise power spectra follow a non-Gaussian distribution. Therefore, we binned both the observed and the simulated power spectra logarithmically by a factor of 1.6 in frequency, as suggested by Papadakis & Lawrence (1993). We include at least two data points into each bin. To obtain the best-fit models of the observed power spectra, we calculated the standard goodness-of-fit parameter

$$\chi^2 = \sum_{i=1}^{N} \frac{\left[\overline{\log P(f_i)} - \langle\overline{\log P_s(f_i)}\rangle\right]^2}{\sigma^2_{\overline{\log P_s(f_i)}}}, \tag{7.1}$$

where $\overline{\log P(f_i)}$ is the ith value of the binned logarithmic periodogram of the observed lightcurve, and $\langle\overline{\log P_s(f_i)}\rangle$ and $\sigma^2_{\overline{\log P_s(f_i)}}$ are the average and the variance of the power spectra of the simulated lightcurves, respectively. In reality, covariance between power spectrum bins must be taken into account in addition to the variance. In principle, powers at different bins are uncorrelated with the frequency bins used in the Scargle periodogram (Scargle 1982). However, the observed power spectra actually suffer from convolution of the true spectra with a bias function, so-called 'Fejer kernel' (Priestley 1981), which comes from complex red-noise leak and aliasing of the spectra and generates possible correlation between different bins. However, this effect is already accounted in our Monte-Carlo simulation and thus we used the variance instead of using the full variance-covariance matrix. We determined the β value ($\beta_{\rm best}$) for which χ^2 is minimized ($\chi^2_{\rm min}$) and obtained the errors of $\beta_{\rm best}$ from the boundaries of the inter-

val in β where χ^2 becomes $\chi^2_{\rm min} + 1$. Since our simulation is limited to a resolution of 0.1 in β, we added an additional binning error of 0.05 in squares. We note that Isobe et al. (2015) obtained the best-fit model power spectra of their *Monitor of All Sky X-ray Image* (MAXI) lightcurves of Mrk 421 using this method. We illustrate the typical behavior of χ^2/d.o.f. as function of β for three sources in Figure 7.2; these three sources are representative of sources showing fast, moderate, and slow flux variability, respectively. Table 7.1 shows the best-fit values of β for our sources plus their errors.

Significance levels. We determined a 3σ (99.7%) significance level for each sampling frequency from the set of 5 000 simulated periodograms with $\beta_{\rm best}$ as we did in Park & Trippe (2014). A spectral power that exceeds the significance level at a certain sampling frequency might indicate the presence of a (quasi-)periodic signal. In Figure 7.5, we show the observed power spectra, the expected distributions resulting from averaging over 5 000 simulated power spectra with $\beta_{\rm best}$, and the significance levels of the three sources presented in Figure 7.2.

7.3.2 Fractal Dimension

The variability of a lightcurve can also be quantified via its fractal dimension (see e.g., Falconer 1990 for an exhaustive review). Basically, this quantity describes how much a given plane – flux density vs. time in our case – is filled by the graph of a given function. If small (large) scale fluctuations dominate, corresponding to smaller (larger) values of β in periodograms, the lightcurve fills a larger (smaller) fraction of the flux–time plane. The fractal dimension has been used to estimate the strength of spatial clustering of gas or stars and the effects of projection onto the sky plane (see e.g., Sánchez et al. 2005, 2010 and references therein). We specifically used the box-counting dimension defined by

$$d_f = -\lim_{\epsilon \to 0} \frac{\log N(\epsilon)}{\log \epsilon}, \tag{7.2}$$

where $N(\epsilon)$ is the number of cells of (dimensionless) size ϵ occupied by the lightcurve. In practice, ϵ is limited by the sampling of the lightcurve. For each lightcurve, we normalized the time axis to the interval from 0 to 1 and the flux density to zero mean

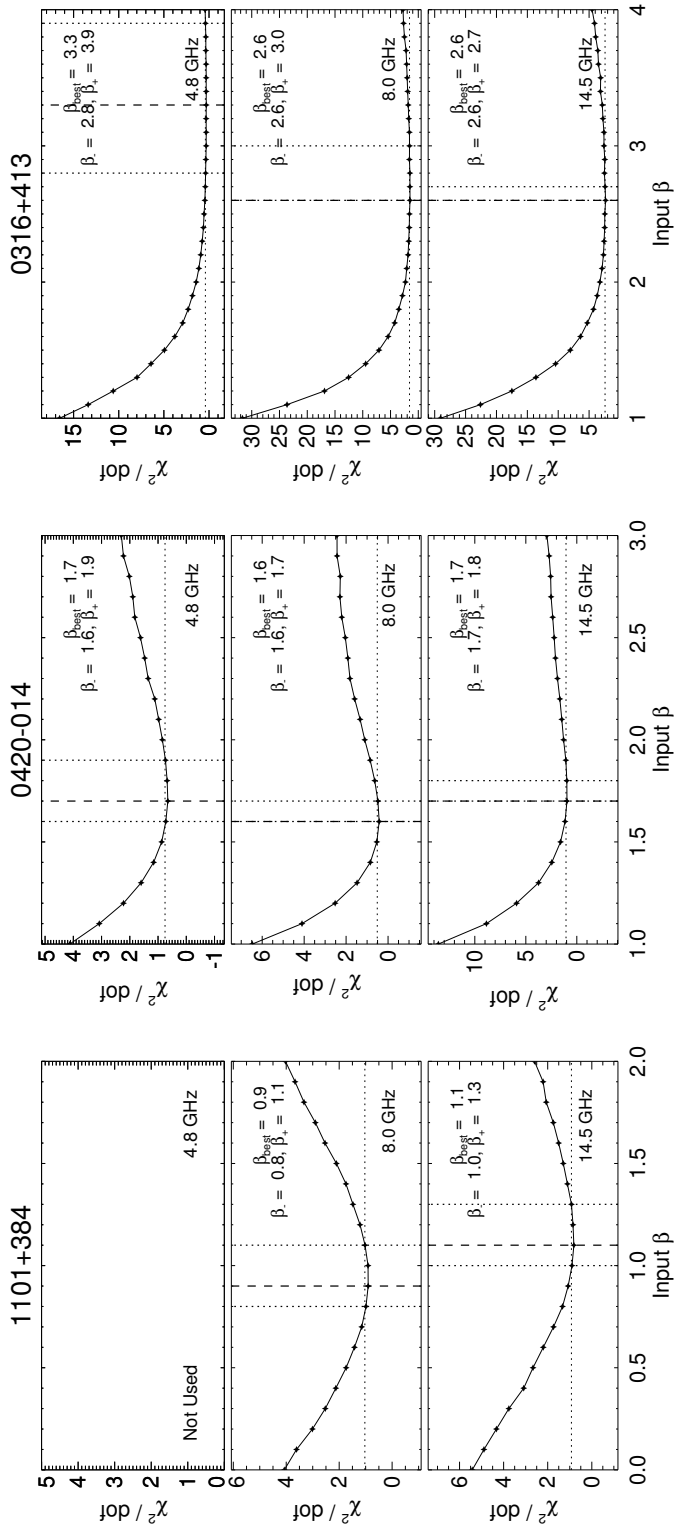

Figure 7.2. χ^2/d.o.f. of model power spectra as function of β for three sources. 'Not Used' means that we excluded the data from our analysis because the number of data points is smaller than 150. Horizontal dotted lines are the $\chi^2_{\rm min} + 1$ lines, i.e., the 68% significance levels. Vertical dashed lines show the values of β that minimize χ^2, $\beta_{\rm best}$. Vertical dotted lines indicate the two β values with $\chi^2 = \chi^2_{\rm min} + 1$, β_- and β_+.

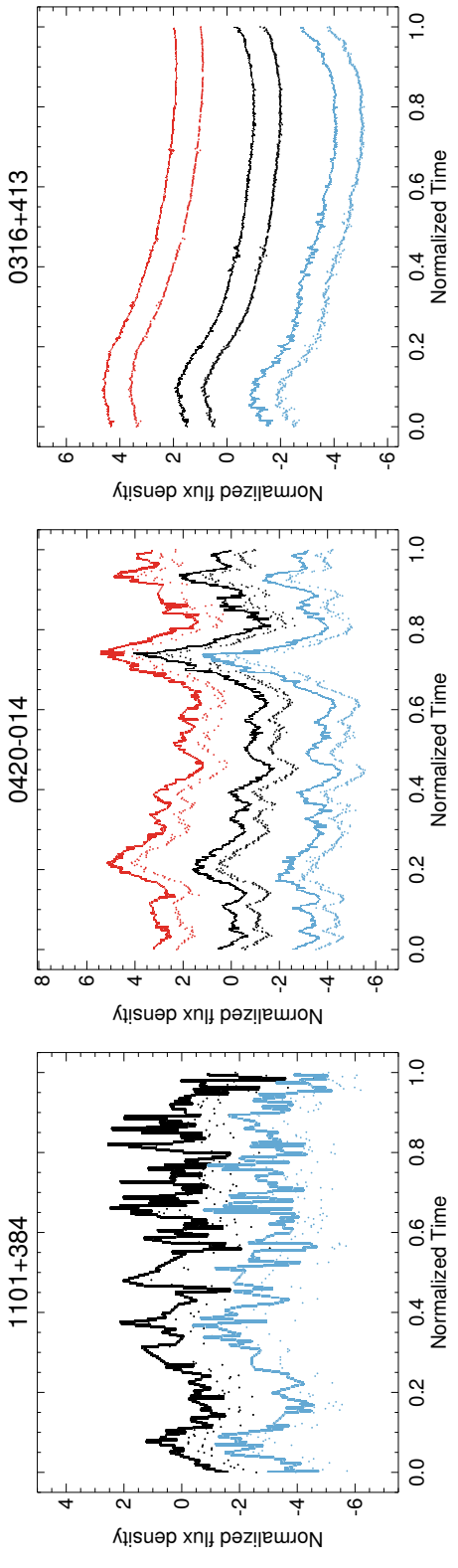

Figure 7.3. Illustration of fractal (box counting) dimension analysis of lightcurves. Each panel shows normalized lightcurves (dotted lines) and corresponding filled grid cells (solid lines, see Section 7.3.2 for details) in flux density versus time for one of the three sources presented in Figure 7.2. Red, black, and blue colours indicate the data points at 4.8, 8, 14.5 GHz, respectively. Lightcurves and filled grid cells are offset by 1 Jy for a given frequency, different frequencies are offset by 3 Jy for clarity.

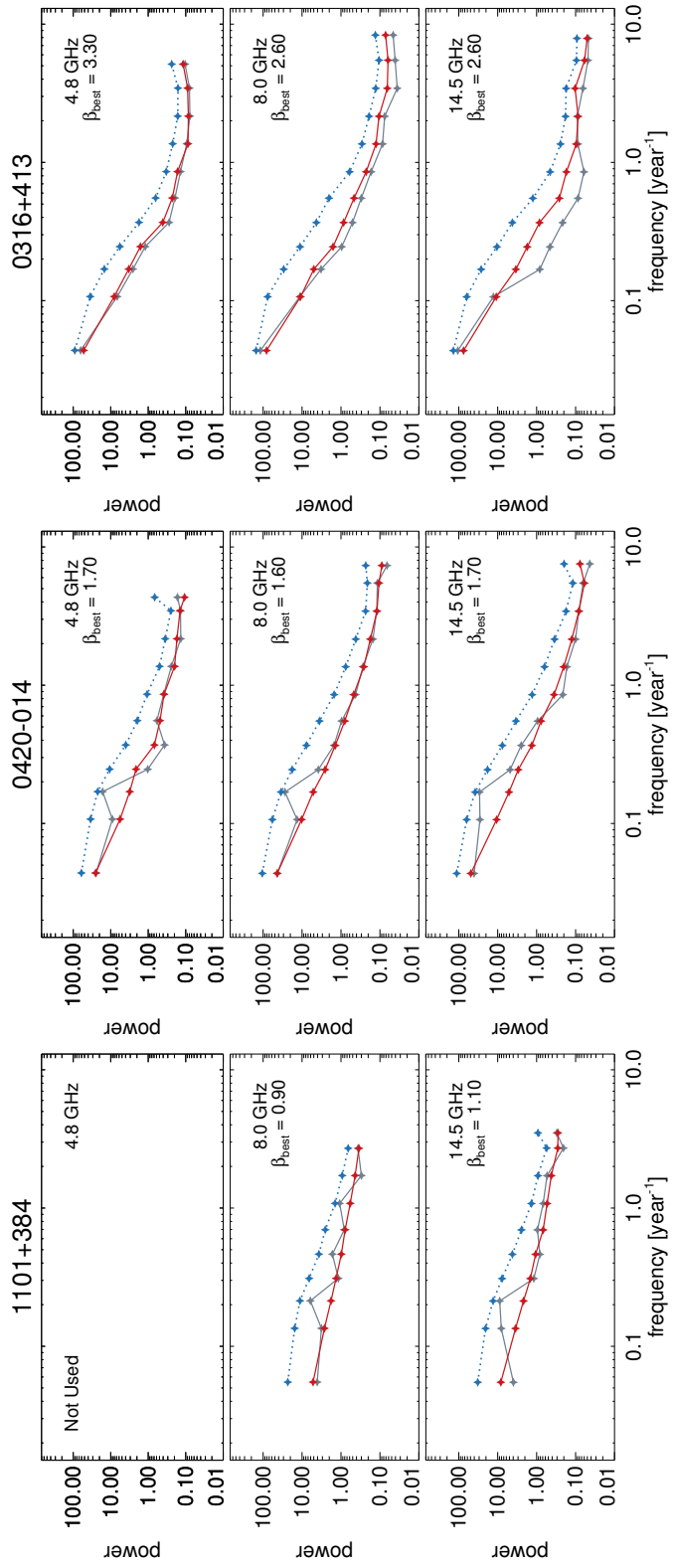

Figure 7.4. Binned logarithmic periodograms (black solid lines), best-fit simple power law models (red solid lines), and 3σ significance levels (blue dotted lines) for the three sources presented in Figure 7.2. In each diagram, $\beta_{\rm best}$ is noted.

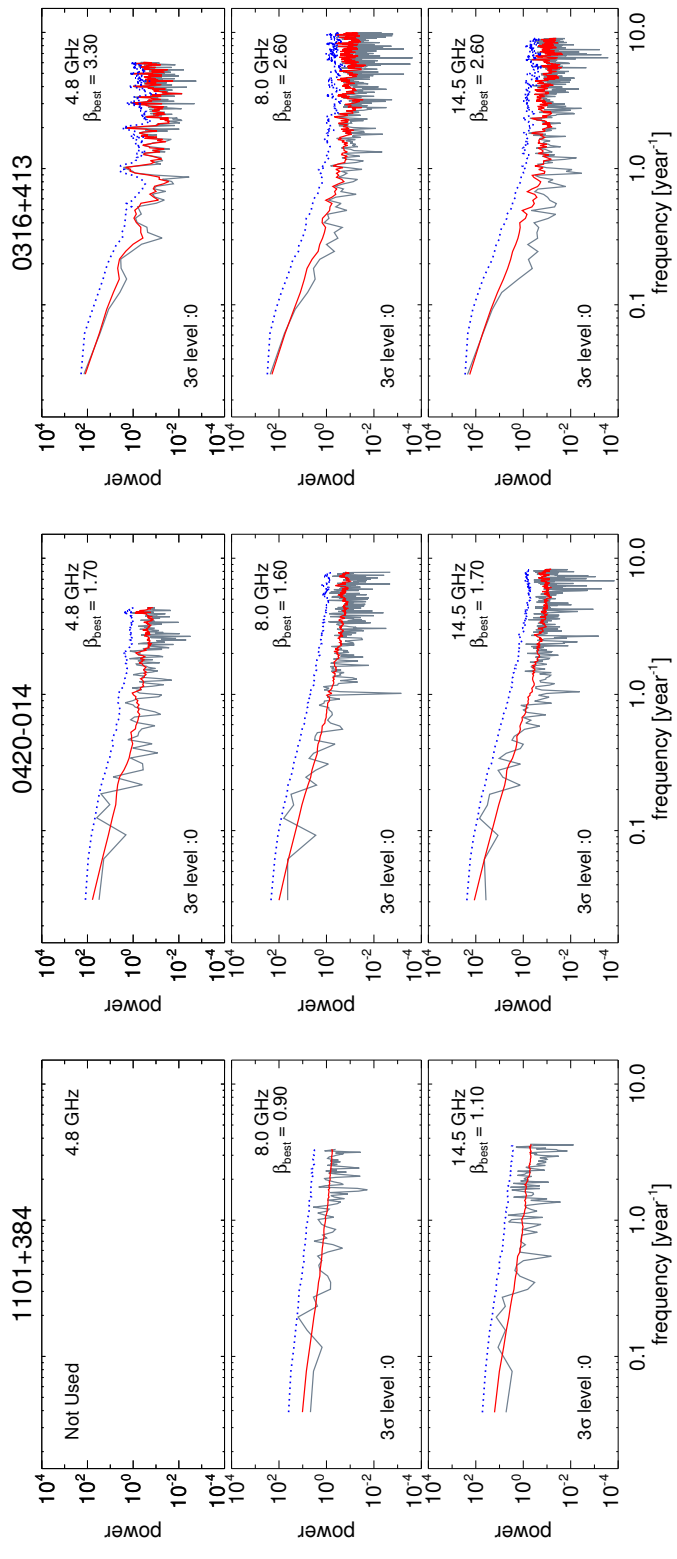

Figure 7.5. Same as Figure 7.4, for un-binned power spectra. In each diagram the number of data points exceeding the significance threshold ('3σ level : ...') is noted.

and unity standard deviation. We divided the normalized time axis into n sections with binsize ϵ and the normalized flux axis into n sections of size $10/n$ (because the flux densities happen to lie in the range of -5 to 5 for all lightcurves). In Figure 7.3, we show the normalized lightcurves and corresponding filled grid cells for the three sources presented in Figure 7.2.

7.3.3 Fitting Lightcurves Piecewise with Gaussian Peaks

Radio lightcurves of radio bright AGNs (mostly blazars) are characterized by multiple flaring events. Many studies have described flares either as exponentially rising and decaying (e.g., Valtaoja et al. 1999; Chatterjee et al. 2008, 2012; Abdo et al. 2010) or Gaussian (e.g., Pyatunina et al. 2006, 2007; Mohan et al. 2015) outbursts of radiation. As already noted by Valtaoja et al. (1999), the decomposition (or deconvolution) of lightcurves into several flares (specifically, the one-dimensional CLEAN method) do not work well at observing frequencies below 22 GHz where the overlap of individual flares is very strong because of the rather long evolutionary timescales of the outbursts. Thus, we divided the lightcurves of our sources into several pieces by visual inspection and fitted a single Gaussian function to each piece. We note that this process is different from the aforementioned deconvolution because we only analysed discrete (non-overlapping) segments of the lightcurves. In this case, the *amplitude* of the model flares can be substantially overestimated. However, our primary aim is to obtain the *duration* of the flares, for which our procedure is sufficient. In Figure 7.6, we show the observed lightcurves, the model lightcurves generated by combining the individual best-fit Gaussians, and the residuals between the data and the models of the three sources presented in Figure 7.2 at 14.5 GHz as an example. The model lightcurves represent the data very well in general, with the exception of some narrow spikes that are not caught by the smooth Gaussian profiles. Table 7.1 shows the median duration of flares for each lightcurve. Here, σ, the duration of the flare, refers to the Gaussian width, i.e., $f(t) \propto \exp[-(t-t_0)^2/2\sigma^2]$.

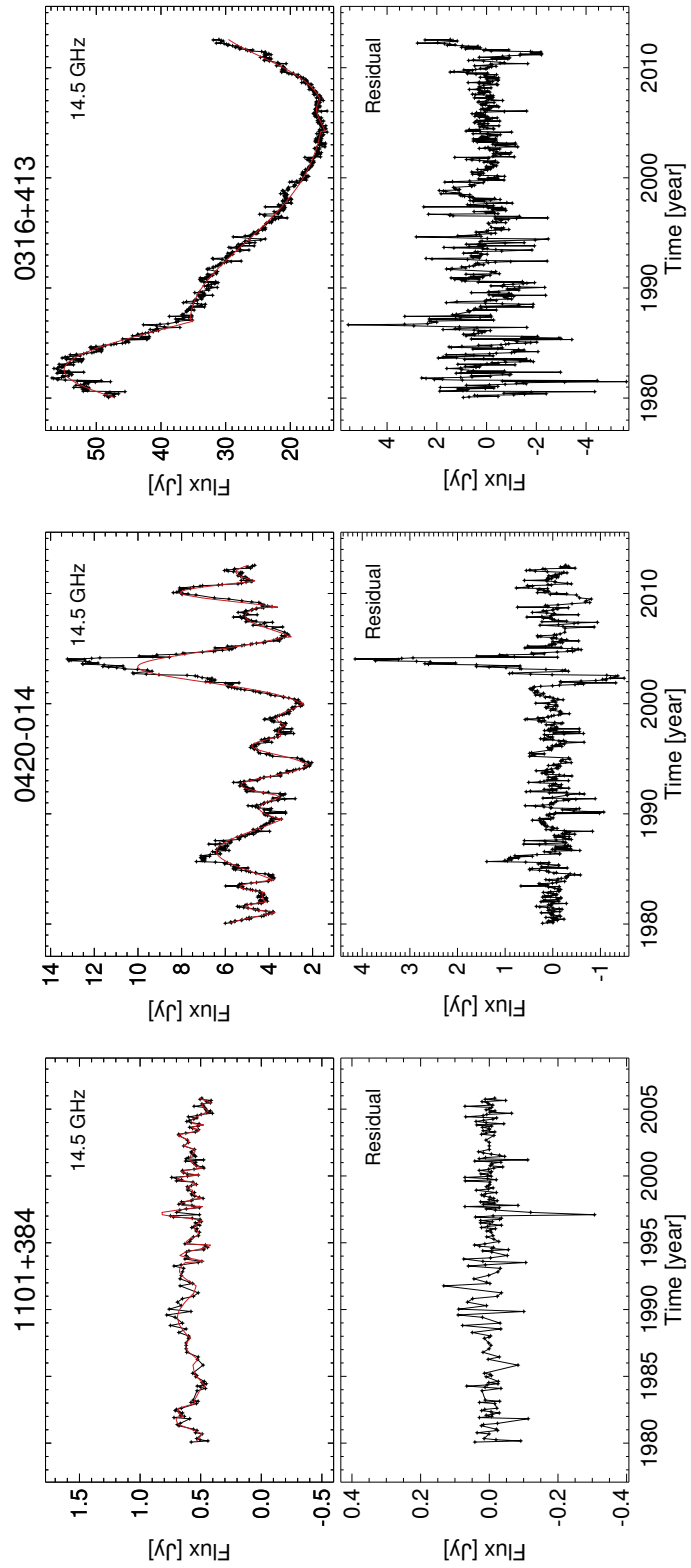

Figure 7.6. *Top panels*: Lightcurves (black solid lines) and model lines composed of Gaussian flares (red solid lines, see Section 7.3.3) of the three sources presented in Figure 7.2 at 14.5 GHz. *Bottom panels*: Residuals between data and models.

7.3.4 Derivatives of Lightcurves

We devised a new method to obtain variability timescales free from any *a priori* assumption on the functional form of flux variations (as we did in Section 7.3.3). The main idea is to take the derivative of a lightcurve as function of time, $\Delta S_\nu/\Delta t$ with ΔS_ν and Δt being the difference in flux density and time between adjacent data points, respectively, and to obtain the distribution function of the derivative values. Before taking the derivative, we normalized the lightcurves to zero mean and unity standard deviation. We used bootstrapping for estimating the errors of the distributions, which turned out to be close to binomial errors. We fitted a single Gaussian function to each distribution function, which was usually a good representation. We obtained the standard deviations of the best-fit Gaussians, $\sigma_{\rm der}$. Smaller values of $\sigma_{\rm der}$ mean that more time is necessary to make a certain amount of change in flux density. Accordingly, the inverse of $\sigma_{\rm der}$ provides an effective variability timescale; in our case, the unit of $\sigma_{\rm der}$ is $\rm yr^{-1}$. In Figure 7.7, we show the distribution functions of the derivatives and the fitted Gaussian functions of the three sources shown in Figure 7.2. We provide the $\sigma_{\rm der}$ values for our sources in Table 7.1.

7.3.5 Black Hole Masses and Accretion Rates

In order to examine if there is any correlation between variability timescale and black hole mass or accretion rate (and thus Eddington ratio), we searched the literature for the black hole masses $M_{\rm BH}$ and the disk luminosities $L_{\rm disk}$ of our sources. There has been significant progress in measuring the black hole mass of AGNs with various methods, including stellar dynamics (e.g., Kormendy & Richstone 1995; Ferrarese & Ford 2005), gas dynamics (e.g., Macchetto et al. 1997), the black hole mass–bulge luminosity relation ($M_{\rm BH}$-$L_{\rm bulge}$ relation; e.g., McLure & Dunlop 2001), single-epoch spectroscopy using the size–luminosity relation for AGN broad line regions (BLR) derived from reverberation mapping (e.g., Kaspi et al. 2000; McLure & Jarvis 2002; Kaspi et al. 2005), and the relation between the black hole mass and the velocity dispersion σ of the stellar system around the black hole, i.e., the $M_{\rm BH}$-σ relation (e.g., Gebhardt et al. 2000;

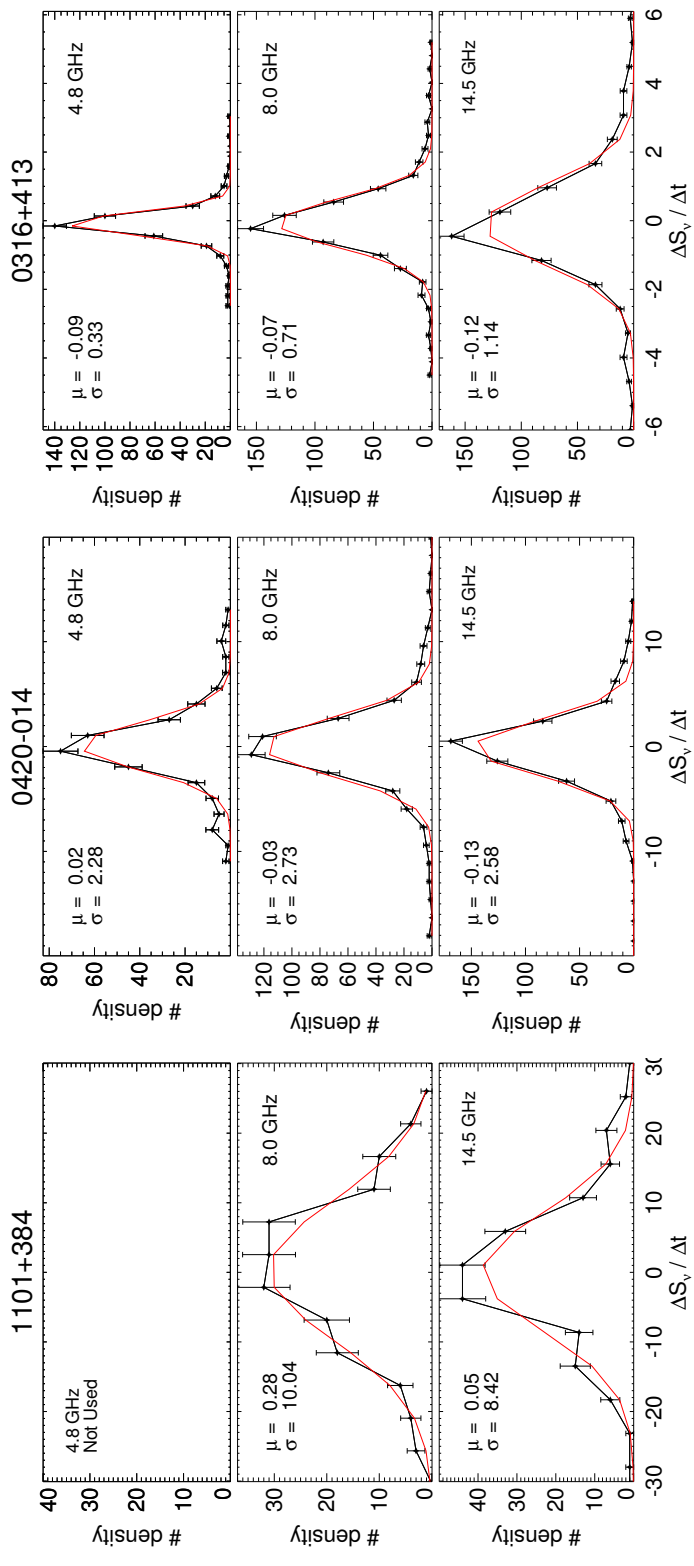

Figure 7.7. Distributions of the derivatives of the normalized lightcurves (black solid lines) and the best-fit Gaussian functions (red solid lines, see Section 7.3.4) of the three sources presented in Figure 7.2. Errors were estimated via bootstrapping with 1 000 random resamplings of given data set. The means and the standard deviations of the best-fit Gaussians are μ and σ, respectively.

Merritt & Ferrarese 2001; Tremaine et al. 2002). Using these empirical relations is a reasonable choice in our case; direct estimates of the black hole masses via, e.g., reverberation mapping, would require a dedicated long-term monitoring program which is beyond the scope of our work. A few studies have presented the black hole masses for radio bright AGNs, including many of our sources, with various methods (Gu et al. 2001; Woo & Urry 2002; Falomo et al. 2002, 2003a,b; Barth et al. 2003; Wang et al. 2004; Liu et al. 2006). However, some authors did not consider the contribution of non-thermal continuum emission of jets to the observed optical continuum luminosity in their single epoch spectroscopic mass measurements. This leads to overestimates of the sizes of BLRs and thus of the black hole masses. Liu et al. (2006) showed that the non-thermal contribution is indeed significant for their sample of radio loud AGNs. Therefore, we had to recalculate the black hole masses given in the abovementioned works. Our calculations use (a) emission line luminosities, which are almost not affected by the non-thermal continuum, and (b) the relation between the continuum luminosity and the emission line luminosity of radio quiet AGNs (Liu et al. 2006).

We used the data for three emission lines, Hβ, Mg II, and C IV (mainly from Wang et al. 2004; Liu et al. 2006; and Torrealba et al. 2012) for estimating black hole masses via single epoch spectroscopy. We used the relation between black hole mass, full width at half maximum (FWHM), and luminosity of Hβ line of Vestergaard & Peterson (2006),

$$\frac{M_{\rm BH}}{M_\odot} = 10^{6.67} \left[\frac{\rm FWHM(H\beta)}{1000\ {\rm km\ s^{-1}}}\right]^2 \left[\frac{L(\rm H\beta)}{10^{42}\ {\rm ergs\ s^{-1}}}\right]^{0.63} \tag{7.3}$$

and the corresponding relation of Vestergaard & Osmer (2009) for the Mg II line,

$$\frac{M_{\rm BH}}{M_\odot} = 10^{6.96} \left[\frac{\rm FWHM(Mg\,II)}{1000\ {\rm km\ s^{-1}}}\right]^2 \left[\frac{L_{5100\text{Å}}}{10^{44}\ {\rm ergs\ s^{-1}}}\right]^{0.5} \tag{7.4}$$

where $L_{5100\text{Å}}$ is the monochromatic luminosity at 5100 Å. For using the latter relation, we first converted the Mg II luminosity to Hβ luminosity following Francis et al. (1991) who found the ratio of the luminosities between these emission lines to be $L(\rm H\beta) : L(Mg\,II) = 22 : 34$. Then, we obtained $L_{5100\text{Å}}$ from the relation between the monochromatic luminosity at 5100Å and the Hβ luminosity for radio-quiet AGNs

presented in Liu et al. (2006), assuming the same relation holds for radio-loud AGNs:

$$L_{5100\text{Å}} = 0.843 \times 10^2 L_{\text{H}\beta}^{0.998}. \quad (7.5)$$

For the C IV lines, we followed Liu et al. (2006) who assumed that the radius of C IV emitting BLRs is about half of that of Hβ emitting BLRs (see references therein) and used the BLR size–luminosity relation of Kaspi et al. (2005) for Hβ. We recalculated the black hole masses presented in Wang et al. (2004) obtained via single epoch spectroscopy, using the aforementioned methods, scaling relations, and our adopted cosmological parameters that are slightly different from those in their work. We used the black hole masses from Liu et al. (2006) without any modification because they already took the contribution by non-thermal emission into account. We also made use of the optical spectroscopic atlas of the MOJAVE / 2 cm AGN sample of Torrealba et al. (2012) and estimated black hole masses from their velocity dispersions and line luminosities.

We also included black hole masses derived via the M_{BH}-σ relation (Falomo et al. 2003a,b; Barth et al. 2003), the rotation velocity of H_2 gas around the black hole (Wilman et al. 2005), and the M_{BH}-L_{bulge} relation (Bettoni et al. 2003) from the literature. We unified the black hole masses derived from various M_{BH}-σ relations into that of Tremaine et al. (2002). We summarized all black hole masses we obtained in Table 7.3. The absolute magnitudes of host galaxies, M_R, shown in Table 7.3 were obtained by using cosmological parameter values ($H_0 = 50$ km s^{-1} Mpc^{-1} and $\Omega_0 = 0$; see Falomo et al. 2003a) different from ours. We did not modify them because the same parameter values were used to derive the M_{BH}-L_{bulge} relation in Bettoni et al. (2003). We averaged the black hole masses for each source (if there was more than one measurement)[4].

The uncertainty of a given black hole mass is hard to quantify because of different geometries and kinematics of BLRs that give rise to errors in single epoch spectroscopic mass measurements (e.g., Vestergaard & Peterson 2006; Park et al. 2012), intrinsic scatter in the M_{BH}-σ relation (e.g., Kormendy & Ho 2013), insufficient bolometric

[4]We used the geometric mean for the averaging of the black hole masses. We note that using the geometric and the arithmetic mean in linear space led to almost the same result.

corrections of monochromatic continuum luminosities (Trippe 2015), and potentially further effects. We adopt an error of 0.3 dex if the averaged black hole mass involves the $M_{\rm BH}$-σ relation or single epoch spectroscopy with Hβ and Mg II lines ($M_{\rm BH}$(Hβ), $M_{\rm BH}$(Mg II)), and of 0.4 dex if only $M_{\rm BH}$(C IV) or a black hole mass obtained with the $M_{\rm BH}$-$L_{\rm bulge}$ relation was available. The above values were adopted based on the discussion on errors in black hole mass estimation with single epoch spectroscopy of Ho et al. (2012), the intrinsic scatter in the $M_{\rm BH}$-σ relation shown in Kormendy & Ho (2013), and the scatter found in the $M_{\rm BH}$-$L_{\rm bulge}$ relation of Bettoni et al. (2003).

We obtained the disk luminosities in Eddington units using the adopted black hole masses and the relation $L_{\rm Edd} \approx 1.5 \times 10^{38} (M_{\rm BH}/M_{\odot})$ erg s^{-1} (cf., e.g., Netzer 2013), which can be used to obtain accretion rates and Eddington ratios when employing certain reasonable assumptions (see Section 7.4.4). The disk luminosity was calculated by assuming $L_{\rm disk} \approx 10 L_{\rm BLR}$ according to Ghisellini et al. (2011), where $L_{\rm BLR}$ is the BLR luminosity and was obtained following Celotti et al. (1997) who showed that $L_{\rm BLR}/L_{{\rm Ly}\alpha} = 5.56$, based on, e.g., Francis et al. (1991). We averaged the disk luminosities for each source if multiple values from different line luminosities were available (mostly from Wang et al. 2004; Liu et al. 2006, and Torrealba et al. 2012). We obtained measurement uncertainties for the disk luminosities from those sources with $L_{\rm disk}$ derived from various emission lines, which allowed us to use the standard deviation of the luminosities as error. Since this was possible for only some of our sources, we adopt the mean values of their errors as typical errors for the other sources. We note that the estimated errors are governed by the assumption of constant line ratios rather than measurement errors in the luminosity of each line.

7.4 Results and Discussion

7.4.1 General Features of Power Spectra

Using the procedure outlined in Section 7.3.1, we obtained best-fit β values for our sources ranging from $\approx$1 to $\approx$3. The observed power spectra are in general well described

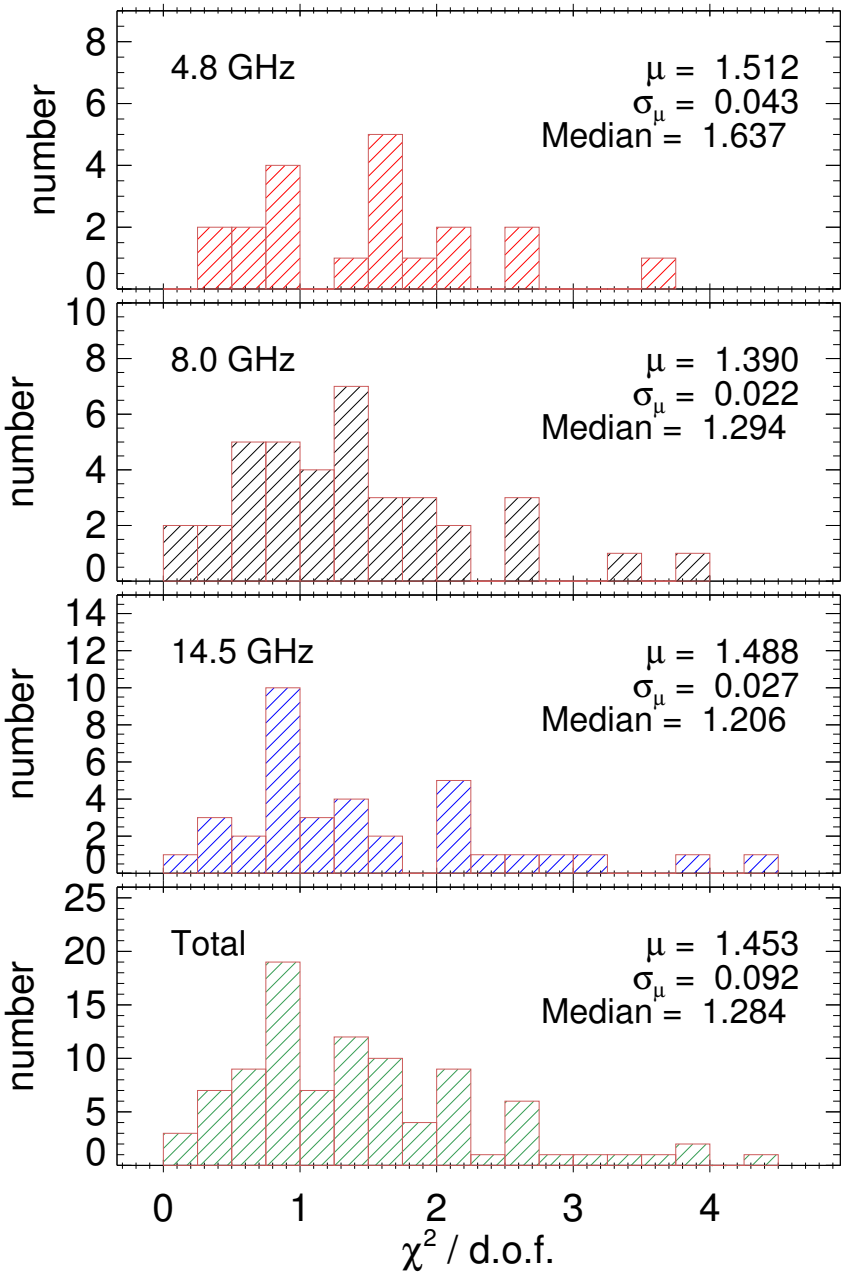

Figure 7.8. Distribution of χ^2/d.o.f. for best-fit model periodograms calculated as outlined in Section 7.3.1. From top to bottom, panels show the results for 4.8 GHz, 8 GHz, 14.5 GHz, and all lightcurves combined, respectively. The mean (μ), the standard error of mean (σ_μ), and the median of the distribution are noted in each panel.

by simple powerlaw models. In Figure 7.8, we show the distribution of χ^2/d.o.f. of our best-fit models, which is concentrated around unity, though with notable scatter. We deal with a few sources with large χ^2/d.o.f. in Section 7.4.5. We found the timescales $\tau_{\rm med}$ to range from ≈0.3 to ≈6.5 years and $\sigma_{\rm der}$ to range from ≈0.3 to ≈10 yr^{-1} over all sources. We note that our best-fit model periodograms reproduce the local peaks seen in the observed power spectra for some sources (e.g.,1253−055 in Figure 7.1 and 0316+413 in Figure 7.5). This result indicates that such patterns are introduced by the sampling of the lightcurves, not by source-intrinsic variability. Accordingly, interpreting any local peak in a power spectrum as an indication for quasi-periodic oscillations requires careful modelling of the power spectrum in order to prevent false positives.

7.4.2 Distributions of Fractal Dimension

We show the relation between β and the fractal (box-counting) dimension of the lightcurves (cf. Section 7.3.2), d_f, in Figure 7.9. We find a strong anti-correlation with correlation coefficients (Pearson and Spearman rank) around -0.8.[5] At least qualitatively, this seems rather obvious because a larger fractal dimension means that a light curve fills more grid cells. This in turn implies a more strongly fluctuating lightcurve which comes with a smaller value of β. Even though, we present here for the first time the quantitative relation between β and d_f,

$$\beta = -(4.43 \pm 0.26) d_f + (7.65 \pm 0.35). \tag{7.6}$$

This relation holds over a wide range of β values from ≈1 to ≈3 within errors with no notable dependency on observing frequency. This result provides a good independent check of our methodology.

[5]Obtaining meaningful correlation coefficients requires that the data under study are uncorrelated. This is not always strictly the case in our analysis because we include data originating from different lightcurves (at two or three frequencies) from the same source. However, the lightcurves at different frequencies are quite different in general and show different sampling patterns. Therefore, we do not average data in frequency except when studying parameters (such as black hole mass) that cannot depend on frequency.

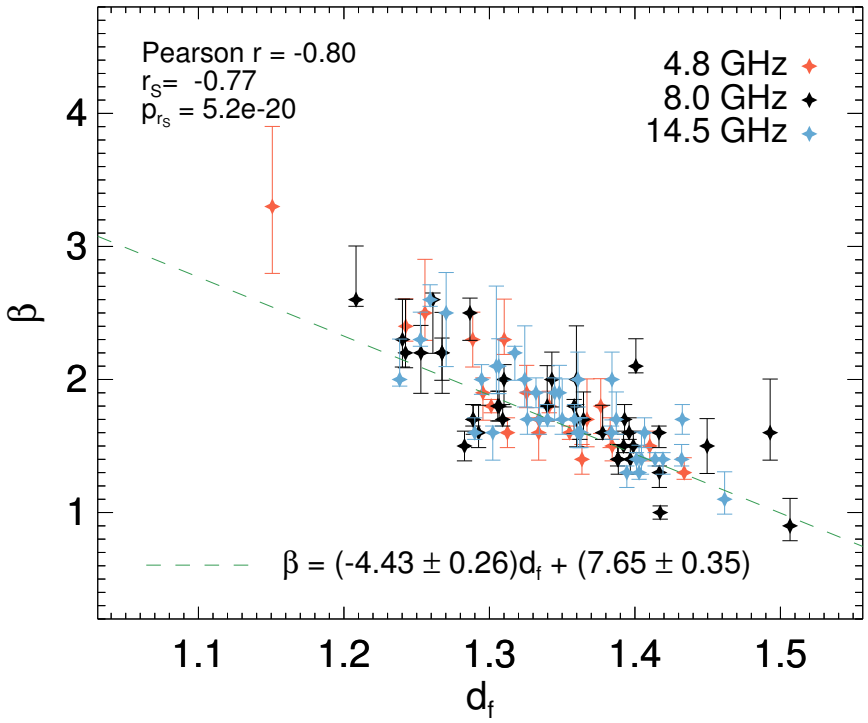

Figure 7.9. Power spectral index β versus fractal dimension d_f. Red, black, and blue points are 4.8, 8, and 14.5 GHz data, respectively. The green dashed line is the best-fit line to the data; the best-fit parameters are shown below at the bottom of the plot. The Pearson correlation coefficient r, the Spearman rank correlation coefficient r_s, and the statistical false-alarm probability of r_s, p_{r_s}, are noted in the top left of the diagram.

7.4.3 β as an Indicator of Variability Timescale

We find a strong correlation between the power spectral index β and the logarithm of the median duration of the flares obtained in Section 7.3.3 (left panel of Figure 7.10). The best-fit linear relation is $\beta \propto 0.99 \log \tau_{\rm med}$,[6] where $\tau_{\rm med}$ is the median duration of flares. This result implies that the longer the overall duration of the flares of radio bright

[6] Actually, χ^2 fitting assumes that errors are symmetric, whereas we obtained asymmetric errors for β. To be conservative, we used the larger error for fitting.

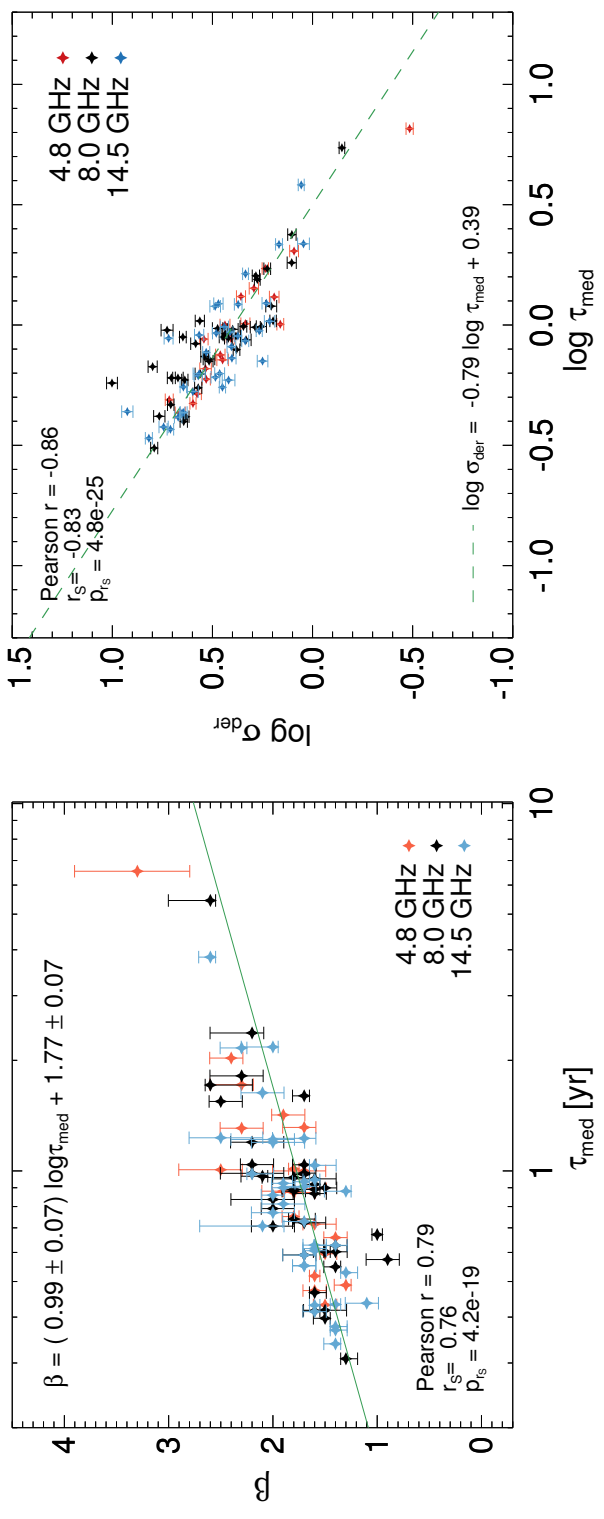

Figure 7.10. *Left:* Power law index β as function of median duration of flares, $\tau_{\rm med}$. Red, black, and blue are 4.8, 8, and 14.5 GHz data, respectively. The green solid line is the best-fit line, the corresponding parameters are shown at the top of the plot. The Pearson correlation coefficient r, the Spearman rank correlation coefficient r_s, and the false-alarm probability of r_s, p_{r_s}, are given at the bottom left. *Right:* Logarithm of the width of the distribution of the derivatives of lightcurves, $\log \sigma_{\rm der}$, as function of $\log \tau_{\rm med}$. The green dashed line is the best-fit line, the best-fit parameters are provided at the bottom of the plot.

AGNs, the steeper the power spectra. Technically, such behavior is straightforward to understand: if a source shows flares with long duration, its lightcurve is dominated by long-term variability, which leads to steeper power spectra. However, the duration of flares is arguably related to fundamental physical processes in the AGN (like shocks in jets), and thus to various physical parameters (e.g., Marscher & Gear 1985; Fromm et al. 2011). In turn, this indicates that β can be used to derive some physical parameters of AGNs (to be specified below).

Else than AGN variability at high observing frequencies (especially X-rays), radio variability has not received much attention because of the difficulties in quantifying the properties of the variability. The power spectra of AGNs at radio wavelengths usually show featureless simple power-law noise as seen in Figure 7.5 but no characteristic break frequencies as found in X-rays. From the relation between β and the median duration of flares, we conclude that the slope of the power spectra represents the variability timescales of radio bright AGNs. This implies that measurements of β are able to reveal the complex accretion and jet physics of AGNs.

The left panel of Figure 7.10 shows that the data points at large $\tau_{\rm med}$ tend to lie above the best fit line. This is mainly because the number of flares becomes very small (three to five) for sources with large flare durations, thus making the use of the median problematic. In addition, the approach used in Section 7.3.3 makes a strong assumption, namely that all lightcurves can be described as sequences of flares with Gaussian profiles – an assumption that may or may not be generally valid.

In order to arrive at a more robust estimate, we focus on the parameter $\sigma_{\rm der}$, the width of the distribution of the derivatives of a lightcurve obtained in Section 7.3.4, instead of $\tau_{\rm med}$ in the following. The parameter $\sigma_{\rm der}$ is inversely proportional to the effective variability timescale of a given lightcurve. It uses all data in a lightcurve, making its use statistically more rigorous than using the median duration of flares. In addition, the (statistical) errors of $\sigma_{\rm der}$ are known. As shown in the right panel of Figure 7.10, $\log \sigma_{\rm der}$ and $\log \tau_{\rm med}$ indeed show a strong anti-correlation. The scatter around the best-fit line in that figure and the fact that the two quantities do not show

a one-to-one relation demonstrate the limited accuracy of the median duration of flares as a proxy for an effective variability timescale. Indeed, $\sigma_{\rm der}$ does contain information on flaring activity, especially the duration of flares: if the variability is dominated by flares with longer duration, this will lead to smaller $\sigma_{\rm der}$ regardless of our choice of models for fitting the lightcurves (compare Figure 7.6 and 7.7).

We analyzed the relation between β and $\log \sigma_{\rm der}$. A linear regression returns $\beta \propto -(1.39 \pm 0.08) \log \sigma_{\rm der}$ (see the left panel of Figure 7.11). We employed the FITEXY estimator (Press et al. 1992) for a linear fit to data with errors on both axes.[7] We checked whether the observed relation between β and $\log \tau_{\rm med}$ also appears in simulated data using red-noise only lightcurves. We generated 100 artificial lightcurves using the method of Timmer & König (1995) with β ranging from 1 to 2.8. The simulated lightcurves were sampled at equal intervals. We added Gaussian noise amounting to 2% of the standard deviation of a given lightcurve to take the effect of measurement noise into consideration. We obtained $\sigma_{\rm der}$ from the distribution of the derivatives of the normalized simulated lightcurves as we did for the observed lightcurves. The relation between β and $\log \sigma_{\rm der}$ for the simulated data is shown in the right panel of Figure 7.11. Overall, the data points are described well by a power-law function, the slope is (within $\sim 2\sigma$) consistent with the observed one. We note that the value of the constant term is arbitrary because the unit of time is arbitrary.

The consistency between observed and simulated $\beta - \log \sigma_{\rm der}$ relations indicates that the observed relation is actually a generic feature of red noise lightcurves. One might ask if this conclusion is consistent with the presence of distinct flares in the radio lightcurves of AGNs – flares are deterministic, whereas red-noise time series are stochastic by nature. When a flare begins, the flux density increases during the Compton and synchrotron stages (see e.g., Marscher & Gear 1985; Valtaoja et al. 1992; Fromm et al. 2011) but decays eventually. Accordingly, we have to conclude that the aperiodic occurrence of flares makes an AGN lightcurve a red-noise time series. The duration of

[7] We refer the reader to Tremaine et al. (2002) who discuss the advantages and disadvantages of this method over other fitting algorithms and to Kelly (2007) who deal with more complicated situations.

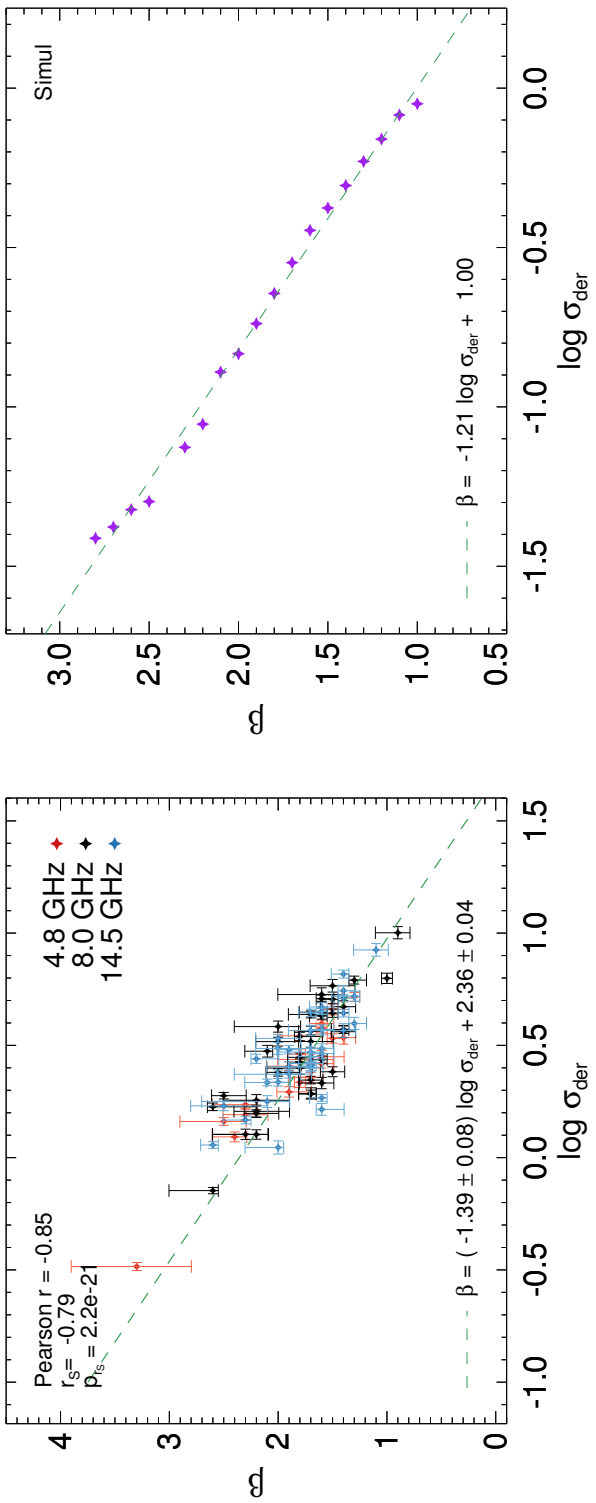

Figure 7.11. *Left:* Power law index β as function of $\log \sigma_{\rm der}$ (which is defined in Section 7.3.4, in units of $\rm yr^{-1}$). Red, black, and blue colours indicate 4.8, 8, and 14.5 GHz data, respectively. The green dashed line shows the best-fit line (using errors on both axes with the FITEXY estimator; cf. Section 7.4.3). The error bars of $\log \sigma_{\rm der}$ were obtained by using the standard error propagation of the errors in $\sigma_{\rm der}$. The Pearson correlation coefficient r, the Spearman rank correlation coefficient r_s, the false-alarm probability of r_s, p_{r_s}, and the result of the linear regression are noted in the diagram. *Right:* Same as the left panel, for *simulated* red-noise lightcurves (see Section 7.4.3 for details).

flares changes with time and flares occur at random times, leading to frequent superposition of flares (see, e.g., Figure 7.6). This behaviour might originate from underlying physical processes such as a long-term, red-noise like variability of accretion rate and/or particle injection rate into jets that is physically correlated over a time comparable to the observation period. In this case, we expect to find power spectra with a single slope over a large range of sampling frequencies. However, as we will see below, a few sources show a flattening of their power spectra at low sampling frequencies; this implies that the timescales over which an emission process is correlated can be shorter than the observation period, roughly on the order of the typical duration of flares. We will discuss the possible origin of featureless red-noise power spectra in more detail in Section 7.4.5.

7.4.4 Relation between β and the Accretion Rate

The reason why different radio bright AGNs show different variability patterns, specifically different β, is not well-studied. In the case of radio-quiet, optical/X-ray bright AGNs and GBHs, a well-known scaling relation between the timescales that correspond to the break frequencies in their power spectra and the black hole mass indicates that their variability timescales are determined by the size of the emitting region (e.g., M$^{\rm c}$Hardy et al. 2004; Uttley & M$^{\rm c}$Hardy 2005; Kelly et al. 2009, 2011). This size would be proportional to the Schwarzschild radius which in turn scales linearly with the black hole mass. However, it is not clear if a similar scaling relation also holds for radio bright AGNs. Radio bright AGNs emit their flux from relativistic jets instead of accretion disks, and emit synchrotron radiation instead of thermal radiation. Therefore, one first needs to find a physical mechanism that determines the duration of radio flares.

As noted in Section 7.3.3, our lightcurves can be described as sequences of Gaussian – and thus symmetric in time – flux peaks. Time-symmetric flares from blazars have been observed at multiple observing frequencies (see, e.g., Hovatta et al. 2008 for radio, Chatterjee et al. 2012 for optical and γ-ray, and Abdo et al. 2010 for γ-ray observations). The symmetry in time has been interpreted as the result of rise and decay timescales being determined by the crossing time of radiation (or particles) through the emission

region. Jorstad et al. (2005) showed that the radiative cooling time is shorter than the cooling timescale of adiabatic expansion for almost all jet components in their VLBI blazar sample. Therefore, one may expect the duration of flares to be given by the sizes of emission regions.

In most cases, radio flares of AGNs are associated with the inner regions of jets (often identified with compact VLBI cores). Especially, there is growing evidence for interaction of moving jets with (probably) stationary cores, leading to strong flares at high energies (from optical to γ-rays) and, likewise, at cm/mm wavelengths (Savolainen et al. 2002; León-Tavares et al. 2010; Arshakian et al. 2010). The cm/mm flares show much broader flare widths and time delays relative to the high energy flares, likely due to relatively long cooling timescales and high optical depths (e.g., Savolainen et al. 2006; Jorstad et al. 2010; Marscher et al. 2008, 2010, 2012; Marscher 2013). If the core is a conical, standing shock (commonly assumed to be a recollimation shock, see e.g., Cawthorne 2006; Cawthorne et al. 2013; Marscher 2006, 2014), then the duration of flares would be determined by the crossing time of jet material through the shock. The core might actually consist of multiple stationary shocks; stationary knots in addition to the cores have been discovered by VLBI for many, usually nearby, sources (e.g., Jorstad et al. 2005, 2010; Cohen et al. 2014).

In this scenario, higher rates of matter injection into AGN jets would lead to longer flare durations, or variability timescales, if the particle densities and bulk velocities of inner jets are similar across our sample. These assumptions are supported by observations of the particle densities in the jets of several blazars (O'Sullivan & Gabuzda 2009a) and the fact that the location of standing shocks is expected to be at the end of the acceleration and collimation zone of the jet (e.g., Marscher et al. 2008; Marscher 2014). The rate of matter injection into the jet, $\dot{M}_{\rm jet}$, would (largely) determine variability timescales in radio bright AGNs. In a given time interval an AGN with higher $\dot{M}_{\rm jet}$ would show, say, one major flare while those with smaller $\dot{M}_{\rm jet}$ would show multiple minor flares. Recent theoretical studies actually show that the rate of electron injection into jets can play an important role in determining the slope of power spectra

(Finke & Becker 2014, 2015).

Ghisellini et al. (2014) found a correlation between the jet power $P_{\rm jet}$ and the accretion power of blazars of the form $P_{\rm jet} \propto \dot{M}_{\rm acc}$, where $\dot{M}_{\rm acc}$ is the accretion rate. The jet power $P_{\rm jet}$ is given by the kinetic energy per time, i.e., $P_{\rm jet} \approx (\Gamma - 1)\dot{M}_{\rm jet}c^2$, where Γ is the Lorentz factor. Since our sources are luminous blazars and usually show superluminal proper motions, their Lorentz factors are located in a rather narrow range (cf. Ghisellini et al. 2014). Thus, we have $P_{\rm jet} \propto \dot{M}_{\rm jet} \propto \dot{M}_{\rm acc}$. Evidence for the proportionality between $\dot{M}_{\rm jet}$ and $\dot{M}_{\rm acc}$ has been provided by Chatterjee et al. (2009, 2011) who discovered that significant dips in the X-ray light curves of the radio galaxies 3C 111 and 3C 120 are followed by ejections of new superluminal jet components. This indicates that X-ray emitting matter in hot coronae and/or the innermost accretion disks is ejected in a jet outflows. Combining the various arguments, we examined if radio bright AGNs indeed show a scaling relation between the variability timescales and the accretion rates.

When comparing the observed variability timescales with other parameters we need to correct for the effects of Doppler boosting. The observed variability timescale is decreased relative to the intrinsic one, $\tau_{\rm var}$, by the Doppler factor $\delta = 1/\Gamma(1 - \beta\cos\theta)$, where Γ is the Lorentz factor, β is the jet speed in units of speed of light, and θ is the angle between the jet axis and the line of sight. If cosmological redshift is non-negligible, the total Doppler factor is $\delta_z = \delta/(1 + z)$. If we assume that the variability timescales of our sources scale with the accretion rate to a power α, i.e., $\tau_{\rm var} \propto \dot{M}^{\alpha}_{\rm acc}/\delta_z$, then we find from the relation $\beta \propto 1.39 \log \tau_{\rm var}$ (see Section 7.4.3)

$$\beta \propto 1.39\alpha \log \dot{M}_{\rm acc} - 1.39 \log \delta_z. \tag{7.7}$$

The Doppler factor is difficult to measure directly because the two parameters involved, intrinsic jet speed and viewing angle, are hard to disentangle in many cases. Nevertheless, Hovatta et al. (2009) obtained the Doppler factors of many of our sources. They decomposed their lightcurves obtained at 22 and 37 GHz into exponentially rising and decaying flares. They assumed that the brightness temperature derived from the flux variability differs from the radiating particle–magnetic field energy equipartition

temperature by the Doppler factor (Readhead 1994, see also Lähteenmaki & Valtaoja 1999; Lähteenmaki et al. 1999; Savolainen et al. 2010). In addition, Jorstad et al. (2005) obtained the Doppler factors for some of our sources assuming that the observed variability timescales differ from the light crossing time across the emitting region because of Doppler boosting affecting observed jet components. For 1101+384 and 1652+398, we took the values from Lico et al. (2012) and Tavecchio et al. (1998), respectively. We note that the Doppler factor of 1101+384 measured by Lico et al. (2012) is somewhat different from that of Tavecchio et al. (1998). However, we adopted the argument of the former that different Doppler factors for radio and high energy photons are necessary for this source. We refer the readers to Katarzyński et al. (2001) who obtained $\delta = 7 - 14$ for 1652+398, depending on their models for the observed spectral energy distribution. This result is consistent with that of Tavecchio et al. (1998) and we adopted their value, $\delta = 10$. We note, however, that this value could be biased because it was derived from modelling of spectral energy distribution of higher energy photons and their emission region could be different from radio emission region. In total, we were able to retrieve the Doppler factors for 39 out of 43 sources; the values are shown in Table 7.1. Where Doppler factors from both Hovatta et al. (2009) and Jorstad et al. (2005) were available, we first took the average of all values of the latter because they provided individual Doppler factors for each jet component of a given source. Then, we took the average of the Doppler factor of Hovatta et al. (2009) and the averaged one of Jorstad et al. (2005). We used the standard deviation of the logarithms of the Doppler factors of Jorstad et al. (2005) as the error of $\log \delta$, i.e., $\sigma_{\log \delta}$, for each source. Variations in the values for different jet components might originate from intrinsic variability of the Doppler factors and/or measurement errors. For some sources, only the values of Hovatta et al. (2009) were available; in those cases, we assigned the average $\sigma_{\log \delta}$ from sources for which we could actually estimate the error (≈ 0.147 dex) as "typical" error. We note that this value is actually consistent with the estimate of uncertainty of variability Doppler factors, $\approx 30\%$, in a recent study (Liodakis & Pavlidou 2015).

The disk luminosity, in units of Eddington luminosity, is an indicator of accretion rate because the normalized accretion rate is given by $\dot{m} \equiv \dot{M}_{\rm acc}/\dot{M}_{\rm Edd} = L_{\rm disk}/\eta L_{\rm Edd}$, where η is the radiative efficiency of accretion. According to the standard, geometrically thin accretion disk theory (Shakura & Sunyaev 1973), η depends on the location of the innermost stable orbit of the disk and thus on the spin of the black hole. Ghisellini et al. (2014) showed that jet launching and acceleration must be extremely efficient for blazars to explain the excess of jet power over accretion power. This requires almost maximally rotating black holes (See also e.g., Tchekhovskoy et al. 2011 and Zamaninasab et al. 2014). Therefore, our sources likely have η values close to the limiting case $\eta \approx 0.3$ chosen by Ghisellini et al. (2014). In summary, we compared the intrinsic variability timescales (Doppler-corrected) with the accretion power, $\dot{M}_{\rm acc}c^2$, where the accretion rate is derived from the disk luminosity assuming $\eta = 0.3$, in the left panel of Figure 7.12. We note that we rearranged Equation 7.7 in order to avoid displaying large errors along one axis.

Despite some scatter, we find a strong correlation. We note that the correlation coefficients become significantly larger when we exclude the FSRQ 1928+738 from the calculation which is arguably an outlier. We suspect that the Doppler factor of this source is systematically underestimated ($\delta_z = 1.5$), even though it shows quite fast superluminal motion with a maximum jet speed of 8.16 times the speed of light without showing any indication of counter jet emission (Lister et al. 2013). The Spearman rank correlation coefficient – which is less sensitive to outliers – shows that the positive correlation between $\log \dot{M}_{\rm acc}c^2$ and $\beta + 1.39 \log \delta_z$ is statistically significant, with the false alarm probability $p_{\rm r_s}$ being about 0.01%. We performed a linear regression using the errors on both axes with the FITEXY estimator (Section 7.4.3) and obtained a slope of 0.36 ± 0.04. This value translates into $\alpha = 0.26 \pm 0.03$ according to Equation 7.7. The value of $\chi^2_{\rm red} = \chi^2/{\rm d.o.f.}$ is close to one, especially when (the value given in the bracket) 1928+738 is excluded; this indicates a good agreement of model and data over five orders of magnitude in accretion power. In the right panel of Figure 7.12, we binned the data in the left panel logarithmically in accretion power with a binsize of 0.5 dex

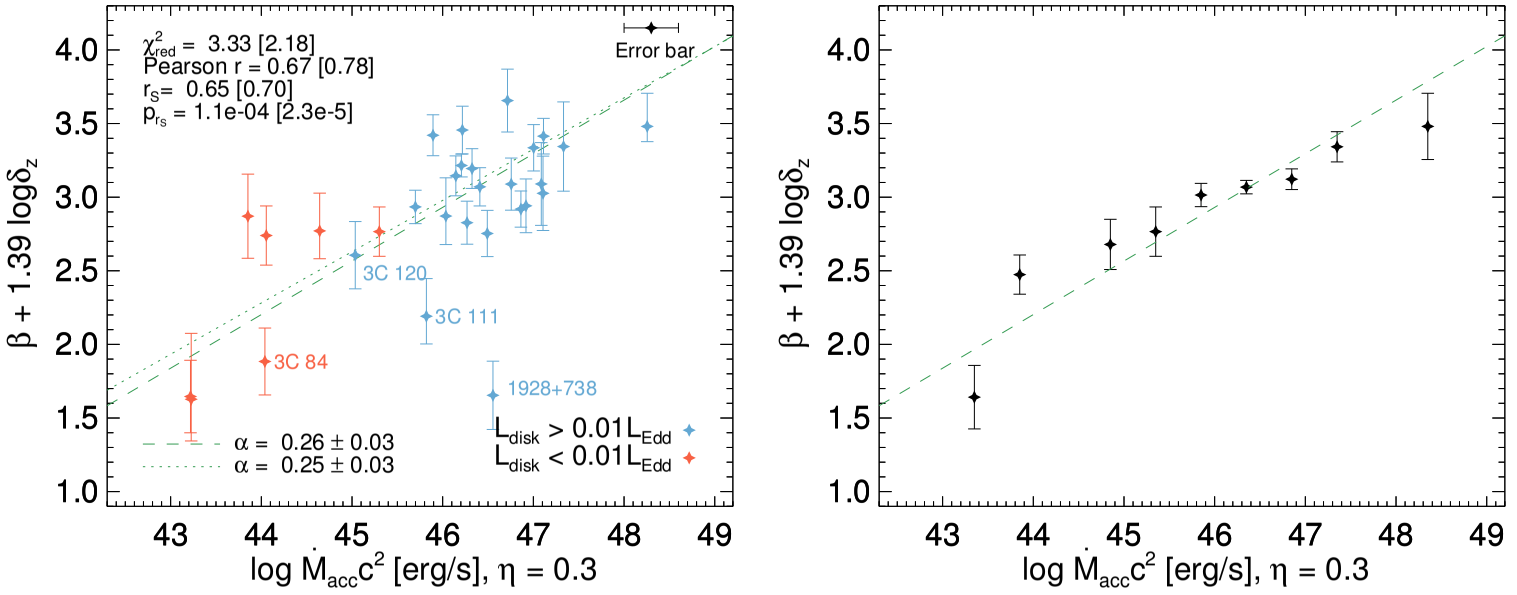

Figure 7.12. *Left*: The parameter $\beta + 1.39 \log \delta_z$ as function of accretion disk luminosity. The sources are divided into two groups based on their disk luminosities in Eddington units (see Section 7.4.4 for details): sources with disk luminosities $> 0.01 L_{\rm Edd}$ in blue, those with $< 0.01 L_{\rm Edd}$ in red. The typical error along the abscissa, 0.29 dex, is illustrated by the black data point with error bars in the top right. The green dashed (dotted) line illustrates a linear regression with (without) including the outlier 1928+738, using the errors along both axes. The best-fit slopes divided by 1.39, denoted α, and their statistical error are provided at the bottom. The χ^2/d.o.f of the best-fit model, the Pearson correlation coefficient r, the Spearman rank correlation coefficient r_s, and the false-alarm probability of r_s, p_{r_s}, are noted. The values in the bracket are obtained excluding the outlier 1928+738 in the calculation. *Right*: Same as the left panel but with all the data after binning logarithmically in accretion power with a binsize of 0.5 dex.

and the best fit line from the un-binned data is shown together.

We investigated possible differences in the scaling relation for the two classes of radio bright AGNs, i.e., BLOs and FSRQs. We divided our sources into those with disk luminosities above and those with disk luminosities below 1% of the Eddington luminosity, which corresponds to FSRQs and BLOs, respectively. This approach is based on Ghisellini et al. (2011) who showed that using the ratio of disk or BLR luminosity and Eddington luminosity is more adequate to distinguish FSRQs and BLOs compared to the classical one using the equivalent width of emission lines. The value of $\approx 1\%$ is known to divide different accretion regimes of AGNs (e.g., Ghisellini et al. 2011; Heckman & Best 2014) and the same parameter can also be used to distinguish FR 1 and FR 2 radio galaxies (e.g., Baum et al. 1995). We counted FR I galaxies, in our case 3C 84, as BLOs and the FR II galaxy 3C 111 and 3C 120 as FSRQ (see Table 7.3). This is in accord with, e.g., Padovani (1992), Maraschi & Rovetti (1994), and Cavaliere & D'Elia (2002) who suggested that FR I and FR II radio galaxies are the parent populations of BLOs and FSRQs respectively. However, as seen in the left panel of Figure 7.12, we do not see any indication of difference in the scaling relation between different classes of radio bright AGNs, although the small number of BLOs and the fact that all BLOs in our sample are among the most radio-loud objects prevent us to draw strong conclusions.

The fact that all our sources share the same scaling relation regardless of their source types implies that the variability timescales of radio bright AGNs are determined by a relatively simple physical process – only weakly (if at all) dependent on jet powers (e.g., Ghisellini et al. 2011), radiative cooling mechanisms (e.g., Ghisellini et al. 2009a), and possible differences in the geometry of magnetic field lines pervading in jets (e.g., Marscher et al. 2002b; Lister & Homan 2005, see also Lyutikov et al. 2005). The clear relation between variability timescales of AGNs at radio wavelengths and accretion rates measured at optical wavelengths comes as a surprise: this behavior indicates that the radio variability of radio-bright AGNs is governed by the accretion process. However, the rather shallow ($\alpha \approx 0.25$) slope in the scaling relation is hard to explain in the frame

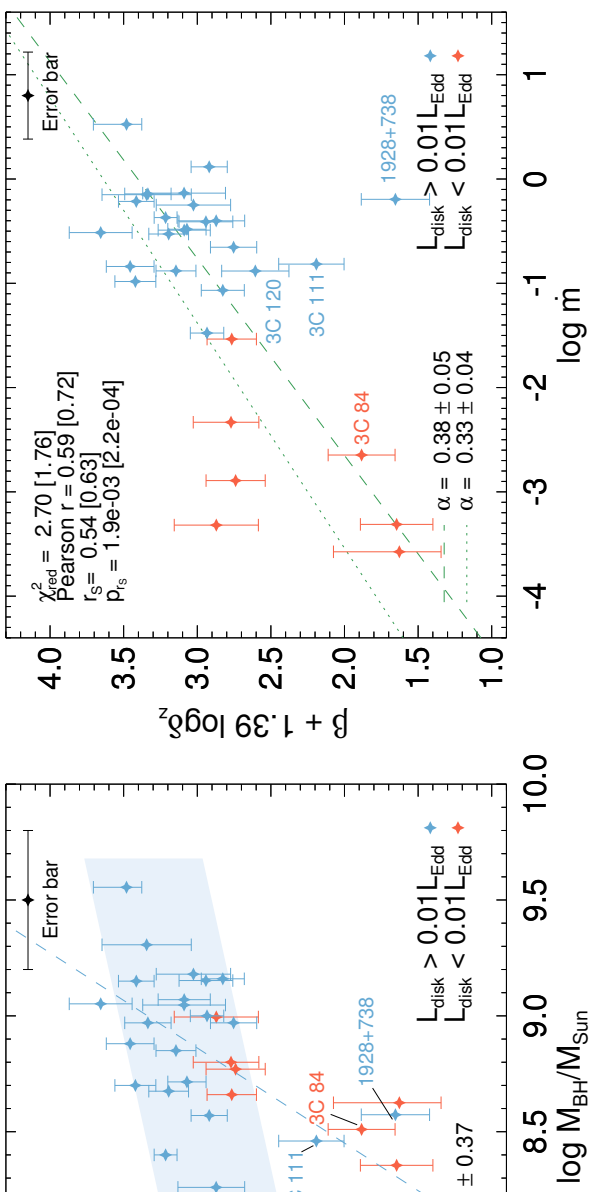

Figure 7.13. *Left:* Same as the left panel of Figure 7.12 but with the black hole mass on the abscissa. The typical error along the abscissa, 0.3 dex, is illustrated by the black data point with error bars in the top right. The blue dashed line illustrates a linear regression, using the errors along both axes. The blue shaded region indicates a relation with slope $\alpha = 1/4$ (drawn manually). The best-fit slope divided by 1.39, i.e., α, and its statistical error are provided at the bottom. The χ^2/d.o.f of the best-fit model, the Pearson correlation coefficient r, the Spearman rank correlation coefficient r_s, and the false-alarm probability of r_s, p_{r_s}, are noted. *Right:* Same as the left panel in Figure 7.12 but with the Eddington ratio on the abscissa. The typical error along the abscissa, 0.42 dex, obtained via standard error propagation of the errors in $\log \dot{M}_{\rm acc}$ and $\log M_{\rm BH}$, is illustrated by the black data point with error bars in the top right.

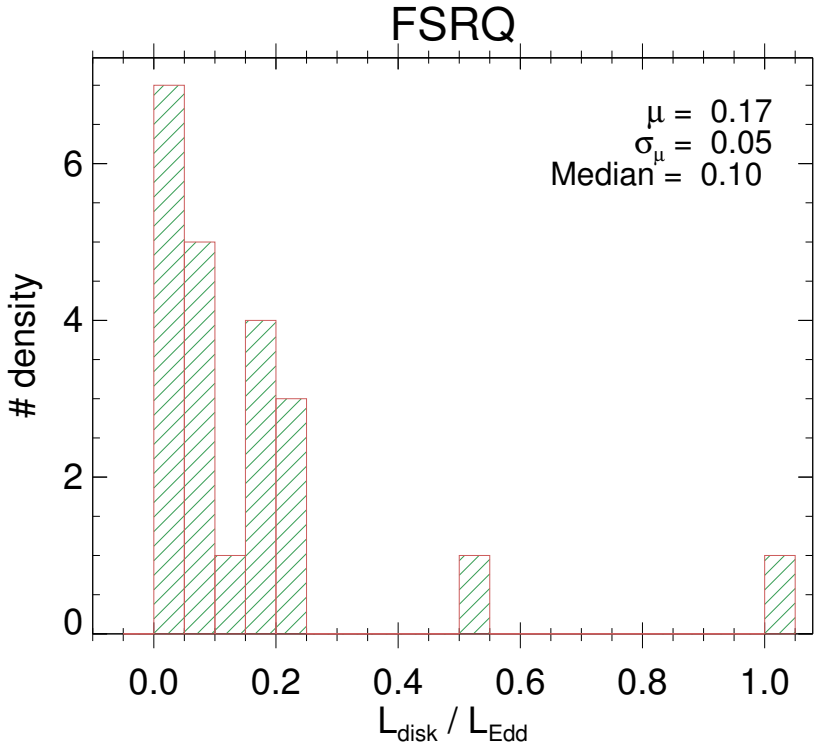

Figure 7.14. Distribution of the disk luminosities, in units of Eddington luminosity, for FSRQs. The mean (μ), the standard error of mean (σ_μ), and the median of the distribution are noted.

of a simple conical jet scenario. If (a) flares arise when a conical jet flow passes through a standing shock and (b) jet opening angles do not vary substantially among different AGNs, one arrives at a simple relation between the accretion rate and the length of the jet along the jet direction, l, namely: $\dot{M}_{\rm acc}\Delta t \propto \rho l^3$. Here Δt is a rest-frame time interval (which is different from the observer frame interval by a factor $(1+z)$) and ρ is the mass density of the jet. If the jet is in a steady state, we can expect $\rho \propto l^{-2}$ which leads to a linear proportionality between $\dot{M}_{\rm acc}$ and l – thus the intrinsic variability timescale is proportional to the accretion rate. However, the slope we find, 0.25, is quite different from the one expected from this simple scenario. This might be the result of complicated jet geometries, such as localized emission regions (often referred to as "blobs"), or

quasi-spherical emission regions, which have succeeded in explaining the broadband variable emission of blazar jets (e.g., Bloom & Marscher 1996; Mastichiadis & Kirk 1997; Böttcher & Chiang 2002, but see also e.g., Marscher & Gear 1985; Marscher & Travis 1996; Marscher 2006). In this case, one would expect a proportionality $\tau_{\rm var} \propto r \propto \dot{M}_{\rm acc}^{1/3}$, where r is the size of the blobs, if (a) there is no density gradient in the blobs and (b) the density does not vary substantially from source to source. In addition, recollimation of jets (e.g., Daly & Marscher 1988), strong superposition of multiple flares arise in different shock regions and possible time delays at cm wavelengths (e.g., Jorstad et al. 2010), and shock-shock interactions in jets (e.g., Fromm et al. 2011) might play an important role. The possible effect of superposition of multiple flares might be investigated by using high-frequency data (mm/sub-mm wavelengths). Numerical simulations would be also helpful to investigate the complicated coupling behavior between mass accretion rate and jet structure (e.g., Tchekhovskoy et al. 2011; Marscher 2014).

As illustrated in Figure 7.13, we checked if the intrinsic variability timescale is related to Eddington ratio and black hole mass. In the left panel, the scaling with black hole mass shows a large scatter, with correlation coefficients of ≈ 0.4, indicating a moderate correlation. This correlation is probably a consequence of the correlation seen in Figure 7.12 because (i) all the FSRQs (except the outlier 1928+738) follow the relation with $\alpha = 1/4$ due to their Eddington ratio being concentrated around ≈ 0.1 (see Figure 7.14) and (ii) the BLOs lie systematically below the FSRQs with similar black hole masses, which indicates their low accretion rates lead to low variability timescales. In the right panel, we see a correlation of time scale and Eddington ratio with correlation coefficients as high as 0.7 when excluding 1928+738. This, too, is probably a corollary of the β–$\dot{M}_{\rm acc}$ relation because our sources span only ≈ 1 dex in black hole mass (as can be seen in the left panel of Figure 7.12) and more than four orders of magnitude in accretion rate.

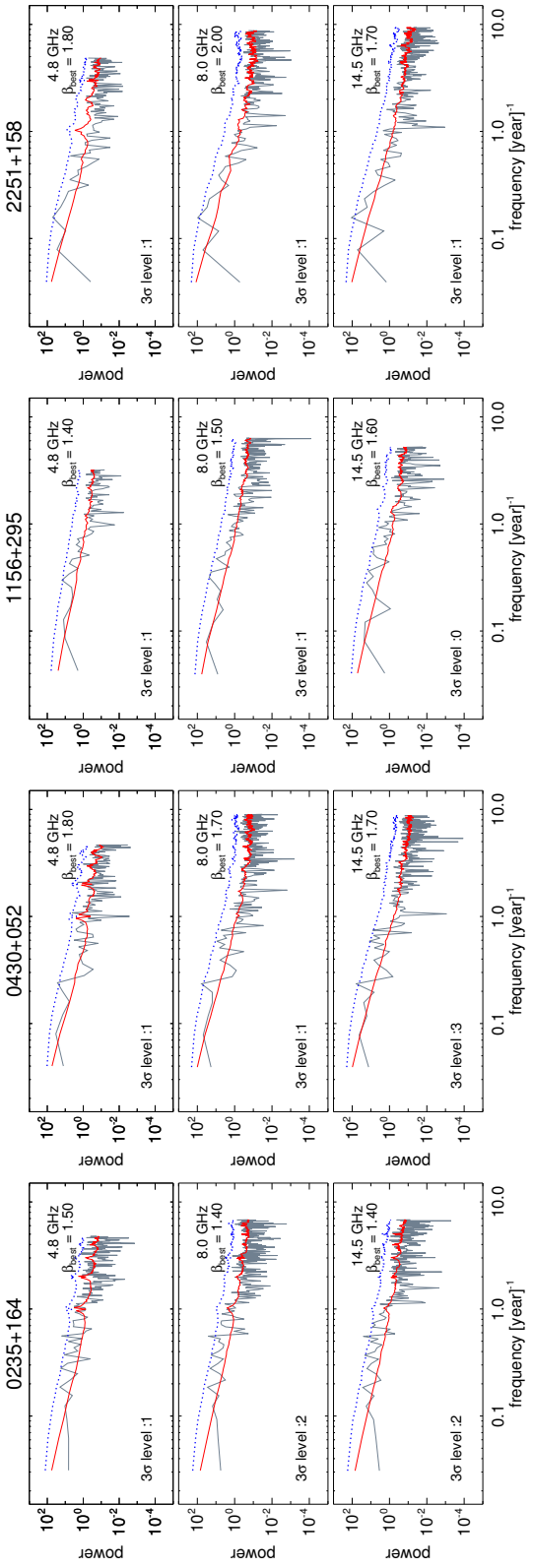

Figure 7.15. Same as Figure 7.5 but for the four sources with significant (3σ) excess spectral power at two or three observing frequencies (see Section 7.4.5 for details).

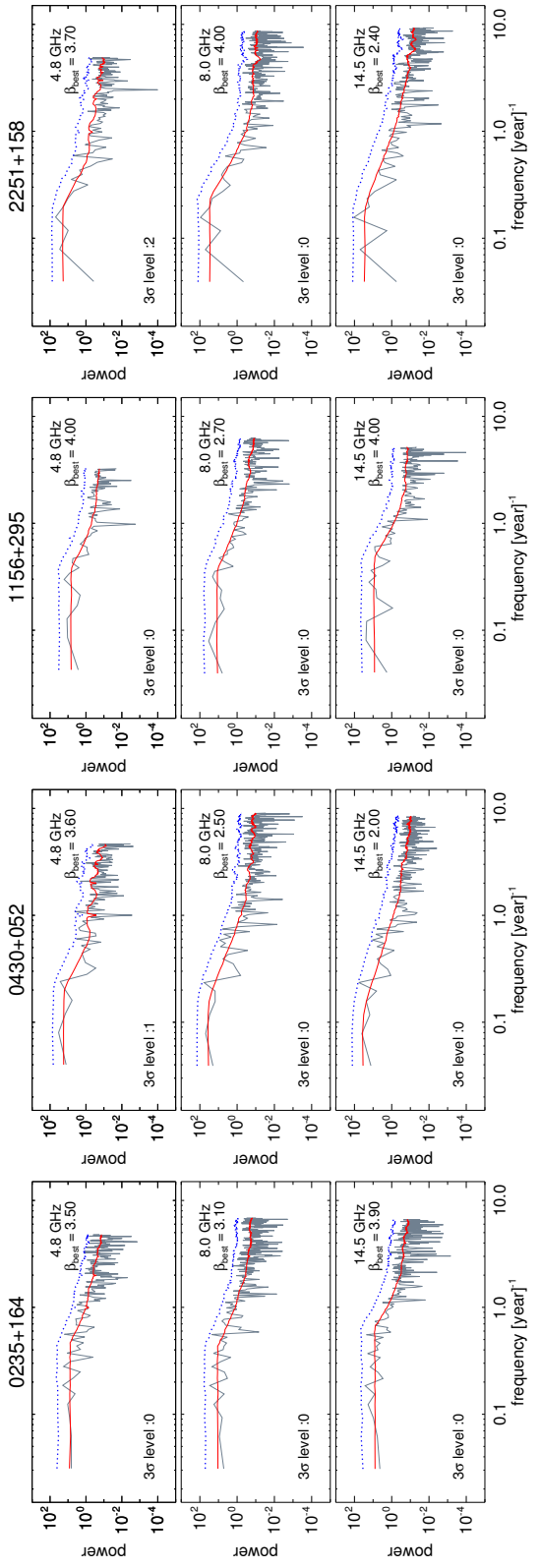

Figure 7.16. Same as Figure 7.15 but with the best-fit broken power-law models (red solid lines) instead of simple powerlaws. In each diagram the value of the best-fit slope β above the break frequencies is noted. (The model curves are flat below the break frequencies.) The apparent excess spectral power noted in Figure 7.15 is now modeled properly for each source.

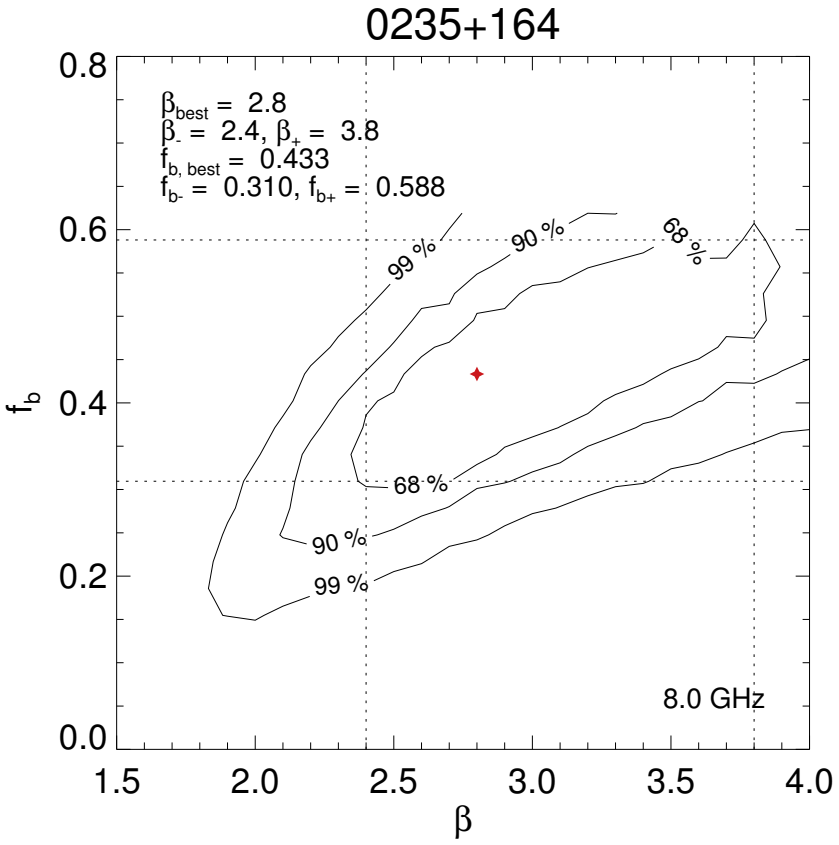

Figure 7.17. χ^2 contours of the broken power-law model for the periodogram of 0235+164 at 8.0 GHz. Parameters are break frequency, f_b, and power spectral index, β (see Section 7.4.5 for details).

7.4.5 Broken Power-law Periodograms

A simple power-law model explains the observed power spectra of most of our sources successfully without any indication for statistically significant QPO signals. However, there are four sources out of which each shows significant excess spectral power simultaneously at two or three observing frequencies and at similar sampling frequencies: 0235+164, 0430+052, 1156+295, and 2251+158. This excess power might indicate the presence of QPOs. We show the power spectra, the best-fit power-law models, and the

corresponding 3σ significance levels in Figure 7.15.

Actually, the candidate QPO signals are located at rather low sampling frequencies and the power spectra appear to flatten below those frequencies. Thus, we tested if the periodograms can be (or have to be) modeled as broken power-laws with break frequencies f_b. We performed Monte Carlo simulations as we did in Section 7.3.1 but this time with broken power-law models. We assumed that β becomes zero below the break frequency.[8] We computed sets of models with break frequencies ranging from $\approx$0.05 to $\approx$0.7 yr^{-1} and power-law indices β (above the break frequencies) ranging from 1.5 to 4.0. We obtained 1 000 artificial lightcurves for each combination of f_b and β. After mapping the observed sampling pattern into the artificial lightcurves, we obtained the binned logarithmic power spectra and took the average of them for each bin. Then, we calculated χ^2 using Equation 7.1. We show the χ^2 contours for 0235+164 at 8.0 GHz – $\chi^2_{\rm min} + 2.30, 4.61, 9.21$, corresponding to 68%, 90%, and 99% significance levels, respectively – (e.g., Wall & Jenkins 2012), as function of β and f_b in Figure 7.17. We obtained the values and the unmarginalized 1σ errors of the best-fit β and f_b. The best-fit broken power-law periodograms for the four sources in question are shown in Figure 7.16. Within errors, the periodograms are completely described by the models. We note that the χ^2/d.o.f values are reduced significantly when changing from simple to broken power-law models: from 3.03, 1.44, 2.21, and 2.51 to 0.77, 0.48, 0.69, and 1.22 for 0235+164, 0430+052, 1156+295, and 2251+158, respectively.

We note that the best-fit values for β in the broken power-law models tend to be very high, up to the simulation limit of 4.0. The formal errors of these values are large, ranging from 0.3 to about 1.2 – meaning that β is not well constrained. Thus, using the broken power-law results for other analyses, e.g., the scaling relations of variability timescale with black hole mass, would lead to highly uncertain results. We suspect that our assumption of flat power spectra below the break frequencies results in the high power spectral indices we observe. Our primary interest was to investigate whether there

[8] In principle, both power spectral indices below and above the break frequency are free parameters (e.g., Uttley et al. 2002), but we aimed at models with the smallest number of free parameters that actually describe the data.

is indication for broken power-law periodograms at least for a few sources. For most of our targets, the two models – simple vs. broken power-law – are not distinguishable within errors. Therefore, we stick to the best-fit values of β obtained with the simple power-law models throughout this paper.

As noted already in Section 7.4.3, the origin of the featureless red-noise power spectra of AGN (mostly blazars) radio lightcurves is not understood. This is in contrast to the case of broken power-law periodograms typically seen in the X-ray and optical lightcurves of non-blazars (i.e., Seyferts and quasars). One possibility is that the emission is correlated over very long timescales – comparable to the observation time covered by UMRAO database, $\approx$ 30 years. If the radio emission of AGNs is directly linked to the accretion flows, the spatial correlation of accretion flows (see e.g., Kelly et al. 2009, 2011) for radio-bright AGNs is much stronger than for nonblazars. However, many of our sources, especially the FSRQs, are active at optical bands as well; they should have accretion disks which are similar to X-ray/optical bright nonblazars. An alternative scenario involves the special feature of blazars lightcurves: the flares. Even if the power spectra of accretion flows or matter injection flows into jets have break frequencies at relatively high sampling frequencies, the break frequencies can move toward low sampling frequencies if the duration of the flares is long enough to cause substantial overlap of individual emission events. Such overlap effectively increases the timescales for flux variations, resulting in higher spectral power at lower sampling frequencies. The location of the break frequencies would depend on the degree of superposition.

To test this scenario, we employed a simple simulation of lightcurves. We generated 100 artificial lightcurves $f(t)$, each composed of multiple exponential flares, according to

$$\begin{aligned} f(t) &= f_{\max} \exp[(t - t_0)/T_r], \quad \text{for t} < \text{t}_0 \text{ and} \\ &= f_{\max} \exp[-(t - t_0)/T_d], \quad \text{for t} > \text{t}_0, \end{aligned} \tag{7.8}$$

where $f_{\max}$ is the peak amplitude of the flare, t is the time, t_0 is the time of the peak, and T_r and T_d are the rise and decay timescales, respectively (Chatterjee et al. 2012). This model is based on the assumption that AGN radio lightcurves can indeed

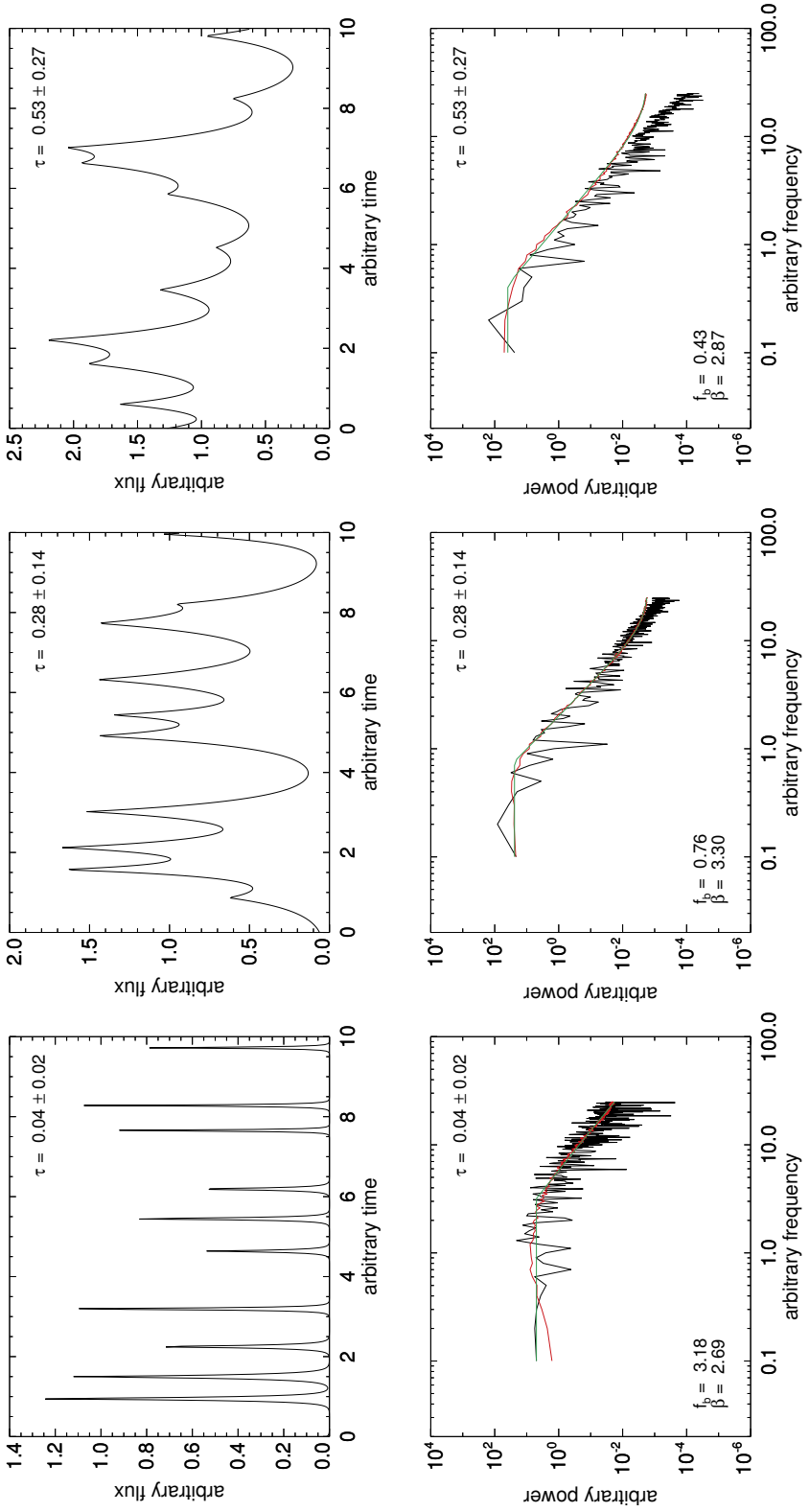

Figure 7.18. *Top panels*: Simulated lightcurves with a combination of exponential flares with randomized amplitude, duration, and separation between the flares for three different mean duration values (see Section 7.4.5 for details). *Bottom panels*: One realization of the power spectra (black solid lines), mean power spectra of 100 realizations (red solid lines), and fitted lines with broken power-law models (green solid lines).

Table 7.2. Variability timescales of two sources

Source	Obs freq.	f_b(obs) [yr^{-1}] (1)	τ/t_0(sim) (2)	τ/t_0(obs) (3)	Difference [%] (4)
0235+164	4.8	0.47	0.51	0.59	13
	8.0	0.43	0.57	0.57	0.41
	14.5	0.65	0.33	0.40	17
1156+295	4.8	0.38	0.67	0.68	2
	8.0	0.36	0.74	0.66	12
	14.5	0.48	0.49	0.71	31

Note. — (1) Break frequencies found from Monte Carlo simulations using broken power-law models. (2) Values of τ/t_0 expected theoretically from the relation shown in Figure 7.19 and the observed break frequencies. (3) Observed values of τ/t_0 from fitting Gaussian flares piecewise to the lightcurves. (4) Relative difference between (2) and (3), in units of percent.

be decomposed into exponential flux peaks whenever the overlap between flares is not too strong (e.g., Valtaoja et al. 1999; Hovatta et al. 2009). For each lightcurve, we initially generated 20 flares that span 20 units (that can be identified with years) in time. From this, we took the half of the data points located in the middle of each lightcurves to avoid having lightcurves that converge to zero at the beginning and at the end. As a result, we have 10 artificial flares that span 10 units on average for each lightcurve. For each flare, we used $f_{\max}$ uniformly randomly distributed from 0.5 to 1.5 units to randomize the amplitudes of flares, t_0 from $n - 0.5$ to $n + 0.5$ units for the nth flare to make aperiodic variability, and $T_r = T_d$ from 0.5 to 1.5, multiplied by a characteristic timescale τ. This timescale controls the degree of overlap of flares. We varied τ from ≈ 0.03 to ≈ 0.7 units and obtained the average of the periodograms for each τ value. This averaged periodogram we fitted with a broken power-law model with three parameters: the power-law index β above the break frequency f_b (the slope below f_b being zero), and a constant offset for taking into account aliasing. One realization of a lightcurve, the corresponding power spectrum, the averaged power spectrum, and the best-fit broken power-law model for each of three different values of τ are shown in Figure 7.18. When τ is small compared to the average separation between two flares (i.e., one unit) there is almost no overlap between flares; the break frequency appears at sampling frequencies well above one frequency unit. As τ increases, it becomes more difficult to disentangle individual flares and the break frequency moves toward lower sampling frequencies – as expected.

We obtained the break frequencies of the simulated power spectra as function of τ/t_0. We found a power-law relation, $f_b = 0.28 \times (\tau/t_0)^{-0.76}$. We scaled the errors on f_b such that $\chi^2/\text{d.o.f.} = 1$ for the best-fit model.[9] As shown in Figure 7.19, the break frequency decreases with increasing τ/t_0 and, at $\tau/t_0 \gtrsim 0.7$, converges to a value located close to the lowest sampling frequency. Accordingly, periodograms from lightcurves that show extensive overlap of flares appear as simple power-laws – as is indeed the case for

[9]Obtaining absolute errors on the break frequencies requires reliable error estimates for the simulated power spectra at each sampling frequency. This cannot be achieved in a straightforward manner because spectral powers do not follow Gaussian distributions .

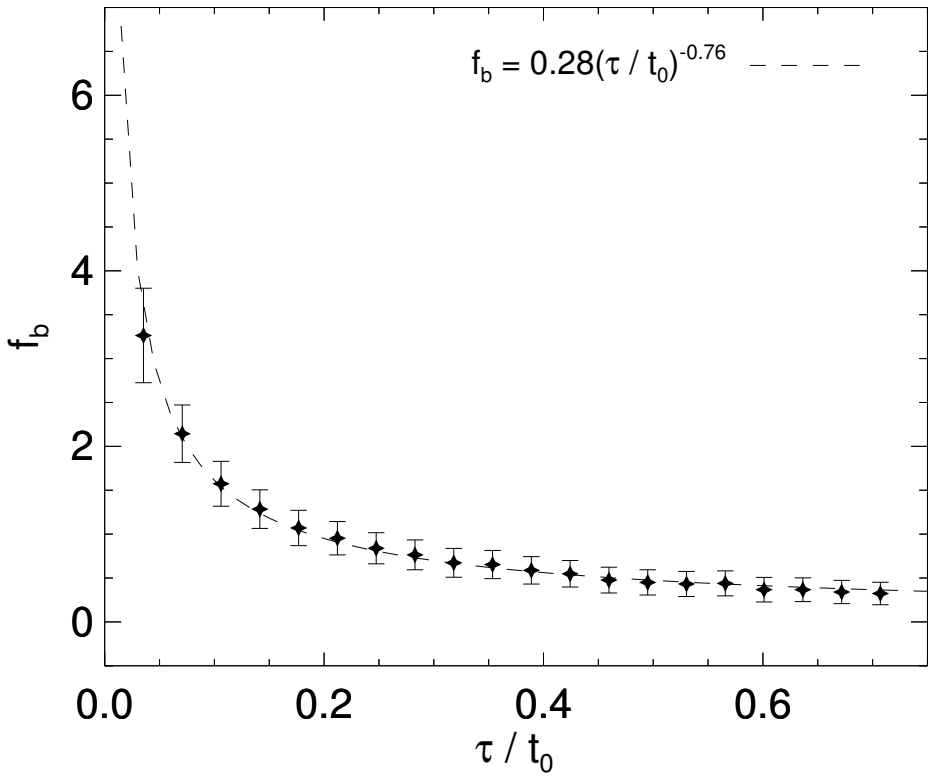

Figure 7.19. Break frequency as function of the ratio of mean duration to mean separation of flares. The black dashed line indicates the best-fit power-law function; the corresponding formula is shown on the top right. Error bars are scaled to $\chi^2/\text{d.o.f.} \equiv 1$ for the best-fit model.

most of our target AGNs.

It is now possible to check the degree of agreement between the observed break frequencies as function τ/t_0 and the simulation results. On the one hand, the break frequencies found in 0430+052 and 2251+158 are very small, $\approx 0.2\,\mathrm{yr}^{-1}$, meaning that a wide range of τ/t_0 is consistent with the observed value for f_b (see also Figures 7.15 and 7.16). 0235+164 and 1156+295, on the other hand, show relatively large break frequencies, $\approx 0.5\,\mathrm{yr}^{-1}$ and $\approx 0.4\,\mathrm{yr}^{-1}$, respectively. We took the median duration and

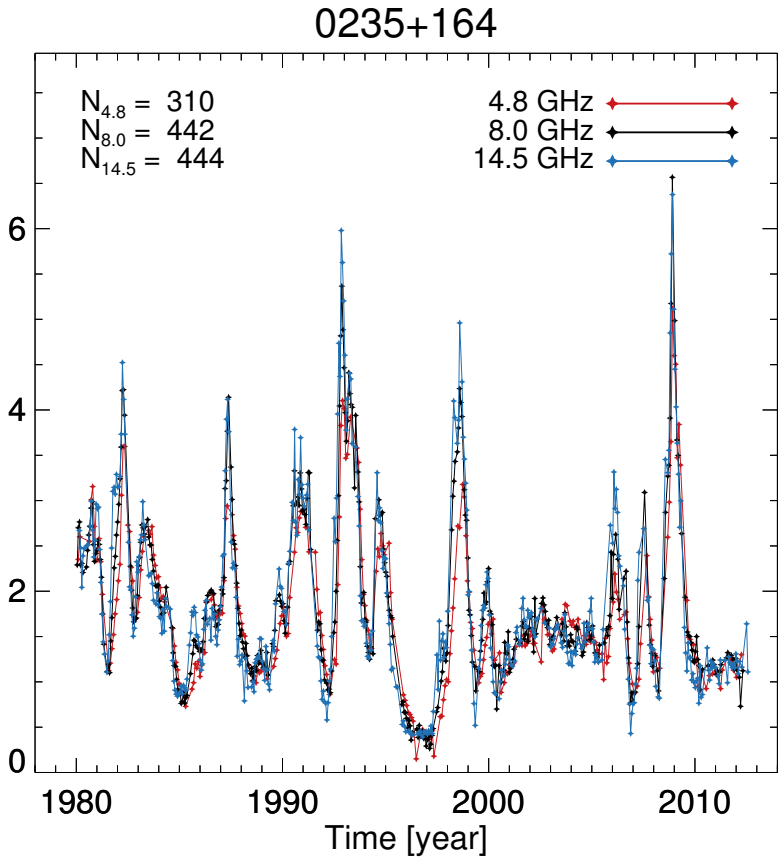

Figure 7.20. Lightcurves of 0235+164 (after binning and flagging). Red, black, and blue solid lines indicate 4.8, 8, and 14.5 GHz data, respectively. The number of data points, N_ν, is noted explicitly for each frequency ν.

the median separation of the flares we obtained in Section 7.3.3 (for each source and each observing frequency) and calculated the observational values for τ/t_0. Since we used Gaussian flares in our lightcurve fitting but exponential flares in the simulations, we multiplied the observed τ/t_0 by $\sqrt{2}$ to compare the e-folding timescales of observed and simulated flares; these values are denoted τ/t_0(obs) in Table 7.2. We inserted the observed break frequencies into the theoretical f_b–τ/t_0 power-law relation and obtained the theoretical ratio τ/t_0(sim). The difference between τ/t_0(obs) and τ/t_0(sim) is on the order of 10% typically and reaches 31% at most (see Table 7.2). Therefore, we

conclude that the observation of red-noise periodograms for most of our target sources is consistent with being due to strong temporal overlap of flares. The main reason for this might be the relatively long variability timescales of AGNs at centimeter wavelengths. We show the lightcurves of 0235+164, for which the break in the periodogram is quite prominent, in Figure 7.20. The duration of the individual flares is short compared to their typical separation; indeed, it seems that there is no substantial overlap between the flares – which is consistent with our scenario.

7.4.6 Comparison with Other Studies

So far, we discussed long-term UMRAO lightcurves of AGNs with jets approximately aligned with the line of sight (even for the radio galaxies). Naturally, we have to ask if the variability patterns we observe agree with those for nonblazars and for blazars at other observing frequencies. Kelly et al. (2011) concluded that the slope of X-ray periodograms (below the high-frequency break) of 10 Seyfert galaxies does not correlate with black hole mass. This indicates that, for Seyferts, factors such as the amplitude of the driving noise field are more important than black hole mass in determining the structure of flux variability. The noise field is arguably related to the viscous, thermal, and radiative response of accretion disks to perturbations (Kelly et al. 2011). In contrast, radio variability of AGNs is governed by the crossing time of radiation and/or disturbances through the emission region. This also explains the quite low break frequencies observed in AGN radio periodograms. In optical and X-ray power spectra of nonblazars, break frequencies are found at timescales of less than a few years (Kelly et al. 2009, 2011).

Blazars usually show symmetric flares across multiple wavelengths – see, e.g., Valtaoja et al. (1999) and Hovatta et al. (2009) for 22 and 37 GHz data respectively, Chatterjee et al. (2012) for optical and γ-rays, and Abdo et al. (2010) for γ-rays. As the observing frequency increases, the rise and decay times of flares become shorter (e.g., Chatterjee et al. 2012; Rani et al. 2013) due to the shorter cooling times of higher energy particles (cf., e.g., Marscher 1996). Therefore, we may expect (1) smaller power

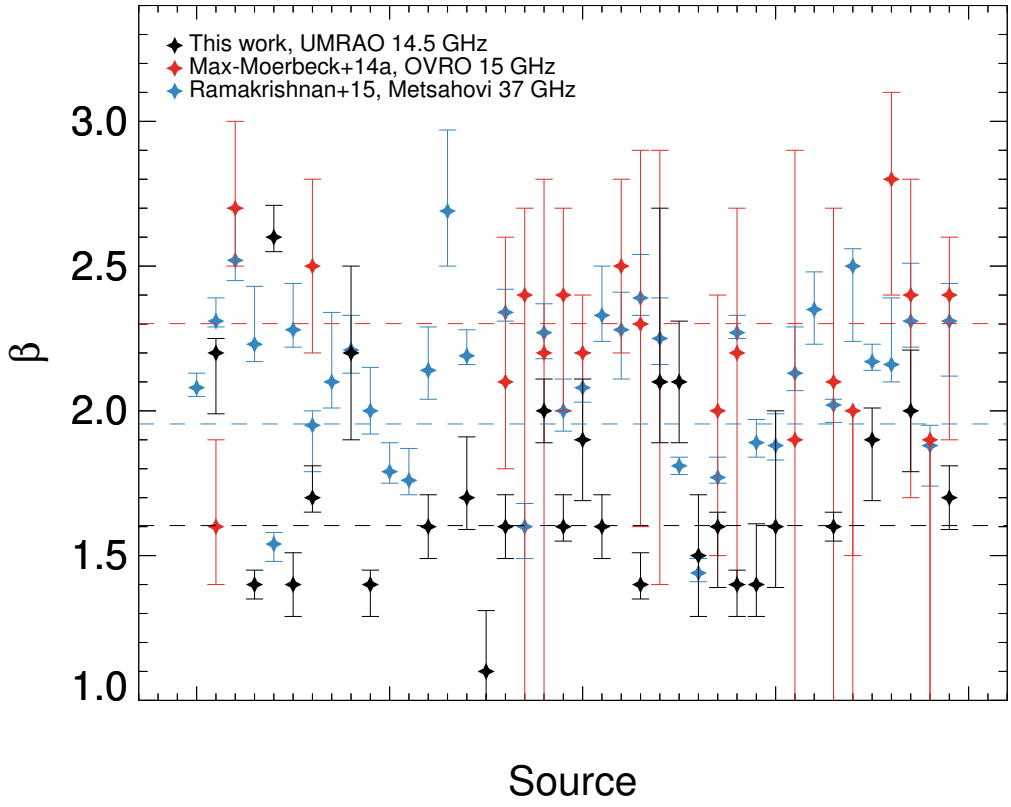

Figure 7.21. Observed values of β for all sources covered by three different studies: this work, using UMRAO 14.5 GHz data (black); Max-Moerbeck et al. (2014a) using OVRO 15 GHz data (red); and Ramakrishnan et al. (2015) using Metsähovi 37 GHz data (blue). A given abscissa value indicates a given source. The horizontal dashed lines indicate weighted averages of the β values found in each study.

spectral indices β and (2) observations of broken power-law periodograms at higher frequencies. Trippe et al. (2011) showed that the power spectra of six radio bright AGNs at millimeter wavelengths have $\beta \approx 0.5$, which is much smaller than the values we find in this work. However, windowing effects (especially red-noise leak and aliasing) were not taken into consideration then, making it hard to conclude on the general behavior of mm-radio periodograms.

Recent studies have shown that the power spectra of many radio bright AGNs are quite steep, $\beta > 2$ for most sources, at 15 GHz from the Owens Valley Radio Observatory (OVRO) 40 m monitoring program (Max-Moerbeck et al. 2014a) and at 37 GHz from the Metsähovi AGN monitoring program (Ramakrishnan et al. 2015). This behaviour is quite different from our expectation in that (i) the OVRO result is not in agreement with our result even though the observing frequency is very similar and (ii) the 37 GHz power spectra are much steeper than ours even though the observing frequency is higher. We present β values obtained in our study and those studies together in Figure 7.21. Though the errors of Max-Moerbeck et al. (2014a) are too large to make a qualitative comparison, the overall level of β of the OVRO 15 GHz observations (weighted mean $\beta_{\rm wmean} = 2.30$) seem to be larger than that of the Metsähovi 37 GHz observations ($\beta_{\rm wmean} = 1.95$), which is in agreement with our expectation. However, the systematic difference between those studies and our study ($\beta_{\rm wmean} = 1.60$) needs to be investigated.

The main difference between the methods of estimation of β in our study and their studies is interpolation of lightcurves and using a sampling window function. They employed linear interpolation when there is gap in their lightcurves after binning and convolved the lightcurves with an Hanning sampling window function, which is effective in reducing red-noise leak (Max-Moerbeck et al. 2014b). Interpolation might lead to suppression of amplitude in power spectra at high frequencies because it adds *correlated* signals to lightcurves, which would result in steeper power spectra than the true power spectra. This might be the reason why quite steep power spectra are seen in those studies. However, the detailed simulation of Max-Moerbeck et al. (2014b) indicates that this might not be the case. In contrast, we didn't use any interpolation in the lightcurves and employed the Scargle periodogram which can be applied to irregularly sampled lightcurves (Scargle 1982). In this case, the periodogram strongly suffers from red noise leak and aliasing and the shape is distorted significantly as seen in Max-Moerbeck et al. (2014b). However, simulated power spectra must be distorted in the same way since we mapped the same sampling pattern of the observed lightcurves into

the simulated ones, which is seen clearly in Figure 7.1 and the right panel of Figure 7.5. The local peaks and the breaks in the observed power spectra, probably generated by the distortion effect, are recovered in the simulated ones as well. Therefore, it is hard to easily understand the reason for the systematic difference in the measured β and it must be investigated in future studies. Nevertheless, it would not affect our results and conclusions because the tight correlation between β and fractal dimension (Figure 7.9) tells us that β of one source relative to other sources might be still correct.

In the γ ray regime, Abdo et al. (2010) found periodogram slopes of 1.4 ± 0.1 and 1.7 ± 0.3 averaged over nine FSRQs and six BLOs, respectively. These values are compatible to the values which we find in this work, whereas we would actually expect smaller values of β in the high-energy regime. We note however that averaging power spectra of different sources is likely to lead to spurious results – as noted in Section 7.4.1, even for sources of the same AGN type β covers a wide range of values (from $\approx$1 to $\approx$3). Sobolewska et al. (2014) used longer *Fermi* lightcurves than those used in Abdo et al. (2010) (4 years vs. 11 months) and modeled them in the time domain based on the assumption of a mixed OU process. For their sample of 13 blazars, they obtained $\beta \lesssim 1$. They also found low-frequency breaks for two sources, 3C 66A and PKS 2155. Shimizu & Mushotzky (2013) found slopes around 0.85 for the hard X-ray lightcurves of three blazars and a broken power-law periodogram for 3C 273 (see also M$^{\rm c}$Hardy 2008). The above results are in agreement with our scenario of β becoming smaller, and broken power-law periodograms becoming more prominent, at higher observing frequencies. Contrary to this trend, Chatterjee et al. (2012) found slopes up to 2.3 for a few blazars at optical wavelengths. We also note that, when comparing radio, optical, and high-energy emission, we are looking at radiation from different physical emission mechanisms or different emission regions. For example, Ramakrishnan et al. (2016) showed that the variability of blazars at optical and γ ray are well correlated, while it was less certain between radio and optical bands. Accordingly, a comparison between radio and optical lightcurves may be questionable, while a comparison between optical and X-rays/γ-ray lightcurves is more straightforward.

7.5 Conclusions

We studied long-term (25–32 years), high-quality radio lightcurves of 43 radio bright AGNs – 27 FSRQs, 13 BLOs, and 3 radio galaxies – at 4.8, 8, and 14.5 GHz. We investigated the physical origin of different variability patterns found in the radio lightcurves of different sources by means of peridogram analyses. Our work leads us to the following principal conclusions:

1. The power spectra of 39 out of 43 sources are in agreement with simple power-law periodograms without any indication for (quasi-)periodic signals. Power spectral indices range from ≈1 to ≈3. We find a strong anti-correlation between the power spectral index and the fractal dimension of the lightcurves, thus quantifying the one-to-one relation between the geometry of lightcurves and the slopes of periodograms as $\beta \propto -4.43 d_f$, where β is the power spectral index and d_f is the fractal dimension.

2. We find that β is a proxy for the variability timescale $\tau_{\rm var}$. We discover a strong correlation between β and the median duration of flares. We apply an improved measure for variability timescales, the width of the distribution of the derivatives of lightcurves, $\sigma_{\rm der}$. We find the relation $\beta \propto -1.39 \log \sigma_{\rm der}$.

3. When taking into account relativistic Doppler boosting and cosmological redshift, β shows a correlation with the accretion rate. We find the relation $\beta \propto 1.39\alpha \log \dot{M}_{\rm acc}$, corresponding to $\tau_{\rm var} \propto \dot{M}_{\rm acc}^{\alpha}$, with $\alpha = 0.25 \pm 0.03$. At this point, we cannot explain the specific value $\alpha \approx 1/4$.

4. For four sources in our sample – 0235+164, 0430+052, 1156+295, and 2251+158 – we find that broken power-law models provide significantly better fits to the observed periodograms than simple power-law models. From random realizations of lightcurves composed of sequences of exponential flares, we obtain a theoretical power-law relation between break frequency f_b and scaled duration of flares τ/t_0. We find that, within errors, our observed values for f_b and τ/t_0 agree with the

theoretical relation.

5. We conclude that the periodograms of AGN lightcurves follow broken power-laws intrinsically. The strong overlap of subsequent flares in cm-radio lightcurves leads to correlation of the observed flux over long timescales and thus to red-noise power spectra (simple power-law periodograms). Accordingly, we expect observations of smaller β values and broken power-law periodograms at higher observing frequencies that probe shorter cooling timescales. This is indeed observed for the X/γ ray lightcurves of blazars; for optical lightcurves, the case remains ambiguous.

Black hole masses and disk luminosities (in Eddington units)

Object	$\log M_{\rm BH}$	$M_{\rm BH}$ Estimator	Ref.	Adopted	$L_{\rm disk}/L_{\rm Edd}$
	(1)	(2)	(3)	(4)	(5)
0133+476	8.75	$L(\mathrm{H}\beta) = 20.97 \times 10^{42}$ erg s^{-1}, FWHM(Hβ) = 4223 km s^{-1}	Tor12	8.88	4.3e-2
	9.01	L(Mg II) $= 28.10 \times 10^{42}$ erg s^{-1}, FWHM(Mg II) = 5367 km s^{-1}			
0235+164	9.00	Fitting the spectral energy distribution (SED)	Ghi09	9.00	1.0e-2[a]
0316+413	8.49	$M_{\rm BH}$-σ relation, σ = 246 km s^{-1}	Heck85	8.51	6.8e-4
	8.51	$M_{\rm BH}$-σ relation, σ = 248 km s^{-1}	NW95		
	8.53	H_2 rotation curve	Wil05		
0333+321	9.25	Single epoch Mg II line	Liu06	9.56	1.0e-0
	9.86	L(Mg II) $= 6091 \times 10^{42}$ erg s^{-1}, FWHM(Mg II) = 3735 km s^{-1}	Tor12		
0336−019	8.89	Single epoch Hβ line	Liu06	8.97	6.6e-2
	9.05	L(Mg II) $= 52.68 \times 10^{42}$ erg s^{-1}, FWHM(Mg II) = 4781 km s^{-1}	Tor12		

Table 7.3. (1) Logarithm of the black hole mass calculated by us or taken from the literature. (2) Methods used to determine black hole masses. We do not name the method if we adopt literature values without modification. We converted the luminosities provided in Wang et al. (2004) into the values in the table by converting their $L_{\rm BLR}$ into line luminosities and updated cosmological parameters. (3) References for the black hole masses (listed below). (4) Adopted values for the (logarithmic) black hole masses, which are the averages of (1) for each source. (5) Disk luminosities in Eddington units.

[a] $L_{\rm disk}/L_{\rm Edd}$ calculated from the $L_{\rm disk}$ values in Ghisellini et al. (2011) or from using their $L_{\rm BLR}$ values, assuming $L_{\rm disk} \approx 10 L_{\rm BLR}$ (Ghisellini et al. 2011; Calderone et al. 2013) if $L_{\rm disk}$ is not available.

REFERENCES.— Bar03: Barth et al. (2003); Fal02: Falomo et al. (2002); Fal03a: Falomo et al. (2003a); Fal03b: Falomo et al. (2003b); Ghi09: Ghisellini et al. (2009b); Heck85: Heckman et al. (1985); Kas00: Kaspi et al. (2000); Kol14: Kollatschny et al. (2014); Liu06: Liu et al. (2006); NW95: Nelson & Whittle (1995); Tor12: Torrealba et al. (2012); Ves06: Vestergaard & Peterson 2006; Wang04: Wang et al. (2004); Wil05: Wilman et al. (2005)

Black hole masses and disk luminosities (in Eddington units)

Object	$\log M_{\rm BH}$	$M_{\rm BH}$ Estimator	Ref.	Adopted	$L_{\rm disk}/L_{\rm Edd}$
	(1)	(2)	(3)	(4)	(5)
0415+379	8.46	$L(\mathrm{H}\beta) = 7.85 \times 10^{42}$ erg s^{-1}, FWHM(Hβ) = 4100 km s^{-1}	Tor12	8.46	4.6e-2
0420−014	8.41	Single epoch Hβ line	Liu06	8.72	9.9e-2
	9.02	L(Mg II) $= 43.37 \times 10^{42}$ erg s^{-1}, FWHM(Mg II) = 4846 km s^{-1}	Tor12		
0430+052	7.36	Hβ reverberation mapping	Kas00	7.70	4.0e-2
	8.13	$M_{\rm BH}$-σ relation, σ = 200 km s^{-1}	Woo02		
	8.03	Hβ reverberation mapping	Kol14		
	7.62	$L(\mathrm{H}\beta) = 1.29 \times 10^{42}$ erg s^{-1}, FWHM(Hβ) = 2750 km s^{-1}	Tor12		
	7.57	$L(\mathrm{H}\beta) = 1.82 \times 10^{42}$ erg s^{-1}, FWHM(Hβ) = 2328 km s^{-1}	Ves06		
0607−157	7.78	$L(\mathrm{H}\beta) = 1.44 \times 10^{42}$ erg s^{-1}, FWHM(Hβ) = 3200 km s^{-1}	Tor12	7.78	4.0e-2
0923+392	9.09	Single epoch Hβ line	Liu06	9.15	1.2e-1
	9.57	$L(\mathrm{H}\beta) = 77.18 \times 10^{42}$ erg s^{-1}, FWHM(Hβ) = 7200 km s^{-1}	Wang04		
	8.81	$L(\mathrm{H}\beta) = 25.11 \times 10^{42}$ erg s^{-1}, FWHM(Hβ) = 4250 km s^{-1}	Tor12		
	9.14	L(Mg II) $= 73.05 \times 10^{42}$ erg s^{-1}, FWHM(Mg II) = 4927 km s^{-1}	Tor12		
1055+018	9.16	L(Mg II) $= 34.07 \times 10^{42}$ erg s^{-1}, FWHM(Mg II) = 6039 km s^{-1}	Tor12	9.16	2.6e-2
1101+384	8.29	$M_{\rm BH}$-σ relation, σ = 219 km s^{-1}	Bar03	8.35	1.5e-4[a]
	8.42	$M_{\rm BH}$-σ relation, σ = 236 km s^{-1}	Fal02		
1156+295	8.54	Single epoch Hβ line	Liu06	8.68	8.9e-2
	8.81	L(Mg II) $= 28.77 \times 10^{42}$ erg s^{-1}, FWHM(Mg II) = 4245 km s^{-1}	Tor12		
1226+023	8.74	Hα, Hβ, Hγ reverberation mapping	Kas00	8.97	2.2e-1
	8.92	Single epoch Hβ line	Liu06		
	9.00	$L(\mathrm{H}\beta) = 85.17 \times 10^{42}$ erg s^{-1}, FWHM(Hβ) = 3800 km s^{-1}	Tor12		
	9.22	$L(\mathrm{H}\beta) = 186.21 \times 10^{42}$ erg s^{-1}, FWHM(Hβ) = 3627 km s^{-1}	Ves06		

Table 7.3. Continued.

Black hole masses and disk luminosities (in Eddington units)

Object	$\log M_{\rm BH}$	$M_{\rm BH}$ Estimator	Ref.	Adopted	$L_{\rm disk}/L_{\rm Edd}$
	(1)	(2)	(3)	(4)	(5)
1253−055	8.70	L(C IV) $= 26.61 \times 10^{42}$ erg s^{-1}, FWHM(C IV) $= 8613$ km s^{-1}	Tor12	8.70	3.1e-2
1308+326	8.77	L(Mg II) $= 29.95 \times 10^{42}$ erg s^{-1}, FWHM(Mg II) $= 4016$ km s^{-1}	Wang04	8.85	3.9e-2
	8.93	L(Mg II) $= 21.33 \times 10^{42}$ erg s^{-1}, FWHM(Mg II) $= 5267$ km s^{-1}	Tor12		
1335−127	8.64	L(Mg II) $= 9.33 \times 10^{42}$ erg s^{-1}, FWHM(Mg II) $= 4602$ km s^{-1}	Wang04	8.64	2.4e-2
1510−089	8.20	Single epoch Hβ line	Liu06	8.40	1.3e-1
	8.46	L(Hβ) $= 17.68 \times 10^{42}$ erg s^{-1}, FWHM(Hβ) $= 3180$ km s^{-1}	Wang04		
	8.54	L(Hβ) $= 21.94 \times 10^{42}$ erg s^{-1}, FWHM(Hβ) $= 3250$ km s^{-1}	Tor12		
1633+382	8.67	Single epoch Mg II line	Liu06	9.05	2.2e-1
	9.27	L(Mg II) $= 78.33 \times 10^{42}$ erg s^{-1}, FWHM(Mg II) $= 5583$ km s^{-1}	Tor12		
	9.20	L(C IV) $= 318.55 \times 10^{42}$ erg s^{-1}, FWHM(C IV) $= 6499$ km s^{-1}	Tor12		
1641+399	9.27	Single epoch Hβ line	Liu06	9.05	9.2e-2
	9.14	L(Hβ) $= 46.51 \times 10^{42}$ erg s^{-1}, FWHM(Hβ) $= 5140$ km s^{-1}	Wang04		
	8.46	L(Hβ) $= 10.80 \times 10^{42}$ erg s^{-1}, FWHM(Hβ) $= 3700$ km s^{-1}	Tor12		
	9.32	L(Mg II) $= 102.18 \times 10^{42}$ erg s^{-1}, FWHM(Mg II) $= 5520$ km s^{-1}	Tor12		
	9.07	L(C IV) $= 192.96 \times 10^{42}$ erg s^{-1}, FWHM(C IV) $= 6710$ km s^{-1}	Tor12		
1652+398	8.78	$M_{\rm BH}$-σ relation, $\sigma = 291$ km s^{-1}	Fal02	9.00	1.3e-4[a]
	9.21	$M_{\rm BH}$-σ relation, $\sigma = 372$ km s^{-1}	Bar03		
1749+096	8.66	$M_{\rm bh}$-$L_{\rm bulge}$ relation	Fal03a	8.66	8.8e-3[a]
1803+784	7.92	Single epoch Hβ line	Liu06	8.26	1.2e-1
	8.17	L(Mg II) $= 13.38 \times 10^{42}$ erg s^{-1}, FWHM(Mg II) $= 2451$ km s^{-1}	Wang04		
	8.69	L(Hβ) $= 15.59 \times 10^{42}$ erg s^{-1}, FWHM(Hβ) $= 4320$ km s^{-1}	Tor12		

Table 7.3. Continued.

Black hole masses and disk luminosities (in Eddington units)

Object	$\log M_{\rm BH}$	$M_{\rm BH}$ Estimator	Ref.	Adopted	$L_{\rm disk}/L_{\rm Edd}$
	(1)	(2)	(3)	(4)	(5)
1921−293	9.14	$L(\mathrm{H}\beta) = 7.35 \times 10^{42}$ erg s^{-1}, FWHM(Hβ) = 9134 km s^{-1}	Wang04	9.14	9.0e-3
	8.35	Single epoch Hβ line	Liu06		
1928+738	8.64	$L(\mathrm{H}\beta) = 28.60 \times 10^{42}$ erg s^{-1}, FWHM(Hβ) = 3360 km s^{-1}	Wang04	8.57	1.9e-1
	8.73	$L(\mathrm{H}\beta) = 39.20 \times 10^{42}$ erg s^{-1}, FWHM(Hβ) = 3360 km s^{-1}	Tor12		
2007+777	8.80	$M_{\rm bh}$-$L_{\rm bulge}$ relation	Fal03a	8.80	1.4e-3[a]
	8.52	$L(\mathrm{MgII}) = 39.48 \times 10^{42}$ erg s^{-1}, FWHM(MgII) = 2800 km s^{-1}	Wang04		
2134+004	9.44	$L(\mathrm{Mg\ II}) = 235.34 \times 10^{42}$ erg s^{-1}, FWHM(Mg II) = 5194 km s^{-1}	Tor12	9.18	1.7e-1
	9.58	$L(\mathrm{C\ IV}) = 794.82 \times 10^{42}$ erg s^{-1}, FWHM(Hβ) = 7418 km s^{-1}	Tor12		
	8.87	Single epoch Mg II line	Liu06		
2145+067	9.64	$L(\mathrm{Mg\ II}) = 457.33 \times 10^{42}$ erg s^{-1}, FWHM(Mg II) = 5517 km s^{-1}	Tor12	9.31	2.1e-1
	9.41	$L(\mathrm{C\ IV}) = 663.85 \times 10^{42}$ erg s^{-1}, FWHM(C IV) = 6423 km s^{-1}	Tor12		
2200+420	8.77	$M_{\rm bh}$-$L_{\rm bulge}$ relation	Fal03a	8.77	3.8e-4[a]
2223−052	8.57	$L(\mathrm{C\ IV}) = 247.89 \times 10^{42}$ erg s^{-1}, FWHM(C IV) = 3449 km s^{-1}	Wang04	8.57	3.9e-1
2230+114	9.08	$L(\mathrm{Mg\ II}) = 71.21 \times 10^{42}$ erg s^{-1}, FWHM(Mg II) = 4583 km s^{-1}	Tor12	9.07	9.7e2
	9.06	$L(\mathrm{C\ IV}) = 255.71 \times 10^{42}$ erg s^{-1}, FWHM(C IV) = 5990 km s^{-1}			
	8.86	Single epoch Hβ line	Liu06		
2251+158	9.30	$L(\mathrm{Mg\ II}) = 125.98 \times 10^{42}$ erg s^{-1}, FWHM(Mg II) = 5162 km s^{-1}	Tor12	9.15	1.8e-1
	9.29	$L(\mathrm{C\ IV}) = 250.01 \times 10^{42}$ erg s^{-1}, FWHM(C IV) = 7875 km s^{-1}	Tor12		

Table 7.3. Continued.

Chapter 8

No asymmetric outflows from Sagittarius A* during the pericenter passage of the gas cloud G2[†]

Abstract

The gas cloud G2 that falls toward Sagittarius A* (Sgr A*), the supermassive black hole at the center of the Milky Way, is assumed to provide valuable information on the physics of accretion flows and the environment of the black hole. We observed Sgr A* with four European stations of the Global Millimeter Very Long Baseline Interferometry Array (GMVA) at 86 GHz on 1 October 2013 when parts of G2 had already passed the pericenter. We searched for a possible transient asymmetric structure – such as jets or winds from hot accretion flows – around Sgr A* that might be caused by accretion of material from G2. The interferometric closure phases remained zero within errors during the observation time. We therefore conclude that Sgr A* did not show signifi-

[†]The contents of this chapter was originally published in Astronomy & Astrophysics (Park et al. 2015)

cant asymmetric (in the observer frame) outflows in late 2013. Using simulations, we constrain the size of the outflows that we could have missed to ≈2.5 mas along the major axis and ≈0.4 mas along the minor axis of the beam, corresponding to approximately 232 and 35 Schwarzschild radii, respectively; we thus probe spatial scales on which the jets of radio galaxies are thought to convert magnetic into kinetic energy. Because probably less than 0.2 Jy of the flux from Sgr A* can be attributed to accretion from G2, the effective accretion rate is $\eta\dot{M} \lesssim 1.5 \times 10^9\ \mathrm{kg\,s^{-1}} \approx 7.7 \times 10^{-9}\, M_\oplus\,\mathrm{yr^{-1}}$ for material from G2. Exploiting the relation of kinetic jet power to accretion power of radio galaxies shows that the rate of accretion of matter that is finally deposited in jets is limited to $\dot{M} \lesssim 10^{17}\,\mathrm{kg\,s^{-1}} \approx 0.5 M_\oplus\,\mathrm{yr^{-1}}$. Accordingly, G2 appears to be mostly stable against loss of angular momentum and subsequent (partial) accretion at least on timescales $\lesssim$1 year.

8.1 Introduction

With a mass of $M_\bullet \approx 4.3 \times 10^6 M_\odot$ and located at the center of the Milky Way at a distance of $R_0 \approx 8$ kpc, Sagittarius A* (Sgr A*) is the nearest supermassive black hole (see, e.g., Genzel et al. 2010 for a review). Thanks to its proximity, the Galactic center serves as an excellent laboratory for the astrophysics of galactic nuclei; for the given mass and distance, 1 milliarcsecond ≡ 8 a.u. ≡ 94 R_S, with R_S denoting the Schwarzschild radius. Sgr A* is characterized by its low luminosity compared to active galactic nuclei (AGN), with a bolometric luminosity $\lesssim 2 \times 10^{-8}$ of its Eddington luminosity (see Narayan et al. 1998 and references therein). Sgr A* shows a slightly inverted radio spectrum peaking at mm-to-submm wavelengths (Zylka et al. 1992; Falcke et al. 1998; Melia & Falcke 2001; Bower et al. 2015).

The emission mechanism of Sgr A* is a matter of ongoing debate. On the one hand, radiatively inefficient accretion flows (RIAFs; e.g., Yuan et al. 2003) successfully reproduce the observed fluxes at various wavelengths. On the other hand, multiple studies (Falcke, & Markoff 2000; Markoff et al. 2001; Yuan et al. 2002; Markoff et al. 2007; Falcke et al. 2009) have pointed out that parts of the emission need to originate from jets,

which is supported by observational evidence for the presence of jets (Yusef-Zadeh et al. 2012; Li, Morris & Baganoff 2013). The current lack of structural information on Sgr A* prevents an unambiguous decision between competing theories. At the short-wavelength side of the submm-bump, where the emission becomes optically thin, instruments with the necessary spatial resolution are not available. At wavelengths of more than a few millimeters, the source structure is washed out by interstellar scattering (e.g., Bower et al. 2006). Lu et al. (2011) found evidence that the shape and orientation of the elliptical Gaussian changes with frequency; this could be interpreted as an intrinsic structure that is slightly misaligned with the scattering disk, which shines through toward higher frequencies. In addition, recent Very Long Baseline Interferometry (VLBI) observations at 43 GHz have been able to resolve an intrinsic elliptical structure with a preferred geometrical axis (Bower et al. 2014). This structure might indicate an existence of jets, but could also be the result of an elongated accretion flow such as a black hole crescent (e.g., Kamruddin, & Dexter 2013).

Recently, a gas cloud labeled G2 was observed to move toward Sgr A* on a nearly radial orbit (Gillessen et al. 2012). So far, mainly two possible structures of G2 have been discussed, with the first scenario being that G2 is a localized overdense region within an extended gas streamer. This agrees with observations reporting that G2 is composed of a compact head and a more widespread tail (Gillessen et al. 2013b; Pfuhl et al. 2015). The two components are on approximately the same orbit and are connected by a faint bridge in position-velocity diagrams, indicating that they might share the same origin. According to this scenario, the pericenter passage started in early 2013 (Gillessen et al. 2013a) and lasted over one year ,while G2 has been stretched substantially along its orbit by tidal shearing caused by the gravitational potential of Sgr A* (Pfuhl et al. 2015). Test particle simulations have provided a good explanation for the dynamics of G2; the results showed that hydrodynamic effects have not been significant (e.g., Pfuhl et al. 2015; see also Schartmann et al. 2012). The second possibility under discussion is that G2 is a circumstellar cloud around a star that provides stabilizing gravity and continuously replenishes the gas. Studies supporting this scenario highlighted that the

tail might only be a fore- or background feature and might not be physically connected to G2 (Phifer et al. 2013; Valencia-S., et al. 2015). Recent observations have also shown that G2 survived its pericenter passage as a compact source, which might be a clue that G2 is a star enshrouded by gas and/or dust (Witzel et al. 2014; Valencia-S., et al. 2015). This scenario was modeled analytically (Miralda-Escudé 2012; Scoville & Burkert 2013) and explored with the help of numerical simulations (Ballone et al. 2013; De Colle et al. 2014; Zajaček et al. 2014).

Interactions with the accretion flows toward Sgr A* might cause G2 to lose angular momentum, and as a result, parts of it may be accreted by the black hole (Anninos et al. 2012; Burkert et al. 2012; Schartmann et al. 2012). Accordingly, an increased radio luminosity (e.g., Mahadevan 1997; Mościbrodzka et al. 2012) as well as an increase in source size might be expected (e.g., Mościbrodzka et al. 2012). In addition, radio-bright outflows such as jets or wind-like outflows related to RIAFs (Yuan et al. 2003; Mościbrodzka et al. 2012; Liu & Wu 2013) might become observable on spatial scales of $\lesssim 1$ mas. To search for such transient structures, we performed VLBI observations with four European stations of the Global Millimeter VLBI Array (GMVA) at 86 GHz, providing an angular resolution down to $\approx$0.3 mas. Our observing frequency of 86 GHz is in a region where scattering vanishes and is weaker in the images of Sgr A* at frequencies lower than about 43 GHz (Bower et al. 2004, 2006; Shen et al. 2005).

8.2 Observations and data analysis

We observed Sgr A* at 86 GHz on 1 October 2013 using four GMVA stations of the European VLBI Network (EVN): Effelsberg (EF), Pico Veleta (PV), Plateau de Bure (PB), and Yebes (YS). A combination of the low declination of Sgr A* ($-29°$), the high latitude of the stations (the minimum latitude being 37° for Pico Veleta), and a technical problem at Yebes station limited our observing times to around 1.5 hours for Yebes and 2.5 hours for the other stations. We observed both circular polarizations except for Yebes station, where only left circular polarization (LCP) data were obtained. The data were recorded with the Mark 5 VLBI system (two-bit sampling) using the

digital baseband converter (DBBC) in polyphase-filter bank mode with a bandwidth of 32 channels, each 16 MHz wide (total bandwidth 512 MHz). All data were correlated with the DifX VLBI correlator of the MPIfR (Bonn, Germany). Our calibrators (fringe-finding sources) were NRAO 530 and 1633+38.

We followed the standard procedures for initial phase and amplitude calibration using the AIPS software package (Greisen 2003) and applied phase self-calibration using the Caltech Difmap package (Shepherd 1997) with a point-source model. The geometry of our observation resulted in a very elongated beam (point spread function) with full widths at half maximum (FWHM) of 3.02 mas and 0.33 mas, respectively, at a position angle of $-22°$. For the flux density of Sgr A* we found a value of $\approx 1.4 \pm 0.3$ Jy).

We used the evolution of closure phases to search for asymmetric, extended emission around Sgr A*. A closure phase is the sum of the interferometric phases of the three baselines in a closed triangle of stations; it is free from antenna-based phase errors (e.g., Thompson et al. 2001). The closure phase for a centrally symmetric brightness distribution is zero. The amount of deviation from zero and the timescales of fluctuations of the closure phases can be used to probe the structure of an asymmetric source even if it cannot be imaged (due to lack of flux or insufficient *uv* plane coverage). This technique was previously used by Krichbaum et al. (2006) and Lu et al. (2011), who found the closure phases of Sgr A* to be consistent with zero throughout their observations in October 2005 and May 2007.

We extracted the closure phases from the visibility data for three independent triangles of the VLBI stations, initially binned into 10-second time bins. We flagged data with large errors (larger than the standard deviation of the data for a given triangle) and obvious outliers. The fraction of flagged data is 8.9%, 7.9%, and 6.0% for the triangles EF-PB-PV, EF-PV-YS, and PB-PV-YS, respectively; the difference between the results obtained with and without flagging is insignificant, however. We took the weighted average of the remaining values for each scan of 6 minutes; the resulting data set is shown in Fig. 8.1. We obtained a combined reduced χ^2 value of 1.34 for all the

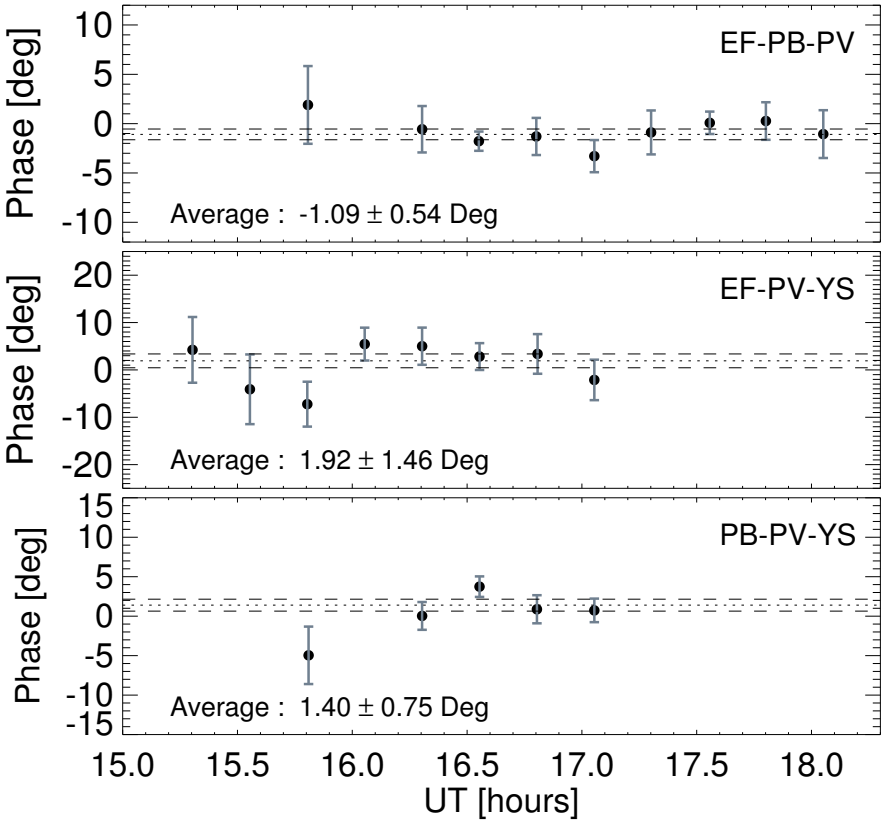

Figure 8.1. Closure phases vs. time for three independent VLBI triangles. Each data point denotes a closure phase measurement averaged over one scan of six minutes; error bars correspond to 1σ errors. Dotted lines indicate weighted averages of all data points, dashed lines represent the corresponding standard errors of mean. Average phase values are noted in each diagram. Phases for the triangle EF-PB-PV are extracted from Stokes I data, phases for the other triangles from LL data.

closure phases for all the independent triangles based on the null hypothesis that the closure phase is zero all the time. The corresponding false-alarm probability (p-value) is 0.136; this value is clearly too high to reject the null hypothesis (this outcome did not change when choosing bin sizes other than 6 min). Consequently, we conclude that the closure phases agree with zero during the observing time.

8.3 Discussion

The absence of a deviation of the closure phases from zero – within typical errors of a few degrees – implies the absence of asymmetric structure around Sgr A* at the time of our observation. A priori, bipolar, symmetric jets can account for zero closure phases. However, if the jet axis is oriented partly along the line of sight, the flux observed from the jet approaching the observer (f_+) is amplified while that from the receding jet (f_-) is dimmed by the Doppler effect. If the jets on both sides of the black hole have the same luminosity intrinsically, the observed ratio of the two fluxes is

$$\frac{f_+}{f_-} = \left(\frac{1+\beta\cos\theta}{1-\beta\cos\theta}\right)^{2+\alpha} \tag{8.1}$$

(e.g., Beckmann & Shrader 2012), where β is the jet speed in units of speed of light, θ is the angle between the jet axis and the line of sight, and α is the spectral index defined via the flux density $S_\nu \propto \nu^\alpha$. Various observational constraints ($\alpha \approx 0.5$, $\beta \lesssim 0.1$; Lu et al. 2011) and model predictions for transient jets ($\theta \approx 60°$, $\beta \approx 0.7$; Falcke et al. 1998, 2009) place the flux ratios to be expected at between ≈1 and ≈6. Accordingly, even intrinsically symmetric jets from Sgr A* might appear asymmetric in the observer frame.

To constrain the size of outflows that we could have missed, we performed simple simulations. We placed artificial, unipolar secondary sources next to a primary point source model representing Sgr A* and compared the closure phases obtained from the resulting artificial visibility data with the observations. We considered two geometries: a single-point source and a jet composed of ten equally spaced point sources (knots) with equal fluxes. We probed four orientations for the simulated outflows (see Fig. 8.2): along the major axis, along the minor axis of the beam, the jet direction claimed by Li, Morris & Baganoff (2013), and the jet direction claimed by Yusef-Zadeh et al. (2012). We used total fluxes of 0.2 Jy and 0.55 Jy for the artificial sources; these values ensure that our simulated outflows are sufficiently faint to not violate the constraints given by the known recent brightness evolution of Sgr A* (0.2 Jy from the mean variability of ≈15% from June 2013 to February 2014 at 41 GHz, with 0.55 Jy corresponding to

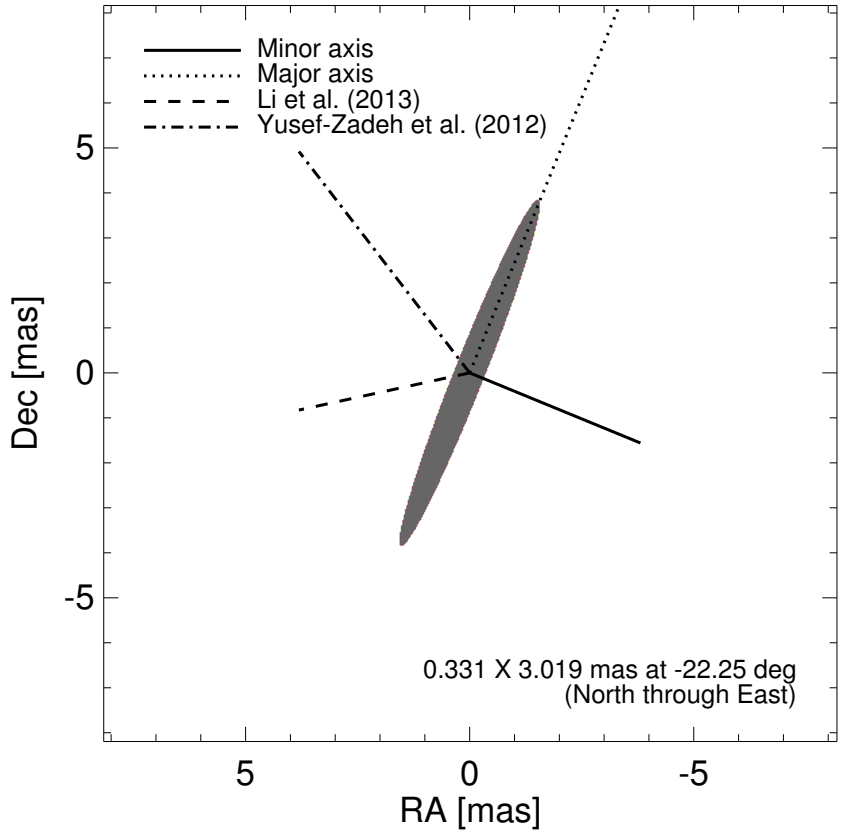

Figure 8.2. Outflow orientations assumed in our simulation. The gray ellipse (with FWHM and position angle as noted) indicates the beam, dashed lines indicate four outflow orientations: along the major axis, along the minor axis, along the jet direction claimed by Li, Morris & Baganoff (2013), and along the direction claimed by Yusef-Zadeh et al. (2012).

the strongest variation in the same period (Chandler & Sjouwerman 2014)). For each simulation setup, we measured the average of absolute values of the closure phases for each triangle. We varied the distances of the model sources (for the jet model: the largest distance) from Sgr A* until we found a critical distance at which the absolute values of the simulated closure phases exceeded those of the observations by more than the 1σ error at all triangles. We summarize our results in Table 8.1. As expected, the critical distances are smaller for brighter outflows. Jet-like structures lead to larger critical distances than equally luminous single, compact sources. As a consequence of

the very elongated beam, the critical distances for sources located along the major axis of the beam are larger by a factor of ≈7 than for those located along the minor axis. In a few cases (denoted 'N/A' in Table 8.1), the absolute values of the simulated closure phases were similar to those of the observations for all distances of the model sources, meaning that we were unable to identify a critical distance. Overall, our observations limit the extension of asymmetric (in the observer frame) jet-like outflows from Sgr A* to projected distances of ≈2.5 mas along the major axis and ≈0.4 mas along the minor axis.

Our analysis limits the (projected) extension of linear outflows to about 232 and 35 Schwarzschild radii, respectively, for outflows with fluxes of about 0.2 Jy; obviously, outflows substantially fainter could be larger and still remain undetected. Unfortunately, the resolution of our observations is not sufficient to probe structures in accretion flows that are expected to occur on scales $\lesssim 10\,R_{\rm S}$ (cf., e.g., Broderick et al. 2011); those observations will probably have to await the Event Horizon Telescope (cf. Fish et al. 2014). When referring to radio galaxies for comparison, especially to M 87, which has a central black hole with small angular diameter (≈10 μas) second only to Sgr A*, a distance of tens of Schwarzschild radii appears to be critical for the formation of AGN jets. Recent VLBI observations of the jet of M 87 find a transition in the collimation geometry at a distance of about $100\,R_{\rm S}$, with the jet opening angle being smaller outside this boundary; this has been interpreted as $\approx 100\,R_{\rm S}$ being the characteristic distance for the conversion of magnetic to kinetic energy in a magnetically launched jet (Hada et al. 2013). Accordingly, Sgr A* is potentially a very important test case for AGN jet physics *if* a jet is ever detected.

Our nondetection of outflows is consistent with earlier null results from VLBI observations of Sgr A* at 86 GHz (Krichbaum et al. 1998; Lo et al. 1998; Shen et al. 2005; Lu et al. 2011) even though we observed Sgr A* at an epoch of potentially increased accretion. Our results are in line with other recent observations finding that Sgr A* has been quiescent from radio to X-rays in 2013 and 2014 (Akiyama et al. 2013; Brunthaler & Falcke 2013; Chandler & Sjouwerman 2014; Degenaar et al. 2014). In addition, the zero

Size constraints for outflows from Sgr A*.

		Minor axis		Major axis		Li+ 2013		YZ+ 2012	
	Triangle	0.2 Jy	0.55 Jy	0.2 Jy	0.55 Jy	0.2 Jy	0.55 Jy	0.2 Jy	0.55 Jy
Point source	EF-PB-PV	0.22 [21]	0.19 [18]	1.21 [114]	1.10 [104]	0.44 [41]	0.39 [36]	0.22 [20]	0.19 [18]
	EF-PB-YS	0.22 [21]	0.19 [18]	1.85 [174]	1.62 [152]	N/A	0.56 [52]	0.22 [20]	0.19 [18]
	PB-PV-YS	0.24 [22]	0.21 [20]	1.66 [156]	1.51 [142]	0.59 [55]	0.47 [44]	0.23 [22]	0.21 [20]
	Average	0.23 [21]	0.20 [19]	1.57 [148]	1.41 [133]	0.51 [48]	0.47 [44]	0.22 [21]	0.20 [18]
Knotty jet	EF-PB-PV	0.36 [34]	0.28 [26]	1.84 [173]	1.52 [143]	0.67 [63]	0.54 [51]	0.35 [33]	0.27 [25]
	EF-PB-YS	0.39 [36]	0.28 [26]	2.97 [279]	2.32 [218]	N/A	N/A	0.37 [34]	0.27 [26]
	PB-PV-YS	0.37 [34]	0.30 [28]	2.58 [243]	2.10 [198]	N/A	0.72 [68]	0.36 [33]	0.29 [27]
	Average	0.37 [35]	0.29 [27]	2.47 [232]	1.98 [186]	0.67 [63]	0.63 [60]	0.36 [34]	0.28 [26]

Table 8.1. Critical distances (see Sect. 8.3 for details) for various cases: four directions for the location of the artificial sources – along the major axis of the beam, along the minor axis, along the jet direction claimed by Li, Morris & Baganoff (2013), and along the direction claimed by Yusef-Zadeh et al. (2012); two total flux densities of the artificial sources – 0.2 Jy and 0.55 Jy; and two simple geometries – a single-point source and a knotty jet composed of ten equidistant point-like components. Values outside [inside] brackets are in units of milliarcseconds [Schwarzschild radii]. All values are projected distances.

closure phases within errors can set some constraints on the substructure in scattering disks of Sgr A* (e.g., Gwinn et al. 2014); this substructure must remain symmetric on spatial scales of from submas to a few mas depending on an axis in the geometry of the substructure.

As noted above, the radio flux density that can realistically be attributed to accretion of parts of G2 is $S_\nu \approx 0.2$ Jy, translating into a radio luminosity $L_\mathrm{R} = 4\pi R_0^2 \nu S_\nu \approx 1.3 \times 10^{26}$ W $\approx 0.3\,L_\odot$ (for $\nu = 86$ GHz). Without making further assumptions, we can state that this value corresponds to an effective accretion rate $\eta\dot{M} = L_\mathrm{R}/c^2 \approx 1.5 \times 10^9\ \mathrm{kg\,s^{-1}} \approx 7.7 \times 10^{-9}\,M_\oplus\,\mathrm{yr^{-1}}$, with $\eta \in [0, 1]$ being the matter-to-light conversion efficiency and c denoting the speed of light. However, in addition, we have to take into account that accreted matter might not be converted into electromagnetic radiation, but into jets, with the presence of jets being an ad hoc working hypothesis. In this case, a rough quantitative estimate of the accretion rate is provided by the relation of jet power to accretion power of radio galaxies: for highly sub-Eddington accretion (as is the case for Sgr A*), kinetic jet power P_jet and accretion power $P_\mathrm{acc} \equiv \dot{M}c^2$ are related as $P_\mathrm{jet} \approx 0.01 P_\mathrm{acc}$ (e.g., Allen et al. 2006; Trippe 2014). The powers P_jet and L_R in turn are empirically relatedas $P_\mathrm{jet} \approx 5.8 \times 10^{36}\,(L_\mathrm{R}/10^{33})^{0.7}$ W (Cavagnolo et al. 2010). Combining the two relations and using, again, $L_\mathrm{R} \lesssim 0.2$ Jy implies an accretion rate $\dot{M} \lesssim 10^{17}\,\mathrm{kg\,s^{-1}} \approx 0.5\,M_\oplus\,\mathrm{yr^{-1}}$. We note that this calculation assumes a highly idealized situation, neglecting interactions between G2 and the accretion flow around Sgr A*. Given the low accretion rates as well as the complexity of the accretion flows, it seems realistic that relatively large amounts of matter could be "peeled off" G2 and driven out of the accretion zone by winds or other noncollimated outflows.

These limits on accretion rates, which are always substantially lower than the total mass of G2 (with details depending on which structure of G2 is assumed), are consistent with the observed kinematics of G2 during its pericenter passage: as noted by several studies, the orbit was purely Keplerian even after the pericenter passage (Witzel et al. 2014; Pfuhl et al. 2015; Valencia-S., et al. 2015). This indicates that G2 did not experience a notable loss of angular momentum and energy, which indicates rather

weak interactions with the hot gas around Sgr A*. As suggested by several studies based on hydrodynamical simulations, the viscous timescale can be on the order of years (Burkert et al. 2012; Schartmann et al. 2012; Mościbrodzka et al. 2012), meaning that it could take a few more years to see AGN-like (mostly in radio mode associated with hot accretion flows and jets, see Yuan & Narayan 2014 for a review) activity in Sgr A*. Overall, our analysis suggests that G2 is mostly stable against loss of angular momentum and subsequent (partial) accretion at least on timescales $\lesssim$1 year.

Bibliography

Aaron, S., 1997, EVN Memo #78, "Calibration of VLBI polarization data", http://pc.astro.brandeis.edu/pdfs/evnmemo78.pdf

Aartsen, M. G., et al. 2018, Science, 361, eaat1378

Abdo, A. A., Ackermann, M., Agudo, I., et al. 2010, ApJ, 721, 1425

Abdo, A. A., Ackermann, M., Ajello, M., et al. 2010, ApJ, 722, 520

Abramowicz, M.A., Bao, G., Lanza, A., & Zhang, X. -H. 1991, A&A, 245, 454

Acciari, V. A., Aliu, E., Arlen, T., et al. 2009, Sci, 325, 444

Acero, F., Ackermann, M., Ajello, M., et al. 2015, ApJS, 218, 23

Acero, F., Ackermann, M., Ajello, M., et al. 2016, ApJS, 223, 26

Ackermann, M., Ajello, M., Atwood, W. B., et al. 2015, ApJ, 810, 14

Agudo, I., Gómez, J.-L., Martí, J.-M., et al. 2001, ApJ, 549, L183

Agudo, I., Marscher, A. P., Jorstad, S. G., et al. 2012, ApJ, 747, 63

Agudo, I., Thum, C., Gómez, J. L., & Wiesemeyer, H. 2014, A&A, 566, 59

Agudo, I., Thum, C., Molina, S. N., et al. 2018a, MNRAS, 474, 1427

Agudo, I., Thum, C., Ramakrishnan, V., et al. 2018b, MNRAS, 473, 1850

Ahnen, M. L., Ansoldi, S., Antonelli, L. A., et al. 2017, A&A, 603, A29

Akiyama, K., Kino, M., Sohn, B.-W., et al. 2013, The Galactic Center: Feeding and Feedback in a Normal Galactic Nucleus, Proc. IAU, IAU Symp., 303, 288

Akiyama, K., Lu, R.-S., Fish, V. L., et al. 2015, ApJ, 807, 150

Akiyama, K., Kuramochi, K., Ikeda, S., et al. 2017, ApJ, 838, 1

Aleksić, J., Anderhub, H., Antonelli, L. A., et al. 2011a, A&A, 530, A4

Aleksić, J., Anderhub, H., Antonelli, L. A., et al. 2011b, ApJ, 730, L8

Aleksić, J., Ansoldi, S., Antonelli, L. A., et al. 2014, A&A, 569, A46

Algaba, J. C. 2013, MNRAS, 429, 3551

Algaba, J. C., Asada, K., & Nakamura, M. 2016, ApJ, 823, 86

Algaba, J.-C., Gabuzda, D. C., & Smith, P. S. 2011, MNRAS, 411, 85

Algaba, J.-C., Gabuzda, D. C., & Smith, P. S. 2012, MNRAS, 420, 542

Algaba, J. C., Lee, S.-S., Rani, B., et al. 2018, ApJ, 859, 128

Algaba, J.-C., Nakamura, M., Asada, K., & Lee, S.-S. 2017, ApJ, 834, 65

Algaba, J.-C., Zhao, G.-Y., Lee, S.-S., et al. 2015, JKAS, 48, 237

Allen, S. W., Dunn, R. J. H., Fabian, A. C., Taylor, G. B., & Reynolds, C. S. 2006, MNRAS, 372, 21

Aller, H. D., Aller, M. F., Latimer, G. E., & Hodge, P. E. 1985, ApJS, 59, 513

Aller, M. F., Aller, H. D., & Hughes, P. A. 2003, ApJ, 586, 33

An, T., Sohn, B. W., & Imai, H. 2018, NatAs, 2, 118

Anninos, P., Fragile, P. C., Wilson, J., & Murray, S. D. 2012, ApJ, 759, 132

Arshakian, T. G., León-Tavares, J., Lobanov, A. P., et al. 2010, MNRAS, 401, 1231

Asada, K., Inoue, M., Nakamura, M., Kameno, S., & Nagai, H. 2008, ApJ, 682, 798

Asada, K., Inoue, M., Uchida, Y., et al. 2002, PASJ, 54, L39

Asada, K., & Nakamura, M. 2012, ApJ, 745, L28

Asada, K., Nakamura, M., Doi, A., Nagai, H., & Inoue, M. 2014, ApJ, 781, L2

Attridge, J. M., Roberts, D. H., & Wardle, J. F. C. 1999, ApJ, 518, L87

Attridge, J. M., Wardle, J. F. C., & Homan, D. C. 2005, ApJ, 633, 85

Atwood, W. B., Abdo, A. A., Ackermann, M., et al. 2009, ApJ, 697, 1071

Balbus, S. A., & Hawley, J. F. 1991, ApJ, 376, 214

Hawley, J. F., & Balbus, S. A. 2002, ApJ, 573, 738

Ballone, A., Schartmann, M., Burkert, A., et al. 2013, ApJ, 776, 13

Balmaverde, B., Baldi, R. D., & Capetti, A. 2008, A&A, 486, 119

Barnacka, A., Moderski, R., Behera, B., Brun, P., & Wagner, S. 2014, A&A, 567, A113

Barth, A. J., Ho, L., C., & Sargent, W. L. W. 2003, ApJ, 583, 134

Baum, S. A., Zirbel, E. L., & O'Dea, C. P. 1995, ApJ, 451, 88

Beckmann, V., & Shrader, C. 2012, Active Galactic Nuclei, Weinheim: Wiley-VCH

Begelman, M. C. 2012, MNRAS, 420, 2912

Begelman, M. C., & Li, Z.-Y. 1994, ApJ, 426, 269

Benlloch, S., Wilms, J., Edelson, R., et al. 2001, ApJ, 562, L121

Bettoni, D., Falomo, R., Fasano, G., & Govoni, F. 2003, A&A, 399, 869

Bicknell, G. V., & Begelman, M. C. 1996, ApJ, 467, 597

Bird, S., Harris, W. E., Blakeslee, J. P., & Flynn, C. 2010, A&A, 524, A71

Biretta, J. A., Sparks, W. B., & Macchetto, F. 1999, ApJ, 520, 621

Biretta, J. A., Zhou, F., & Owen, F. N. 1995, ApJ, 447, 582

Blakeslee, J. P., Jordán, A., Mei, S., et al. 2009, ApJ, 694, 556

Blandford, R. D., & Begelman, M. C. 1999, MNRAS, 303, L1

Blandford, R. D., & Begelman, M. C. 2004, MNRAS, 349, 68

Blandford, R. D., & Königl, A. ApJ, 232, 34

Blandford, R., Meier, D., & Readhead, A. 2018, ARA&A, in press (arXiv:1812.06025)

Blandford, R. D., & Payne, D. G. 1982, MNRAS, 199, 883

Blandford, R. D., & Znajek, R. L. 1977, MNRAS, 179, 433

Błażejowski, M., Sikora, M., Moderski, R., & Madejski, G. M. 2000, ApJ, 545, 107

Blinov, D., Pavlidou, V., Papadakis, I., et al. 2015, MNRAS, 453, 1669

Bloom, S. D., & Marscher, A. P. 1996, ApJ, 461, 657

Boccardi, B., Krichbaum, T. P., Bach, U., et al. 2016, A&A, 585, A33

Bodo, G., & Tavecchio, F. 2018, A&A, 609, A112

Boettcher, M., Harris, D. E., & Krawczynski, H. 2012, Relativistic Jets from Active Galactic Nuclei (Berlin: Wiley)

Bogovalov, S., & Tsinganos, K. 2005, MNRAS, 357, 918

Bonning, E., Urry, C. M., Bailyn, C., et al. 2012, ApJ, 756, 13

Böttcher, M. & Chiang, J. 2002, ApJ, 581, 127

Böttcher, M., Reimer, A., Sweeney, K., & Prakash, A. 2013, ApJ, 768, 54

Bower, G. C., Broderick, A., Dexter, J., et al. 2018, ApJ, 868, 101

Bower, G. C., Dexter, J., Markoff, S., Rao, R., & Plambeck, R. L. 2017, ApJ, 843, L31

Bower, G. C., Falcke, H., Herrnstein, R. M., et al. 2004, Science, 304, 704

Bower, G. C., Goss W. M., Falcke H., et al. 2006, ApJ, 648, L127

Bower, G. C., Markoff, S., Brunthaler, A., et al. 2014, ApJ, 790, 1

Bower, G. C., Markoff, S., Dexter, J., et al. 2015, ApJ, 802, 69

Bower, G. C., Wright, M. C. H., Falcke, H., & Backer, D. C. 2003, ApJ, 588, 331

Britzen, S., Fendt, C., Eckart, A., & Karas, V. 2017, A&A, 601, A52

Broderick, A. E., & Loeb, A. 2009, ApJ, 697, 1164

Broderick, A. E., & McKinney, J. C. 2010, ApJ, 725, 750

Broderick, A. E., Fish, V. L., Doeleman, S. S., & Loeb, A. 2011, ApJ, 738, 38

Broderick, A. E., Narayan, R., Kormendy, J., et al. 2015, ApJ, 805, 179

Bromberg, O., & Levinson, A. 2009, ApJ, 699, 1274

Bromberg, O., & Tchekhovskoy, A. 2016, MNRAS, 456, 1739

Brunthaler, A., & Falcke, H. 2013, ATel, 5159, 1

Bu, D.-F., & Mosallanezhad, A. 2018, A&A, 615, A35

Bu, D.-F., Yuan, F., Gan, Z.-M., & Yang, X.-H. 2016a, ApJ, 818, 83

Bu, D.-F., Yuan, F., Gan, Z.-M., & Yang, X.-H. 2016b, ApJ, 823, 90

Burkert, A., Schartmann, M., Alig, C., et al. 2012, ApJ, 750, 58

Burn, B. J. 1966, MNRAS, 133, 67

Calderone, G., Ghisellini, G., Colpi, M., & Dotti, M. 2013, MNRAS, 431, 210

Cantiello, M., Blakeslee, J. P., Ferrarese, L., et al. 2018, ApJ, 856, 126

Canvin, J. R., Laing, R. A., Bridle, A. H., & Cotton, W. D. 2005, MNRAS, 363, 1223

Cavagnolo, K. W., McNamara, B. R., Nulsen, P. E. J., et al. 2010, ApJ, 720, 1066

Cavaliere, A., & D'Elia, V. 2002, ApJ, 571, 226

Cawthorne, T. V. 2006, MNRAS, 367, 851

Cawthorne, T. V., Jorstad, S. G., & Marscher, A. P. 2013, ApJ, 772, 14

Casadio, C., Gómez, J. L., Grandi, P., et al. 2015, ApJ, 808, 162

Casadio, C., Krichbaum, T., Marscher, A., et al. 2017, Galaxies, 5, 67

Celotti, A., Padovani, P., & Ghisellinni, G. 1997, MNRAS, 286, 415

Chael, A. A., Johnson, M. D., Narayan, R., et al. 2016, ApJ, 829, 11

Chandler, C. J., & Sjouwerman, L. O. 2014, ATel, 6247

Chatterjee, R., Jorstad, S. G., Marscher, A. P., et al. 2008, ApJ, 689, 79

Chatterjee, R., Marscher, A. P., Jorstad, S. G., et al. 2009, ApJ, 704, 1689

Chatterjee, R., Marscher, A. P., Jorstad, S. G., et al. 2011, ApJ, 734, 43

Chatterjee, R., Bailyn, C. D., Bonning, E. W., et al. 2012, ApJ, 749, 191

Chen, Y. J., Zhao, G.-Y., & Shen, Z.-Q. 2011, MNRAS, 416, L109

Cheung, C. C., Harris, D. E., & Stawarz, Ł. 2007, ApJ, 663, L65

Ciaramella, A., Bongardo, C., Aller, H.D., et al. 2004, A&A, 419, 485

Clausen-Brown, E., Lyutikov, M., & Kharb, P. 2011, MNRAS, 415, 2081

Cohen, M. H., Meier, D. L., Arshakian, T. G., et al. 2014, ApJ, 787, 151

Condon, J. J., & Ransom, S. M. 2016, Essential Radio Astronomy (Princeton, NJ: Princeton Univ. Press)

Conway, R. G., Haves, P., Kronberg, P. P., et al. 1974, MNRAS, 168, 137

Crenshaw, D. M., Kraemer, S. B., & George, I. M. 2003, ARA&A, 41, 117

Crenshaw, D. M., & Kraemer, S. B. 2012, ApJ, 753, 75

Croke, S. M., & Gabuzda, D. C. 2008, MNRAS, 386, 619

Daly, R. A., & Marscher, A. P. 1988, ApJ, 334, 539

D'Ammando, F., Raiteri, C. M., Villata, M., et al. 2011, A&A, 529, A145

De Colle, F., Raga, A. C., Contreras-Torres, F. F., & Toledo-Roy, J. C., ApJ, 789, L33

De Villiers, J.-P., Hawley, J. F., Krolik, J. H., & Hirose, S. 2005, ApJ, 620, 878

Degenaar, N., Reynolds, M., Miller, J., et al. 2014, ATel, 6458, 1

Dermer, C. D., Schlickeiser, R., & Mastichiadis, A. 1992, A&A, 256, L27

Dexter, J., McKinney, J. C., & Agol, E. 2012, MNRAS, 421, 1517

Do, T., Ghez, A.M., Morris, M.R., et al. 2009, ApJ, 691, 1021

Dodds-Eden, K., et al. 2011, ApJ, 728, 37

Dodson, R., Edwards, P. G., & Hirabayashi, H. 2006, PASJ, 58, 243

Dodson, R., Rioja, M. J., Molina, S. N., & Gómez, J. L. 2017, ApJ, 834, 177

Doeleman, S. S., Fish, V. L., Schenck, D. E., et al. 2012, Science, 338, 355

Doeleman, S. S., Weintroub, J., Rogers, A. E. E., et al. 2008, Nature, 455, 78

Dotson, A., Georganopoulos, M., Meyer, E. T., & McCann, K. 2015, ApJ, 809, 164

Edelson, R. A., & Krolik, J. H. 1988, ApJ, 333, 646

EHT Collaboration, et al. 2019a, ApJ, 875, L1

EHT Collaboration, et al. 2019b, ApJ, 875, L2

EHT Collaboration, et al. 2019c, ApJ, 875, L3

EHT Collaboration, et al. 2019d, ApJ, 875, L4

EHT Collaboration, et al. 2019e, ApJ, 875, L5

EHT Collaboration, et al. 2019f, ApJ, 875, L6

Eichler, D. 1993, ApJ, 419, 111

Emmanoulopoulos, D., M^{c}Hardy, I. M., & Uttley, P. 2010, MNRAS, 404, 931

Fabian, A. C. 2012, ARAA, 50, 455

Falcke, H., Goss, W. M., Matsuo, H., et al. 1998, ApJ, 499, 731

Falcke, H., & Markoff, S. 2000, A&A, 362, 113

Falcke, H., Markoff, S., & Bower, G. C. 2009, A&A, 496, 77

Falconer, K. 1990, Fractal Geometry: Mathematical Foundations and Applications (Chicester: Wiley)

Falomo, R., Kotilainen, J. K., & Treves, A. 2002, ApJ, 569, L35

Falomo, R., Carangelo, N., & Treves, A. 2003, MNRAS, 343, 505

Falomo, R., Kotilainen, J. K., Carangelo, N., & Treves, A. 2003, ApJ, 595, 624

Fan, J. H. 1999, MNRAS, 308, 1032

Fan, J. H., Liu, Y., Yuan, Y. H., et al. 2007, A&A, 462, 547

Fanaroff, B. L., & Riley, J. M. 1974, MNRAS, 167, 31P

Farnes, J. S., Gaensler, B. M., & Carretti, E. 2014, ApJS, 212, 15

Farnsworth, D., Rudnick, L., & Brown, S. 2011, AJ, 141, 191

Ferrarese, L., & Ford, H. 2005, Space Sci. Rev. 116, 523

Finke, J. D., & Becker, P. A. 2014, ApJ, 791, 21

Finke, J. D., & Becker, P. A. 2015, ApJ, 809, 85

Fish, V. L., Johnson, M. D., Doeleman, S. S., et al. 2016, ApJ, 820, 90

Fish, V. L., Johnson, M. D., Lu, R.-S., et al. 2014, ApJ, 795, 134

Fomalont, E. B. 1999, Synthesis Imaging in Radio Astronomy II, 180, 301

Fossati, G., Maraschi, L., Celotti, A., Comastri, A., & Ghisellini, G. 1998, MNRAS, 299, 433

Francis, P. J., Hewett, P. C., Foltz, C. B., et al. 1991, ApJ, 373, 465

Fromm, C. M., Perucho, M., Ros, E., et al. 2011, A&A, 531, A95

Fromm, C. M., Perucho, M., Mimica, P., & Ros, E. 2016, A&A, 588, A101

Fromm, C. M., Ros, E., Perucho, M., et al. 2013, A&A, 557, 105

Fuentes, A., Gómez, J. L., Martí, J. M., & Perucho, M. 2018, ApJ, 860, 121

Fujita, Y., & Nagai, H. 2017, MNRAS, 465, L94

Gabuzda, D. C., Knuettel, S., & Reardon, B. 2015, MNRAS, 450, 2441

Gabuzda, D. C., Murray, É., & Cronin, P. 2004, MNRAS, 351, L89

Gabuzda, D. C., Nagle, M., & Roche, N. 2018, A&A, 612, A67

Gabuzda, D. C., Rastorgueva, E. A., Smith, P. S., & O'Sullivan, S. P. 2006, MNRAS, 369, 1596

Gardner F. F., & Whiteoak J. B. 1966, ARA&A, 4, 245

Gaspari, M., Ruszkowski, M., & Oh, S. P. 2013, MNRAS, 432, 3401

Gebhardt, K., Adams, J., Richstone, D., et al. 2011, ApJ, 729, 119

Gebhardt, K., Bender, R., Bower, G., et al. 2000, ApJ, 539, L13

Gebhardt, K., & Thomas, J. 2009, ApJ, 700, 1690

Genzel, R., Eisenhauer, F., & Gillessen, S. 2010, Rev. Mod. Phys., 82, 3121

Ghisellini, G., Celotti, A., Fossati, G., Maraschi, L., & Comastri, A. 1998, MNRAS, 301, 451

Ghisellini, G., Maraschi, L., & Tavecchio, F. 2009, MNRAS, 396, L105

Ghisellini, G., Padovani, P., Celotti, A., & Maraschi, L. 1993, ApJ, 407, 65

Ghisellini, G., Tavecchio, F., Chiaberge, M., et al. 2005, A&A, 432, 401

Ghisellini, G., Tavecchio, F., Foschini, L., et al. 2010, MNRAS, 402, 497

Ghisellini, G., Tavecchio, F., Foschini, L., & Ghirlanda, G. 2011, MNRAS, 414, 2674

Ghisellini, G., Tavecchio, F., & Ghirlanda, G. 2009, MNRAS, 399, 2041

Ghisellini, G., Tavecchio, F., Maraschi, L., Celotti, A., & Sbarrato, T. 2014, Nature, 515, 376

Ghisellini, G., Righi, C., Costamante, L., & Tavecchio, F. 2017, MNRAS, 469, 255

Giannios, D., Uzdensky, D. A., & Begelman, M. C. 2009, MNRAS, 395, L29

Gillessen, S., Genzel, R., Fritz, T. K., et al. 2012, Nature, 481, 51

Gillessen, S., Genzel, R., Fritz, T. K., et al. 2013, ApJ, 763, 78

Gillessen, S., Genzel, R., Fritz, T. K., et al. 2013, ApJ, 774, 44

Gillessen, S., Plewa, P. M., Widmann, F., et al. 2018, ApJ, in press (arXiv:1812.01416)

Ginzburg, V.L. & Syrovatskii, S.I. 1965, ARA&A, 3, 297

Giovannini, G., Savolainen, T., Orienti, M., et al. 2018, Nature Astronomy, 2, 472

Giroletti, M., Hada, K., Giovannini, G., et al. 2012, A&A, 538, L10

Giroletti, M., Giovannini, G., Feretti, L., et al. 2004, ApJ, 600, 127

Globus, N., & Levinson, A. 2016, MNRAS, 461, 2605

Gómez, J. L., Marscher, A. P., Alberdi, A., et al. 2002, VLBA Scientific Memo #30

Gómez, J. L., Lobanov, A. P., Bruni, G., et al. 2016, ApJ, 817, 96

Gómez, J. L., Martí, J. M., Marscher, A. P., Ibáñez, J. M., & Marcaide, J. M. 1995, ApJ, 449, L19

Gómez, J. L., Martí, J. M., Marscher, A. P., et al. 1997, ApJ, 482, 33

Gracia, J., Tsinganos, K., & Bogovalov, S. V. 2005, A&A, 442, L7

Gracia, J., Vlahakis, N., Agudo, I., Tsinganos, K., & Bogovalov, S. V. 2009, ApJ, 695, 503

Greisen, E. W. 2003, in Information Handling in Astronomy – Historical Vistas, ed. A. Heck (Dordrecht: Kluwer), Astrophys. Space Sci. Libr., 285, 109

Gu, M., Cao, X., & Jiang, D. R. 2001, MNRAS, 327, 1111

Gupta, A. C., Krichbaum, T. P., Wiita, P. J., et al. 2012, MNRAS, 425, 1357

Gurwell, M. A., Peck, A. B., Hostler, S. R., Darrah, M. R., & Katz, C. A. 2007, in ASP Conf. Ser. 375, From Z-Machines to ALMA: (Sub)Millimeter Spectroscopy of Galaxies, ed. A. J. Baker et al. (San Francisco, CA: ASP), 234

Gwinn, C. R., Kovalev, Y. Y., Johnson, M. D., & Soglasnov, V. A. 2014, ApJ, 794, L14

Heckman, T. M., & Best, P. N. 2014, ARA&A, 52, 589

Heckman, T. M., Illingworth, G. D., Miley, G. K., et al. 1985, ApJ, 299, 41

Hada, K. 2017, Galaxies, 5, 2

Hada, K., Doi, A., Kino, M., et al. 2011, Nature, 477, 185

Hada, K., Doi, A., Wajima, K., et al. 2018, ApJ, 860, 141

Hada, K., Giroletti, M., Giovannini, G., et al. 2015, arXiv:astro-ph/1504.01808

Hada, K., Kino, M., Doi, A., et al. 2013, ApJ, 775, 70

Hada, K., Kino, M., Doi, A., et al. 2016, ApJ, 817, 131

Hada, K., Park, J., Kino, M., et al. 2017, PASJ, 69, 71

Hardee, P. E. 2000, ApJ, 533, 176

Hardee, P. E., & Eilek, J. A. 2011, ApJ, 735, 61

Harris, D. E., Biretta, J. A., Junor, W., et al. 2003, ApJ, 586, L41

Harris, D. E., Cheung, C. C., Stawarz, Ł., Biretta, J. A., & Perlman, E. S. 2009, ApJ, 699, 305

Harrison C. M. 2014. Observational constraints on the influence of active galactic nuclei on the evolution of galaxies. PhD Thesis, Durham Univ., Durham, UK

Hartman, R. C., Bertsch, D. L., Fichtel, C. E., et al. 1992, ApJ, 385, L1

Hartman, R. C., Böttcher, M., Aldering, G., et al. 2001, ApJ, 553, 683

Heckman, T. M., & Best, P. N. 2014, ARA&A, 52, 589

H.E.S.S. Collaboration, Abramowski, A., Acero, F., et al. 2013, A&A, 554, A107

Hirose, S., Krolik, J. H., De Villiers, J.-P., & Hawley, J. F. 2004, ApJ, 606, 1083

Ho, L. C. 2008, ARA&A, 46, 475

Ho, L. C., Goldoni, P., Dong, X.-B., et al. 2012, ApJ, 754, 11

Hodgson, J. A., Lee, S.-S., Zhao, G.-Y., et al. 2016, JKAS, 49, 137

Hodgson, J. A., Krichbaum, T. P., Marscher, A. P., et al. 2017, A&A, 597, A80

Homan, D. C. 2012, ApJ, 747, L24

Homan, D. C., Kovalev, Y. Y., Lister, M. L., et al. 2006, ApJ, 642, 115

Homan, D. C., Lister, M. L., Kovalev, Y. Y., et al. 2015, ApJ, 798, 134

Hovatta, T., Aller, M. F., Aller, H. D., et al. 2014, A&A, 147, 143

Hovatta, T., Lindfors, E., Blinov, D., et al. 2016, A&A, 596, 78

Hovatta, T., Lister, M. L., Aller, M. F., et al. 2012, AJ, 144, 105

Hovatta, T., Nieppola, E., Tornikoski, M., et al. 2008, A&A, 485, 51

Hovatta, T., O'Sullivan, S., Martí-Vidal, I., Savolainen, T., & Tchekhovskoy, A. 2018, A&A, in press (arXiv:1803.09982)

Hovatta, T., Tornikoski, M., Lainela, M., et al. 2007, A&A, 469, 899

Hovatta, T., Valtaoja, E., Tornikoski, M., & Lähteenmäki, A., 2009, A&A, 494, 527

Hughes, P. A. 2005, ApJ, 621, 635

Hughes, P. A., Aller, H. D., & Aller, M. F. 1985, ApJ, 298, 301

Hughes, P. A., Aller, H. D., & Aller, M. F. 1992, ApJ, 396, 469

Hughes, P. A., Aller, M. F., & Aller, H. D. 2011, ApJ, 735, 81

Liddle, A. R. 2004, MNRAS, 351, L49

Ichimaru, S. 1977, ApJ, 214, 840

Igumenshchev, I. V., & Abramowicz, M. A. 2000, ApJS, 130, 463

Igumenshchev, I. V., & Narayan, R. 2002, ApJ, 566, 137

Igumenshchev, I. V., Narayan, R., & Abramowicz, M. A. 2003, ApJ, 592, 1042

Isobe, N., Sato, R., Ueda, Y., et al. 2015, ApJ, 798, 27

MAGIC Collaboration, Acciari, V. A., Ansoldi, S., et al. 2018, A&A, 619, A159

Jeffreys H. 1961, Theory of probability, 3rd edn, Oxford Univ. Press, Oxford

Johnson, M. D., Fish, V. L., Doeleman, S. S., et al. 2015, Science, 350, 1242

Johnson, M. D., Narayan, R., Psaltis, D., et al. 2018, ApJ, 865, 104

Jones, D. L., Tingay, S. J., Murphy, D. W., et al. 1996, ApJ, 466, L63

Jones, D. L., & Wehrle, A. E. 1997, ApJ, 484, 186

Jorstad, S., & Marscher, A. 2016, Galaxies, 4, 47

Jorstad, S. G., Marscher, A. P., Larionov, V. M., et al. 2010, ApJ, 715, 362

Jorstad, S. G., Marscher, A. P., Lister, M. L., et al. 2005, AJ, 130, 1418

Jorstad, S. G., Marscher, A. P., Mattox, J. R., et al. 2001, ApJ, 556, 738

Jorstad, S. G., Marscher, A. P., Morozova, D. A., et al. 2017, ApJ, 846, 98

Jorstad, S. G., Marscher, A. P., Smith, P. S., et al. 2013, ApJ, 773, 147

Jorstad, S. G., Marscher, A. P., Stevens, J. A., et al. 2007, AJ, 134, 799

Junor, W., Biretta, J. A., & Livio, M. 1999, Nature, 401, 891

Kamruddin, A. B., & Dexter, J. 2013, MNRAS, 434, 765

Kang, S., Lee, S.-S., & Byun, D.-Y. 2015, JKAS, 48, 257

Kaspi, S., Smith, P. S., Netzer, H., et al. 2000, ApJ, 533, 631

Kaspi, S., Maoz, D., Netzer, H., et al. 2005, ApJ, 629, 61

Kass R. E., & Raftery A. E. 1995, Journ. American Stat. Assoc., 90, 773

Katarzyński, K., Sol, H., & Kus, A. 2001, A&A, 367, 809

Kato, S. 2000, PASJ, 53, 1

Kawashima, T., Matsumoto, Y., & Matsumoto, R. 2017, PASJ, 69, 43

Kelly, B. C. 2007, ApJ, 665, 1489

Kelly, B. C., Bechtold, J., & Siemiginowska, A. 2009, ApJ, 698, 895

Kelly, B. C., Sobolewska, M., & Siemiginowska, A. 2011, ApJ, 730, 52

Kembhavi, A. K., & Narlikar, J. V. 1999, Quasars and Active Galactic Nuclei, Cambridge: Cambridge University Press

Kharb, P., Gabuzda, D. C., O'Dea, C. P., et al. 2009, ApJ, 694, 1485

Kim, D.-W., Trippe, S., Lee, S.-S., et al. 2017, JKAS, 50, 167

Kim, J.-Y., Krichbaum, T. P., Lu, R.-S., et al. 2018, A&A, 616, A188

Kim, J.-Y., Krichbaum, T. P., Marscher, A. P., et al. 2018, A&A, in press (arXiv:1811.07815)

Kim, J.-Y., Lu, R.-S., Krichbaum, T. P., et al. 2016, Galaxies, 4, 39

Kim, J. -Y., & Trippe, S. 2013, JKAS, 46, 65

Kim, J.-Y., Trippe, S., Sohn, B. W., et al. 2015, JKAS, 48, 285

Kino, M., Niinuma, K., Zhao, G.-Y., et al. 2015a, PKAS, 30, 633

Kino, M., Takahara, F., Hada, K., & Doi, A. 2014, ApJ, 786, 5

Kino, M., Takahara, F., Hada, K., et al. 2015b, ApJ, 803, 30

Krolik, J. H. 1999, Active Galactic Nuclei: Princeton University Press

Kollatschny, W., Ulbrich, K., Zetzl, M., et al. 2014, A&A, 566, 106

Komissarov, S. S., Barkov, M. V., Vlahakis, N., & Königl, A. 2007, MNRAS, 380, 51

Komissarov, S. S., & Falle, S. A. E. G. 1997, MNRAS, 288, 833

Komissarov, S. S., Vlahakis, N., Königl, A., & Barkov, M. V. 2009, MNRAS, 394, 1182

Kormendy, J., & Ho, L. C. 2013, ARA&A, 51, 511

Kormendy, J., & Richstone, D. 1995, ARA&A, 33, 581

Kovalev, Y. Y., Lister, M. L., Homan, D. C., & Kellermann, K. I. 2007, ApJ, 668, L27

Koyama, S., Kino, M., Giroletti, M., et al. 2016, A&A, 586, A113

Kravchenko, E. V., Kovalev, Y. Y., & Sokolovsky, K. V. 2017, MNRAS, 467, 83

Krichbaum, T. P., Graham, D. A., Witzel, A., et al. 1998, A&A, 335, L106

Krichbaum, T. P., Graham, D. A., Bremer, M., et al. 2006, JPhCS, 54, 328

Kuo, C. Y., Asada, K., Rao, R., et al. 2014, ApJ, 783, L33

Lähteenmäki, A., Valtaoja, E., & Wiik, K. 1999, ApJ, 511, 112

Lähteenmäki, A., & Valtaoja, E. 1999, ApJ, 521, 493

Laing, R. A. 1996, in ASP Conf. Ser. 100, Energy Transportation in Galaxies and Quasars, ed. P. E. Hardee, A. H. Bridle, & J. A. Zensus (San Francisco, CA: ASP), 241

Lawrence, A., & Papadakis, I. 1993, ApJ, 414, 85

Lawrence, A., Watson, M. G., Pounds, K. A., & Elvis, M. 1987, Nature, 325, 694

Lee, S.-S., Byun, D.-Y., Oh, C. S., et al. 2011, PASP, 123, 1398

Lee, S.-S., Byun, D.-Y., Oh, C. S., et al. 2015b, JKAS, 48, 229

Lee, S.-S., Oh, C. S., Roh, D.-G., et al. 2015a, JKAS, 48, 125

Lee, S.-S., Petrov, L., Byun, D.-Y., et al. 2014, AJ, 147, 77

Lee, S.-S., Wajima, K., Algaba, J.-C., et al. 2016, ApJS, 227, 8

León-Tavares, J., Lobanov, A. P., Chavushyan, V. H., et al. 2010, ApJ, 715, 335

León-Tavares, J., Valtaoja, E., Tornikoski, M., et al. 2011, A&A, 532, 146

Leppänen, K. J., Zensus, J. A., & Diamond, P. J. 1995, AJ, 110, 2479

Li, Z.-Y., Chiueh, T., & Begelman, M. C. 1992, ApJ, 394, 459

Li, Z., Morris, M. R., & Baganoff, F. K. 2013, ApJ, 779, 154

Lico, R., Gómez, J. L., Asada, K., & Fuentes, A. 2017, MNRAS, 469, 1612

Lico, R., Giroletti, M., Orienti, M., et al. 2012, A&A, 545, 117

Liodakis, I., & Pavlidou, V. 2015, MNRAS, 454, 1767

Lisakov, M. M., Kovalev, Y. Y., Savolainen, T., Hovatta, T., & Kutkin, A. M. 2017, MNRAS, 468, 4478

Lister, M. L., Aller, H. D., Aller, M. F., et al. 2009, AJ, 137, 3718

Lister, M. L., Aller, M. F., Aller, H. D., et al. 2013, AJ, 146, 120

Lister, M. L., Aller, M. F., Aller, H. D., et al. 2016, AJ, 152, 12

Lister, M. L., & Homan, D. C. 2005, AJ, 130, 1389

Lister, M. L., & Smith, P. S. 2000, ApJ, 541, 66

Liu, H. T., & Bai, J. M. 2006, ApJ, 653, 1089

Liu, Y., Jiang, D. R., & Gu, M. F. 2006, ApJ, 637, 669

Liu, H. B., Wright, M. C. H., Zhao, J.-H., et al. 2016, A&A, 593, A107

Liu, H. & Wu, Q. 2013, ApJ, 764, 17

Lo, K. Y., Shen, Z.-Q., Zhao, J.-H., & Ho, P. T. P. ApJ, 1998, 508, L61

Lobanov, A. P. 1998, A&A, 330, 79

Lobanov, A., Hardee, P., & Eilek, J. 2003, AJ, 130, 1389

Lu, R.-S., Broderick, A. E., Baron, F., et al. 2014, ApJ, 788, 120

Lu, R.-S., Fish, V. L., Akiyama, K., et al. 2013, ApJ, 772, 13

Lu, R.-S., Krichbaum, T. P., Eckart A., et al. 2011, A&A, 525, A76

Lu, R.-S., Krichbaum, T. P., Roy, A. L., et al. 2018, ApJ, 859, 60

Ly, C., Walker, R. C., & Wrobel, J. M. 2004, AJ, 127, 119

Ly, C., Walker, R. C., & Junor, W. 2007, ApJ, 660, 200

Lyubarskii, Y. E. 1997, MNRAS, 292, 679

Lyubarsky, Y. 2009, ApJ, 698, 1570

Lyutikov, M., Pariev, V. I., & Gabuzda, D. C. 2005, MNRAS, 360, 869

Macchetto, F., Marconi, A., Axon, D. J., et al. 1997, ApJ, 489, 579

MacDonald, N. R., Marscher, A. P., Jorstad, S. G., & Joshi, M. 2015, ApJ, 804, 111

MacDonald, N. R., Jorstad, S. G., & Marscher, A. P. 2017, ApJ, 850, 87

Machida, M., Matsumoto, R., & Mineshige, S. 2001, PASJ, 53, L1

Mahadevan, R. 1997, ApJ, 477, 585

Mahmud, M., Coughlan, C. P., Murphy, E., Gabuzda, D. C., & Hallahan, D. R. 2013, MNRAS, 431, 695

Mahmud, M., Gabuzda, D. C., & Bezrukovs, V. 2009, MNRAS, 400, 2

Mannheim, K. 1993, A&A, 269, 67

Maraschi, L., Ghisellini, G., & Celotti, A. 1992, ApJ, 397, L5

Maraschi, L., & Rovetti, F. 1994, ApJ, 436, 79

Markoff, S., Falcke, H., Yuan, F., & Biermann, P. L. 2001, A&A, 379, L13

Markoff, S., Bower, G. C., & Falcke, H. 2007, MNRAS, 379, 1519

Markowitz, A., Edelson, R., Vaughan, S., et al. 2003, ApJ, 593, 96

Marrone, D. P., Moran, J. M., Zhao, J.-H., & Rao, R. 2006, ApJ, 640, 308

Marrone, D. P., Moran, J. M., Zhao, J.-H., & Rao, R. 2007, ApJ, 654, L57

Marscher, A. P. 1996, in ASP Conf. Ser. 110, Blazar Continuum Variability, ed. H. R. Miller, J. R. Webb, & J. C. Noble (San Francisco, CA: ASP), 248

Marscher, A. P. 2006, in AIP Conf. Proc. 856, Relativistic Jets: The Common Physics of AGN, Microquasars, and Gamma Ray Bursts, ed. P. A. Hughes & J. N. Bregman (Melville, NY: AIP), 1

Marscher, A. P. 2009, in ASP Conf. Ser. 402, Approaching Micro-Arcsecond Resolution with VSOP-2: Astrophysics and Technologies, ed. Y. Hagiwar et al. (San Francisco, CA: ASP), 194

Marscher, A. P. 2008, Extragalactic Jets: Theory and Observation from Radio to Gamma Ray, 386, 437

Marscher, A. P. 2013, EPJWC, 61, 04001

Marscher, A. P. 2014, ApJ, 780, 87

Marscher, A. P. 2016, Galaxies, 4, 37

Marscher, A. P., & Gear, W. K. 1985, ApJ, 298, 114

Marscher, A. P., & Travis, J. P. 1996, A&AS, 120, 537

Marscher, A. P., Jorstad, S. G., Agudo, I., MacDonald, N. R., & Scott, T. L. 2012, arXiv:1204.6707

Marscher, A. P., Jorstad, S. G., D'Arcangelo, F. D., et al. 2008, Nature, 452, 966

Marscher, A. P., Jorstad, S. G., Gómez, J.-L., et al. 2002a, Nature, 417, 625

Marscher, A. P., Jorstad, S. G., Mattox, J. R., & Wehrle, A. E. 2002b, ApJ577, 85

Marscher, A. P., Jorstad, S. G., Larionov, V. M., et al. 2010, ApJ, 710, L126

Martí, J. M., Perucho, M., & Gomez, J. L. 2016, ApJ, 831, 163

Martí-Vidal, I., Marcaide, J. M., Alberdi, A., et al. 2011, A&A, 533, 111

Martí-Vidal, I., Muller, S., Vlemmings, W., et al. 2015, Science, 348, 311

Mastichiadis, A., & Kirk, J. G. 1997, A&A, 320, 19

Mattox, J. R., Bertsch, D. L., Chiang, J., et al. 1996, ApJ, 461, 396

Max-Moerbeck, W., Hovatta, T., Richards, J. L., et al. 2014, MNRAS, 445, 428

Max-Moerbeck, W., Richards, J. L., Hovatta, T., et al. 2014, MNRAS, 445, 437

M^{c}Hardy, I. M., Papadakis, I. E., Uttley, P., et al. 2004, MNRAS, 348, 783

M^{c}Hardy, I. M., Koerding, E., Knigge, C., et al. 2006, Nature, 444, 730

M^{c}Hardy, I. 2008, Proc. Blazar Variability across the Electromagnetic Spectrum, PoS (BLAZARS2008) (Trieste: SISSA Proc. Sci), 14

McKinney, J. C. 2006, MNRAS, 368, 1561

McKinney, J. C., Tchekhovskoy, A., & Blandford, R. D. 2013, Science, 339, 49

McKinney, J. C., & Gammie, C. F. 2004, ApJ, 611, 977

Mckinney, J. C., Tchekhovskoy, A., & Blandford, R. D. 2012, MNRAS, 423, 3083

McLure, R. J., & Dunlop, J. S. 2001, MNRAS, 327, 199

McLure, R. J., & Jarvis, M. J. 2002, MNRAS, 337, 109

McNamara, B. R., Rohanizadegan, M., & Nulsen, P. E. J. 2011, ApJ, 727, 39

Mei, S., Blakeslee, J. P., Côté, P., et al. 2007, ApJ, 655, 144

Meier, D. L. Black Hole Astrophysics: The Engine Paradigm (Springer, 2012)

Meier, D. L., Koide, S., & Uchida, Y. 2001, Science, 291, 84

Melia, F., & Falcke, H. 2001, ARA&A, 39, 309

Merritt, D., & Ferrarese, L. 2001, ApJ, 547, 140

Mertens, F., & Lobanov, A. P. 2015, A&A, 574, A67

Mertens, F., & Lobanov, A. P. 2016, A&A, 587, A52

Mertens, F., Lobanov, A. P., Walker, R. C., & Hardee, P. E. 2016, A&A, 595, A54

Meyer, L., Ghez, A. M., Schödel, R., et al. 2012, Science, 338, 84

Meyer, E. T., Sparks, W. B., Biretta, J. A., et al. 2013, ApJ, 774, L21

Middelberg, E., Roy, A. L., Walker, R. C., & Falcke, H. 2005, A&A, 433, 897

Miralda-Escudé, J. 2012, ApJ, 758, 86

Mizuno, Y., Gómez, J. L., Nishikawa, K.-I., et al. 2015, ApJ, 809, 38

Mohan, P., Agarwal, A., Mangalam, A., et al. 2015, MNRAS, 452, 2004

Montroll, E.W. & Shlesinger, M.F. 1982, Proc. Natl. Acad. Sci. USA, 79, 3380

Mosallanezhad, A., Bu, D., & Yuan, F. 2016, MNRAS, 456, 2877

Mościbrodzka, M., Dexter, J., Davelaar, J., & Falcke, H. 2017, MNRAS, 468, 2214

Mościbrodzka, M., Falcke, H., & Shiokawa, H. 2016, A&A, 586, A38

Mościbrodzka, M., Shiokawa, H., Gammie, C. F., & Dolence, J. C. 2012, ApJ, 752, L1

Mou, G., Yuan, F., Bu, D., Sun, M., & Su, M. 2014, ApJ, 790, 109

Murphy, E., Cawthorne, T. V., & Gabuzda, D. C. 2013, MNRAS, 430, 1504

Mukherjee, S., Feigelson, E. D., Babu, G. J., et al. 1998, ApJ, 508, 314

Nagai, H., Fujita, Y., Nakamura, M., et al. 2017, ApJ, 849, 52

Nagai, H., Haga, T., Giovannini, G., et al. 2014, ApJ, 785, 53

Nakamura, M., & Asada, K. 2013, ApJ, 775, 118

Nakamura, M., Asada, K., Hada, K., et al. 2018, ApJ, 868, 146

Nakamura, M., Garofalo, D., & Meier, D. L. 2010, ApJ, 721, 1783

Nakamura, M., & Meier, D. L. 2014, ApJ, 785, 152

Narayan, R., & Fabian, A. C. 2011, MNRAS, 415, 3721

Narayan, R., & McClintock, J. E. 2008, New Astronomy Reviews, 51, 733

Narayan, R., Igumenshchev, I. V., & Abramowicz, M. A. 2000, ApJ, 593, 798

Narayan, R., Igumenshchev, I. V., & Abramowicz, M. A. 2003, PASJ, 55, 69

Narayan, R., Mahadevan, R., Grindlay, J. E., et al. 1998, ApJ, 492, 554

Narayan, R., Sadowski, A., Penna, R. F., & Kulkarni, A. K. 2012, MNRAS, 426, 3241

Narayan, R., & Yi, I. ApJ, 1994, 428, L13

Narayan, R., & Yi, I. 1995a, ApJ, 444, 231

Narayan, R., & Yi, I. 1995b, ApJ, 452, 710

Nelson, C. H., & Whittle, M. 1995, ApJS, 99, 67

Nemmen, R. S., & Tchekhovskoy, A. 2015, MNRAS, 449, 316

Netzer, H. 2013, The Physics and Evolution of Active Galactic Nuclei (Cambridge: Cambridge University Press)

Nieppola, E., Hovatta, T., Tornikoski, M., et al. 2009, AJ, 137, 5022

Niinuma, K., Kino, M., Doi, A., et al. 2015, ApJ, 807, L14

Niinuma, K., Lee, S.-S., Kino, M., et al. 2014, PASJ, 66, 103

Nokhrina, E. E., Gurvits, L. I., Beskin, V. S., et al. 2019, MNRAS, submitted (arXiv: 1904.05665)

Orienti, M., Koyama, S., D'Ammando, F., et al. 2013, MNRAS, 428, 2418

O'Sullivan, S. P., Brown, S., Robishaw, T., et al. 2012, MNRAS, 421, 3300

O'Sullivan, S. P. & Gabuzda, D. C. 2009, MNRAS, 393, 429

O'Sullivan, S. P. & Gabuzda, D. C. 2009b, MNRAS, 400, 26

O'Sullivan, S. P., Purcell, C. R., Anderson, C. S., et al. 2017, MNRAS, 469, 4034

Oh, J., Trippe, S., Kang, S., et al. 2015, JKAS, 48, 299

Ostrowski, M. 1998, A&A, 335, 134

Owen, F. N., Hardee, P. E., & Cornwell, T. J. 1989, ApJ, 340, 698

Owen, F. N., Eilek, J. A., & Keel, W. C. 1990, ApJ, 362, 449

Owen, F. N., Eilek, J. A., & Kassim, N. E. 2000, ApJ, 543, 611

Pacholczyk, A. G. 1970, Radio Astrophysics (San Francisco: W. H. Freeman)

Padovani, P. 1992, MNRAS, 257, 404

Pang, B., Pen, U.-L., Matzner, C. D., Green, S. R., & Liebendörfer, M. 2011, MNRAS, 415, 1228

Papadakis, I. E., & Lawrence, A. 1993, MNRAS, 261, 612

Park, J., Hada, K., Kino, M., et al. 2019a, ApJ, 871, 257

Park, J., Hada, K., Kino, M., et al. 2019c, ApJ, submitted

Park, J., Kam, M., Trippe, S., et al. 2018, ApJ, 860, 112

Park, J., Lee, S.-S., Kim, J.-Y., et al. 2019, ApJ, in press (arXiv:1904.11118)

Park, J.-H., & Trippe, S. 2014, ApJ, 785, 76

Park, J., & Trippe, S. 2017, ApJ, 834, 157

Park, J.-H., Trippe, S., Krichbaum, T. P., et al. 2015, A&A, 576, L16

Park, D., Woo, J.-H., Treu, T., et al. 2012, ApJ, 747, 30

Park, J. -H., & Trippe, S. 2012, JKAS, 45, 147

Pasetto, A., Carrasco-González, C., O'Sullivan, S., et al. 2018, A&A, 613, 74

Pen, U.-L., Matzner, C. D., & Wong, S. 2003, ApJ, 596, L207

Penna, R. F., Narayan, R., & Sadowski, A. 2013, MNRAS, 436, 3741

Penna, R. F., Sadowski, A., Kulkarni, A. K., & Narayan, R. 2013b, MNRAS, 428, 2255

Perley, R. A., & Butler, B. J. 2013, ApJS, 206, 16

Perley, R. A., Dreher, J. W., & Cowan, J. J. 1984, ApJ, 285, L35

Perlman, E. S., Adams, S. C., Cara, M., et al. 2011, ApJ, 743, 119

Perlman, E. S., Biretta, J. A., Zhou, F., Sparks, W. B., & Macchetto, F. D. 1999, AJ, 117, 2185

Perlman, E. S., Biretta, J. A., Sparks, W. B., Macchetto, F. D., & Leahy, J. P. 2001, ApJ, 551, 206

Pfuhl, O., Gillessen, S., Eisenhauer, F., et al. 2015, ApJ, 798, 111

Phifer, K., Do, T., Meyer, L., et al. 2013, ApJ, 773, L13

Piran, T. 2003, Nature, 422, 268

Plambeck, R. L., Bower, G. C., Rao, R., et al. 2014, ApJ, 797, 66

Porth, O., Fendt, C., Meliani, Z., & Vaidya, B. 2011, ApJ, 737, 42

Porth, O., & Komissarov, S. S. 2015, MNRAS, 452, 1089

Potter, W. J., & Cotter, G. 2013a, MNRAS, 429, 1189

Potter, W. J., & Cotter, G. 2013b, MNRAS, 431, 1840

Potter, W. J., & Cotter, G. 2015, MNRAS, 453, 4070

Press, W. H. 1978, Comment. Astrophys., 7, 103

Press, W. H., & Rybicki, G. B. 1989, ApJ, 338, 277

Press, W. H., Teukolsky, S. A., Vetterling, W. T., & Flannery, B. P. 1992, Numerical Recipes in FORTRAN (2nd ed.; Cambridge: Cambridge Univ. Press)

Priestley, M. B. 1981, Spectral Analysis and Time Series (London: Elsevier)

Prieto, M. A., Fernández-Ontiveros, J. A., Markoff, S., Espada, D., & González-Martín, O. 2016, MNRAS, 457, 3801

Prince, R., Majumdar, P., & Gupta, N. 2017, ApJ, 844, 62

Pu, H.-Y., Wu, K., Younsi, Z., et al. 2017, ApJ, 845, 160

Pushkarev, A. B., Gabuzda, D. C., Vetukhnovskaya, Y, N., & Yakimov, V. E. 2005, MNRAS, 356, 859

Pushkarev, A. B., Hovatta, T., Kovalev, Y. Y., et al. 2012, A&A, 545, 113

Pushkarev, A. B., Kovalev, Y. Y., Lister, M. L., & Savolainen, T. 2017, MNRAS, 468, 4992

Pyatunina, T. B., Kudryavtseva, N. A., Gabuzda, D. C., et al. 2006, MNRAS, 373, 1470

Pyatunina, T. B., Kudryavtseva, N. A., Gabuzda, D. C., et al. 2007, MNRAS, 381, 797

Qian, Q., Fendt, C., & Vourellis, C. 2018, ApJ, 859, 28

Quataert, E., & Gruzinov, A. 2000, ApJ, 539, 809

Rafferty, D. A., McNamara, B. R., Nulsen, P. E. J., & Wise, M. W. 2006, ApJ, 652, 216

Raiteri, C. M., Villata, M., Acosta-Pulido, J. A., et al. 2017, Nature, 552, 374

Ramakrishnan, V., Hovatta, T., Nieppola, E., et al. 2015, MNRAS, 452, 1280

Ramakrishnan, V., Hovatta, T., Tornikoski, M., et al. 2016, MNRAS, 456, 171

Ramakrishnan, V., León-Tavares, J., Rastorgueva-Foi, E. A., et al. 2014, MNRAS, 445, 1636

Rani, B., Gupta, A. C., Joshi, U. C., et al. 2010, ApJ, 719, L153

Rani, B., Krichbaum, T. P., Fuhrmann, L., et al. 2013, A&A, 552, A11

Rani, B., Krichbaum, T. P., Marscher, A. P., et al. 2015, A&A, 578, 123

Rani, B., Wiita, P. J., & Gupta, A. C. 2009, ApJ, 696, 2170

Readhead, A. C. S. 1994, ApJ, 426, 51

Reid, M. J., Biretta, J. A., Junor, W., Muxlow, T. W. B., & Spencer, R. E. 1989, ApJ, 336, 112

Rioja, M. J., Dodson, R., Jung, T., et al. 2014, AJ, 148, 84

Rioja, M. J., Dodson, R., Malarecki, J., & Asaki, Y. 2011, AJ, 142, 157

Roberts, D. H., Wardle, J. F. C., & Brown, L. F. 1994, ApJ, 427, 718

노오현 압축성 유체 유동, 2004 (서울대학교 출판원)

Russell, H. R., McNamara, B. R., Edge, A. C., et al. 2013, MNRAS, 432, 530

Russell, H. R., Fabian, A. C., McNamara, B. R., & Broderick, A. E. 2015, MNRAS, 451, 588

Russell, H. R., Fabian, A. C., McNamara, B. R., et al. 2018, MNRAS, 477, 3583

Sadowski, A., Narayan, R., Penna, R., & Zhu, Y. 2013, MNRAS, 436, 3856

Saito, S., Stawarz, Ł, Tanaka, Y. T., et al. 2015, ApJ, 809, 171

Sánchez, N., Alfaro, E. J., & Pérez, E. 2005, ApJ, 625, 849

Sánchez, N., Añez, N., Alfaro, E. J., & Odekon, M. C. 2010, ApJ, 720, 541

Sanders, R. H. 1983, ApJ, 266, 73

Savolainen, T., Homan, D. C., Hovatta, T., et al. 2010, A&A, 512, A24

Savolainen, T., Wiik, K., Valtaoja, E., et al. 2002, A&A, 394, 851

Savolainen, T., Wiik, K., Valtaoja, E., & Tornikoski, M. 2006, A&A, 446, 71

Scargle, J. D. 1982, ApJ, 263, 835

Schartmann, M., Burkert, A., Alig, C., et al. 2012, ApJ, 755, 155

Schödel, R., Krips, M., Markoff, S., et al. 2007, A&A, 463, 551

Schwarz, G. 1978, Ann. Stat., 6, 461

Scoville, N., & Burkert, A. 2013, ApJ, 768, 108

Shakura, N. I., & Sunyaev, R. A. 1973, A&A, 24, 337

Shepherd, M. C. 1997, in Astronomical Data Analysis Software and Systems VI, eds. G. Hunt, & H. E. Payne (San Francisco: ASP), ASP Conf. Ser., 125, 77

Shen, Z.-Q., Lo, K. Y., Liang, M.-C., et al. 2005, Nature, 438, 62

Shimizu, T. T., & Mushotzky, R. F. 2013, ApJ, 770, 60

Sikora, M., Begelman, M. C., & Rees, M. J. 1994, ApJ, 421, 153

Simonetti, J. H., Cordes, J. M., & Heeschen, D. S. 1985, ApJ, 296, 46

Sironi, L., & Spitkovsky, A. 2014, ApJ, 783, L21

Smith, P.S., Montiel, E., Rightley, S., et al. 2009, arXiv:0912.3621, 1094 2009 Fermi Symposium, eConf Proceedings C091122

Sobolewska, M. A., Siemiginowska, A., Kelly, B. C., & Nalewajko, K. 2014, ApJ, 786, 143

Sokoloff, D. D., Bykov, A. A., Shukurov, A., et al. 1998, MNRAS, 299, 189

Sokolovsky, K. V., Kovalev, Y. Y., Pushkarev, A. B., & Lobanov, A. P. 2011, A&A, 532, 38

Sol, H., Pelletier, G., & Asséo, E. 1989, MNRAS, 237, 411

Spada, M., et al. 2001, MNRAS, 325, 1559

Sparks, W. B., Biretta, J. A., & Macchetto, F. 1996, ApJ, 473, 254

Stawarz, Ł., Aharonian, F., Kataoka, J., et al. 2006, MNRAS, 370, 981

Stawarz, Ł., & Ostrowski, M. 2002, ApJ, 578, 763

Stawarz, Ł., Siemiginowska, A., Ostrowski, M., & Sikora, M. 2005, ApJ, 626, 120

Stone, J. M., Pringle, J. E., & Begelman, M. C. 1999, MNRAS, 310, 1002

Tavecchio, F., & Ghisellini, G. 2008, MNRAS, 385, L98

Tavecchio, F., & Ghisellini, G. 2014, MNRAS, 443, 1224

Tavecchio, F., Maraschi, L., & Ghisellini, G. 1998, ApJ, 509, 608

Tavecchio, F., Maraschi, L., Sambruna, R. M., & Urry, C. M. 2000, ApJ, 544, 23

Tavecchio, F., & Mazin, D. 2009, MNRAS, 392, L40

Taylor, G. B., Gugliucci, N. E., Fabian, A. C., et al. 2006, MNRAS, 368, 1500

Taylor, A. R., Stil, J. M., & Sunstrum, C. 2009, ApJ, 702, 1230

Tchekhovskoy, A. 2015, ASSL, 414, 45

Tchekhovskoy, A., McKinney, J. C. & Narayan, R. 2008, MNRAS, 388, 551

Tchekhovskoy, A., McKinney, J. C. & Narayan, R. 2009, ApJ, 699, 1789

Tchekhovskoy, A., McKinney, J. C. & Narayan, R. 2012, J. Phys. Conf. Ser. 372, 012040

Tchekhovskoy, A., Narayan, R., & McKinney, J. C. 2011, MNRAS, 418, L79

Thompson, D. J., Djorgovski, S., & de Carvalho, R. 1990, PASP, 102, 1235

Thompson, A. R., Moran, J. M., & Swenson, G. W. Jr. 2001, Interferometry and Synthesis in Radio Astronomy. New York: Wiley. 2nd ed.

Thorne, K. S. 1974, ApJ, 191, 507

Thum, C., Agudo, I., Molina, S. N., et al. 2018, MNRAS, 473, 2506

Timmer, J., & König, M. 1995, ApJ, 300, 707

Toma, K., & Takahara, F. 2013, Progr. Theor. Exper. Phys., 2013, 083E02

Tombesi, F., Cappi, M., Reeves, J. N., et al. 2010, A&A, 521, A57

Tombesi, F., Tazaki, F., Mushotzky, R. F., et al. 2014, MNRAS, 443, 2154

Tomimatsu, A., & Takahashi, M. 2003, ApJ, 592, 321

Torrealba, J., Chavushyan, V., Cruz-González, I., et al. 2012, Rev. Mex. Astron. Astrofis., 48, 9

Tremaine, S., Gebhardt, K., Bender, R., et al. 2002, ApJ, 574, 740

Tribble, P. C. 1991, MNRAS, 250, 726

Trippe, S. 2014, JKAS, 47, 15

Trippe, S. 2014, JKAS, 47, 159

Trippe, S. 2015, JKAS, 48, 203

Trippe, S., Krips, M., Piétu, V., et al. 2011, A&A, 533, 97

Tsinganos, K., & Bogovalov, S. 2002, MNRAS, 337, 553

Ulrich, M.-H., Maraschi, L., & Urry, C. M. 1997, ARAA, 35, 445

Urry, C. M., & Padovani, P. 1995, PASP, 107, 803

Uttley, P., & M^{c}Hardy, I. M. 2005, MNRAS, 363, 586

Uttley, P., M^{c}Hardy, I. M., & Papadakis, I. E. 2002, MNRAS, 332, 231

Valencia-S., M., Eckart, A., Zajaček, M., et al. ApJ, 800, 125

Valtaoja, E., Lähteenmäki, A., Teräsranta, H., & Lainela, M. 1999, ApJS, 120, 95

Valtaoja, E., Teräsranta, H., Urpo, S., et al. 1992, A&A, 254, 71

Vaughan, S. 2005, A&A, 431, 391

Vaughan, S. 2010, MNRAS, 402, 307

Vestergaard, M., & Peterson, B. M. 2006, ApJ, 641, 689

Vestergaard, M., & Osmer, P. S. 2009, ApJ, 699, 800

Vlahakis, N. Theory of Relativistic Jets. In The Formation and Disruption of Black Hole Jets (eds. Contopoulos, I., Gabuzda, D., & Kylafis, N.) 177-206 (Astrophys. Space Sci. Libr. Vol. 414, Springer, 2015).

Vlahakis, N., & Königl, A. 2003, ApJ, 596, 1080

Vlahakis, N., & Königl, A. 2004, ApJ, 605, 656

Vlahakis, N., Tsinganos, K., Sauty, C., & Trussoni, E. 2000, MNRAS, 318, 417

Wajima, K., Hagiwara, Y., An, T., et al. 2016, in Proc. Workshop Frontiers in Radio Astronomy and FAST Early Sciences Symposium 2015, ed. L. Qain & D. Li (San Francisco, CA: ASP), 81

Walker, R. C., Dhawan, V., Romney, J. D., Kellermann, K. I., & Vermeulen, R. C. 2000, ApJ, 530, 233

Walker, R. C., Hardee, P. E., Davies, F. B., Ly, C., & Junor, W. 2018, ApJ, 855, 128

Wall, J. V., & Jenkins, C. R. 2012, Practical Statistics for Astronomers (Cambridge: Cambridge Univ. Press)

Walsh, J. L., Barth, A. J., Ho, L. C., & Sarzi, M. 2013, ApJ, 770, 86

Wang, Q. D., Nowak, M. A., Markoff, S. B., et al. 2013, Science, 341, 981

Wang, C.-C., & Zhou, H.-Y. 2009, MNRAS, 395, 301

Wardle, J. F. C., Cawthorne, T. V., Roberts, D. H., & Brown, L. F. 1994, ApJ, 437, 122

Wardle, J. F. C., & Kronberg, P. P. 1974, ApJ, 194, 249

Wang, J.-M., Luo, B., & Ho, L. C. 2004, ApJ, 615, L9

Webb, J. R., Smith, A. G., Leacock, R. J., et al. 1988, AJ, 95, 374

Weżgowiec, M., Urbanik, M., Beck, R., Chyży, K. T., & Soida, M. 2012, A&A, 545, A69

Wilman, R. J., Edge, A. C., & Johnstone, R. M. 2005, MNRAS, 359, 755

Wilson, M. J., & Falle, S. A. E. G. 1985, MNRAS, 216, 971

Witzel, G., Ghez, A. M., Morris, M. R., et al. 2014, ApJ, 796, L8

Wong, K.-W., Irwin, J. A., Yukita, M., et al. 2011, ApJ, 736, L23

Wong, K.-W., Irwin, J. A., Shcherbakov, R. V., et al. 2014, ApJ, 780, 9

Woo, J.-H., & Urry, C. M. 2002, ApJ, 579, 530

Xie, F.-G., & Yuan, F. 2012, MNRAS, 427, 1580

Yoon, D., Yuan, F., Gan, Z.-M., et al. 2018, ApJ, 864, 6

Yuan, F., & Narayan, R. 2014, ARA&A, 52, 529

Yuan, F., Bu, D., & Wu, M. 2012, ApJ, 761, 130

Yuan, F., Wu, M., & Bu, D. 2012, ApJ, 761, 129

Yuan, F., Gan, Z., Narayan, R., et al. 2015, ApJ, 804, 101

Yuan, F., Markoff, S., & Falcke, H. 2002, A&A, 383, 854

Yuan, F., Quataert, E., & Narayan, R. 2003, ApJ, 598, 301

Yuan, F., Yoon, D., Li, Y.-P., et al. 2018, ApJ, 857, 121

Yuan, M. S., Tran, H., Wills, B., & Wills, D. 2001, in ASP Conf. Ser. 227, Blazar Demographics and Physics, ed. P. Padovani & C. M. Urry (San Francisco: ASP), 150

Yusef-Zadeh, F., Arendt, R., Bushouse, H., et al. 2012, ApJ, 758, L11

Zacharias, M., Dominis Prester, D., Jankowsky, F., et al. 2019, Galaxies, 7, 41

Zajaček, M., Karas, V., & Eckart, A. 2014, A&A, 565, A17

Zamaninasab, M., Clausen–Brown, E., Savolainen, T., & Tchekhovskoy, A. 2014, Nature, 510, 126

Zamaninasab, M., Savolainen, T., Clausen–Brown, E., et al. 2013, MNRAS, 436, 3341

Zamaninasab, M., Savolainen, T., Clausen-Brown, E., et al. 2013, MNRAS, 436, 3341

Zavala, R. T., & Taylor, G. B. 2002, ApJ, 566, 9

Zavala, R. T., & Taylor, G. B. 2003, ApJ, 589, 126

Zavala, R. T., & Taylor, G. B. 2004, ApJ, 612, 749

Zavala, R. T., & Taylor, G. B. 2005, ApJ, 626, 73

Zhao, G.-Y., Algaba, J. C., Lee, S. S., et al. 2018, AJ, 155, 26

Zylka, R., Mezger, P. G., & Lesch, H. 1992, A&A, 261, 119

Appendix A

Appendices for Chapter 2

A.1 Errors in linear polarization quantities

In this appendix, we present the details of error estimation for linear polarization quantities. We used the following equations to estimate the errors in linear polarization quantities (Roberts et al. 1994; Hovatta et al. 2012),

$$\sigma_P = \frac{\sigma_Q + \sigma_U}{2} \tag{A.1}$$

$$\sigma_{\rm EVPA} = \frac{\sigma_P}{2P}, \tag{A.2}$$

where σ_P, $\sigma_{\rm EVPA}$, σ_Q, and σ_U are uncertainties in the polarized intensity, EVPA, Stokes Q and U data, respectively. σ_Q and σ_U are estimated by adding different noise terms in quadrature, i.e.,

$$\sigma^2 = \sigma^2_{\rm rms} + \sigma^2_{\rm Dterm} + \sigma^2_{\rm CLEAN} \tag{A.3}$$

$$\sigma_{\rm Dterm} = \frac{\sigma_\Delta}{(N_{\rm ant} N_{\rm IF} N_{\rm scan})^{1/2}} (I^2 + (0.3 I_{\rm peak})^2)^{1/2} \tag{A.4}$$

$$\sigma_{\rm CLEAN} = 1.5 \sigma_{\rm rms}, \tag{A.5}$$

where $\sigma_{\rm rms}$, $\sigma_{\rm Dterm}$, and $\sigma_{\rm CLEAN}$ denote rms noise, D-term errors, and CLEAN errors, respectively. We estimated the rms noise in the residual maps after the CLEAN procedure in *Difmap* by shifting the maps by about a hundred times the beam size, corresponding to an off-center rms noise. We note that the rms noise in Stokes Q and U maps and in different sub-bands are similar and provide an average of them for each data set in (3) in Table A.1. σ_{Δ} is the D-term scatter (provided in (4) in Table A.1, see below), $N_{\rm ant}$ the number of antennas, $N_{\rm IF}$ the number of IFs, $N_{\rm scan}$ the number of scans with independent parallactic angles, and $I_{\rm peak}$ the peak of the total intensity map. We present the stations participating in the observations in Table A.1. In our case, $N_{\rm IF} = 1$ because we analyzed each sub-band data separately. We assumed $N_{\rm scan} = 8$ because all our data sets observed M87 as a primary target in a full-track observing mode. We assumed the error from imperfect EVPA calibration of 3° because relatively small errors are expected, as can be seen in Figure 2.1 (see also Section 2.2), and added this error to Equation A.2 in quadrature.

We estimated the D-term scatters by comparing the D-terms obtained from different sources. However, this was not always possible because some data sets did not have more than one source that is suitable for D-term calibration or because of a small number of scans (less than three) on other D-term calibrators. Specifically, we obtained reliable D-terms for BJ020A and BJ020B using three sources, OQ 208, OJ 287, and M87, because all of these are suitable for D-term calibration, i.e., either weakly polarized or moderately polarized but having compact geometries, and they are observed in multiple scans over large parallactic angle ranges (see e.g., Roberts et al. 1994; Aaron 1997; Park et al. 2018 for details of D-term calibration). We present the D-terms of different antennas obtained from different sources in Figure A.1 (top for BJ020A and middle for BJ020B). The scatter in the D-terms obtained by using different sources is about $\approx 0.25\%$ for both left-handed circularly polarized (LCP) and RCP data.

For the BC210 data sets, we could obtain a reasonably small scatter of $\approx 0.4\%$ only for the BC210D data (the bottom panel of Figure A.1), using M87 and 0716+714, because the number of scans on 0716+714 is at most two or three and two antennas

Table A.1. Information about data and errors

Project code (1)	Stations (2)	rms error (3)	D-term scatter (4)	$P_{\rm false}$ (5)	$N_{\rm false}$ (6)	$N_{\rm obs}$ (7)
BJ020A	VLBA	0.139	0.26	8.72×10^{-5}	38	3081
BJ020B	VLBA	0.128	0.25	1.34×10^{-6}	0	2824
BC210B	VLBA, −MK, −OV	0.090	0.41*	$< 3.64 \times 10^{-7}$	0	3427
BC210C	VLBA, −MK, −KP	0.092	0.41*	$< 3.96 \times 10^{-7}$	0	4947
BC210D	VLBA, −KP, $-\frac{1}{2}$PT	0.074	0.41	2.04×10^{-5}	7	1345
BH135F	VLBA	0.174	0.41*	2.50×10^{-7}	0	1125
BC167C	VLBA	0.173	0.41*	$< 2.62 \times 10^{-7}$	0	863
BC167E	VLBA	0.175	0.41*	1.33×10^{-5}	2	775

Note. — (1) Project code of VLBA observations. (2) VLBA stations participating in the observations. (3) Averages of off-center rms errors in Stokes Q and U maps in units of mJy/beam. (4) Scatter in the D-terms obtained with different sources in units of %. We could not derive reliable D-term scatters in some data sets (marked with *) and thus assumed that the errors for these data sets are similar to that of session BC210D, 0.41% (see Appendix A.1 for more details). (5) Probability of detecting false RMs with the RM values and χ^2_r similar to the observed ones (Appendix A.2). $P_{\rm false}$ is obtained from integrating the FPDF between the minimum and maximum observed RMs for each data set presented in Table 2.2. $<$ in front of the values for some sessions means that we could not find any pixel of false RM and we provide an upper limit. (6) Number of pixels of false RMs expected to be seen in the jet. (7) Number of pixels of observed RMs in the jet.

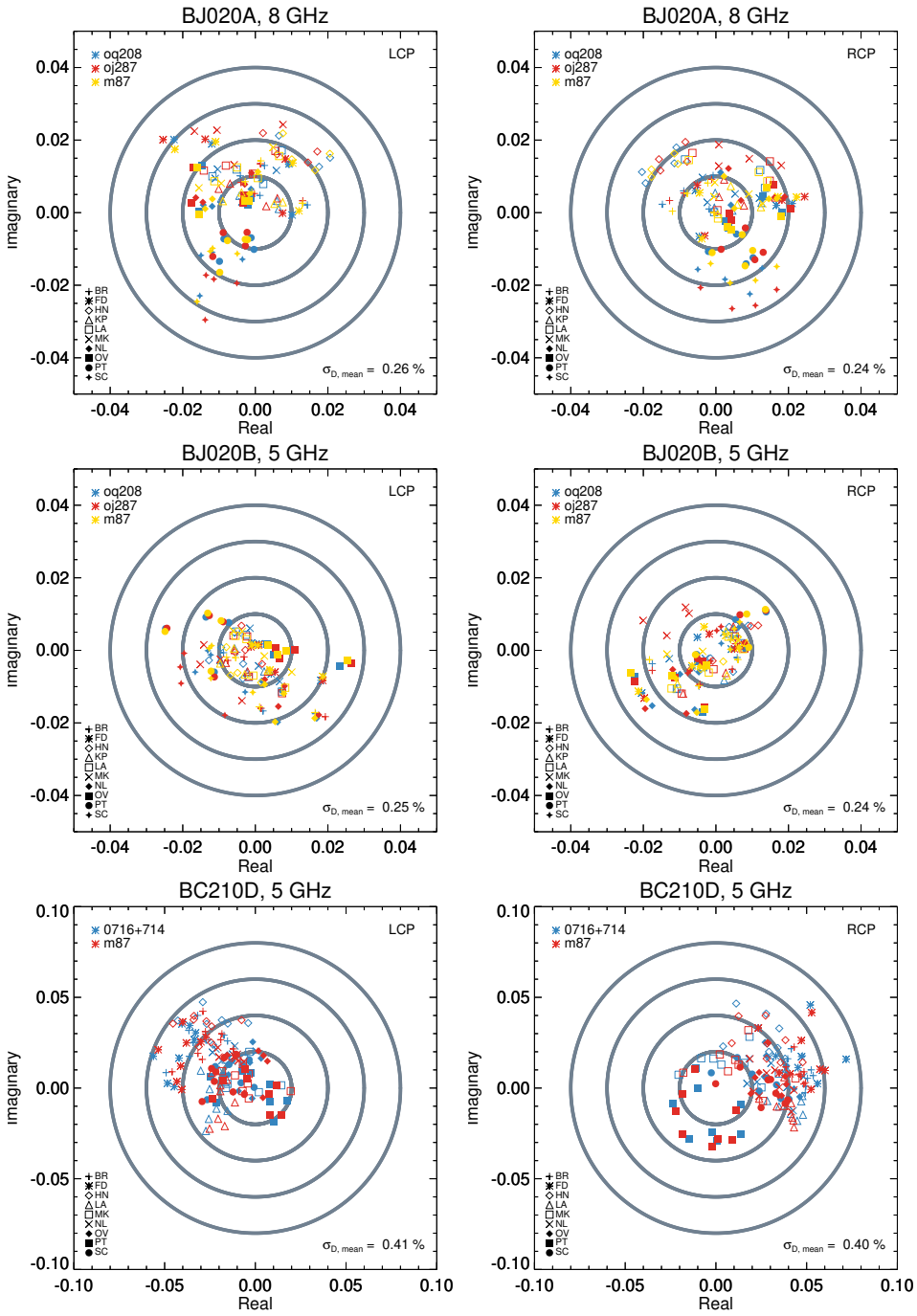

Figure A.1. D-terms obtained by using different calibrator sources (different colors) in the complex plane for the BJ020A, BJ020B, and BC210D data in the top, middle, and bottom panels, respectively. The left (right) panels are for the LCP (RCP) data. The average scatter in the D-terms is noted on the bottom right of each panel.

were missing in the other two data sets. However, the D-terms measured by using M87 for BC210B and BC210C data sets are likely quite reliable because we obtained clear linear polarization in all different sub-bands that are consistent with the results of BJ020B and BC210D (Figure A.3). Thus, we assumed that the D-term scatters for these data sets are similar to that of BC210D and used 0.41%.

For the L band (2 GHz) data sets, we could not obtain the D-term scatters because only three sources, M87, 3C 273, and 3C 286, were observed. M87 can serve as a good D-term calibrator thanks to its very low degree of linear polarization. However, the other two sources show quite strong ($\gtrsim$ 10%) linear polarization over large extended jet regions and thus they are not suitable for D-term calibration. We assumed that the D-term scatters of these data sets are the same as those of BC210D, i.e., 0.41%. This is because the D-term scatters of the VLBA tend to be larger at higher observing frequencies (e.g., Gómez et al. 2002).

A.2 Significance level of RM

We obtained RM for each pixel where the linear polarization intensity exceeds 1.5σ in all sub-bands, with σ being the full uncertainty (Equation A.1, A.3). As there are at least four independently processed sub-bands per data set, the total (Gaussian) probability of false detection of RM is $< 3.2 \times 10^{-4}$. However, linear polarization intensity does not follow a Gaussian probability distribution for a small signal-to-noise ratio (Wardle & Kronberg 1974; Trippe 2014). Thus, we need to carefully check the potential chance of detection of artifacts in the observed RMs. This kind of test has been done by performing extensive simulations in previous studies (e.g., Roberts et al. 1994; Hovatta et al. 2012; Algaba 2013; Mahmud et al. 2013). They generate simulated data sets with the known polarized intensity distributions, e.g., a uniform fractional polarization and EVPA across the source's total intensity structure, and add errors introduced by various effects discussed in Appendix A.1. The significance level can be inferred from the number of simulated data sets where the input polarized model is distorted.

However, this approach might not apply to our study because the observed linear

polarization is very patchy in all data sets possibly due to substantial depolarization (Section 2.3.5). We present an alternative approach to infer the significance levels of the observed RMs. If the criterion of 1.5σ cutoff is not strict enough and this introduces many false RMs in the jet, then one should expect to see many similar RMs outside the jet region (where the total intensity emission of the jet is not significant) as well. This is because all the error sources, i.e., random errors, CLEAN errors, and D-term errors can be distributed across the entire map, not specific to the jet region. Although the D-term errors depend on the total intensity (Equation A.4), this intensity is usually smaller than ≈ 30 mJy/beam where significant RMs are observed in the jet. Thus, the second term in Equation A.4 is always dominant, and it would be fair to compare the observed RMs in the jet with the false RMs outside the jet region generated by errors.

For the regions outside the jet, we computed the number of pixels that satisfy the following two conditions: (i) polarized intensity above 1.5σ is detected in all sub-bands and (ii) $\chi^2_r \lesssim 1.1-1.5$ are obtained for the λ^2 fit to the EVPAs, similarly to the observed RMs (We note, however, that the results are not significantly changed when we did not consider χ^2_r). This calculation was done by using the maps having similar fields-of-view to those of the jet to properly compare with the observed jet RMs and to avoid the bandwidth-smearing and the time-average smearing effects. We obtained histograms of false RMs and divided them by the total number of pixels outside the jet region in the maps, which can serve as the false-alarm probability distribution functions (FPDFs) of detecting RM.

In Figure A.2, we present the FPDF for the 8 GHz data as an example. The probability of detecting false RMs with $-10{,}163 \lesssim \mathrm{RM} \lesssim -3{,}374$ rad/m^2 (the range of observed RMs at 8 GHz, see Table 2.2) with good λ^2 fits, obtained from integrating the hatched region, is 8.72×10^{-5} ($P_{\rm false}$). Accordingly, one can expect to detect false RMs in the jet region in approximately 38 pixels ($N_{\rm false}$), while significant RMs are detected in more than 3,000 pixels ($N_{\rm obs}$). We present the values of $P_{\rm false}$, $N_{\rm false}$, and $N_{\rm obs}$ for all data sets in Table A.1. The values of $P_{\rm false}$ for the other data sets, obtained by integrating the FPDF between the minimum and maximum observed RMs (Table 2.2)

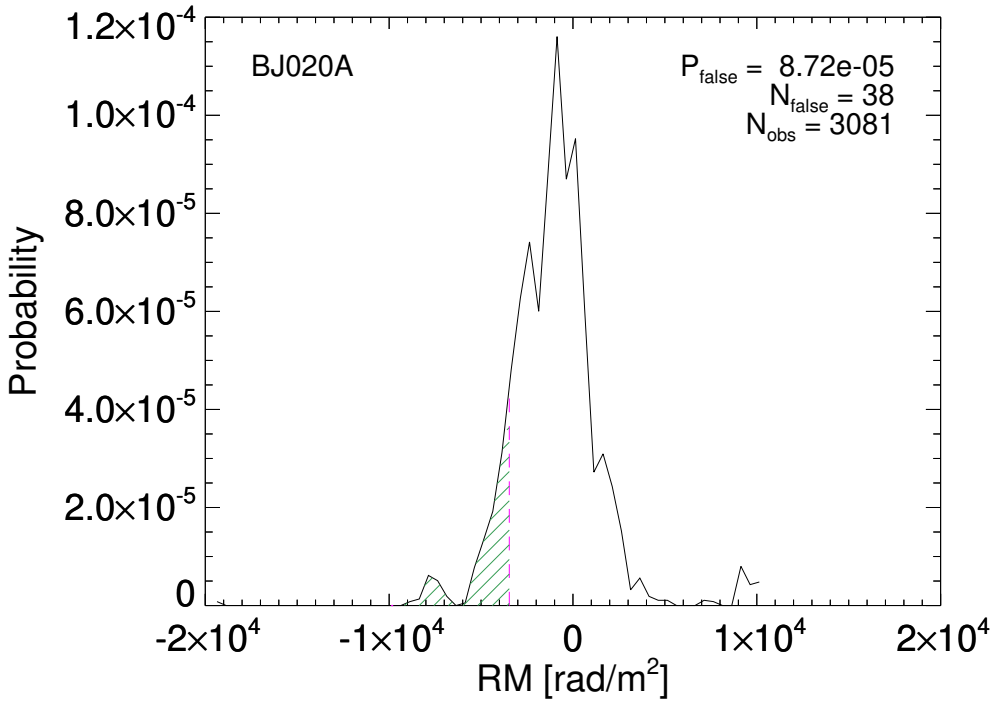

Figure A.2. False-alarm probability distribution function of detecting RM with the 1.5σ cutoff for BJ020A data set. $P_{\rm false}$ denotes a false-alarm probability of detecting RMs similar to the observed ones, obtained by integrating the green hatched region. $N_{\rm false}$ is the number of pixels of false RMs expected to be seen in the jet and $N_{\rm obs}$ the number of pixels of observed RMs in the jet.

for each data set, are even smaller, resulting in very small or zero $N_{\rm false}$.

In Table A.2, we present $P_{\rm false}$ obtained by using five different signal-to-noise ratio cutoffs. When 1σ cutoff is used, $P_{\rm false}$ values are non-negligible, up to $\approx 2 \times 10^{-3}$ for BJ020A data set. However, $P_{\rm false}$ decreases rapidly as the cutoff level increases for all data sets, becoming smaller than $\approx 9 \times 10^{-5}$ with 1.5σ cutoff. Therefore, we conclude that almost all of the observed RMs obtained by using the 1.5σ cutoff is intrinsic to the source.

Table A.2. $P_{\rm false}$ for different SNR cutoffs

Session	$P_{\rm false}$				
	1σ	1.5σ	2σ	2.5σ	3σ
BJ020A	2.45×10^{-3}	8.72×10^{-5}	8.00×10^{-7}	$< 2.67 \times 10^{-7}$	$< 2.67 \times 10^{-7}$
BJ020B	4.32×10^{-4}	1.34×10^{-6}	$< 2.67 \times 10^{-7}$	$< 2.67 \times 10^{-7}$	$< 2.67 \times 10^{-7}$
BC210B	5.89×10^{-5}	$< 3.64 \times 10^{-7}$	$< 3.64 \times 10^{-7}$	$< 3.64 \times 10^{-7}$	$< 3.64 \times 10^{-7}$
BC210C	5.88×10^{-4}	$< 3.96 \times 10^{-7}$	$< 3.96 \times 10^{-7}$	$< 3.96 \times 10^{-7}$	$< 3.96 \times 10^{-7}$
BC210D	2.43×10^{-4}	2.04×10^{-5}	$< 2.62 \times 10^{-7}$	$< 2.62 \times 10^{-7}$	$< 2.62 \times 10^{-7}$
BH135F	2.66×10^{-4}	2.50×10^{-7}	$< 2.50 \times 10^{-7}$	$< 2.50 \times 10^{-7}$	$< 2.50 \times 10^{-7}$
BC167C	2.15×10^{-5}	$< 2.62 \times 10^{-7}$	$< 2.62 \times 10^{-7}$	$< 2.62 \times 10^{-7}$	$< 2.62 \times 10^{-7}$
BC167E	2.69×10^{-4}	9.06×10^{-6}	1.01×10^{-6}	$< 2.52 \times 10^{-7}$	$< 2.52 \times 10^{-7}$

Note. — $P_{\rm false}$ values using different signal-to-noise ratio cutoffs. $<$ in front of the values means that we could not find any pixel of false RM and we provide an upper limit.

A.3 RM maps for all observations

We present the RM maps for the whole 2 and 5 GHz data sets in Figure A.3. The RMs in different epochs at the same observing frequency are detected in similar locations of the jet, notably at ≈ 170 and $\approx 320 - 370$ mas from the core at 2 GHz and at $\approx 20 - 30$ and $\approx 150 - 200$ mas from the core at 5 GHz. We note that the difference in the locations of some RMs might be due to relatively large time gaps (three months – 17 years) between different data sets, given that the jet is known to move relativistically already at distances less than ≈ 10 mas from the core (Mertens et al. 2016; Hada et al. 2017; Walker et al. 2018).

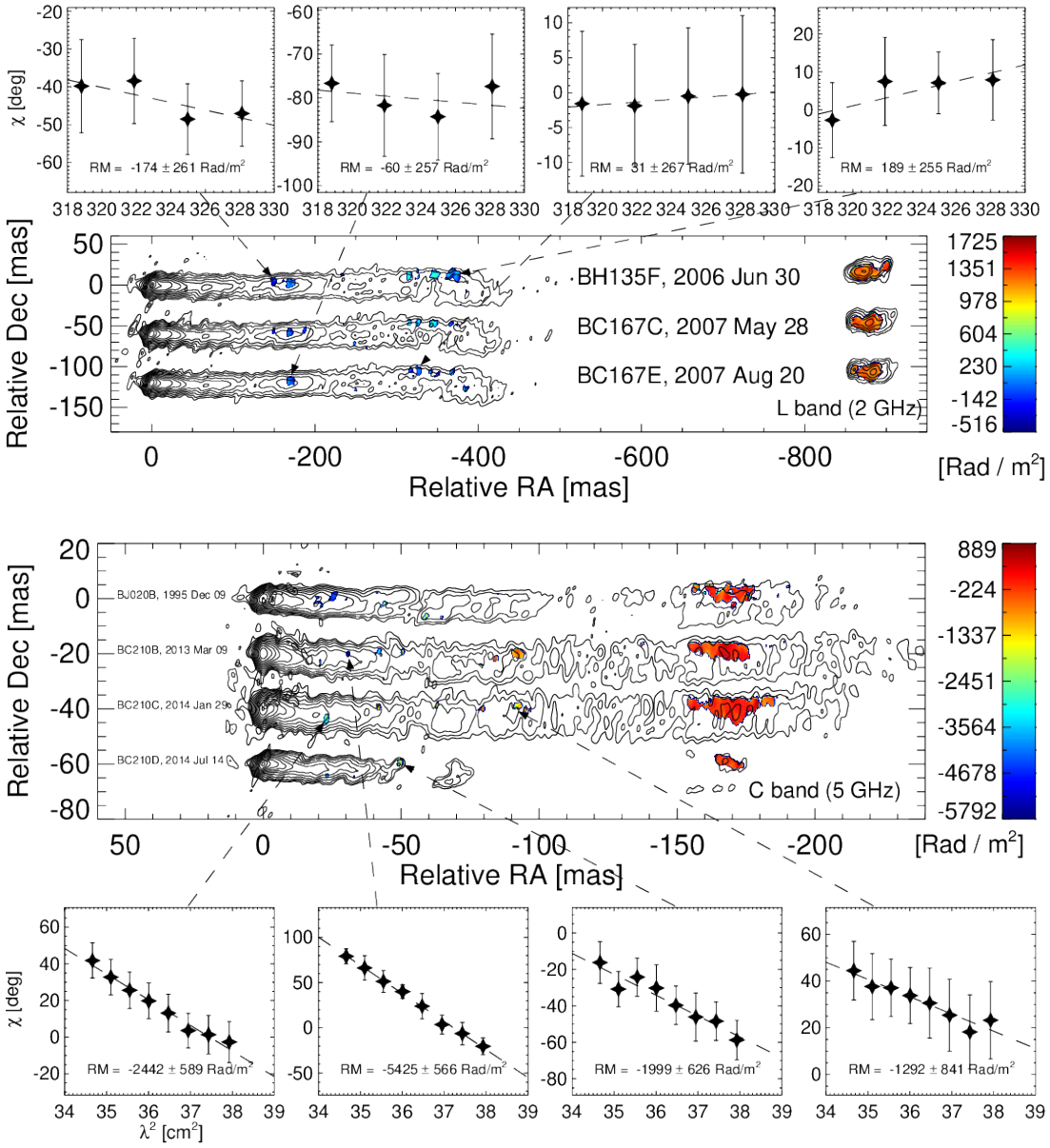

Figure A.3. RM maps and EVPA–λ^2 diagrams of three data sets we analyzed at 2 GHz (top) and four at 5 GHz (bottom). The maps in different epochs are shifted along the declination axis. All maps are rotated clockwise by 23°. The session and the observation date are noted for each map. Contours start at 0.79 and 0.60 mJy per beam for the 2 GHz and 5 GHz maps, respectively, and increase by factors of 2. Most of the extended jet emission is missing in the data from session BC210D because KP and half of PT antennas were missing (Table A.1), resulting in a significant loss of short baselines.

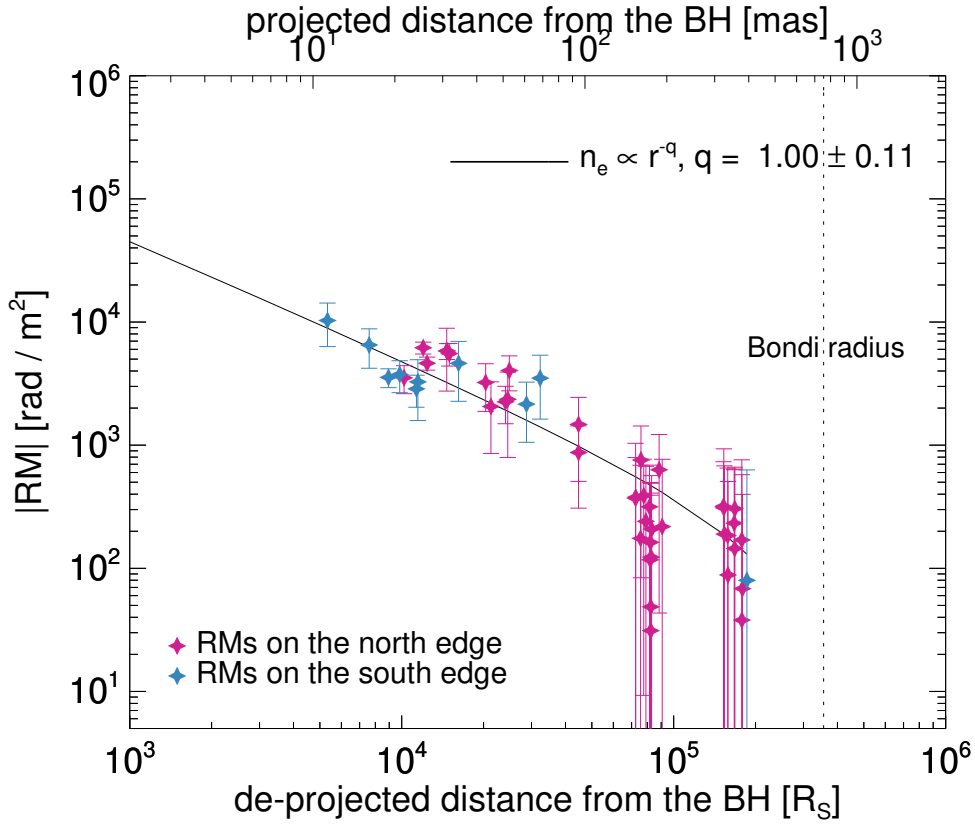

Figure A.4. Same as Figure 2.4 but with data points obtained on the northern and southern jet edges shown in different colors.

A.4 Radial RM profiles for the northern and southern jet edges

In Figure A.4, we present the absolute values of RM as a function of de-projected distance for the RMs detected on the northern and southern jet edges with different colors. We determined whether the observed RMs are located in the north or south edges by comparing the position of the RMs with the brightness centroid of the transverse intensity profile at the given distances. We found that out of 49 regions where significant RMs are detected, 10 are located in the southern jet edges.

Appendix B

Appendices for Chapter 3

B.1 WISE Analysis

In Section 3.4.3, we present the results of an application of the WISE technique to our KaVA data. We found that the observed displacement vectors of SSPs show either (i) radial, outward motions consistently observed in many epochs, or (ii) quasi-stationary or inward motions with relatively large dispersion in the positions of SSPs. We assumed that the former group represents real jet motions, while the latter may not. In this appendix, we present the whole displacement vectors and discuss the validity of our assumption.

In Figure B.1, we show the displacement vectors on top of the stacked maps of CLEAN images at 22 and 43 GHz. The results for four different SWD and IWD scales are displayed on the maps shifted along the y-axis. One can see that a lot of displacement vectors show quasi-stationary motions with non-negligible dispersion in the positions of SSPs. Some vectors show inward motions, e.g., one at a distance $\approx$ 11 mas on a scale of 0.3 mas at 22 GHz, and those at a distance $\approx$ 4 mas on scales of 0.18, 0.24, and 0.36 mas at 43 GHz. In contrast, a few vectors show gradual outward motions, e.g., those at a distance $\approx$ 5 mas on scales of 0.4 and 0.6 mas at 22 GHz, and those at a distance $\approx$ 1.5 mas on scales of 0.12, 0.18, 0.24 mas at 43 GHz. We note that the displacement vectors obtained on different SWD/IWD scales in the same parts of

the jet are significantly different from each other at several locations, e.g., at distances ≈ 3.5 and ≈ 5 mas at 22 GHz and at ≈ 1.5 mas at 43 GHz.

This result is puzzling in the sense that all displacement vectors likely belong to two groups that show quite different characteristics from each other, not in between them. This behavior is clearly different from what is seen by Mertens et al. (2016) who presented that most of the detected displacement vectors show outward motions without an indication of back and forth motions ubiquitous in the jet. Besides, the dependence of the results on SWD scales implies that the WISE results may be affected by the limited angular resolution of our KaVA data.

In Figure B.2, we present the apparent speeds derived from the detected displacement vectors presented in Figure B.1, together with those obtained in our `modelfit` analysis (Section 3.4.1 and 3.4.2), as functions of projected distance from the core. We note that our `modelfit` results represent average speeds of the jet at given distances because we did not perform our analysis for the north and south jet limbs separately and we measured a single velocity for each jet region. If both groups of our WISE results, i.e., (i) the radial, outward motions at relatively fast speeds, and (ii) the quasi-stationary or inward motions, are intrinsic to the jet, one may expect that the data points obtained by our `modelfit` analysis would be located between the two groups at a given distance. However, the `modelfit` results are consistent with the former group within errors, although the comparison is limited to specific jet distances. Therefore, we conclude that the former group represents real jet motions, while the latter may not and is possibly affected by the limited angular resolution of the KaVA. Also, when different speeds are obtained in the same parts of the jet for different SWD/IWD scales in the former group, we used the results for the smallest scale to be less affected by the resolution effect.

Nevertheless, we note that our conclusion based on the comparison with the results of other methods can be affected by the fact that other methods have their own limitations as well, as described in Section 3.4.4. One of the possible ways to verify that the quasi-stationary or inward motions are caused by the limitations of our observa-

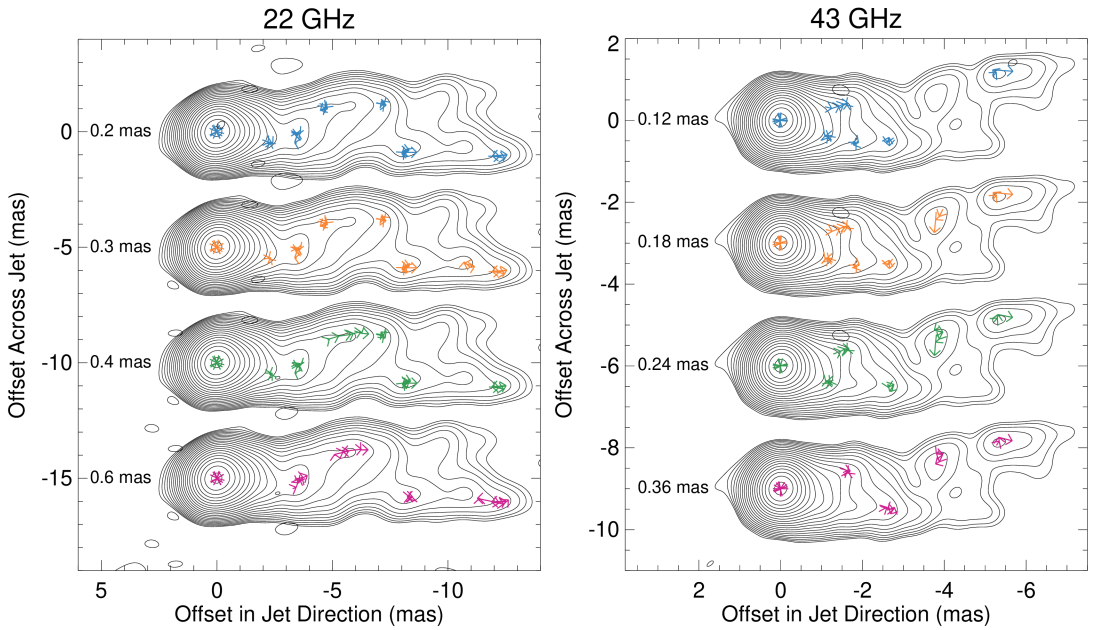

Figure B.1. Same as Figure 3.6 but showing whole displacement vectors of the SSPs detected by WISE. The results for four different SWD/IWD scales are shown in the four stacked CLEAN maps shifted along the y-axis.

tions is to investigate whether similar results are obtained with the data observed in an on-going and future KaVA/EAVN monitoring program or not (Y. Cui et al. 2019, in preparation). We note that we found similar results when we applied the WISE technique to our KaVA monitoring data in 2013–2014 at 22 GHz (Hada et al. 2017). In that study, the displacement vectors showed a dichotomy as well and those showing radial, outward motions were consistent with the trend of jet acceleration found in the `modelfit` analysis. This result may support our assumption that the radial, outward motions represent real jet motions in the present study. We note that future monitoring observations of the M87 jet with the EAVN, thanks to its improved angular resolution by a factor of up to ≈ 2.5 compared to the KaVA (An et al. 2018), will make it possible to investigate a potential effect of the angular resolution of the KaVA on the WISE results more quantitatively.

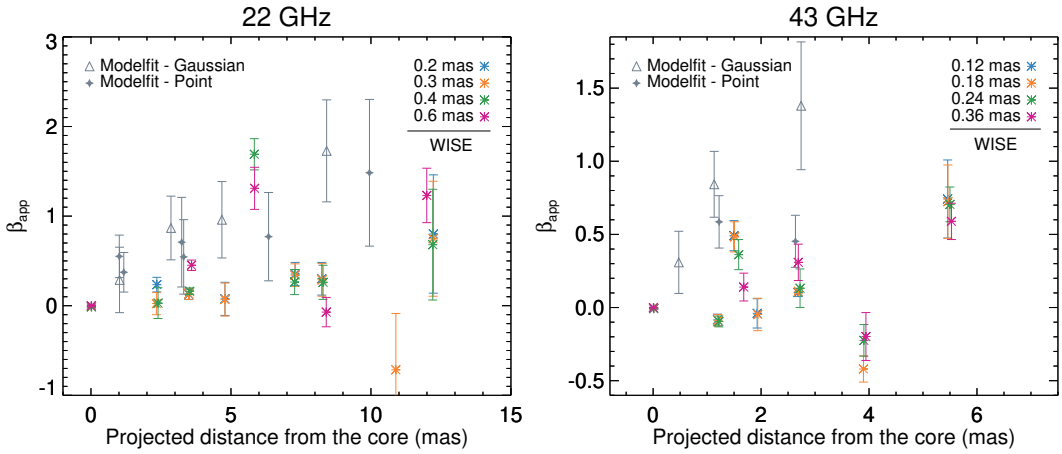

Figure B.2. Apparent speeds in units of the speed of light as functions of projected distance from the core in units of mas detected by the WISE analysis (asterisks) on four different SWD/IWD scales (shown in different colors), and detected by the `modelfit` analysis obtained in Section 3.4.1 (grey open upward triangles) and 3.4.2 (grey filled diamonds) at 22 (left panel) and 43 GHz (right panel).

Appendix C

Appendices for Chapter 4

C.1 D-Term calibration and evolution

We show examples of calibration of instrumental polarization in Figure C.1. The calibrated complex visibility ratio, LR/LL with L and R referrring to left and right hand circular polarization, respectively, from the calibrator sources used for D-term calibration of our 2017 January data is shown on the complex plane. KVN antennas are on alt-azimuth mounts and instrumental polarization does not (usually) change over time as antennas change the direction of pointing. Target parallactic angles change over time, causing the polarization signal received by the alt-az antennas to vary. Since we perform parallactic angle correction in the early stage of data pre-processing, the polarization signal intrinsic to the target remains constant in the LR/LL plane while the instrumental polarization signal rotates with parallactic angle. Therefore, the rotation of the visibility ratio on the complex plane in Figure C.1 is (mostly) due to instrumental polarization. See Roberts et al. (1994) and Aaron (1997) for details of instrumental polarization calibration.

Amplitudes and phases of D-terms can be derived from the rotating pattern by assuming that the center of rotation does not vary with time. This is true only when (i) the antenna D-terms do not vary during the observation, which is true in most cases, and (ii) the calibration sources are either unpolarized or are polarized but spatially un-

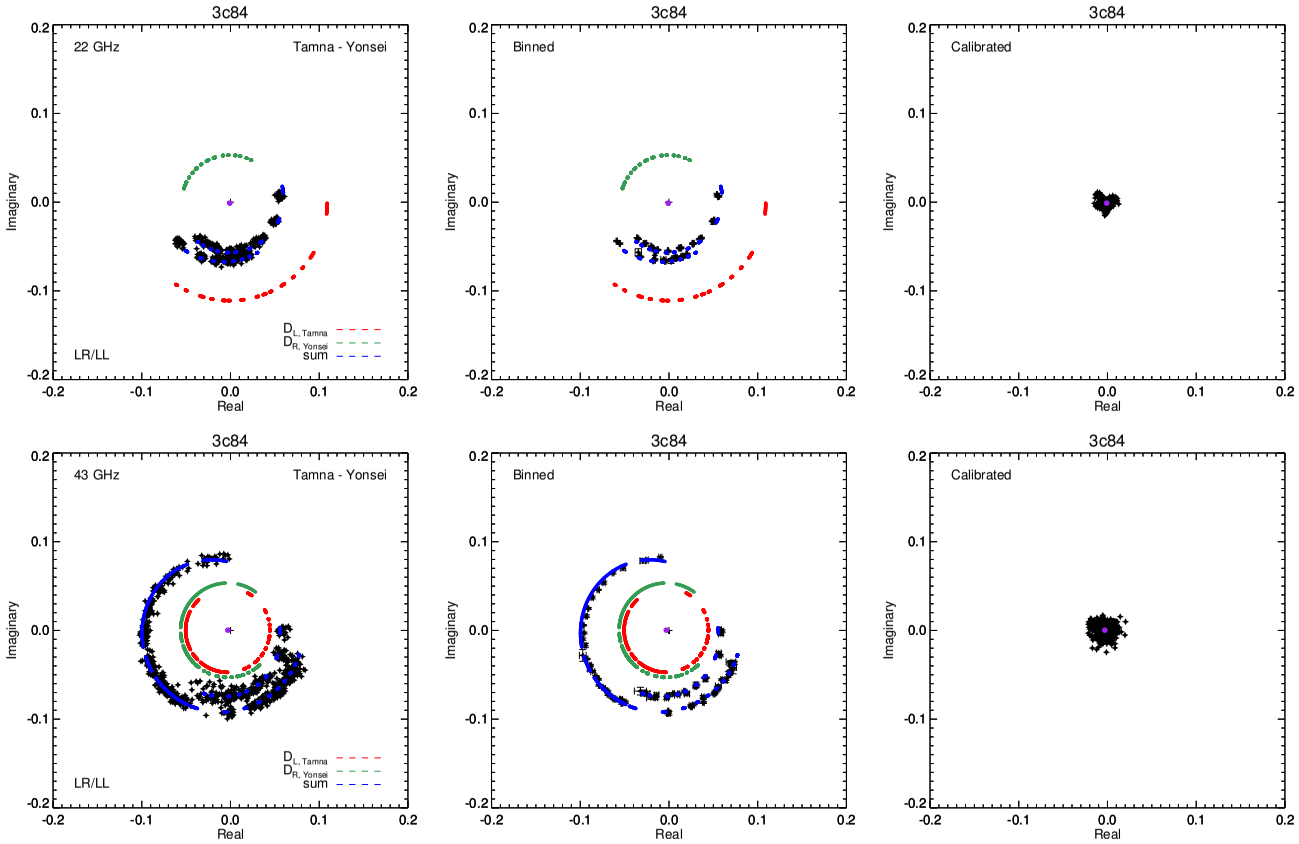

Figure C.1. *Left:* Visibility ratio LR/LL at 22, 43, and 86 GHz (top to bottom panels) for the baseline Tamna–Yonsei in January 2017 on the complex plane. The plots include: observed ratios (black data points); expected visibility ratios due to instrumental polarization for the Tamna (red) and Yonsei (green) antennas; sum of the ratios from the two antennas (blue). *Center:* Same as the left panels but with data being binned in time. *Right:* Visibility ratios after instrumental polarization calibration. Purple dots mark the centers of distributions.

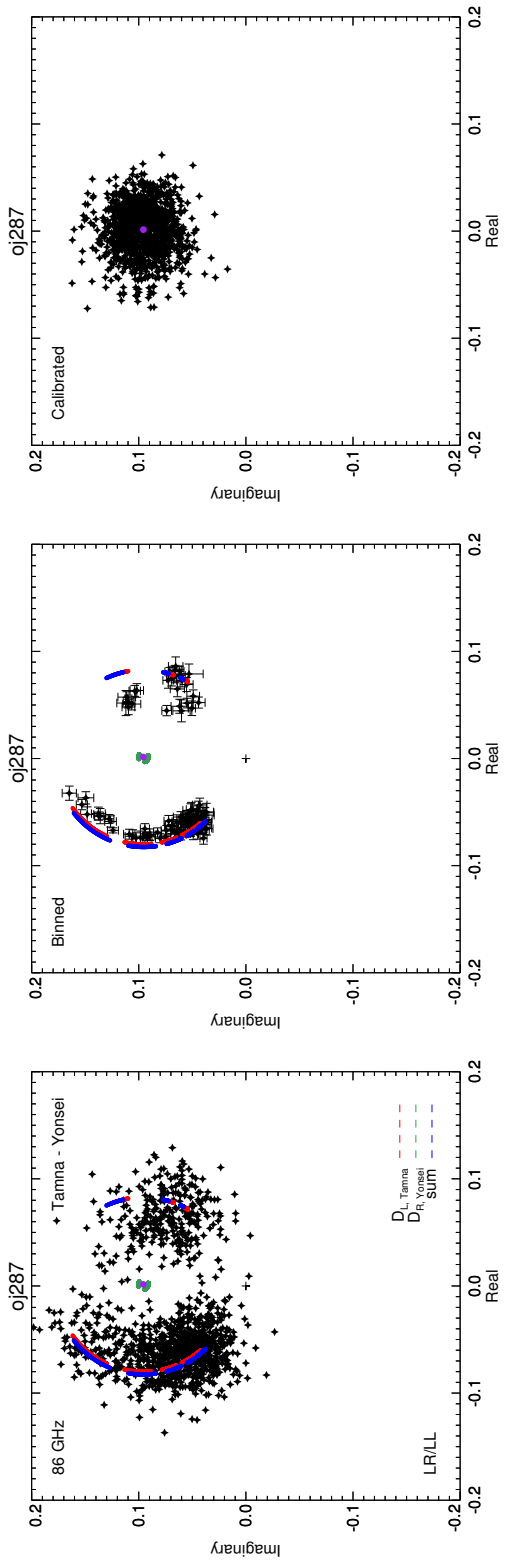

Figure C.1. *Continued.*

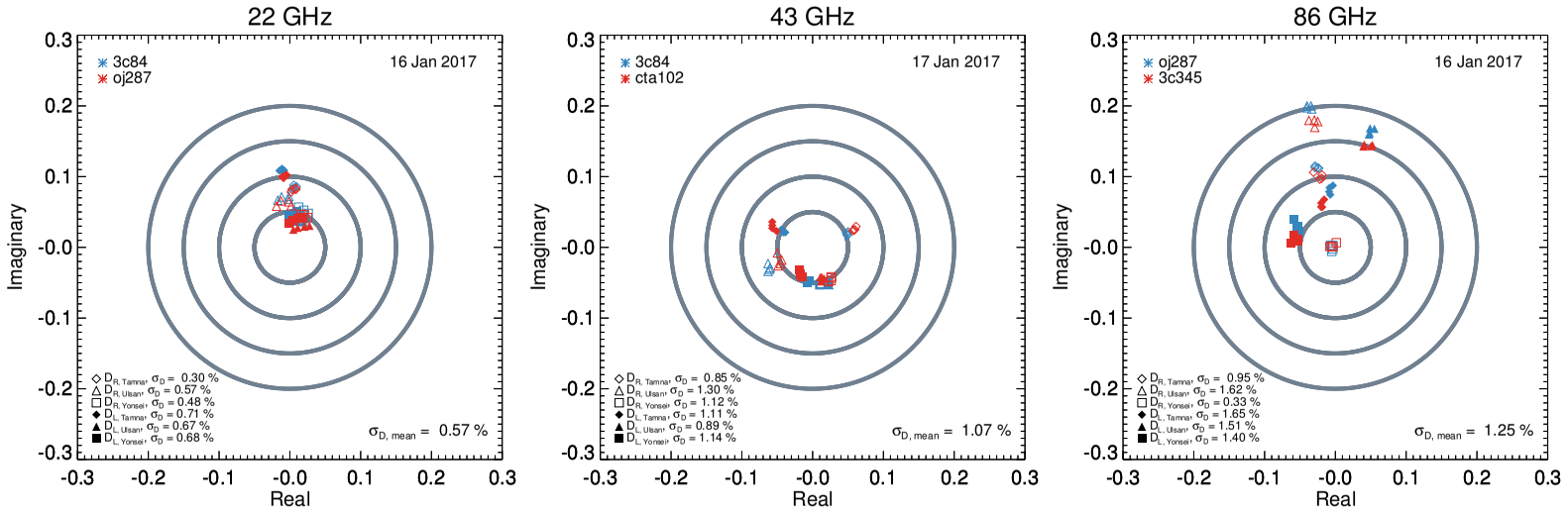

Figure C.2. D-terms obtained using different calibrator sources (different colors) in the complex plane for the KVN 22, 43, and 86 GHz bands in the left, center, and right panels, respectively. The standard deviations of the D-terms for each antenna and for each polarization are noted on the bottom left of each panel. Their mean values are noted on the bottom right of each panel.

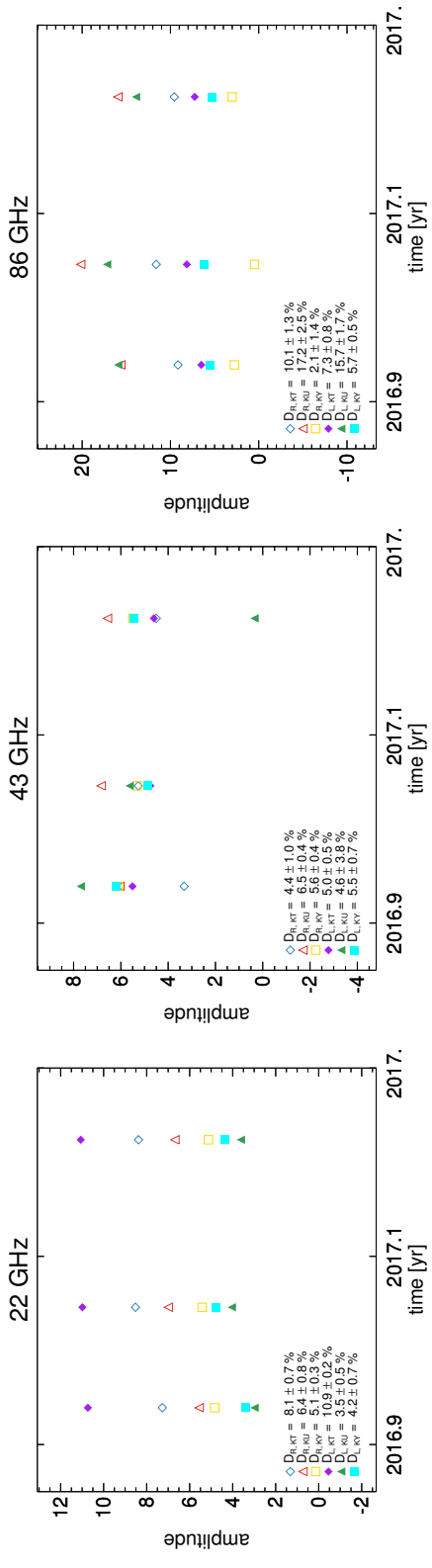

Figure C.3. D-terms amplitudes as function of time. Means and standard devations are noted on the bottom left of each panel.

resolved. As we have 6 independent visibility ratios from three baselines and 6 unknown D-terms for three antennas and two polarizations, solutions of D-terms can be obtained from fitting the pattern observed in the complex plane.

The green and red lines in the left and the central panels of Figure C.1 correspond to the expected LR/LL variation caused by the D-terms of two antennas, as obtained from the AIPS task LPCAL. The blue lines are the sum of contributions of the two D-terms, which is in good agreement with the data. The right panels show the visibility ratio after the D-term correction; the data are clustered around fixed points which mark polarization signals intrinsic to the target AGNs. The scatter is mostly due to thermal noise in the data; the noise becomes larger at higher observing frequencies.

Even precise D-term measurements may be affected by substantial systematic errors like non-stationary centers of rotation in the complex plane. Our calibrator sources are not perfectly un-polarized (or are polarized with sub-structure), and the D-terms may not always be constant during an observation run. We can estimate the errors on the D-terms by comparing the values obtained from different instrumental polarization calibrators as we did in Figure C.2. We use the standard devations of the D-terms obtained using different calibrators as errors. The errors are usually less than 1–2% but sometimes up to 3%. These errors will be transferred to the polarization quantities we used in our analysis and we considered these errors as described in Section 4.2.

The D-terms of the VLBA antennas are known to vary only on timescales of months or longer (e.g., Gómez et al. 2002). In Figure C.3 we check the stability of the KVN D-terms; their amplitudes seem to be mostly stable over $\approx$ 4 months but sometimes show non-negligible variability. Their standard deviations are usually less than 1–2% – in agreement with the formal errors of the D-terms.

C.2 Reliability check of KVN polarimetry

Thanks to the extensive monitoring of blazars, specifically by the MOJAVE program at 15 GHz and the VLBA-BU program[1] at 43 GHz, we could check if our KVN maps

[1] https://www.bu.edu/blazars/VLBAproject.html

are consistent with contemporaneous VLBA images. We picked 3C 273, which shows complex jet structure in both total intensity and polarization and thus is not used for our analysis of blazar cores, as reference source and compared (a) our KVN 22 GHz data observed on 2016 December 9 with the MOJAVE 15 GHz data observed one day after, (b) our KVN 43 GHz data observed on 2016 December 10 with the BU data observed on 2016 December 24, and (c) our KVN 86 GHz data observed on 2016 December 10 with the BU data in Figure C.4. The top panels show polarization maps generated from the KVN and VLBA data next to each other. The VLBA maps are convolved with the corresponding KVN beam.

The VLBA and KVN distributions of fractional jet polarization at 15 GHz and 22 GHz, respectively, are in good agreement with each other, showing higher degrees of polarization – up to $\approx$ 70% – at the northern edge of the jet located $\approx$ 10 mas from the core. Likewise, the 43-GHz VLBA and KVN data are consistent with each other except that the KVN maps show more polarized emission in the outer jet, i.e., $\approx$ 10 mas from the core. This might be because there is a time gap of $\approx$ 2 weeks between the observations and/or the KVN has only short baselines (with the maximum baseline length less than 500 km) and thus is more sensitive to the extended emission. However, the 86 GHz KVN map shows an additional polarization component near the core region, while the 43 GHz VLBA map does not have such a component but has an extended polarization near the core from the inner jet polarization component (at $\approx$ 1 mas from the core) by convolution of a large beam. Interestingly, the core of this source is usually unpolarized (e.g., Jorstad et al. 2005; Attridge et al. 2005; Hada et al. 2016), which has been attributed to strong Faraday depolarization or intrinsically very low polarization at the core. Its inner jet components at $\lesssim$ 1 mas from the core show $|\mathrm{RM}| \approx$ a few $\times 10^4$ rad/m^2 (Attridge et al. 2005; Jorstad et al. 2007; Hada et al. 2016). Therefore, our result might indicate a detection of core polarization of 3C 273 at 86 GHz presumably because of less depolarization at higher frequency. We will verify this possibility in a forthcoming paper with more data at 86 and 129 GHz (Park et al. in preparation).

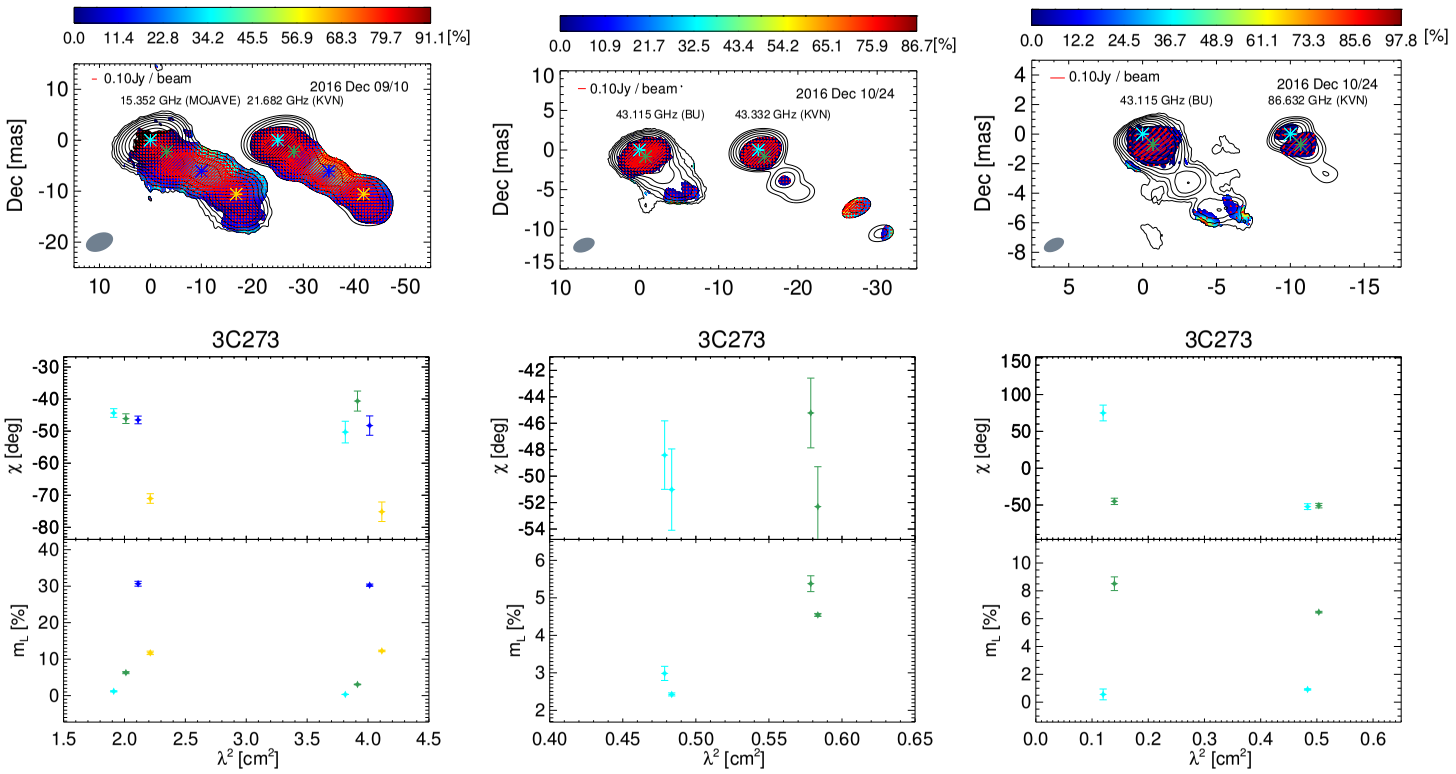

Figure C.4. *Top panels:* Same as the left panel of Figure 4.1 but showing contemporaneous VLBA images along our KVN images of 3C 273. *Left:* MOJAVE 15 GHz vs. KVN 22 GHz, *Center:* BU 43 GHz vs KVN 43 GHz, *Right:* BU 43 GHz vs KVN 86 GHz. The VLBA maps are convolved with the beam of the corresponding KVN maps. *Bottom panels:* EVPA and degree of linear polarization as a function of λ^2. Colors indicate the polarization quantities at the jet locations marked by asterisks in the upper panel images. For clarity, we shifted values obtained from the same map along the λ^2 axis.

The bottom panels of Figure C.4 show EVPA and degree of polarization as a function of λ^2 at a few locations in the jet marked in the top panels. The 15-GHz VLBA and 22-GHz KVN results are, to first order, consistent with each other but show non-negligible differences. This might be due to Faraday rotation with a RM of a few hundred rad/m^2 in the jet, as reported by many other studies (e.g., Hovatta et al. 2012) and possibly different polarization structure in the jet at different frequencies. The VLBA and KVN data at 43 GHz are consistent with each other within errors, especially when considering the time gap of ≈ 2 weeks. Similarly, The VLBA 43 GHz and KVN 86 GHz data are in agreement with each other for the inner jet component at ≈ 1 mas from the core, taking into account the time gap and the small rotation measure. Therefore, we conclude that the polarimetry mode of KVN is reliable.

Conclusion

Active Galactic Nuclei (AGNs) release an enormous amount of energy (up to $\approx 10^{48}$ erg s^{-1}) in the form of radiation across various wavelengths and mechanical energy carried by collimated jets. They are powered by the gravitational potential energy of matter accreted by the central supermassive (with a mass of $10^6 - 10^{10} M_\odot$) black holes. It is believed that they play an important role in the evolution of galaxies and clusters via AGN feedback. Jets in AGNs are thought to be one of the most efficient tools that AGNs transfer their huge energy to the interstellar and intergalactic medium. For example, observations of the cavities of X-ray emitting hot gas in groups and clusters filled by large-scale radio jets are direct evidence for the interaction between the jets and the ambient medium. Furthermore, AGN jets are the source of γ-ray photons at energies up to TeV, indicating that they are efficient particle accelerators.

Understanding the mechanism of launching, propagation, and energy dissipation of AGN jets has improved significantly in the last couple of decades. Large-scale magnetic fields which are strongly twisted in the black hole's ergosphere or the inner part of the accretion disk play a crucial role in launching and powering of AGN jets. The electromagnetic energy of the strong magnetic fields is gradually converted into the kinetic energy of the jets. Jet collimation by the pressure of an external confining medium is essential for efficient energy conversion. Thus, jet collimation and acceleration are believed to occur at the same time at distances less than around 10^5 Schwarzschild radii from the jet base (corresponding to $\lesssim 1$ pc for a black hole with a mass of $M_{\rm BH} = 10^8 M_\odot$). The relativistic jet is subject to move through an interstellar medium having a complex pressure profile and several standing, recollimation shocks can naturally form. These shocks may be the sites of dissipation of the jet kinetic energy and the origin of high energy photons.

Nevertheless, the details of the above processes are still poorly understood yet. Especially, finding observational evidence to test or confirm the theoretical predictions has been quite limited. The physical scales of the jet launching site (corresponding to

$\approx$ 20 AU for $M_{\rm BH} = 10^8 M_\odot$), the acceleration and collimation zone (ACZ, $\lesssim$ 1 pc for $M_{\rm BH} = 10^8 M_\odot$), and the energy dissipation sites ($\gtrsim$ 1 pc for $M_{\rm BH} = 10^8 M_\odot$) are quite different, which requires to have a "multi-scale view" of AGN jets. In this regard, we explicitly make use of various methodologies and tools such as very long baseline interferometry (VLBI), polarimetry, power spectra of AGN light curves, and so on.

Firstly, we study how the jet of a nearby radio galaxy M87 is highly collimated and accelerated to relativistic speeds. Thanks to the proximity of M87 and its very massive black hole, the ACZ of the jet can be resolved very well with the very long baseline array (VLBA). We study Faraday rotation in the jet inside the Bondi radius, where information of hot accretion flows surrounding the jet is imprinted. We find that the Faraday rotation measures (RMs) systematically decrease with increasing distance. We apply models of hot accretion flows and find that the decrease of RM is described well by a gas density profile $\rho \propto r^{-1}$. This result is in good agreement with the picture that substantial winds, nonrelativistic un-collimated gas outflows launched from hot accretion flows, collimate the jet. We also perform a kinematic analysis of the jet with the intensive monitoring data obtained by the KVN and VERA array (KaVA) and find that the jet is accelerated from subluminal to superluminal speeds in the same region as the collimation zone. Our findings are consistent with the theoretical predictions that (i) AGN jets are collimated by the pressure of an external medium, most likely sub-relativistic winds launched in the outer parts of the accretion disk, and (ii) the collimation leads to efficient conversion of the electromagnetic energy of the jet into the kinetic energy.

Secondly, we investigate the nature of the radio cores of eight blazars with multifrequency polarimetric observations with the Korean VLBI Network (KVN). The core-shift effect, the shift of the core positions towards the jet base at higher frequencies due to the frequency dependence of synchrotron self-absorption, has been observed in many AGN jets, which suggests that the cores are a surface of optically thick-to-thin transition (so-called a $\tau = 1$ surface). However, strong multi-wavelength flares in blazars tend to be associated with the passage of traveling knots of the jets through

the cores, indicating that the cores are physical structures such as standing recollimation shocks. In the former case, the core-shift effect will be present even at very high frequencies until the core position reaches the jet base. In the latter case, the core-shift effect will vanish at a certain frequency, e.g., at a few hundred GHz, where the recollimation shock becomes fully optically thin. We try to test the models with the KVN observations based on the fact that the core RM is expected to increase with observing frequency if there is core-shift effect at those frequencies. We find that the core RMs between 43 and 86 GHz are systematically higher than those between 22 and 43 GHz for our target sources, which implies that the cores are affected by the core-shift effect at these frequencies. However, when we compare our KVN data with contemporaneous optical polarization data for a few sources, we find indication that the increase of RM with frequency saturates at frequencies of a few hundred GHz. This may suggest that blazar cores are physical structures rather than simple $\tau = 1$ surfaces at least for those sources.

Thirdly, we study the mechanism of γ-ray emission from a quasar PKS 1510–089 which is bright and highly variable in γ-rays. It is commonly believed that inverse Compton scattering of soft photons by relativistic electrons in AGN jets is responsible for the γ-ray emission. However, both the location of the γ-ray emission sites in the jets and the origin of the soft photons are still unclear. PKS 1510–089 showed strong and complex γ-ray flares in mid-2015 and we investigate the origin of the flares by analyzing (i) long-term radio, optical, and γ-ray light curves and (ii) jet kinematics and linear polarization using VLBA data observed between late-2015 and mid-2017 at 43 GHz. We find that a strong radio flare trails the γ-ray flares in 2015, showing a gradual transition from an optically thick to thin spectrum during the flare. We detect two laterally separated knots that emerge from the radio core nearly simultaneously during the γ-ray flares. The linear polarization maps showed an edge-brightened structure near the core in the active state in 2016. These observations point to that the γ-ray flares may originate from compression of the knots by a standing shock in the core. Also, our results suggest that the jet may consist of multiple complex layers showing time-

dependent behavior, rather than of a simple structure of a fast jet spine and a slow jet sheath.

Fourthly, we investigate the long-term radio variability of many radio-loud AGNs by exploiting the database of the University of Michigan Radio Astronomy Observatory monitoring program (UMRAO). While the mechanism of variability at optical and X-ray wavelengths of radio-quiet AGNs has been extensively studied and found to be related to the accretion disk and the hot corona above the disk, that of radio variability of radio-loud AGNs is still a matter of debate. We first explore the long-term radio light curves of four blazars spanning 32 years in time at 4.8, 8, and 14.5 GHz. We find that the periodograms (temporal power spectra) of the light curves are consistent with simple *red-noise* spectra ($P(f) \propto f^{-\beta}, \beta > 0$) without any indication of (quasi-)periodic oscillations, by performing Monte Carlo simulations to take into account possible effects of limited sampling of the light curves on the periodograms. We extend our study to the long-term light curves of 43 AGNs at the same frequencies and find similar results. We discover that there is a strong correlation between the intrinsic variability timescales of our sources, which can be inferred from the periodogram modeling (β) and the known Doppler factors, and the accretion rate over five orders of magnitude in accretion rate. Our results suggest that the long-term radio variability of AGNs, which is thought to occur near the radio cores of their jets located far from the jet bases, is governed by their accretion processes.

Finally, we focus on the peculiar gas cloud G2 which passed through the vicinity of Sagittarius A* (Sgr A*), the supermassive black hole at the center of the Milky Way, in late-2013. Previous studies predicted that interactions with the accretion flows toward Sgr A* may cause G2 to lose its angular momentum and parts of this cloud would be accreted onto the black hole. This would result in an enhanced activity of Sgr A* such as jets which have been inferred to exist in Sgr A* from the modeling of spectral energy distribution but not been directly detected by observations possibly due to their small size or luminosity in quiescent states. To search for such transient structures, we performed observations with the Global Millimeter VLBI Array (GMVA) at 86 GHz,

providing an angular resolution down to ≈0.3 mas, on 1 October 2013 when parts of G2 had already passed the pericenter. We find that the interferometric closure phases remained zero within errors, indicating that Sgr A* did not show significant asymmetric outflows during the pericenter passage of G2. Our results are consistent with the reports that Sgr A* has been quiescent from radio to X-rays in 2013 and 2014. G2 might be a star enshrouded by gas and/or dust or G2 is a gas cloud but it takes more years, comparable to viscous timescale, for a part of its gas to be accreted onto the black hole and to induce any enhanced AGN-like activity in Sgr A*.

요 약

활동성은하핵 (AGN) 은 여러 파장대에 걸친 복사에너지 및 제트에 담겨있는 역학적 에너지의 형태로 막대한 양의 에너지를 분출한다. 그 에너지의 원천은 중심부의 초거대블랙홀로 빨려 들어가는 물질들의 중력적 위치 에너지가 다른 형태의 에너지로 변환되는 과정에서 나온다. 활동성은하핵은 은하와 은하단의 진화에 중요한 역할을 했을 것으로 예상된다. 제트는 활동성은하핵이 주변 물질에 에너지를 전달하는 데 가장 효율적인 도구 중의 하나로 여겨진다. 예를 들면, 은하군 및 은하단의 엑스선을 방출하는 뜨거운 가스에 생긴 구멍이 전파 영역에서 관측되는 제트로 채워져 있는 경우가 종종 발견되는데, 이는 제트와 주변 물질간의 상호 작용을 보여주는 직접적인 증거로 볼 수 있다. 게다가, 활동성은하핵의 제트는 감마선 및 중성미자와 같은 고에너지 방출원이기도 하며 효율적인 입자 가속기로써의 역할을 한다.

제트의 분출, 전파 및 에너지 소멸 기작에 대한 이해는 지난 수십 년 간 상당히 발전되어 왔다. 블랙홀의 작용권 (ergosphere) 및 강착 원반 (accretion disk) 의 중심부에서 강하게 구부러진 광범위한 자기장이 제트의 방출 및 에너지 공급에 핵심적인 역할을 할 것으로 예상된다. 강한 자기장에 담겨있는 전자기적 에너지는 점진적으로 제트의 운동 에너지로 변환된다. 제트를 둘러싸고 있는 물질의 압력에 의한 제트의 시준 (collimation) 현상이 이 변환 과정에 상당한 영향을 미친다. 그러므로 제트의 시준과 가속은 동시에 일어나며, 제트의 시작점으로부터 약 10^5 슈바르츠실드 반지름 안쪽의 거리 (10^8배의 태양질량을 가진 경우 1 pc 정도의 거리에 해당) 에서 일어날 것으로 예상된다. 가속 이후 상대론적 속도로 움직이는 제트는 복잡한 압력 분포 구조를 가진 성간 물질을 통과하게 되며 이 과정에서 여러 개의 정지된 (stationary) 재시준 (recollimation) 충격파가 형성될 수 있다. 이러한 충격파에서 제트의 운동 에너지가 소멸될 수 있으며 고에너지 광자들이 형성될 수 있다.

그럼에도 불구하고, 위에 기술된 현상들의 자세한 부분들은 아직 연구가 부족하다. 특히, 이론적 예측들을 검증하거나 확인하는 관측적 증거들은 상당히 부족한 현황이다. 제트가 분출되는 지역 (10^8배의 태양질량을 가진 경우 20 AU 정도에 해당), 가속 및 시준되는 지역 (약 1 pc 미만의 거리) , 에너지 소멸 지역 (약 1 pc 이의 거리) 의 물리적 범위는 상당히 다르며 이로 인해 제트의 "여러 규모의 모습"을 연구할 필요가 있다. 따라서, 이 논문에서 우리는 초장기선 간섭계, 편광, 광상도 곡선의 파워 스펙트럼 등의 다양한

방법론과 도구들을 이용해서 연구를 진행할 것이다.

첫째로, 우리는 가까운 전파 은하 M87의 제트가 어떻게 고도로 시준되며 상대론적 속도까지 가속되는 지 연구할 것이다. M87은 가깝고 굉장히 무거운 블랙홀을 가지고 있기 때문에 제트의 시준 및 가속 영역은 VLBA (Very Long Baseline Array) 로 상당히 잘 분해할 수 있다. 우리는 M87 제트의 본디 반경 (Bondi radius) 안쪽 영역에서의 파라데이 회전을 연구했는데, 여기에는 제트를 둘러싸고 있는 뜨거운 강착 흐름 (Hot accretion flows) 에 대한 정보가 담겨 있다. 우리는 파라데이 회전값 (Faraday rotation measures) 이 거리가 증가함에 따라 점진적으로 감소하는 것을 발견했다. 우리는 뜨거운 강착 흐름 모형들을 이용해서 관측된 파라데이 회전값 분포가 $\rho \propto r^{-1}$ 기체 밀도 분포와 잘 맞는다는 것을 발견하였다. 이 결과는 wind라고 부르는 뜨거운 강착 흐름으로부터 방출된 시준되지 않은 (un-collimated) 비상대론적 기체 분출이 제트를 시준시키는 모형과 잘 부합한다. 우리는 또한 M87 제트의 운동학을 KaVA (KVN and VERA array) 를 이용한 모니터링 관측을 통해 연구했고 제트가 시준되고 있는 영역에서 상대론적 속도까지 점진적으로 가속됨을 발견하였다. 우리의 관측 결과들은 다음과 같은 이론적 예측들과 일치한다; (i) 활동성은하핵의 제트는 주변 물질에 의해 시준되는데, 이 물질은 아마도 강착 원반의 바깥쪽에서 방출된 비상대론적 wind일 것이다. (ii) 제트의 시준은 제트의 강한 전자기장 에너지를 효율적으로 운동 에너지로 바꾸는 데 도움을 준다.

둘째로, 우리는 여덟 개의 blazar의 전파 코어 (radio core)의 특성을 KVN (Korean VLBI Network) 의 다주파수 편광 관측을 통해 조사한다. 코어 위치가 싱크로트론 자체 흡수 (synchrotron self-absorption) 에 의해 더 높은 주파수에서 제트 기저 (jet base) 쪽으로 이동하는 코어 이동 효과 (core-shift effect) 가 여러 AGN 제트들에서 발견되었고, 이는 코어가 제트의 $\tau = 1$ 표면에 대응된다는 것을 의미한다. 하지만, blazar 들에서 관측되는 강한 다주파수 플레어 (flare) 가 움직이는 제트 무리 (knot) 가 코어를 통과할 때 나타나는 경향이 있다는 관측 결과는 반대로 코어가 정지된 재시준 충격파 등과 같은 물리적 구조라는 것을 나타낸다. 전자의 경우에는 코어 이동 효과는 코어가 제트 기저 영역에 해당될 때 까지 지속되며 굉장히 높은 주파수에서도 나타날 것이다. 후자의 경우에는 코어 이동 효과가 재시준 충격파가 완전히 투명해지게 되는 주파수, 예를 들면 수백 GHz, 에 이르른 다음에는 나타나지 않을 것이다. 우리는 코어의 파라데이 회전 값이 코어 이동 효과가 존재할 때 고주파수로 갈수록 커진다는 사실에 입각하여 위 모형들을 KVN 관측을

통해 테스트한다. 우리는 조사된 천체들의 코어의 파라데이 회전값이 22 GHz와 43 GHz 사이에서보다 43 GHz와 86 GHz 사이에서 더 크다는 것을 발견하였는데, 이는 해당 주파수에서 코어가 여전히 코어 이동 효과의 영향을 받고 있다는 것을 나타낸다. 하지만, 몇몇 천체들의 경우 광학 편광 결과와 비교했을 때 파라데이 회전값이 수백 GHz 정도에서 더 이상 증가하지 않을 가능성이 있다는 것을 발견하였다. 이것이 사실이라면 해당 천체들의 경우 코어는 단순한 $\tau = 1$ 표면이 아닌 물리적 구조라는 것을 의미한다.

셋째로, 우리는 감마선 하늘에서 밝고 강한 변동성을 보이는 퀘이사 PKS 1510–089의 감마선 분출 기작을 연구한다. 흔히들 활동성은하핵의 제트의 상대론적 전자들에 의한 낮은 에너지 광자들의 (soft photons) 역-콤프턴 산란 (inverse Compton scattering)이 blazar의 감마선 분출을 만들어 내는 것으로 일컬어진다. 그러나 제트의 어떤 부분에서 이 현상이 일어나며 낮은 에너지 광자들은 어디에서 오는 지에 대해서는 아직도 불분명하다. PKS 1510–089는 2015년에 강하고 복잡한 감마선 폭발 (flare) 을 일으켰는데 우리는 (i) 긴 시간대의 전파, 광학, 감마선 광도 곡선 및 (ii) 2015년 말부터 2017년까지 43 GHz 에서 관측된 VLBA 데이터를 이용한 제트의 운동학 및 선형 편광을 분석함으로써 이 폭발의 원인을 알아보고자 한다. 우리는 강한 전파 폭발이 2015년 감마선 폭발 직후에 일어났다는 것과, 전파 폭발 도중 광학적으로 두꺼운 스펙트럼에서 얇은 스펙트럼으로의 전이를 일으켰다는 것을 발견하였다. 우리는 또한 감마선 폭발과 거의 동시에 두 개의 측면으로 분리된 제트 무리 (knot) 가 코어로부터 빠져나오는 것을 관측했다. 선형 편광 지도는 2016년의 활동 상태 (active state) 에 코어 주변에서 측면이 밝아진 구조를 나타낸다. 이러한 관측 결과들은 코어에 있는 정지 충격파에 의해 제트 무리가 압축되면서 감마선 폭발이 일어났다는 가설을 지지한다. 게다가 우리가 찾은 결과는 제트가 단순히 빠른 spine 및 느린 sheath 구조가 아닌 복잡하고 시간에 따라 변하는 여러 개의 층으로 구성되어 있을 가능성을 제시한다.

넷째로, 우리는 미시간 대학교 전파 천문 관측소의 모니터링 프로그램을 이용하여 많은 radio-loud 활동성은하핵들의 장기간 전파 변동성을 조사한다. radio-quiet 활동성은하핵들의 광학 및 엑스선 영역에서의 변동성 기작은 활발히 연구되어 왔고, 그 결과 강착원반 및 원반 위쪽의 뜨거운 코로나와 관련이 있다는 것이 발견되었지만, radio-loud 활동성 은하핵들의 전파 변동성 기작은 아직 논의가 진행중이다. 우리는 첫째로 32년간 4.8, 8, 14.5 GHz 에서 관측된 네 개의 blazar의 장기간 전파 광도 곡선을 분석한다. 우리는

그 광도 곡선들의 periodogram (시간적 파워 스펙트럼) 이 단순한 *red-noise* 스펙트럼 ($P(f) \propto f^{-\beta}, \beta > 0$) 과 일치하며, 광도 곡선에서의 어떠한 주기적 진동의 가능성도 찾지 못했는데, 이는 몬테 카를로 시뮬레이션 (Monte Carlo Simulation) 을 통해 광도 곡선의 제한된 샘플링이 periodogram에 미치는 영향을 고려함으로써 연구되었다. 우리는 이 연구를 같은 주파수에서의 43개의 활동성은하핵 광도 곡선으로 확장하였고 위와 비슷한 결과를 얻었다. 우리는 연구된 천체들의 고유 변동성 시간 스케일 (intrinsic variability timescale) – 위의 periodogram 모델링 (β값) 및 알려진 도플러 인자 (Doppler factor) 를 통해 유추할 수 있는 – 과 강착 속도 (accretion rate) 간의 강한 상관 관계가 있다는 것을 발견하였는데, 이 관계는 넓은 강착 속도 범위에 걸쳐서 나타났다. 이 결과는 제트 기저로부터 먼 지역에 위치해 있는 코어 주변부에서 일어날 것으로 예측되는 활동성은하핵의 장기간 전파 변동성이 블랙홀 주변부의 강착 과정과 밀접한 관련이 있다는 것을 암시한다.

마지막으로, 우리는 우리 은하 중심부의 초거대블랙홀 Sgr A* 근처를 2013년 말에 지나간 특이한 가스 구름 G2에 초점을 맞춘다. 이전 연구들은 G2와 블랙홀로 빨려 들어가는 강착 흐름 (accretion flows) 간의 상호 작용을 통해 G2가 각운동량을 잃어버릴 것이고 이로 인해 G2의 일부분이 블랙홀로 빨려 들어갈 것으로 예측했다. 이 현상은 Sgr A*에서 제트와 같은 활동을 나타낼 수도 있는데, 제트는 스펙트럼 에너지 분포 (Spectral energy distribution) 모델링 등을 통해 Sgr A* 에 존재할 것으로 예상되어 왔으나 아마도 그 크기나 밝기가 너무 작기 때문에 그 동안 직접적으로 관측된 적은 없다. 이러한 일시적 현상을 찾기 위해 우리는 약 0.3 밀리각초의 분해능을 제공하는 86 GHz에서의 GMVA (Global Millimeter VLBI Array) 관측을 2013년 10월 1일에 수행하였는데, 이 때는 G2의 일부분이 이미 근일점을 지나간 후였다. 우리는 간섭계 관측 물리량 중의 하나인 closure phase가 0과 일치한다는 것을 발견하였고, 이 결과는 Sgr A*가 G2의 근일점 통과 기간 동안 비대칭적인 분출을 보이지 않았다는 것을 의미한다. 우리의 결과는 Sgr A*가 2013년과 2014년에 전파 및 엑스선 영역에서 조용했다는 다른 관측 결과들과 일맥상통한다. G2는 가스 및 먼지로 뒤덮인 별이거나, 가스 구름이라 하더라도 일부분이 빨려들어가서 Sgr A*의 활동으로 연결되는 데는 viscous timescale에 필적하는 몇 년 정도가 더 걸릴 것으로 예상된다.

주요어: 활동성 은하핵, 제트, 상대론적 특성, 비열적 방출 기작, 편광, 강착 및 강착원반, 간섭계

학 번: 2013-20392